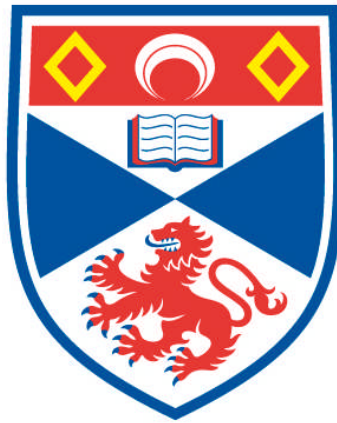


**DISTANCE MEASUREMENTS USING PULSED EPR:  
NONCOVALENTLY BOUND NITROXIDE AND TRITYL SPIN  
LABELS**

**Gunnar Widtfeldt Reginsson**

**A Thesis Submitted for the Degree of PhD  
at the  
University of St Andrews**



**2013**

**Full metadata for this item is available in  
Research@StAndrews:FullText  
at:**

**<http://research-repository.st-andrews.ac.uk/>**

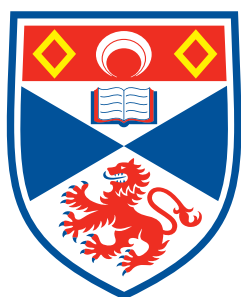
**Please use this identifier to cite or link to this item:**

**<http://hdl.handle.net/10023/3680>**

**This item is protected by original copyright**

# Distance measurements using pulsed EPR: Noncovalently bound nitroxide and trityl spin labels

Gunnar Widtfeldt Reginsson



University of  
St Andrews



This thesis is submitted in partial fulfilment for  
the degree of PhD at the University of St Andrews and  
University of Iceland

April 2013

**1. Candidate's declarations:**

I, Gunnar Widtfeldt Reginsson hereby certify that this thesis, which is approximately 39,000 words in length, has been written by me, that it is the record of work carried out by me and that it has not been submitted in any previous application for a higher degree.

I was admitted as a research student in June, 2010 and as a candidate for the degree of PhD in June, 2011; the higher study for which this is a record was carried out in the University of St Andrews between 2010 and 2012.

Date ..... signature of candidate .....

**2. Supervisor's declaration:**

I hereby certify that the candidate has fulfilled the conditions of the Resolution and Regulations appropriate for the degree of PhD in the University of St Andrews and that the candidate is qualified to submit this thesis in application for that degree.

Date ..... signature of supervisor .....

signature of supervisor .....

**3. Permission for electronic publication: (to be signed by both candidate and supervisor)**

In submitting this thesis to the University of St Andrews I understand that I am giving permission for it to be made available for use in accordance with the regulations of the University Library for the time being in force, subject to any copyright vested in the work not being affected thereby. I also understand that the title and the abstract will be published, and that a copy of the work may be made and supplied to any bona fide library or research worker, that my thesis will be electronically accessible for personal or research use unless exempt by award of an embargo as requested below, and that the library has the right to migrate my thesis into new electronic forms as required to ensure continued access to the thesis. I have obtained any third-party copyright permissions that may be required in order to allow such access and migration, or have requested the appropriate embargo below.

The following is an agreed request by candidate and supervisor regarding the electronic publication of this thesis:

Access to printed copy and electronic publication of thesis through the University of St Andrews and University of Iceland.

Date ..... signature of candidate ..... signature of supervisor .....

signature of supervisor .....

"If you're not prepared to be wrong, you'll never come up with anything original." - Ken Robinson

"It is very easy to answer many of these fundamental biological questions; you just look at the thing!" - Richard Feynman

## **Abstract**

The function of biomacromolecules is controlled by their structure and conformational flexibility. Investigating the structure of biologically important macromolecules can, therefore, yield information that could explain their complex biological function. In addition to X-ray crystallography and nuclear magnetic resonance (NMR) methods, pulsed electron paramagnetic resonance (EPR) methods, in particular the pulsed electron-electron double resonance (PELDOR) technique has, during the last decade, become a valuable tool for structural determination of macromolecules. Long-range distance constraints obtained from pulsed EPR measurements, make it possible to carry out structural refinements on structures from NMR and X-ray methods. In addition, EPR yields distance distributions that give information about structural flexibility.

The use of EPR for structural studies of biomacromolecules requires in most cases site-specific incorporation of paramagnetic centres known as spin labelling. To date, spin labelling nucleic acids has required complex spin labelling chemistry. The first application of a site-directed and noncovalent spin labelling method for distance measurements on DNA is described. It is demonstrated that noncovalent spin labelling with a rigid spin label can afford detailed information on internal DNA dynamics using PELDOR. Furthermore, it is shown that noncovalent spin labelling can be used to study DNA-protein complexes.

PELDOR can also yield information about spin label orientation. Therefore, spin labels with limited flexibility can be used to measure the relative orientation of the spin-labelled sites. Although information on orientation can be obtained from 9.7 GHz PELDOR measurements in selected applications, measurements at 97 GHz or higher, increases orientation selection. It is shown that PELDOR measurements on semi-rigid and rigid nitroxide biradicals using a home-built high-power 97 GHz EPR spectrometer (Hiper) and model-based simulations yield quantitative information on spin label orientations and dynamics.

The most widely used spin labels for EPR studies on biomacromolecules are the aminoxyl (nitroxide) radicals. The major drawbacks of nitroxide spin labels include low sensitivity for distance measurements, fast spin-spin relaxation in solution and limited stability in reducing environments. Carbon-centered triarylmethyl (trityl) radicals have properties that could eliminate some of the limitations of nitroxide spin labels. To evaluate the use of trityl spin labels for nanometer distance measurements, model systems with trityl and nitroxide spin labels were measured using PELDOR and Double Quantum Coherence (DQC). This study shows that trityl spin labels yield reliable information on interlabel distances and dynamics, establishing the trityl radical as a viable spin label for structural studies on biomacromolecules.

## Abstract in Icelandic

Hlutverk og virkni lífsameinda byggir á byggingu þeirra og stellingajafnvægi. Ákvörðun á byggingu þeirra og lögun getur því varpað ljósi á líffræðilega virkni þeirra. Helstu aðferðir sem beitt er til að ákvarða byggingu lífsameinda eru röntgengeislagreining á kristöllum (e. X-ray crystallography) og kjarnspunagreining (e. nuclear magnetic resonance, NMR). Á síðasta áratug hefur púlsuð rafeindaspunataekni (e. pulsed electron paramagnetic resonance, EPR), aðallega PELDOR (e. pulsed electron-electron double resonance), verið notuð í auknum mæli til rannsókna á byggingu mikilvægra lífsameinda. Nanómetra fjarlægðir, mældar með púlsuðum EPR mælingum, gera kleift að betrubæta byggingar sem ákvarðaðar hafa verið með röntgengeislagreiningum og NMR aðferðum. EPR veitir einnig upplýsingar um fjarlægðadreifingu sem má nota til að meta hreyfingu í stellingajafnvægi lífsameinda.

Notkun EPR til rannsókna á byggingu lífsameinda krefst í flestum tilfellum staðbundinnar innleiðingar á stakeindum. Betur þekkt sem staðbundin spunamerking (e. site-directed spin labelling). Spunamerkingar kjarnsýra hafa hingað til krafist flókinna efnasmíða. Staðbundin spunamerking á deoxýríbósakjarnsýrum (e. DNA) án samgildra efnatengja er hér notuð til að rannsaka byggingu og stellingajafnvægi DNA og DNA-prótein komplexa með PELDOR. Sýnt er fram á að ósamgild spunamerking með stífu spunamerki getur gefið upplýsingar um hreyfanleika tvíþátta DNA.

PELDOR getur einnig veitt upplýsingar um innbyrðis afstöðu spunamerkja. Spunamerki með takmarkaðan sveigjanleika má þess vegna nota til að mæla innbyrðis afstöðu spunamerktra þátta á lífsameindum. Í einstaka tilfellum er hægt að fá upplýsingar um innbyrðis afstöðu spunamerkja með 9,7 GHz PELDOR mælingum en PELDOR mælingar við 97 GHz eða hærri tíðni eru næmari fyrir innbyrðis afstöðu spunamerkja. Sameindir með hálf-stífar og stífar amínóxýl (nítroxíð) spunamerki voru mældar með PELDOR á heimasníðuð EPR tæki (Hiper) sem er með 97 GHz tíðni og 1 kW örbylgjugjafa. Niðurstöðurnar sýndu að

PELDOR mælingar með Hiper og hermun byggð á líkönum gefa magnbundnar upplýsingar um innbyrðis afstöðu spunamerkja og sveigjanleika sameinda.

Algengustu spunamerkin fyrir EPR mælingar á lífsameindum eru amínóxyl (nítroxíð) stakeindir. Helstu annmarkar nítroxíð spunamerkja eru lítil næmni fyrir fjarlægðarmælingar, stuttur líftími EPR merkis í lausn og takmarkaður stöðugleiki stakeindarinnar í afoxandi umhverfi. Önnur stakeind sem gæti nýst vel sem spunamerki fyrir lífsameindir er triarylmethyl (trítýl) stakeindin. Trítýl stakeindin er kolefnis-stakeind og hefur ekki áður nefnda annmarka nítroxíðs. Til að meta notagildi trítýl stakeinda sem spunamerki fyrir nanómetra fjarlægðarmælingar voru smíðaðar stífar sameindir með trítýl og nítroxíð spunamerkjum. Niðurstöður úr PELDOR og DQC (e. double quantum coherence) mælingum sýndu að trítýl spunamerki gefa nákvæmar upplýsingar um fjarlægðir milli spunamerkja og stellingajafnvægi sameinda. Trítýl stakeindir gætu því reynst mjög hentugar sem spunamerki fyrir rannsóknir á byggingu og hreyfingu lífssameinda.



## **Acknowledgements**

I would first of all like to thank my supervisors, Prof. Olav Schiemann and Prof. Snorri Th. Sigurdsson for their guidance and support during my studies. Their scientific enthusiasm and critical judgment has inspired me to become a better scientist. I would also like to thank current and past group members of the Sigurdsson and Schiemann groups for their collaborations and enjoyable discussions.

I wish to thank the University of St Andrews and the School of Biology to grant me a SORSAS Award for the duration of my doctoral studies. Without it, this work would not have been possible.

Last but not least I give my deepest gratitude to my wife, Lilja and our children, María, Sara and Magnús for their love and support.

## Abbreviations

Ap	Apurinic and apyrimidinic
BOP	Benzotriazol-1-yloxytris(dimethylamino)-phosphonium hexafluorophosphate
C	Cytosine
CH <sub>3</sub> CN	Acetonitrile
CW-EPR	Continuous wave electron paramagnetic resonance
DEER	Double electron-electron resonance
DMF	Dimethylformamide
DNA	Deoxyribonucleic acid
DPAGE	Denaturing polyacrylamide gel electrophoreses
DQC	Double quantum coherence
EDTA	Ethylenediaminetetracarboxylic acid
EMSA	Electrophoretic mobility shift assay
EPR	Electron paramagnetic resonance
ESEEM	Electron spin echo envelope modulation
Et <sub>3</sub> N	Triethylamine
EtOAc	Ethyl acetate
FFT	Fast Fourier transform
FRET	Fluorescence resonance energy transfer
G	Guanine/Gauss
HSC	Harmonic segmented chain
HOBt	1-Hydroxybenzotriazole
K	Kelvin
LacI	<i>lac</i> repressor
NC-SDSL	Noncovalent site-directed spin labelling
NMR	Nuclear magnetic resonance
MES	2-(N-morpholino)ethanesulfonic acid
MPD	2-methyl-2,4-pentanediol
ns	Nanoseconds
PAGE	Polyacrylamide gel electrophoresis
PDB	Protein data bank

PEG	Polyethylene glycol
PELDOR	Pulsed electron-electron paramagnetic resonance
PNE	10 mM Na <sub>2</sub> HPO <sub>4</sub> , 100 mM NaCl, 0.1 mM Na <sub>2</sub> EDTA, pH 7.0
PTSA	4-toluensulfonic acid
RNA	Ribonucleic acid
RMSD	Root-mean-square deviation
SDSL	Site-directed spin labelling
TBAF	Tetrabutylammonium fluoride
THF	Tetrahydrofuran
TLC	Analytical thin layer chromatography
TWT	Traveling-wave tube
U	Uracil
UV	Ultraviolet
μs	Micro seconds
Å	Angstrom

## Table of Contents

<b>Abstract</b>	<b>4</b>
<b>Abstract in Icelandic</b>	<b>6</b>
<b>Acknowledgements</b>	<b>8</b>
<b>Abbreviations</b>	<b>9</b>
<b>Table of Contents</b>	<b>11</b>
<b>List of Figures</b>	<b>14</b>
<b>List of Tables</b>	<b>19</b>
<b>1 Introduction</b>	<b>20</b>
<b>1.1 Probing macromolecular structure by PELDOR and site-directed spin labelling</b>	<b>22</b>
<b>1.2 EPR spectroscopy</b>	<b>25</b>
1.2.1 Basics of EPR	25
1.2.2 CW-EPR spectrum and nitroxides	29
1.2.3 Interactions between electrons	32
1.2.4 Pulsed EPR	35
<b>1.3 Spin labelling</b>	<b>48</b>
1.3.1 Spin labelling proteins	48
1.3.2 Spin labelling nucleic acids	51
<b>1.4 Aims of this research</b>	<b>58</b>
<b>2 Structure of spin-labelled nucleobase <math>\zeta</math> and phenoxazine derivative</b>	<b>60</b>
<b>2.1 Introduction</b>	<b>60</b>
<b>2.2 Materials and methods</b>	<b>60</b>
2.2.1 Small molecule crystallization and structure determination	60
2.2.2 Density function theory calculations	61
<b>2.3 X-ray crystallography of <math>\zeta</math> and phenoxazine derivative</b>	<b>61</b>
<b>2.4 DFT calculations of <math>\zeta</math> and phenoxazine</b>	<b>62</b>
<b>2.5 Summary</b>	<b>64</b>
<b>2.6 Acknowledgment</b>	<b>65</b>
<b>3 PELDORSIM: Model-based simulations of PELDOR time traces</b>	<b>66</b>
<b>3.1 Introduction</b>	<b>66</b>
<b>3.2 Constructing the vector model</b>	<b>67</b>
<b>3.3 Calculating PELDOR time traces</b>	<b>71</b>
<b>3.4 Acknowledgement</b>	<b>75</b>
<b>4 Molecular geometry, flexibility and exchange coupling measured by high-field PELDOR</b>	<b>76</b>
<b>4.1 Introduction</b>	<b>76</b>
<b>4.2 Materials and methods</b>	<b>79</b>
4.2.1 Sample preparation	79
4.2.2 Pulse EPR measurements	79
4.2.3 Data analysis and simulations	80
4.2.4 Molecular modelling	80
4.2.5 CW-EPR simulations	81
4.2.6 PELDOR simulations	81
4.2.7 Original PELDOR time traces	82
<b>4.3 PELDOR measurements on bisnitroxide model systems</b>	<b>82</b>

4.3.1	CW-EPR measurements	82
4.3.2	PELDOR measurements	83
4.3.3	Biradical <b>17</b>	86
4.3.4	Biradicals <b>18</b> and <b>19</b>	89
<b>4.4</b>	<b>Summary</b>	<b>93</b>
<b>4.5</b>	<b>Acknowledgment</b>	<b>94</b>
<b>5</b>	<b>DNA structure and dynamics observed with PELDOR and noncovalent site-directed spin labelling</b>	<b>95</b>
<b>5.1</b>	<b>Introduction</b>	<b>95</b>
<b>5.2</b>	<b>Materials and methods</b>	<b>97</b>
5.2.1	General procedures	97
5.2.2	Synthesis and purification of DNA oligomers	97
5.2.3	Hybridization of oligonucleotides	98
5.2.4	Preparation of <b>dsDNA 1</b>	98
5.2.5	Preparation of <b>dsDNA 2</b>	99
5.2.6	EMSA	99
5.2.7	Preparation of <b>dsDNA 2</b> with Lac repressor	99
5.2.8	Preparation of <b>dsDNA 3</b>	100
5.2.9	Preparation of <b>dsDNA 3</b> with Lac repressor	100
5.2.10	Pulse EPR measurements	100
5.2.11	Data analysis and modeling	101
5.2.12	Simulation of PELDOR time traces	101
5.2.13	Original PELDOR time traces	103
<b>5.3</b>	<b>PELDOR measurements on dsDNA 1</b>	<b>104</b>
<b>5.4</b>	<b>LacI-induced DNA bending observed by PELDOR</b>	<b>109</b>
<b>5.5</b>	<b>LacI-induced bending of covalently spin-labelled DNA</b>	<b>116</b>
<b>5.6</b>	<b>Summary</b>	<b>119</b>
<b>5.7</b>	<b>Note</b>	<b>119</b>
<b>5.8</b>	<b>Acknowledgment</b>	<b>120</b>
<b>6</b>	<b>Trityl Radicals as Spin Labels for Nanometer Distance Measurements</b>	<b>121</b>
<b>6.1</b>	<b>Introduction</b>	<b>121</b>
<b>6.2</b>	<b>Materials and methods</b>	<b>122</b>
6.2.1	General	122
6.2.2	Measurement of the inversion pulse excitation profile	123
6.2.3	Original PELDOR and DQC time traces	124
6.2.4	Data analysis and simulations	124
<b>6.3</b>	<b>Structures of trityl-nitroxide biradical 21 and trityl-trityl biradical 22</b>	<b>126</b>
<b>6.4</b>	<b>CW-EPR measurements on biradicals 21 and 22</b>	<b>127</b>
<b>6.5</b>	<b>PELDOR and DQC measurements on trityl-nitroxide biradical 21</b>	<b>129</b>
6.5.1	PELDOR	129
6.5.2	Simulations of PELDOR time traces	131
6.5.3	Excitation profile of the inversion pulse	133
6.5.4	PELDOR measurements on trityl-nitroxide biradical using different inversion/detection positions	134
6.5.5	DQC	137
<b>6.6</b>	<b>PELDOR and DQC measurements on trityl-trityl biradical 22</b>	<b>141</b>
6.6.1	PELDOR	141
6.6.2	DQC	144
6.6.3	DQC measurements at 50 - 100 K	146
<b>6.7</b>	<b>Signal-to-noise ratio comparison</b>	<b>149</b>
<b>6.8</b>	<b>Summary</b>	<b>150</b>

<b>6.9 Acknowledgments</b>	<b>151</b>
<b>7 Conclusions</b>	<b>152</b>
<b>References</b>	<b>154</b>
<b>Appendices</b>	<b>170</b>
<b>A.1 X-ray crystallography of <math>\zeta</math> and phenoxazine derivative</b>	<b>170</b>
A.1.1 Crystallographic Information File (CIF) for crystal structure of phenoxazine derivative	170
A.1.2 Crystallographic Information File (CIF) for crystal structure of $\zeta$	175
<b>A.2 DFT calculations of <math>\zeta</math> and phenoxazine</b>	<b>181</b>
A.2.1 Coordinates for $\zeta$ in the planar conformation from DFT calculations	184
A.2.2 Coordinates for $\zeta$ in the bent conformation from DFT calculations	188
<b>A.3 Matlab script for PELDOR simulation program and user interface</b>	<b>189</b>
A.3.1 User interface	189
A.3.2 Simulation program	200
A.3.3 Functions used in simulation program	222
A.3.4 Cooperative twist-stretch dynamics model for short dsDNA	226
A.3.5 Harmonic segmented chain (HSC) model for <b>21</b>	230
A.3.6 Dynamics model for <b>17</b>	238
A.3.7 Dynamics model for <b>19</b>	241
A.3.8 Manual for PELDOR simulation program	245
<b>Publications</b>	<b>252</b>
<b>Research articles</b>	<b>252</b>
<b>Review articles</b>	<b>252</b>
<b>Talks at conferences and seminars</b>	<b>253</b>
<b>Posters</b>	<b>253</b>
<b>Original research articles</b>	<b>254</b>

## List of Figures

1.2.1	States of the spin magnetic moment for a $S = 1/2$ spin.	24
1.2.2	Precession of a spin magnetic moment around a magnetic field.	25
1.2.3	Energy-levels for an unpaired electron in a magnetic field.	26
1.2.4	Energy-level diagram for an unpaired electron with hyperfine coupling to a $I = 1$ nucleus.	27
1.2.5	Molecular structure of a nitroxide moiety.	28
1.2.6	Simulated nitroxide CW-EPR spectra.	29
1.2.7	A vector diagram showing the angle $\theta$ between the interspin vector and Z-axis.	33
1.2.8	Two-pulse Hahn-echo sequence.	36
1.2.9	Four-pulse PELDOR sequence.	37
1.2.10	Simulated PELDOR time trace.	38
1.2.11	Six-pulse DQC sequence.	43
1.2.12	Energy-level diagram for two $S = 1/2$ electrons	45
1.3.1	Nitroxide spin labels for site-directed spin labelling of proteins and peptides.	48
1.3.2	Examples of nitroxide spin labels for nucleic acids.	52
2.3.1	Crystal structures of phenoxazine and nitroxide spin-labelled nucleobase $\zeta$ .	61

2.4.1	Crystal structure of 10-mer DNA duplex spin-labelled with $\zeta$ .	62
3.2.1	Vector model of semi-rigid nitroxide biradical.	67
3.2.2	Unit vectors in three-dimensional space.	67
3.2.3	Vector diagram of a nitroxide biradical in the laboratory frame.	68
3.2.4	User interface for vector model parameters.	69
3.3.1	User interface for peldorsim.	74
4.1.1	Two-pulse detected nitroxide field swept EPR spectra.	75
4.1.2	Structure of nitroxide biradicals.	77
4.2.1	Experimental PELDOR time trace for compounds <b>17-19</b> before background correction.	81
4.3.1	W-band CW-EPR spectra for compounds <b>17-19</b> .	82
4.3.2	An echo detected field sweep for compound <b>17</b> .	83
4.3.3	PELDOR data for compounds <b>17-19</b> .	85
4.3.4	Structures and vector models for biradicals <b>17-19</b> .	86
4.3.5	Experimental PELDOR time trace for biradical <b>18</b> .	90
4.3.6	Experimental PELDOR time trace for biradical <b>19</b> .	92
5.1.1	Molecular structure of $\zeta$ spin label and DNA abasic site.	95
5.2.1	Molecular model of DNA and definition of geometric parameters.	102
5.5.2	Original PELDOR time traces for noncovalently	



	spin-labelled DNA.	102
5.3.1	CW-EPR spectra of $\zeta$ spin label and noncovalently spin-labelled <b>dsDNA 1</b> .	104
5.3.2	EPR spectrum and relative orientation of the <b>g</b> -matrix for a nitroxide.	105
5.3.3	PELDOR data for <b>dsDNA 1</b> .	106
5.3.4	Molecular models of noncovalently spin-labelled <b>dsDNA 1</b> .	107
5.4.1	Lac repressor dimer bound to a 21-mer symmetric Lac operator.	109
5.4.2	Electrophoretic mobility shift assay of LacI and <b>dsDNA 2</b> .	107
5.4.3	PELDOR data for noncovalently spin-labelled <b>dsDNA 2</b> with and without LacI.	111
5.4.4	PELDOR data for <b>dsDNA 2</b> and <b>dsDNA 2 + LacI</b> .	113
5.4.5	Diagram showing the distance between DNA abasic sites and spin label orientation upon DNA bending.	114
5.5.1	PELDOR data for covalently spin-labelled <b>dsDNA 3</b> with and without LacI.	116
5.5.2	PELDOR data for <b>dsDNA 3</b> and <b>dsDNA 3 + LacI</b> .	117
6.1.1	Chemical structure of trityl radical.	121
6.2.1	Original PELDOR and DQC time traces.	123

<b>6.3.1</b>	Chemical structures of <b>21</b> and <b>22</b>	125
<b>6.4.1</b>	CW-EPR spectra of trityl-nitroxide biradical <b>21</b> .	126
<b>6.4.2</b>	CW-EPR spectra of trityl biradical <b>22</b> .	127
<b>6.5.1</b>	Echo detected field swept spectrum of trityl-nitroxide biradical <b>21</b> .	128
<b>6.5.2</b>	PELDOR data from trityl-nitroxide biradical.	129
<b>6.5.3</b>	Diagram showing the segmented chain model.	131
<b>6.5.4</b>	Chemical structure of trityl-nitroxide biradical.	131
<b>6.5.5</b>	Simulated PELDOR time traces and excitation profiles.	133
<b>6.5.6</b>	PELDOR experiments on trityl-nitroxide biradical with different inversion/detection positions.	134
<b>6.5.6</b>	Two-pulse ESEEM measurements of trityl-nitroxide biradical.	135
<b>6.5.8</b>	Echo detected field sweep of trityl-nitroxide biradical.	137
<b>6.5.9</b>	Six-pulse DQC data from trityl-nitroxide biradical.	138
<b>6.5.10</b>	Six-pulse DQC data on semi-rigid nitroxide biradical.	139
<b>6.6.1</b>	Chemical structure of <b>22</b>	141
<b>6.6.2</b>	Two-pulse echo detected field sweep of trityl biradical.	141
<b>6.6.3</b>	Four-pulse PELDOR on trityl-biradical with detection and inversion at same position.	142
<b>6.6.4</b>	Four-pulse PELDOR on trityl biradical with detection pulses at 13 MHz offset.	143

<b>6.6.5</b>	Six-pulse DQC on trityl biradical.	144
<b>6.6.6</b>	Two-pulse ESEEM measurements on trityl biradical.	145
<b>6.6.7</b>	DQC time traces on trityl biradical at 50 and 80 K.	146
<b>6.6.8</b>	DQC tim trace on trityl biradical at 100 K	147
<b>6.6.9</b>	Distance distributions from DQC on trityl biradical.	148
<b>6.7.1</b>	PELDOR on nitroxide biradical and DQC on trityl biradical.	149

## List of Tables

<b>2.4.1</b>	DNA sequence used in crystallization trials.	63
<b>4.3.1</b>	Parameters used for simulations of CW-EPR spectra for nitroxide biradical <b>1-3</b> .	82
<b>4.3.2</b>	Structural parameters for nitroxide biradical <b>1-3</b> determined from DFT, PELDOR and simulations.	87
<b>5.3.1</b>	Noncovalently and covalently spin-labelled DNA sequences.	103
<b>5.3.2</b>	Interspin distances for all dsDNA.	108
<b>5.4.1</b>	Geometric parameters for PELDOR simulations on noncovalently and covalently spin-labelled DNAs.	112
<b>6.4.1</b>	Simulation parameters for trityl-nitroxide and trityl biradical.	127
<b>6.5.1</b>	Interspin distance for trityl-nitroxide and trityl biradical.	130
<b>6.5.2</b>	Dynamics parameters for trityl-nitroxide and	132

## 1 Introduction

It is widely accepted that the three-dimensional structure of biological macromolecules controls their function. Maybe one of the best-known example is the structure of the double-stranded DNA helix, reported by Watson and Crick in 1953 (1). Therefore, if the structure of a macromolecule can be determined, its *in-vivo* function can be assessed. The method of choice to obtain three-dimensional structures of biomacromolecules at atomic-scale resolution is X-ray crystallography. Although it is capable of yielding detailed structural information, X-ray crystallography reports on the structure of molecules in the solid state, which does not necessarily represent a biologically relevant state. Nuclear magnetic resonance (NMR) methods on the other hand can be used to obtain both high-resolution structure and dynamics of biomacromolecules in solution, by measuring short-range constraints ( $< 5 \text{ \AA}$ ) and torsion angles (2, 3). Structural determination by NMR is limited to macromolecules that are less than about 100 kDa in molecular weight, which poses the most serious limitation to the method (4). Fluorescence resonance energy transfer (FRET), a method for measuring distances between fluorescent dye molecules in the range of 10-100  $\text{\AA}$  (5), is a very powerful method for determining the structure and dynamics of biomacromolecules in solution. The single-molecule FRET (sm-FRET) technique is especially valuable, since it can be used to observe real-time dynamics of single molecules (6). Disadvantages of FRET include uncertainty in extracting inter-dye distances and the need to label the biomacromolecule with two different fluorophores (6).

Electron paramagnetic resonance (EPR) is another magnetic resonance technique that is highly important to structural biology. EPR is a technique that detects unpaired electrons with high sensitivity and affords accurate distance measurements between paramagnetic centres and information on molecular dynamics. EPR can be used to study biomacromolecules that cannot be crystallised for X-ray studies, are too large for NMR and are embedded in membranes and cells which is a more natural environment for structural studies. In the late sixties, when researchers started to label proteins and nucleic acids

with nitroxide spin labels, continuous wave EPR (CW-EPR) became a valuable tool to measure short range distances ( $< 20 \text{ \AA}$ ) and dynamics on biomacromolecules in solution (7, 8). In the last decade, pulsed electron-electron double resonance (PELDOR or DEER), a pulsed EPR technique that is capable of measuring distances in the range of 17-80  $\text{\AA}$  between paramagnetic centres, has seen increased application to problems in structural biology (9, 10). Structural determination by EPR has two major drawbacks. First, the macromolecule needs to be labelled with a paramagnetic molecule (spin label) which poses constraints on the number of distances that can be obtained. Second, the macromolecule sample needs to be either immobilised or frozen for distance measurements. Beside these methods, small angle scattering and cryo-electron microscopy are also valuable tools to resolve the structure of biomacromolecules (11, 12).

In summary, the pros and cons of four powerful methods for applications in structural biology have been briefly reviewed. None of these methods can single-handedly yield a complete picture of a biomacromolecular function-structure relationship. Therefore, the true potential of these methods to determine molecular structure and dynamics is only obtained when these techniques are combined. In the following section, the application of PELDOR/DEER to biologically relevant molecules will be reviewed through several examples.

## **1.1 Probing macromolecular structure by PELDOR and site-directed spin labelling**

Pulsed EPR methods that are most commonly used for distance measurements on biomacromolecules and synthetic polymers are PELDOR and double quantum coherence (DQC). This section will mainly be concerned with applications of PELDOR to measure long-range distance constraints and conformational distribution in biomacromolecules. Detailed explanations of PELDOR, DQC and spin labelling techniques will be given in subsequent sections.

In short, the PELDOR technique measures the dipole-dipole coupling between a pair of spin labels (most commonly nitroxides) that have been site-specifically incorporated onto the biomolecule or polymer under study. As previously mentioned, spin-labelled macromolecules need to be immobilized to prevent averaging of the dipole-dipole coupling to zero. In almost all cases, the spin-labelled sample is shock frozen and measured at 50-80 K to slow down the spin relaxation rate of the nitroxide spin labels. The frozen sample represents, to a good approximation, an ensemble of conformations for the solubilised macromolecule. Distribution in interlabel distances can, therefore, be interpreted in terms of conformational dynamics of the macromolecule and spin labels. The effect of freezing rate on the conformational dynamics of proteins and hence the distance distribution measured with PELDOR was convincingly demonstrated in a recent work on spin-labelled T4 lysozyme by Freed and coworkers. There it was shown that rapidly freezing the protein sample yielded a broader distance distribution compared to the slowly frozen sample. The mean interspin distance was not found to be dependent on the freezing rate, suggesting that freezing causes negligible perturbation to the protein structure (13). Hubbell and Freed also recently reported distance measurements on T4 lysozyme in liquid solution using trityl spin labels and immobilisation of the protein (14).

EPR only detects paramagnetic molecules and is, therefore, not affected by large spectral overlaps as in the case of NMR. Thus, PELDOR is not limited by the size of the macromolecule. A doubly spin-labelled protein or nucleic acid only provides a single distance constraint. Given the time and effort needed for the

preparation of most spin-labelled macromolecules and that not all sites can be spin-labelled without causing structural perturbations, the number of distances obtained from a PELDOR study is considerably smaller than obtained from NMR. Nonetheless, a set of sparse long-range distance constraints from PELDOR can be used to obtain a low-resolution structure. This was illustrated with a study on the sodium/proline transporter PutP of *Escherichia coli*. 16 distance constraints from PELDOR measurements and a coarse-grained helix-loop-helix model were used to model the conformation of the IX domain. It was shown that the IX domain of PutP has a kink that plays a role in closing and opening of the transporter (15).

In conjunction with structural data from X-ray and/or NMR, long-range distance constraints from PELDOR can be used for structure refinements and to assess if a macromolecule has a different structure in solution compared to the solid state. To obtain accurate distances between spin-labelled sites on macromolecules, the conformations of the spin labels have to be modelled. This can be done by using a rotamer library (16) as demonstrated in a recent study on electron transfer flavoprotein (ETF) from *Paracoccus denitrificans*. ETF was spin-labelled with the MTSSL nitroxide spin label and distances between spin labels and the native flavin adenine dinucleotide (FAD) radical measured with PELDOR at X- and Q-band. Using structural information from crystal structures, molecular dynamics simulations, MTSSL rotamer library and three nitroxide-FAD distances obtained from PELDOR, it was determined that the FAD-containing domain of ETF in solution adopts orientations that are different than observed from the crystal structure. This conclusion was also in agreement with data obtained from small-angle solution X-ray scattering (17). Rhodopsin, a pigment in photoreceptor cells, is known to undergo a conformational change on light activation. To quantify the conformational change of rhodopsin the transmembrane helices were spin-labelled with MTSSL spin labels on the cytoplasmic end. Measuring 16 distances between spin labels with PELDOR and using geometry optimization and a crystal structure of rhodopsin in the inactive state, it was demonstrated that a 5 Å outward tilt of the transmembrane helix 6 (TM6) represents the largest conformational change upon light activation (18).



An example of combined application of FRET and PELDOR is a study on the F/E subunits of archaeal RNA polymerase. The F/E subunits were spin-labelled with MTSSL spin labels and fluorophores to probe any structural alterations upon RNA binding. Distances from PELDOR and FRET, before and after addition of RNA, indicated that binding of RNA has negligible influence on the structure of the F/E complex (19).

Characterizing the structure of large multimeric membrane proteins by X-ray crystallography and NMR can be difficult due to sample inhomogeneity and molecular size, respectively. In a recent study, site-directed spin labelling and PELDOR was used to probe the solution structure of heptameric mechanosensitive channel of small conductance (MscS) from *Escherichia coli*. The transmembrane helices of MscS monomers were spin-labelled with MTSSL at their membrane embedded regions. PELDOR data from seven helical positions together with modelling of spin label rotamers onto crystal structures showed the detergent solubilized MscS to be predominantly in the open state, confirming the open crystal structure and contradicting previous models produced from CW-EPR and extrapolated motion dynamics (EMD) studies (20).

In summary, this section has reviewed some of the applications of PELDOR to problems in structural biology. The examples referenced herein show that PELDOR and site-directed spin labelling can be applied to various systems and if carefully designed, distance measurements between spin labels can yield valuable information not obtainable by other methods.

## 1.2 EPR spectroscopy

### 1.2.1 Basics of EPR

Electrons have an intrinsic property called a *spin*, which is described by the spin quantum number  $S$ . A single unpaired electron has a spin quantum number of  $S = 1/2$ . Associated with the electron spin is a spin angular momentum  $\mathbf{s}$  and an antiparallel spin magnetic momentum  $\boldsymbol{\mu} = g_e\beta_e\mathbf{s}$ , where  $g_e$  is the electron  $g$ -factor and  $\beta_e$  the Bohr magneton (21). The projection of the spin magnetic moment onto an arbitrary axis has a magnitude that is described by the quantum number  $m_s$ , which can take on values between  $-S$  and  $S$  in integral increments. The electron can, therefore, assume  $2S + 1$  spin states. An unpaired electron with  $S = 1/2$  can, therefore, take on two possible spin states with  $m_s = \pm 1/2$  (Figure 1.2.1). A nitroxide radical has only a single unpaired electron and is, therefore, described by  $S = 1/2$ . Other paramagnetic centres, e.g. transition-ions, can have more than one unpaired electron. In this case  $S > 1/2$  (22).

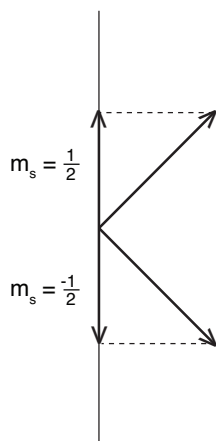


**Figure 1.2.1.** A diagram showing the two possible states of the spin magnetic momentum  $\boldsymbol{\mu}$  and its projection onto an arbitrary axis for a spin with  $S = 1/2$ .

If a single unpaired electron is placed within a magnetic field the electron spin magnetic momentum can be described, by classical mechanics, as precessing about an axis parallel to the direction of the applied magnetic field  $\mathbf{B}_0$  (conventionally assigned to the  $Z$ -axis) (Figure 1.2.2).

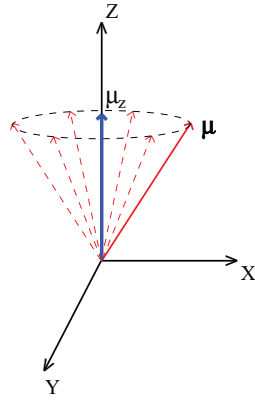


**Figure 1.2.2.** A diagram showing the spin magnetic moment  $\mu$  (red vector) precessing around a magnetic field aligned with the Z-axis. The Z component of the spin magnetic moment  $\mu_z$  (blue vector) is depicted for the  $m_s = -1/2$  state.

The z-component of the spin magnetic momentum will have a magnitude given by Eq. 1.2.1 and the precession will have a frequency known as the *Larmor frequency* (Eq. 1.2.2), where  $B_0$  is the magnitude of the applied magnetic field and  $h$  is the Planck constant (22).

$$\mu_z = -g_e \beta_e m_s \quad (1.2.1)$$

$$\nu = \frac{g_e \beta_e B_0}{h} \quad (1.2.2)$$

The interaction between the magnetic field and the magnetic moment of the electron, which is known as the *Zeeman interaction*, lifts the degeneracy of the  $2S + 1$  electron spin states. Figure 1.2.3 illustrates how the energy difference between the two spin states ( $m_s = \pm 1/2$ ) of a single electron with  $S = 1/2$  increases as the magnitude of the magnetic field is increased (22).

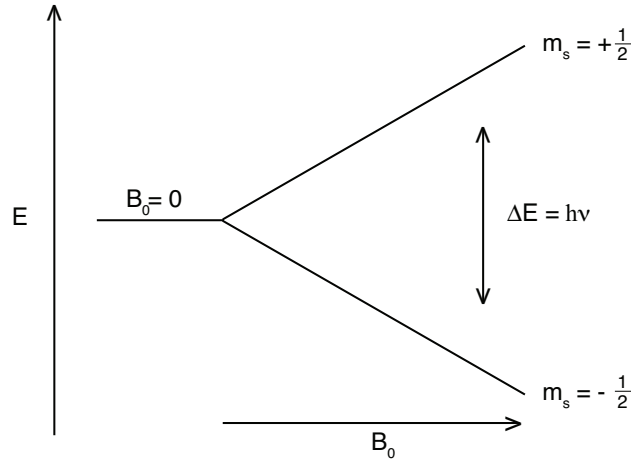


**Figure 1.2.3.** Energy-level diagram for a single unpaired electron in a magnetic field  $\mathbf{B}_0$ .  $\Delta E$  is the energy required for the transition between the two spin states,  $m_s = \pm 1/2$ . See text for a description of the various symbols in the figure.

For an unpaired electron with  $S = 1/2$ , the energy of the Zeeman interaction for the two spin states ( $m_s = \pm 1/2$ ) is given by Eq. 1.2.3. It can also be seen from Eq. 1.2.3 that the  $m_s = -1/2$  spin state is lower in energy than the  $m_s = 1/2$  spin state. The energy difference between the two states is then given by Eq. 1.2.4.

$$E = -\mu_z B_0 = m_s g_e \beta_e B_0 \quad (1.2.3)$$

$$\Delta E = g_e \beta_e B_0 = h\nu \quad (1.2.4)$$

$$\frac{N_{upper}}{N_{lower}} = \exp\left(-\frac{\Delta E}{k_b T}\right) \quad (1.2.5)$$

In a sample of  $N$  electrons in thermodynamic equilibrium, the populations of the spin states is given by the Boltzmann distribution (Eq. 1.2.5), where  $k_b$  is the Boltzmann constant and  $T$  is the temperature of the sample in Kelvin. A transition between the two spin states of a  $S = 1/2$  electron in a magnetic field is induced by introducing an oscillating magnetic field  $\mathbf{B}_1$  perpendicular to the direction of the static magnetic field  $\mathbf{B}_0$ . This additional magnetic field  $\mathbf{B}_1$ , is provided by circularly polarized microwaves. For a transition to occur, the frequency of the microwave radiation has to match the Larmor frequency, or in other words, fulfil Eq. 1.2.2. When the microwave frequency matches the Larmor frequency the microwaves are said to be in *resonance* with the electron spin.

Thus far the discussion has mainly been focused on an isolated unpaired electron in a static magnetic field. The interaction of this isolated electron with a magnetic field is described in relation to the constant free-electron g-factor  $g_e$ . In general, an unpaired electron belonging to a paramagnetic molecule interacts with its neighbour electrons and nuclei through spin-orbit coupling, causing the g-value to depend on the orientation of the paramagnetic center relative to the magnetic field (g-anisotropy) (22). Because the surroundings of the unpaired electron have an effect on the spin magnetic momentum, EPR spectroscopy is a tool to probe the atomic structure of paramagnetic centres. The interaction between the magnetic momenta of an unpaired electron and neighbouring nuclei splits each electronic spin state into  $2I+1$  levels, where the spin quantum number of the nuclei is given by  $I$ . This interaction, which is both isotropic and anisotropic, is known as the *nuclear hyperfine interaction*. Figure 1.2.4 shows how the energy levels for an unpaired electron with  $S = 1/2$  are split by a nucleus with  $I = 1$ , assuming an isotropic hyperfine coupling. The anisotropic g-value and hyperfine coupling are represented by  $3 \times 3$  matrices, denoted as  $\mathbf{g}$  and  $\mathbf{A}$ , respectively. Likewise, nuclei that are in the vicinity of the nitroxide can have an effect on the  $\mathbf{g}$  and  $\mathbf{A}$  values of the unpaired electron for example through hydrogen bonding and polarity changes. EPR measurements can, therefore, report on solvent composition.

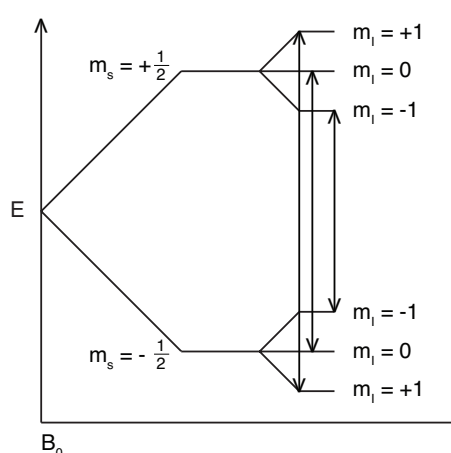


**Figure 1.2.4.** Energy-level diagram for an unpaired  $S = 1/2$  electron and  $I = 1$  nucleus. The hyperfine coupling is isotropic. The magnetic field  $B_0$  is constant. The  $m_I$  are the spin states of the nucleus. Arrows correspond to the allowed EPR transitions.

### 1.2.2 CW-EPR spectrum and nitroxides

In this section, the method of obtaining an electron paramagnetic resonance (EPR) spectrum and the way in which the interactions between an unpaired electron and a magnetic field manifest themselves in the EPR spectrum, will be considered. In particular, the EPR spectrum for a nitroxide radical will be discussed. The two leading methods of obtaining an EPR signal are by continuous wave- (CW) and pulsed EPR, with the latter method discussed in the next section. The CW-EPR method uses a low-power microwave source with fixed frequency. The net absorption of microwaves, by the paramagnetic sample under study, is then monitored as the magnitude of the magnetic field  $\mathbf{B}_0$  is varied. To increase the signal to noise ratio, the EPR absorption signal is modulated by sinusoidal variation of the magnetic field  $\mathbf{B}_0$ , this results in an EPR spectrum that is the first derivative of the absorption spectrum.

The commonly used nitroxide radical has the unpaired electron delocalised between a nitrogen- and an oxygen atom (Figure 1.2.5). Both the  $g$ -value and hyperfine coupling to the  $^{14}\text{N}$  ( $I = 1$ ) are anisotropic. The EPR lines for the nitroxide, therefore, depend on the orientation of the nitroxide molecule relative to the magnetic field  $\mathbf{B}_0$ . The principal components of the nitroxide  $g$ - and  $\mathbf{A}$ -matrices are approximately co-linear (23). The  $x$ -component of  $g$  and  $\mathbf{A}$  is parallel with the N-O bond, the  $z$ -component is normal to the plane of the nitroxide ring-system and the  $y$ -component is orthogonal to both  $x$ - and  $z$ -components (Figure 1.2.5).

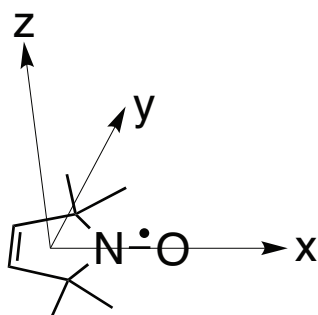


**Figure 1.2.5** Molecular structure of a nitroxide moiety. Arrows illustrate the orientation of the  $g$ - and  $\mathbf{A}$ -matrix principal components relative to the molecule.

Simulated CW-EPR spectra for a single crystal nitroxide radical illustrate how the orientation of the nitroxide radical, relative to the magnetic field, gives rise to different EPR spectra (Figure 1.2.6 a).

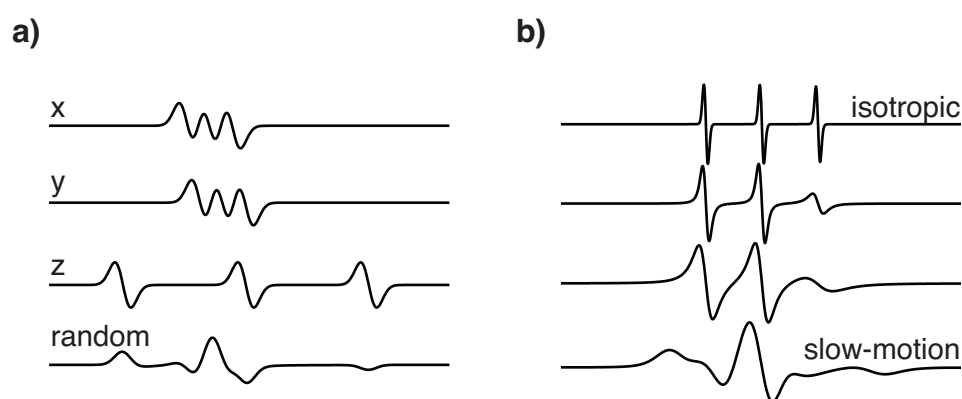


**Figure 1.2.6.** Simulated nitroxide CW-EPR spectra. **a)** First derivative CW-EPR spectra for a single crystal nitroxide. Aligning the three principal components of the  $g$ -matrix,  $g_x$ ,  $g_y$  and  $g_z$ , parallel to the magnetic field  $\mathbf{B}_0$  results in three different EPR spectra, labelled  $x$ ,  $y$  and  $z$ , respectively. The spectrum for a powder sample, where the orientation of nitroxide molecules is random, results in a spectrum that is a sum of spectra from all possible orientations. **b)** First derivative CW-EPR spectra for a nitroxide moiety in solution (isotropic) and in solvent with increasing viscosity, top to bottom respectively.

In each case the  $^{14}\text{N}$  hyperfine coupling splits the signal into three peaks with the  $z$ -component of the  $^{14}\text{N}$  hyperfine coupling matrix the largest, as can be seen from the spectrum with the  $z$ -component parallel to the magnetic field (Figure 1.2.6 a). If the nitroxide sample is a powder, where the nitroxide molecules are randomly oriented, the EPR spectrum no longer depends on the orientation of the sample and represents a summation over all orientations of the  $\mathbf{g}$  and  $\mathbf{A}$  matrices relative to the magnetic field  $\mathbf{B}_0$  (Figure 1.2.6 a). The EPR spectrum of a nitroxide, in powder or frozen glass, becomes broad and asymmetric (Figure 1.2.6 a, random spectrum).

Until now the discussion has been on nitroxide samples in a crystal or a powder. In both cases the orientation of the nitroxide molecule relative to the magnetic field  $\mathbf{B}_0$  has been constant during the EPR measurement. For molecules in solution, rapid and constant collisions will cause the molecules to tumble with a

characteristic rotational correlation time  $\tau_c$  which is about the average time it takes a molecule to tumble through an angle of one radian (24). If a nitroxide in solution has a rotational frequency  $\tau_c^{-1}$  that is much faster than the microwave frequency  $\omega_0$  the anisotropic  $\mathbf{g}$  and  $\mathbf{A}$  interactions will get time-averaged, resulting in EPR spectra determined by apparently 'isotropic'  $g$ - and  $^{14}\text{N}$  hyperfine coupling values that are an average of the  $\mathbf{g}$  principal values and the isotropic component of the hyperfine coupling, respectively. Simulated EPR spectra of a nitroxide in solution with increasing viscosity clearly illustrate how tumbling of the nitroxide affects the EPR spectrum (Figure 1.2.6 b). A nitroxide in solution with  $\tau_c^{-1} \gg \omega_0$  has an 'isotropic' EPR spectrum consisting of three equally spaced peaks with equal intensity (Figure 1.2.6 b). Increasing the viscosity of the solution or decreasing the temperature slows down the tumbling of the molecules and the anisotropic interactions will no longer be completely averaged. The 'isotropic' EPR spectrum becomes broader and asymmetric, as shown by the second and third spectra from top in figure 1.2.6 b. As the molecular tumbling is further decreased the spectrum starts to resemble the rigid-limit spectrum from a powder sample (Figure 1.2.6 b, 'slow-motion' spectrum). CW-EPR measurements can, therefore, give insight into the mobility of nitroxide radicals.

Hitherto, this section has described the basics of electron spin energy levels and how the atomic structure of a paramagnetic center can influence the EPR spectrum. The anisotropic nature of spin centres has a direct effect on the EPR spectrum yielding information on the structure and relative orientation of the spin centre (25). The EPR spectrum can also report on the degree of molecular tumbling of radicals in solution and has been used to measure molecular dynamics (26). The spin density of the nitroxide radical is affected by hydrogen bonding and solvent polarity. The EPR spectrum of nitroxide radicals is, therefore, sensitive to the solvent composition. Nitroxides and EPR have been used to measure pH, and solvent accessibility of spin labels (27, 28).



### 1.2.3 Interactions between electrons

Two unpaired electrons that are very close spatially and/or are able to interact through bonds will have their energy levels split by the electron-exchange coupling  $J$ , which is isotropic for most organic radicals. If two electrons are separated by more than about 0.8 nm (29) and are not able to interact through chemical bonds then the exchange coupling becomes negligible. However, in the same way as the spin magnetic moment of an unpaired electron can interact with the magnetic moment of a nuclei at a distance (hyperfine coupling) the spin magnetic momenta of two unpaired electrons, spatially separated by the distance  $\mathbf{r}$ , can interact through space by means of the anisotropic electron spin dipole-dipole interaction. An unpaired electron with  $S = 1/2$  (spin  $A$ ) will have each of the two spin states  $m_s = \pm 1/2$  split into two states by the dipole-dipole coupling to another unpaired electron with  $S = 1/2$  (spin  $B$ ). The dipole coupling between two unpaired electrons  $A$  and  $B$ , is described by the Hamiltonian operator (Eq. 1.2.6).

$$\hat{\mathcal{H}}_{AB} = \frac{\mu_0}{4\pi\hbar} g_A g_B \beta_e^2 \left[ \frac{\hat{\mathbf{S}}_A^T \cdot \hat{\mathbf{S}}_B}{r^3} - \frac{3(\hat{\mathbf{S}}_A^T \cdot \mathbf{r})(\hat{\mathbf{S}}_B^T \cdot \mathbf{r})}{r^5} \right] \quad (1.2.6)$$

$\mathbf{S}$  is the spin operator,  $\mu_0$  the permeability of vacuum and  $\hbar$  is the Planck constant divided by  $2\pi$  ( $\hbar/2\pi$ ). The subscripted  $A$  and  $B$  denote electrons  $A$  and  $B$ . Equation 1.2.6 can be converted to equation 1.2.7 by expressing the orientation of the interspin vector  $\mathbf{r}$  in spherical coordinates (30).

$$\hat{\mathcal{H}}_{AB} = \frac{\mu_0}{4\pi\hbar r^3} g_A g_B \beta_e^2 (A + B + C + D + E + F) \quad (1.2.7)$$

The terms in the bracket are given by the following expressions,

$$\begin{aligned}
A &= S_z^A S_z^B (1 - 3\cos^2\theta) \\
B &= -\frac{1}{4} (S_+^A S_-^B + S_-^A S_+^B) (1 - 3\cos^2\theta) \\
C &= -\frac{3}{2} (S_+^A S_z^B + S_z^A S_+^B) \sin\theta \cdot \cos\theta \cdot e^{-i\varphi} \\
D &= -\frac{3}{2} (S_-^A S_z^B + S_z^A S_-^B) \sin\theta \cdot \cos\theta \cdot e^{i\varphi} \\
E &= -\frac{3}{4} S_+^A S_+^B \sin^2\theta \cdot e^{-2i\varphi} \\
F &= -\frac{3}{4} S_-^A S_-^B \sin^2\theta \cdot e^{2i\varphi}
\end{aligned}$$

where  $S_z$ ,  $S_+$ ,  $S_-$  are spin operators and  $\theta$ ,  $\varphi$  describe the orientation of the interspin vector relative to the magnetic field  $\mathbf{B}_0$ . If the dipole-dipole coupling  $\omega_{AB}$  between two electrons  $A$  and  $B$  is small compared to the resonance difference between electrons  $A$  and  $B$ ,  $\omega_{AB} \ll |\omega_A - \omega_B|$ , all terms except  $A$  in Eq. 1.2.7 can be safely neglected. Furthermore, assuming the delocalization of the unpaired electrons is small relative to the distance between them, the electron spins can be described by the point-dipole approximation (31). With these approximations valid the dipole-dipole interaction, in angular frequency ( $2\pi\nu_{AB}$ ), is given by Eq. 1.2.8.

$$\omega_{AB} = \frac{\mu_0 g_A g_B \beta_e^2}{4\pi \hbar r^3} (1 - 3\cos^2(\theta)) \quad (1.2.8)$$

Note that the frequency of the electron dipole-dipole interaction depends on the angle  $\theta$  between the interspin vector and the applied magnetic field  $\mathbf{B}_0$  (Figure 1.2.7) and also on the inverse of the interspin distance  $r$ .

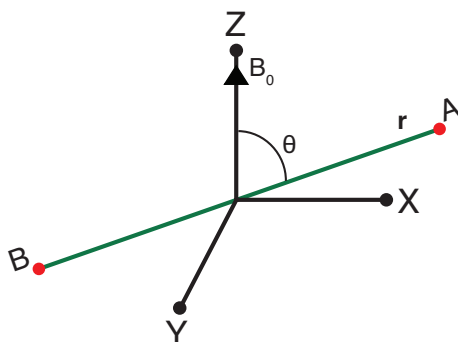


**Figure 1.2.7.** A vector diagram showing the angle  $\theta$  between an interspin vector  $\mathbf{r}$  (green) and the Z-axis, which is parallel to the direction of the magnetic field  $\mathbf{B}_0$ . The spin centres  $A$  and  $B$  are denoted by red dots.

If the point-dipole approximation fails due to spin delocalization, the dipole-dipole interaction has to be calculated by considering the interaction of each spin-bearing atom of spin centre  $A$  with each spin-bearing atom of spin centre  $B$ . The interaction matrix  $d_{ij}$  is described by Eq. 1.2.9 (32).

$$d_{ij} = -\frac{\mu_0 \beta_e^2}{4\pi \hbar} g_A g_B \sum_m \sum_n \rho_m \rho_n \frac{r_{mn}^2 \delta_{ij} - 3r_{mni} r_{mnj}}{r_{mn}^5} \quad (1.2.9)$$

Here  $\delta_{ij}$  is the Kronecker delta and  $\rho$  the spin density. The  $m$  and  $n$  subscripts denote the atoms carrying spin density from the  $A$  and  $B$  electrons, respectively and the  $i$  and  $j$  subscripts denote the components of the interaction matrix. The  $i$  and  $j$  components of the interatomic distance vectors ( $r_{mni}$  and  $r_{mnj}$ ) are relative to the molecular frame of the  $A$  electron.

If the absolute resonance difference between two electrons is less than the absolute dipole-dipole coupling,  $|\omega_{AB}| \gg |\omega_A - \omega_B|$ , the  $B$  term in Eq. 1.2.7 has to be included and Eq. 1.2.8 becomes Eq. 1.2.10. Equation 1.2.8 is valid for nitroxide radicals as long as the interspin distance exceeds 1.5 nm (29).

$$\omega_{AB} = \frac{3\mu_0 g_A g_B \beta_e^2}{8\pi \hbar r^3} (1 - 3\cos^2(\theta)) \quad (1.2.10)$$

If the dipole-dipole coupling is approximately equal to the resonance difference of spins  $A$  and  $B$   $|\omega_{AB}| \sim |\omega_A - \omega_B|$ , the situation becomes more complicated and

the extraction of interspin distances from EPR data becomes less reliable (33, 34). At the end of section 1.2.2 it was discussed how the anisotropic  $\mathbf{g}$  and  $\mathbf{A}$  interactions become time-averaged by molecular tumbling in solution. Likewise, if a molecule with a pair of coupled spin centres is rapidly tumbling in solution the angle between the interspin vector and the magnetic field  $\theta$  will be rapidly changing and the dipole-dipole coupling will get time-averaged. Because the average of the dipole-dipole coupling is zero, no coupling will be observed if the rotational frequency of the interspin vector is much larger than the dipole-dipole coupling (24). For this reason, systems under study have to be immobilized. For biomacromolecular systems this is normally achieved by freezing the sample into a homogeneous glass. Other methods to prevent fast tumbling include attachment of the biomacromolecule to a solid support (14) or using viscous solvents (35).

If the dipole-dipole interaction between paramagnetic centres is larger or at least of the same order as the inherent spectral linewidth of either paramagnetic center, the dipolar coupling will be visible as splitting of EPR lines or broadening and CW-EPR methods can be used to determine the interspin distance. In the specific case of nitroxide radicals interspin distances in the range of 0.5–1.7 nm can be measured reliably using CW-EPR (36, 29). For larger interspin distances the splitting from the dipole-dipole coupling can no longer be resolved from the inhomogeneously broadened nitroxide EPR spectrum. To reliably measure distances beyond 1.7 nm the dipole-dipole interaction has to be isolated from the inhomogeneously broadened nitroxide spectrum. This can be achieved using various pulsed EPR techniques, two of which will be discussed in the next section.

#### 1.2.4 Pulsed EPR

As mentioned above (Section 1.2.2), pulsed EPR is another method to acquire an EPR spectrum. In contrast to CW-EPR, where the EPR spectrum is obtained by continuously irradiating the sample with microwaves of a fixed frequency, pulsed EPR uses short (nanoseconds) high-power microwave pulses. As previously discussed, when an unpaired electron is placed in a magnetic field  $\mathbf{B}_0$

the spin magnetic moment can be described as precessing about the direction of  $\mathbf{B}_0$ , assigned to lie parallel to the Z-axis. Considering a very large number of unpaired electrons in a magnetic field, discussion of the individual spin magnetic moments can be replaced by the total magnetization  $\mathbf{M}$ , which follows the rules of classical mechanics. Applying a resonant microwave pulse of length  $t_p$  along the X-axis will induce a magnetic field  $\mathbf{B}_1$  perpendicular to  $\mathbf{B}_0$  and rotate  $\mathbf{M}$  about the X-axis through an angle  $\alpha$  (Eq. 1.2.11) (31).

$$\alpha = \frac{g\beta_e B_1}{\hbar} t_p \quad (1.2.11)$$

Microwave pulses that rotate  $\mathbf{M}$  through an angle of either 90 or 180 ° are known as  $\pi/2$  and  $\pi$  pulses, respectively. The approximate frequency bandwidth at half height of a microwave pulse with length  $t_p$  is given by Eq. 1.2.12. Hence, shorter pulses lead to broader excitation bandwidth (31).

$$\Delta\nu[MHz] \approx \frac{1.207}{t_p[\mu s]} \quad (1.2.12)$$

Immediately after a  $\pi/2$  microwave pulse, all the individual spin magnetic moments will be phase-correlated and aligned along the Y-axis. This is known as *spin coherence*. Following a microwave pulse, the systems is no longer at equilibrium and the total magnetization must relax back to its equilibrium position, which is parallel to the magnetic field  $\mathbf{B}_0$ . Two relaxation processes, the *spin-lattice relaxation* and the *spin-spin relaxation*, mainly determine the rate of the relaxation. The spin-lattice relaxation involves the flipping of spins to recover the magnetization along the  $\mathbf{B}_0$  and the Boltzmann population difference. This process is characterized by an exponential time constant  $T_1$ . The spin-spin relaxation, also known as the transverse relaxation, describes the decay of the magnetization in the X-Y plane due to loss in phase-correlation between individual spin magnetic moments. This process is described by another exponential time constant  $T_2$ . In a pulsed EPR spectrometer only the magnetization in the X-Y plane is detected. The signal obtained after a resonant  $\pi/2$  pulse is, therefore, a transient free induction decay (FID). Fourier

transforming the FID then yields the EPR spectrum. Because most paramagnetic centres have a relatively fast spin relaxation rate and a broad spectral width it is technically less demanding to use a two-pulse sequence containing a  $\pi/2$  and  $\pi$  pulse to obtain a so-called Hahn echo (Figure 1.2.8).

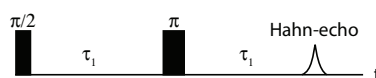


**Figure 1.2.8.** Two-pulse Hahn-echo sequence. Microwave pulses are separated by the time delay  $\tau_1$ . The Hahn-echo comes at  $\tau_1$  after the last pulse.

An absorptive EPR spectrum is obtained by integrating the Hahn-echo as the amplitude of the magnetic field  $B_0$  is swept. An EPR spectrum acquired with this method is known as an echo-detected EPR spectrum (ED-EPR).

### 1.2.5 PELDOR and DQC

Various pulse sequences have been developed to measure the dipole-dipole coupling between paramagnetic centres. While the majority of the methods rely on extracting the dipolar coupling from an oscillating signal, the dipolar coupling between paramagnetic centres can also be extracted from the spin relaxation enhancement of the dipolar coupling (37). In this case, the dipolar coupled spin centres must have reasonably different relaxation rates. The pulsed EPR methods that have gained the most widespread application for distance measurements on synthetic polymers and biomacromolecules are pulsed electron-electron double resonance (PELDOR) and double quantum coherence (DQC). This section will start with a general description of the PELDOR technique, followed by a detailed discussion on how the PELDOR time trace is generated and a distance distribution is extracted from the PELDOR data. Second, the technique of DQC will be discussed.

PELDOR, which is also known as double electron-electron resonance (DEER), is a double frequency pulsed EPR technique for precise and reliable distance measurements between paramagnetic centres (38). PELDOR has been used to

measure distances in the range of 1.6–8 nm, mostly between nitroxide spin labels. To obtain reliable distances from PELDOR, the excitation band-width of the microwave pulses has to be larger than the dipolar coupling (39, 29). This determines the lower limit of the distance range. Distances are obtained from PELDOR by measuring the intensity of a spin echo with time. To obtain reliable results the time window of the PELDOR experiment needs to be long enough to observe at least one period of the dipole-dipole frequency. The upper limit of the distance range is, therefore, set by the spin-spin relaxation rate of the paramagnetic centres (40). With PELDOR, the dipole-dipole interaction between a pair of paramagnetic centres is separated from the interactions that are the cause of inhomogeneously broadened spectra in CW-EPR. These include unresolved hyperfine interactions and  $g$ -anisotropy. The four-pulse PELDOR sequence (41) (Figure 1.2.9), used throughout in this thesis, is an extension of the original three-pulse PELDOR technique (42, 43).

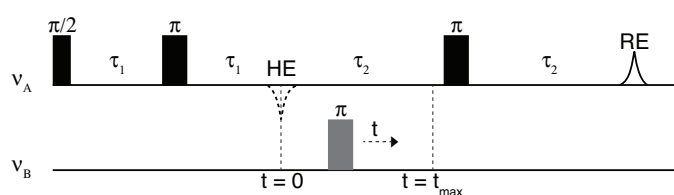


**Figure 1.2.9.** Four-pulse PELDOR sequence. The PELDOR time trace is recorded by moving the inversion pulse at  $\nu_B$  from  $t < 0$  to  $t = t_{\max}$ . The delays  $\tau_1$  and  $\tau_2$  of the detection pulses at  $\nu_A$  are kept constant, except when ESEEM modulation is being suppressed (see Chapter 5).

The basic idea behind the PELDOR technique is to create a signal from an ensemble of spins (spins  $A$ ) — that are coupled via electron dipole-dipole coupling to spins in another spin ensemble (spins  $B$ ) — using selective microwave pulses, i.e. pulses that don't excite the complete EPR spectrum. The signal from the  $A$  spins is then modulated by applying a selective  $\pi$  pulse to the  $B$  spins ensemble. A three-pulse sequence, denoted as the 'detection sequence', has a frequency of  $\nu_A$  and is in resonance with  $A$  spins. The pulses in the detection sequence are applied with constant time separations,  $\tau_1$ , and  $\tau_2$ . The  $\pi$ -pulse that inverts the  $B$  spins is denoted as the 'inversion pulse' and has a frequency of  $\nu_B$ . The inversion pulse is applied in between the second and third

detection pulses at time  $t$ . In a PELDOR experiment the integral intensity of the refocused echo (RE) is monitored as the time-position of the inversion pulse is incremented in equal steps from an initial position  $t < 0$  between the second detection pulse and the Hahn-echo (HE) to a position right before the third detection pulse  $t = t_{\max}$  (Figure 1.2.9). This results in a time trace that oscillates with the frequency of the dipole-dipole interaction (Figure 1.2.10 a).

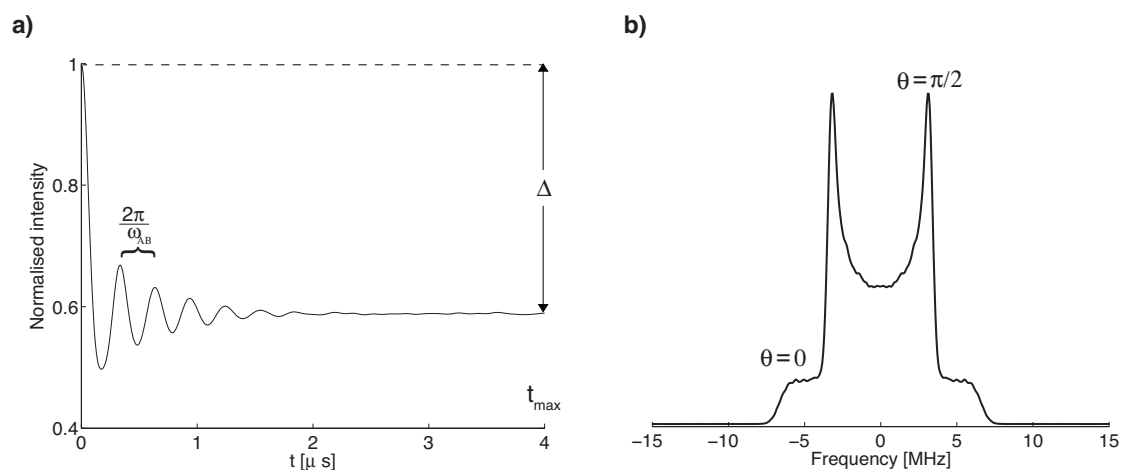


**Figure 1.2.10.** **a)** Simulated PELDOR time trace. The modulation depth is denoted by  $\Delta$  and the period of the dipolar modulation is shown by the curly bracket. **b)** Fourier transformation of the PELDOR time trace in **a)**. The perpendicular  $\theta = \pi/2$  and parallel  $\theta = 0$  components are indicated by their respective labels.

When the inversion pulse coincides with the HE, the PELDOR signal is at its maximum intensity. This point is the ‘zero-time’ of the PELDOR time trace and corresponds to the time  $t = 0$  (Figures 1.2.9 and 1.2.10 a). To reliably extract broad distance distributions between paramagnetic centres the time trace should ideally start at zero-time (41). In the three-pulse PELDOR sequence the inversion pulse has to cross the first detection pulse in order to observe the zero-time. This cannot be done without introducing strong artefacts at the start of the PELDOR time trace (41) and the zero-time is, therefore, not obtained. This is known as ‘dead-time’ and is a disadvantage of three-pulse PELDOR. Fourier transformation of the PELDOR time trace yields the dipolar spectrum in frequency-domain, which has the shape of a ‘Pake pattern’ (Figure 1.2.10 b). The dipolar spectrum is dominated by two large peaks and two smaller shoulders, on either side of the zero frequency. The larger peaks correspond to couplings from



spin-pairs having the interspin vector at an angle of  $90^\circ$  relative to  $\mathbf{B}_0$ ,  $\theta = 90^\circ$ . The shoulders correspond to spin-pairs with  $\theta = 0^\circ$  (Figure 1.2.10 b). For systems in a disordered powder and with a well-defined interspin distance, reading off the dipolar frequency from the  $\theta = 90^\circ$  peaks and using Eq. 1.2.8 or 1.2.10 yields the interspin distance. If the system is flexible, the interspin distance will be described by a distribution and has to be determined by fitting the PELDOR time trace. This will be discussed in more details below.

To better understand why the PELDOR signal oscillates with the frequency of the dipole-dipole interaction, the dynamics of the total magnetization  $\mathbf{M}$  have to be considered. The first detection pulse, with a rotation angle of  $\pi/2$  radians, flips the magnetization of an  $A$  spin ensemble  $90^\circ$  into the X-Y plane. Immediately after the pulse the magnetic moments of the individual  $A$  spins start to precess in the X-Y plane with different Larmor frequencies due to off-resonance effects, inhomogeneous broadening and the dipole-dipole coupling. Each individual spin magnetic moment will, therefore, acquire a relative phase difference. The second detection pulse, with a rotation angle of  $\pi$  radians, reverses the precession of all the spin magnetic moments in the  $A$  spin ensemble and hence reverses the dephasing acquired during  $\tau_1$  and creates a Hahn echo at  $2 \times \tau_1$ . Following the first two detection pulses and during the time-evolution of the  $A$  spin magnetic moments the inversion pulse, with a rotation angle of  $\pi$  radians and frequency  $\nu_B$ , flips the spin magnetization of a  $B$  spin ensemble  $180^\circ$ . Spins in the  $A$  ensemble, that are dipole-dipole coupled to spins in the  $B$  ensemble, will, therefore, change their Larmor frequency by the electron dipole-dipole coupling  $\omega_{AB}$ . The change in Larmor frequency by  $\omega_{AB}$  will, therefore, result in a phase change  $\phi = t \omega_{AB}$  of coupled  $A$  spins. Note that when the inversion pulse is applied at time  $t = 0$  (the zero-time) the phase change is also 0. The third and last detection pulse, with a flip angle of  $\pi$  radians, again reverses the precession of all  $A$  spin magnetic moments and creates a refocused echo (RE) at  $2(\tau_1 + \tau_2)$ . Due to the acquired phase change  $\phi$  caused by the inversion pulse at time  $t$  the normalised intensity of the refocused echo  $V$  as a function of time  $t$  is given by

$$V(t) = \prod_i \{1 - \lambda_i [1 - \cos(\omega_{AB}^i t)]\} \quad (1.2.13)$$

where  $\lambda$  is the fraction of  $B$  spins that are both coupled to a spin in the  $A$  spin ensemble and excited by the inversion pulse. This fraction also determines the modulation depth of the PELDOR time trace (Figure 1.2.10 a). The product in Eq. 1.2.13 runs over the number  $i$  of  $B$  spins coupled to the same  $A$  spin. In a disordered powder sample of molecules with two paramagnetic centres  $A$  and  $B$ , separated by a constant interspin distance  $r$ , a single  $A$  spin will be dipolar coupled to the  $B$  spin on the same molecule, this is known as intramolecular coupling. In addition, a single  $A$  spin will be dipolar coupled to all the other spins in the sample. This is known as intermolecular coupling. The PELDOR signal is, therefore, composed of an intramolecular part ( $V_{\text{intra}}$ ) and an intermolecular part ( $V_{\text{inter}}$ ). If the spatial distribution of the molecules can be assumed to be homogeneously distributed, which is valid for most experimental applications, then the intermolecular couplings are composed of a large number of random couplings with a large distance distribution. In this case  $V_{\text{inter}}$  can be derived from Eq. 1.2.13 as an exponential function and the PELDOR signal becomes a product of  $V_{\text{intra}}$  and  $V_{\text{inter}}$ . The background function, or  $V_{\text{inter}}$ , of the PELDOR time trace, is described by

$$B(t) = \exp(-kt^{D/3}) \quad (1.2.14)$$

where  $D$  is the dimension of the distribution of molecules and the constant  $k$  can be experimentally determined from a sample of molecules with only one spin centre. The normalised PELDOR signal is then given by

$$V(t) = \left( 1 - \lambda \left[ 1 - \int_0^{\pi/2} \cos(\omega_{AB} t) \sin\theta \, d\theta \right] \right) B(t) \quad (1.2.15)$$

where the integration is over all angles  $\theta$  of the interspin vector relative to the magnetic field  $\mathbf{B}_0$ , weighted by  $\sin(\theta)$ . If orientation correlation between the spin centres and the interspin vector  $\mathbf{r}$  can be neglected, which is valid for almost all

applications using nitroxides at X-band and even at higher frequencies (44),  $V_{intra}$  can be further simplified and expressed by Eq. 1.2.16

$$V_{intra}(t) = \int_{r_{min}}^{r_{max}} K(t, r)P(r)dr \quad (1.2.16)$$

$$K(t, r) = \int_0^1 \cos(\omega_{AB}t) d \cos\theta$$

where  $P(r)$  is a distance distribution function and  $K(t,r)$  is a kernel function. Using Eq. 12.16 and the Tikhonov regularization algorithm (45), the interspin distance distribution  $P(r)$  can be determined by fitting the background corrected PELDOR time trace.

If a paramagnetic centre has an anisotropic EPR spectrum (e.g. nitroxide radical) and its orientation relative to the interspin vector  $\mathbf{r}$  is not random, the fraction of excited  $B$  spins, given by  $\lambda$  in Eq. 1.2.15, can no longer be assumed to be constant and has to be included in the integral of Eq. 1.2.15.  $V_{intra}$  is then described by Eq. 1.2.17

$$V_{intra}(t) = 1 - \left( \int_0^{\pi/2} \lambda_{AB}(\theta)[1 - \cos(\omega_{AB}t)] \sin\theta d\theta \right) \quad (1.2.17)$$

where  $\lambda_{AB}$  quantifies the fraction of excited spins that now depends on the orientation of the spin centres and the interspin vector relative to the magnetic field  $\mathbf{B}_0$ . Depending on the position and excitation band-width of the microwave pulses, not all possible values for  $\theta$  will contribute equally to the PELDOR signal. In the case of orientation correlation and/or highly selective microwave pulses, especially at frequencies of 97 GHz (W-band) and higher,  $V_{intra}$  becomes orientation selective and can no longer be simplified to Eq. 1.2.16. Instead, the distance distribution has to be obtained directly from Eq. 1.2.17 using numerical simulations. This will be further discussed in chapters 3 and 4.

If an exchange coupling (Section 1.2.3) between a pair of unpaired electrons becomes detectable, the energy of the electron-electron interaction has to be

described by the Hamiltonian  $H_{AB} = S_A D S_B + S_A S_B J$  where  $D$  is the anisotropic dipole-dipole coupling matrix and  $J$  is the isotropic electron-electron exchange constant. The dipolar interaction between a pair of paramagnetic centres  $\omega_{dip}$  is then described by Eq. 1.2.18.

$$\omega_{dip} = \omega_{AB} + J \quad (1.2.18)$$

PELDOR can successfully separate the contribution of exchange coupling from the dipole-dipole coupling and in addition determine the sign and magnitude of the exchange coupling constant (46). Application of PELDOR to nitroxide biradicals with exchange coupling is described in chapter 4.

If a molecule contains not only two, but  $N$  identical paramagnetic centres that are positioned at specific sites on a molecule and with no rotational correlations, then a single  $A$  spin will be dipolar coupled to  $N-1$   $B$  spins within the same molecule. The intramolecular contribution to the PELDOR signal will then be a product of  $N(N-1)/2$  pair-interactions and will no longer be expressed by Eq. 1.2.15. If all  $N$  spin centres within a single molecule are equally excited by the inversion pulse the intramolecular PELDOR signal is expressed by Eq. 1.2.19.

$$V_{intra}(t) = \frac{1}{N} \sum_j^N \prod_{k \neq j}^N \left( 1 - \lambda \int_0^{\pi/2} [1 - \cos(\omega_{AB}^{kj} t)] \sin \theta \, d\theta \right) \quad (1.2.19)$$

Using Eq. 1.2.19, the number of interacting spins in a single molecule  $N$  can be determined from the intensity of the intramolecular PELDOR signal when all dipolar modulation has been damped  $V_\lambda$  and the fraction of spins excited by the inversion pulse  $\lambda$  (Eq. 1.2.20)(47, 48).

$$N = \frac{\ln V_\lambda}{\ln (1 - \lambda)} + 1 \quad (1.2.20)$$

For a mixture of molecules with different number of coupling spin centres, the intramolecular PELDOR signal is a weighted sum of signals from each species of molecules.  $V_\lambda$  is then described by

$$V_\lambda = \frac{\sum_i s_i x_i V_{\lambda i}}{\sum_i s_i x_i} \quad (1.2.21)$$

were  $s_i$  is a scaling factor for molecule  $i$ , that accounts for any difference in the transversal relaxation between molecules and  $x_i$  is the fraction of  $i$  molecules in the mixture (48). The number of spin centres within the same molecule and even the fraction of specific species can, therefore, be determined from PELDOR. This can be applied to measure the number of monomers in multimeric protein complexes (49).

Another effective way to measure the dipole-dipole coupling between paramagnetic centres is the double quantum coherence (DQC) method. DQC was first developed to measure the dipolar coupling between a pair of spin magnetic moments in NMR (50). Later Jack Freed and coworkers introduced DQC-EPR for double quantum coherence measurements on paramagnetic systems using EPR (51). DQC-EPR solely detects the electron dipole-dipole coupling in a time-domain experiment by using a pulse sequence that includes a double-quantum coherence filter (52, 53). In contrast to PELDOR, DQC is a single frequency pulsed EPR technique that has been used to measure distances in the range of 1.6-7.2 nm (54, 55). Various DQC pulse sequences have been developed, but the dead-time free six-pulse DQC sequence has seen the largest use for biomacromolecular applications (Figure 1.2.11).

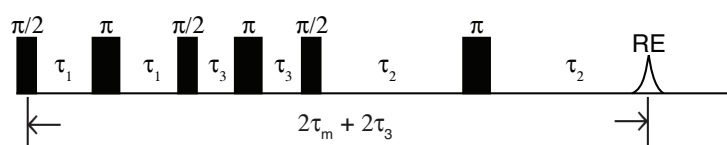


**Figure 1.2.11.** Six-pulse DQC sequence. The DQC time trace is recorded by increasing  $\tau_1$  and decreasing  $\tau_2$  in equal increments.  $\tau_m = \tau_1 + \tau_2$  and  $\tau_3$  are kept constant.

The six-pulse DQC sequence is split into three regions. The first region ( $\pi/2$ - $\tau_1$ - $\pi$ - $\tau_1$ - $\pi/2$ ) is the DQC-generator. The second region is the evolution period ( $\tau_3$ - $\pi$ - $\tau_3$ ). The third and last region ( $\pi/2$ - $\tau_2$ - $\pi$ - $\tau_2$ -refocused echo) is the DQC-detector. A DQC time trace is obtained by measuring the integral intensity of the refocused

echo (RE) as  $\tau_1$  and  $\tau_2$  are increased and decreased in equal increments, respectively. Because  $\tau_m = \tau_1 + \tau_2$  and  $\tau_3$  are constant during the experiment, the position of the RE is constant. In the same way as for PELDOR, the intensity of the refocused echo is modulated by the electron dipole-dipole coupling, which results in a time trace that oscillates with the frequency of the dipolar interaction (Eq. 1.2.18). To successfully measure the electron dipole-dipole coupling using “allowed” DQC pathways the microwave pulses should ideally be non-selective, i.e. they should excite the whole EPR spectrum (54). Explaining how the refocused echo is modulated by the dipole-dipole coupling unfortunately cannot be done in terms of the total magnetization and precession of spin magnetic moments, as was done for PELDOR. Instead, the interaction between the two-spin system and microwave pulses has to be explained mathematically by the Product Operator (PO) method, (56) which is beyond the scope of this dissertation. Nevertheless, the basics of each region of the DQC sequence can be explained in terms of spin coherences and transitions and still retain the general idea of the DQC method. Before continuing, a few terms have to be defined. As described at the start of section 1.2.4, a  $\pi/2$  pulse applied to an ensemble of spins creates spin coherence. For a coupled pair of  $S = 1/2$  spins this coherence can be described as *inphase*- and *antiphase* coherence. If the spin magnetic moments of spin *A* and *B* are either aligned with the laboratory X- or Y-axis, the coherence is inphase. If the spin magnetic moment for one spin is perpendicular and the other parallel to the magnetic field, the coherence is antiphase. While the inphase coherence is observed, the antiphase coherence cannot be directly detected in an EPR experiment. A coupled pair of  $S = 1/2$  spins has a total of six possible transitions (Figure 1.2.12).

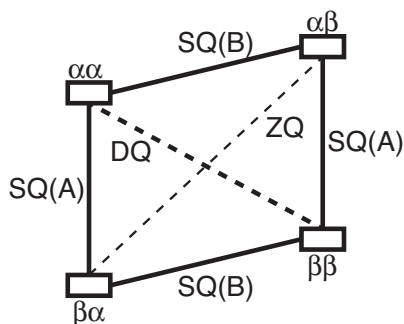


**Figure 1.2.12.** Energy-level diagram for two  $S = 1/2$  electrons. Allowed single-quantum (SQ) transitions of spin  $A$  or  $B$  are denoted by solid lines. Forbidden zero-quantum (ZQ) and double quantum (DQ) transitions are denoted by dashed lines.  $\alpha$  and  $\beta$  represent the spin states of the electrons.

Four of these are *single-quantum* (SQ) transitions, where only one spin changes its spin state. The two remaining transitions are *zero-quantum* (ZQ) and *double-quantum* (DQ) transitions, where both spins change their spin state simultaneously. With inphase- and antiphase coherences and SQ, ZQ and DQ transitions defined, the regions of the DQC sequence can be further explained assuming an isolated pair of dipole-dipole coupled  $S = 1/2$  spins and non-selective microwave pulses. DQC-generator: The first pulse excites both spins and creates inphase and antiphase SQ coherences. During  $\tau_1$  the dipole-dipole coupling introduces coherent oscillations between the inphase and antiphase coherences. The  $\pi$  pulse in the middle of the region refocuses the coherences and the last  $\pi/2$  pulse converts antiphase SQ coherences into DQ coherence that is not directly observed. Evolution: The DQ coherence created by the DQC-generator is allowed to evolve during  $2\tau_3$ . The  $\pi$  pulse refocuses the coherence to maximize the refocused echo in the last region. DQC-detector: In the last part of the DQC sequence the undetectable DQ coherence is converted into antiphase SQ coherence by the  $\pi/2$  pulse. This coherence then evolves during  $\tau_2$  into a detectable inphase coherence, is refocused by the final  $\pi$  pulse and appears as an echo at  $2\tau_2$ . In summary, the DQC pulse sequence effectively isolates the DQ coherence signal from all other coherences (54).

As previously described for PELDOR, the experimentally observed DQC signal is likewise a product of an intramolecular and intermolecular dipolar coupling. However, since an analytical expression is not known for the intermolecular signal, the DQC modulation depth does not yield information on the number of

coupled spins (14) and determining the width and shape of distance distributions becomes complicated (57). In addition to intermolecular couplings the DQC signal is also affected by relaxation decay, which is mainly due to spin-spin relaxation  $T_2$  and decay of the double quantum coherence  $T_2^{DQC}$ . The relaxation of the DQC signal is described by Eq. 1.2.22 (31).

$$R(\tau_1, \tau_2, T_2, T_2^{DQC}) = \exp(-2((\tau_1 + \tau_2)/T_2) - 2(\tau_3/T_2^{DQC})) \quad (1.2.22)$$

The intermolecular contribution and the relaxation decay, collectively known as the background function  $B(t)$ , is most commonly removed by fitting an exponential function to the experimental DQC time trace, as demonstrated in chapter 6.

In the case of allowed DQC pathways, the normalized intramolecular DQC time trace is given by Eq. 1.2.23 (31).

$$V_{intra}(\tau_1, \tau_2) = \cos(\omega_{dip}(\tau_1 - \tau_2)) + \cos(\omega_{dip}(\tau_1 + \tau_2)) \quad (1.2.23)$$

The maximum of the DQC signal and the zero-time of the time trace is obtained when  $\tau_1 = \tau_2$ . Eq. 1.2.23 can be used to simulate background-free DQC time traces. Although the requirement of non-selective pulses is a limiting factor, especially for measurement of paramagnetic centres with a broad EPR spectrum, it does eliminate possible complications due to orientation selection. Furthermore, since the whole EPR spectrum is excited, sensitivity is increased compared to PELDOR, where only a portion of the EPR spectrum is excited. Calculations of excitation profiles reveals that about 19% of the spin-pairs actually contribute to the observed dipolar modulation, while for an optimum setup only 6% of the spin-pairs contribute to the PELDOR dipolar modulation (38). Therefore, in favorable cases the signal to noise ratio for DQC is expected to be three times larger compared to PELDOR.

In summary, this section has outlined two pulsed EPR methods to measure distance distributions between paramagnetic centres, PELDOR and DQC. Of these methods, PELDOR has gained more popularity, in part because the method is



easily applied using commercial spectrometers. For distance measurements between paramagnetic centres with very narrow EPR spectra, DQC becomes the superior method since PELDOR is limited by the requirement of selective pulses that can only have a limited excitation profile overlap (Chapter 6). On the other hand, for spin centres with very broad EPR spectra PELDOR has an advantage because the whole EPR spectrum does not need to be excited by the microwave pulses. In cases where orientation selection is not desirable or high sensitivity is needed, DQC is the method of choice. Another useful property of PELDOR is the possibility to count the number of spin centres within a cluster (48).

### 1.3 Spin labelling

To obtain distance constraints or information on local dynamics using EPR, the system being studied has to contain paramagnetic centres. Although the majority of proteins and nucleic acids are diamagnetic, some contain intrinsic paramagnetic centres in the form of cofactors, metal clusters and metal ions. Examples of structural studies where these intrinsic paramagnetic centres have been used as spin probes, include distance measurements between a Cu and an iron centre in the *cytochrome c oxidase-cytochrome c* complex using dipolar relaxation experiments (58), high-field PELDOR measurements between a pair of tyrosyl radicals in a dimer of R2 subunit ribonucleotide reductase (RNR) (59) and distance measurements between iron-sulfur (FeS) clusters in complex I of *Thermus thermophilus* using PELDOR (60). The affinity and structure of the intrinsic Mn<sup>2+</sup> binding site in the hammerhead ribozyme was investigated by CW- and pulsed EPR methods (61, 62). For structural studies on diamagnetic systems by EPR, spin probes have to be incorporated at selected sites and with high specificity. In this section, some of the most successful methods of incorporating paramagnetic centres into biomacromolecules will be reviewed.

#### 1.3.1 Spin labelling proteins

In 1965, McConnell and coworkers were the first to chemically attach nitroxide radicals to biomolecules to study pH-dependent structural transitions of poly-L-lysine and bovine serum albumin from the EPR linewidth. They termed the attachment of a paramagnetic centres to biomolecules as 'spin labelling' (63).

Almost 20 years later, Berliner introduced the nitroxide spin label (1-oxyl-2,2,5,5-tetramethylpyrroline-3-methyl-methanethiosulfonate (MTSSL) **1** (Figure 1.3.1) that reacts specifically to the thiol group on the cysteine amino acid and forms a covalent disulfide bond (64).

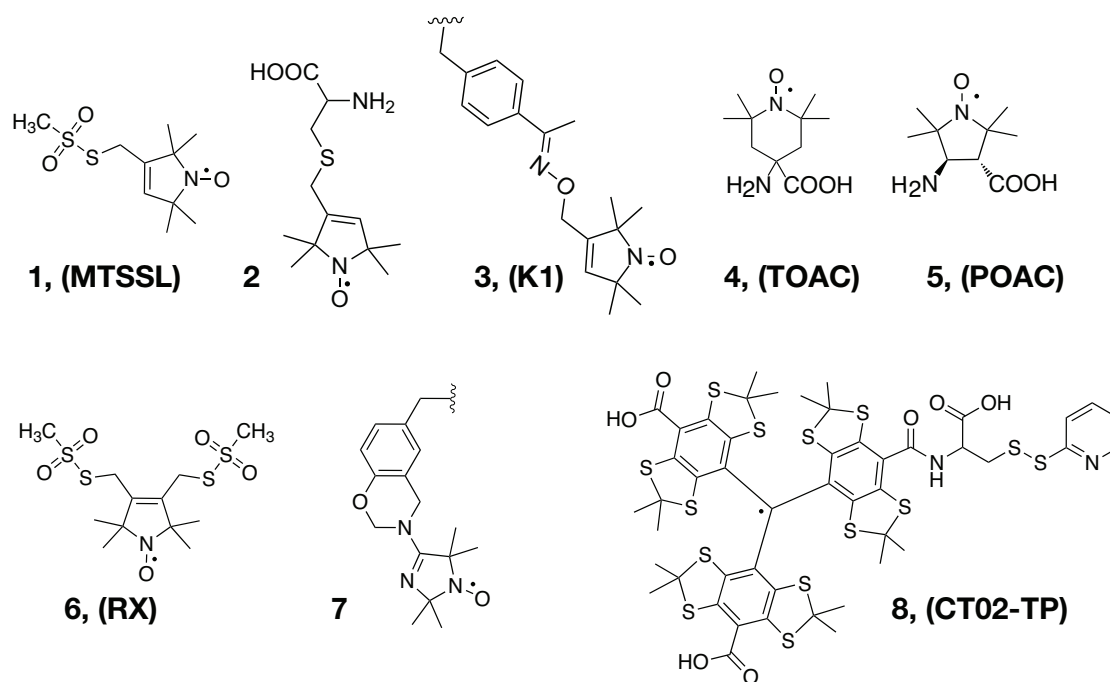


**Figure.1.3.1.** Nitroxide spin labels for site-directed spin labelling of proteins and peptides. **1)** The MTSSL spin label that reacts to thiols. **2)** Unnatural spin-labelled amino acid. **3)** Unnatural amino acid *p*-acetyl-L-phenylalanine bound to a nitroxide. **4)** TOAC, a rigid spin-labelled unnatural amino acid. **5)** POAC, a rigid nitroxide spin-labelled unnatural amino acid. **6)** A nitroxide spin label that binds to proteins via two disulfide bonds. **7)** A tyrosine-selective spin label. **8)** A trityl spin label that reacts to cysteine residues.

The breakthrough in spin labelling came in 1989, when Wayne L. Hubbell and coworkers introduced site-directed spin labelling (SDSL) by combining site-specific mutagenesis and nitroxide spin labelling (28, 65). Selected amino acids on the protein were substituted with cysteines and subsequently reacted with the MTSSL spin label, yielding proteins with spin labels only at selected positions. If the protein contains native cysteines then these are replaced by suitable amino acids. The activity of the protein has to be confirmed to verify that the modifications have not affected the structure of the protein. The site-directed spin labelling method and spin labels described above have two major disadvantages. First, native cysteines that might be functionally important to the

protein have to be substituted. Second, the nitroxide is attached to the protein by a flexible linker that complicates both measurements of dynamics and distances. One way to make SDSL applicable to proteins containing functional cysteines, is by performing the spin labelling during the biosynthesis of the protein by means of incorporation of unnatural and spin-labelled amino acids. The incorporation of a spin-labelled unnatural amino acid **2** (Figure 1.3.1) was demonstrated on T4 lysozyme (66, 67). Unfortunately, this method was hampered by low expression efficiency and difficulties in spin labelling different positions on the protein. Another method to incorporate spin-labelled amino acids uses the unnatural amino acid *p*-acetyl-L-phenylalanine (*p*-AcPhe) (68) containing a keto functional group. The *p*-AcPhe was genetically incorporated into T4 lysozyme and subsequently reacted with a nitroxide spin label that contained a hydroxylamine functional group **3** (Figure 1.3.1) (69). Although the T4 lysozyme mutants containing the *p*-AcPhe were expressed in good yields the spin label **3** was shown to have a larger mobility compared to the MTSSL spin label. Unnatural amino acids containing spin labels can also be incorporated during the solid-phase synthesis of peptides. Two spin-labelled amino acids that have been incorporated into several peptides are TOAC **4** (70) and POAC **5** (71) (Figure 1.3.1). The nitroxide moiety of TOAC has very limited conformational flexibility and is, therefore, well suited for precise measurements of secondary structure of peptides using EPR (72, 73). The POAC spin label also has a rigid nitroxide moiety and was partly developed to overcome the low coupling yields of amino acids following incorporation of the TOAC spin label. The structure of  $\beta$ -peptides, spin-labelled with the POAC spin label, was assessed using CW-EPR (74). Although incorporating TOAC and POAC spin labels into peptides during solid-phase synthesis can yield accurate information on the structure and dynamics of peptides the method is limited to relatively short peptides. Furthermore, CW-EPR at 9 and 94 GHz on a series of peptides spin-labelled with the TOAC spin label showed that the helical structure of the peptide was not uniform and did not represent the typical types of peptide helix (75).

Since its introduction, the MTSSL spin label (**1**) has become the most commonly used spin label for SDSL on biomacromolecules. Recent additions to the family of

spin labels for protein spin labelling include the semi-flexible RX spin label **6** (Figure 1.3.1) that is essentially a MTSSL that binds to proteins via two disulfide bridges (76) and an alternative nitroxide spin label that binds selectively to tyrosines **7** (Figure 1.3.1) (77). X-ray crystallography, CW-EPR and PELDOR on T4 lysozyme, spin-labelled with the RX spin label revealed the label to be highly constrained, yielding narrow distance distributions and precise information on dynamics (76). A small protein containing four structurally important cysteine residues and one native tyrosine was spin-labelled with the tyrosine-selective spin label **7** and studied by CW-EPR (77). This study demonstrated an alternative spin label for site-directed spin labelling of proteins containing structurally important cysteine residues. In chapter 6 of this dissertation, the use of trityl radicals for distance measurements using DQC and PELDOR are demonstrated. Soon after this work was completed and during the review process of the subsequent research article, (78) Hubbell and coworkers demonstrated the use of a thiol reactive trityl radical **8** (Figure 1.3.1) for SDSL of proteins. Distance measurements on proteins in liquid solution were demonstrated using DQC and T4 lysozyme mutants, spin-labelled with the trityl-based spin label **8** (14).

Because many proteins contain site-specific binding sites for ligands, these proteins can be noncovalently spin-labelled by using spin-labelled ligands. The first application of noncovalent protein spin labelling was shown by Stryer and Griffith in 1965. A 2,4-dinitrophenyl moiety was spin-labelled with a nitroxide and its affinity and interaction with an antidinitrophenyl antibody investigated using CW-EPR (79). Other examples of spin labels for noncovalent spin labelling of proteins include spin-labelled monophosphate which was used to study the binding of phosphate to ribonuclease (80), spin-labelled acetyl CoA for the study of thermodynamic properties of citrate synthase (81) and spin-labelled sulfonamide that was used to noncovalently spin label bovine carbonic anhydrase (82).

### 1.3.2 Spin labelling nucleic acids

The helical structure of nucleic acids and its building blocks make nucleic acids very amenable to modifications that do not perturb the structure. In addition,

chemical synthesis of nucleic acids is a lot easier than peptide synthesis. This has made it possible to develop various spin labels and spin labelling methods for nucleic acids. These include spin-labelled intercalators and nitroxide spin labels covalently bound to the phosphate backbone, sugar moieties or nucleobases of RNA and DNA (83). In this section a brief summary will be given of the different methods and sites used for spin labelling of nucleic acids.

In 1965 McConnell and Ohnishi demonstrated the first application of EPR spectroscopy to nucleic acids by showing that the chlorpromazine radical cation intercalates in DNA (63). The most straight-forward method of spin labelling nucleic acids is by spin-labelled ligands that bind noncovalently to the nucleic acid duplex. The interaction of several spin-labelled intercalators and groove-binding compounds with nucleic acids has been studied by EPR spectroscopy. Examples include carcinogenic aromatic amines (84), an adenine-phenoxyacridine conjugate that intercalates close to an abasic site (85, 86) and nitroxide labelled ruthenium complexes that were shown to bind to DNA via surface binding and intercalation using EPR and time-resolved luminescence measurements (87). Although spin-labelled intercalators can serve as useful spin labels for EPR studies on nucleic acids they don't always have good binding affinity and their binding is in most cases not selective. Compounds that bind covalently to nucleic acids through cross-links have been labelled with nitroxides and used as sequence- and site-specific spin labels. Psoralen derivatives were spin-labelled with nitroxides and site-specifically incorporated into DNA using photoaddition. EPR studies showed the dynamics of the spin-labelled psoralen to be correlated with the global tumbling of the DNA (88). The anticancer drug cisplatin has also been nitroxide spin-labelled and used for NMR paramagnetic relaxation enhancement studies. The sequence-specific cross-linking of the spin-labelled cisplatin yielded important 60-120 nm distance constraints from NMR measurements (89).

In 1967 Yamane and Smith were the first to chemically attach nitroxide spin labels to nucleic acids (90). Three nitroxide reagents were reacted to DNA and RNA and the conformational flexibility of the spin labels assessed using CW-EPR.

These spin labels and others that followed were unfortunately not site-selective. Three years later Hoffman and coworkers utilized a nitroxide labelled N-hydroxysuccinimide ester, that reacts selectively to  $\alpha$ -amino groups, to spin label a tRNA containing a single valine amino acid (91). This first application of site-directed spin labelling to nucleic acids was used to study the motional dynamics of the spin-labelled site as a function of temperature and ionic strength (91). The chemical synthesis of nucleic acids containing nitroxide spin labels at specific sites was first reported by Hopkins and coworkers in 1988 (92). A nitroxide was attached to the base moiety of deoxyuridine **9** (Figure 1.3.2) and the spin label phosphoramidite incorporated during synthesis of the oligonucleotide. The spin label was found not to perturb the structure of the DNA and to have limited intrinsic freedom of motion (92).

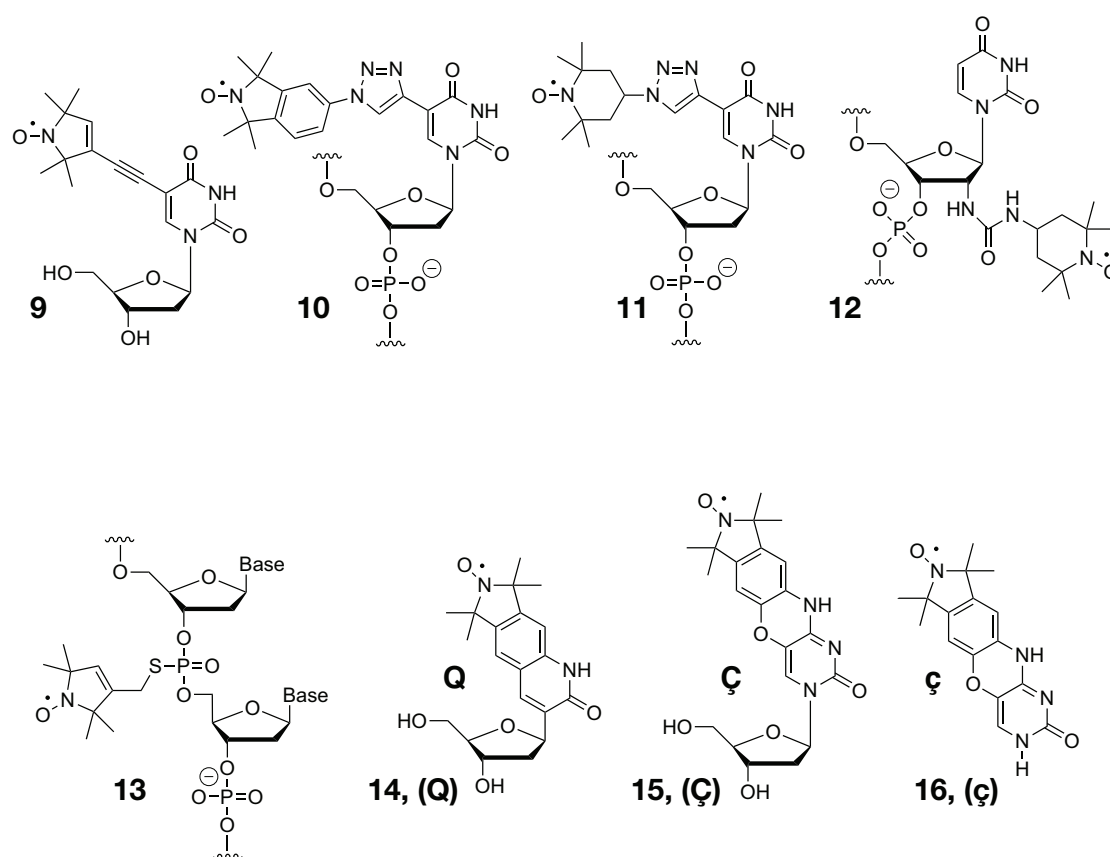


**Figure 1.3.2.** Examples of nitroxide spin labels for nucleic acids. **9,14** and **15** are incorporated during nucleic acid synthesis. Label **10** and **11** are incorporated post-synthetically via click-chemistry to DNA. Labels **12** and **13** are incorporated post-synthetically to nucleic acids. Label **16** binds noncovalently to abasic sites in DNA.

This same spin label was later incorporated into a series of DNAs by Schiemann, Engels and coworkers during solid-phase synthesis, using an on-column coupling reaction. The spin-labelled DNA duplexes were used to establish a nanometer distance ruler using PELDOR measurements (93). Recently, spin labels **10** and **11** (Figure 1.3.2) were synthesized and incorporated into DNA following the synthesis of the oligonucleotides (post synthetically) using click-chemistry. Spin label **10** was used to detect abasic sites and structural deformations in DNA from mismatches using CW-EPR (94). Interspin distances between a pair of **11** in DNA duplexes were measured using CW-EPR and PELDOR (95). Other examples of nucleobase spin labelling include the labelling of guanine in DNA by incorporating 2-fluorohypoxanthine modified guanine into oligonucleotides during solid-phase synthesis followed by reaction with 4-amino nitroxide reagent (96) and the nitroxide labelling of guanine, adenine and cytosine nucleobases of RNA using the convertible nucleosides method (97). The latter spin labels were used to study the secondary structures of RNA using PELDOR (98).

Methods to spin label the sugar moiety of nucleic acids have also been developed. The 2' position of uridine in RNA was spin-labelled by reacting 2'-amino modified RNA oligomers with a nitroxide containing an isocyanate functional group **12** (Figure 1.3.2) (99). Spin label **12** was subsequently used to investigate the structure and dynamics of HIV-1 TAR RNA upon binding of small molecules using CW-EPR (100). The sugar moieties of DNA have also been spin-labelled by incorporating 2'-O-propargyl modified uridine into DNA and reacting the modified oligomers with an azido functionalized nitroxide using click-chemistry (101). Distance measurements on spin-labelled DNA by PELDOR indicated a rather large flexibility of the spin label (101).

The phosphate backbone of nucleic acids offers a convenient place for spin labelling since the surface bound spin labels are less likely to perturb the secondary structure of nucleic acids and there is no need for synthesising spin-labelled or modified nucleosides. Spin label **13** (Figure 1.3.2) was prepared by synthesizing a RNA containing a single deoxyribo-phosphorothioate linkage

and reacting it with a thiol specific nitroxide spin label (102). This spin label was applied to distance measurements on DNA using PELDOR. The analysis of the data was complicated by the inherent flexibility of the spin label and the existence of two phosphorothioate diastereomers (103). Another example of phosphate backbone spin labelling is by substituting one of the nonbridging oxygen atoms with an amine during oligonucleotide synthesis and subsequent reaction with an amino-functionalised nitroxide (104). The terminal phosphates of DNA have also been spin-labelled by activating the phosphate groups and reacting the oligonucleotide with a nitroxides containing an amino functional group. This spin labelling technique was used to investigate the conformation of single- and double-stranded DNA with damaged and non-nucleotide inserts using distance measurements by PELDOR (105).

To obtain accurate distance measurements and inherent dynamics on nucleic acids the spin labels should ideally be completely rigid to make data analysis unambiguous. Hopkins and coworkers were the first to report the synthesis and application of a completely rigid spin label for nucleic acids (106). The structurally rigid spin label was obtained by fusing a five-membered nitroxide to the ring structure of a nonnatural nucleobase **14** (Figure 1.3.2). The rigid spin label known as **Q** forms a base pair with 2-aminopurine. The **Q** spin label has been successfully used to study DNA sequence-dependent dynamics (107). Sigurdsson and coworkers later prepared the rigid spin label **Ç** (Figure 1.3.2) by fusing a nitroxide containing isoindol to cytidine (108). **Ç** was shown by X-ray crystallography to stack inside the DNA duplex and form a base-pair to guanine without structural perturbations to the DNA duplex (109). Together with PELDOR, **Ç** has yielded detailed information on the internal motions of short DNA duplexes (110). Recently the **Ç** spin label was modified (**Çm**) for incorporation into RNA. CW-EPR measurements on a series of RNAs spin-labelled with **Çm** demonstrated that the rigid spin label can yield detailed information on the global RNA structure (111).

As previously mentioned at the start of this section, spin-labelled intercalators have been used to noncovalently spin label nucleic acids although they have very



limited use for site-directed spin labelling. Recently Sigurdsson and coworkers reported a method for noncovalent site-directed spin labelling (NC-SDSL) by using abasic sites in oligonucleotides as receptors for a spin-labelled base. The nucleobase of the  $\zeta$  spin label ( $\zeta$ ) (Figure 1.3.2) was shown to bind with high affinity and specificity to an abasic site opposite guanine at a temperature of  $-30^{\circ}\text{C}$  (112). In chapter 2 the structure of  $\zeta$  using X-ray crystallography is described. A study on the structure and internal dynamics of DNA using  $\zeta$  and PELDOR is then described in chapter 5.

All the spin labelling methods discussed so far have involved spin labelling either during or following the chemical synthesis of the oligonucleotide. Since chemical synthesis of nucleic acids is limited to a length of about 50 nucleotides, incorporation of spin labels during transcription to study larger nucleic acid systems is of interest. In fact, before the first site-directed spin labelling of nucleic acids by chemical synthesis, Bobst and coworkers reported spin labelling of uridine in RNA by an enzymatic method (113, 114). The 5' terminal guanine in RNA has also been spin-labelled by incorporating 5'-guanosine monophosphorothioate during transcription and coupling to a thiol-specific nitroxide reagent (115). More recently, spin label **9** was used for site-directed and enzymatic spin labelling of DNA (116). Major drawbacks of enzymatic methods are incorporation of spin labels at multiple sites, difficulties controlling the amount of incorporated spin labels and lack of compatibility of spin-labelled nucleotides to the enzymatic reactions.

Although the stable nitroxide radical is the most commonly used spin label for SDSL of nucleic acids, methods have been developed to site-specifically incorporate  $\text{Mn}^{2+}$  and  $\text{Gd}^{3+}$  ions to DNA. Using the commercially available phosphoramidite of an EDTA-derivatized deoxythymidine, DNA duplexes were spin-labelled with  $\text{Mn}^{2+}$  and used for the study of DNA-protein structure by NMR paramagnetic relaxation enhancement (117). A DNA duplex was spin-labelled with  $\text{Gd}^{3+}$  by incorporating a  $\text{Gd}^{3+}$  tag to a modified nucleotide on the 5' end by click-chemistry. The  $\text{Gd}^{3+}$  spin label was used to measure interspin distances of about 6 nm on DNA using PELDOR (118).

In summary, the various methods and spin labels that have been developed for spin labelling proteins and nucleic acids have been reviewed. For every method of spin labelling, the nitroxide radical has become by far the most common spin label. Spin labelling proteins is mainly done by post-synthetic methods since chemical synthesis of proteins is only feasible for relatively short peptide chains. On the contrary, spin labelling nucleic acids is mainly done by incorporating spin-labelled or functionalized nucleotides either during or following the solid-phase synthesis of the oligonucleotide. From the various methods of incorporating spin centres into proteins and nucleic acids and the examples of applications reviewed, it is clear that spin labelling has made an invaluable contribution to the study of biomacromolecular structure and dynamics using EPR spectroscopy.

## 1.4 Aims of this research

The overall goal of the work described in this doctoral dissertation was to advance some of the methods used for nanometer distance measurements by EPR. As discussed in the previous section, spin labelling nucleic acids with site-specific spin labels requires laborious chemistry that can be discouraging for a wide application of spin labelling to study the structure and dynamics of nucleic acids. Since distance measurement by PELDOR is a powerful method for structural studies it is important to develop a facile method for site-directed spin labelling of nucleic acids for PELDOR measurements. In chapter 2, X-ray and computational study on the structure of the rigid spin label  $\zeta$  is described.  $\zeta$  binds noncovalently to DNA and thereby eliminates the need for advanced spin labelling chemistry. Chapter 5 describes the application of the  $\zeta$  spin label to structural studies on DNA and DNA-protein complex using PELDOR and simulations.

Analysing data from PELDOR in terms of distances between spin labels or spin-labelled sites is often the most difficult part of a PELDOR study. Depending on the spin labels and the nature of the spin-labelled system, various methods and computer programs have been developed to make the analysis of PELDOR data as robust and easy as possible. Chapter 3 describes the development of a Matlab-based program that can simulate PELDOR time traces and distance distributions from a predefined model. Simulations based on a model are necessary to analyse orientation selective PELDOR data. As described in chapter 5, this simulation program was used to analyse the orientation selective PELDOR time traces that were obtained from DNA, spin-labelled with the rigid  $\zeta$  spin label.

PELDOR yields information on spin label orientation, especially at high magnetic fields. This property of PELDOR is valuable to resolve structural information from biomacromolecules. Chapter 4 concerns a study on orientation selective PELDOR measurements at 97 GHz, using a home-built high-power EPR spectrometer (Hiper). By measuring nitroxide biradicals with limited flexibility and using model-based simulations, it is shown that PELDOR data with high

orientation selectivity can yield quantitative information on spin label orientation and flexibility. The PELDOR simulation program described in chapter 3 was used to simulate the orientation selective PELDOR measurements obtained from rigid and semi-rigid biradicals.

Finally, chapter 6 describes the use of trityl spin labels for distance measurements. Although site-directed spin labelling for distance measurements has come a long way since its beginnings, structural studies by EPR are limited by rather few options of available spin labels. A radical that has been widely used for EPR imaging and oxymetry is the carbon centered triarylmethyl (trityl) radical. Since the trityl radical has properties that could eliminate some of the limitations of nitroxide spin labels the possibility of using trityl radicals as spin labels for nanometer distance measurements was evaluated.

## 2 Structure of spin-labelled nucleobase $\zeta$ and phenoxazine derivative

### 2.1 Introduction

As discussed in section 1.3.2, the structure and dynamics of nucleic acids have been studied using EPR spectroscopy and various spin labels. The extraction of dynamics and distances from nucleic acids using EPR is appreciably complicated by the inherent flexibility of the spin label. Thus, rigid spin labels that can be incorporated into DNA or RNA without perturbing the helical structure are highly valuable for detailed structural investigations. In addition, rigid spin labels give access to the relative spin label orientation from PELDOR measurements. The rigid spin label  $\zeta$  (Figure 1.3.2) that forms a Watson-Crick base pair with guanine has yielded information on the mobility of single nucleotides (119), spin label orientation in DNA (120) and complex internal dynamics of short DNA helices (110). A drawback of many spin labelling techniques is the extensive chemistry and purification that is required. This is especially true for spin labelling with the  $\zeta$  spin label. To simplify the site-directed spin labelling of nucleic acids, Sigurdsson and coworkers reported the use of an abasic site in oligonucleotides as a receptor for the nucleobase of  $\zeta$  ( $\zeta$ ) (112) (Figure 1.3.2). To aid the analysis of EPR data and confirm the integrity of the nucleic acid structure, it is beneficial to obtain structural information on the spin label and/or spin-labelled nucleic acids with atomic-resolution. This chapter describes the study on the structure of the  $\zeta$  spin label and its phenoxazine precursor using X-ray crystallography and *ab initio* calculations. The crystal structure of  $\zeta$  incorporated into DNA is also discussed.

### 2.2 Materials and methods

#### 2.2.1 Small molecule crystallization and structure determination

Yellow crystals of the  $\zeta$  spin label were obtained by slow evaporation from ethanol. Yellowish-brown crystals of the phenoxazine were obtained by slow evaporation from 3:1 dichloromethane:methanol solution. Crystals of  $\zeta$  and phenoxazine were mounted on a Rigaku MM007/Mercury X-ray diffractometer (confocal optics Mo K $\alpha$  radiation, 0.71073 Å). X-ray diffraction experiments were

performed at 93 K. Intensity data were collected using accumulated area detector frames spanning at least a hemisphere of reciprocal space for all structures. Data were integrated using Crystal Clear. All data were corrected for Lorentz, polarization and long-term intensity fluctuations. Absorption effects were corrected on the basis of multiple equivalent reflections. The structures were solved by direct methods. Hydrogen atoms bound to carbon were idealized. Structural refinements were obtained with full-matrix least-squares based on F<sup>2</sup> by using the program SHELXTL (121). The theta(max) resolution of the small molecule structure of phenoxazine was 27.52 and the theta(max) resolution of the small molecule structure of **ϕ** was 25.3.

### 2.2.2 Density function theory calculations

Density function theory (DFT) calculations on the spin-labelled nucleobase **ϕ** were performed with the B3LYP functional, the 6-31G\* basis set and unrestricted spin-wave functions using Gaussian03 (122). To obtain a geometry optimized structure and single point energy for the bent spin label, the atoms of the spin label's phenoxazine moiety were frozen to the position obtained from the small molecule crystal structure and hydrogen atoms were added to the vacant positions. The constraints on the phenoxazine moiety were then relaxed to obtain the energy optimized structure and single point energy of the unbent spin label. The vibrational frequencies for both geometry-optimized structures were all positive, indicating the structures represent an energy minimum. The single point energy for the bent and planar spin label was -2 795 044 kJ/mol and -2 795 046 kJ/mol respectively. The unbent structure is 2 kJ/mol less in energy. The frequency for the bending motion around the oxazine linkage is 18.8 and 28.3 cm<sup>-1</sup> for the planar and the bent conformation, respectively.

### 2.3 X-ray crystallography of **ϕ** and phenoxazine derivative

If **ϕ** is to be used for measurements of distances and orientations on nucleic acids it is important to evaluate the structure of **ϕ**. Crystal structures of a phenoxazine derivative (Figure 2.3.1 a), and **ϕ** (Figure 1.3.2 b) were obtained by crystallizing the compounds from ethanol. Analyses of the crystals by X-ray crystallography, performed by Prof. Alexandra Slawin, revealed the phenoxazine derivative to be

planar (Figure 2.3.1 a) but the  $\zeta$  spin label to have a bend of about  $20^\circ$  at the oxazine linkage between the cytosine and benzene rings (Figure 2.3.1 b).

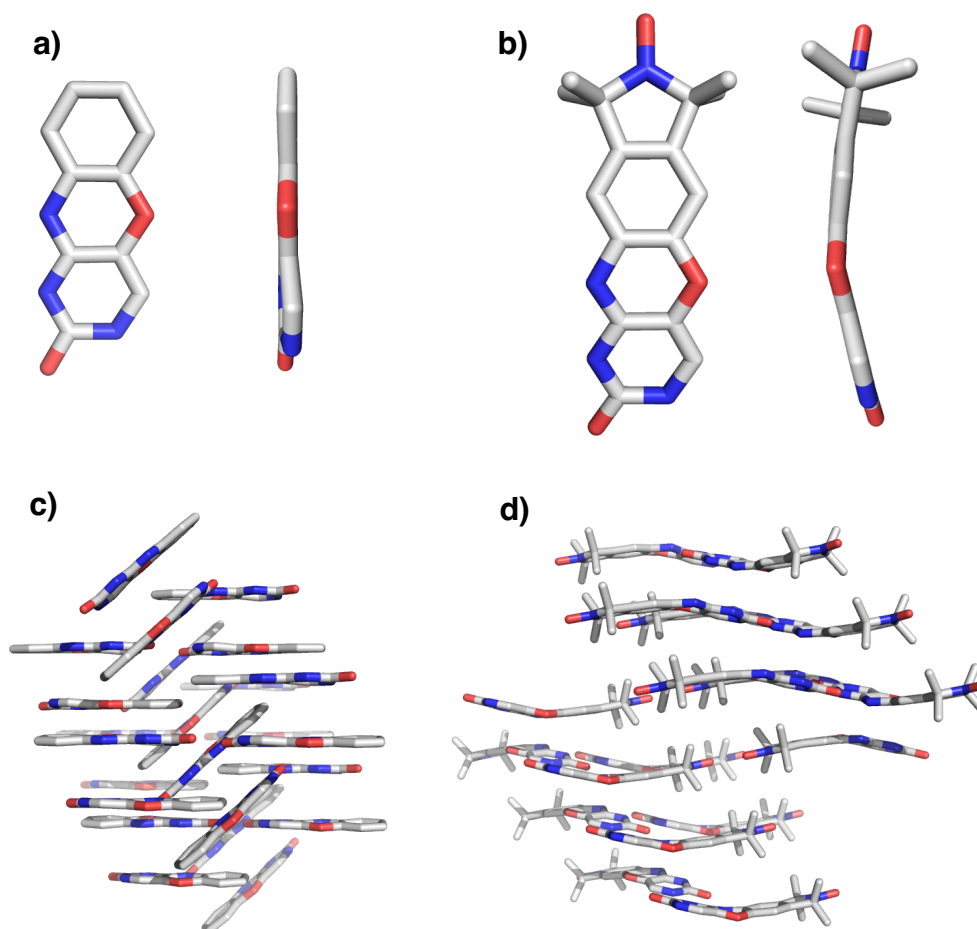


**Figure 2.3.1.** Crystal structures of **a)** phenoxazine and **b)** nitroxide spin-labelled nucleobase  $\zeta$ . The crystal packing of the phenoxazine and  $\zeta$  is shown in **c)** and **d)**, respectively.

## 2.4 DFT calculations of $\zeta$ and phenoxazine

The only difference between the phenoxazine derivative and  $\zeta$  is the nitroxide moiety. The bent geometry of the spin label could, therefore, be due to either effects from crystal packing or the antiaromaticity of the label. The  $16\pi$  electrons of the spin label could cause non-planarity of the ring system. To evaluate if the bent geometry of the spin label could be a possible conformation in solution, density functional theory (DFT) calculations were done on  $\zeta$ , in both bent and planar conformation, by Prof. Michael Bühl and Dr. Sudip Roy. For the calculations of the optimized geometry of the bent spin label the coordinates

from the crystal structure of  $\zeta$  were used as an initial structure. The structure was then energy minimized while keeping the position of the atoms in the phenoxazine moiety frozen. The geometry optimized structure of a planar spin label was then obtained by relaxing the constraints on the phenoxazine atoms and calculating the energy minimum. Single point energy calculations of the bent and planar spin labels showed the energy difference of the structures to be only 1.31 kJ/mol. Vibrational frequency calculations on the bent and planar structures of  $\zeta$  showed all frequencies to be positive. In addition, the frequencies of the bending motion about the oxazine linkage were determined as 18 and 28  $\text{cm}^{-1}$  for the planar and bent conformations, respectively. These results from calculations of optimum geometry, single point energy and frequencies show that the planar and bent conformations of  $\zeta$  could belong to the same energy minimum. Since very little energy is needed to bend the spin label, crystal packing could force the spin label into the bent conformation. If crystal packing can cause bending of the spin label; could the incorporation into a nucleic acid have the same effect? To answer this question, a 10-mer DNA duplex containing the rigid spin label  $\zeta$  was crystalized by T. E. Edwards (109). The high-resolution X-ray structure obtained showed the  $\zeta$  spin label to have a planar geometry within the DNA duplex and no clear indication of bending motion about the oxazine linkage (Figure 2.4.1).

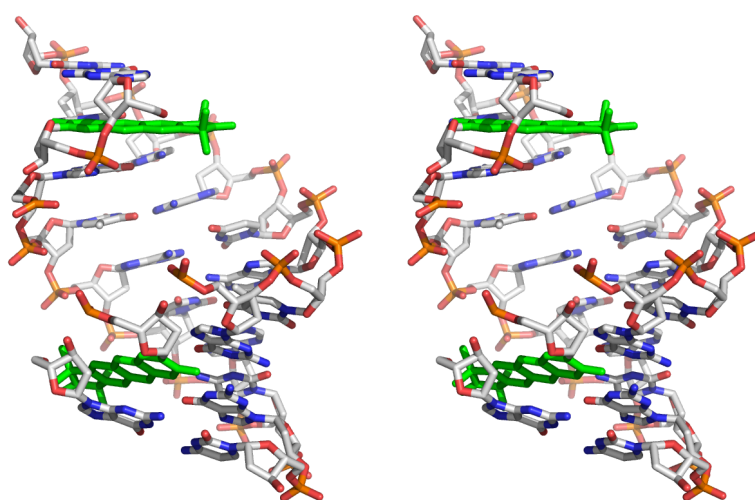




**Figure 2.4.1.** A stereo view of a crystal structure of the 10-mer DNA duplex spin-labelled with  $\zeta$ . The  $\zeta$  spin labels are in green stick representation. The structure was adapted from PDB ID 3OT0 (109).

The planar geometry of the spin label within the DNA is probably the preferred conformation, made stable by hydrogen bonds to the base-pairing G and stacking interactions to adjacent nucleobases. To obtain a structure of  $\zeta$ , bound noncovalently to a DNA abasic site, two DNA duplexes, containing abasic sites, were crystallized (Table 2.4.1). The first duplex had the same sequence as the DNA that was spin-labelled with  $\zeta$  (109), except the  $\zeta$  nucleotides were replaced by abasic sites. The second DNA was a 14-mer containing only one abasic site at position 8 from the 5' side (Table 2.4.1). Crystallisation plates using the hanging-drop method and the same crystallisation conditions as in (109) were prepared using the 10-mer and 14-mer DNA duplexes with and without 1 equivalent per abasic site of  $\zeta$ . Only crystals of the abasic 14-mer DNA without  $\zeta$  were obtained but unfortunately they did not diffract sufficiently for structure determination by X-ray analysis.

**Table 2.4.1.** DNA sequences used in crystallisation trials.

DNA	DNA sequence <sup>[a]</sup>
10-mer DNA	5'-GFGTAU*ACGC-'3 3'-CGCAU*ATGFG-'5
14-mer DNA	5'-GACCTCGFATCGTG-'3 3'-CTGGAGCGTAGCAC-'5

[a] F denotes abasic sites and U\* denotes 2'-O-methyluridine.

## 2.5 Summary

In summary, the structure of the spin-labelled nucleobase  $\zeta$  and a phenoxazine derivative was determined using X-ray crystallography and DFT calculations. The crystal structure of  $\zeta$  showed the spin label to have a bent geometry in contrast to the phenoxazine which crystallised in a planar geometry. DFT calculations confirmed that the  $\zeta$  spin label could go between a planar and bent conformation without much energy cost. An X-ray crystal structure of the  $\zeta$  spin label, covalently linked to a 10-mer A-form DNA, showed the  $\zeta$  spin label to be in

a planar conformation. It can, therefore, be concluded that the  $\zeta$  spin label is most probably in a planar geometry when stacked inside a DNA duplex. For further information on the X-ray crystallography structures of the 10-mer DNA duplex,  $\zeta$  spin label and phenoxazine derivatives, see the original research article at the end of this dissertation.

## **2.6 Acknowledgment**

The  $\zeta$  spin label and phenoxazine derivative were synthesized by Dr. Sandip A. Shelke. The synthesis of the 10-mer DNA with the  $\zeta$  spin label was carried out by Dr. Pavol Cekan. X-ray crystallisation of the 10-mer DNA with  $\zeta$  was obtained by Dr. Thomas E. Edwards. I would like to thank Prof. Alexandra Slawin for X-ray measurements and analysis of the  $\zeta$  spin label and phenoxazine derivative and Prof. Michael Bühl and Dr. Sudip Roy for assistance with the setup and execution of DFT calculations.

### 3 PELDORSIM: Model-based simulations of PELDOR time traces

#### 3.1 Introduction

Measuring distance constraints and conformational distributions on biomolecular systems by SDSL and PELDOR relies on measuring the dipolar coupling between spin labels. Interpreting the observed changes and distribution of interspin distances, in terms of inherent spin label dynamics and structural changes, is in very few cases an easy task (10). If the orientation of the spin labels is not correlated to the orientation of the interspin vector and exchange coupling is negligible, DeerAnalysis (123, 124), a Matlab-based program, can be used to extract distance information from PELDOR time traces. PELDOR yields information on the distance distribution between spin centres. therefore, in order to interpret the measured distance distribution in terms of distances between the spin-labelled sites, the inherent flexibility of the spin labels has to be disentangled from the experimental distance distribution. For proteins the site of spin labelling is most commonly a sulfur atom of a cysteine residue and for nucleic acids the spin-labelled site is an atom of the base, sugar or phosphate backbone moieties. If the conformation of spin labels is mainly governed by rotations of the atomic bonds within the spin label and linker the distance distribution inherent to the spin label can be simulated using a rotamer library (16). The Matlab-based program, MMM (125) is an application that can simulate PELDOR time traces and distance distributions calculated from rotamers on *in-silico* spin-labelled systems. The simulated time traces and distance distributions are then compared with the experimental data to assess distances and structural dynamics belonging to the spin-labelled macromolecule. A recent addition to the list of tools for analysing PELDOR data is MtsslWizard (126). MtsslWizard simulates distance distributions between spin labels from *in-silico* spin-labelled proteins by generating random values for each dihedral angle within the linker of the MTSSL spin label and then checks for clashes between spin label and protein. The program, which is a plugin for PyMOL (127), was shown to produce distance distributions with an excellent agreement to experiments (126). If the relative orientation of the spin labels is correlated to the orientation of the

interspin vector the interpretation of PELDOR data becomes more complicated. Various model-based approaches have been applied to directly analyse orientation selective PELDOR data in terms of mutual spin label orientations and distances. One approach is to construct a model of the spin-labelled system and using geometric parameters that yield the best fit between simulated and experimental PELDOR data to derive the mutual orientation of the spin labels (128, 129). Another approach is to apply a fitting algorithm to find a set of mutual spin label orientations that give the best fit to the experimental data. The spin label orientations can either be found from a grid search (130) or a database of simulated time traces (131).

In this chapter a Matlab-based program, that simulates PELDOR time traces and distance distributions from a geometric model, will be described in detail. A model of the spin-labelled system is constructed from geometric parameters of spin labels and spin-labelled molecule. The conformational distribution of spin labels is then approximated by a distribution in these geometric parameters. The PELDOR time traces are simulated by generating a number of model conformers and calculating the PELDOR time trace for each conformer, taking into account the field position of detection and inversion pulses and their excitation profiles. The script for the complete program can be found in the appendices.

### **3.2 Constructing the vector model**

To describe how a model is constructed, the generation of a vector model for a simple semi-rigid nitroxide biradical is described. A biradical can be represented by a rigid molecule that has both ends spin-labelled with a nitroxide spin label via flexible linkers. In terms of vectors, the rigid molecule is described by a single vector. The nitroxide moieties, including their linkers, are described by another set of vectors attached to the rigid molecule (Figure 3.2.1). In this particular model, the interspin vector lies parallel to the blue vector and its length is the combined length of the green, blue and red vectors.



**Figure 3.2.1.** A semi-rigid nitroxide biradical described by a vector model. The blue vector represents the rigid molecule. The red and green vectors represent the nitroxide moieties and their flexible linkers (spin labels A and B). The relative orientation of nitroxides A and B is described by the unit vectors, x, y, z. The interspin vector  $r$  between the spin centres is shown by the black vector below.

Mathematically, a vector can be defined as a line between two coordinates in two- or three-dimensional space. A three-dimensional space can be defined by three vectors, all originating from the same point and orthogonal to each other (Figure 3.2.2). The three vectors are commonly labelled as X, Y and Z. A vector lying in this space and originating at the center of the coordinate system  $[0\ 0\ 0]$  is described by the coordinate of its endpoint in terms of the X-, Y- and Z-directions. A unit vector (a vector that has length of one arbitrary unit) that is parallel to the Z-direction is then denoted as  $[0\ 0\ 1]$  (Figure 3.2.2). In Matlab, a straight line connecting two points is created by the *line* function. The unit vector  $[0\ 0\ 1]$  can then be drawn in Matlab as `line([0 0],[0 0],[0 1])`.

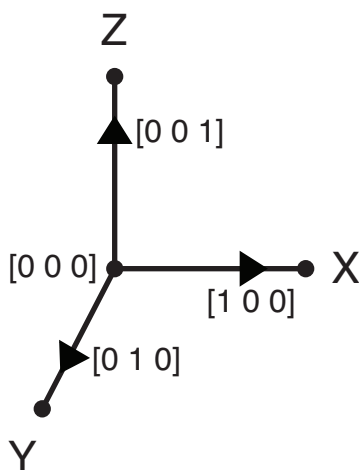


**Figure 3.2.2.** Representation of unit vectors in three-dimensional space. The direction of each unit vector is described in terms of its  $[X\ Y\ Z]$  components.

For the model shown in figure 3.2.1, the positions of the nitroxides spin centres are represented by the endpoint-coordinates of the red and green vectors. The

length of the interspin vector  $\mathbf{r}$  can be calculated from the coordinates of the spin centres by the following equation,

$$r = \sqrt{(A_x - B_x)^2 + (A_y - B_y)^2 + (A_z - B_z)^2} \quad (1)$$

where  $A$  and  $B$  are the spin centres and  $x$ ,  $y$  and  $z$  the components of the coordinates. To describe conformational flexibility of the nitroxide spin labels, the position and orientation of the spin centres have to be considered. The flexibility in position can be modelled by varying the length and relative angles of the vectors representing the spin labels. To add information on the orientation of spin centres, each spin label vector is assigned additional three unit vectors labelled  $x$ ,  $y$ ,  $z$  that represent the principle components of the  $\mathbf{g}$ - and  $\mathbf{A}$ -matrices and define the orientation of the spin centre relative to the applied magnetic field  $\mathbf{B}_0$  (Figure 3.2.3).

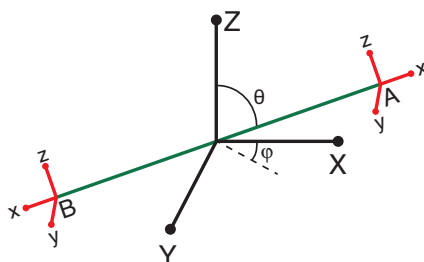


**Figure 3.2.3.** A vector diagram of a nitroxide biradical in the laboratory frame  $\{X, Y, Z\}$ . The interspin distance vector is represented by the green line and the frames of spin centres  $A$  and  $B$  by red vectors. The orientation of the interspin distance vector relative to the applied magnetic field is represented by  $\theta$  and  $\varphi$ .

The principal components of the nitroxide  $\mathbf{g}$ - and  $^{14}\text{N}$  hyperfine coupling matrices are assumed to be collinear, which is a valid approximation. The conformational dynamics of the semi-rigid nitroxide biradicals is simulated by creating 20,000 instances of the vector model, each representing a single molecular conformer. For the model in figure 3.2.1, only the angle between the vectors representing the spin labels and rigid molecule will have a random value ( $0 - 2\pi$ ). Calculating the distance between the spin centres for each conformer and assigning all distances to discrete intervals (binning) yields a simulated nitroxide-nitroxide distance distribution. To give easy access to the model

variables, a user interface was created. Figure 3.2.4 shows the window for the model editing user interface, where model parameters can be easily edited by the user.

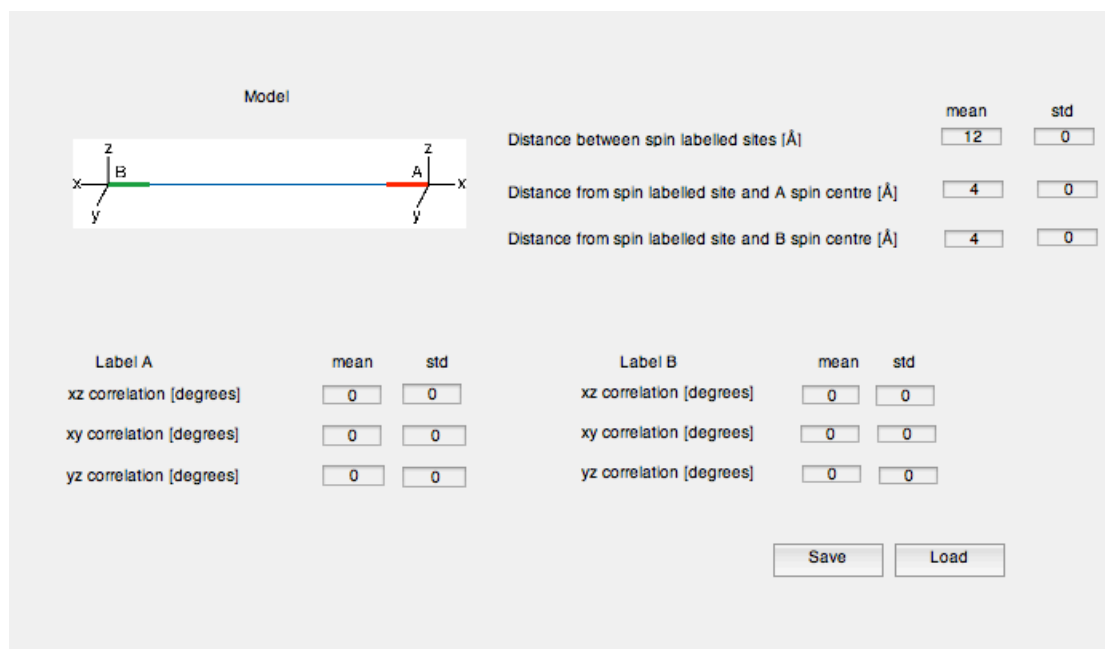


**Figure 3.2.4.** User interface for vector model parameters. The conformational dynamics of spin labels is defined through correlations with a normal distribution. The xz correlation represents rotation of the spin label about its  $g_y$  component, which results in a mutual rotation of the  $g_x$  and  $g_z$  components. Using the right mixture of correlations various modes of spin label motion can be modelled.

Parameters that can be varied include the lengths of the rigid molecule and spin labels and the relative orientation and position of spin centres. Lengths are given in Å as a mean value and one standard deviation (mean and std, respectively). The position and orientation of spin centres is described in terms of correlations that are also given as a mean value and one standard deviation (mean and std, respectively). The relative orientations of spin centres are defined in degrees. As an example, the xz correlation describes spin label motion that rotates the spin centre about the y- component of the  $\mathbf{g}$ - and  $\mathbf{A}$  matrices. Rotation about the y-component only changes the orientation of the z- and x- components and is, therefore, labelled as xz correlation. If the xz correlation for spin label A is given a mean value of  $90^\circ$  the red vector will be rotated clockwise about the y-component. This changes the position and orientation of the A spin center,

relative to the molecule and also the angle of the interspin vector relative to the direction of the magnetic field  $\mathbf{B}_0$  (Z-axis). The other correlations can be rationalised in the same manner.

### 3.3 Calculating PELDOR time traces

After having constructed an ensemble of conformers the interspin distance vector  $\mathbf{r}$  for each molecular conformer is computed from the known positions of the spin centres. The interspin vector is given a random orientation in the laboratory frame  $\{X, Y, Z\}$  by assigning random values to the polar and azimuthal angles  $\theta$  and  $\varphi$ , respectively (Figure 3.2.3). The polar angle  $\theta$  is weighted by  $\sin(\theta)$  to simulate the random orientations in a disordered powder sample. By convention the direction of the magnetic field  $\mathbf{B}_0$  is set parallel to the Z-axis. The polar angle  $\theta$  is, therefore, the angle between the interspin vector and the Z-axis.

Now that the molecular conformers have been generated the next task is to calculate the resonance frequency for each spin centre. To compute the resonance frequency, the orientation of the  $\mathbf{g}$ - and  $\mathbf{A}$ -frames  $\{x, y, z\}$  in the laboratory frame  $\{X, Y, Z\}$  need to be calculated. When the molecular conformers were constructed the orientation of the  $\mathbf{g}$ - and  $\mathbf{A}$ -frames in the laboratory frame was known. However, since the orientation of the interspin vectors is now random and the  $\{x, y, z\}$  frames are correlated to the interspin vector, the orientations of the  $\mathbf{g}$ - and  $\mathbf{A}$ -frames in the laboratory frame have to be computed using a rotation matrix. The orientation of the  $\{x, y, z\}$  frame in the  $\{X, Y, Z\}$  frame, which can also be visualized as the orientation of  $\mathbf{B}_0$  in the  $\{x, y, z\}$  frame, is given as a coordinate  $O'$  in the  $\{X, Y, Z\}$  frame and is computed using equation 3.3.1, where  $RM$  is a rotation matrix and  $O$  the coordinate of either the  $\mathbf{g}$ - or  $\mathbf{A}$ -frame before the transformation.  $\mathbf{r}$  and  $\mathbf{r}'$  are the coordinates of the interspin vector before and after a random orientation in the laboratory frame, respectively.

$$O'_{[XYZ]} = RM(O_{[XYZ]}, \mathbf{r}) \times \mathbf{r}' \quad (3.3.1)$$

The rotation matrix  $RM$  in Eq. 3.3.1 has the following Matlab script:



```

%Rotation matrix that rotates the vector u to the direction of
%vector v.
function [R]=RotationMatrix(u,v)
uvangle=acos(dot(u,v));%calculate the angle between u and v.
k=cross(u,v); k = k/norm(k);%calculate the cross product between u
and v and normalize the resulting vector.
kx=[0 -k(1,3) k(1,2);k(1,3) 0 -k(1,1);-k(1,2) k(1,1) 0];%the cross
product in matrix form.
R=eye(3,3)+(kx.*sin(uvangle))+((1-cos(uvangle))*kx^2);%Calculate the
rotation matrix with Rodrigues' rotation formula.

```

The 20,000 molecular conformers now represent a macroscopic sample of the semi-rigid nitroxide biradical in either a powder or a frozen glass, where all possible orientations of the molecule and spin labels, relative to the magnetic field  $\mathbf{B}_0$ , are sampled. The resonance frequencies for each spin centre are computed from the orientation  $(\theta, \varphi)$  and principal values of the  $\mathbf{g}$ - and  $^{14}\text{N}$  hyperfine coupling matrices using equations 3.3.2 - 3.3.4. Equations 3.3.2 and 3.3.3 describe the effective values for the  $\mathbf{g}$ - and  $^{14}\text{N}$  hyperfine coupling matrices in the laboratory frame where  $g_{xx}$ ,  $g_{yy}$  and  $g_{zz}$  are the principal values of the  $\mathbf{g}$ -matrix and  $A_{xx}$ ,  $A_{yy}$  and  $A_{zz}$  are the principal values of the  $^{14}\text{N}$  hyperfine coupling matrix. In equation 3.3.4  $\beta_e$  is the Bohr magneton and  $m_I$  is the quantum number for the spin state of a hyperfine-coupled nuclei.

$$g_{eff} = (g_{xx} \times \cos(\varphi) \times \sin(\theta))^2 + (g_{yy} \times \sin(\varphi) \times \sin(\theta))^2 + (g_{zz} \times \cos(\theta))^2 \quad (3.3.2)$$

$$A_{eff} = (A_{xx} \times \cos(\varphi) \times \sin(\theta))^2 + (A_{yy} \times \sin(\varphi) \times \sin(\theta))^2 + (A_{zz} \times \cos(\theta))^2 \quad (3.3.3)$$

$$\nu_{res} = \beta_e \times B_0 \times \sqrt{g_{eff}} + m_I \times \sqrt{A_{eff}} \quad (3.3.4)$$

For 20,000 molecular conformers there are 40,000 nitroxide spins. Since each of these nitroxide spins has a  $^{14}\text{N}$  nuclear spin with three possible values for the quantum number  $m_I$  (-1, 0 1), this yields a total number of 120,000 resonance frequencies.

To simulate PELDOR time traces the fraction of spins that are excited by the detection and inversion pulses needs to be quantified by calculating the excitation profiles for the detection  $I_{v1}$  and inversion  $I_{v2}$  pulses. Assuming ideal

square pulses the excitation profiles for the detection sequence and inversion pulse are described by equations 3.3.5 and 3.3.6, respectively (132).

$$\xi = \frac{\pi/2}{t_{\pi/2}} \quad (3.3.5)$$

$$\xi' = \frac{\pi}{t_{\pi}} \quad (3.3.6)$$

$$\zeta^2 = \xi^2 + (\omega - \omega_r)^2 \quad (3.3.7)$$

$$\zeta'^2 = \xi'^2 + (\omega - \omega_r)^2 \quad (3.3.8)$$

$$I_{\nu_1} = \frac{\xi}{\zeta} \sin(\zeta t_{\pi/2}) \frac{\xi'^4}{4\zeta'^4} [1 - \cos(\zeta' t_{\pi})]^2 \quad (3.3.9)$$

$$I_{\nu_2} = \frac{\xi'^2}{2\zeta'^2} [1 - \cos(\zeta' t_{\pi})] \quad (3.3.10)$$

In equations 3.3.5 and 3.3.6 the lengths of the  $\pi/2$  and  $\pi$  pulses are given by  $t_{\pi/2}$  and  $t_{\pi}$ , respectively. The  $(\omega - \omega_r)$  in equations 3.3.7 and 3.3.8 is the frequency offset of the microwave pulses,  $\omega$  being the frequency of the microwave pulse and  $\omega_r$  the resonance frequency of the spin centre, calculated by Eq. 3.3.2 - 3.3.4. The contribution from each conformer, or specifically each intramolecular spin pair, to the PELDOR signal is computed from the fraction of spins *A* excited by the detection sequence  $I_{\nu_1}(A)$  weighted by the inversion probability of spin *B*  $I_{\nu_2}(B)$  and the fraction of spins *B* excited by the detection sequence  $I_{\nu_1}(B)$  weighted by the inversion probability of spin *A*  $I_{\nu_2}(A)$  (Eq. 3.3.11).

$$\Psi(\theta, \Phi_A, \Phi_B, \nu_1, \nu_2) = I_{\nu_1}(A)I_{\nu_2}(B) + I_{\nu_1}(B)I_{\nu_2}(A) \quad (3.3.11)$$

The PELDOR time trace for each spin pair depends on the orientation of the interspin vector relative to the magnetic field  $\mathbf{B}_0$ , the orientation of the  $\mathbf{g}$ - and  $\mathbf{A}$ -frames  $\Phi$  and on the frequency of the detection and inversion pulses,  $\nu_1$  and  $\nu_2$  respectively. The intensity of the PELDOR signal at time zero, where the effect from the inversion pulse is zero, is computed by Eq. 3.3.12, where the summation is over the number of molecular conformers *N*.

$$V_0 = \sum_{i=1}^N I_{\nu_1}(A) + I_{\nu_1}(B) \quad (3.3.12)$$

For  $N$  spin pairs, each with a finite number  $R$  of orientations, the intensity of the refocused echo  $V$  as a function of the position of the inversion pulse  $t$  is described by equation 3.3.13.

$$V(t) = V_0 + \sum_{i=1}^N \sum_{j=1}^R \Psi^{i,j} [\cos(Dt) - 1] \quad (3.3.13)$$

$D$  is the dipolar coupling (Eq. 3.3.14),

$$D = \frac{\mu_0 g_A g_B \beta_e^2}{4\pi \hbar r_i^3} (1 - 3\cos^2(\theta_{i,j})) + J_i \quad (3.3.14)$$

where  $\mu_0$  is the permeability of vacuum,  $g$  the isotropic  $g$ -value,  $\hbar$  the reduced Planck constant,  $r$  the interspin distance and  $J$  the isotropic exchange coupling constant. The PELDOR time trace  $V(t)$  is then obtained by computing  $V_0$ ,  $\Psi$ ,  $\theta$  and  $r$  for each molecular conformer and using Eq.3.3.13. Calculation of six time traces from 20,000 conformers takes about 10 seconds to compute on a 2.8 GHz Intel Core 2 duo processor. Figure 3.3.1 shows the user interface for the simulation program. The user manual for the program can be found in the appendices.

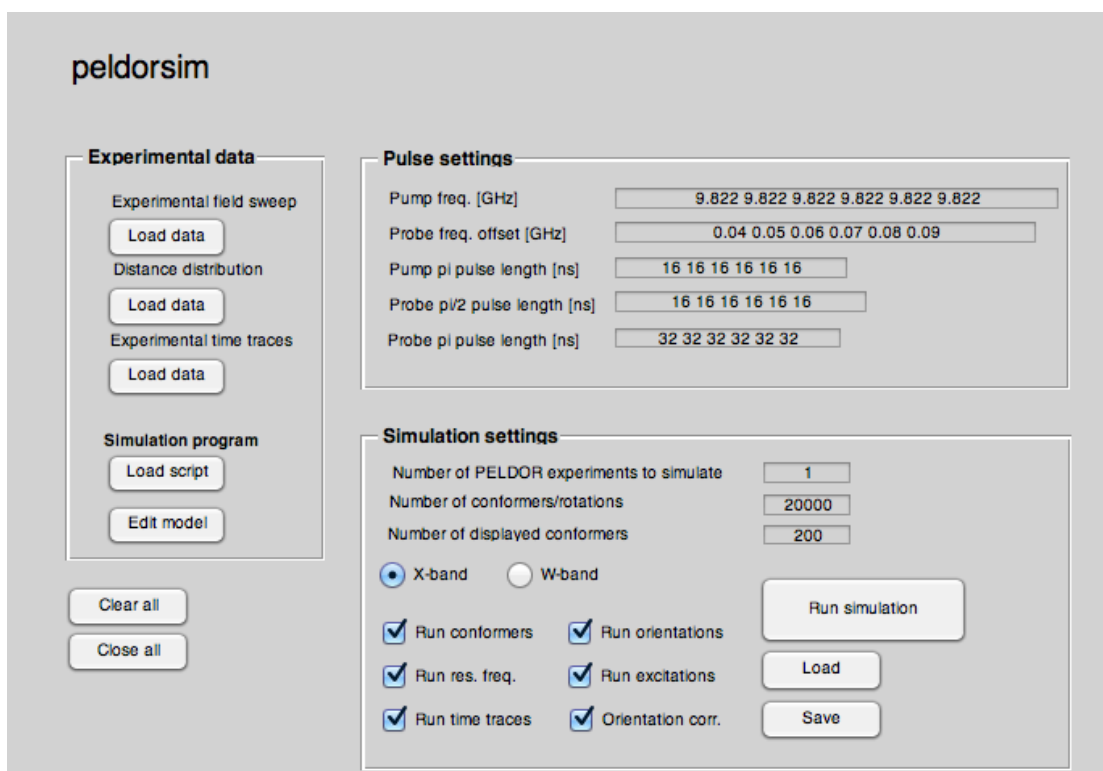


**Figure 3.3.1.** User interface for peldorsim. The various buttons and fields are described in the user manual found in the appendices.

The PELDOR simulation program described here was successfully used to simulate orientation selective PELDOR time trace for nitroxide biradicals (Chapter 4), spin-labelled DNA (Chapter 5) and nitroxide-trityl and trityl-trityl biradicals (Chapter 6). Each of these examples used a geometric model different from the one described here.

### 3.4 Acknowledgement

The Matlab script for the generation of random orientations on a sphere with  $\sin(\theta)$  weighting is based on a Mathematica code written by Dr. Graham Smith. The functions *eppload*, *basecorr* and *smooth* from the EasySpin package (133) are used within the peldorsim script.

## 4 Molecular geometry, flexibility and exchange coupling measured by high-field PELDOR

### 4.1 Introduction

As previously discussed, pulsed EPR, especially pulsed electron-electron double resonance (PELDOR) (41, 42), has in the last 10 years become a valuable technique to determine the structure and conformational flexibility of biomacromolecules. Using either paramagnetic centres that are intrinsic to the biomolecule or site specifically incorporating spin labels, PELDOR is used to measure the distance between spin centres and to relate the obtained distance constraints and their distributions to conformational states (134, 38). Utilizing PELDOR it is possible to measure distances between paramagnetic centres in the range of 1.5 to 8 nm but it is also possible to measure the relative orientation of the paramagnetic centres (59, 135). At X-band (9.7 GHz) the anisotropic nitroxide EPR spectrum (Figure 4.1.1 a) is not resolved with respect to the  $g$ -matrix and only partially with respect to the  $^{14}\text{N}$  hyperfine coupling matrix orientations, which makes orientation selection in PELDOR rather weak.

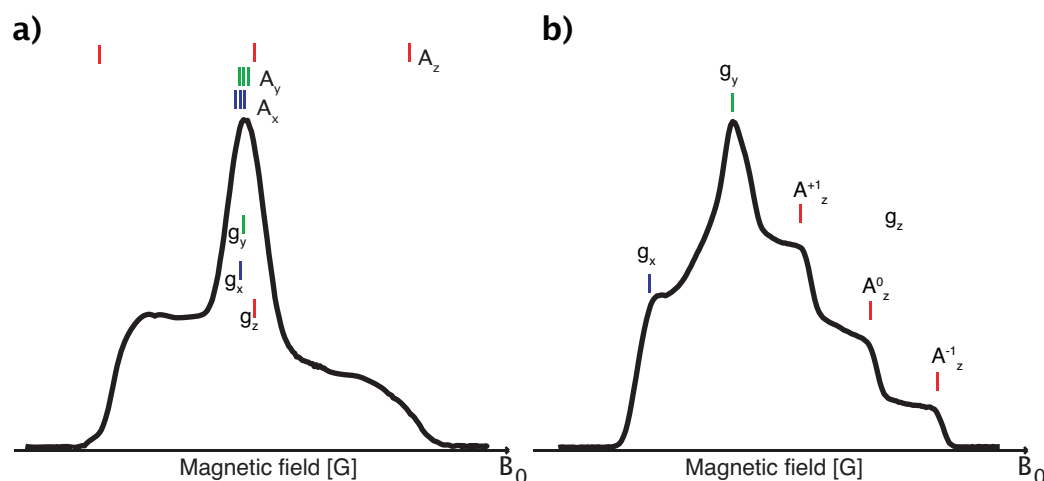


**Figure 4.1.1.** Two-pulse detected field swept EPR spectra. **a)** X-band nitroxide EPR spectrum. Colored sticks indicate the field positions of the  $g$ - and  $^{14}\text{N}$  hyperfine coupling matrix components. **b)** W-band nitroxide EPR spectrum. Colored sticks indicate the field positions of the  $g$ - and  $^{14}\text{N}$  hyperfine coupling matrix components.

The most widely used nitroxide spin label MTSSL (Figure 1.3.1) has an inherent flexibility in the four atom linker (16) which gives a broad orientation and

distance distribution unless the spin label has restricted motion at the spin labelling site as was e.g. demonstrated on the potassium ion channel (136) and the *Shigella flexneri* Spa15 chaperone (137). Nitroxide spin labels with restricted inherent flexibility have been developed and used with PELDOR at X-band to obtain information on spin label orientation and conformational distribution. Examples are DNAs spin-labelled with the rigid spin label **Ç** (120, 138, 110) and copper nitroxide biradical model systems (139, 140). A spin label for protein systems that has the potential to yield information on orientation from PELDOR at X-band is the RX spin label, which is attached to proteins via two linkers. The lab of Hubbell recently demonstrated the greatly reduced mobility of this label and applied it to measurements of protein dynamics and distances (141, 76).

Working at higher frequencies results in an EPR spectrum with increased resolution. At W-band (94 GHz) (135, 142-144) or 180 GHz (G-band) (59, 110, 145) the **g**-matrix orientations become better resolved (Figure 4.1.1 b) and as a result orientation selection in PELDOR measurements is increased. To date, most high-frequency spectrometers that are being used have the disadvantage of low microwave power, which decreases the modulation depth of PELDOR time traces. In addition, because of the low microwave power that is available relatively high Q single-mode resonators have to be used to increase the sensitivity. This limits the available bandwidth of the spectrometer, frequency separation between inversion and detection pulses and hence the possibility to excite a full set of orthogonal orientations. A promising way to gain increased bandwidth from high Q resonators is to use bimodal resonators with separate modes that can be individually tuned for the inversion and detection pulses. Bennati and coworkers recently demonstrated PELDOR measurements at W-band using a home-built bimodal resonator (142).

In this study a home-built W-band pulse EPR spectrometer (HiPER) with 1 kW microwave power and a flat 1 GHz instantaneous bandwidth (146) was used for PELDOR measurements on three bisnitroxide model systems (Figure 4.1.2). Bisnitroxide **17** and similar compounds are known to be semi-flexible and to contain negligible exchange coupling (140, 128). Bisnitroxides **18** and **19** are

known to have a fairly rigid structure and a small exchange coupling (46). These three compounds, therefore, serve as good model systems for determination of molecular structure, flexibility and exchange coupling. It is shown here that HiPER makes it possible to obtain PELDOR data with high orientation selection and large modulation depths. Since the PELDOR modulation contains information on the dipolar coupling it is important for the sensitivity of PELDOR to have a deep modulation depth. A measurement methodology is demonstrated which yields a set of PELDOR time traces from which a highly constrained data set is obtained. A detailed insight into the conformational flexibility and exchange coupling of the bisnitroxide model systems is obtained from simulations of the PELDOR time traces. This study demonstrates that W-band PELDOR has the potential to be an accurate and quantitative tool for the assessment of relative orientations of nitroxide spin labels, which can be correlated to the structure and dynamics of the underlying biological system.

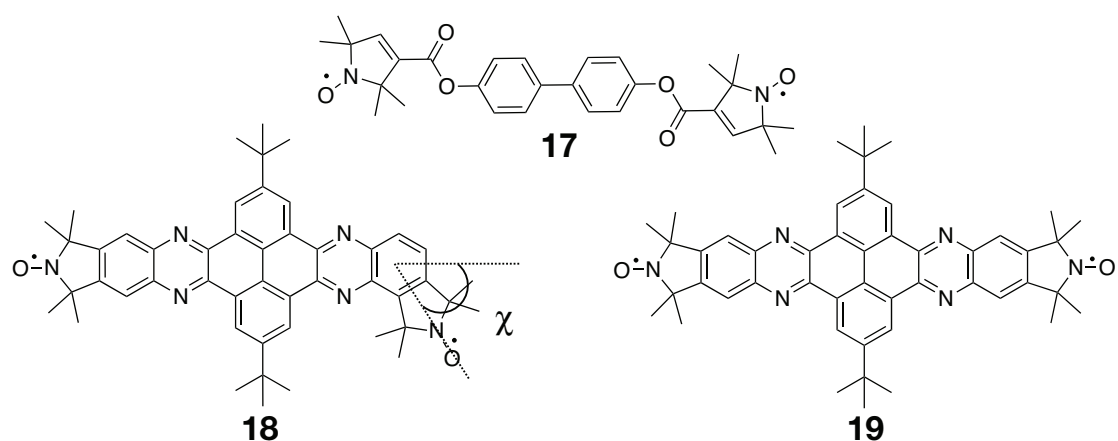


**Figure 4.1.2.** Structure of nitroxide biradicals **17** - **19**. For **18**,  $\chi$  denotes the angle between the nitroxide  $g_x$  components. The synthesis of these bisnitroxides has been previously described (140, 46).

## 4.2 Materials and methods

### 4.2.1 Sample preparation

Biradical **17** (100  $\mu\text{M}$ ) was dissolved in molten d14 o-terphenyl obtained from Chem Service (98% $\text{C}$ ). The synthesis of **17** has been described elsewhere (140). Biradicals **18** and **19** (100  $\mu\text{M}$ ) were dissolved in d-8 toluene obtained from Cambridge Isotope Laboratories Incorporation (99.5%). The samples ( $\sim 50 \mu\text{L}$ ) were shock-frozen in liquid nitrogen before loading into the spectrometer. The synthesis of **18** and **19** have been described elsewhere (46).

### 4.2.2 Pulse EPR measurements

Pulse EPR measurements were recorded using a home-built W-band EPR spectrometer using a non-resonant sample holder operating in reflection and induction mode, which has been described before (146). All frequency, phase and pulse control of both inversion and detection frequencies is performed at frequencies near 7.8 GHz, before multiplication to 94 GHz and amplification to beyond 1 kW. The frequency of both low noise inversion and detection pulse sources may be separately phase locked at any frequency within a 1 GHz bandwidth at W-band, which allows complete coverage of the nitroxide spectrum. Phase coherent, heterodyne detection of the detection pulse frequency is performed with an IF frequency of 1800 MHz, with excellent electronic phase stability. The inversion pulse source is not phase related to the local oscillator. High power amplification is performed using an Extended Interaction Klystron Amplifier (EIKA) (CPI, Communications & Power Industries) operating at 94 GHz with a 1 GHz instantaneous bandwidth. Power is transmitted to the sample and to the detector through low loss quasi-optics, where free space isolators provide  $> 90 \text{ dB}$  isolation between source and sample and  $> 70 \text{ dB}$  isolation between sample and detector. The sample is contained in a 3 mm O.D., 2.5 mm I.D. quartz tube that is placed within a non-resonant sample holder that is designed to be pre-cooled and permit cold sample loading. High isolation ( $> 40 \text{ dB}$ ) between source and detector is maintained by operating in induction mode. The sample is irradiated by a single linear polarisation and the orthogonal polarisation is detected. This technique also allows conventional, very fast (ns), low power (few



Watt) switches to be used for receiver protection. For measurements at cryogenic temperatures a continuous flow helium cryostat (CF935) and a temperature control system (ITC 502) from Oxford instruments were used. All pulsed experiments were performed at 50 K. The PELDOR experiments were done using the 4 pulse sequence,  $\pi/2(\nu_A) - \tau_1 - \pi(\nu_A) - (\tau_1+t) - \pi(\nu_B) - (\tau_2-t) - \pi(\nu_A) - \tau_2 - echo$ . The length of the  $\pi/2$  and  $\pi$  detection pulses ( $\nu_A$ ) were 8 and 16 ns respectively. The length of the inversion pulse ( $\nu_B$ ) varied between 14 and 21 ns, depending on sample and field position. The time delay between the first two detection pulses ( $d_1$ ) was set to 300 ns. The inversion pulse position was incremented by 5 ns. The sequence repetition rate was 2.5 KHz with 3000 shots per point. Interferences from  $^{14}\text{N}$  nuclear modulations, which might be expected and that would show up predominately at the end of the time trace, were not discernible in neither the PELDOR time traces nor the Fourier transformed time traces, and indeed have not yet been seen in any PELDOR experiments using this instrumentation. Each PELDOR time trace for biradicals **17**, **18** and **19** was measured in approximately 30 minutes.

#### 4.2.3 Data analysis and simulations

A three dimensional homogeneous background model was fitted and subtracted from the experimental PELDOR time traces using DeerAnalysis 2011. The starting time for the background fit was adjusted to minimize any singularity in the dipolar spectrum at zero frequency. The orientation averaged PELDOR time traces were constructed by normalising the original time traces and summing them up. This is also a common strategy for orientation selected NMR residual dipolar coupling patterns (147).

#### 4.2.4 Molecular modelling

Geometry optimised structures of biradicals **17-19** were obtained using density functional theory (DFT) as implemented in the program Orca (148). DFT calculations were done using the B3LYP functional and 6-31G\* basis set (149).

#### 4.2.5 CW-EPR simulations

The W-band CW-EPR spectra recorded of **17-19** were simulated using the program EasySpin (133). All spectra were simulated without including dipolar or exchange couplings.

#### 4.2.6 PELDOR simulations

PELDOR time traces were simulated with a home-written Matlab® program (Chapter 3). The biradicals were represented by vector models, from which the distance distribution and PELDOR time traces were calculated. The uncertainty in simulation parameters was assessed qualitatively by varying each simulation parameter individually. The difference in a parameter value giving noticeably different simulations was assigned as the error for that variable.

## 4.2.7 Original PELDOR time traces

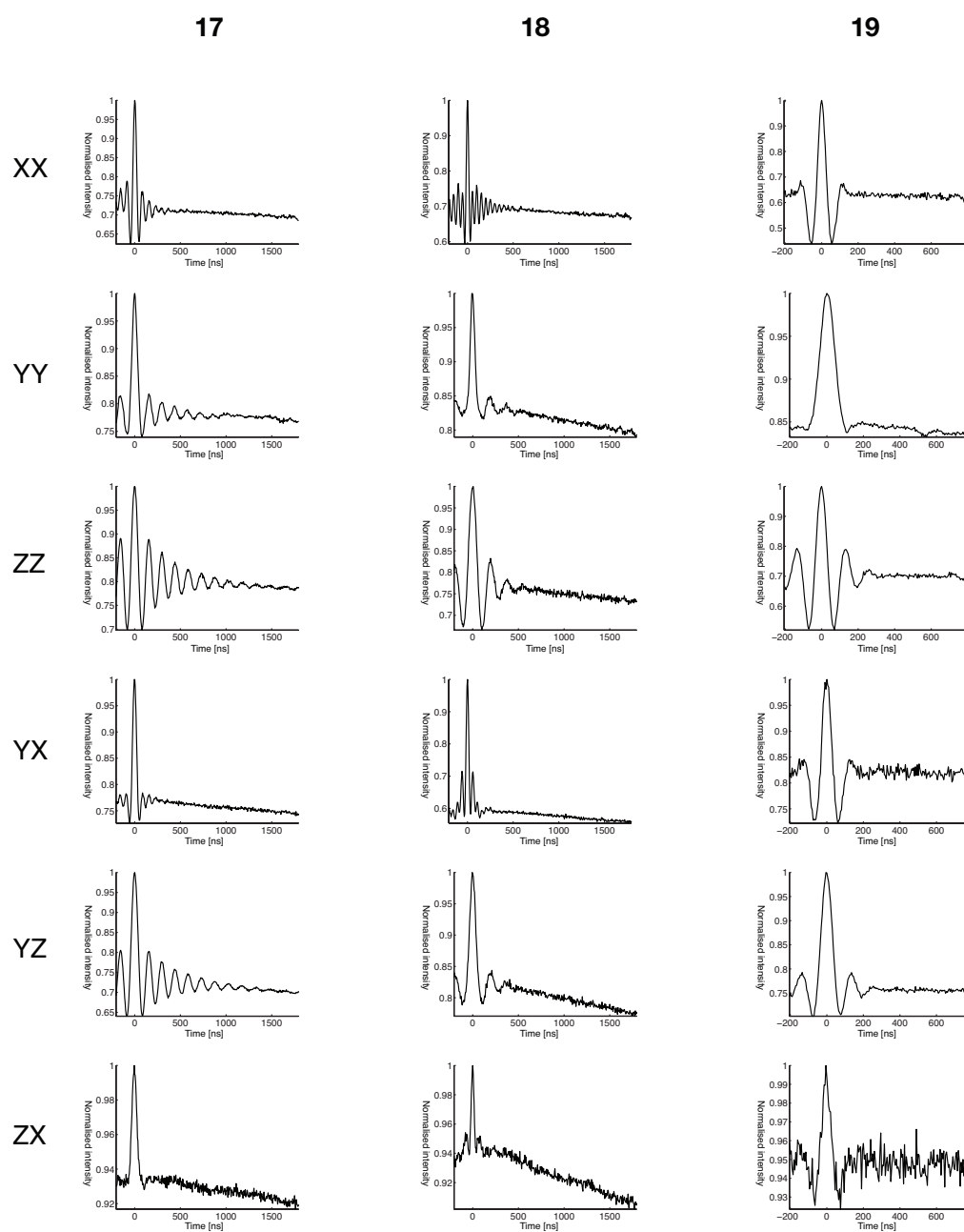


**Figure 4.2.1.** Experimental PELDOR time traces for compounds **17-19** before background correction. ZX denotes inversion pulse on  $g_z$  and detection sequence on  $g_x$  etc. The time traces are normalized with respect to maximum intensity.

## 4.3 PELDOR measurements on bisnitroxide model systems

### 4.3.1 CW-EPR measurements

To confirm the purity and assess the EPR parameters of the bisnitroxides continuous wave-EPR (CW-EPR) spectra at 110 K were recorded of all three bisnitroxide samples using HiPER (Figure 4.3.1). A typical W-band nitroxide EPR

spectrum was obtained from all three compounds with no discernible splittings from dipolar- or exchange couplings. The CW-EPR spectra were simulated to obtain principal values of the  $\mathbf{g}$ - and  $^{14}\text{N}$  hyperfine coupling matrices and linewidths to use for the simulation of PELDOR time traces. Table 4.3.1 summarizes the parameters obtained from the EPR simulations.

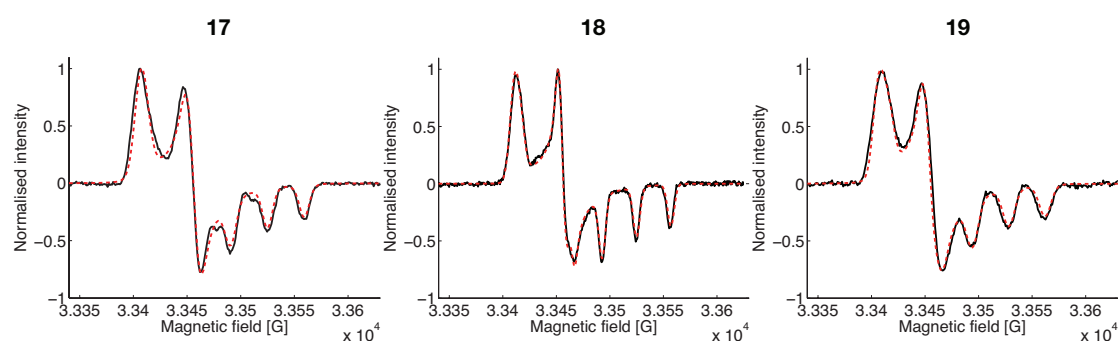


**Figure 4.3.1.** W-band CW-EPR spectra of **17**, **18** and **19** at 110 K (solid black) with simulations overlaid (dashed red).

**Table 4.3.1.** Parameters used for the simulations of the cw EPR spectra of compounds **17-19**.

Parameters	<b>17</b>	<b>18</b>	<b>19</b>
$g_{xx}, g_{yy}, g_{zz}$ <sup>[a]</sup>	2.0104, 2.0073, 2.0033	2.01, 2.0072, 2.0033	2.0101, 2.0073, 2.0031
g-strain <sup>[b]</sup>	0.0004, 0.0003, 0.0001	0.0005, 0.0002, 0.0003	0.0003, 0.0003, 0.0005
$A_{xx}, A_{yy}, A_{zz}$ <sup>[c]</sup>	8, 6, 96	10, 12, 90	16, 13, 95
A-strain <sup>[d]</sup>	0, 0, 12	5, 0, 5	1, 1, 5
Linewidth <sup>[e]</sup>	0.8, 0.13	0.4, 0.02	0.7, 0.11

[a] The absolute values for the principal g-values are not precise since a precise value for the static field was not known. [b, d] The g-strain is given in absolute values and A-strain in MHz. The strain is listed in the following order, (x, y, z). [c] The  $^{14}\text{N}$  hyperfine coupling values are in MHz. [e] The linewidths (Gaussian, Lorentzian) is the peak to peak linewidth in mT.

#### 4.3.2 PELDOR measurements

When the NO-bond of the nitroxide is oriented parallel to the magnetic field  $\mathbf{B}_0$  the nitroxide is said to be oriented in the x-direction. When  $\mathbf{B}_0$  is oriented orthogonal to the plane of the five-membered ring system the nitroxide is

oriented in the z-direction and in the y-direction when  $\mathbf{B}_0$  is orthogonal to both the x- and z-directions. This convention can be rationalized by observing the orientation of the  $\mathbf{g}$ -matrix relative to the nitroxide molecule (Figure 4.3.2, inset).

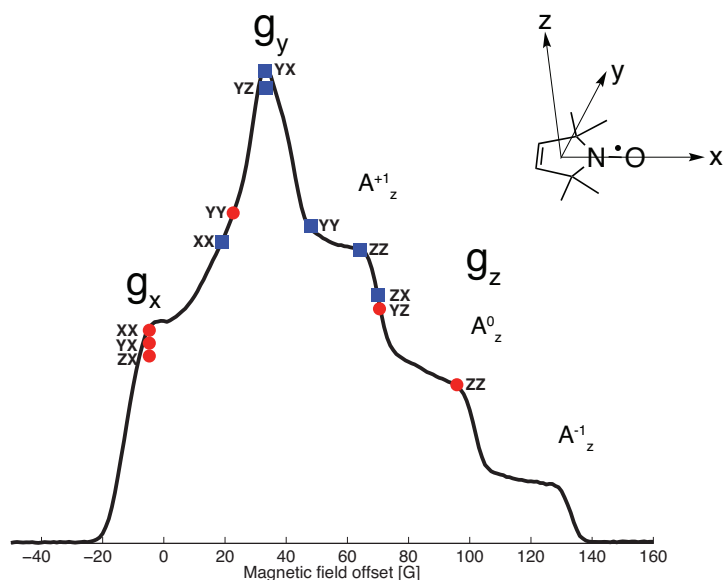


**Figure 4.3.2.** An echo detected field sweep of 17. Red dots and blue squares show the positions of the PELDOR detection and inversion pulses, respectively. The dots and squares are labelled with their respective PELDOR experiment. The inset shows a nitroxide and the relative orientation of the  $\mathbf{g}$ -matrix illustrated by arrows.

At W-band frequencies, the nitroxide  $\mathbf{g}$ -matrix becomes sufficiently resolved so that it becomes possible to selectively excite nitroxides with specific orientations. Thus, by exciting the  $A$  spins of nitroxides oriented in a particular direction via the detection pulse sequence and then monitor the effect of inverting the  $B$  spins of nitroxides oriented in the same or an orthogonal direction one obtains orientation selective PELDOR experiments with a modulation depth that is determined by the fraction of  $B$  spins that were excited by the inversion pulse. The frequency and decay rate of the PELDOR modulation is determined by the distribution of distances between coupled spins and the distribution in orientations of spin labels relative to the magnetic field  $\mathbf{B}_0$ . In this study, six separate PELDOR experiments were recorded to correlate pairs of  $A$  and  $B$  spins that are oriented in the x-, y-, or z-direction with respect to the magnetic field  $\mathbf{B}_0$ . Therefore, six inversion/detection PELDOR correlation measurements labelled as XX, YY, ZZ, YX, YZ and ZX are described for each

bisnitroxide, where for example ZX means that the inversion pulse excites spins that are oriented in the z-direction and the detection sequence excites spins oriented in the x-direction. It was also determined using HiPER and these bisnitroxides that this particular set of six PELDOR experiments gives a highly constrained data set for the determination of relative spin label orientation.

In order to know where to place the detection and inversion pulses on the nitroxide EPR spectrum an echo detected field swept spectrum of each bisnitroxide was recorded (Figure 4.3.2). Because HiPER does not use a resonator (works in reflection mode) it is not limited by the band-width of a resonator. This allows one to position the PELDOR inversion and detection pulses at any field position on the nitroxide spectrum and to measure not only the correlation between the XX, YY and ZZ orientations but also the cross-correlations XY, XZ and YZ which need a large frequency difference between the inversion and detection pulse, e.g. 210 MHz for XZ.

The set of six PELDOR time traces with these different inversion/detection combinations for each of the three biradicals are shown in figure 4.3.3 a, d, g. The 1 kW microwave power of HiPER and its high sensitivity made it possible to acquire PELDOR time traces with an average signal-to-noise ratio (S/N) of 100 in about 30 minutes. The time traces have a modulation depth as large as 40%, this is close to the 50% modulation depth that can be obtained from X-band measurements (140, 46) and also considerably larger than the 6% modulation depth that is obtained from W-band PELDOR on a power-upgraded Bruker Elexsys 680 spectrometer using either a single or dual mode cavity (135, 142). The modulation depth obtained here using HiPER is also larger than the 20% modulation depth achieved with a home-built spectrometer (150). Because the bisnitroxide samples used in this study are not strictly identical to the ones used for the other studies in the above comparison of maximum modulation depth, it should be kept in mind that the observed PELDOR modulation depth also depends on the relative orientation and degree of correlation between the coupled spin centres. A detailed analysis of the PELDOR time traces obtained for the bisnitroxides **17-19** is discussed below.

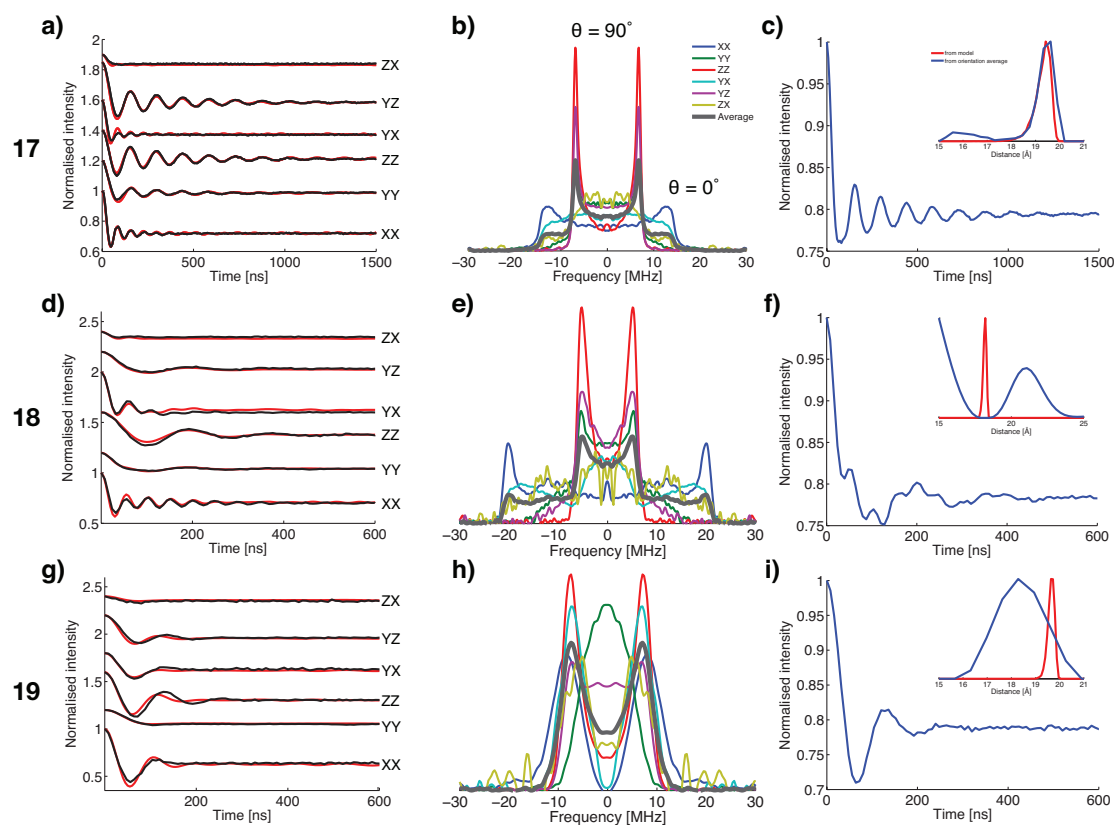


**Figure 4.3.3.** PELDOR data for compounds **17-19**. **(a,d,g)** Background corrected time traces (black) with simulated time traces overlaid (red). ZX denotes inversion pulse on  $g_z$  and detection sequence on  $g_x$  etc. The time traces are displaced on the y-axis for clarity. **(b,e,h)** Fourier transformed spectra of the six individual time traces, plus the Fourier transformation of their sum (black line). **(c,f,i)** Sum of all time traces and distance distribution from simulation (red) and summed time trace (blue).

### 4.3.3 Biradical **17**

The PELDOR time traces obtained for **17** show a large variation in the frequency and depth of the PELDOR modulation. This is a consequence from the high degree of orientation selection obtained at W-band frequencies (Figure 4.3.3 a). From the dipolar spectra (Fourier transformed time traces), a qualitative picture is obtained of the spin label orientations relative to the interspin vector. The largest selection of the parallel ( $\theta = 0^\circ$ ) and perpendicular ( $\theta = 90^\circ$ ) dipolar components is obtained with the XX and ZZ experiments, respectively. This indicates that the nitroxide  $g_x$  and  $g_z$  matrix components are largely oriented parallel and perpendicular respectively, to the interspin vector or the molecular backbone, since it is approximately parallel to the interspin vector (Figure 4.1.2). One nitroxide (spin A) must, therefore, have its  $g_x$  matrix component largely oriented perpendicular to the  $g_z$  matrix component of the other nitroxide within

the same biradical (spin  $B$ ). This is also supported by the negligible modulation in the ZX experiment (Figure 4.3.3 a). In order to characterize the mutual orientation and inherent flexibility of the nitroxide spin labels in a more quantitative manner the PELDOR time traces were simulated with a lab-written Matlab® program (Chapter 3) that is based on an approach published by Prisner and coworkers (128). The first step is to obtain a geometry-optimised structure of **17** from density functional theory (DFT) calculations. Measuring the lengths of the molecular linker and nitroxide moieties from the geometry-optimised structure then yields a set of initial geometric values for the construction of a vector model where each nitroxide, including the ester group, and the connecting bridge were represented by three independent vectors (Figure 4.3.4 a).

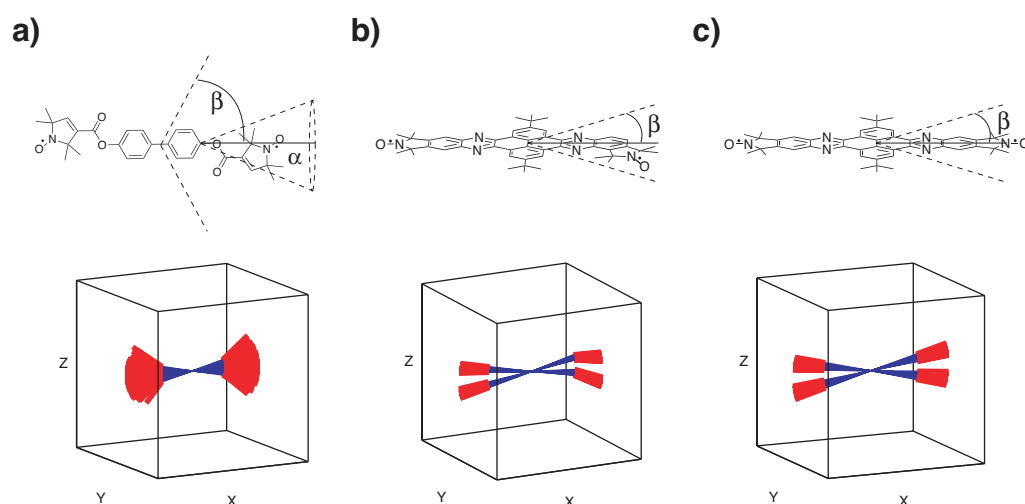


**Figure 4.3.4.** (a-c) Structures and corresponding geometrical vector models used in the simulation program for biradicals **17** to **19**, respectively. Blue lines represent the connecting bridge. Red lines represent the nitroxide moieties including the ester groups. Each model shows the conformations of 20 conformers. The molecular flexibility is described by the backbone bending angle  $\beta$  and the flexibility of the nitroxide moiety by the cone angle  $\alpha$ .

In this vector model for **17** the two nitroxide groups were allowed to have a free rotation around the phenolic bond with the N-O bond ( $g_x$  matrix component) moving on a cone with a mean opening angle of  $25^\circ$ . The  $g_z$  and  $g_y$  matrix components have a random position in the zy-plane. A bending motion with a single normal distribution was used to model the flexibility of the molecular linker about the biphenyl bond (Figure 4.3.4 a). Generating an ensemble of conformers and measuring the distance between the nitroxide spin centres



(defined as the center of the N-O bond) for each conformer yields a simulated distance distribution that can be compared to the distance distribution obtained from the PELDOR experiments. PELDOR time traces were simulated using the spin Hamiltonian parameters, obtained by simulating the CW-EPR spectrum of **17** (Table 4.3.1), and the geometrical parameters from the geometry optimised structure of **17**. The values for the cone angle ( $\alpha$ ) and flexibility of the molecular linker ( $\beta$ ) were iterated until one set of values gave a good fit between all six simulated and experimental PELDOR time traces. The geometric parameters that yielded simulations with the best fit to the experimental time traces (Figure 4.3.3 a) are summarized in Table 4.3.2. The simulated mean distance of 19.3 Å is in good agreement with the static distance of 19.8 Å obtained from the geometry-optimised structure. The value for the cone angle and linker flexibility determined from the PELDOR simulations is in good agreement with results from previous X-band PELDOR studies on analogues nitroxide biradical systems (139, 140, 128). It was not possible to find an alternative set of geometric parameters (Table 4.3.2) with the same quality of global-fit to all six PELDOR time traces using this model-based simulation. The obtained solution is, therefore, believed to be unique.

**Table 4.3.2.** Structural parameters determined from DFT calculations, PELDOR measurements and simulations.

Biradical	$r_{\text{DFT}}$ [Å] <sup>[a]</sup>	$r_{\text{PELDOR}}$ [Å] <sup>[b]</sup>	$\alpha$ [°] <sup>[c]</sup>	$\beta$ [°] <sup>[d]</sup>	$\chi$ [°] <sup>[e]</sup>
<b>17</b>	19.8	19.30 ± 0.68 (0.15, 0.01)	25 ± 10 (3, 2.5)	0 ± 10 (5, 2.5)	-
<b>18</b>	18.4	18.04 ± 0.26 (0.03, 0.01)	-	10 ± 5 (4, 1.4)	60
<b>19</b>	20	19.70 ± 0.30 (0.03, 0.01)	-	10 ± 5 (3, 1.5)	0

[a] Interspin distances obtained from DFT calculations. The interspin distance was measured between the centres of the N-O bonds. [b] The distance distribution obtained by simulation of the PELDOR time traces is represented as a mean value ± two standard deviations. The error of the mean value, standard deviation is in brackets. The width of the distance distribution is defined as two times the standard deviation. [c] The angle of the cone  $\alpha$  is given as a normal distribution with mean value ± two standard deviations. The error of the mean value, standard deviation is in brackets. [d] The bending of the backbone  $\beta$  is given as a normal distribution with mean value ± two standard deviations. The width of the bending is defined as two standard deviations. The error of the mean value, standard deviation is in brackets. [e] For **19**, the angle between the  $g_x$  components  $\chi$  is defined as 0°.

If the orientation correlation of coupled spin centres is negligible or very weak, the distance distribution can be easily obtained from the background subtracted time trace using Tikhonov regularization, which is implemented into the program DeerAnalysis (123). Since the time traces for **17** show a strong orientation selection, which indicates a strong correlation in spin label orientation, they cannot be treated individually in DeerAnalysis to obtain the distance distribution. Adding together the six time traces yields a good approximation to an orientation averaged time trace (151). This orientation averaged time trace can then be converted to the distance-domain using Tikhonov regularization. This is demonstrated for **17** in figure 4.3.3 c. The distance distribution from the orientation averaged time trace is in very good agreement with the distribution from the simulated molecular conformer ensemble, apart from a small broad peak at 15-17 Å. An interspin distance in this range would correspond to very unlikely molecular conformers. This peak is, therefore, attributed to artefacts due to incomplete orientation averaging (151).

#### 4.3.4 Biradicals **18** and **19**

A set of six PELDOR experiments was recorded for biradicals **18** and **19** at approximately the same field positions as for **17** (Figure 4.3.3 d, g). The time traces for **18** show a large variation in modulation frequency and depth depending on pulse positions. The most prominent modulation is seen for the XX, ZZ and YX experiments (Figure 4.3.3 d). The dipolar spectra for the XX and YX experiments show an intense parallel component while the ZZ experiment shows an intense perpendicular component (Figure 4.3.3 e). From these observations it can be inferred that the  $g_x$  and  $g_y$  matrix components are mostly parallel to the molecular linker and the  $g_z$  matrix component is perpendicular to the molecular linker. However, unlike for **17**, any interpretation from the time traces has to be done with care as the dipolar spectra show that the modulation frequencies of the parallel and perpendicular components are not consistent with a simple dipolar model where  $\nu_{\parallel} = -2\nu_{\perp}$  but the need for including an exchange coupling term into the analysis. This also does not come as a surprise as it was previously determined at X-band that **18** and **19** are exchange coupled systems (46). To obtain the distance distribution and quantify the relative spin label orientation

and conformational distribution, the PELDOR time traces for **18** were simulated using the Hamiltonian parameters obtained from CW-EPR simulations (Table 4.3.1), geometric parameters from a geometry-optimised structure (Figure 4.1.2) and taking into account an exchange coupling constant,  $J$  (Figure 4.3.3 d). The lengths of the nitroxide moieties, molecular linker and angles as obtained from the geometry-optimized structure of **18** were used as initial mean values for the construction of a simple vector model (Figure 4.3.4 b). One nitroxide was aligned such that its  $g_x$  matrix component was parallel to the molecular linker and the  $g_x$  and  $g_y$  matrix components of the other nitroxide were rotated  $60^\circ$  about its  $g_z$  matrix component. The  $g_z$  components of both nitroxides were perpendicular to the molecular linker. The molecular backbone that includes the nitroxide moieties was allowed to have a discrete and normally distributed bending motion in the molecular  $zx$  plane and about the center of the molecule. Such bending motion has also been observed by X-ray crystallography of analogue molecules (152). Including an exchange coupling of  $-3.2 \pm 0.8$  MHz and a discrete molecular bending of  $\pm 10^\circ$  resulted in the best fit between simulated and experimental PELDOR time traces. The exchange coupling is in excellent agreement with the value determined at X-band (46). In order to simulate the observed modulation depth of all six time traces for **18** and **19** (see below) it was necessary to include a discrete bending motion of the molecule into the vector model. At X-band (46) a bending of  $\pm 5^\circ$  was only included to rectify the observed distribution in  $J$ , which was required to fit the decay of the time traces. The increased orientation selection at W-band and the possibility to probe different orientation correlations with HiPER verifies and gives a more quantitative picture of this bending mode. The distance distribution obtained from the simulated ensemble of molecular conformers has a mean distance of  $18.04 \text{ \AA}$ , in agreement with the distance from the geometry-optimised structure (Table 4.3.2). The dipole-dipole coupling  $\nu_{AB}$  and exchange coupling constant  $J$  can be extracted from the dipolar spectra using equations 4.3.1 and 4.3.2 (46).

$$\nu_{AB} = \frac{\nu_{\perp} - \nu_{\parallel}}{3} \quad (4.3.1)$$

$$J = \frac{2\nu_{\perp} + \nu_{\parallel}}{3} \quad (4.3.2)$$

Since the perpendicular  $\nu_{\perp}$  and parallel  $\nu_{\parallel}$  frequency singularities of the dipolar spectrum can be either read of as a positive or negative frequency  $J$ ,  $\nu_{AB}$  and hence the interspin distance  $r$ , could have more than one possible solution. In the X-band study of **18** it was difficult to distinguish between two sets of solutions for  $r$  and  $J$  (46). To see if the W-band PELDOR data makes it possible to find only one set of  $r$  and  $J$ , that results in simulations with a good fit, the HiPER PELDOR time traces were simulated with both solutions sets determined at X-band (46). One of these solution set is in agreement with the values used for the simulations in figure 4.3.3 d, but the other solution set has an exchange coupling constant of -10.5 MHz and an interspin distance of 20.7 Å (46). Using this latter set did not result in simulations with good fits to any of the six W-band time traces (Figure 4.3.5). These results show that the higher degree of orientation selectivity at W-band makes it easier to determine a unique set of values for the exchange coupling and interspin distance.

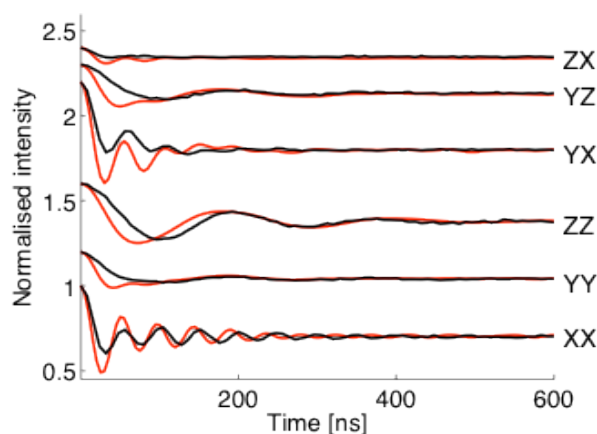


**Figure 4.3.5.** Experimental (solid black) and simulated (dashed red) time traces for bisnitroxide **18**. The simulated time traces were calculated using an interspin distance of 20.7 Å and exchange coupling of -10.5 MHz

Analysing the orientation averaged time trace of **18** using DeerAnalysis yields a broad distance distribution with two major distances. Comparing the distance distributions from the orientation average and simulated conformers ensemble

shows that there is no agreement (Figure 4.3.3 f). The large discrepancy between the distance distributions is caused by the inherent exchange coupling which is not accounted for in DeerAnalysis.

As was done for **18**, the PELDOR time traces for **19** were simulated using spin Hamiltonian parameters obtained from CW-EPR simulations and the same vector- and dynamics model that was used to simulate the PELDOR time traces of **18** with the only exception that the two nitroxide  $g_x$  matrix components are antiparallel (Figure 4.3.4 c). Including an exchange coupling constant of  $2.5 \pm 1.7$  MHz, as was determined from the X-band study (46), resulted in the best overall fit to the experimental data (Figure 4.3.3 g). The distance distribution obtained from the simulated conformational ensemble has a mean value of  $19.7 \text{ \AA}$ , in agreement with the distance from the geometry-optimised structure of **19** (Table 4.3.2). The distance distribution from the orientation averaged time trace of **19** gives a single distance with a broad distribution that does not agree with the simulated distance distribution (Figure 4.3.3 i). Again, this is most likely due to the inherent exchange coupling which is not accounted for in DeerAnalysis.

The time traces for **19** do not show the same amount of difference in modulation frequency as biradical **18** (figure 4.3.3 g). This is also evident from the dipolar spectra that don't show a clear distinction between the parallel and perpendicular components (Figure 4.3.3 h). This was also observed in the X-band study and was attributed to the overlap of the parallel and perpendicular component due to the presence of an exchange coupling (46). This made it impossible to distinguish between two solutions for  $r$  and  $J$  via simulations (46). One solution set had  $r$  approaching infinity and  $J = \pm 8.3$  MHz while the other had the same values as used for the simulations of the W-band time traces Figure 4.3.3 g). Using an interspin distance of  $10 \text{ m}$  (as an approximation for infinity) and an exchange coupling of  $\pm 8.3$  MHz as initial values for the simulations of the W-band time traces yielded simulations with worse fit to the experimental time traces, particularly for the YY and YZ experiments (Figure 4.3.6).

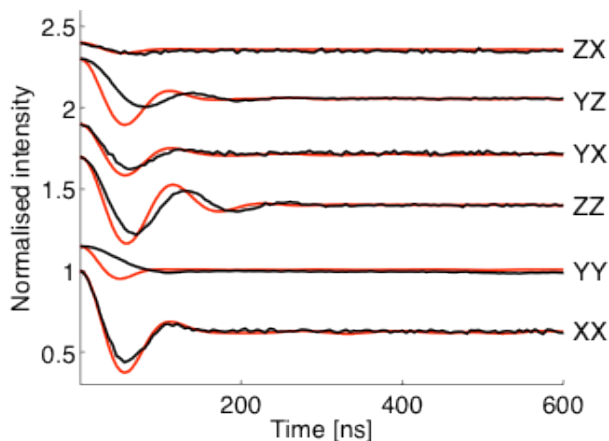


**Figure 4.3.6.** Experimental (solid black) and simulated (dashed red) time traces for bisnitroxide **19**. The simulated time traces were done using an interspin distance of 10 m and an isotropic exchange coupling of 8.5 MHz (-8.5 MHz gives identical solutions).

These results also demonstrate that the higher degree of orientation selection at W-band makes it easier to distinguish between possible solutions sets for the exchange coupling and interspin distance.

#### 4.4 Summary

To summarise, this study has shown that by using a 1 kW microwave power EPR spectrometer operating in reflection mode, it is possible to obtain high sensitivity orientation selective PELDOR time traces that can be quantitatively modelled to provide accurate information on the relative orientation of spin centres and conformational distribution of both semi-rigid and exchange coupled rigid biradicals. Conformational flexibility of nitroxide spin labels and molecular linker measured for the semi-rigid biradical **17** was in very good agreement with that determined from structurally analogous biradicals at X-band frequencies (139, 128). It became possible to quantitatively determine the relative spin label orientation in biradicals **18** and **19** and specifically, the change in the orientation of the  $g_x$  and  $g_y$  matrix components was resolved, something that was not possible at X-band (46). In addition, the flexibility of the molecular linker in biradical **18** and **19** was quantitatively determined with less uncertainty than at X-band (46). The exchange coupling in **18** and **19** was separated from the W-band PELDOR time traces via simulations and a unique set of solutions for the interspin distance and exchange coupling was determined with less ambiguity

than at X-band. Acquiring PELDOR with the HiPER spectrometer offers the possibility to probe the correlation between all principal **g**-matrix components and makes it possible to acquire a detailed and quantitative description of spin label orientation and conformational distribution on a set of semi-rigid and rigid nitroxide biradicals.

#### **4.5 Acknowledgment**

I would like to thank Dr. Robert I. Hunter for his help with the operation of the spectrometer and acquiring the PELDOR experiments and Dr. Hassane El Mkami for his assistance with the W-band CW-EPR measurements.

## **5 DNA structure and dynamics observed with PELDOR and noncovalent site-directed spin labelling**

### **5.1 Introduction**

Biological functions of nucleic acids include information storage, translation, transcription and protein synthesis from genetic information. Furthermore, DNA has the potential to become important for digital information storage (153). These complex roles of nucleic acids in biological processes is greatly determined by their inherent structure and conformational flexibility. Understanding the structure-function relationship, therefore, requires determining the structure and conformational flexibility of nucleic acids and their complexes with proteins and small molecules. Expression of genes is regulated by controlled transcription and translation. This is achieved by sequence-specific binding of DNA by proteins. Binding of DNA to proteins have been studied using several techniques, such as foot printing (154), photochemical cross-linking (155) and various spectroscopic approaches (156). The interaction between DNA and proteins can lead to major conformational changes (157, 158) and studying the rearrangements in molecular details requires high-resolution techniques, such as X-ray crystallography (159) or NMR spectroscopy (160, 161). Obtaining high-resolution structures of nucleic acid-protein complexes is in most case not straightforward and static crystal structures give limited information on the dynamics that could have a role in gene regulation mechanisms (162). Structural studies in solution have been performed through long-range distance measurements using fluorescence resonance energy transfer (FRET) but this technique is limited by the uncertainty in orientation of the dyes (5). On the other hand, the use of rigid spin labels and EPR enables measurements of accurate distances and orientation information on frozen samples (163).

Site-directed spin labelling of nucleic acids by nitroxide spin labels has successfully been used to obtain information on dynamics and structure via continues wave (CW)- and pulsed EPR techniques (164, 165). A complicating factor of most nitroxide spin labels is the large inherent flexibility of the linker used to attach the spin label to the nucleotides. To obtain precise information on



dynamics and distances between spin-labelled sites on nucleic acids, the conformational flexibility of the spin label has to be kept to a minimum. The rigid spin label  $\zeta$  (Figure 1.3.2 and Chapter 2) which is a cytidine analogue fused to a nitroxide has been shown to yield precise distance measurements and information on subtle dynamics of DNA (120, 108, 119, 166, 167, 110) due to the restricted flexibility of the nitroxide moiety. However, spin labelling DNA with  $\zeta$  requires elaborate organic synthesis since the spin label needs to be incorporated during DNA synthesis. This greatly hampers the wide application of site-directed spin labelling by  $\zeta$  to nucleic acids for structure determination. To simplify site-directed spin labelling of nucleic acids a non-covalent and site-directed spin labelling strategy (NC-SDSL) was developed (112), utilizing the rigid spin label  $\zeta$  (Figure 1.3.2 and Chapter 2) that binds to DNA abasic sites via hydrogen-bonding and stacking interactions. It was shown by CW-EPR that the  $\zeta$  spin label binds tightly to abasic sites in duplex DNA via non-covalent interactions to base-pairs flanking the abasic site and guanine (G) opposite the abasic site (Figure 5.1.1) (112, 168).

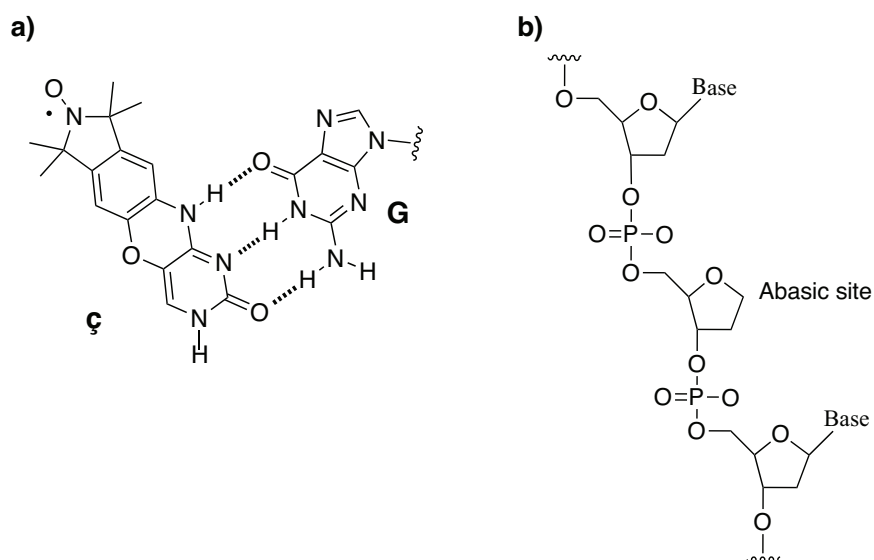


**Figure 5.1.1.** Molecular structure of  $\zeta$  spin label and DNA abasic site. **a)**  $\zeta$  spin label base-paired with Guanine. **b)** Structure of an abasic site in DNA.

DNA containing abasic sites at chosen positions are commercially available. Therefore, spin labelling nucleic acids by this NC-SDLS method is as simple as mixing spin label and DNA. In this study it is shown that the specificity and

binding efficiency of  $\zeta$  for abasic sites in duplex DNAs is high enough to yield PELDOR time traces with resolved modulation and orientation selectivity. Furthermore, the NC-SDSL method is applied to the DNA/Lac repressor system, enabling measurement of DNA bending and dynamics. This demonstrates that non-covalent spin labelling can also be performed in the presence of DNA binding proteins.

## 5.2 Materials and methods

### 5.2.1 General procedures

NaCl, and 2-(N-morpholino)ethanesulfonic acid (MES) (Fluka).  $\text{Na}_2\text{HPO}_4 \cdot 6 \text{H}_2\text{O}$ , ethanol and EDTA were obtained from Fischer Scientific. Ethylene glycol was obtained from Aldrich. Deuterated ethylene glycol (98%) and deuterium oxide (99%) was obtained from Cambridge Isotope Laboratories.

### 5.2.2 Synthesis and purification of DNA oligomers

29-mer  $\zeta$ -labeled DNA oligomers were synthesized and purified as previously reported (119). DNA oligomers containing abasic sites were synthesized by a trityl-off synthesis on a 1.0  $\mu\text{mol}$  scale (1000 Å CPG columns) using an automated ASM 800 Biosset DNA synthesizer and phosphoramidites with standard protecting groups. 1,2-dideoxy D-ribose CED phosphoramidite were used as a building block for abasic oligomer synthesis. The DNA oligomers were deprotected in concentrated ammonia solution at 55 °C for 8 h and purified by 20% denaturing polyacrylamide gel electrophoreses (DPAGE). The oligonucleotides were visualized by UV shadowing and the bands excised from the gel were crushed and soaked in TEN buffer (10 mM Tris pH 7.5, 250 mM NaCl, 1 mM  $\text{Na}_2\text{EDTA}$ ). The DNA elution solutions were filtered through a 0.45  $\mu\text{m}$  polyethersulfone membrane (disposable filter device from Whatman) and desalted using Sep-Pak cartridge (Waters Corporation) according to manufacturer's instructions. After removing the solvent under vacuum, the oligonucleotides were dissolved in de-ionized and sterilized water (200  $\mu\text{L}$ ). All commercial phosphoramidites, CPG columns and solutions for DNA synthesis were purchased from ChemGenes Corporation.

29-mer DNA oligomers containing 19-mer LacI operator sequence and abasic sites were purchased from Eurogentec. Purification was done with DPAGE and quality control by MALDI-TOF Mass spectrometry.

The concentration of DNA oligomers was calculated from Beer's law based on measurements of absorbance at 260 nm, using a 50 Bio UV-VIS spectrometer from Varian, equipped with a 100  $\mu$ L cell (optical path length = 1 cm). Extinction coefficients of DNA oligomers were determined, using the UV WinLab oligonucleotide calculator (V2.85.04, Perkin Elmer). ssDNA oligomers solutions (1  $\mu$ L) were dissolved in sterilized water (99  $\mu$ L) and transferred to spectrometer cell for measurements. Sterilized water was used as a reference sample. Evaporation of solvents under vacuum was carried out on a SPD 111V speed-vac from Savant equipped with a vapour trap and vacuum inversion. Preparation of all DNA samples for EPR measurements were done in sterile Biopur Eppendorf tubes (2 mL) with cap.

### 5.2.3 Hybridization of oligonucleotides

Hybridization of all DNA oligomers was performed with a PCH-2 heating block from Grant-bio. Complementary DNA strands were annealed according to the following program: 90 °C for 2 minutes, 60 °C for 5 minutes, 50 °C for 5 minutes, 40 °C for 5 minutes, 22 °C for 15 minutes. DNA samples were stored at -30 °C.

### 5.2.4 Preparation of **dsDNA 1**

Synthesized and purified DNA oligomers were reconstituted with sterile water in Biopur Eppendorf tubes (2 mL). Noncovalently spin-labelled DNA duplexes were prepared by mixing appropriate single-stranded DNA oligomers (5 nmol) with two equivalents of spin label **ç** dissolved in ethanol (10 nmol). The water/ethanol solution was evaporated under vacuum and the dry sample dissolved in phosphate buffer ( $\text{Na}_2\text{HPO}_4$  10 mM, NaCl 100 mM,  $\text{Na}_2\text{EDTA}$  0.1 mM, pH 7.00) (100  $\mu$ L). After annealing the DNA oligomers the solvent was removed under vacuum. The dry sample was dissolved in sterile water with 20% (v/v) ethylene glycol (100  $\mu$ L). All samples were transferred to a quartz EPR tube,

rapidly frozen in (1:4 methylcyclohexane:iso-pentane at -165 °C) and stored in liquid nitrogen.

#### 5.2.5 Preparation of **dsDNA 2**

29-mer DNA oligomers (4 nmol) were mixed with two equivalents of  $\zeta$  dissolved in ethanol (8 nmol) and annealed in phosphate buffer (Na<sub>2</sub>HPO<sub>4</sub> 10 mM, NaCl 100 mM, Na<sub>2</sub>EDTA 0.1 mM, pH 7.00) (100  $\mu$ L). The solvent was removed under vacuum and the dry sample dissolved in MES buffer (MES 20 mM pH 6.0, NaCl 300 mM, in <sup>2</sup>H<sub>2</sub>O) (80  $\mu$ L) and deuterated ethylene glycol (20  $\mu$ L). The sample was transferred to an EPR tube, rapidly frozen in freezing mixture and stored in liquid nitrogen.

#### 5.2.6 EMSA

Aliquots of LacI from *Escherichia coli* (150  $\mu$ M) in MES buffer (MES 20 mM pH 6.0, NaCl 300 mM, 50% in <sup>2</sup>H<sub>2</sub>O) were prepared. <sup>32</sup>P-labeled 29-mer dsDNA (50 nM) was incubated for 20 min. at room temperature with two equivalents of  $\zeta$  spin label and Lac repressor, titrated at 0.25, 0.5, 0.75, 1.25, 2.5, 5, and 12.5  $\mu$ M, in MES buffer (MES 20 mM pH 6.0, NaCl 300 mM, 100% in <sup>2</sup>H<sub>2</sub>O), before loaded onto 12% native acrylamide gel (90 mM Tris-Borate, 2 mM EDTA). Gel were run at 130V for 4 hours, exposed to phosphor imaging screen and visualized using a Fuji FLA5000 imager.

#### 5.2.7 Preparation of **dsDNA 2** with Lac repressor

29-mer DNA oligomers (4 nmol) were mixed with two equivalents of  $\zeta$  dissolved in ethanol (8 nmol) and annealed in phosphate buffer (Na<sub>2</sub>HPO<sub>4</sub> 10 mM, NaCl 100 mM, Na<sub>2</sub>EDTA 0.1 mM, pH 7.00) (100  $\mu$ L). The solvent was removed under vacuum and the dry sample dissolved in MES buffer (MES 20 mM pH 6.0, NaCl 300 mM, 50% in <sup>2</sup>H<sub>2</sub>O) containing Lac repressor (315  $\mu$ M) (80  $\mu$ L) and deuterated ethylene glycol (20  $\mu$ L). The sample was transferred to an EPR tube and rapidly frozen in freezing mixture approximately 10 min. after addition of LacI. The sample was stored in liquid nitrogen.

### 5.2.8 Preparation of **dsDNA 3**

29-mer DNA oligomers (4 nmol) spin-labelled with the  $\zeta$  spin label were annealed in phosphate buffer ( $\text{Na}_2\text{HPO}_4$  10 mM, NaCl 100 mM,  $\text{Na}_2\text{EDTA}$  0.1 mM, pH 7.00) (100  $\mu\text{L}$ ). The solvent was removed under vacuum and the dry sample dissolved in MES buffer (MES 20 mM pH 6.0, NaCl 300 mM, in  $^2\text{H}_2\text{O}$ ) (80  $\mu\text{L}$ ) and deuterated ethylene glycol (20  $\mu\text{L}$ ). The sample was transferred to an EPR tube, rapidly frozen in freezing mixture and stored in liquid nitrogen.

### 5.2.9 Preparation of **dsDNA 3** with Lac repressor

29-mer DNA oligomers (4 nmol) spin-labelled with the  $\zeta$  spin label were annealed in phosphate buffer ( $\text{Na}_2\text{HPO}_4$  10 mM, NaCl 100 mM,  $\text{Na}_2\text{EDTA}$  0.1 mM, pH 7.00) (100  $\mu\text{L}$ ). The solvent was removed under vacuum and the dry sample dissolved in MES buffer (MES 20 mM pH 6.0, NaCl 300 mM, 50% in  $^2\text{H}_2\text{O}$ ) containing Lac repressor (315  $\mu\text{M}$ ) (80  $\mu\text{L}$ ) and deuterated ethylene glycol (20  $\mu\text{L}$ ). The sample was transferred to an EPR tube and rapidly frozen in freezing mixture approximately 10 min. after addition of LaCl. The sample was stored in liquid nitrogen.

### 5.2.10 Pulse EPR measurements

Pulse EPR measurements were done using a Bruker ELEXSYS E580 X-band EPR spectrometer with a standard flex line probe head, housing a dielectric ring resonator (MD4). For measurements at cryogenic temperatures a continuous flow helium cryostat (CF935) and a temperature control system (ITC 502) from Oxford instruments were used. All pulsed experiments were performed at 50 K. For PELDOR measurements a double microwave frequency setup available from Bruker was used. Microwave pulses were amplified with an (TWT) amplifier (117X) from Applied Systems Engineering. PELDOR experiments were done using the 4 pulse sequence,  $\pi/2(\nu_A) - \tau_1 - \pi(\nu_A) - (\tau_1+t) - \pi(\nu_B) - (\tau_2-t) - \pi(\nu_A) - \tau_2 - echo$ . To eliminate receiver offsets the  $\pi/2(\nu_A)$  pulse was phase-cycled by applying the microwave pulse consecutively through the  $+\langle x \rangle$  and  $-\langle x \rangle$  channels and subtracting the signals. The length of the detection pulses ( $\nu_A$ ) were set to 16 ns ( $\pi/2$ ) and 32 ns ( $\pi$ ). The frequency of the inversion pulse ( $\nu_B$ ) was set at the

maximum of the nitroxide field sweep spectrum and the length was set to 16 ns. Amplitude and phase of the pulses was set to optimize the refocused echo. The frequency of the detection pulses ( $\nu_A$ ) was 40 to 90 MHz higher than the frequency of the inversion pulse ( $\nu_B$ ). All PELDOR spectra were recorded with a shot repetition time of 4000 to 5000  $\mu$ s, video amplifier bandwidth of 20 MHz and amplifier gain of 51 to 57 dB.  $\tau_1$  was set to 200 ns for samples in protonated matrix and to 380 ns for samples in deuterated matrix. Proton and deuterium modulation was suppressed by incrementing  $\tau_1$  by 8 ns 8 times and adding the consecutive spectra. The time increment of the inversion pulse was set to either 12 or 30 ns.

#### 5.2.11 Data analysis and modeling

Experimental PELDOR time traces were background subtracted and Fourier transformed using DeerAnalysis2011 (123). Distance distributions were generated from orientation averaged time traces using Tikhonov regularization as implemented in DeerAnalysis2011. The equilibrium geometry of spin label  $\zeta$  was calculated using density functional theory (DFT) with the B3LYP functional and 6-31G\* basis set as implemented in Spartan (Wavefunction). B-form DNA structures were modeled with the make-na server from <http://casegroup.rutgers.edu/Biomer/index.html>. Abasic sites were introduced into the DNA duplexes by deleting the corresponding cytosine and replacing the glycosidic bond with hydrogen using PyMol (DeLano Scientific LLC).

#### 5.2.12 Simulation of PELDOR time traces

Simulation of PELDOR time traces and distance distributions were done using peldorsim (Chapter 3) where the spin label pair in DNA was represented by a vector model. The conformational distribution and dynamics of the spin labels was modeled using the cooperative twist-stretch dynamics model for short dsDNA (110). The spin labels and their equilibrium positions were represented by vectors, positioned relative to the center of the DNA helix axis. The equilibrium position of the spin labels was obtained from a molecular model of the DNA duplexes with  $\zeta$  spin labels docked into the abasic sites (Figure 5.2.1). The position of spin labels was parameterized by defining three variables: DNA

radius ( $R$ ), DNA length ( $L$ ) and torsion angle ( $\phi$ ). The equilibrium value for  $R$  was defined as the distance spin labels are shifted away from the center of the DNA helix axis (Figure 5.2.1 b).  $R$  was allowed to have a standard deviation of 0.65 Å as previously determined (110). The equilibrium value for the DNA length was defined as the height between spin labels (Figure 5.2.1 a) and the distribution in  $L$  was given by Eq. 5.2.1 (110) where  $\sigma_R$  is the standard deviation in  $R$  and  $n$  is the number of base pairs between the spin labels.

$$\sigma_L = \frac{\sigma_R * n}{-3.2} \quad \text{Eq. 5.2.1}$$

The equilibrium angle between the N-O bonds of the spin labels  $\phi$  was determined from the DNA molecular models. The distribution (two standard deviations) in  $\phi$  was previously determined to be 22° per helical turn (110). Since the spin labels in **dsDNA 1** and **dsDNA 2** are approximately 1 and 2 helical turns apart the distribution in  $\phi$  was determined to be 22° and 48°, respectively. The length of the vectors representing the spin labels  $L_c$  was 9.5 Å. This distance corresponds to the distance from the center of the N-O bond to the other end of the spin label that is approximately located at DNA helix axis (Figure 5.2.1 b). The equilibrium values for the height and torsion angle between spin labels were adjusted slightly until a good fit to the modulation frequency was obtained. The equilibrium values and distributions in  $R$ ,  $L$  and  $\phi$  for all dsDNAs are summarised in table 5.4.1.

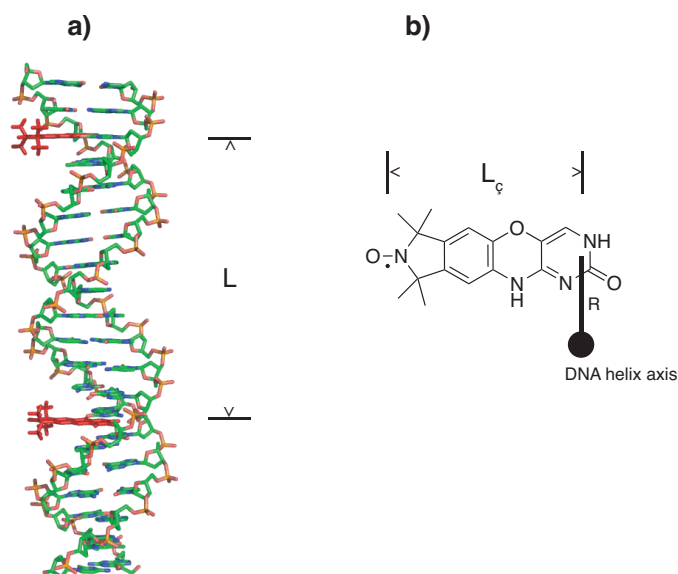


**Figure 5.2.1.** Molecular model of DNA and definition of geometric parameters. **a)** Molecular model of **dsDNA 1** with  $\zeta$  spin labels docked inside abasic sites. The spin labels are red. The height between the spin labels, assigned as the DNA length parameter is shown. **b)**  $\zeta$  spin label with illustrations defining the DNA radius  $R$  and spin label length  $L_\zeta$ .

### 5.2.13 Original PELDOR time traces

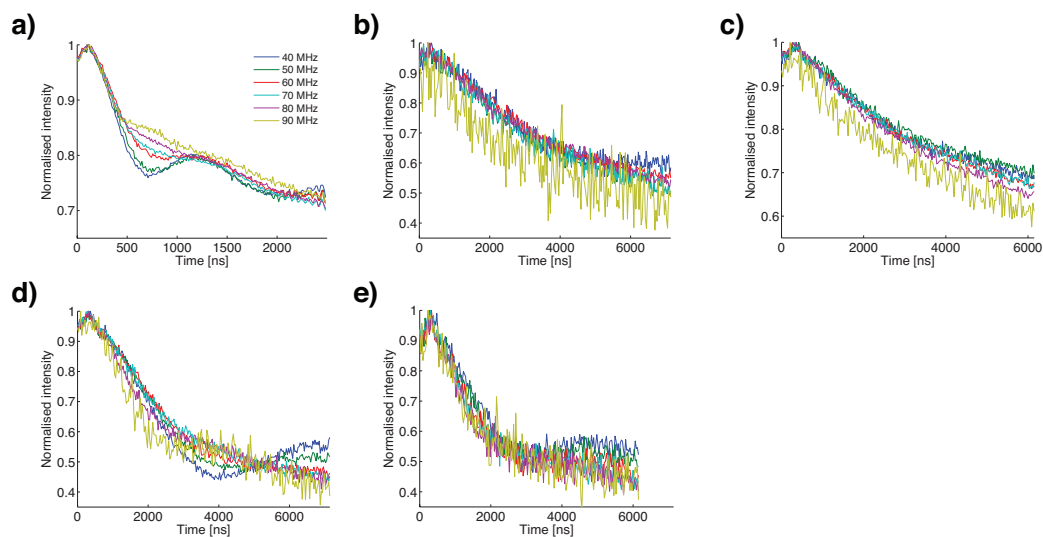


**Figure 5.2.2.** Original PELDOR time traces of noncovalently spin-labelled **a)** **dsDNA 1**, **b)** **dsDNA 2**, **c)** **dsDNA 2 + Lacl**, **d)**  $\zeta$  spin-labelled **dsDNA 3** and **e)**  $\zeta$  spin-labelled **dsDNA 3 + Lacl**.



### 5.3 PELDOR measurements on dsDNA 1

A 20-mer DNA duplex **dsDNA 1** (Table 5.3.1) was mixed with 2 equivalents of spin label  $\zeta$  and then hybridized in phosphate buffer containing 20% ethylene glycol as cryoprotectant to ensure a homogeneously frozen sample.

**Table 5.3.1.** Sequences for dsDNA noncovalently and covalently spin-labelled with  $\zeta$  and  $\zeta$ , respectively

DNA	DNA sequence
<b>dsDNA 1</b>	5'-GATGCGFGCGCGCGACTGAC-3' 3'-CTACGCGCGCGCGCTGAFTG-5'
<b>dsDNA 2</b>	5'-GCGFATTGTGAGCGGATAACAATTTGGCG-3' 3'-CGCGTAACTCGCCTATTGTTAAAFCGC-5'
<b>dsDNA 3</b>	5'-GCGÇATTGTGAGCGGATAACAATTTGGCG-3' 3'-CGCGTAACTCGCCTATTGTTAAACCGC-5'

Abasic sites are denoted by F. The bold sequence in **dsDNA 2** and **dsDNA 3** is the 19-mer Lac repressor consensus sequence.

Spin label binding was confirmed by measuring the noncovalently spin-labelled **dsDNA 1** and a sample of  $\zeta$  in phosphate buffer with 20% (v/v) ethylene glycol with CW-EPR at 0 - 40 °C (Figure 5.3.1). As the temperature is decreased the viscosity of the  $\zeta$  spin label sample increases and the linewidth of the EPR spectrum becomes broader due to the decreased rotational correlation time. At -40 °C the  $\zeta$  spin label sample is completely frozen and the spectrum resembles the rigid nitroxide spectrum recorded at -173 °C (Figure 5.3.1). The EPR spectrum for the noncovalently spin-labelled **dsDNA 1** starts to show peaks from spin labels with slow tumbling rate as the temperature is decreased from 0 to -10 °C, as shown by the \* in figure 5.3.1. Since these peaks are not visible in the spectrum for the  $\zeta$  spin label at -10 °C they must belong to spin labels that are bound to DNA, which has a slower tumbling rate in solution due to its larger size. As the temperature is decreased further, the peaks from slowly tumbling spin labels increase in intensity, indicating that the binding of spin labels to the DNA increases with decreased temperature. At a temperature of -30 °C the EPR spectrum shows negligible contribution from spin labels with fast tumbling

(unbound spin labels). This is evident from the reduced intensity of the corresponding peaks, shown by + at -20 °C in figure 5.3.1. It was observed that the samples of noncovalently spin-labelled DNA and  $\zeta$  spin label start to become frozen at  $\sim -30$  °C and completely frozen at -40 °C.

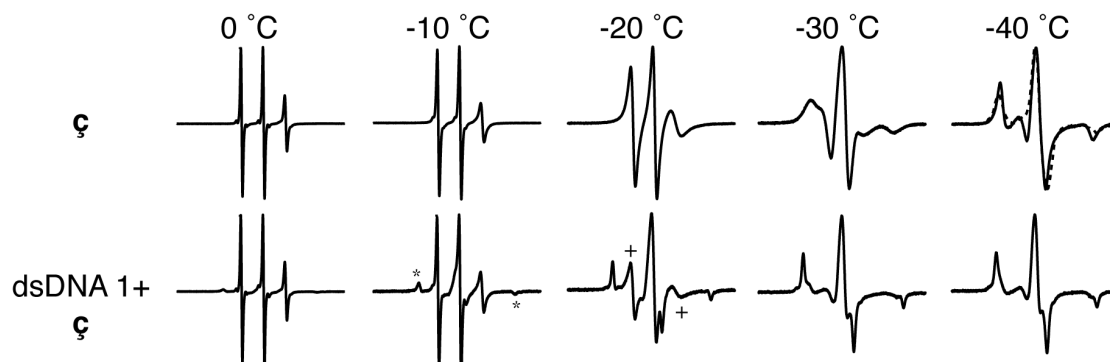


**Figure 5.3.1.** CW-EPR spectra of  $\zeta$  spin label (top) and noncovalently spin-labelled **dsDNA 1** (bottom) recorded at 0 to -40 °C. Spectrum from free  $\zeta$  spin label at -173 °C is shown as a broken line overlaid with the spectrum at -40 °C. Samples were dissolved in phosphate buffer with 20% ethylene glycol. \* and + symbols show EPR transitions from slow and fast tumbling spin labels, respectively.

The noncovalently spin-labelled **dsDNA 1** was measured with 4-pulse PELDOR (41) at 50 K, placing the inversion pulse at the maximum of the nitroxide spectrum and the detection pulse sequence on the low-field side of the spectrum. This setup results in 40 to 90 MHz frequency difference (offset) between detection and inversion pulse position (Figure 5.3.2 b). At 90 MHz offset the detection sequence excites predominantly the z-component of the  $^{14}\text{N}$  hyperfine matrix,  $A_{zz}$ . Decreasing the offset to 40 MHz results in an increased excitation of  $A_{xx}$ ,  $A_{yy}$  and off-diagonal components.

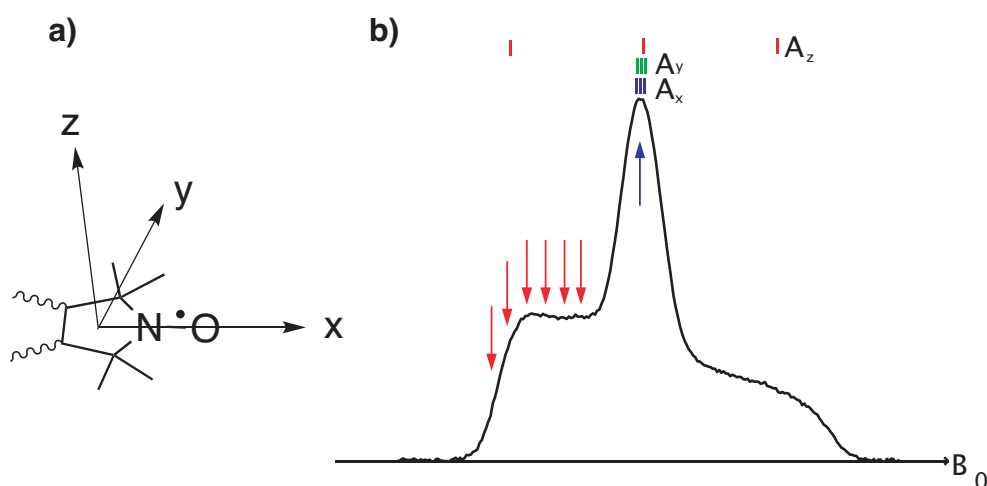


**Figure 5.3.2.** The  $g$ -matrix frame and EPR spectrum for a nitroxide. **a)** A nitroxide and the relative orientation of the  $g$ -matrix's principal components. **b)** An echo-detected EPR spectrum for **dsDNA 1** at X-band. The blue arrow indicates the position of the inversion pulse. The red arrows indicate the position of the detection pulses at 40-90 MHz offsets between the frequencies of the detection and inversion pulses. The sticks at the top of the figure show the approximate positions of the  $^{14}\text{N}$  hyperfine coupling components.

Measuring **dsDNA 1** with PELDOR at 40 to 90 MHz offset, in steps of 10 MHz, resulted in time traces with decreased modulation depth and shorter modulation frequency (Figure 5.3.3 a, b). The modulation depth for these PELDOR experiments will primarily depend on the relative orientation of spin labels, degree of orientation correlation, excitation width of the inversion pulse and on the ratio between coupled spin pairs in DNA and the total spin concentration (48). Therefore, comparing the modulation depth obtained for the noncovalently spin-labelled **dsDNA 1** to that obtained for the same DNA sequence covalently spin-labelled with  $\zeta$  (120), (which is 100% doubly spin-labelled) is a means of quantifying the degree of noncovalent binding, assuming the relative orientation and orientation correlation for the spin labels is similar for both DNA. The noncovalently spin-labelled **dsDNA 1**, at 40 MHz offset, has a modulation depth of 0.16 (Figure 5.3.3 a). Comparing this to the modulation depth of about 0.45, obtained from the covalently labelled **dsDNA 1** (120) indicates that  $0.16/0.45=36\%$  of the **dsDNA 1** duplexes contain two noncovalently bound spin labels. Identical results were obtained from the other frequency offsets. The degree of doubly labeled DNA could not be increased by increasing the concentration ratio of spin label to duplex DNA, nor by varying the flanking bases for both abasic sites (168). Rapidly freezing the samples of noncovalently

spin-labelled DNA either before or after cooling the sample to  $\sim -30$  °C did not have an appreciable effect on the modulation depth and there was no indication of the  $\zeta$  spin labels getting reduced, either before or after, adding DNA and buffer solution.

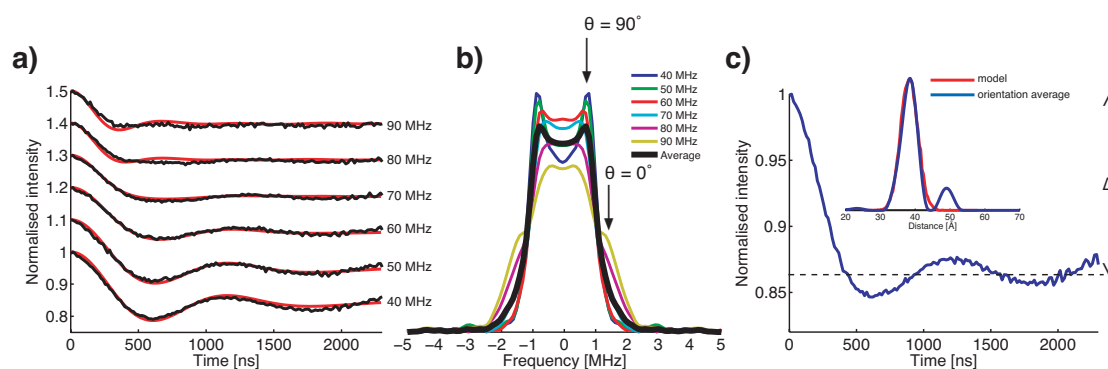


**Figure 5.3.3.** PELDOR data for **dsDNA 1**. **a)** PELDOR time traces of noncovalently spin-labelled **dsDNA 1** (black) with simulated time traces overlaid (red). The time traces have been background subtracted, normalized and displaced on the y-axis for clarity. **b)** Fourier transformation of the experimental and orientation averaged time traces. Arrows point to the perpendicular and parallel components. **c)** Orientation averaged time trace and distance distribution from simulation (red) and orientation average (blue).  $\Delta$  represents the modulation depth.

The dependence of the dipolar frequency on the offset between detection and inversion pulses can be seen in the Fourier transformed time traces (Figure 5.3.3 b). The dipolar spectra show that the parallel component of the dipolar spectrum ( $\theta = 0^\circ$ ) increases in intensity as the detection sequence is moved from 40 to 90 MHz offset. The same trend was also observed for the covalently spin-labelled **dsDNA 1** (120) and indicates that the  $A_z$  component of  $\zeta$  is approximately parallel to the interspin vector  $\mathbf{r}$  (Figure 5.3.4 a). The PELDOR time traces for the noncovalently spin-labelled **dsDNA 1** show that the orientation of the  $\zeta$  spin labels is correlated with the orientation of the interspin vector  $\mathbf{r}$ . Therefore, the interspin distance distribution cannot be reliably obtained from any single time trace using DeerAnalysis (38), as is most commonly done when orientation correlation can be neglected. Instead, the time traces recorded at 40 - 90 MHz offset are all added together which gives an approximate orientation averaged time trace that can be analysed using DeerAnalysis (151). The orientation averaged time trace, its Fourier transformation and corresponding distance

distribution are shown in figure 5.3.3 b-c. The distance distribution from the orientation averaged time trace has a mean distance of 38 Å (Figure 5.3.3 c inset), nearly identical to that previously determined for the covalently spin-labelled **dsDNA 1** (37±1 Å) (120).

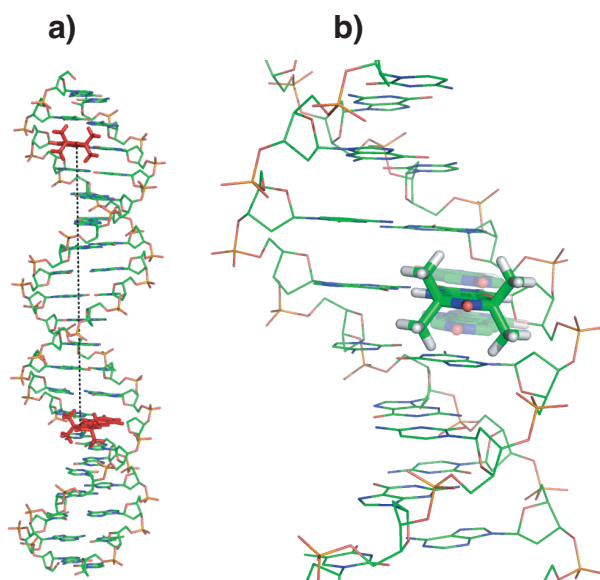


**Figure 5.3.4.** Molecular models of noncovalently spin-labelled **dsDNA 1**. **a)** Molecular model of **dsDNA 1** showing the relative positioning of the  $\zeta$  spin labels (red) and the distance vector between them (broken black line). **b)** A close-up view of  $\zeta$  (stick representation) within the DNA abasic site. The conformational dynamics of the spin label, as implemented in the PELDOR simulations, are depicted. The transparent spin labels show how the spin labels move away from an equilibrium position upon cooperative twist-stretching of the DNA helix. The conformational dynamics of the DNA helix have been omitted and the methyl groups of the transparent spin labels have been removed for clarity.

To obtain more precise distance distribution and information on orientation and conformational dynamics of the spin labels, PELDOR time traces were simulated with peldorsim, a Matlab program that simulates PELDOR time traces from a model of dipolar coupled spin pairs (Chapter 3) (169). The cooperative twist-stretch dynamics model for short dsDNA (170, 171) was used to model the noncovalently spin-labelled **dsDNA 1** (see Materials and methods). This dynamics model was recently successfully used to determine the dynamics of short dsDNA by analysing and simulating a series of PELDOR data obtained from DNA, covalently spin-labelled with the  $\zeta$  spin label (110). Using the same dynamics parameters that were determined for the covalently spin-labelled dsDNA (110), except for the mean distance, yields simulated time traces with

good agreement to the experimental time traces (Figure 5.3.3 a). The simulated distance distribution is also in agreement with the distribution from the orientation averaged time trace (Figure 5.3.3 c). All six time traces for noncovalently spin-labelled **dsDNA 1** were simulated with the same set of geometrical parameters. The interspin distance obtained from PELDOR, simulations and modeling of DNA duplexes are summarized in table 5.3.2.

**Table 5.3.2.** Interspin distances for all dsDNA

dsDNA	$r_{DA}$ [Å] <sup>[a]</sup>	$r_{Simulation}$ [Å] <sup>[b]</sup>	$r_{MM/X-ray}$ [Å] <sup>[c]</sup>
<b>dsDNA 1</b>	$38.0 \pm 4.4$	$38.6 \pm 5$ (0.4, 0.1)	38
<b>dsDNA 2</b>	$69.2 \pm 7.6$	$70.0 \pm 9.6$ (1, 0.1)	73
<b>dsDNA 2 +LacI</b>	$64.6 \pm 8.2$	$65.0 \pm 10.6$ (1, 0.1)	67
<b>dsDNA 3</b>	$68.1 \pm 8.0$	$68.0 \pm 9.6$ (1, 0.1)	73
<b>dsDNA 3 +LacI</b>	$62.1 \pm 8.2$	$62.2 \pm 10.6$ (1, 0.1)	67

[a] Mean distance  $\pm$  two standard deviations from orientation averaged PELDOR time traces using DeerAnalysis 2011. The mean value is calculated for the most probable distance. [b] Mean distance  $\pm$  two standard deviations. The error of the mean value, standard deviation is in brackets. [c] Interspin distances obtained from molecular modeling using B-form DNA duplexes. The interspin distance for **dsDNA 2** and **dsDNA 3** bound to LacI was estimated by modelling spin labels into the X-ray structure of a 21-mer dsDNA bound to LacI (pdb id. 1LBG).

#### 5.4 LacI-induced DNA bending observed by PELDOR

To evaluate the applicability of noncovalent spin labelling for distance measurements on DNA/protein complexes the binding of the Lac repressor protein (LacI) to the consensus Lac operator DNA sequence was used as a proof of principle experiment (Figure 5.4.1). The LacI protein binds specifically to a consensus DNA sequence, known as an operator, and distorts the DNA from the B-form by bending the operator sequence through an angle of  $\sim 45^\circ$  (172-174). If the LacI protein is able to bind to a DNA that contains a LacI operator and two

abasic sites to each side of the LacI operator, occupied by the spin label  $\zeta$ , then the accompanied bending of the DNA should show a change in the interspin distance measured by PELDOR.

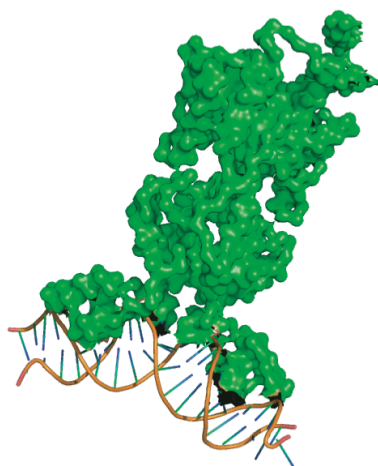


**Figure 5.4.1.** Lac repressor dimer bound to a 21-mer symmetric Lac operator (PDB 1LBG) (175). The Lac repressor is represented in surface mode. The Lac operator DNA is represented in cartoon mode.

A 29-mer dsDNA containing a 19-mer LacI consensus sequence and two abasic sites (**dsDNA 2**, table 5.3.1) was noncovalently spin-labelled. Electrophoretic mobility shift assay (EMSA) was used to verify that the LacI repressor protein (LacI from *Escherichia coli*) binds to **dsDNA 2** (Figure 5.4.2). The 29-mer DNA duplex was radiolabelled with  $^{32}\text{P}$  and incubated (50 nM) with LacI prior to electrophoresis and imaging. The DNA was clearly seen to shift upon protein binding, yielding a dissociation constant of approximately 1  $\mu\text{M}$  LacI (Figure 5.4.2), suggesting that the protein is fully bound to the DNA at the concentrations used for EPR experiments. Similar binding dissociation constant was obtained in the presence or absence of  $\zeta$  spin labels. The binding affinity determined for **dsDNA 2** is weaker than published previously for the LacI repressor using membrane filtering (176). This is most likely due to the relatively short length of **dsDNA 2**, the presence of two abasic sites and the use of the gel-shift technique, which tends to underestimate binding affinity due to the extended incubation times.

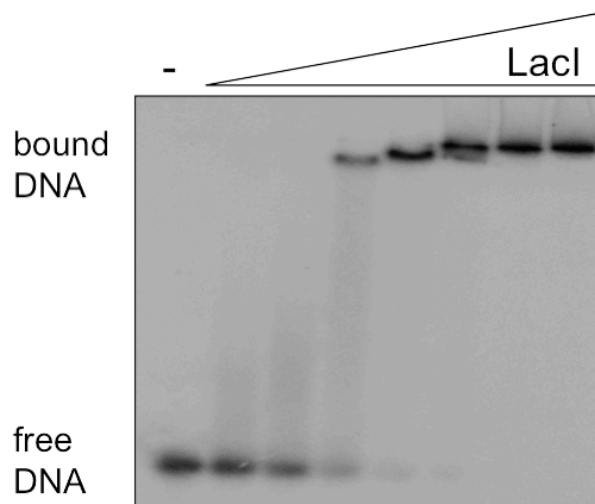


**Figure 5.4.2.** Electrophoretic mobility shift assay showing binding of the Lac repressor to **dsDNA 2** in the presence of the spin label  $\zeta$ . DNA (50 nM) was titrated with 0, 0.25, 0.5, 0.75, 1.25, 2.5, 5 and 12.5  $\mu\text{M}$  Lacl dimer prior to separation by gel electrophoresis and gel visualization. A dissociation constant of approximately 1  $\mu\text{M}$  was observed. At high protein concentrations a second, more retarded species is observed. This is likely due to the known propensity for Lacl to tetramerise.

**dsDNA 2**, noncovalently spin-labelled with 2 equivalents of spin label  $\zeta$  was measured with PELDOR at 40 to 90 MHz frequency offsets, before and after adding the Lacl protein. The 40 MHz offset PELDOR time trace of **dsDNA 2** in the absence of Lacl has a modulation depth of 0.2 (Figure 5.4.3 a), corresponding to ca. 40% doubly spin-labelled DNA. This degree of binding is comparable to that observed for **dsDNA 1**, taking into account the different label orientation and errors from determining the modulation depth. The variation in modulation frequency with frequency offset is not as clear for **dsDNA 2** as **dsDNA 1** (Figure 5.4.3 a) but increasing the offset from 40 to 90 MHz leads to a decreased modulation depth. Fourier transforming the individual time traces shows less pronounced orientation selection for **dsDNA 2** (Figure 5.4.3 c). This could be due to the increased interspin distance, flexibility or that the angle between the interspin vector and the z-component of the spin labels'  $^{14}\text{N}$  hyperfine coupling matrix ( $A_{zz}$ ) is around  $45^\circ$  (120). Since **dsDNA 2** has a substantially longer interspin distance than **dsDNA 1** the PELDOR time window had to be extended to 7 microseconds to observe at least one full period of the dipolar modulation. The longer time window leads to a considerably reduced intensity of the



monitored echo and a time trace with worse signal-to-noise ratio than for **dsDNA 1**.

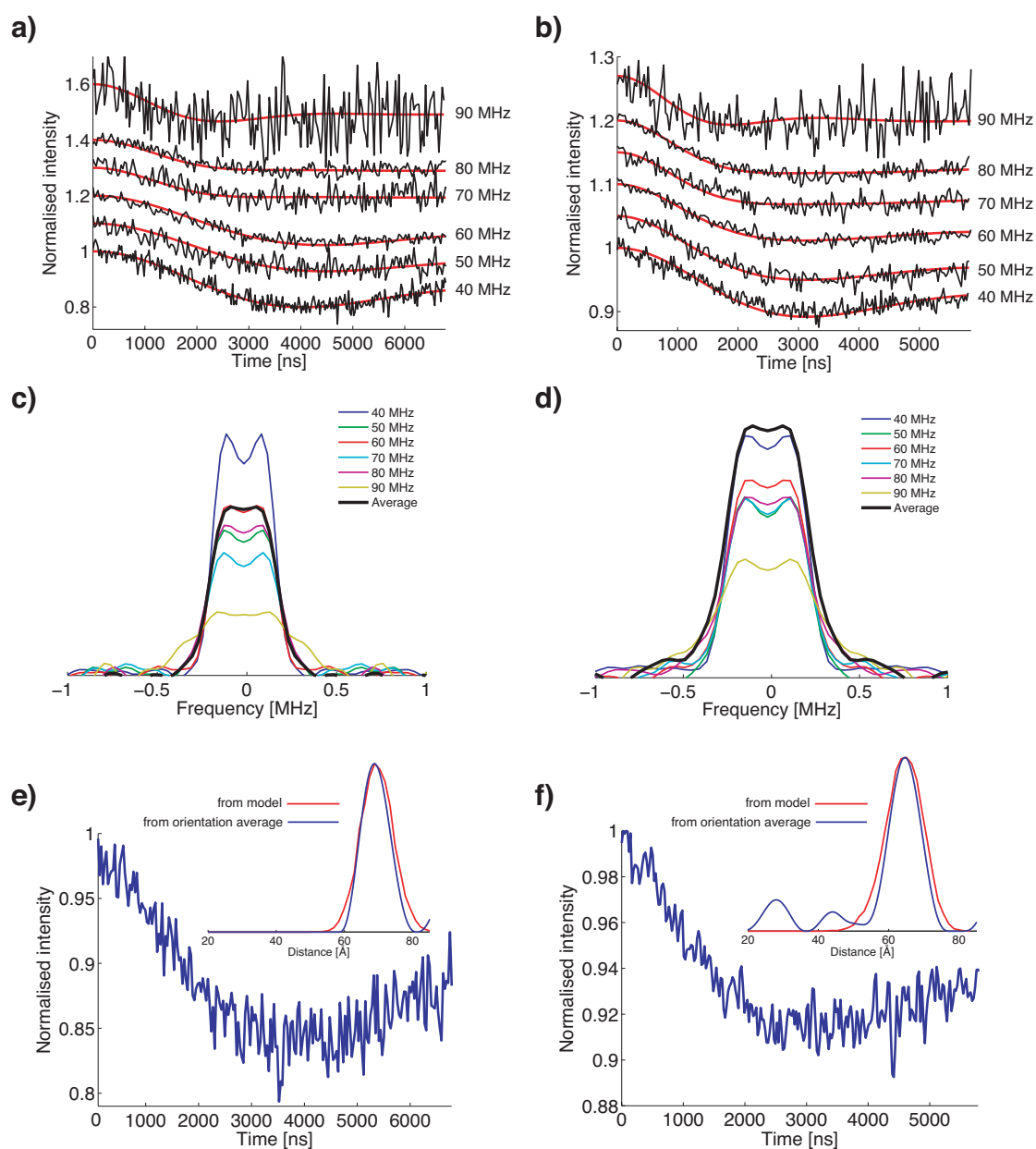


**Figure 5.4.3.** PELDOR data for noncovalently spin-labelled **dsDNA 2** with and without LaCl at 40 to 90 MHz offsets. **a,b)** Background corrected PELDOR time traces of **dsDNA 2** with and without LaCl (black), respectively, overlaid with the corresponding simulated time traces (red). The time traces have been displaced on the y-axis for clarity. **c)** and **d)** are the respective Fourier transformations of the time traces in **a)** and **b)**. The black spectra are the Fourier transformations of the respective orientation averaged time traces shown in **e)** and **f)**. **e)** and **f)** are the orientation averaged PELDOR time trace of **dsDNA 2** without and with LaCl, respectively. The inset shows the distance distribution obtained from the summed time traces using DeerAnalysis (blue) and the distribution obtained from the model based simulations (red).

The orientation averaged PELDOR time trace for **dsDNA 2** yields a distance distribution with a mean value of 69.2 Å (Figure 5.4.3 e, inset), which is similar to the mean distance of 68.1 Å obtained by PELDOR measurements on an identical DNA covalently spin-labelled with  $\zeta$  (**dsDNA 3**, Table 5.4.1). Simulating the PELDOR time traces for **dsDNA 2** using the cooperative twist-stretch dynamics model (110) yields a distance distribution with a mean distance of 70 Å (Figure 5.4.3 e inset), in good agreement with the distance distribution obtained from the orientation averaged time trace.

**Table 5.4.1.** Geometric parameters of the molecular model for simulation of PELDOR time traces.

dsDNA	DNA Radius (R) [Å]	DNA Length (L) [Å]	Torsion ( $\phi$ ) [°]
<b>dsDNA 1</b>	2.7 ± 1.30(0.01)	37.2 ± 4.46(0.03)	75 ± 22(0.2)
<b>dsDNA 2</b>	2.7 ± 1.30(0.01)	70 ± 9.02(0.03)	60 ± 48(0.2)
<b>dsDNA 2 +LacI</b>	2.7 ± 1.30(0.01)	65.4 ± 10.4(0.03)	75 ± 48(0.2)
<b>dsDNA 3</b>	2.7 ± 1.30(0.01)	67.6 ± 9.02(0.03)	60 ± 48(0.2)
<b>dsDNA 3 +LacI</b>	2.7 ± 1.30(0.01)	62.1 ± 10.1(0.03)	80 ± 48(0.2)

The DNA radius, DNA length and torsion angle (angle between the spin labels N-O bond) are given as mean value ± two standard deviations. The uncertainty in the standard deviation is given within brackets.

The PELDOR experiments for **dsDNA 2** in the presence of LacI yielded time traces with visible modulation but a weakly resolved orientation selection (Figure 5.4.3 b, d). At 40 MHz offset the modulation depth is 0.1, which translates into 20% double spin-labelled DNA. The apparent decrease in spin label affinity for **dsDNA 2** in the presence of LacI is attributed to the deformation of DNA and abasic sites and overlap between the abasic sites and the LacI, which impedes the insertion of spin labels. However, the labelling efficiency and specificity are

still large enough to yield PELDOR time traces with visible modulation. A mean distance of 64.6 Å is obtained from the orientation averaged PELDOR time trace (Figure 5.4.3 f, inset). Comparing the orientation averaged PELDOR time traces and distance distributions for **dsDNA 2** and **dsDNA 2 + LacI** clearly shows how the interspin distance becomes shorter upon binding of the LacI (Figure 5.4.4).

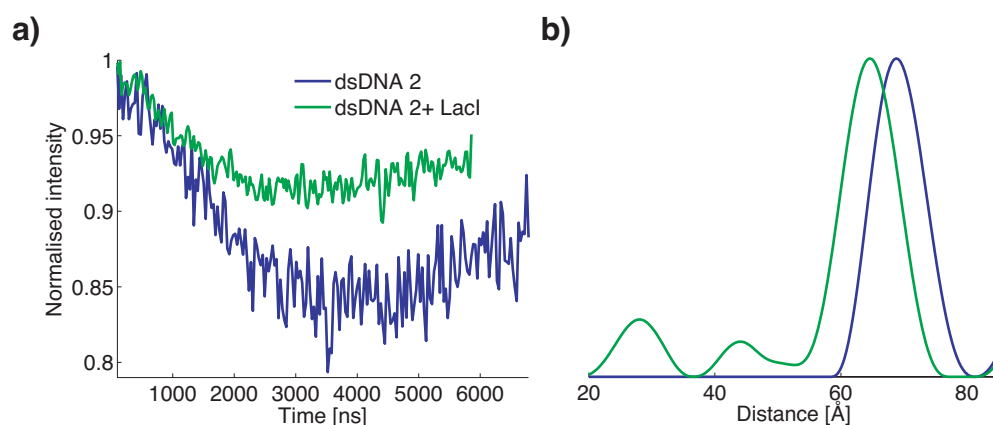


**Figure 5.4.4.** PELDOR data for **dsDNA 2** and **dsDNA 2 + LacI**. **a)** Background corrected orientation averaged time traces. **b)** Distance distributions from the time traces in **a)** obtained by Tikhonov regularization.

To assess how much the LacI bends **dsDNA 2**, the mean distances obtained from the orientation averaged time traces on **dsDNA 2** and **dsDNA + LacI** are used. Trigonometry and these distances (105) yields a bending angle of 42° which is in good agreement with the bending angle of ~ 45°, observed from crystal structure on a 21-mer operator sequence (174) and the angle of 48.5° obtained from PELDOR measurements on covalently spin-labelled **dsDNA 2** (**dsDNA 3**, Table 5.3.1). Although this approach of using only the mean distances obtained from orientation averaged time traces results in a 42° bending of the DNA, it does not take into account that the spin labels stick out from the DNA helix and change their relative orientation when LacI bends the DNA. Furthermore, addition of time traces acquired at discrete field positions does not represent a complete orientation averaged time trace (57). Assuming the conformational dynamics of the DNA does not drastically change upon binding of LacI, the twist-stretch dynamics model used for simulation of PELOR time traces and distance distributions for **dsDNA 1** and **dsDNA 2** could also be used to simulate PELDOR time traces for **dsDNA 2 + LacI**. To an approximation the LacI bends the

operator symmetrically around the central base pair, which is valid according to the x-ray structure (175). Simple trigonometry estimates that a  $42^\circ$  bending of the DNA should decrease the distance between the two abasic sites by about 4.6 Å and tilt each spin label  $\sim 21^\circ$  towards the interspin vector (Figure 5.4.5).

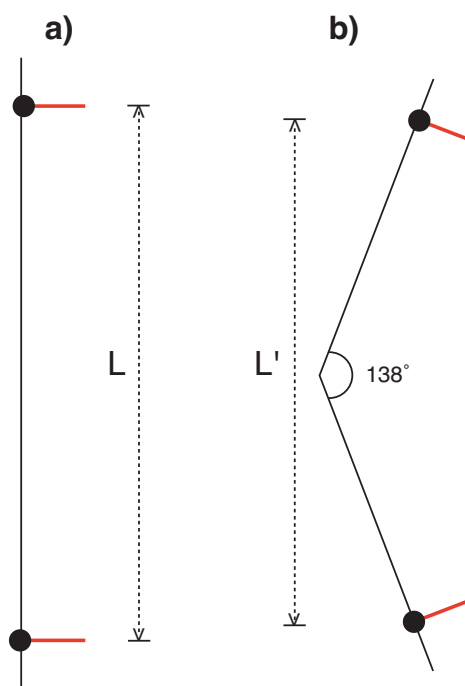


**Figure 5.4.5.** Diagram illustrating the change in distance between the DNA abasic sites and spin label orientation upon DNA bending. The **dsDNA 2** is represented by black solid lines, abasic sites by black circles and spin labels by red lines. **a)** Unbound **dsDNA 2**. The distance between the abasic sites (the height between spin labels) is denoted by  $L$ . **b)** **dsDNA 2** after being bent  $42^\circ$  about the center by the LacI protein. The distance between the abasic site, which now has become shorter, is denoted by  $L'$ .

These geometric parameters were combined with the twist-stretch dynamics model to simulate the PELDOR time traces for **dsDNA 2 + LacI** (Figure 5.4.3). Furthermore, in order to simulate the experimental modulation frequency it was necessary to increase the equilibrium angle between the N-O bonds of the spin labels (torsion angle) by  $15^\circ$ , relative to the angle used for **dsDNA 2** in the absence of LacI. The need to change the torsion angle can be rationalized by the unwinding of the DNA operator sequence upon binding to LacI (175). The parameters for the dynamics model that resulted in the best fit between simulations and experimental time traces (Figure 5.4.3 b) are listed in table 5.4.1. The simulated distance distribution for **dsDNA 2 + LacI** has a mean distance of

65 Å, which is only 0.4 Å longer than obtained from the orientation averaged time trace using DeerAnalysis (Table 5.3.2).

### 5.5 **LacI-induced bending of covalently spin-labelled DNA**

To evaluate the effects from abasic sites and noncovalently bound spin labels on PELDOR measurements of **dsDNA 2** the same 29-mer DNA sequence was covalently spin-labelled with the  $\zeta$  spin label (120) (**dsDNA 3**, Table 5.3.1) and measured with PELDOR at 40-90 MHz frequency offsets, before and after adding LacI. The PELDOR time traces of **dsDNA 3** with and without LacI show a pronounced modulation at almost all frequency offset and a modulation depth of 0.46 at 40 MHz offset (Figure 5.5.1 a, b). The Fourier transformed time traces show an increased parallel component as the frequency offset is increased from 40 to 90 MHz, which is in agreement with **dsDNA 2** (Figure 5.5.1 c, d). Analysing the orientation averaged time traces for **dsDNA 3** and **dsDNA 3 + LacI** with Tikhonov regularization yields a mean interspin distance of 68.1 and 62.1 Å, respectively (Table 5.3.2).

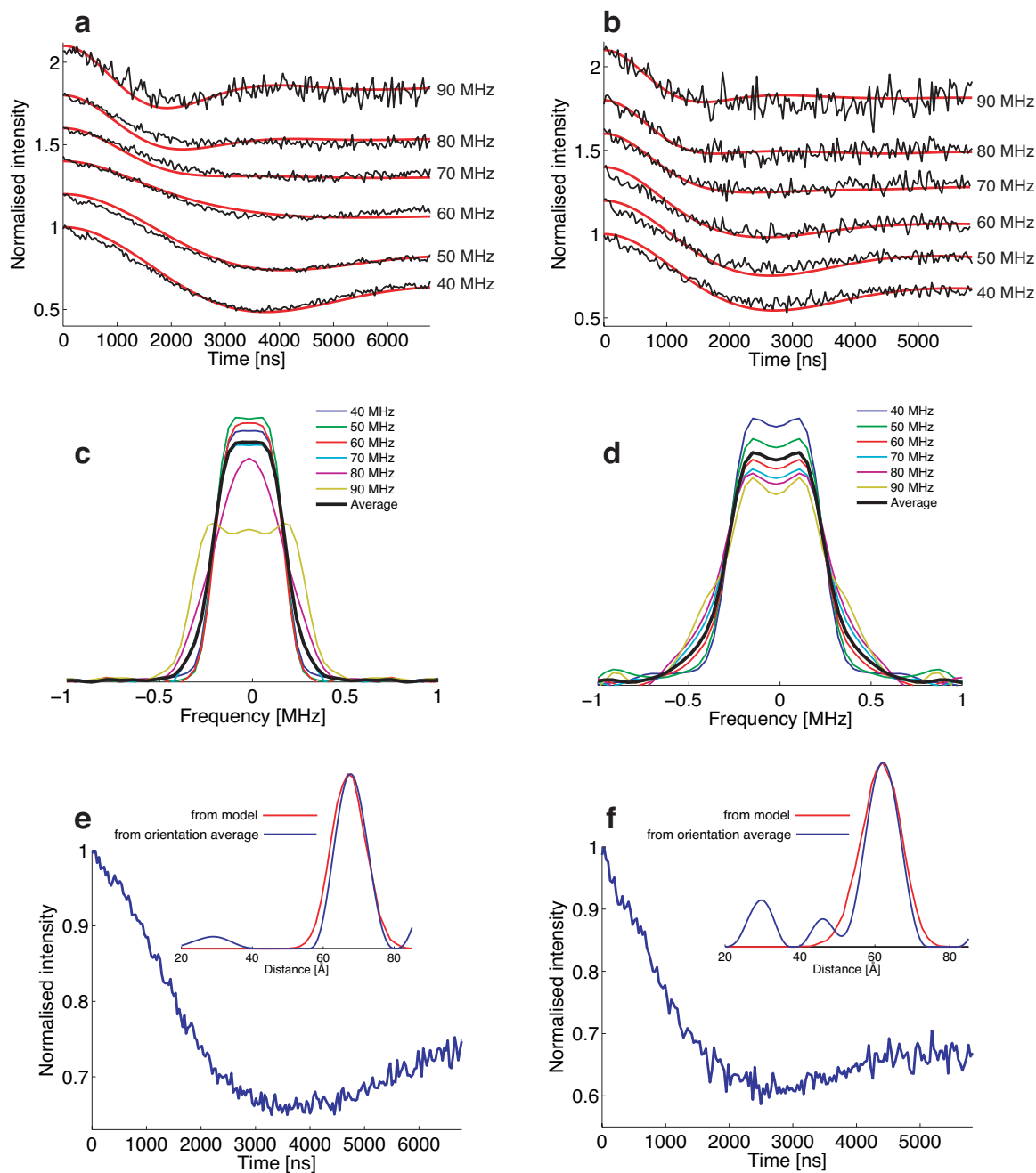


**Figure 5.5.1.** PELDOR data for covalently spin-labelled **dsDNA 3** with and without LaCl at 40 to 90 MHz offsets. **a,b)** Background corrected PELDOR time traces of **dsDNA 3** with and without LaCl (black), respectively, overlaid with the corresponding simulated time traces (red). The time traces have been displaced on the y-axis for clarity. **c, d)** Respective Fourier transformations of the time traces in **a)** and **b)**. The black spectra are the Fourier transformations of the respective orientation averaged time traces shown in **e)** and **f)**. **e, f)** Summed PELDOR time trace of **dsDNA 3** without and with LaCl, respectively. The inset shows the distance distribution obtained from the orientation averaged time traces using DeerAnalysis (blue) and the distance distribution obtained from the model based simulations (red).

The change in interspin distance upon addition of LacI is clearly seen when comparing the orientation averaged time traces and corresponding distance distributions for **dsDNA 3** and **dsDNA 3 + LacI** (Figure 5.5.2).

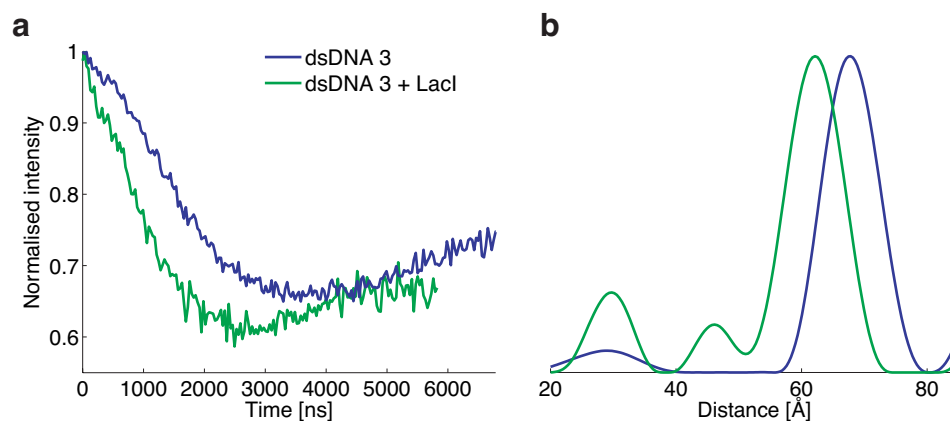


**Figure 5.5.2.** PELDOR data for **dsDNA 3** and **dsDNA 3 + LacI**. **a)** Background corrected orientation averaged time traces. **b)** Distance distributions from the time traces in **a)** obtained by Tikhonov regularization.

Using trigonometry and these mean distances, the bending angle of the **dsDNA 3** bound to LacI can be estimated as  $48.5^\circ$ . This is  $6.5^\circ$  larger bending than for the noncovalently spin-labelled DNA, **dsDNA 2**. The PELDOR time traces for **dsDNA 3** were also simulated using the same dynamics model and parameters as for simulations of time traces for **dsDNA 2** and the bending angle determined from the orientation averaged time traces of **dsDNA 3** (Table 5.3.2). The simulated time traces have an excellent fit to the experimental time traces and the simulated distance distributions fit nicely to the distance distribution from the orientation averaged PELDOR time traces (Figure 5.5.1 e, f and Table 5.3.2). PELDOR measurements on **dsDNA 3** and **dsDNA 3 + LacI** resulted in interspin distances that are 1.1 and 2.5 Å shorter compared to **dsDNA 2** and **dsDNA 2 + LacI**, respectively. The small differences in mean interspin distance and LacI induced bending between covalently and noncovalently spin-labelled DNAs is most likely due to the structural perturbation from the abasic sites and the exact position of the spin labels within the DNA duplex.

## 5.6 Summary

In summary, this study has shown how a noncovalent and site-directed spin labelling (NC-SDLS) strategy facilitates the measurements of distances and conformational dynamics of DNA using PELDOR. To illustrate this, a 20-mer DNA duplex and a 29-mer DNA/protein complex were noncovalently spin-labelled with the rigid spin label  $\zeta$  and the interspin distance, label orientation and conformational dynamics measured. PELDOR time traces that show clear modulation and orientation selectivity were obtained. The measurements on the 20-mer DNA resulted in data that was in very good agreement with that obtained from an identical DNA sequence covalently spin-labelled with  $\zeta$ . Although the affinity for noncovalently bound spin labels was decreased for the DNA/LacI complex it was still possible to detect the bending of DNA upon LacI binding, which showed that the LacI protein was able to bind to the DNA in the presence of noncovalently bound spin labels. Measuring the DNA/LacI complex enabled us to evaluate the limits for the noncovalent spin labelling method to be close to 70 Å for the maximum distance, 20% for the double spin labelling efficiency and 4.5 Å as a detectable distance change. Most importantly, this study shows that the facile NC-SDSL method is capable of yielding good quality PELDOR data. Since DNA containing abasic sites at specific nucleotide positions is commercially available, site-directed spin labelling of DNA can become widely applicable and should facilitate structural determination by EPR.

## 5.7 Note

Preliminary PELDOR studies using this noncovalent spin labelling method and  $\zeta$  were performed during my MSc studies and published in my MSc thesis. Specifically the PELDOR measurements on **dsDNA 2** and **dsDNA 2 + LacI** at 40, 60 and 80 MHz offsets shown in the present study were previously performed as part of my MSc studies and published in my MSc thesis. All other PELDOR measurements described in this study, including the measurements at 50, 70 and 90 MHz offset for **dsDNA 2** and **dsDNA 2 + LacI**, I performed as part of my PhD. The writing of the Matlab program to simulate PELDOR time traces using the cooperative twist-stretch dynamics model for short dsDNA as described here, and all detailed analysis into the conformational flexibility of the noncovalently



spin-labelled DNA and DNA/protein complex were all performed during my PhD and have not been submitted towards any other degree.

## **5.8 Acknowledgment**

The  $\zeta$  spin label, **dsDNA 1** and covalently spin-labelled **dsDNA 3** were synthesized by Dr. Sandip A. Shelke. I would like to thank Biljana Petrovic-Stojanovska for preparing the LacI protein and Dr. Christophe Rouillon for carrying out the EMSA on **dsDNA 2** and LacI.

## 6 Trityl Radicals as Spin Labels for Nanometer Distance Measurements

### 6.1 Introduction

As mentioned in previous chapters, electron paramagnetic resonance (EPR) methods such as pulsed electron-electron double resonance (PELDOR) and double quantum coherence (DQC) are very powerful tools to quantitatively measure nanometer distances in the range of ~1.4 to 8 nm (134, 38, 177, 9). To obtain distances between selected sites on biological macromolecules by EPR, most often site-directed spin labelling is required. To date, the most prominent spin labels are aminoxyl (nitroxide) radicals (178), a stable radical that can be readily incorporated to proteins (179), nucleic acids (180), organic polymers (151), lipids (181) and nanoparticles (182). Despite being a versatile spin label the nitroxide has the disadvantage of rather low sensitivity for EPR based distance measurements, rapid relaxation at ambient temperatures and only limited stability (> 60 min) under reducing environments (183) which makes distance measurements on systems within cells very demanding (184).

In this study the potential of using carbon-centred triarylmethyl (trityl) radicals as spin labels for nanometer distance measurements is evaluated. Specifically the tetrathiatriarylmethyl radical **20** (185) is used as the spin label (Figure 6.1.1). This trityl spin label has a narrow single peak EPR spectrum with very weak <sup>13</sup>C satellite lines (Figure 6.1.1) and has a transverse relaxation time  $T_m$  in the microsecond regime at room temperature in the liquid state (186, 187). The substituted aryl groups of the trityl protect it against dimerization and the trityl radical is stable in reducing environments for several hours (188, 189). The narrow EPR spectrum, slow transverse relaxation and high bio-stability are all properties that could help to overcome some of the limitations of using nitroxide spin labels.

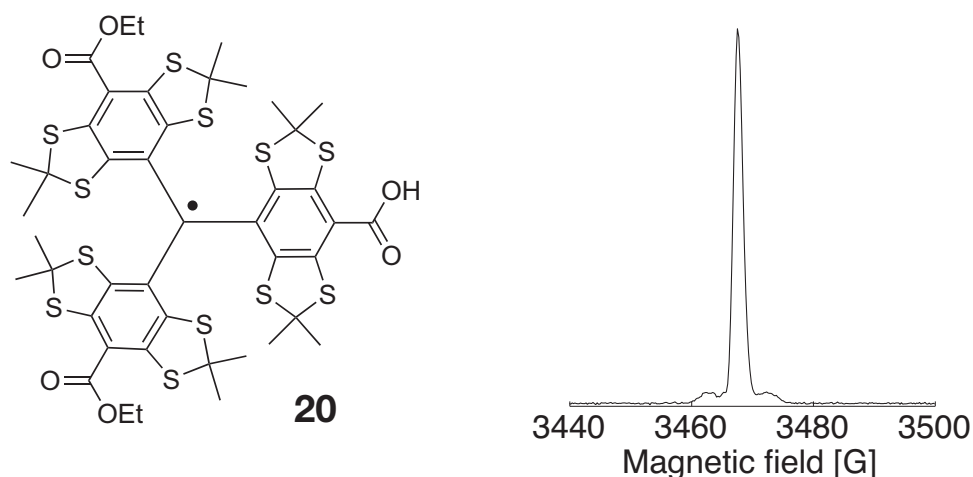


**Figure 6.1.1.** The chemical structure of **20** and its echo-detected X-band EPR spectrum.

## 6.2 Materials and methods

### 6.2.1 General

**EPR:** Pulsed EPR measurements were done on a Bruker ELEXSYS E580 X-band EPR spectrometer equipped with the SpecJet-II and PatternJet-II combination. All pulsed experiments were performed at 50 K unless otherwise stated using a standard flex line probe head with a dielectric ring resonator (MD5) together with a continuous flow helium cryostat (CF935) and a temperature control system (ITC 502) from Oxford Instruments. Continuous wave EPR measurements were performed on a Bruker EMX spectrometer equipped with a liquid nitrogen setup from Oxford Instruments. Samples of **21**, **22** and the nitroxide biradical **17** were dissolved in deuterated toluene to yield a spin concentration of 200  $\mu\text{M}$  and a final volume of 100 microliter. The samples were frozen in liquid nitrogen before the EPR measurements at cryogenic temperatures. Field-swept spectra were recorded by detecting the echo created by the Hahn echo pulse sequence  $\pi/2 - \tau - \pi$ . The pulse lengths were 12 and 24 ns for the  $\pi/2$  and  $\pi$  pulse, respectively. The delay  $\tau$  between the pulses was 380 ns. The whole echo was recorded with a 450 ns acquisition window. For the PELDOR measurements a double microwave frequency setup available from Bruker was used. Microwave pulses were amplified with a 1kW TWT amplifier (117X) from Applied Systems Engineering.

PELDOR experiments were done using the 4-pulse sequence,  $\pi/2(\nu_A) - \tau_1 - \pi(\nu_A) - (\tau_{1+t}) - \pi(\nu_B) - (\tau_{2-t}) - \pi(\nu_A) - \tau_2 - \text{echo}$ . To eliminate receiver offsets the  $\pi/2(\nu_A)$  pulse was phase-cycled. The length of the detection pulses ( $\nu_A$ ) were 16 ns ( $\pi/2$ ) and 32 ns ( $\pi$ ) unless otherwise stated. The frequency of the inversion pulse ( $\nu_B$ ) was set at the maximum of the trityl field sweep spectrum and the length was 16 ns unless otherwise stated. Amplitude and phase of the pulses was set to optimize the refocused echo. All PELDOR spectra were recorded with a shot repetition time of 3000  $\mu\text{s}$ , a video amplifier bandwidth of 20 MHz and an amplifier gain of 51 to 57 dB.  $\tau_1$  was 380 ns, which corresponds to a blind spot for deuterium Larmor frequency. Proton modulation was suppressed by incrementing  $\tau_1$  8 times by 8 ns and adding the consecutive spectra. The time increment of the inversion pulse was 14 ns for compound **21** and 20 ns for compound **22**.

DQC EPR measurements were performed using the six-pulse sequence,  $\pi/2 - \tau_1 - \pi - \tau_1 - \pi/2 - \tau_3 - \pi - \tau_3 - \pi/2 - \tau_2 - \pi - \tau_2 - \text{echo}$ . The dipolar signal was filtered out by a 64-step phase-cycling program (54). To suppress nuclear modulation,  $\tau_1$  and  $\tau_2$  were incremented 4 times by 108 ns and the spectra added together. The initial value for  $\tau_1$  was 280 ns and the initial value for  $\tau_2$  was between 4000 and 6500 ns.  $\tau_3$  was held constant at 30 ns. The DQC time trace was recorded by increasing  $\tau_1$  and decreasing  $\tau_2$  by 20 ns steps. The  $\pi/2$  and  $\pi$  pulse length was 8 and 16 ns, respectively for the DQC EPR measurements on **21** and 12 and 24 ns for the DQC EPR on **22**. The DQC echo was recorded with an acquisition window of 40 ns.

### 6.2.2 Measurement of the inversion pulse excitation profile

The excitation profile of the 16 ns  $\pi$  pulse was obtained experimentally by measuring a Hahn echo on the maximum of the trityl EPR spectrum of **21**, using a  $\pi/2 - \pi$  pulse sequence of the microwave detection source. The field position of an optimized inversion pulse of 16 ns, using the inversion microwave source, was then swept. A 40 ns integration window was used to measure the area under the Hahn echo as the frequency of the inversion pulse was swept. The width of

the integration window, delay between the  $\pi/2$  and  $\pi$  detection pulse and their lengths had negligible effects on the observed excitation profile.

### 6.2.3 Original PELDOR and DQC time traces

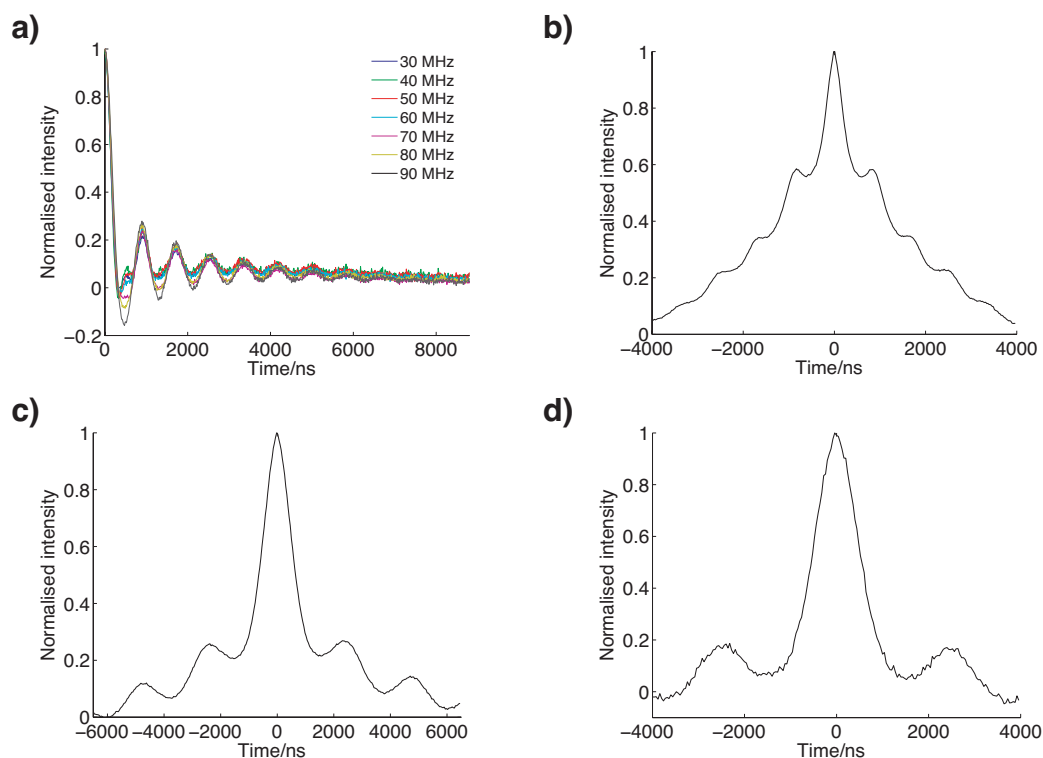


**Figure 6.2.1.** Original PELDOR and DQC time traces. **a)** Original PELDOR time traces for **21**. **b)** Original DQC time trace for **21**. **c)** Original DQC time trace for **22**. **d)** Original DQC time trace for **22** at 100 K.

### 6.2.4 Data analysis and simulations

The orientation-averaged PELDOR time trace for **21** was acquired by normalizing the original time traces and adding them. The individual PELDOR time traces for **21** were recorded with the same settings, including video amplifier gain and number of scans. PELDOR time traces were background corrected by fitting an exponential function (Eq. 6.2.1) to the experimental time trace using the function `exponfit` from the EasySpin toolbox (133) and dividing the experimental time trace with the fitted function.

$$a + b * e^{-kx} \quad (6.2.1)$$

Since DQC time traces were recorded to each side of the zero-time, the data points on each side were added together to make a single time trace from zero time to the maximum of the time window. The DQC time traces were background corrected by subtracting a fitted exponential function (Eq. 6.2.1) from the experimental time trace. One exception was the DQC time trace of **21**, which had a background that fitted better to a polynomial of degree 5. The reason for this might be that the nitroxide spectrum is not fully excited. The starting point for the fitting of the exponential and polynomial functions to the experimental DQC time trace was chosen that gave the best fit between the background corrected and simulated time trace. Dipolar spectra and distance distributions from PELDOR and DQC data were then obtained from the background corrected time traces using DeerAnalysis2011 (123). To obtain more information on the conformational dynamics of the system, the PELDOR and DQC time traces for **21** and **22** were simulated with peldorsim, a Matlab program that uses a conformational model and takes orientation selectivity into account (Chapter 3). For simulations of PELDOR time traces the excitation profiles of the detection sequence and inversion pulse are calculated. The excitation profile for the detection sequence was calculated according to equation 3.3.9 (Chapter 3). The profile for the inversion pulse was calculated by multiplying equation 3.3.10 (Chapter 3) with a Gaussian function and a factor of 0.9 in order to approximate as close as possible the experimentally determined excitation profile for the 16 ns inversion pulse. The DQC time traces were simulated assuming no orientation selection and complete excitation of the EPR spectrum using Eq. 1.2.23 (Section 1.2.5). The transverse spin relaxation  $T_m$  was evaluated by fitting an exponential decay function to the experimental two-pulse ESEEM time traces using the Bruker Xepr program (Bruker). Two-pulse ESEEM experiments were acquired with two-step phase-cycling. Evaluation of signal to noise in experimental time traces was done by fitting a polynomial function to the part of the original data that contains the least amount of modulations. The root-mean-square deviation between the polynomial function and the experimental data was then used to quantify the signal to noise ratio.

### 6.3 Structures of trityl-nitroxide biradical **21** and trityl-trityl biradical **22**

To evaluate trityls as spin labels for nanometer distance measurements two biradicals were synthesized using poly(para-phenyleneethynylene)s (PolyPPEs) polymers as the tether between spin labels (Figure 6.3.1) (78).

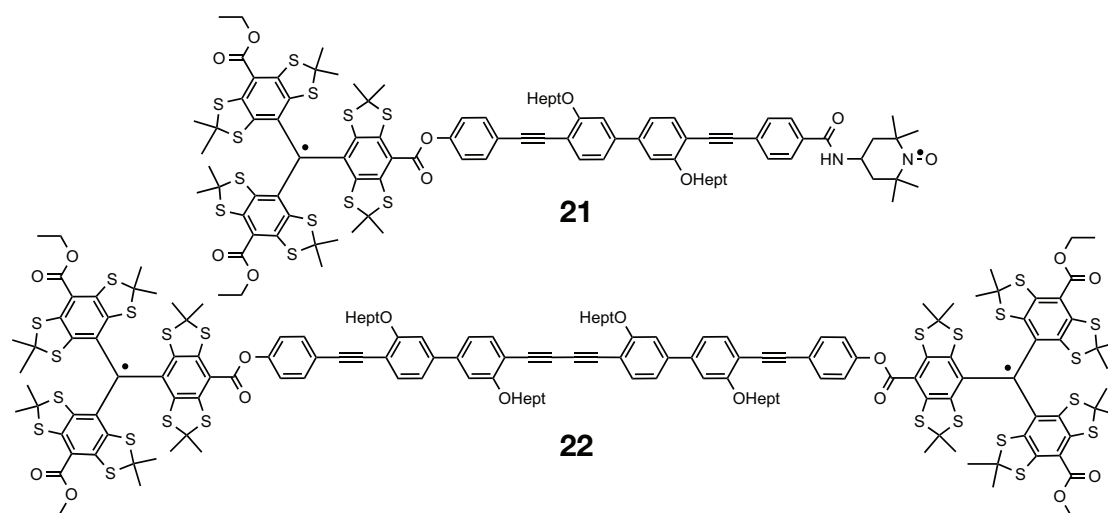


**Figure 6.3.1.** chemical structures of trityl-nitroxide biradical **21** and trityl biradical **22**.

The structure and conformational flexibility of this class of polymers, which has found wide use in material science (190, 191), has previously been studied by PELDOR in combination with nitroxide labeling (192, 151). Compound **21** contains one nitroxide and one trityl. First, this biradical enables a direct comparison to PELDOR measurements on similar compounds spin-labelled with two nitroxides. Second, a biradical with a combination of trityl and nitroxide spin labels will be useful to assess the possibilities of using a combination of trityls and nitroxides for biological heterodimers.

The two radicals in compounds **21** and **22** are connected by a linear tether consisting of aryl and acetylene units that are linked through a series of Sonogashira cross-coupling reactions (78).

#### 6.4 CW-EPR measurements on biradicals **21** and **22**

The trityl-nitroxide biradical **21** and trityl biradical **22** were measured with continuous wave electron paramagnetic resonance (CW-EPR) at both 295 and 130 K to confirm the presence of the radicals. The EPR spectra of **21** show the narrow peak from the trityl overlapping with the nitroxide spectrum (Figure 6.4.1). While the nitroxide part of the spectrum becomes considerably broader for the frozen sample, the spectrum for the trityl shows negligible broadening. Simulating the EPR spectra of **21** using the EasySpin toolbox (133) confirmed that the ratio of trityl to nitroxide is 1:1 (Figure 6.4.1 and Table 6.4.1).

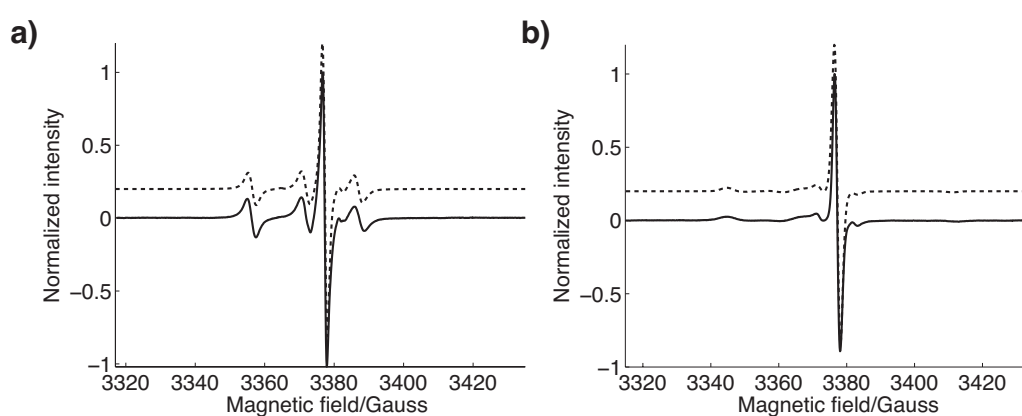


**Figure 6.4.1.** CW-EPR spectra of **21**. **a)** CW-EPR spectrum at 295 K (solid line) and simulated spectrum (broken line). **b)** CW-EPR spectrum at 130 K (solid line) and simulated spectrum (broken line). Simulated spectra have been displaced on the vertical axis for clarity.

The EPR spectra obtained from biradical **22** at 295 and 130 K show a single narrow peak and small satellite signals from  $^{13}\text{C}$  hyperfine coupling (Figure 6.4.2). Overall the trityl spectrum does not become appreciably broader when freezing the sample. The EPR spectra for **22** were also simulated using the EasySpin toolbox (Figure 6.4.2 and Table 6.4.1).



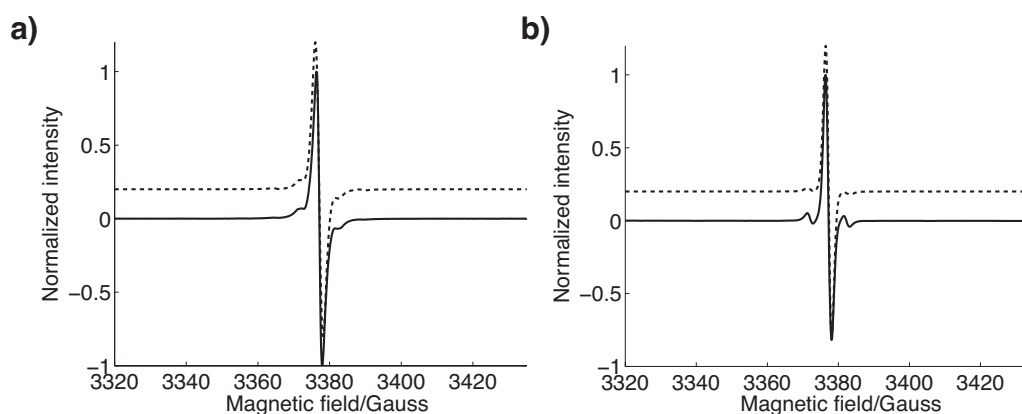


**Figure 6.4.2.** CW-EPR spectra of **22**. **a)** CW-EPR spectrum at 295 (solid line) and simulated spectrum (broken line). **b)** CW-EPR spectrum at 130 K (solid line) and simulated spectrum (broken line). Simulated spectra have been displaced on the vertical axis for clarity.

**Table 6.4.1.** Simulation parameters for **21** and **22** at 295 and 130 K.

Parameters	<b>21</b>		<b>22</b>
	Nitroxide	Trityl	
$g_{xx}, g_{yy}, g_{zz}$	2.0093, 2.0059, 2.0018	2.0030, 2.0027, 2.0021 <sup>(1)</sup>	2.0030, 2.0027, 2.0021 <sup>(1)</sup>
$A_{xx}, A_{yy}, A_{zz}$ <sup>[a]</sup>			
<sup>14</sup> N Nitroxide nitrogen	18, 18, 93	-	-
<sup>13</sup> C Central carbon <sup>(2)</sup>	-	20.6, 20.6, 160.1	20.6, 20.6, 160.1
<sup>13</sup> C 1-Phenyl carbon	-	25, 25, 34	25, 25, 34
<sup>13</sup> C 2,6-Phenyl carbon	-	18, 18, 36.7	18, 18, 36.7
Linewidth <sup>[b]</sup>	295 K	0.12, 0.13	0.10, 0.07
	130 K	0.35, 0.01	0.15, 0.04
Rotational correlation time <sup>[c]</sup>	$1.4 \cdot 10^{-14}$	$1.4 \cdot 10^{-14}$	$1.4 \cdot 10^{-14}$
Weight	0.5	0.5	-

[a] The hyperfine coupling values are in MHz. Only carbon atoms with the largest hyperfine couplings were included in the simulation for the trityl. [b] The linewidths (Gaussian, Lorentzian) is the peak to peak linewidth in mT. [c] Isotropic rotational correlation times for simulation at 295 K are in seconds. The rotational correlation time was fixed to this value to produce a fast-motion spectrum. (1) A. J. Fielding, P. J. Carl, G. R. Eaton, S. S. Eaton, *Appl. Magn. Reson.* 2005, 28, 231–238. (2) M. K. Bowman, C. Mailer, H. J. Halpern, *J. Magn. Reson.* 2005, 172, 254–367.

## 6.5 PELDOR and DQC measurements on trityl-nitroxide biradical **21**

### 6.5.1 PELDOR

A sample of **21** was dissolved in d8-toluene to 200  $\mu\text{M}$  and measured with four-pulse PELDOR at 50 K. In order to get the optimum PELDOR signal, the detection sequence should solely excite the nitroxide spectrum and the inversion pulse should at least excite the complete trityl spectrum, although without too large excitation overlap between the detection and inversion pulses. By placing the inversion pulse on the center of the trityl spectrum it is then possible to place the detection sequence on the nitroxide spectrum with 30 - 90 MHz frequency difference between detection and inversion pulses (Figure 6.5.1). Since the width of the trityl peak is only about 2 G, a 16 ns inversion pulse with an excitation bandwidth of 16 G at half-height should completely excite the whole trityl EPR spectrum and invert all of the trityl spin centres.

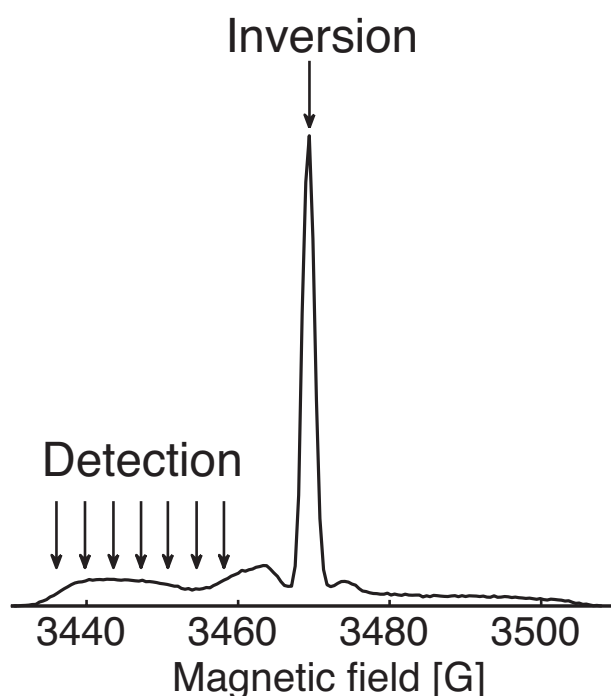


**Figure 6.5.1.** Echo detected field swept EPR spectrum of compound **21**. Field positions of the PELDOR detection and inversion pulses are indicated by arrows.

Figure 6.5.2 shows the PELDOR data obtained from **21**. A modulation depth  $\Delta$  of 90% was observed experimentally for all frequency offset of the detection pulses (Figure 6.5.1). This indicates that the trityl is not completely excited by the

inversion pulse. The deviation from the expected 100% modulation depth is attributed to the inversion pulse not having an excitation profile of an ideal  $\pi$  pulse. This is discussed in more details in section 6.5.3. The modulation depth of 90% obtained here from **21** is still twice the modulation depth obtained for nitroxide biradicals at X-band (48, 49).

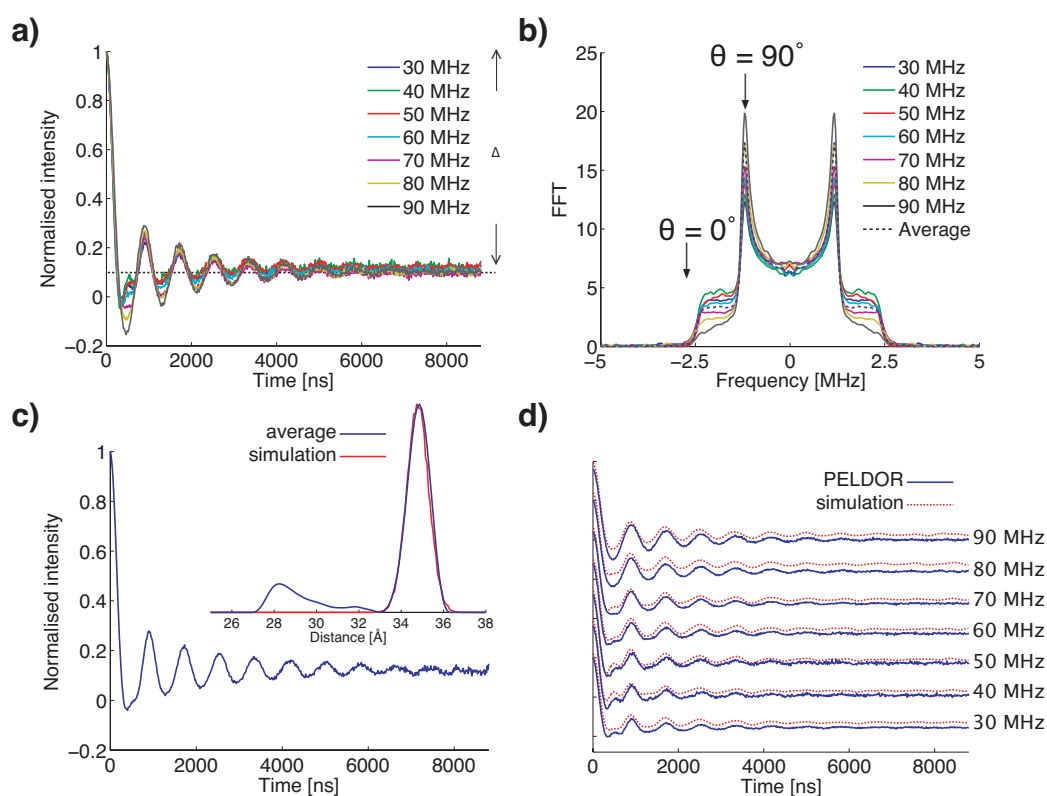


**Figure 6.5.2.** PELDOR data obtained from **2**. **a)** Background-subtracted time traces. **b)** Fourier transformed time traces in **a)**. **c)** Orientation averaged time trace and distance distributions obtained from DeerAnalysis (blue line) and via simulations (red line). **d)** Background corrected time traces (blue line) and simulated time traces (broken red line). Experimental and simulated time traces have been displaced on the vertical axis for clarity. Original time traces are shown in materials and methods section.

Fourier transforming the PELDOR time traces from **21** reveals that the intensity of the perpendicular component ( $\theta = 90^\circ$ ) of the dipolar coupling increases while the intensity of the parallel component ( $\theta = 0^\circ$ ) decreases as the detection frequency is moved from 30 to 90 MHz offset (Figure 6.5.2). This shows that although the modulation depth is invariant with position of the detection sequence for such mixed trityl/nitroxide labeled systems any inherent orientation selection will be decoded in the frequency of the PELDOR

modulation, making orientation-selective PELDOR measurements still possible and with much improved modulation depth compared to bisnitroxides (120). To obtain a distance distribution from the PELDOR time traces of **21** using Tikhonov regularization, the individual orientation selective time traces at different frequency offset have to be added together to yield an orientation averaged time trace (Figure 6.5.2 c). The distance distribution is then obtained from the orientation averaged time trace using DeerAnalysis (123) (Figure 6.5.2 c, inset). The mean distance from the orientation averaged time trace is in agreement with the distance obtained from molecular mechanics calculations on **21** (Table 6.5.1) The small peak at around 28 Å in the distance distribution is attributed to incomplete orientation averaging since its peak value corresponds to the over-weighted parallel dipolar component (Figure 6.5.2 b).

**Table 6.5.1.** Interspin distances for **21** and **22** obtained from molecular mechanics, simulations, and from PELDOR and DQC, both in combination with DeerAnalysis. All distances are given as a mean value  $\pm$  two standard deviations.

	$r_{\text{sim}} [\text{Å}]$ [a]	$r_{\text{PELDOR}} [\text{Å}]$ [a]	$r_{\text{DQC}} [\text{Å}]$ [a]	$r_{\text{MM}} [\text{Å}]$
<b>21</b>	$34.8 \pm 1.1$	$34.8 \pm 1.0$	$34.8 \pm 1.2$	35
<b>22</b>	$48.8 \pm 1.3$	$48.7 \pm 1.6$	$48.9 \pm 1.4$	51

[a] The mean distance  $\pm$  two standard deviations is given for the most probable peak.

## 6.5.2 Simulations of PELDOR time traces

Because the PELDOR time traces of **21** are orientation-selective the experimental time traces were simulated using the peldorsim program (Chapter 3) in order to obtain a more precise distance distribution and further information on the conformational dynamics of the biradicals. A dynamics model is needed for the simulation of time traces. Therefore, a model for **21** was constructed by treating the backbone and spin labels of **21** as a chain of rigid segments linked by joints, as was previously done for a set of structurally similar nitroxide biradicals (192, 151). The PELDOR simulations were obtained from 20,000 conformers. The conformers were generated by using a harmonic segmented chain (HSC) model (Figure 6.5.3) (192, 151).

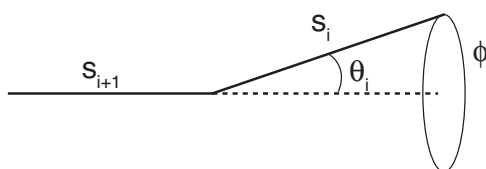


**Figure 6.5.3.** Segmented chain model. Each rigid segment  $s_i$  is allowed to bend and rotate about its joint with  $\theta_i$  and  $\phi$ , respectively. The bending angles  $\theta_i$  are the bending angles for the molecular linker-, nitroxide spin label- and trityl spin label- segments  $\theta_S$ ,  $\theta_N$ ,  $\theta_T$ , respectively. They are described by a normal distribution and the torsion angle  $\phi$  is uniformly distributed between 0 and  $2\pi$ .

The following are defined as segments: bonds between the center of the nitroxide N-O bond and the carbon atom of the amide group, the bonds between the trityl radical center and the oxygen atom of the ester group, each benzene group and each remaining bond between atoms in the molecular linker (Figure 6.5.4). These rigid segments are allowed to bend with a normal distribution  $\theta_i$  and rotate uniformly between 0 and  $2\pi$  ( $\phi$ ) about the atoms, which act as joints. Mean segment lengths and bending angles  $\theta_i$  were obtained from molecular mechanics calculations. The mean lengths of the segments are the following: 2.8 Å (benzen), 1.5 Å (benzen-benzen bond), 1.4 Å (benzene-acetylene bond), 1.2 Å (acetylene), 1.5 Å (benzene-oxygen bond), 1.4 Å (benzene-carbon bond), 5.8 Å (nitroxide spin label), 6 Å (trityl spin label). All segments within the molecular linker have a mean bending angle of  $0^\circ$ . The nitroxide and trityl spin label segments have a mean bending angle of  $24^\circ$  and  $12.7^\circ$ , respectively. Distributions in lengths and flexibility of segments, that resulted in the best fit between simulated and experimental PELDOR time traces are summarized in Table 6.5.2.

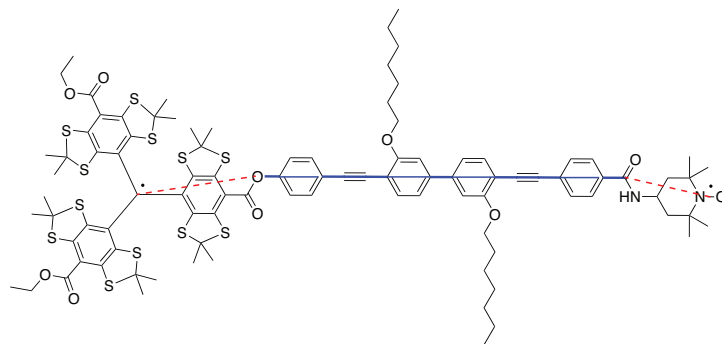


**Figure 6.5.4.** Chemical structure of **21**. The molecular linker segments are indicated by blue solid lines and the spin label segments are indicated by red broken lines.

**Table 6.5.2.** Dynamics parameters used for conformational model of **21** and **22**.

	$\sigma_r^{[a]}$	$\theta_S^{[b]}$	$\theta_N^{[b]}$	$\theta_T^{[b]}$
<b>21</b>	0.13(0.03)	$0 \pm 2.9(1)$	$24(3) \pm 2.9(1)$	$12.7(3) \pm 2.9(1)$
<b>22</b>	0.13(0.03)	$0 \pm 2.9(1)$	-	$12.7(3) \pm 2.9(1)$

[a]  $\sigma_r$  describes the average standard deviation in the length of each segment.<sup>[8]</sup> [b]  $\theta_S$ ,  $\theta_N$ ,  $\theta_T$ , describe the bending angle  $\theta_i$  of the molecular linker-, nitroxide spin label- and trityl spin label-segments, respectively. All segments within the molecular linker have the same bending distribution  $\theta_S$ . The degree of bending for each segment is described as the mean value  $\pm$  two standard deviations. Number in bracket is the error of the corresponding parameter.

The dynamics model constructed for **21** and the EPR parameters determined from CW-EPR spectra were used to reproduce the orientation selective PELDOR time traces (Figure 6.5.2 d). The dynamics model also provided an excellent fit to the distance distribution from the orientation averaged time trace (Figure 6.5.2 c, inset and Table 6.5.1). The parameters determined here for the dynamics of **21** are in excellent agreement with those determined from similar compounds, using nitroxide spin labelling and PELDOR (192). The PELDOR measurements and model-based simulations on **21** indicate that the size of the trityl spin label has negligible influence on the dynamics of the polyPPEs. In addition, the symmetric spin delocalization of the trityl spin label does not appear to have an effect on the measured interspin distance, at least not for distances equal to or beyond that measured for **21**.

### 6.5.3 Excitation profile of the inversion pulse

The excitation profile of the 16 ns optimized inversion pulse, used in the PELDOR experiments on biradical **21**, was experimentally obtained from a frequency swept spectrum (Figure 6.5.5 b). Simulating the experimental PELDOR time traces for **21** using a theoretical excitation profile (38) for an ideal square inversion pulse results in time traces with 100% modulation depth. On the other hand, using an excitation profile that approximates the experimentally determined profile for the 16 ns inversion pulse results in simulated time traces with 90% modulation depth, in agreement with the experimental PELDOR time traces. Simulated PELDOR time traces at 70 MHz offset using the theoretical and experimental  $\pi$  pulse profiles are shown as an example in figure 6.5.5 a.

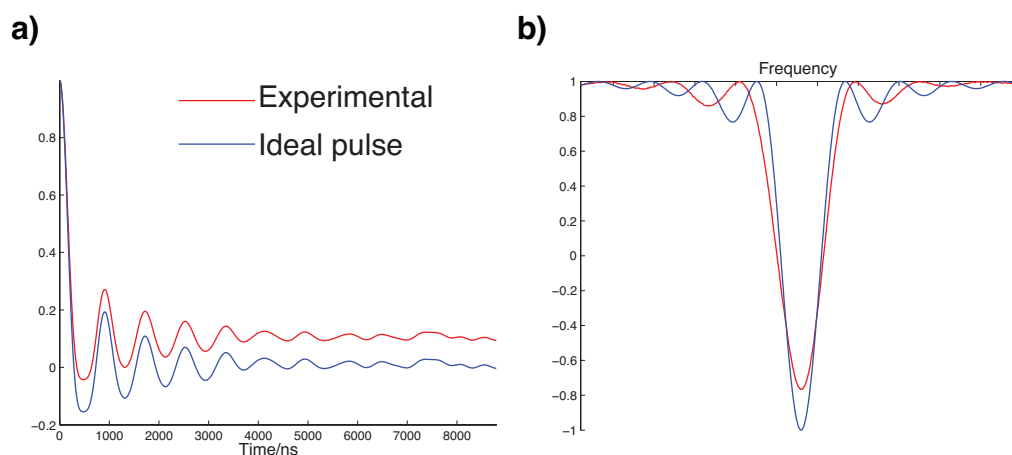


**Figure 6.5.5.** Simulated PELDOR time traces and excitation profiles. **a)** Simulated PELDOR time traces for **21** at 70 MHz offset using a theoretical (blue) and experimental (red) excitation profile for the inversion pulse. **b)** Theoretical (blue) and experimental (red) excitation profiles for a 16 ns  $\pi$  pulse.

#### 6.5.4 PELDOR measurements on trityl-nitroxide biradical using different inversion/detection positions

In all the above PELDOR experiments on biradical **21**, the inversion pulse was positioned on the trityl spectrum and the detection sequence on the nitroxide spectrum. To further investigate PELDOR measurements on biradical **21**, PELDOR experiments with different detection/inversion positions were performed. First, the inversion pulse was positioned on the nitroxide spectrum and the detection pulse sequence on the trityl spectrum with 70 MHz frequency difference (Figure 6.5.6 a, blue labels).

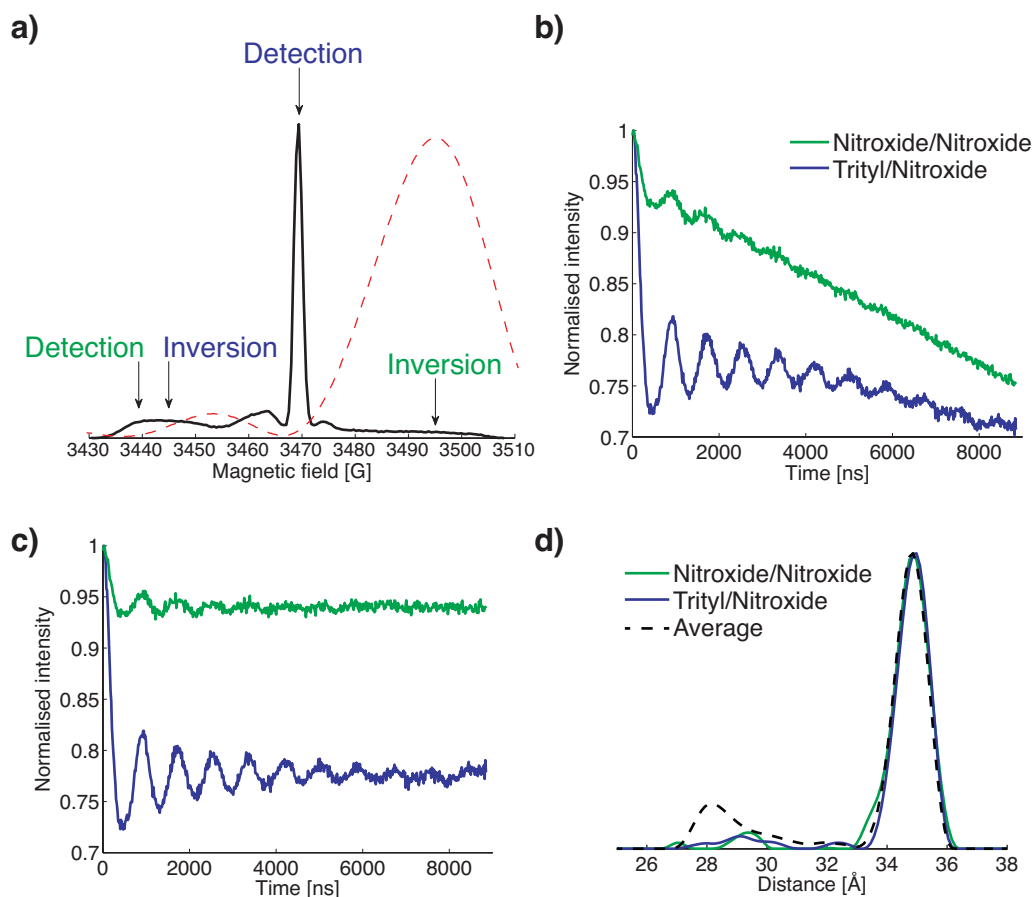


**Figure 6.5.6.** PELDOR experiments with different inversion/detection position on **21**. **a)** Echo detected field swept spectrum of **21** and positions of the inversion and detection pulses. The excitation profile of the inversion pulse is shown as red broken line. **b)** Original PELDOR time traces of **21** obtained by positioning the detection pulse sequence on the trityl spectrum and inversion pulse on the nitroxide spectrum (blue) and detection and inversion pulses on the nitroxide spectrum (green). **c)** Background corrected time traces in **b)**. **d)** Distance distribution from the time traces in **b)** and from the orientation averaged time trace (black broken line).

The detection sequence, now placed on the narrow trityl spectrum, will excite a larger fraction of spins, which should result in an increased signal-to-noise ratio (S/N) for the refocused echo. On the other hand, the inversion pulse, which is now placed on the broad nitroxide spectrum, will only excite a fraction of nitroxide spins that are coupled to the trityl spin labels. This will lead to a decreased PELDOR modulation depth. Acquiring a PELDOR time trace with this setup resulted in a time trace with a considerably reduced S/N, compared to the setup where the inversion pulse was on the trityl spectrum, and a modulation depth of only 25% (Figure 6.5.6 b, c). The reason for the decreased S/N of the PELDOR time trace with the detection sequence placed on the trityl spectrum is attributed to the shorter  $T_m$  of the trityl compared to the nitroxide at 50 K.



Two-pulse electron spin echo envelope modulation (ESEEM) measurements at 50 K revealed a  $T_m$  of 2.8  $\mu\text{s}$  and 8.4  $\mu\text{s}$  for the trityl and nitroxide spin labels, respectively (Figure 6.5.7).

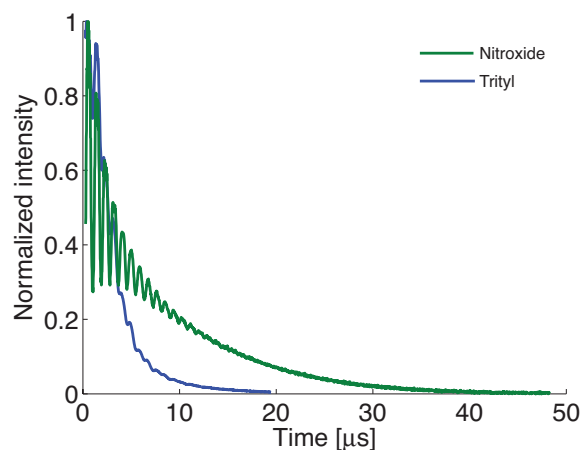


**Figure 6.5.7.** Two-pulse ESEEM measurements of compound **21** at 50 K.  $T_m$  values of 8.4 and 2.8  $\mu\text{s}$  are obtained from the ESEEM time traces on the nitroxide spin label (green) and trityl spin label (blue), respectively.

Furthermore, placing the detection sequence on the trityl results in a PELDOR echo with a comparable intensity, but which is broader by a factor of 3.4, relative to the echo obtained with the detection on the nitroxide.

In a second PELDOR experiment, the inversion and observer pulses were both positioned on the nitroxide spectrum with a frequency separation of 168 MHz (Figure 6.5.6 a, green labels). Since the sample of **21** does not contain biradicals with two nitroxides, this setup should in fact not yield an intramolecular dipolar modulation. However, the PELDOR time trace obtained from **21**, with both inversion and detection on the nitroxide spectrum, has a visible modulation with a depth of 6% (Figure 6.5.6 b, c). This modulation is attributed to the inversion pulse exciting a small portion of the trityl spectrum due to the side-bands of the excitation profile (Figure 6.5.6 a). Using DeerAnalysis to analyze the time traces from these alternative PELDOR setups yields distance distributions that are in very good agreement with the distribution obtained from the orientation averaged PELDOR time trace, where the detection sequence was placed on the

nitroxide spectrum and the inversion pulse on the trityl spectrum (Figure 6.5.6 d).

### 6.5.5 DQC

Another elegant pulse EPR technique to detect the dipolar electron-electron coupling between spin centres is double quantum coherence (DQC) (52, 53). First introduced by Freed and coworkers (51), DQC-EPR solely detects the dipolar electron-electron coupling in a time-domain experiment by using a pulse sequence that includes a double-quantum coherence filter. To successfully measure the dipolar coupling using “allowed” DQC pathways, the microwave pulses should ideally be non-selective (54). Measuring nitroxides, which have a broad EPR spectrum, with DQC using allowed pathways is, therefore, technically demanding. To our knowledge, DQC measurements on nitroxide samples, using commercially available EPR spectrometers, have not yet been reported without large ESEEM modulation and ‘forbidden’ coherence pathways due to the lack of high enough microwave power.

Because the trityl radical has a much narrower spectral width than nitroxides, biradical **21** was measured with DQC at X-band frequencies using a E580 FT-EPR spectrometer equipped with a dielectric resonator from Bruker. The shortest  $\pi/2$  pulse length possible with this spectrometer and resonator was about 8 ns. The DQC experiments were, therefore, acquired using  $\pi/2$  and  $\pi$  pulse lengths of 8 and 16 ns, respectively to be able to excite as much as possible of the spectrum of **21**. The DQC experiments were performed using the six-pulse DQC sequence published by Borbat and Freed (54). A two-pulse echo detected field swept spectrum of **21** was recorded and the frequency of the microwave source positioned at the center of the trityl peak (Figure 6.5.8).

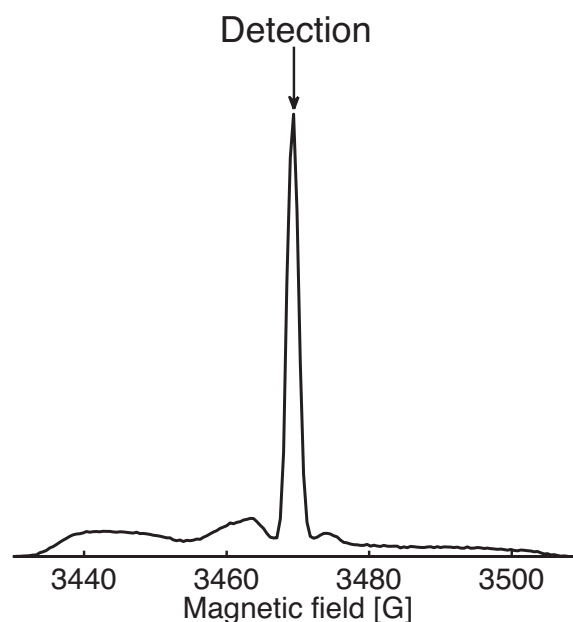


**Figure 6.5.8.** Echo detected field sweep of **21**. The field position of the DQC pulse sequence is indicated by the arrow.

The six-pulse DQC experiment on **21** yielded a time trace with a well-defined modulation (Figure 6.5.9 a). A polynomial of degree 5 was fitted to the DQC time trace and subtracted from the original data to obtain a background corrected time trace (Figure 6.5.8 b). PELDOR time traces are normally background corrected by fitting an exponential function to the original data and dividing the PELDOR time trace with the fitted function. Since the DQC data decays to zero at the end of the time-window, the fitted polynomial function has to be subtracted and not divided from the original DQC time trace to avoid distortions to the background corrected time trace from division with very small numbers or even zero. The dipolar spectrum, obtained by Fourier transforming the background corrected time trace, shows a not quite complete, Pake pattern (Figure 6.5.9 c) which is indicating that the EPR spectrum of **21** is not completely excited by the DQC pulses.

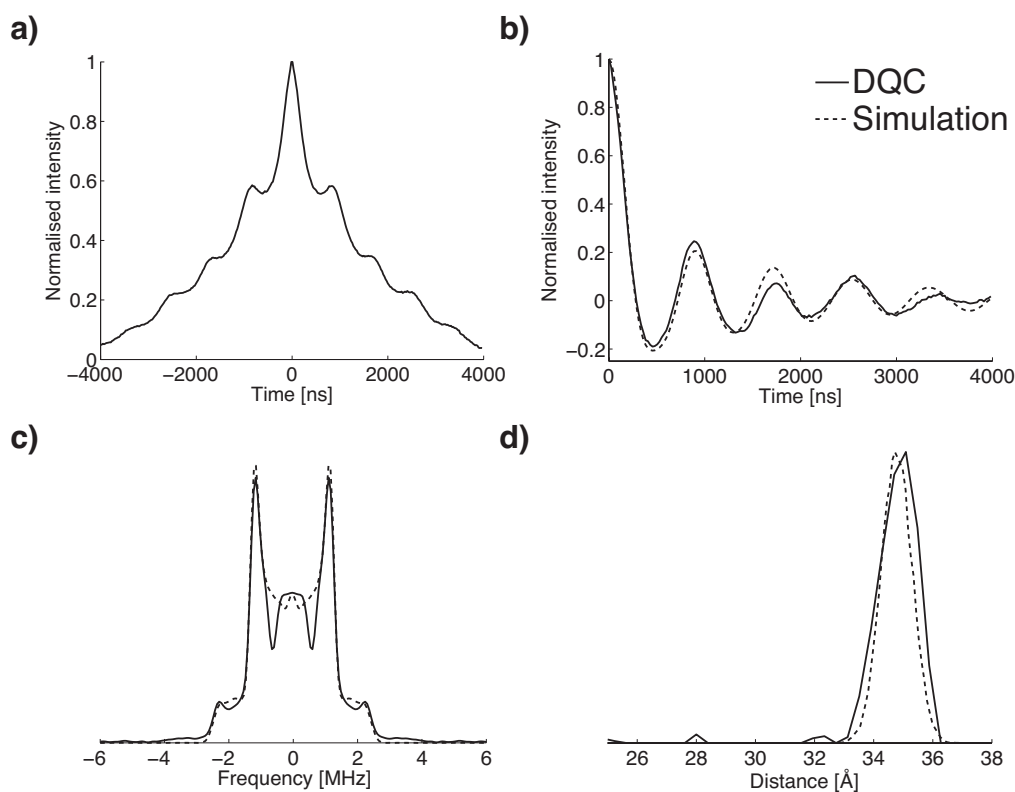


**Figure 6.5.9.** Six-pulse DQC data obtained from **21**. **a)** DQC time trace. **b)** Background corrected time trace (solid line) and simulated time trace (broken line). **c)** Fourier transformation of the time traces in **b)**. **d)** Distance distributions from the DQC time trace using DeerAnalysis (solid line) and the simulation model (broken line).

Analyzing the background corrected DQC time trace with Tikhonov regularization, as implemented in DeerAnalysis yielded a distance distribution with a mean value of 34.8 Å (Figure 6.5.9 d), in agreement with the distance distribution obtained from the orientation averaged PELDOR time trace and the model-based PELDOR simulations (Table 6.5.1). These results indicate that it might be sufficient to completely excite the dipolar coupling on one of the two spin centres in order to obtain a DQC time trace without substantial interference from forbidden coherence transfers and orientation selection (54, 31). To further evaluate the data, the DQC time trace and distance distribution were simulated using the same dynamics model as developed for the simulation of PELDOR time traces for **21**. The DQC time trace was simulated assuming complete excitation of the EPR spectrum. Although the simulated time trace has a modulation frequency that fits to the experimental time trace there are small discrepancies in the decay of the modulation (Figure 6.5.9 b), which is most likely due to lack of

complete excitation of the EPR spectrum of **21**. Fourier transforming the simulated time trace also shows that the experimental dipolar spectrum is not complete (Figure 6.5.9 c). Nevertheless, the simulated distance distribution is shown to fit nicely to the experimental distribution obtained from DeerAnalysis.

To assess the possibility of obtaining a DQC time trace of a nitroxide biradical with the commercial EPR spectrometer setup used here, a semi-rigid nitroxide biradical (see compound **17** in Chapter 4), dissolved in deuterated toluene and with a spin concentration of 1 mM, was measured with six-pulse DQC at 50 K (Figure 6.5.10). The interspin distance for this nitroxide biradical was determined to be 19.8 Å from DFT calculations and 19.3 Å using PELDOR at W-band (Chapter 4).

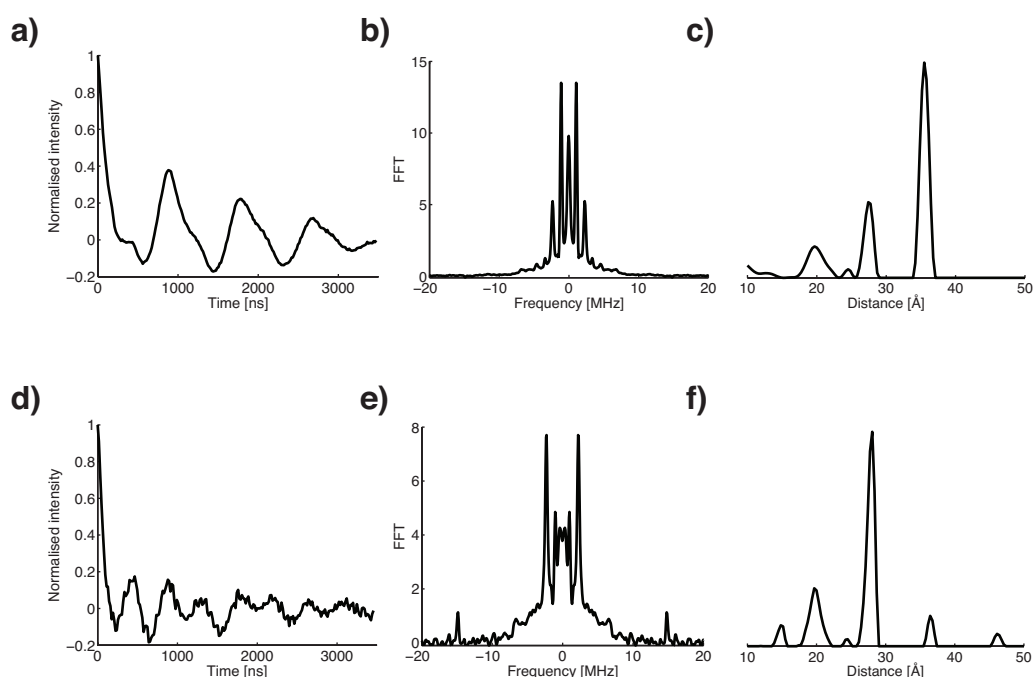


**Figure 6.5.10.** Six-pulse DQC data obtained from a semi-rigid nitroxide biradical **17**. **a,d)** Background corrected DQC time trace. **b,e)** Fourier transformation of the time traces in **a,b)**. **c,f)** Distance distribution from the time trace in **a,b)**.

The shortest pulse lengths for the  $\pi/2$  and  $\pi$  pulses, achievable for this sample, were 12 and 24 ns, respectively. To suppress nuclear modulations from either protons or solvent deuterium, four time traces with varying initial pulse delays were added together. Using suppression of proton modulation the DQC time

trace shows very strong modulation from coupling to deuterium (Figure 6.5.10 a). This unwanted deuterium modulation shows up as peaks at about  $\pm 1$  and  $\pm 2.2$  MHz in the dipolar spectrum (Figure 6.5.10 b) with corresponding distances of about 28 Å and 35 Å. The distance distribution also has a smaller peak at 19.7 Å. Acquiring the DQC time trace with suppression of deuterium modulation results in a time trace that shows a less pronounced deuterium modulation but a stronger modulation from protons (Figure 6.5.10 d). The dipolar spectrum has the most pronounced peaks at about  $\pm 14.9$  and  $\pm 2.2$  MHz from proton and deuterium modulation, respectively. The strong deuterium modulation has, therefore, not been fully suppressed by modulation suppression. The distance distribution from the DQC time trace with deuterium modulation suppression has the largest peak at about 28 Å and a smaller peak at 19.7 Å. The small peak at 19.7 Å in the distance distributions from both DQC experiments is most likely from the dipolar coupling since this distance is close to the 19.8 Å determined by DFT calculations. It should be noted that the W-band PELDOR (Chapter 4) experiment on **17** was performed in a matrix of deuterated o-terphenyl, which has a higher melting temperature than toluene. This could explain the slightly shorter distance measured by PELDOR.

To summarize, these measurements show that measuring interspin distances between a pair of nitroxide spin labels using DQC and a similar commercial EPR spectrometer setup results in time traces that include strong signals from nuclear modulations. This results in a high degree of uncertainty with respect to the measured dipolar coupling.

## 6.6 PELDOR and DQC measurements on trityl-trityl biradical **22**

### 6.6.1 PELDOR

In the discussion above, the experimental results from PELDOR and DQC experiments on the trityl-nitroxide biradical **21** were shown and discussed. In this section, distance measurements on the trityl biradical **22** using PELDOR and DQC will be presented.

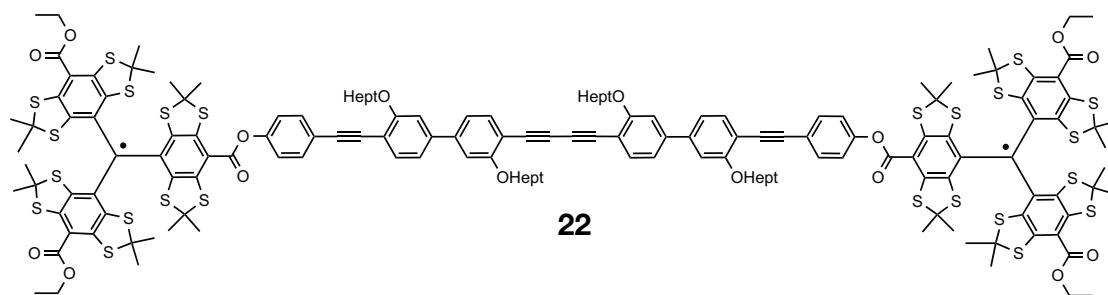


**Figure 6.6.1.** Chemical structure of **22**.

The trityl biradical **22** was dissolved in *d*8-toluene to 200  $\mu\text{M}$  and measured with four-pulse PELDOR at 50 K. The trityl has an EPR spectrum with a width of only 2 G (Figure 6.6.2). Thus, a trityl EPR spectrum is about a factor of 30 narrower than for a typical nitroxide biradical, which has a width of about 70 G. The reduced width of the trityl compared to a nitroxide translates into increased signal intensity for the trityl biradical system by roughly the same factor of 30. Since the EPR spectrum of the trityl is so narrow, setting up a PELDOR experiment without substantial frequency overlap between detection and inversion pulses becomes difficult.

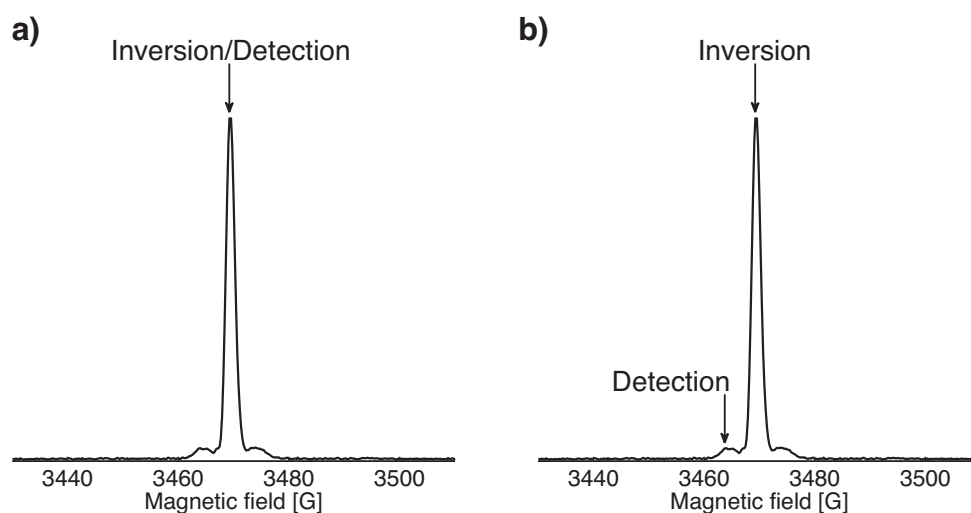


**Figure 6.6.2.** Two-pulse echo detected field sweep at X-band of **22**. **a, b)** Positions of the PELDOR inversion pulse and detection sequence are indicated by arrows. The small satellites to each side of the sharp peak are from hyperfine interaction to  $^{13}\text{C}$ .

The trityl biradical **22** was first measured with PELDOR by positioning both the detection sequence and inversion pulse on the center of the narrow trityl peak

(Figure 6.6.2 a). The length of the inversion pulse was 60 ns and the lengths of the  $\pi/2$  and  $\pi$  pulses, in the detection sequence, were 16 and 32 ns, respectively. The length of the inversion pulse was set to 60 ns instead of 16 ns in an effort to minimize the excitation overlap of detection and inversion pulses. This PELDOR setup, which is actually a single frequency '2+1' experiment without phase coherence between the detection and inversion pulses (193), yielded a highly distorted PELDOR time trace with very strong ESEEM modulation from interactions between the trityl radical and solvent deuterium ( $S = 1$ ) (Figure 6.6.3). This distorted PELDOR time trace is attributed to the large frequency overlap between detection and inversion pulses.

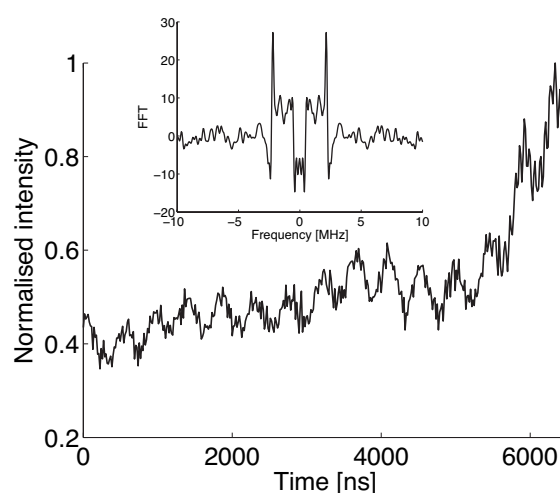


**Figure 6.6.3.** 4-pulse PELDOR of **22** and the corresponding dipolar spectrum (inset).

To decrease the overlap between detection and inversion pulses, the trityl biradical **22** was measured with a slightly different PELDOR setup. Again, the inversion pulse was placed on the center of the narrow trityl peak but now the detection sequence was positioned on the  $^{13}\text{C}$  satellite on the low-field side, 13 MHz away from the inversion pulse (Figure 6.6.2 b). The length of the inversion pulse was still 60 ns but the lengths of the  $\pi/2$  and  $\pi$  pulses in the detection sequence were increased to 32 and 64 ns respectively, in order to decrease further the overlap with the excitation profile of the inversion pulse. The time trace obtained from **22** using this PELDOR setup has a well-defined modulation and a modulation depth of about 38% (Figure 6.6.4 a).



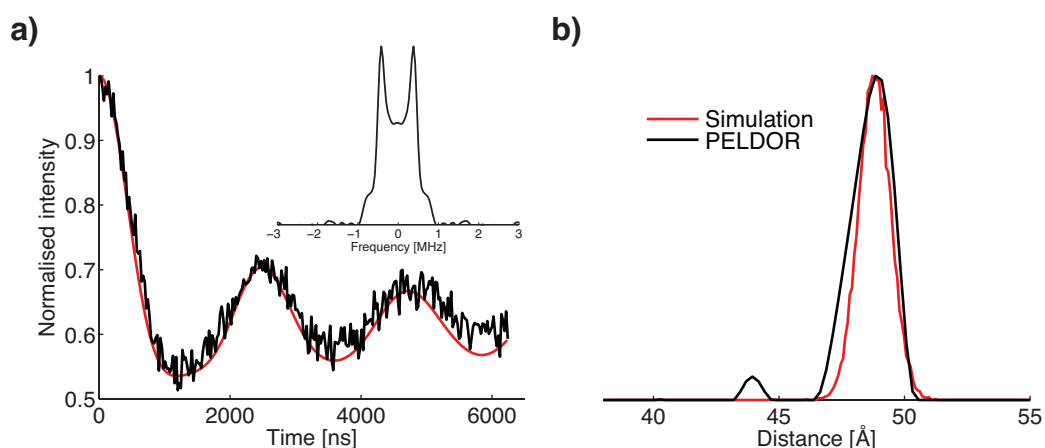


**Figure 6.6.4.** 4-pulse PELDOR of **22**. **a)** Background corrected PELDOR time trace (black) and simulated time trace (red). The experimental dipolar spectrum is shown as inset. **b)** Distance distribution obtained from the PELDOR time trace (black) and dynamics model (red).

The S/N is rather poor which is due to detection of the low intensity  $^{13}\text{C}$  satellites. The distance distribution obtained from Tikhonov regularization on the background corrected PELDOR time trace has a mean value of 48.7 Å (Figure 6.6.4 b), which is in agreement with the interspin distance obtained from molecular mechanics calculations (Table 6.5.1). The PELDOR time trace for **22** was also simulated using a segmented-chain dynamics model that was constructed in the same way as the model for the trityl-nitroxide biradical **21** (Figure 6.5.3). The dynamics parameters for this model were the same as for the model of **21** (Table 6.5.2). The simulated PELDOR time trace is in very good agreement with the experimental data (Figure 6.6.4 a). The simulated distance distribution, generated from the dynamics model, also fits nicely to the distance distribution obtained from the PELDOR time trace using DeerAnalysis (Figure 6.6.4 b). These results show that although the trityl has a narrow spectral width it is still possible to obtain accurate PELDOR data of reasonable quality from trityl biradicals.

## 6.6.2 DQC

As discussed in the previous section, the dipolar coupling of trityl biradical **22** can be measured with PELDOR, although with less than optimum signal-to-noise ratio and modulation depth. The narrow spectral width of the trityl biradical should make DQC the preferred method to measure the dipolar coupling. DQC

measurements on **22** yielded a time trace with excellent signal-to-noise ratio and a well-defined modulation. The DQC time trace was background corrected by subtracting an exponential function from the original time trace (Figure 6.6.5 a). Analyzing the background corrected DQC time trace with DeerAnalysis yields a distance distribution with a mean value of 48.9 Å, in excellent agreement with the mean distance obtained from PELDOR measurement on **22** (Table 6.5.1).

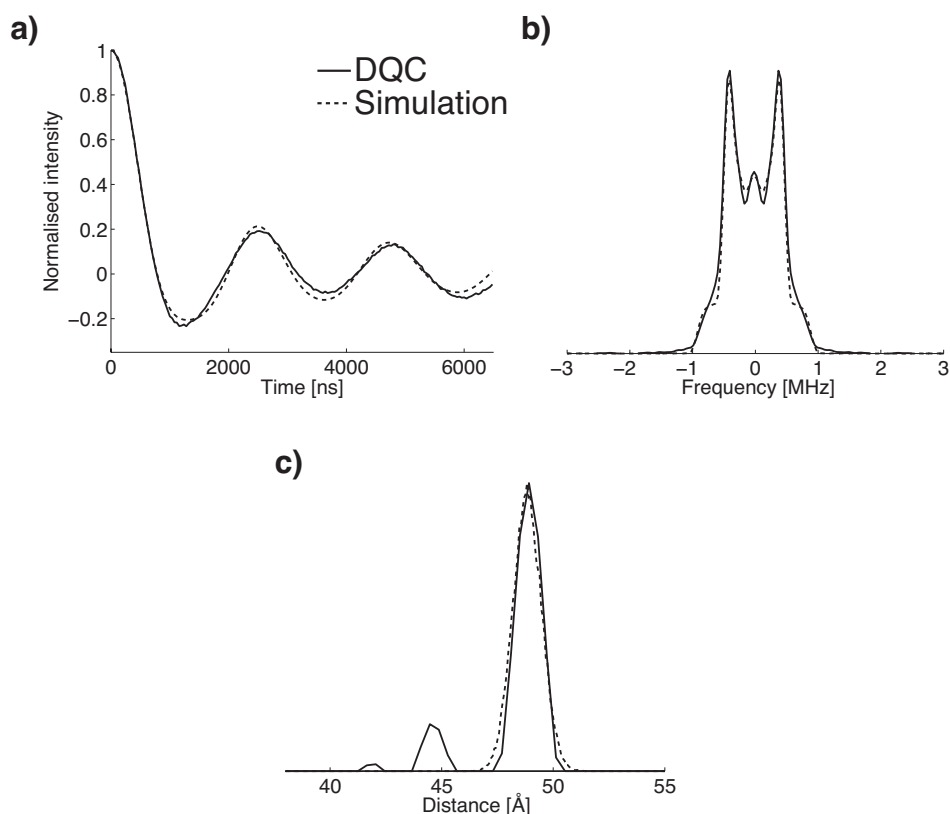


**Figure 6.6.5.** Six-pulse DQC data obtained from **22**. **a)** Background-corrected time trace (solid line) and simulated time trace (broken line). **b)** Fourier transform of the time traces in **a)**. **c)** Distance distributions from the DQC time trace in **a)** using DeerAnalysis (solid line) and the model based simulation (broken line).

The DQC time trace for **22** was simulated using the same dynamics model as used to simulate the PELDOR time trace of **22**. The simulated DQC time trace almost completely replicates the experimental time trace (Figure 6.6.5 a). The distance distribution obtained from the model-based simulation is also in very good agreement with the distribution obtained from the experimental DQC time trace using DeerAnalysis (Figure 6.6.5 c).

### 6.6.3 DQC measurements at 50 - 100 K

Two-pulse ESEEM measurements on trityl biradical **22** in deuterated toluene at 50, 80 and 100 K were performed to measure the transverse spin relaxation  $T_m$  at these temperatures (Figure 6.6.6). From these measurements, the  $T_m$  was estimated to be 2.6, 3.2 and 1.6  $\mu\text{s}$  at 50, 80 and 100 K, respectively.

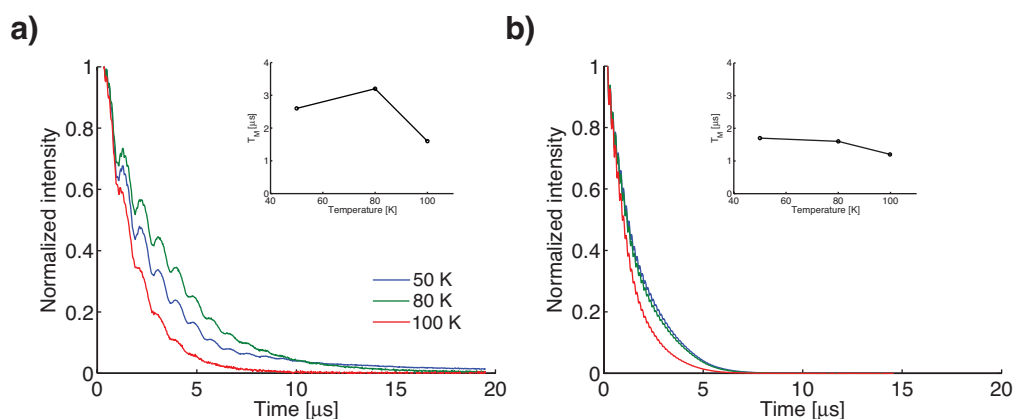


**Figure 6.6.6.** Two-pulse ESEEM measurements of trityl biradical **22** at 50 - 100 K. **a)** In deuterated toluene **22** has a  $T_m$  value of 2.6, 3.2 and 1.6  $\mu\text{s}$  at 50, 80 and 100 K, respectively. **b)** In THF **22** has a  $T_m$  value of 1.7, 1.6 and 1.2  $\mu\text{s}$  at 50, 80 and 100 K, respectively. The insets show the change in  $T_m$  with temperature.

Interestingly, the  $T_m$  at 80 K was a factor of 1.2 higher than at 50 K. On the contrary, for biradical **22** in tetrahydrofuran (THF) the  $T_m$  was estimated as 1.7, 1.6 and 1.2  $\mu\text{s}$  at 50, 80 and 100 K, respectively, with the maximum  $T_m$  at 50 K. The increase in  $T_m$  observed for **22** in deuterated toluene is, therefore, most likely due to the solvent and its temperature-dependent behavior. The overall decrease in  $T_m$  for **22** in THF compared to deuterated toluene is mostly due to the THF not being deuterated. Since the  $T_m$  for **22** in deuterated toluene increases going from 50 to 80 K, **22** was measured with DQC at both 50 and 80 K to assess if measuring at 80 K would improve the S/N for the DQC time trace (Figure 6.6.7).

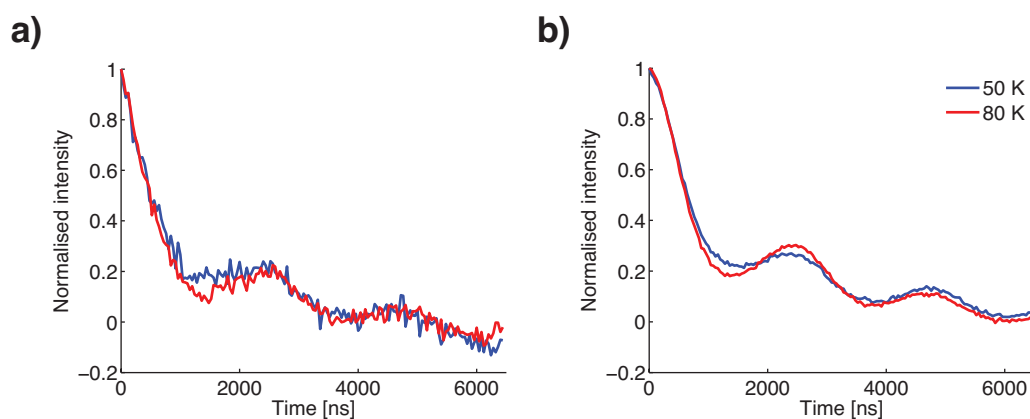


**Figure 6.6.7.** DQC time trace of trityl biradical **22** recorded at 50 K (blue) and 80 K (red). **a)** DQC time traces after 3 min. of acquisition. **b)** DQC time traces after 2 h. of acquisition. All experimental settings were identical for both time traces.

Comparing the original DQC time traces (Figure 6.6.7 a), it can be seen that the S/N ratio becomes slightly larger when measuring at 80 K. To evaluate the gain in S/N ratio, the degree of noise in these time traces was evaluated by fitting a polynomial of degree 10 to the complete time trace and calculating the root-mean-square deviation (rmsd) of the fitted polynomial from the experimental time trace. The S/N ratio was found to be about 1.3 times larger for the measurement at 80 K, which is about the same as the increase in  $T_m$ . More importantly, measuring at 80 K does not result in a reduced S/N, as is the case for most nitroxide spin labels (194). Being able to perform PELDOR or DQC measurements at higher temperatures than about 70 K without sacrificing S/N is important, since liquid nitrogen can then be used instead of more expensive liquid helium. Furthermore, when the DQC experiments shown in figure 6.6.7 a were allowed to average for 2 hours it became clear that the DQC time trace at 80 K was slightly less damped compared to the time trace at 50 K (Figure 6.6.7 b). This apparent reduction in the decay rate of the DQC time trace might be due to a change in the background function since it depends on the transverse spin relaxation  $T_m$  (53).

From the  $T_m$  measurements on the trityl biradical **22** in deuterated toluene it was also observed that the transverse spin relaxation was still about 1.6  $\mu\text{s}$  at a temperature of 100 K. To observe the dipolar coupling the spin system has to be immobile on the time scale of the dipolar coupling (Section 1.2.3). Since the

solvent used is toluene, a temperature of 100 K was chosen as the highest temperature possible for distance measurements on **22** to make sure the sample was still frozen. A DQC experiment on trityl biradical **22** at this temperature yielded a time trace with an excellent S/N of 60 after 20 hours of measurement time (Figure 6.6.8).

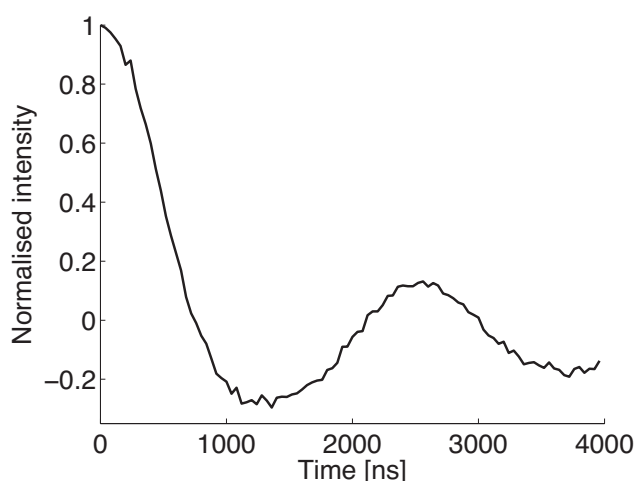


**Figure 6.6.8.** Background corrected DQC time trace obtained from **22** at 100 K.

The time window of the DQC experiment had to be decreased from 6.5 to 4  $\mu$ s to compensate for the decreased  $T_m$ . Increasing the temperature from 50 to 100 K results in a decreased transverse relaxation time  $T_m$  by only a factor of 1.6 and a reduction in S/N by a factor of 2.7. Although the shorter transverse spin relaxation time results in a reduced S/N and a shorter time window for the time evolution of the dipolar coupling, the S/N is also reduced by the reduction in Boltzmann population difference of spin states with higher temperature.

The distance distributions obtained from the DQC time trace on **22** at 50 and 100 K using DeerAnalysis are in excellent agreement with respect to the mean value of the most probable distance. The width of the distance distribution at 100 K is somewhat broader which could be due to a slightly different background correction (Figure 6.6.9).

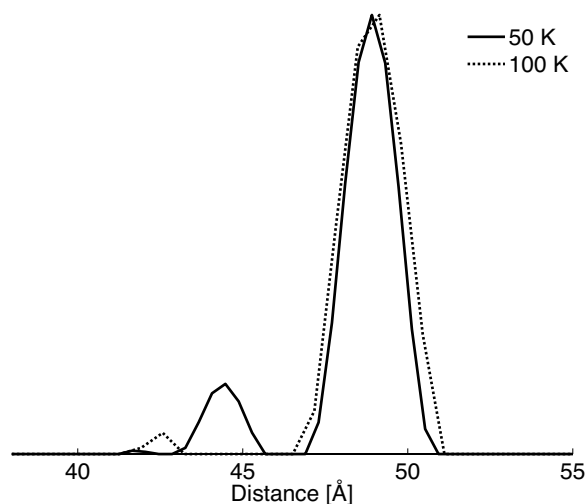


**Figure 6.6.9.** Distance distributions obtained from DQC on **22** at 50 K (solid line) and 100 K (broken line).

It was not possible to perform PELDOR measurements on a nitroxide biradical (Chapter 6.7) at 100 K since a spin echo could not be observed. Although, it should be noted that nitroxide spin labels can be used for distance measurements at temperatures higher than 100 K if the *gem*-dimethyl groups are replaced by spirocyclohexyl groups (194) or the solvent used is ortho-terphenyl (195).

In summary, the transverse spin relaxation behavior of the trityl radical in deuterated toluene allows distance measurements at 80 K without loss in S/N and at 100 K with a reasonable S/N and time window length.

## 6.7 Signal-to-noise ratio comparison

To assess the difference in the signal-to-noise ratio for PELDOR and DQC, a semi-rigid nitroxide biradical **17** (Chapter 4) (Figure 6.7.1 inset) of same concentration and volume as trityl biradical **22** was measured with PELDOR at 50 K (Figure 6.7.1 a). The inversion pulse was placed at the field position corresponding to the maximum signal of the nitroxide spectrum and the detection sequence was placed on the low-field side of the spectrum, at 80 MHz higher frequency than the inversion pulse. Trityl biradical **22** was then measured with DQC for comparison to the PELDOR measurement on the nitroxide biradical. The time window, repetition time and acquisition time were all the

same for both PELDOR and DQC measurements. Measuring the rmsd of a fitted polynomial to the latter two thirds of the PELDOR and DQC time traces reveals a S/N that is a factor of 1.7 better for the DQC measurement (Figure 6.7.1 a). It was noted in section 1.2.5 that in favourable cases the S/N ratio should be 3 times larger for DQC than PELDOR. The reason that the S/N is only 1.7 better for DQC on **22** could be due to the shorter  $T_m$  for the trityl radical, compared to the nitroxide (Figure 6.5.7).

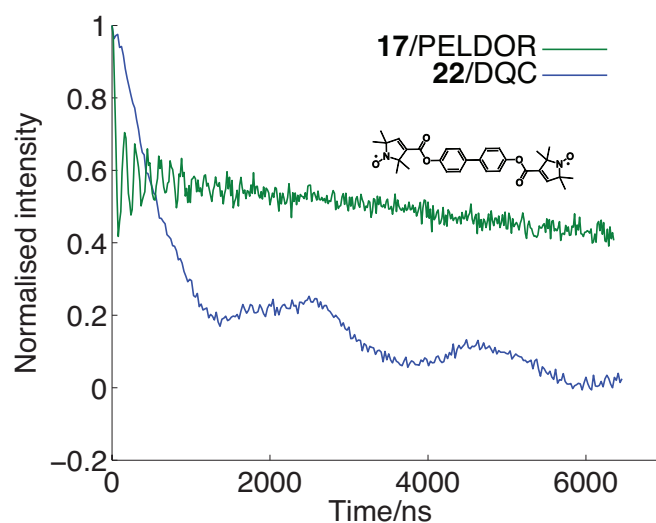


**Figure 6.7.1.** PELDOR on nitroxide biradical **17** (green) and DQC on **22** (blue) at 50 K. Both time traces were recorded for 25 minutes.

## 6.8 Summary

This study has demonstrated that trityl radicals can successfully be used as spin labels for nanometer distance measurements using pulsed EPR methods. Measuring a trityl-nitroxide biradical with PELDOR yielded time traces with almost 100% modulation depth, which is beneficial to the sensitivity of the PELDOR method. DQC measurements on the trityl biradical using a commercial X-band spectrometer showed that for the narrow EPR spectrum of the trityl, DQC yields high quality time traces with improved sensitivity compared to PELDOR on nitroxide biradicals. Trityl spin labels have, therefore, the potential to become important for distance measurements of biological systems, where low signal-to-noise ratio and modulation depth is often the limiting factor of distance measurements. The trityl label is certainly more bulky than a nitroxide, which

could lead to a higher probability of structural distortion to the spin-labelled molecule. As for nitroxides, this will mostly depend on the specific molecular structure and the spin labelling site and will have to be checked in each individual case.

## **6.9 Acknowledgments**

I would like to thank Nitin Chhaban Kunjir for synthesizing and analytically verifying compounds **20** - **22** and their precursors.



## 7 Conclusions

The work presented in this doctoral dissertation has included the use of the nitroxide spin label  $\zeta$ , for distance measurements using PELDOR. The structure of  $\zeta$  was determined by X-ray crystallography and DFT calculations. While the crystal structure of the  $\zeta$  spin label, covalently attached to a DNA, was shown to have a planar conformation, the crystal structure of  $\zeta$  showed the label to have bent geometry. X-ray analysis and DFT calculations indicated that the  $\zeta$  spin label is most probably in a planar geometry when stacked inside a DNA duplex. Noncovalent spin labelling of DNA with  $\zeta$  yielded good quality PELDOR data and was shown to be applicable to distance measurements in DNA-protein complexes.

In another theme of the thesis, orientation selection in PELDOR measurements was utilized to gain information on the relative orientation and flexibility of nitroxide biradicals. It was shown that the structural flexibility of a semi-rigid nitroxide biradical can be quantified by a  $\pm 10^\circ$  bending of the molecular linker and the motion of the nitroxide moieties was found to lie within a cone, with an opening angle of  $25 \pm 10^\circ$ . The structural flexibility of a rigid nitroxide biradical was found to be described by a  $\pm 5^\circ$  bending angle of the molecular backbone. This study was conducted on a home-built high-power EPR spectrometer (Hiper) that operates at 97 GHz and gives access to highly orientation selective PELDOR time traces. It was demonstrated, using Hiper and a PELDOR simulation program, that it is possible to obtain quantitative information on spin label orientation and dynamics.

The last chapter of this thesis presented work on trityl spin labels. Although the nitroxide radical is a highly versatile spin label, its limitations include low sensitivity for EPR based distance measurements, rapid relaxation in solution and limited stability within cells. In this study, the use of trityl radicals as spin labels for nanometer distance measurements was evaluated. PELDOR measurements on a nitroxide-trityl biradical yielded time traces with 90% modulation depth and information on the relative orientation of the nitroxide

spin labels and flexibility of the molecular linker. DQC measurements on a trityl biradical showed that the narrow EPR spectrum of the trityl makes it possible to use DQC on a current commercial EPR spectrometer and measurements can be performed at 80 K without much loss in the signal to noise ratio. PELDOR and DQC measurements on these biradical systems confirmed that trityl radicals have great potential as spin labels for distance measurements on biomacromolecules.

## References

1. Watson, J.D. and Crick, F.H. (1953) Molecular structure of nucleic acids: a structure for deoxyribose nucleic acid. *Nature*, **171**, 737–738.
2. Wagner, G., Hyberts, S.G. and Havel, T.F. (1992) NMR structure determination in solution: A Critique and Comparison with X-Ray Crystallography. *Annu. Rev. Biophys. Biomol. Struct.*, **21**, 167–198.
3. Clore, G.M. and Gronenborn, A.M. (1998) NMR structure determination of proteins and protein complexes larger than 20 kDa. *Curr. Opin. Chem. Biol.*, **2**, 564–570.
4. Lundström, P., Ahlner, A. and Blissing, A.T. (2012) Isotope Labeling Methods for Large Systems. In Atreya, H.S. (ed), *Isotope Labeling in Biomolecular NMR, Advances in Experimental Medicine and Biology*. Springer, Dordrecht, Vol. 992, pp. 3–15.
5. Hillisch, A., Lorenz, M. and Diekmann, S. (2001) Recent advances in FRET: distance determination in protein–DNA complexes. *Curr. Opin. Struct. Biol.*, **11**, 201–207.
6. Roy, R., Hohng, S. and Ha, T. (2008) A practical guide to single-molecule FRET. *Nature methods*, **5**, 507–516.
7. McConnell, H.M. and McFarland, B.G. (1970) Physics and chemistry of spin labels. *Q. Rev. Biophys.*, **3**, 91–136.
8. Eaton, S.S. and Eaton, G.R. (1978) Interaction of spin labels with transition metals. *Coord. Chem. Rev.*, **26**, 207–262.
9. Schiemann, O. and Prisner, T.F. (2007) Long-range distance determinations in biomacromolecules by EPR spectroscopy. *Q. Rev. Biophys.*, **40**, 1–53.
10. Jeschke, G. (2012) DEER Distance Measurements on Proteins. *Annu. Rev. Phys. Chem.*, **63**, 419–446.
11. Petoukhov, M.V. and Svergun, D.I. (2013) Applications of small-angle X-ray scattering to biomacromolecular solutions. *Int. J. Biochem. Cell. Biol.*, **45**, 429–437.
12. Newcomb, C.J., Moyer, T.J., Lee, S.S. and Stupp, S.I. (2012) Advances in cryogenic transmission electron microscopy for the characterization of dynamic self-assembling nanostructures. *Curr. Opin. Colloid Interface Sci.*, **17**, 350–359.
13. Georgieva, E.R., Roy, A.S., Grigoryants, V.M., Borbat, P.P., Earle, K.A., Scholes, C.P. and Freed, J.H. (2012) Effect of freezing conditions on distances and their distributions derived from Double Electron Electron Resonance (DEER): A study of doubly-spin-labeled T4 lysozyme. *J. Magn. Reson.*, **216**, 69–77.

14. Yang,Z., Liu,Y., Borbat,P., Zweier,J.L., Freed,J.H. and Hubbell,W.L. (2012) Pulsed ESR Dipolar Spectroscopy for Distance Measurements in Immobilized Spin Labeled Proteins in Liquid Solution. *J. Am. Chem. Soc.*, **134**, 9950–9952.
15. Hilger,D., Polyhach,Y., Jung,H. and Jeschke,G. (2009) Backbone Structure of Transmembrane Domain IX of the Na<sup>+</sup>/Proline Transporter PutP of Escherichia coli. *Biophys. J.*, **96**, 217–225.
16. Polyhach,Y., Bordignon,E. and Jeschke,G. (2011) Rotamer libraries of spin labelled cysteines for protein studies. *Phys. Chem. Chem. Phys.*, **13**, 2356–2366.
17. Swanson,M.A., Kathirvelu,V., Majtan,T., Frerman,F.E., Eaton,G.R. and Eaton,S.S. (2011) Electron transfer flavoprotein domain II orientation monitored using double electron-electron resonance between an enzymatically reduced, native FAD cofactor, and spin labels. *Protein Sci.*, **20**, 610–620.
18. Altenbach,C., Kusnetzow,A.K., Ernst,O.P., Hofmann,K.P. and Hubbell,W.L. (2008) High-resolution distance mapping in rhodopsin reveals the pattern of helix movement due to activation. *Proceedings of the National Academy of Sciences of the United States of America*, **105**, 7439–7444.
19. Grohmann,D., Klose,D., Klare,J.P., Kay,C.W.M., Steinhoff,H.-J. and Werner,F. (2010) RNA-Binding to Archaeal RNA Polymerase Subunits F/E: A DEER and FRET Study. *J. Am. Chem. Soc.*, **132**, 5954–5955.
20. Pliotas,C., Ward,R., Branigan,E., Rasmussen,A., Hagelueken,G., Huang,H., Black,S.S., Schiemann,O. and Naismith,J.H. (2012) Conformational state of the MscS mechanosensitive channel in solution revealed by pulsed electron–electron double resonance (PELDOR) spectroscopy. *Proc. Natl. Acad. Sci. U. S. A.*, **109**, E2675-E2682.
21. Atherton,N.M. (1993) Principles of electron spin resonance 1st ed. Ellis Horwood PTR Prentice Hall.
22. Weil,J.A. and Bolton,J.R. (2007) Electron Paramagnetic Resonance 2nd ed. Wiley-Interscience, New Jersey.
23. Earle,K.A. and Budil,D.E. (2006) Calculating slow-motion ESR spectra of spin-labeled polymers. In Schlick,S. (ed), *Advanced ESR Methods in Polymer Research*. John Wiley & Sons, Inc., New Jersey, pp. 53–83.
24. Hore,P.J. (1995) Nuclear Magnetic Resonance Oxford University Press, New York.
25. Stoll,S. and Schweiger,A. (2007) EasySpin: Simulating cw ESR Spectra. In Hemminga,M.A., Berliner,L.J. (eds), *ESR Spectroscopy in Membrane Biophysics*. Springer, New York, Vol. 27, pp. 299–321.
26. Mchaourab,H.S., Lietzow,M.A., Hideg,K. and Hubbell,W.L. (1996) Motion of Spin-Labeled Side Chains in T4 Lysozyme. Correlation with Protein Structure

- and Dynamics. *Biochemistry*, **35**, 7692–7704.
27. Smirnova, T.I. and Smirnov, A.I. (2007) High-Field ESR Spectroscopy In Membrane and Protein Biophysics. In Hemminga, M.A., Berliner, L.J. (eds), *ESR Spectroscopy in Membrane Biophysics-Biological Magnetic Resonance*. Springer, Vol. 27.
  28. Altenbach, C., Marti, T., Khorana, H.G. and Hubbell, W.L. (1990) Transmembrane Protein Structure: Spin Labeling of Bacteriorhodopsin Mutants. *Science*, **248**, 1088–1092.
  29. Banham, J., Baker, C., Ceola, S., Day, I., Grant, G., Groenen, E., Rodgers, C., Jeschke, G. and Timmel, C. (2008) Distance measurements in the borderline region of applicability of CW EPR and DEER: A model study on a homologous series of spin-labelled peptides. *J. Magn. Reson.*, **191**, 202–218.
  30. Slichter, C.P. (1990) Principles of Magnetic Resonance. In *Solid-State Sciences*. Springer-Verlag, Heidelberg, Vol. 1.
  31. Schweiger, A. and Jeschke, G. (2001) Principles of pulse electron paramagnetic resonance Oxford University Press, New York.
  32. Mansoorabadi, S.O. and Reed, G.H. (2003) Effects of Electron Spin Delocalization and Non-Collinearity of Interaction Terms in EPR Triplet Powder Patterns. In Telsler, J. (ed), *Paramagnetic Resonance of Metallobiomolecules*. American Chemical Society, Washington, DC, Vol. ACS Symposium Series 858, pp. 82–96.
  33. Jeschke, G. (2002) Determination of the Nanostructure of Polymer Materials by Electron Paramagnetic Resonance Spectroscopy. *Macromol. Rapid Commun.*, **23**, 227–246.
  34. Borbat, P. and Freed, J. (2007) Measuring Distances by Pulsed Dipolar ESR Spectroscopy: Spin-Labeled Histidine Kinases. *Methods Enzymol.*, **423**, 52–116.
  35. Kittell, A.W., Hustedt, E.J. and Hyde, J.S. (2012) Inter-spin distance determination using L-band (1-2 GHz) non-adiabatic rapid sweep electron paramagnetic resonance (NARS EPR). *J. Magn. Reson.*, **221**, 51–56.
  36. Hustedt, E.J. and Beth, A.H. (2000) Structural Information from CW-EPR Spectra of Dipolar Coupled Nitroxide Spin Labels. In Berliner, L.J., Eaton, G.R., Eaton, S.S. (eds), *Biological Magnetic Resonance-Distance Measurements in Biological Systems by EPR*. Kluwer Academic/Plenum Publishers, New York, Vol. 19, pp. 155–184.
  37. Jäger, H., Koch, A., Maus, V., Spiess, H.W. and Jeschke, G. (2008) Relaxation-based distance measurements between a nitroxide and a lanthanide spin label. *J. Magn. Reson.*, **194**, 254–263.
  38. Jeschke, G. and Polyhach, Y. (2007) Distance measurements on spin-labelled

- biomacromolecules by pulsed electron paramagnetic resonance. *Phys. Chem. Chem. Phys.*, **9**, 1895–1910.
39. Maryasov, A.G. and Tsvetkov, Y.D. (2000) Formation of the Pulsed Electron-Electron Double Resonance Signal in the Case of a Finite Amplitude of Microwave Fields. *Appl. Magn. Reson.*, **18**, 583–605.
  40. Ward, R., Bowman, A., Sozudogru, E., El-Mkami, H., Owen-Hughes, T. and Norman, D.G. (2010) EPR distance measurements in deuterated proteins. *J. Magn. Reson.*, **207**, 164–167.
  41. Martin, R., Pannier, M., Diederich, F., Gramlich, V., Hubrich, M. and Spiess, H. (1998) Determination of End-to-End Distances in a Series of TEMPO Diradicals of up to 2.8 nm Length with a New Four-Pulse Double Electron Electron Resonance Experiment. *Angew. Chem. Int. Ed.*, **37**, 2833–2837.
  42. Milov, A.D., Salikhov, K.M. and Shirov, M.D. (1981) Application of the double resonance method to electron spin echo in a study of the spatial distribution of paramagnetic centers in solids. *Soviet physics - Solid state*, **23**, 565–569.
  43. Larsen, R. and Singel, D. (1993) Double electron–electron resonance spin–echo modulation: Spectroscopic measurement of electron spin pair separations in orientationally disordered solids. *J. Chem. Phys.*, **98**, 5134–5146.
  44. Polyhach, Y., Bordignon, E., Tschaggelar, R., Gandra, S., Godt, A. and Jeschke, G. (2012) High sensitivity and versatility of the DEER experiment on nitroxide radical pairs at Q-band frequencies. *Phys. Chem. Chem. Phys.*, **14**, 10762.
  45. Tikhonov, A.N. and Arsenin, V.Y. (1977) *Solutions of Ill-Posed Problems* WILEY, New York.
  46. Margraf, D., Cekan, P., Prisner, T., Sigurdsson, S.T. and Schiemann, O. (2009) Ferro- and antiferromagnetic exchange coupling constants in PELDOR spectra. *Phys. Chem. Chem. Phys.*, **11**, 6708–6714.
  47. Milov, A., Maryasov, A. and Tsvetkov, Y. (1998) Pulsed Electron Double Resonance (PELDOR) and Its Applications in Free-Radicals Research. *Appl. Magn. Reson.*, **15**, 107–143.
  48. Bode, B.E., Margraf, D., Plackmeyer, J., Dürner, G., Prisner, T.F. and Schiemann, O. (2007) Counting the Monomers in Nanometer-Sized Oligomers by Pulsed Electron–Electron Double Resonance. *J. Am. Chem. Soc.*, **129**, 6736–6745.
  49. Hagelueken, G., Ingledew, W.J., Huang, H., Petrovic-Stojanovska, B., Whitfield, C., El-Mkami, H., Schiemann, O. and Naismith, J.H. (2009) PELDOR Spectroscopy Distance Fingerprinting of the Octameric Outer-Membrane Protein Wza from *Escherichia coli*. *Angew. Chem. Int. Ed.*, **48**, 2904–2906.
  50. Ernst, R.R., Bodenhausen, G. and Wokaun, A. (1987) *Principles of Nuclear Magnetic Resonance in One and Two Dimensions* Clarendon, Oxford.

51. Saxena,S. and Freed,J. (1996) Double quantum two-dimensional Fourier transform electron spin resonance: distance measurements. *Chem. Phys. Lett.*, **251**, 102–110.
52. Borbat,P. and Freed,J. (1999) Multiple-quantum ESR and distance measurements. *Chem. Phys. Lett.*, **313**, 145–154.
53. Borbat,P., Mchaourab,H. and Freed,J.H. (2002) Protein Structure Determination Using Long-Distance Constraints from Double-Quantum Coherence ESR: Study of T4 Lysozyme. *J. Am. Chem. Soc.*, **124**, 5304–5314.
54. Borbat,P.P. and Freed,J.H. (2000) Double-Quantum ESR and Distance Measurements. In Berliner,L.J., Eaton,S.S., Eaton,G.R. (eds), *Biological Magnetic Resonance*. Kluwer Academic/Plenum Publishers, New York, Vol. 19, pp. 383–459.
55. Borbat,P., Davis,J.H., Butcher,S.E. and Freed,J.H. (2004) Measurements of Large Distances in Biomolecules Using Double-Quantum Filtered Refocused Electron Spin-Echoes. *J. Am. Chem. Soc.*, **126**, 7746–7747.
56. Sørensen,O.W., Eich,G.W., Levitt,M.H., Bodenhausen,G. and Ernst,R.R. (1983) Product operator formalism for the description of NMR pulse experiments. *Prog. Nucl. Magn. Reson. Spectrosc.*, **16**, 163–192.
57. Jeschke,G. (2012) Interpretation of Dipolar EPR Data in Terms of Protein Structure. In *Series Structure and Bonding*, Springer, Berlin, in press. doi: 10.1007/430\_2011\_61.
58. Lyubenova,S., Siddiqui,M.K., Penning de Vries,M.J.M., Ludwig,B. and Prisner,T.F. (2007) Protein–Protein Interactions Studied by EPR Relaxation Measurements: Cytochrome c and Cytochrome c Oxidase. *J. Phys. Chem. B.*, **111**, 3839–3846.
59. Denysenkov,V., Prisner,T., Stubbe,J. and Bennati,M. (2006) High-field pulsed electron–electron double resonance spectroscopy to determine the orientation of the tyrosyl radicals in ribonucleotide reductase. *Proc. Natl. Acad. Sci. U. S. A.*, **103**, 13386–13390.
60. Roessler,M.M., King,M.S., Robinson,A.J., Armstrong,F.A., Harmer,J. and Hirst,J. (2010) Direct assignment of EPR spectra to structurally defined iron-sulfur clusters in complex I by double electron-electron resonance. *Proc. Natl. Acad. Sci. U. S. A.*, **107**, 1930–1935.
61. Horton,T.E., Clardy,D.R. and Deroose,V.J. (1998) Electron Paramagnetic Resonance Spectroscopic Measurement of Mn 2+Binding Affinities to the Hammerhead Ribozyme and Correlation with Cleavage Activity. *Biochemistry*, **37**, 18094–18101.
62. Kisseleva,N., Khvorova,A., Westhof,E. and Schiemann,O. (2005) Binding of manganese (II) to a tertiary stabilized hammerhead ribozyme as studied by electron paramagnetic resonance spectroscopy. *RNA*, **11**, 1–6.

63. Ohnishi, S.-I. and McConnell, H.M. (1965) Interaction of the Radical Ion of Chlorpromazine with Deoxyribonucleic Acid. *J. Am. Chem. Soc.*, **87**, 2293.
64. Berliner, L.J., Grunwald, J., Hankovszky, H.O. and Hideg, K. (1982) A Novel Reversible Thiol-Specific Spin Label: Papain Active Site Labeling and Inhibition. *Anal. Biochem.*, **119**, 450–455.
65. Altenbach, C., Flitsch, S.L., Khorana, H.G. and Hubbell, W.L. (1989) Structural Studies on Transmembrane Proteins. 2. Spin Labeling of Bacteriorhodopsin Mutants at Unique Cysteines. *Biochemistry*, **28**, 7806–7812.
66. Bain, J.D., Glabe, C.G., Dix, T.A. and Chamberlin, A.R. (1989) Biosynthetic Site-Specific Incorporation of a Non-Natural Amino Acid into a Polypeptide. *J. Am. Chem. Soc.*, **111**, 8013–8014.
67. Noren, C.J., Anthonycahill, S.J., Griffith, M.C. and Schultz, P.G. (1989) A general-method for site-specific incorporation of unnatural amino-acids into proteins. *Science*, **244**, 182–188.
68. Wang, L., Zhang, Z., Brock, A. and Schultz, P.G. (2003) Addition of the keto functional group to the genetic code of Escherichia coli. *Proc. Natl. Acad. Sci. U. S. A.*, **100**, 56–61.
69. Fleissner, M.R., Brustad, E.M., Kálai, T., Altenbach, C., Cascio, D., Peters, F.B., Hideg, K., Peucker, S., Schultz, P.G. and Hubbell, W.L. (2009) Site-directed spin labeling of a genetically encoded unnatural amino acid. *Proc. Natl. Acad. Sci. U. S. A.*, **106**, 21637–21642.
70. Marchetto, R., Schreier, S. and Nakaie, C.R. (1993) A Novel Spin-Labeled Amino Acid Derivative for Use in Peptide Synthesis: (9-Fluorenylmethyloxycarbonyl)-2,2,6,6-tetramethylpiperidine-N-oxyl-4-amino-4-carboxylic Acid. *J. Am. Chem. Soc.*, **115**, 11042–11043.
71. Tominaga, M., Barbosa, S.R., Poletti, E.F., Zukerman-Schpector, J., Marchetto, R., Schreier, S., Paiva, A.C.M.M. and Nakaie, C.R. (2001) Fmoc-POAC: [(9-Fluorenylmethyloxycarbonyl)-2,2,5,5-tetramethylpyrrolidine-N-oxyl-3-amino-4-carboxylic Acid]: A Novel Protected Spin Labeled beta-Amino Acid for Peptide and Protein Chemistry. *Chem. Pharm. Bull.*, **49**, 1027–1029.
72. Smythe, M.L., Nakaie, C.R. and Marshall, G.R. (1995) Alpha-Helical versus 3(10)-Helical Conformation of Alanine-Based Peptides in Aqueous Solution: An Electron Spin Resonance Investigation. *J. Am. Chem. Soc.*, **117**, 10555–10562.
73. Toniolo, C., Valente, E., Formaggio, F., Crisma, M., Pilloni, G., Corvaja, C., Toffoletti, A., Martinez, G.V., Hanson, M.P., Millhauser, G.L., et al. (1995) Synthesis and conformational studies of peptides containing TOAC, a spin-labelled  $\alpha,\alpha$ -disubstituted glycine. *J. Pept. Sci.*, **1**, 45–57.
74. Wright, K., Wakselman, M., Mazaleyra, J.-P., Franco, L., Toffoletti, A., Formaggio, F. and Toniolo, C. (2010) Synthesis and Conformational



- Characterisation of Hexameric beta-Peptide Foldamers by Using Double POAC Spin Labelling and cw-EPR. *Chemistry - A European Journal*, **16**, 11160–11166.
75. Elsässer,C., Monien,B., Haehnel,W. and Bittl,R. (2005) Orientation of spin labels in de novo peptides. *Magn Reson Chem.*, **43**, S26–33.
76. Fleissner,M., Bridges,M., Brooks,E.K., Cascio,D., Kálai,T., Hideg,K. and Hubbell,W.L. (2011) Structure and dynamics of a conformationally constrained nitroxide side chain and applications in EPR spectroscopy. *Proc. Natl. Acad. Sci. U. S. A.*, **108**, 16241–16246.
77. Lorenzi,M., Puppo,C., Lebrun,R., Lignon,S., Roubaud,V., Martinho,M., Mileo,E., Tordo,P., Marque,S.R.A., Gontero,B., et al. (2011) Tyrosine-Targeted Spin Labeling and EPR Spectroscopy: An Alternative Strategy for Studying Structural Transitions in Proteins. *Angew. Chem. Int. Ed.*, **50**, 9108–9111.
78. Reginsson,G.W., Kunjir,N.C., Sigurdsson,S.T. and Schiemann,O. (2012) Trityl Radicals: Spin Labels for Nanometer-Distance Measurements. *Angew. Chem. Int. Ed.*, **18**, 13580–13584.
79. Stryer,L. and Griffith,O.H. (1965) A spin-labeled hapten. *Proc. Natl. Acad. Sci. U. S. A.*, **54**, 1785–1791.
80. Roberts,G.C., Hannah,J. and Jardetzky,O. (1969) Noncovalent binding of a spin-labeled inhibitor to ribonuclease. *Science*, **165**, 504–506.
81. Weidman,S.W., Drysdale,G.R. and Mildvan,A.S. (1973) Interaction of a Spin-Labeled Analog of Acetyl Coenzyme A with Citrate Synthase. Paramagnetic Resonance and Proton Relaxation Rate Studies of Binary and Ternary Complexes. *Biochemistry*, **12**, 1874–1883.
82. Mushak,P. and Coleman,J.E. (1972) Electron Spin Resonance Studies of Spin-labeled Carbonic Anhydrase. *J. Biol. Chem.*, **247**, 373–380.
83. Shelke,S.A. and Sigurdsson,S.T. (2012) Site-Directed Nitroxide Spin Labeling of Biopolymers. In *Series Structure and Bonding*, Springer, Berlin, in press. doi:10.1007/430\_2011\_62.
84. Hong,S. and Piette,L.H. (1976) Electron Spin Resonance Spin-Label Studies of Intercalation of Ethidium Bromide and Aromatic Amine Carcinogens in DNA. *Cancer Res.*, **36**, 1159–1171.
85. Belmont,P., Chapelle,C., Derneunynck,M., Michon,J., Michon,P. and Lhomme,J. (1998) Introduction of a nitroxide group on position 2 of 9-phenoxyacridine: Easy access to spin labelled DNA-binding conjugates. *Bioorganic & medicinal Chemistry Letters*, **8**, 669–674.
86. Thomas,F., Michon,J. and Lhomme,J. (1999) Interaction of a Spin-Labeled Adenine–Acridine Conjugate with a DNA Duplex Containing an Abasic Site Model. *Biochemistry*, **38**, 1930–1937.

87. Ottaviani, M.F., Ghatlia, N.D., Bossmann, S.H., Barton, J.K., Duerr, H. and Turro, N.J. (1992) Nitroxide-Labeled Ru(II)-Polypyridyl Complexes as EPR Probes To Study Organized Systems. 2. Combined Photophysical and EPR Investigations of B-DNA. *J. Am. Chem. Soc.*, **114**, 8946–8952.
88. Spielmann, H.P., Chi, D.Y., Hunt, N.G., Klein, M.P. and Hearst, J.E. (1995) Spin-Labeled Psoralen Probes for the Study of DNA Dynamics. *Biochemistry*, **34**, 14801–14814.
89. Dunham, S.U. and Lippard, S.J. (1995) Long-Range Distance Constraints in Platinated Nucleotides: Structure Determination of the 5' Orientational Isomer of cis-[Pt(NH<sub>3</sub>)(4-aminoTEMPO){d(GpG)}]<sup>+</sup> from Combined Paramagnetic and Diamagnetic NMR Constraints with Molecular Modeling. *J. Am. Chem. Soc.*, **117**, 10702–10712.
90. Smith, I.C.P. and Yamane, T. (1967) Spin-labeled nucleic acids. *Proc. Natl. Acad. Sci. U. S. A.*, **58**, 884–887.
91. Hoffman, B.M., Schofield, P. and Rich, A. (1969) Spin-labeled transfer RNA. *Proc. Natl. Acad. Sci. U. S. A.*, **62**, 1195–1202.
92. Spaltenstein, A., Robinson, B.H. and Hopkins, P.B. (1988) A Rigid and Nonperturbing Probe for Duplex DNA Motion. *J. Am. Chem. Soc.*, **110**, 1299–1301.
93. Schiemann, O., Piton, N., Mu, Y., Stock, G., Engels, J.W. and Prisner, T.F. (2004) A PELDOR-Based Nanometer Distance Ruler for Oligonucleotides. *J. Am. Chem. Soc.*, **126**, 5722–5729.
94. Jakobsen, U., Shelke, S., Vogel, S. and Sigurdsson, S.T. (2010) Site-Directed Spin-Labeling of Nucleic Acids by Click Chemistry: Detection of Abasic Sites in Duplex DNA by EPR Spectroscopy. *J. Am. Chem. Soc.*, **132**, 10424–10428.
95. Ding, P., Wunnicke, D., Steinhoff, H.-J. and Seela, F. (2010) Site-Directed Spin-Labeling of DNA by the Azide-Alkyne 'Click' Reaction: Nanometer Distance Measurements on 7-Deaza-2'-deoxyadenosine and 2'-Deoxyuridine Nitroxide Conjugates Spatially Separated or Linked to a "dA-dT" Base Pair. *Chemistry - A European Journal*, **16**, 14385–14396.
96. Okamoto, A., Inasaki, T. and Saito, I. (2004) Nitroxide-labeled guanine as an ESR spin probe for structural study of DNA. *Bioorganic & medicinal Chemistry Letters*, **14**, 3415–3418.
97. MacMillan, A.M. and Verdine, G.L. (1990) Synthesis of Functionally Tethered Oligodeoxynucleotides by the Convertible Nucleoside Approach. *J. Org. Chem.*, **55**, 5931–5933.
98. Sicoli, G., Wachowius, F., Bennati, M. and Höbartner, C. (2010) Probing Secondary Structures of Spin-Labeled RNA by Pulsed EPR Spectroscopy. *Angew. Chem. Int. Ed.*, **49**, 6443–6447.

99. Edwards, T.E., Okonogi, T.M., Robinson, B.H. and Sigurdsson, S.T. (2001) Site-Specific Incorporation of Nitroxide Spin-Labels into Internal Sites of the TAR RNA; Structure-Dependent Dynamics of RNA by EPR Spectroscopy. *J. Am. Chem. Soc.*, **123**, 1527–1528.
100. Edwards, T.E. and Sigurdsson, S.T. (2002) Electron paramagnetic resonance dynamic signatures of TAR RNA-small molecule complexes provide insight into RNA structure and recognition. *Biochemistry*, **41**, 14843–14847.
101. Flaender, M., Sicoli, G., Fontecave, T., Mathis, G., Saint-Pierre, C., Boulard, Y., Gambarelli, S. and Gasparutto, D. (2008) Site-specific insertion of nitroxide-spin labels into DNA probes by click chemistry for structural analyses by ELDOR spectroscopy. *Nucleic Acids Symp. Ser.*, **52**, 147–148.
102. Qin, P.Z., Butcher, S.E., Feigon, J. and Hubbell, W.L. (2001) Quantitative Analysis of the Isolated GAAA Tetraloop/Receptor Interaction in Solution: A Site-Directed Spin Labeling Study. *Biochemistry*, **40**, 6929–6936.
103. Cai, Q., Kusnetzow, A.K., Hubbell, W.L., Haworth, I.S., Gacho, G.P.C., Van Eps, N., Hideg, K., Chambers, E.J. and Qin, P.Z. (2006) Site-directed spin labeling measurements of nanometer distances in nucleic acids using a sequence-independent nitroxide probe. *Nucleic Acids Res.*, **34**, 4722–4730.
104. Makino, K., Murakami, A., Nagahara, S., Nakatsuji, Y. and Takeuchi, T. (1989) A study on spin-labelled oligonucleotide synthesis and its electron spin resonance behavior in solution. *Free Radical Res. Commun.*, **6**, 311–316.
105. Kuznetsov, N.A., Milov, A.D., Koval, V.V., Samoilova, R.I., Grishin, Y.A., Knorre, D.G., Tsvetkov, Y.D., Fedorova, O.S. and Dzuba, S. (2009) PELDOR study of conformations of double-spin-labeled single- and double-stranded DNA with non-nucleotide inserts. *Phys. Chem. Chem. Phys.*, **11**, 6826–6832.
106. Miller, T.R. and Hopkins, P.B. (1994) Toward the Synthesis of a Second-Generation Nitroxide Spin Probe for DNA Dynamics Studies. *Bioorg. Med. Chem. Lett.*, **4**, 981–986.
107. Miller, T.R., Alley, S.C., Reese, A.W., Solomon, M.S., McCallister, W.V., Mailer, C., Robinson, B.H. and Hopkins, P.B. (1995) A probe for Sequence-Dependent Nucleic Acid Dynamics. *J. Am. Chem. Soc.*, **117**, 9377–9378.
108. Barhate, N., Cekan, P., Massey, A. and Sigurdsson, S. (2007) A Nucleoside That Contains a Rigid Nitroxide Spin Label: A Fluorophore in Disguise. *Angew. Chem. Int. Ed.*, **46**, 2655–2658.
109. Edwards, T.E., Cekan, P., Reginsson, G.W., Shelke, S.A., Ferré-D'Amaré, A.R., Schiemann, O. and Sigurdsson, S.T. (2011) Crystal structure of a DNA containing the planar, phenoxazine-derived bi-functional spectroscopic probe Ç. *Nucleic Acids Res.*, **39**, 4419–4426.
110. Marko, A., Denysenkov, V., Margraf, D., Cekan, P., Schiemann, O., Sigurdsson, S.T. and Prisner, T.F. (2011) Conformational Flexibility of DNA. *J. Am. Chem. Soc.*,

133, 13375–13379.

111. Höbartner, C., Sicoli, G., Wachowius, F., Gophane, D.B. and Sigurdsson, S.T. (2012) Synthesis and Characterization of RNA Containing a Rigid and Nonperturbing Cytidine-Derived Spin Label. *J Org Chem.*, **77**, 7749–7754.
112. Shelke, S.A. and Sigurdsson, S.T. (2010) Noncovalent and Site-Directed Spin Labeling of Nucleic Acids. *Angew. Chem. Int. Ed.*, **49**, 7984–7986.
113. Warwick, P.E., Hakam, A., Bobst, E.V. and Bobst, A.M. (1980) Reactivity of reverse transcriptase toward (s4U, U) n copolymers and spin-labeled nucleic acid lattices. *Proc. Natl. Acad. Sci. U. S. A.*, **77**, 4574–4577.
114. Kao, S.-C., Polnaszek, C.F., Toppin, C.R. and Bobst, A.M. (1983) Internal Motions in Ribonucleic Acid Duplexes As Determined by Electron Spin Resonance with Site-Specifically Spin-Labeled Uridines. *Biochemistry*, **22**, 5563–5568.
115. Macosko, J.C., Pio, M.S., Tinoco, I. and Shin, Y.K. (1999) A novel 5' displacement spin-labeling technique for electron paramagnetic resonance spectroscopy of RNA. *RNA*, **5**, 1158–1166.
116. Obeid, S., Yulikov, M., Jeschke, G. and Marx, A. (2008) Enzymatic Synthesis of multi Spin-labeled DNA. *Nucleic Acids Symp. Ser.*, **52**, 373–374.
117. Iwahara, J., Anderson, D.E., Murphy, E.C. and Clore, G.M. (2003) EDTA-Derivatized Deoxythymidine as a Tool for Rapid Determination of Protein Binding Polarity to DNA by Intermolecular Paramagnetic Relaxation Enhancement. *J. Am. Chem. Soc.*, **125**, 6634–6635.
118. Song, Y., Meade, T.J., Astashkin, A.V., Klein, E.L., Enemark, J.H. and Raitsimring, A. (2011) Pulsed dipolar spectroscopy distance measurements in biomacromolecules labeled with Gd(III) markers. *J. Magn. Reson.*, **210**, 59–68.
119. Cekan, P., Smith, A.L., Barhate, N., Robinson, B.H. and Sigurdsson, S.T. (2008) Rigid spin-labeled nucleoside Ç: a nonperturbing EPR probe of nucleic acid conformation. *Nucleic Acids Res.*, **36**, 5946–5954.
120. Schiemann, O., Cekan, P., Margraf, D., Prisner, T.F. and Sigurdsson, S.T. (2009) Relative Orientation of Rigid Nitroxides by PELDOR: Beyond Distance Measurements in Nucleic Acids. *Angew. Chem. Int. Ed.*, **48**, 3292–3295.
121. Sheldrick, G. (2007) A short history of SHELX. *Acta Crystallogr., Sect. A: Found. Crystallogr.*, **64**, 112–122.
122. Frisch, M.J., Trucks, G.W., Schlegel, H.B., Scuseria, G.E., Robb, M.A., Cheeseman, J.R., J A Montgomery, J., Vreven, T., Kudin, K.N., Burant, J.C., et al. Gaussian 03.
123. Jeschke, G., Chechik, V., Ionita, P., Godt, A., Zimmermann, H., Banham, J., Timmel, C.R., Hilger, D. and Jung, H. (2006) DeerAnalysis2006—a Comprehensive Software Package for Analyzing Pulsed ELDOR Data. *Appl.*

- Magn. Reson.*, **30**, 473–498.
124. DeerAnalysis 2011 (2012) DeerAnalysis 2011. *www.epr.ethz.ch*.
125. MMM 2011 (2012) MMM 2011. *www.epr.ethz.ch*.
126. Hagelueken,G., Ward,R., Naismith,J.H. and Schiemann,O. (2012) MtsslWizard: In Silico Spin-Labeling and Generation of Distance Distributions in PyMOL. *Appl. Magn. Reson.*, **42**, 377–391.
127. PyMOL (2012) PyMOL. *pymol.org*.
128. Margraf,D., Bode,B.E., Marko,A., Schiemann,O. and Prisner,T.F. (2007) Conformational flexibility of nitroxide biradicals determined by X-band PELDOR experiments. *Mol. Phys.*, **105**, 2153–2160.
129. Lovett,J., Bowen,A., Timmel,C., Jones,M., Dilworth,J., Caprotti,D., Bell,S., Wong,L. and Harmer,J. (2009) Structural information from orientationally selective DEER spectroscopy. *Phys. Chem. Chem. Phys.*, **11**, 6840–6848.
130. Abé,C., Klose,D., Dietrich,F., Ziegler,W.H., Polyhach,Y., Jeschke,G. and Steinhoff,H.-J. (2012) Orientation selective DEER measurements on vinculin tail at X-band frequencies reveal spin label orientations. *J. Magn. Reson.*, **216**, 53–61.
131. Marko,A. and Prisner,T.F. (2012) An algorithm to analyze PELDOR data of rigid spin label pairs. *Phys. Chem. Chem. Phys.*, **15**, 619–627.
132. Marko,A., Margraf,D., Yu,H., Mu,Y., Stock,G. and Prisner,T. (2009) Molecular orientation studies by pulsed electron-electron double resonance experiments. *J. Chem. Phys.*, **130**, 064102.
133. Stoll,S. and Schweiger,A. (2006) EasySpin, a comprehensive software package for spectral simulation and analysis in EPR. *J. Magn. Reson.*, **178**, 42–55.
134. Reginsson,G.W. and Schiemann,O. (2011) Pulsed electron-electron double resonance: beyond nanometre distance measurements on biomacromolecules. *Biochem. J.*, **434**, 353–363.
135. Polyhach,Y., Godt,A., Bauer,C. and Jeschke,G. (2007) Spin pair geometry revealed by high-field DEER in the presence of conformational distributions. *J. Magn. Reson.*, **185**, 118–129.
136. Endeward,B., Butterwick,J., MacKinnon,R. and Prisner,T. (2009) Pulsed Electron– Electron Double-Resonance Determination of Spin-Label Distances and Orientations on the Tetrameric Potassium Ion Channel KcsA. *J. Am. Chem. Soc.*, **131**, 15246–15250.
137. Lillington,J.E.D., Lovett,J.E., Johnson,S., Roversi,P., Timmel,C.R. and Lea,S.M. (2011) Shigella flexneri Spa15 Crystal Structure Verified in Solution by

- Double Electron Electron Resonance. *J. Mol. Biol.*, **405**, 427–435.
138. Marko,A., Margraf,D., Cekan,P., Sigurdsson,S.T., Schiemann,O. and Prisner,T.F. (2010) Analytical method to determine the orientation of rigid spin labels in DNA. *Phys. Rev. E.*, **81**, 021911.
139. Bode,B.E., Plackmeyer,J., Bolte,M., Prisner,T.F. and Schiemann,O. (2009) PELDOR on an exchange coupled nitroxide copper(II) spin pair. *J. Organomet. Chem.*, **694**, 1172–1179.
140. Bode,B., Plackmeyer,J., Prisner,T. and Schiemann,O. (2008) PELDOR measurements on a nitroxide-labeled Cu (II) porphyrin: orientation selection, spin-density distribution, and conformational flexibility. *J. Phys. Chem. A.*, **112**, 5064–5073.
141. Bridges,M.D., Hideg,K. and Hubbell,W.L. (2010) Resolving Conformational and Rotameric Exchange in Spin-Labeled Proteins Using Saturation Recovery EPR. *Appl. Magn. Reson.*, **37**, 363–390.
142. Tkach,I., Sicoli,G., Höbartner,C. and Bennati,M. (2011) A dual-mode microwave resonator for double electron–electron spin resonance spectroscopy at W-band microwave frequencies. *J. Magn. Reson.*, **209**, 341–346.
143. Savitsky,A., Dubinskii,A., Flores,M., Lubitz,W. and Möbius,K. (2007) Orientation-resolving pulsed electron dipolar high-field EPR spectroscopy on disordered solids: I. Structure of spin-correlated radical pairs in bacterial photosynthetic reaction centers. *J. Phys. Chem. B.*, **111**, 6245–6262.
144. Flores,M., Savitsky,A., Paddock,M., Abresch,E.C., Dubinskii,A., Okamura,M.Y., Lubitz,W. and Möbius,K. (2010) Electron-Nuclear and Electron-Electron Double Resonance Spectroscopies Show that the Primary Quinone Acceptor QA in Reaction Centers from Photosynthetic Bacteria *Rhodobacter sphaeroides* Remains in the same Orientation Upon Light-Induced Reduction. *J. Phys. Chem. B.*, **114**, 16894–16901.
145. Denysenkov Vasyl,P., Biglino,D., Lubitz,W., Prisner,T.F. and Bennati,M. (2008) Structure of the Tyrosyl Biradical in Mouse R2 Ribonucleotide Reductase from High-Field PELDOR. *Angew. Chem. Int. Ed.*, **47**, 1224–1227.
146. Cruickshank,P.A.S., Bolton,D.R., Robertson,D.A., Hunter,R.I., Wylde,R.J. and Smith,G.M. (2009) A kilowatt pulsed 94 GHz electron paramagnetic resonance spectrometer with high concentration sensitivity, high instantaneous bandwidth, and low dead time. *Rev. Sci. Instrum.*, **80**, 103102.
147. Ashbrook,S.E. (2009) Recent advances in solid-state NMR spectroscopy of quadrupolar nuclei. *Phys Chem Chem Phys.*, **11**, 6892–6905.
148. Neese,F. (2012) ORCA-An ab-initio, Density Functional and Semiempirical Program Package.

149. Hehre,W.J., Ditchfield,R. and Pople,J.A. (1972) Self-consistent molecular orbital methods. XII. Further extensions of gaussian-type basis sets for use in molecular orbital studies of organic molecules. *J. Chem. Phys.*, **56**, 2257.
150. Goldfarb,D., Yaakov,L., Potapov,A., Gorodetsky,Y., Epel,B., Raitsimring,A., Radoul,M. and Kaminker,I. (2008) HYSORE and DEER with an upgraded 95 GHz pulse EPR spectrometer. *J. Magn. Reson.*, **194**, 8–15.
151. Godt,A., Schulte,M., Zimmermann,H. and Jeschke,G. (2006) How Flexible Are Poly (paraphenyleneethynylene) s? *Angew. Chem. Int. Ed.*, **45**, 7560–7564.
152. Baoxiang,G., Wang,M., Cheng,Y., Wang,L., Jing,X. and Wang,F. (2008) Pyrazine-Containing Acene-Type Molecular Ribbons with up to 16 Rectilinearly Arranged Fused Aromatic Rings. *J. Am. Chem. Soc.*, **130**, 8297–8306.
153. Church,G.M., Gao,Y. and Kosuri,S. (2012) Next-Generation Digital Information Storage in DNA. *Science*, **337**, 1628–1628.
154. Galas,D.J. and Schmitz,A. (1978) DNAase footprinting: a simple method for the detection of protein-DNA binding specificity. *Nucleic Acids Res.*, **5**, 3157–3170.
155. Welsh,J. and Cantor,C.R. (1984) Protein--DNA cross-linking. *Trends Biochem. Sci.*, **9**, 505–508.
156. Lohman,T.M. and Bujalowski,W. (1991) Thermodynamic Methods for Model-Independent Determination of Equilibrium Binding Isotherms for Protein-DNA Interactions: Spectroscopic Approaches to Monitor Binding. *Methods Enzymol.*, **208**, 258–290.
157. Rhodes,D., Schwabe,J.W.R., Chapman,L. and Fairall,L. (1996) Towards an Understanding of Protein-DNA Recognition. *Philos. Trans. R. Soc., B*, **351**, 501–509.
158. Luscombe,N.M., Austin,S.E., Berman,H.M. and Thornton,J.M. (2000) An overview of the structures of protein-DNA complexes. *Genome Biol.*, **1**, 001.1–001.10.
159. Frederick,C.A., Grable,J., Melia,M., Samudzi,C., Jen-Jacobson,L., Wang,B.-C., Greene,P., Boyer,H.W. and Rosenberg,J.M. (1984) Kinked DNA in crystalline complex with EcoRI endonuclease. *Nature*, **309**, 327–331.
160. Prestegard,J.H., Al-Hashimi,H.M. and Tolman,J.R. (2000) NMR structures of biomolecules using field oriented media and residual dipolar couplings. *Q. Rev. Biophys.*, **33**, 371–424.
161. Renault,M., Cukkemane,A. and Baldus,M. (2010) Solid-State NMR Spectroscopy on Complex Biomolecules. *Angew. Chem. Int. Ed.*, **49**, 8346–8357.

162. Langowski, J., Benight, A.S., Fujimoto, B.S., Schurr, J.M. and Schomburg, U. (1985) Change of conformation and internal dynamics of supercoiled DNA upon binding of Escherichia coli single-strand binding protein. *Biochemistry*, **24**, 4022–4028.
163. Shelke, S.A. and Sigurdsson, S.T. (2012) Site-Directed Spin Labelling of Nucleic Acids. *Eur. J. Org. Chem.*, **2012**, 2291–2301.
164. Ward, R. and Schiemann, O. (2012) Structural Information from Oligonucleotides. In *Series Structure and Bonding*, Springer, Berlin, in press. doi: 10.1007/430\_2012\_76.
165. Krstić, I., Endeward, B., Margraf, D., Marko, A. and Prisner, T.F. (2012) Structure and dynamics of nucleic acids. *Top Curr Chem.*, **321**, 159–198.
166. Smith, A.L., Cekan, P., Brewood, G.P., Okonogi, T.M., Alemayehu, S., Hustedt, E.J., Benight, A.S., Sigurdsson, S.T. and Robinson, B.H. (2009) Conformational Equilibria of Bulged Sites in Duplex DNA Studied by EPR Spectroscopy. *J. Phys. Chem. B.*, **113**, 2664–2675.
167. Cekan, P., Jonsson, E.Ö. and Sigurdsson, S.T. (2009) Folding of the cocaine aptamer studied by EPR and fluorescence spectroscopies using the bifunctional spectroscopic probe C. *Nucleic Acids Res.*, **37**, 3990–3995.
168. Shelke, S.A. and Sigurdsson, S.T. (2011) Structural changes of an abasic site in duplex DNA affect noncovalent binding of the spin label c. *Nucleic Acids Res.*, **40**, 3732–3740.
169. Reginsson, G.W., Hunter, R.I., Cruickshank, P.A.S., Bolton, D.R., Sigurdsson, S.T., Smith, G.M. and Schiemann, O. (2012) W-band PELDOR with 1kW microwave power: Molecular geometry, flexibility and exchange coupling. *J. Magn. Reson.*, **216**, 175–182.
170. Gore, J., Bryant, Z., Nöllmann, M., Le, M.U., Cozzarelli, N.R. and Bustamante, C. (2006) DNA overwinds when stretched. *Nature*, **442**, 836–839.
171. Marko, J. (1997) Stretching must twist DNA. *EPL (Europhysics Letters)*, **38**, 183–188.
172. Bahl, C.P., Wu, R., Stawinsky, J. and Narang, S.A. (1977) Minimal Length of the Lactose Operator Sequence For the Specific Recognition by the Lactose Repressor. *Proc. Natl. Acad. Sci. U. S. A.*, **74**, 966–970.
173. Bell, C. and Lewis, M. (2000) A closer view of the conformation of the Lac repressor bound to operator. *Nat. Struct. Mol. Biol.*, **7**, 209–214.
174. Lewis, M. (2005) The lac repressor. *C. R. Biologies*, **328**, 521–548.
175. Lewis, M., Chang, G., Horton, N.C., Kercher, M.A., Pace, H.C., Schumacher, M.A., Brennan, R.G. and Lu, P. (1996) Crystal structure of the lactose operon repressor and its complexes with DNA and inducer. *Science*, **271**, 1247–1254.



176. Riggs,A.D., Suzuki,H. and Bourgeois,S. (1970) lac Repressor-Operator Interaction. *J. Mol. Biol.*, **48**, 67–83.
177. Freed,J.H. (2008) New Technologies in Electron Spin Resonance. *Annu. Rev. Phys. Chem.*, **51**, 655–689.
178. Karoui,H., Moigne,F.L., Ouari,O. and Tordo,P. (2010) Stable Radicals: Fundamentals and Applied Aspects of Odd-Electron Compounds - Nitroxide Radicals: Properties, Synthesis and Applications. *Wiley*.
179. Berliner,L.J. (2010) Stable Radicals: Fundamentals and Applied Aspects of Odd-Electron Compounds - Spin Labeling: A Modern Perspective. In Hicks,R.G. (ed). John Wiley & Sons, Ltd.
180. Schiemann,O., Piton,N., Plackmeyer,J., Bode,B., Prisner,T. and Engels,J. (2007) Spin labeling of oligonucleotides with the nitroxide TPA and use of PELDOR, a pulse EPR method, to measure intramolecular distances. *Nat. Protoc.*, **2**, 904–923.
181. Junk,M.J.N., Spiess,H.W. and Hinderberger,D. (2010) The Distribution of Fatty Acids Reveals the Functional Structure of Human Serum Albumin. *Angew. Chem. Int. Ed.*, **49**, 8755–8759.
182. Yulikov,M., Lueders,P., Farooq Warsi,M., Chechik,V. and Jeschke,G. (2012) Distance measurements in Au nanoparticles functionalized with nitroxide radicals and Gd<sup>3+</sup>-DTPA chelate complexes. *Phys. Chem. Chem. Phys.*, **14**, 10732.
183. Swartz,H. and Khan,N. (2005) Biological Magnetic Resonance Eaton,S.S., Eaton,G.R. (eds) Springer, New York.
184. Krstić,I., Hänsel,R., Romainczyk,O., Engels,J.W., Dötsch,V. and Prisner,T.F. (2011) Long-Range Distance Measurements on Nucleic Acids in Cells by Pulsed EPR Spectroscopy. *Angew. Chem. Int. Ed.*, **50**, 5070–5074.
185. Reddy,T., Iwama,T., Halpern,H. and Rawal,V. (2002) General synthesis of persistent trityl radicals for EPR imaging of biological systems. *J Org Chem.*, **67**, 4635–4639.
186. Fielding,A., Carl,P., Eaton,G. and Eaton,S. (2005) Multifrequency EPR of four triarylmethyl radicals. *Appl. Magn. Reson.*, **28**, 231–238.
187. Owenius,R., Eaton,G. and Eaton,S. (2005) Frequency (250 MHz to 9.2 GHz) and viscosity dependence of electron spin relaxation of triarylmethyl radicals at room temperature. *J. Magn. Reson.*, **172**, 168–175.
188. Bobko,A., Dhimitruka,I. and Zweier,J. (2007) Trityl radicals as persistent dual function pH and oxygen probes for in vivo electron paramagnetic resonance spectroscopy and imaging: concept and experiment. *J. Am. Chem. Soc.*, **129**, 7240–7241.

189. Liu, Y., Villamena, F., Sun, J., Xu, Y. and Dhimitruka, I. (2008) Synthesis and characterization of ester-derivatized tetrathiatriarylmethyl radicals as intracellular oxygen probes. *J Org Chem.*, **73**, 1490–1497.
190. Browne, W.R. and Feringa, B.L. (2006) Making molecular machines work. *Nat Nanotechnol.*, **1**, 25–35.
191. Shirai, Y., Osgood, A.J., Zhao, Y., Kelly, K.F. and Tour, J.M. (2005) Directional Control in Thermally Driven Single-Molecule Nanocars. *Nano Lett.*, **5**, 2330–2334.
192. Jeschke, G., Sajid, M., Schulte, M., Ramezani, N., Volkov, A., Zimmermann, H. and Godt, A. (2010) Flexibility of Shape-Persistent Molecular Building Blocks Composed of p-Phenylene and Ethynylene Units. *J. Am. Chem. Soc.*, **132**, 10107–10117.
193. Kurshev, V.V., Raitsimring, A.M. and Tsvetkov, Y.D. (1969) Selection of dipolar interaction by the '2+1' pulse train ESE. *J. Magn. Reson.*, **81**, 441–454.
194. Rajca, A., Kathirvelu, V., Roy, S.K., Pink, M., Rajca, S., Sarkar, S., Eaton, S.S. and Eaton, G.R. (2010) A Spirocyclohexyl Nitroxide Amino Acid Spin Label for Pulsed EPR Spectroscopy Distance Measurements. *Chemistry - A European Journal.*, **16**, 5778–5782.
195. Jeschke, G., Bender, A., Paulsen, H., Zimmermann, H. and Godt, A. (2004) Sensitivity enhancement in pulse EPR distance measurements. *J. Magn. Reson.*, **169**, 1–12.

## Appendices

### A.1 X-ray crystallography of $\zeta$ and phenoxazine derivative

#### A.1.1 Crystallographic Information File (CIF) for crystal structure of phenoxazine derivative

```
data_shelxl

_audit_creation_method          SHELXL-97
_chemical_name_systematic
;
?
;
_chemical_name_common           ?
_chemical_melting_point         ?
_chemical_formula_moiety        ?
_chemical_formula_sum           'C10 H7 N3 O2'
_chemical_formula_weight        201.19

loop_
_atom_type_symbol
_atom_type_description
_atom_type_scatter_dispersion_real
_atom_type_scatter_dispersion_imag
_atom_type_scatter_source
'C' 'C' 0.0033 0.0016
'International Tables Vol C Tables 4.2.6.8 and 6.1.1.4'
'H' 'H' 0.0000 0.0000
'International Tables Vol C Tables 4.2.6.8 and 6.1.1.4'
'N' 'N' 0.0061 0.0033
'International Tables Vol C Tables 4.2.6.8 and 6.1.1.4'
'O' 'O' 0.0106 0.0060
'International Tables Vol C Tables 4.2.6.8 and 6.1.1.4'

_symmetry_cell_setting          monoclinic
_symmetry_space_group_name_H-M  P21/c

loop_
_symmetry_equiv_pos_as_xyz
'x, y, z'
'-x, y+1/2, -z+1/2'
'-x, -y, -z'
'x, -y-1/2, z-1/2'

_cell_length_a                  9.268 (7)
_cell_length_b                  8.872 (6)
_cell_length_c                  11.160 (8)
_cell_angle_alpha               90.00
_cell_angle_beta                112.90 (3)
_cell_angle_gamma               90.00
_cell_volume                    845.3 (11)
_cell_formula_units_Z           4
_cell_measurement_temperature   93 (2)
_cell_measurement_reflns_used   3143
_cell_measurement_theta_min     2.52
_cell_measurement_theta_max     28.24

_exptl_crystal_description      ?
_exptl_crystal_colour           ?
_exptl_crystal_size_max         0.12
_exptl_crystal_size_mid         0.10
_exptl_crystal_size_min         0.01
_exptl_crystal_density_meas     ?
_exptl_crystal_density_diffn    1.581
_exptl_crystal_density_method   'not measured'
_exptl_crystal_F_000            416
_exptl_absorpt_coefficient_mu   0.115
_exptl_absorpt_correction_type  multi-scan
_exptl_absorpt_correction_T_min 0.9863
```

```

_exptl_absorpt_correction_T_max      0.9989
_exptl_absorpt_process_details      'Jacobson, R. (1998) Private communication'

_exptl_special_details
;
?
;

_diffrn_ambient_temperature          93(2)
_diffrn_radiation_wavelength         0.71073
_diffrn_radiation_type               MoK\alpha
_diffrn_radiation_source             'rotating anode'
_diffrn_radiation_monochromator      confocal
_diffrn_measurement_device_type      CCD
_diffrn_measurement_method           '\w and \f scans'
_diffrn_detector_area_resol_mean     ?
_diffrn_standards_number             ?
_diffrn_standards_interval_count     ?
_diffrn_standards_interval_time     ?
_diffrn_standards_decay_%           ?
_diffrn_reflns_number               3564
_diffrn_reflns_av_R_equivalents      0.0949
_diffrn_reflns_av_sigmaI/netI       0.0943
_diffrn_reflns_limit_h_min          -11
_diffrn_reflns_limit_h_max           7
_diffrn_reflns_limit_k_min          -10
_diffrn_reflns_limit_k_max           10
_diffrn_reflns_limit_l_min          -12
_diffrn_reflns_limit_l_max           14
_diffrn_reflns_theta_min            4.78
_diffrn_reflns_theta_max            27.52
_reflns_number_total                 1567
_reflns_number_gt                    873
_reflns_threshold_expression         >2sigma(I)

_computing_data_collection           'CrystalClear (Rigaku Corp., 2004)'
_computing_cell_refinement           'CrystalClear (Rigaku Corp., 2004)'
_computing_data_reduction            'CrystalClear (Rigaku Corp., 2004)'
_computing_structure_solution        'SHELXS-97 (Sheldrick, 1990)'
_computing_structure_refinement      'SHELXL-97 (Sheldrick, 1997)'
_computing_molecular_graphics        'Bruker SHELXTL'
_computing_publication_material      'Bruker SHELXTL'

_refine_special_details
;
Refinement of F2 against ALL reflections. The weighted R-factor wR and
goodness of fit S are based on F2, conventional R-factors R are based
on F, with F set to zero for negative F2. The threshold expression of
F2 > 2sigma(F2) is used only for calculating R-factors(gt) etc. and is
not relevant to the choice of reflections for refinement. R-factors based
on F2 are statistically about twice as large as those based on F, and R-
factors based on ALL data will be even larger.
;

_refine_ls_structure_factor_coef      Fsqd
_refine_ls_matrix_type               full
_refine_ls_weighting_scheme          calc
_refine_ls_weighting_details         'calc w=1/[\s^2^(Fo^2)+(0.0354P)^2+3.3437P] where P=(Fo^2+2Fc^2)/3'
_atom_sites_solution_primary         direct
_atom_sites_solution_secondary       difmap
_atom_sites_solution_hydrogens       geom
_refine_ls_hydrogen_treatment        constr
_refine_ls_extinction_method         none
_refine_ls_extinction_coef           ?
_refine_ls_number_reflns            1567
_refine_ls_number_parameters         136
_refine_ls_number_restraints         0
_refine_ls_R_factor_all              0.1622
_refine_ls_R_factor_gt               0.0844
_refine_ls_wR_factor_ref             0.1915
_refine_ls_wR_factor_gt              0.1503
_refine_ls_goodness_of_fit_ref       1.048
_refine_ls_restrained_S_all         1.048
_refine_ls_shift/su_max              0.001
_refine_ls_shift/su_mean             0.000

```

```

loop_
  _atom_site_label
  _atom_site_type_symbol
  _atom_site_fract_x
  _atom_site_fract_y
  _atom_site_fract_z
  _atom_site_U_iso_or_equiv
  _atom_site_adp_type
  _atom_site_occupancy
  _atom_site_symmetry_multiplicity
  _atom_site_calc_flag
  _atom_site_refinement_flags
  _atom_site_disorder_assembly
  _atom_site_disorder_group
O11 O 0.3157(4) 0.5235(4) 0.5206(3) 0.0267(9) Uani 1 1 d . . .
O1 O -0.0352(4) 0.0958(4) 0.6220(3) 0.0277(9) Uani 1 1 d . . .
N2 N 0.0656(5) 0.3346(5) 0.6628(4) 0.0223(9) Uani 1 1 d . . .
N4 N 0.1692(5) 0.5736(5) 0.6967(4) 0.0234(10) Uani 1 1 d . . .
H4 H 0.1195 0.5918 0.7584 0.028 Uiso 1 1 calc R . .
N14 N 0.1000(4) 0.1797(5) 0.5037(4) 0.0231(10) Uani 1 1 d . . .
H14 H 0.0788 0.0953 0.4586 0.028 Uiso 1 1 calc R . .
C1 C 0.0421(5) 0.2004(6) 0.5984(5) 0.0217(11) Uani 1 1 d . . .
C3 C 0.1506(5) 0.4388(5) 0.6365(4) 0.0191(11) Uani 1 1 d . . .
C5 C 0.2591(5) 0.6884(6) 0.6723(4) 0.0220(11) Uani 1 1 d . . .
C6 C 0.2747(6) 0.8285(6) 0.7307(5) 0.0236(11) Uani 1 1 d . . .
H6 H 0.2216 0.8491 0.7865 0.028 Uiso 1 1 calc R . .
C7 C 0.3675(6) 0.9391(6) 0.7083(5) 0.0283(12) Uani 1 1 d . . .
H7 H 0.3781 1.0347 0.7493 0.034 Uiso 1 1 calc R . .
C8 C 0.4451(6) 0.9103(6) 0.6256(5) 0.0276(12) Uani 1 1 d . . .
H8 H 0.5106 0.9849 0.6118 0.033 Uiso 1 1 calc R . .
C9 C 0.4254(6) 0.7698(6) 0.5630(5) 0.0263(12) Uani 1 1 d . . .
H9 H 0.4765 0.7492 0.5057 0.032 Uiso 1 1 calc R . .
C10 C 0.3316(5) 0.6622(6) 0.5851(5) 0.0230(11) Uani 1 1 d . . .
C12 C 0.2217(5) 0.4179(6) 0.5444(4) 0.0212(11) Uani 1 1 d . . .
C13 C 0.1901(5) 0.2871(6) 0.4775(4) 0.0212(11) Uani 1 1 d . . .
H13 H 0.2302 0.2694 0.4123 0.025 Uiso 1 1 calc R . .

```

```

loop_
  _atom_site_aniso_label
  _atom_site_aniso_U_11
  _atom_site_aniso_U_22
  _atom_site_aniso_U_33
  _atom_site_aniso_U_23
  _atom_site_aniso_U_13
  _atom_site_aniso_U_12
O11 0.034(2) 0.0250(19) 0.0285(18) -0.0016(16) 0.0204(16) -0.0057(16)
O1 0.038(2) 0.0205(19) 0.032(2) -0.0016(16) 0.0217(17) -0.0065(16)
N2 0.024(2) 0.023(2) 0.023(2) -0.0016(19) 0.0130(18) -0.0011(18)
N4 0.031(2) 0.021(2) 0.025(2) 0.0009(19) 0.0190(19) -0.0027(19)
N14 0.028(2) 0.024(2) 0.022(2) -0.0013(19) 0.0136(18) -0.0006(18)
C1 0.020(2) 0.024(3) 0.020(2) 0.003(2) 0.007(2) 0.004(2)
C3 0.022(3) 0.021(3) 0.016(2) 0.005(2) 0.009(2) 0.003(2)
C5 0.022(3) 0.025(3) 0.018(2) -0.003(2) 0.007(2) -0.002(2)
C6 0.028(3) 0.022(3) 0.023(3) 0.003(2) 0.012(2) 0.003(2)
C7 0.033(3) 0.020(3) 0.029(3) -0.003(2) 0.009(2) -0.005(2)
C8 0.028(3) 0.029(3) 0.025(3) 0.003(2) 0.010(2) -0.007(2)
C9 0.024(3) 0.031(3) 0.026(3) 0.000(2) 0.012(2) -0.002(2)
C10 0.022(3) 0.022(3) 0.025(3) 0.002(2) 0.009(2) -0.002(2)
C12 0.022(3) 0.021(3) 0.023(3) -0.001(2) 0.010(2) -0.001(2)
C13 0.024(2) 0.025(3) 0.018(2) -0.001(2) 0.011(2) -0.003(2)

```

```
_geom_special_details
```

```
;
```

All esds (except the esd in the dihedral angle between two l.s. planes) are estimated using the full covariance matrix. The cell esds are taken into account individually in the estimation of esds in distances, angles and torsion angles; correlations between esds in cell parameters are only used when they are defined by crystal symmetry. An approximate (isotropic) treatment of cell esds is used for estimating esds involving l.s. planes.

```
;
```

```

loop_
  _geom_bond_atom_site_label_1
  _geom_bond_atom_site_label_2
  _geom_bond_distance
  _geom_bond_site_symmetry_2
  _geom_bond_publ_flag

```

O11 C12 1.375(6) . ?  
 O11 C10 1.404(6) . ?  
 O1 C1 1.261(6) . ?  
 N2 C3 1.319(6) . ?  
 N2 C1 1.364(6) . ?  
 N4 C3 1.349(6) . ?  
 N4 C5 1.408(6) . ?  
 N14 C1 1.371(6) . ?  
 N14 C13 1.371(6) . ?  
 C3 C12 1.432(6) . ?  
 C5 C6 1.384(7) . ?  
 C5 C10 1.401(7) . ?  
 C6 C7 1.391(7) . ?  
 C7 C8 1.397(7) . ?  
 C8 C9 1.406(7) . ?  
 C9 C10 1.376(7) . ?  
 C12 C13 1.349(7) . ?

loop\_  
 \_geom\_angle\_atom\_site\_label\_1  
 \_geom\_angle\_atom\_site\_label\_2  
 \_geom\_angle\_atom\_site\_label\_3  
 \_geom\_angle  
 \_geom\_angle\_site\_symmetry\_1  
 \_geom\_angle\_site\_symmetry\_3  
 \_geom\_angle\_publ\_flag  
 C12 O11 C10 116.5(4) . . ?  
 C3 N2 C1 118.8(4) . . ?  
 C3 N4 C5 121.0(4) . . ?  
 C1 N14 C13 121.6(4) . . ?  
 O1 C1 N2 121.3(4) . . ?  
 O1 C1 N14 119.2(5) . . ?  
 N2 C1 N14 119.6(4) . . ?  
 N2 C3 N4 118.8(4) . . ?  
 N2 C3 C12 123.3(5) . . ?  
 N4 C3 C12 117.8(4) . . ?  
 C6 C5 C10 119.1(5) . . ?  
 C6 C5 N4 121.3(4) . . ?  
 C10 C5 N4 119.6(5) . . ?  
 C5 C6 C7 120.5(4) . . ?  
 C6 C7 C8 120.2(5) . . ?  
 C7 C8 C9 119.3(5) . . ?  
 C10 C9 C8 119.7(5) . . ?  
 C9 C10 C5 121.1(5) . . ?  
 C9 C10 O11 117.6(4) . . ?  
 C5 C10 O11 121.2(4) . . ?  
 C13 C12 O11 119.8(4) . . ?  
 C13 C12 C3 116.6(4) . . ?  
 O11 C12 C3 123.6(4) . . ?  
 C12 C13 N14 119.9(4) . . ?

_diffraction_measured_fraction_theta_max	0.803
_diffraction_reflns_theta_full	25.00
_diffraction_measured_fraction_theta_full	0.945
_refine_diff_density_max	0.431
_refine_diff_density_min	-0.318
_refine_diff_density_rms	0.079

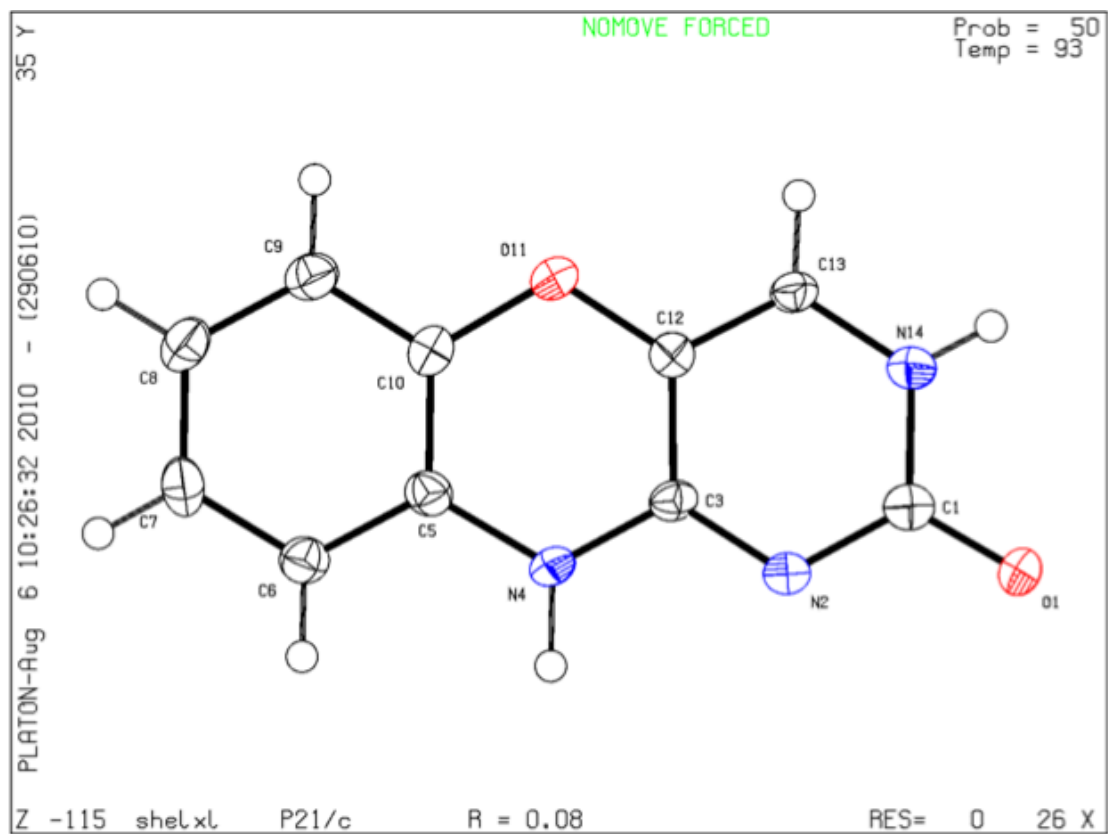


**Figure A1.** Thermal ellipsoid plot of the crystal structure of phenoxazine derivative.

## A.1.2 Crystallographic Information File (CIF) for crystal structure of $\zeta$

```
data_shelxl

_audit_creation_method          SHELXL-97
_chemical_name_systematic ?

_chemical_melting_point         ?
_chemical_formula_moiety        'C16 H15 N4 O3'
_chemical_formula_sum           'C16 H15 N4 O3'
_chemical_formula_weight        311.32

loop_
_atom_type_symbol
_atom_type_description
_atom_type_scatter_dispersion_real
_atom_type_scatter_dispersion_imag
_atom_type_scatter_source
'C' 'C' 0.0033 0.0016
'International Tables Vol C Tables 4.2.6.8 and 6.1.1.4'
'H' 'H' 0.0000 0.0000
'International Tables Vol C Tables 4.2.6.8 and 6.1.1.4'
'N' 'N' 0.0061 0.0033
'International Tables Vol C Tables 4.2.6.8 and 6.1.1.4'
'O' 'O' 0.0106 0.0060
'International Tables Vol C Tables 4.2.6.8 and 6.1.1.4'

_symmetry_cell_setting          monoclinic
_symmetry_space_group_name_H-M  P21/n

loop_
_symmetry_equiv_pos_as_xyz
'x, y, z'
'-x+1/2, y+1/2, -z+1/2'
'-x, -y, -z'
'x-1/2, -y-1/2, z-1/2'

_cell_length_a                  5.731(2)
_cell_length_b                  9.162(4)
_cell_length_c                  31.739(12)
_cell_angle_alpha               90.00
_cell_angle_beta                91.230(12)
_cell_angle_gamma               90.00
_cell_volume                    1666.0(11)
_cell_formula_units_Z           4
_cell_measurement_temperature    93(2)
_cell_measurement_reflns_used    ?
_cell_measurement_theta_min      ?
_cell_measurement_theta_max      ?

_exptl_crystal_description      ?
_exptl_crystal_colour           yellow
_exptl_crystal_size_max         0.10
_exptl_crystal_size_mid         0.03
_exptl_crystal_size_min         0.03
_exptl_crystal_density_meas     ?
_exptl_crystal_density_diffn    1.243
_exptl_crystal_density_method   'not measured'
_exptl_crystal_F_000            696
_exptl_absorpt_coefficient_mu   0.089
_exptl_absorpt_correction_type  multi-scan
_exptl_absorpt_correction_T_min 0.9906
_exptl_absorpt_correction_T_max 0.9972
_exptl_absorpt_process_details  'Jacobson, R. (1998) Private communication'

_exptl_special_details
;
?
;

_diffn_ambient_temperature      93(2)
_diffn_radiation_wavelength     0.71073
```



```

_diffrn_radiation_type           MoK\alpha
_diffrn_radiation_source         'rotating anode'
_diffrn_radiation_monochromator   confocal
_diffrn_measurement_device_type   CCD
_diffrn_measurement_method       '\w and \f scans'
_diffrn_detector_area_resol_mean  ?
_diffrn_standards_number         ?
_diffrn_standards_interval_count  ?
_diffrn_standards_interval_time  ?
_diffrn_standards_decay_%        ?
_diffrn_reflns_number            9668
_diffrn_reflns_av_R_equivalents  0.1135
_diffrn_reflns_av_sigmaI/netI    0.1080
_diffrn_reflns_limit_h_min       -4
_diffrn_reflns_limit_h_max       6
_diffrn_reflns_limit_k_min       -11
_diffrn_reflns_limit_k_max       10
_diffrn_reflns_limit_l_min       -37
_diffrn_reflns_limit_l_max       38
_diffrn_reflns_theta_min         1.28
_diffrn_reflns_theta_max         25.30
_reflns_number_total             2997
_reflns_number_gt                1506
_reflns_threshold_expression      >2sigma(I)

_computing_data_collection        'CrystalClear (Rigaku Corp., 2004)'
_computing_cell_refinement        'CrystalClear (Rigaku Corp., 2004)'
_computing_data_reduction         'CrystalClear (Rigaku Corp., 2004)'
_computing_structure_solution     'SHELXS-97 (Sheldrick, 1990)'
_computing_structure_refinement   'SHELXL-97 (Sheldrick, 1997)'
_computing_molecular_graphics     'Bruker SHELXTL'
_computing_publication_material   'Bruker SHELXTL'

_refine_special_details
;
Refinement of F2 against ALL reflections. The weighted R-factor wR and
goodness of fit S are based on F2, conventional R-factors R are based
on F, with F set to zero for negative F2. The threshold expression of
F2 > 2sigma(F2) is used only for calculating R-factors(gt) etc. and is
not relevant to the choice of reflections for refinement. R-factors based
on F2 are statistically about twice as large as those based on F, and R-
factors based on ALL data will be even larger.
;

_refine_ls_structure_factor_coef  Fsqd
_refine_ls_matrix_type           full
_refine_ls_weighting_scheme       calc
_refine_ls_weighting_details
'calc w=1/[\s2(Fo2)+(0.1337P)2+0.0000P] where P=(Fo2+2Fc2)/3'
_atom_sites_solution_primary      direct
_atom_sites_solution_secondary    difmap
_atom_sites_solution_hydrogens    geom
_refine_ls_hydrogen_treatment     constr
_refine_ls_extinction_method      none
_refine_ls_extinction_coef        ?
_refine_ls_number_reflns         2997
_refine_ls_number_parameters      227
_refine_ls_number_restraints      0
_refine_ls_R_factor_all           0.1676
_refine_ls_R_factor_gt           0.0900
_refine_ls_wR_factor_ref         0.2790
_refine_ls_wR_factor_gt         0.2330
_refine_ls_goodness_of_fit_ref    1.030
_refine_ls_restrained_S_all       1.030
_refine_ls_shift/su_max          0.019
_refine_ls_shift/su_mean         0.001

loop_
_atom_site_label
_atom_site_type_symbol
_atom_site_fract_x
_atom_site_fract_y
_atom_site_fract_z
_atom_site_U_iso_or_equiv
_atom_site_adp_type
_atom_site_occupancy
_atom_site_symmetry_multiplicity

```

```

_atom_site_calc_flag
_atom_site_refinement_flags
_atom_site_disorder_assembly
_atom_site_disorder_group
O1 O -0.9162(6) -0.4009(3) 0.26927(9) 0.0445(9) Uani 1 1 d . . .
C1 C -0.7338(9) -0.4017(5) 0.24815(14) 0.0396(12) Uani 1 1 d . . .
N2 N -0.6463(7) -0.5281(4) 0.23177(11) 0.0387(10) Uani 1 1 d . . .
C3 C -0.4517(9) -0.5278(5) 0.20696(14) 0.0408(12) Uani 1 1 d . . .
H3A H -0.3951 -0.6169 0.1958 0.049 Uiso 1 1 calc R . .
C4 C -0.3428(8) -0.4032(5) 0.19854(13) 0.0372(11) Uani 1 1 d . . .
O5 O -0.1448(6) -0.3993(3) 0.17413(9) 0.0444(9) Uani 1 1 d . . .
C6 C -0.0791(8) -0.2633(5) 0.15902(13) 0.0384(12) Uani 1 1 d . . .
C7 C 0.0664(8) -0.2582(5) 0.12426(14) 0.0407(12) Uani 1 1 d . . .
H7A H 0.1209 -0.3454 0.1116 0.049 Uiso 1 1 calc R . .
C8 C 0.1301(8) -0.1208(5) 0.10850(14) 0.0406(12) Uani 1 1 d . . .
C9 C 0.2708(8) -0.0918(5) 0.06964(15) 0.0425(12) Uani 1 1 d . . .
O10 O 0.3551(6) 0.1460(4) 0.04000(11) 0.0601(11) Uani 1 1 d . . .
N10 N 0.2562(7) 0.0702(5) 0.06883(12) 0.0495(11) Uani 1 1 d . . .
C11 C 0.1315(8) 0.1392(5) 0.10423(14) 0.0442(13) Uani 1 1 d . . .
C12 C 0.0541(8) 0.0069(5) 0.12767(13) 0.0388(12) Uani 1 1 d . . .
C13 C -0.0910(8) -0.0005(5) 0.16193(14) 0.0413(12) Uani 1 1 d . . .
H13A H -0.1427 0.0868 0.1749 0.050 Uiso 1 1 calc R . .
C14 C -0.1608(8) -0.1337(5) 0.17728(13) 0.0358(11) Uani 1 1 d . . .
N15 N -0.3262(7) -0.1415(4) 0.20976(11) 0.0398(10) Uani 1 1 d . . .
C16 C -0.4294(8) -0.2731(5) 0.21686(13) 0.0379(11) Uani 1 1 d . . .
N17 N -0.6177(7) -0.2732(4) 0.24145(11) 0.0371(10) Uani 1 1 d . . .
C18 C 0.1605(9) -0.1520(6) 0.02924(14) 0.0521(14) Uani 1 1 d . . .
H18A H -0.0027 -0.1205 0.0270 0.078 Uiso 1 1 calc R . .
H18B H 0.1673 -0.2589 0.0297 0.078 Uiso 1 1 calc R . .
H18C H 0.2458 -0.1155 0.0050 0.078 Uiso 1 1 calc R . .
C19 C 0.5216(9) -0.1386(6) 0.07349(16) 0.0549(14) Uani 1 1 d . . .
H19A H 0.5914 -0.0983 0.0994 0.082 Uiso 1 1 calc R . .
H19B H 0.6071 -0.1025 0.0492 0.082 Uiso 1 1 calc R . .
H19C H 0.5300 -0.2453 0.0743 0.082 Uiso 1 1 calc R . .
C20 C -0.0717(10) 0.2347(6) 0.08716(16) 0.0547(14) Uani 1 1 d . . .
H20A H -0.1797 0.1742 0.0704 0.082 Uiso 1 1 calc R . .
H20B H -0.0096 0.3127 0.0695 0.082 Uiso 1 1 calc R . .
H20C H -0.1546 0.2777 0.1108 0.082 Uiso 1 1 calc R . .
C21 C 0.3009(10) 0.2352(6) 0.13065(16) 0.0546(14) Uani 1 1 d . . .
H21A H 0.4302 0.1751 0.1415 0.082 Uiso 1 1 calc R . .
H21B H 0.2176 0.2782 0.1543 0.082 Uiso 1 1 calc R . .
H21C H 0.3625 0.3132 0.1129 0.082 Uiso 1 1 calc R . .

```

```

loop_
_atom_site_aniso_label
_atom_site_aniso_U_11
_atom_site_aniso_U_22
_atom_site_aniso_U_33
_atom_site_aniso_U_23
_atom_site_aniso_U_13
_atom_site_aniso_U_12
O1 0.050(2) 0.034(2) 0.0506(18) 0.0014(15) 0.0190(17) -0.0034(15)
C1 0.047(3) 0.034(3) 0.038(2) 0.002(2) 0.002(2) 0.001(2)
N2 0.044(2) 0.032(2) 0.041(2) -0.0034(18) 0.0096(19) 0.0010(18)
C3 0.052(3) 0.029(3) 0.041(2) -0.007(2) 0.002(2) 0.004(2)
C4 0.046(3) 0.029(3) 0.036(2) 0.003(2) 0.010(2) 0.003(2)
O5 0.056(2) 0.0292(18) 0.0488(18) 0.0047(15) 0.0166(17) 0.0015(15)
C6 0.043(3) 0.036(3) 0.036(2) -0.005(2) 0.000(2) 0.003(2)
C7 0.038(3) 0.039(3) 0.044(3) -0.003(2) 0.002(2) -0.001(2)
C8 0.033(3) 0.047(3) 0.042(2) -0.002(2) 0.004(2) -0.005(2)
C9 0.038(3) 0.040(3) 0.050(3) -0.001(2) 0.011(2) -0.004(2)
O10 0.067(3) 0.059(2) 0.055(2) 0.0036(19) 0.018(2) -0.0128(19)
N10 0.054(3) 0.046(3) 0.048(2) 0.003(2) 0.014(2) -0.013(2)
C11 0.041(3) 0.049(3) 0.043(3) -0.001(2) 0.008(2) -0.007(2)
C12 0.041(3) 0.039(3) 0.037(2) 0.002(2) 0.001(2) -0.005(2)
C13 0.042(3) 0.036(3) 0.047(3) -0.003(2) 0.008(2) -0.001(2)
C14 0.039(3) 0.034(3) 0.034(2) 0.000(2) 0.003(2) 0.001(2)
N15 0.045(2) 0.034(2) 0.042(2) 0.0024(18) 0.0119(18) -0.0064(18)
C16 0.040(3) 0.039(3) 0.034(2) 0.000(2) 0.001(2) -0.001(2)
N17 0.046(2) 0.027(2) 0.0383(19) -0.0023(17) 0.0077(18) 0.0003(17)
C18 0.056(4) 0.059(3) 0.042(3) -0.003(3) 0.007(3) -0.004(3)
C19 0.046(3) 0.060(4) 0.059(3) 0.001(3) 0.007(3) -0.004(3)
C20 0.056(4) 0.052(3) 0.056(3) 0.009(3) 0.003(3) -0.005(3)
C21 0.053(3) 0.055(3) 0.056(3) -0.002(3) 0.007(3) -0.019(3)

```

```

_geom_special_details
;

```

All esds (except the esd in the dihedral angle between two l.s. planes) are estimated using the full covariance matrix. The cell esds are taken into account individually in the estimation of esds in distances, angles and torsion angles; correlations between esds in cell parameters are only used when they are defined by crystal symmetry. An approximate (isotropic) treatment of cell esds is used for estimating esds involving l.s. planes.

;

```

loop_
  _geom_bond_atom_site_label_1
  _geom_bond_atom_site_label_2
  _geom_bond_distance
  _geom_bond_site_symmetry_2
  _geom_bond_publ_flag
O1 C1 1.254(5) . ?
C1 N2 1.369(5) . ?
C1 N17 1.370(6) . ?
N2 C3 1.379(6) . ?
C3 C4 1.331(6) . ?
C4 O5 1.388(5) . ?
C4 C16 1.420(6) . ?
O5 C6 1.390(5) . ?
C6 C7 1.398(6) . ?
C6 C14 1.406(6) . ?
C7 C8 1.406(6) . ?
C8 C12 1.392(6) . ?
C8 C9 1.511(6) . ?
C9 N10 1.487(6) . ?
C9 C19 1.502(7) . ?
C9 C18 1.521(7) . ?
O10 N10 1.289(5) . ?
N10 C11 1.486(6) . ?
C11 C12 1.495(6) . ?
C11 C21 1.544(7) . ?
C11 C20 1.545(7) . ?
C12 C13 1.385(6) . ?
C13 C14 1.377(6) . ?
C14 N15 1.417(5) . ?
N15 C16 1.364(6) . ?
C16 N17 1.345(6) . ?

```

```

loop_
  _geom_angle_atom_site_label_1
  _geom_angle_atom_site_label_2
  _geom_angle_atom_site_label_3
  _geom_angle
  _geom_angle_site_symmetry_1
  _geom_angle_site_symmetry_3
  _geom_angle_publ_flag
O1 C1 N2 121.6(4) . . ?
O1 C1 N17 119.4(4) . . ?
N2 C1 N17 119.0(4) . . ?
C1 N2 C3 121.5(4) . . ?
C4 C3 N2 120.3(4) . . ?
C3 C4 O5 121.8(4) . . ?
C3 C4 C16 117.9(4) . . ?
O5 C4 C16 120.3(4) . . ?
C4 O5 C6 116.5(3) . . ?
O5 C6 C7 118.2(4) . . ?
O5 C6 C14 121.3(4) . . ?
C7 C6 C14 120.4(4) . . ?
C6 C7 C8 118.4(4) . . ?
C12 C8 C7 120.7(4) . . ?
C12 C8 C9 112.7(4) . . ?
C7 C8 C9 126.5(4) . . ?
N10 C9 C19 109.8(4) . . ?
N10 C9 C8 99.1(4) . . ?
C19 C9 C8 114.2(4) . . ?
N10 C9 C18 109.0(4) . . ?
C19 C9 C18 110.1(4) . . ?
C8 C9 C18 113.9(4) . . ?
O10 N10 C11 122.2(4) . . ?
O10 N10 C9 121.6(4) . . ?
C11 N10 C9 116.1(4) . . ?
N10 C11 C12 100.6(4) . . ?
N10 C11 C21 110.3(4) . . ?
C12 C11 C21 112.4(4) . . ?

```

N10 C11 C20 110.3(4) . . ?  
C12 C11 C20 113.8(4) . . ?  
C21 C11 C20 109.2(4) . . ?  
C13 C12 C8 120.1(4) . . ?  
C13 C12 C11 128.3(4) . . ?  
C8 C12 C11 111.4(4) . . ?  
C14 C13 C12 120.3(4) . . ?  
C13 C14 C6 120.1(4) . . ?  
C13 C14 N15 120.4(4) . . ?  
C6 C14 N15 119.4(4) . . ?  
C16 N15 C14 117.6(4) . . ?  
N17 C16 N15 116.9(4) . . ?  
N17 C16 C4 121.9(4) . . ?  
N15 C16 C4 121.2(4) . . ?  
C16 N17 C1 119.3(4) . . ?

\_diffrn\_measured\_fraction\_theta\_max 0.995  
\_diffrn\_reflns\_theta\_full 25.30  
\_diffrn\_measured\_fraction\_theta\_full 0.995  
\_refine\_diff\_density\_max 0.495  
\_refine\_diff\_density\_min -0.361  
\_refine\_diff\_density\_rms 0.08

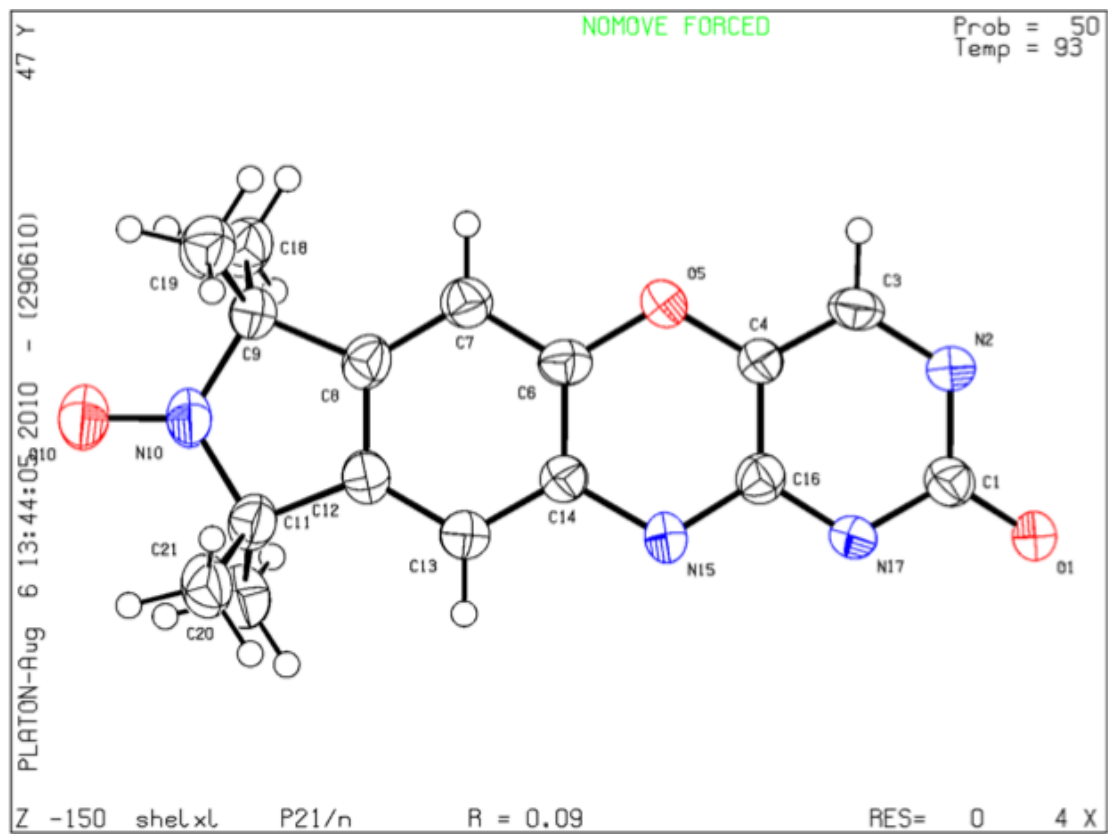


**Figure A2.** Thermal ellipsoid plot of the crystal structure of  $\bar{q}$ .

## A.2 DFT calculations of $\zeta$ and phenoxazine

**Table A.2.1.** Frequencies and intensities from DFT frequency calculations on the geometry optimized  $\zeta$  spin label in the planar conformation.

Frequencies	Intensities	Frequencies	Intensities	Frequencies	Intensities
18.78	0.59	749.19	0.83	1506.65	342.99
30.56	0.68	759.16	27.15	1507.00	2.69
51.24	3.86	765.11	0.35	1515.38	0.14
85.46	2.01	781.86	5.20	1518.13	2.97
99.13	3.59	845.83	13.47	1522.61	219.73
117.41	0.88	867.89	11.67	1526.65	65.19
117.89	1.31	867.98	13.26	1528.84	139.13
166.19	0.04	882.88	8.24	1537.61	6.11
207.29	0.92	885.24	23.28	1539.29	1.21
211.85	0.19	888.61	2.84	1550.50	175.57
213.68	1.22	948.74	0.00	1619.77	547.54
215.16	0.11	949.57	0.15	1646.24	6.48
217.41	0.06	952.83	5.96	1672.81	31.79
258.45	0.70	961.32	2.10	1732.44	131.05
259.67	0.28	1027.21	0.11	1817.52	805.46
261.21	0.99	1028.18	0.08	3056.30	0.02
274.94	0.03	1038.64	1.69	3056.57	32.90
299.72	0.18	1090.63	0.59	3060.74	30.64
317.79	9.65	1141.90	35.24	3061.74	0.60
320.38	0.18	1147.98	25.99	3127.33	0.58
345.07	2.75	1182.84	0.19	3128.78	17.47
353.86	0.58	1183.35	15.28	3132.11	50.77
375.79	23.43	1185.41	18.55	3133.47	7.47
391.24	0.14	1195.58	132.55	3142.04	0.00
412.92	9.42	1203.52	5.66	3142.62	14.33
				3145.47	

---

438.78	0.12	1208.52	10.43	3146.23	5.12
461.46	0.42	1260.24	9.21	3186.01	42.82
503.58	9.67	1277.17	37.61	3213.01	8.94
523.23	0.03	1285.82	11.15	3243.84	2.45
527.68	51.87	1311.49	13.46	3611.05	3.58
535.31	0.88	1334.22	6.17	3622.93	60.63
550.43	18.00	1355.41	20.45		101.80
571.77	1.68	1376.41	467.01		
585.60	1.69	1414.95	0.97		
590.09	109.60	1416.39	26.14		
602.33	2.59	1417.60	13.01		
652.99	6.62	1433.36	0.90		
672.45	1.61	1436.09	23.52		
688.91	0.41	1448.54	210.35		
719.52	1.46	1488.91	53.34		
743.12	3.07	1502.89	0.03		

---

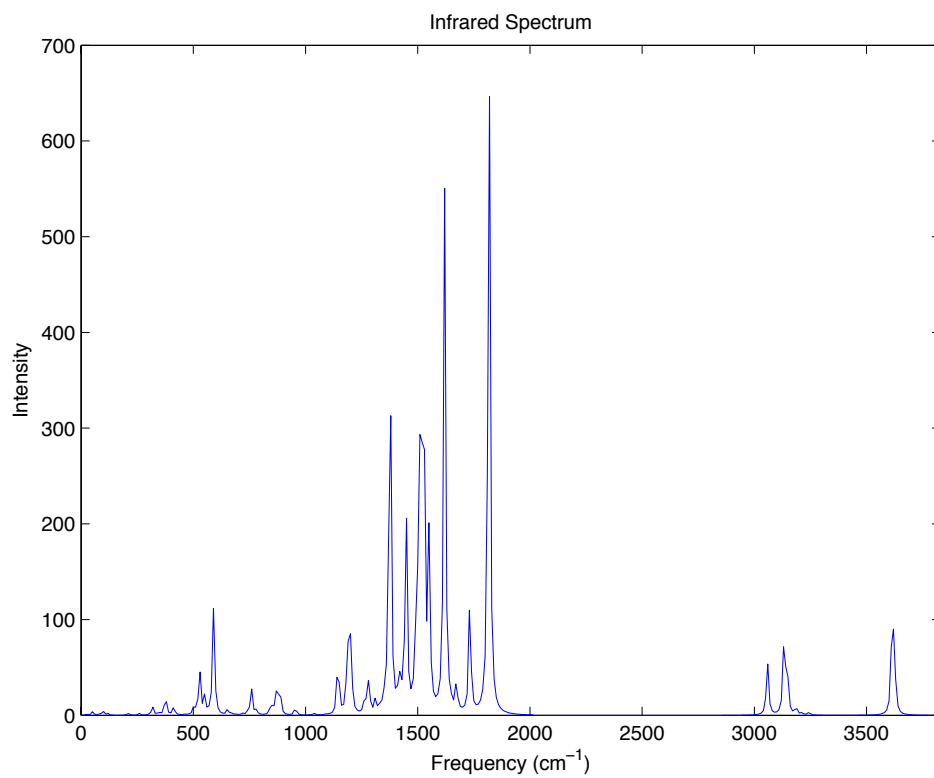


**Figure A.2.1.** DFT IR spectrum of  $\zeta$  in the planar conformation.



### A.2.1 Coordinates for $\zeta$ in the planar conformation from DFT calculations

O	-4.911925	-3.862008	9.219636
C	-4.103746	-3.743416	8.315366
N	-3.616735	-4.904645	7.662796
C	-2.710704	-4.885853	6.638118
H	-2.402788	-5.831082	6.206707
C	-2.236844	-3.692264	6.206022
O	-1.319957	-3.629393	5.173185
C	-0.873438	-2.384873	4.776238
C	0.047798	-2.335180	3.737106
H	0.373679	-3.267540	3.286294
C	0.521377	-1.094888	3.309327
C	1.517882	-0.816636	2.204907
O	2.313785	1.356977	1.493285
N	1.573640	0.672374	2.271680
C	0.710039	1.310703	3.306418
C	0.074885	0.080600	3.918107
C	-0.848992	0.030752	4.960232
H	-1.203759	0.939007	5.441675
C	-1.329324	-1.205756	5.395929
N	-2.258040	-1.313951	6.438204
C	-2.735926	-2.518884	6.873858
N	-3.603113	-2.538057	7.854164
C	1.025685	-1.244663	0.810406
H	0.015720	-0.868994	0.619027
H	1.011747	-2.336621	0.724899
H	1.699319	-0.839949	0.049083
C	2.919242	-1.390575	2.482284
H	3.262326	-1.119030	3.485449
H	3.626178	-0.988559	1.750284
H	2.911194	-2.483000	2.402180
C	-0.300121	2.246975	2.618277
H	-0.955527	1.688313	1.942915
H	0.241988	2.998529	2.036523
H	-0.921932	2.757870	3.361610
C	1.593729	2.100113	4.289540
H	2.292115	1.436478	4.808788
H	0.978042	2.610478	5.038316
H	2.168910	2.849138	3.737014
H	-3.989101	-5.779783	8.006807
H	-2.609853	-0.489892	6.908492

Table A.2.2. Frequencies and intensities from DFT frequency calculations on the geometry optimized  $\zeta$  spin label in the bent conformation.

Frequencies	Intensities	Frequencies	Intensities	Frequencies	Intensities
28.31	0.45	781.46	5.55	1528.24	14.26
41.74	1.06	845.82	17.84	1536.80	5.61
51.64	3.44	868.28	13.75	1538.41	1.36
89.80	0.99	868.57	11.11	1549.01	142.50
95.89	5.10	885.32	0.81	1618.47	476.03
120.80	1.37	887.50	28.03	1646.10	6.06
124.32	0.91	888.23	5.30	1672.84	32.57
166.99	0.05	948.17	0.02	1732.41	125.44
202.63	1.56	948.94	0.36	1818.41	806.12
211.87	0.01	952.70	5.81	3056.39	1.37
214.53	0.06	960.93	2.03	3056.72	31.38
218.63	0.35	1025.55	0.12	3060.95	30.58
223.38	0.88	1026.31	0.10	3061.98	0.64
257.51	0.54	1037.87	1.66	3127.48	0.07
260.33	0.74	1090.38	0.69	3128.81	17.79
263.94	0.70	1140.86	32.57	3132.33	51.59
279.12	1.17	1146.90	28.93	3133.65	6.41
300.51	0.17	1183.70	0.25	3141.87	1.62
318.17	9.69	1184.30	15.15	3142.70	13.30
325.93	1.08	1185.55	18.54	3145.45	7.09
345.44	2.56	1194.95	125.21	3146.34	40.08
353.68	1.18	1203.46	8.78	3186.29	8.81
378.09	18.75	1207.35	9.78	3213.21	2.43
391.87	0.35	1260.64	8.26	3243.65	3.27
413.48	10.37	1273.81	38.23	3601.93	52.56
438.41	0.70	1284.43	11.14	3622.01	102.71

---

463.64	0.26	1311.57	14.17
502.31	9.92	1334.35	4.03
523.16	0.48	1354.44	35.30
531.31	4.66	1373.85	471.31
550.85	3.83	1413.59	0.40
559.83	42.13	1415.20	30.62
573.11	4.50	1416.26	18.72
590.78	2.69	1432.03	2.85
598.07	101.96	1435.28	23.49
603.50	34.78	1448.62	214.19
653.52	8.08	1488.70	59.62
674.10	2.20	1503.81	7.72
689.81	0.93	1504.55	370.66
721.42	2.47	1507.85	3.24
744.32	3.29	1514.70	0.71
751.18	1.08	1517.24	4.02
760.19	27.49	1520.69	311.61
765.47	0.18	1525.94	52.80

---

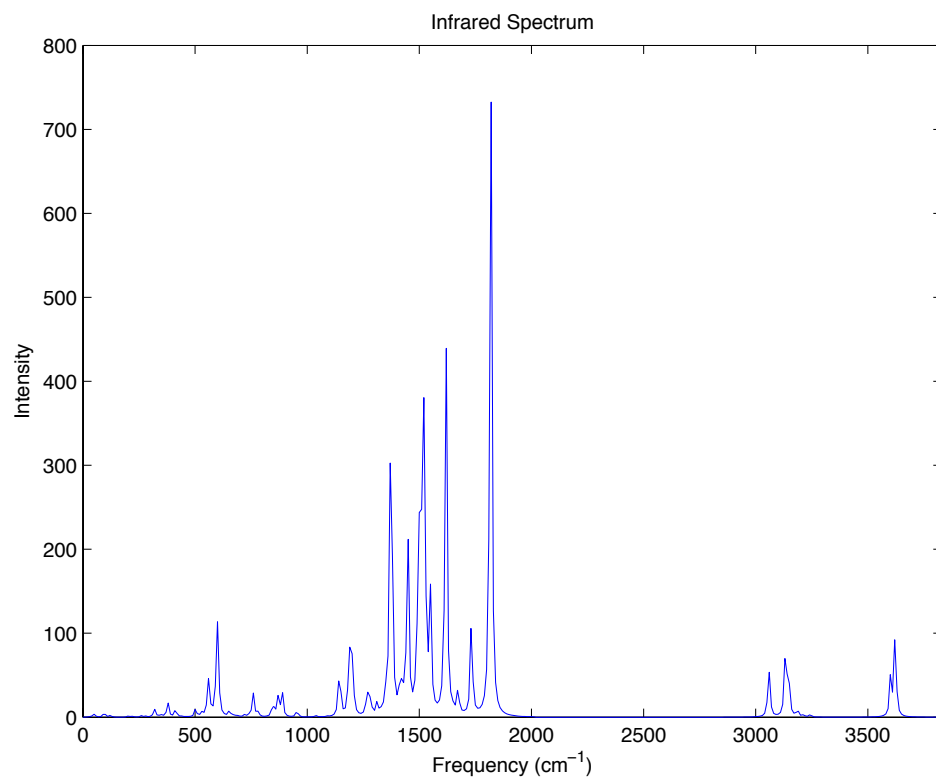


**Figure A.2.2.** DFT IR spectrum of  $\zeta$  in the bent conformation.

## A.2.2 Coordinates for $\zeta$ in the bent conformation from DFT calculations

O	-5.188737	-3.822481	8.916236
C	-4.266471	-3.714672	8.127335
N	-3.764802	-4.875444	7.483490
C	-2.735846	-4.870108	6.582933
H	-2.425860	-5.814143	6.150277
C	-2.137908	-3.691618	6.283641
O	-1.056856	-3.637025	5.423110
C	-0.711337	-2.393927	4.926363
C	0.151494	-2.344974	3.839049
H	0.482470	-3.278134	3.393671
C	0.568038	-1.101970	3.362006
C	1.497357	-0.822270	2.200872
O	2.174243	1.355466	1.386896
N	1.490810	0.669129	2.214072
C	0.687347	1.306931	3.296735
C	0.120654	0.074537	3.968564
C	-0.749147	0.024591	5.056703
H	-1.107633	0.934119	5.532985
C	-1.167161	-1.214588	5.545199
N	-2.040541	-1.331185	6.636733
C	-2.657537	-2.518598	6.934482
N	-3.647848	-2.522819	7.789774
C	0.959404	-1.319457	0.847170
H	-0.074202	-0.994365	0.693279
H	0.990545	-2.413375	0.797584
H	1.577501	-0.912784	0.041070
C	2.933790	-1.327954	2.429286
H	3.311606	-1.008938	3.405652
H	3.587939	-0.922279	1.651647
H	2.968664	-2.421871	2.385013
C	-0.383585	2.213754	2.664328
H	-1.075730	1.632026	2.047686
H	0.104743	2.960849	2.031439
H	-0.959520	2.731583	3.439191
C	1.619534	2.127304	4.207538
H	2.364146	1.484736	4.687555
H	1.045043	2.635921	4.989374
H	2.141298	2.879186	3.607894
H	-4.226475	-5.739463	7.735239
H	-2.451977	-0.502876	7.0490

## A.3 Matlab script for PELDOR simulation program and user interface

### A.3.1 User interface

```
function varargout = peldorsim(varargin)
% peldorsim MATLAB code for peldorsim.fig
%   peldorsim, by itself, creates a new peldorsim or raises the
existing
%   singleton*.
%
%   H = peldorsim returns the handle to a new peldorsim or the
handle to
%   the existing singleton*.
%
%   peldorsim('CALLBACK',hObject,eventData,handles,...) calls the
local
%   function named CALLBACK in peldorsim.M with the given input
arguments.
%
%   peldorsim('Property','Value',...) creates a new peldorsim or
raises the
%   existing singleton*. Starting from the left, property value
pairs are
%   applied to the GUI before peldorsim_OpeningFcn gets called.
An
%   unrecognized property name or invalid value makes property
application
%   stop. All inputs are passed to peldorsim_OpeningFcn via
varargin.
%
%   *See GUI Options on GUIDE's Tools menu. Choose "GUI allows
only one
%   instance to run (singleton)".
%
% See also: GUIDE, GUIDATA, GUIHANDLES

% Edit the above text to modify the response to help peldorsim

% Last Modified by GUIDE v2.5 17-Sep-2012 10:52:30

%Assign variables to the base workspace

% Begin initialization code - DO NOT EDIT
gui_Singleton = 1;
gui_State = struct('gui_Name',       mfilename, ...
                  'gui_Singleton',  gui_Singleton, ...
                  'gui_OpeningFcn', @peldorsim_OpeningFcn, ...
                  'gui_OutputFcn',  @peldorsim_OutputFcn, ...
                  'gui_LayoutFcn',  [], ...
                  'gui_Callback',   []);
if nargin && ischar(varargin{1})
    gui_State.gui_Callback = str2func(varargin{1});
end

if nargout
    [varargout{1:nargout}] = gui_mainfcn(gui_State, varargin{:});
else
    gui_mainfcn(gui_State, varargin{:});
end
% End initialization code - DO NOT EDIT
```

```

% --- Executes just before peldorsim is made visible.
function peldorsim_OpeningFcn(hObject, eventdata, handles, varargin)
% This function has no output args, see OutputFcn.
% hObject    handle to figure
% eventdata  reserved - to be defined in a future version of MATLAB
% handles    structure with handles and user data (see GUIDATA)
% varargin   command line arguments to peldorsim (see VARARGIN)

% Choose default command line output for peldorsim
handles.output = hObject;

% Update handles structure
guidata(hObject, handles);

% UIWAIT makes peldorsim wait for user response (see UIRESUME)
% uiwait(handles.figure1);

% --- Outputs from this function are returned to the command line.
function varargout = peldorsim_OutputFcn(hObject, eventdata, handles)
% varargout  cell array for returning output args (see VARARGOUT);
% hObject    handle to figure
% eventdata  reserved - to be defined in a future version of MATLAB
% handles    structure with handles and user data (see GUIDATA)

% Get default command line output from handles structure
varargout{1} = handles.output;

% --- Executes on button press in RunSimulation.
function RunSimulation_Callback(hObject, eventdata, handles)
% hObject    handle to RunSimulation (see GCBO)
% eventdata  reserved - to be defined in a future version of MATLAB
% handles    structure with handles and user data (see GUIDATA)

%Check if any of the radiobuttons have been de-selected.
if evalin('base','exist(''runConformers'',''var'')');
else
    runConformers = 1;
    assignin('base','runConformers',runConformers);
end

if evalin('base','exist(''runOrientations'',''var'')');
else
    runOrientations = 1;
    assignin('base','runOrientations',runOrientations);
end

if evalin('base','exist(''runFrequency'',''var'')');
else
    runFrequency = 1;
    assignin('base','runFrequency',runFrequency);
end

if evalin('base','exist(''runExcitation'',''var'')');
else
    runExcitation = 1;
    assignin('base','runExcitation',runExcitation);
end

```

```

end

if evalin('base','exist(''runTimeTraces'',''var''));
else
    runTimeTraces = 1;
    assignin('base','runTimeTraces',runTimeTraces);
end

if evalin('base','exist(''OrientationCorrelation'',''var''));
else
    OrientationCorrelation = 1;
    assignin('base','OrientationCorrelation',OrientationCorrelation);
end
end
%Read the variables in the GUI. This makes sure that if variables
have not
%been changed from the default value the default value gets passed to
the
%simulation program.
n = str2double(get(handles.nRotations,'String'));
    assignin('base','n',n);

m = str2double(get(handles.nDispConformers,'String'));
assignin('base','m',m);

N = str2double(get(handles.nExperiments,'String'));
    assignin('base','N',N);

bandCheck = get(handles.XbandButton,'Value');
if bandCheck == 1;
    B0 = 3496*1e-4;%in Tesla - Xband
    assignin('base','B0',B0);
    minfreq = 9.5928e9;
    maxfreq = 9.9848e9;
    assignin('base','minfreq',minfreq);
    assignin('base','maxfreq',maxfreq);
    assignin('base','band','xband');
end

bandCheck = get(handles.WbandButton,'Value');
if bandCheck == 1;
    B0= 3.34727;%in Tesla - Wband
    assignin('base','B0',B0);
    minfreq = 93.58e9;
    maxfreq = 94.41e9;
    assignin('base','minfreq',minfreq);
    assignin('base','maxfreq',maxfreq);
    assignin('base','band','wband');
end

pumpcentrefreq = get(handles.PumpFreq,'String');
pumpcentrefreq = textscan(pumpcentrefreq,'%s');
pumpcentrefreq = str2double(pumpcentrefreq{1}(1:end,1));
pumpcentrefreq = pumpcentrefreq';
assignin('base','pumpcentrefreq',pumpcentrefreq);

probcentrefreq = get(handles.ProbeFreq,'String');
probcentrefreq = textscan(probcentrefreq,'%s');
probcentrefreq = str2double(probcentrefreq{1}(1:end,1));
probcentrefreq = probcentrefreq';

```



```

assignin('base','probecentrefreq',probecentrefreq);

pumppulselength = get(handles.PumpPulseLength,'String');
pumppulselength = textscan(pumppulselength,'%s');
pumppulselength = str2double(pumppulselength{1}(1:end,1));
pumppulselength = pumppulselength';
assignin('base','pumppulselength',pumppulselength);

firstprobepulselength = get(handles.ProbePiHalfLength,'String');
firstprobepulselength = textscan(firstprobepulselength,'%s');
firstprobepulselength =
str2double(firstprobepulselength{1}(1:end,1));
firstprobepulselength = firstprobepulselength';
assignin('base','firstprobepulselength',firstprobepulselength);

secondprobepulselength = get(handles.ProbePiLength,'String');
secondprobepulselength = textscan(secondprobepulselength,'%s');
secondprobepulselength =
str2double(secondprobepulselength{1}(1:end,1));
secondprobepulselength = secondprobepulselength';
assignin('base','secondprobepulselength',secondprobepulselength);

SimPpath = evalin('base','SimPpath');
SimPname = evalin('base','SimPname');
cd(SimPpath)
eval(SimPname);

% --- Executes on button press in loadFS.
function loadFS_Callback(hObject, eventdata, handles)
% hObject    handle to loadFS (see GCBO)
% eventdata  reserved - to be defined in a future version of MATLAB
% handles    structure with handles and user data (see GUIDATA)

[FSname,FSpath] = uigetfile('*.DTA;*.txt;*.asc;*.dat','Load Field
Sweep data');
    assignin('base','FSname',FSname);
    assignin('base','FSpath',FSpath);
% [xFS,yFS] = eprload([FSpath FSname(1:end-4)]);

% --- Executes on button press in RunConformers.
function RunConformers_Callback(hObject, eventdata, handles)
% hObject    handle to RunConformers (see GCBO)
% eventdata  reserved - to be defined in a future version of MATLAB
% handles    structure with handles and user data (see GUIDATA)

% Hint: get(hObject,'Value') returns toggle state of RunConformers
if get(hObject,'Value')
    runConformers = 1;
else
    runConformers = 0;

```

```

end
assignin('base','runConformers',runConformers);

% --- Executes on button press in RunOrientations.
function RunOrientations_Callback(hObject, eventdata, handles)
% hObject    handle to RunOrientations (see GCBO)
% eventdata  reserved - to be defined in a future version of MATLAB
% handles    structure with handles and user data (see GUIDATA)

% Hint: get(hObject,'Value') returns toggle state of RunOrientations
if get(hObject,'Value');
    runOrientations = 1;
else
    runOrientations = 0;
end
assignin('base','runOrientations',runOrientations);

% --- Executes on button press in RunFrequencies.
function RunFrequencies_Callback(hObject, eventdata, handles)
% hObject    handle to RunFrequencies (see GCBO)
% eventdata  reserved - to be defined in a future version of MATLAB
% handles    structure with handles and user data (see GUIDATA)

% Hint: get(hObject,'Value') returns toggle state of RunFrequencies
if get(hObject,'Value');
    runFrequency = 1;
else
    runFrequency = 0;
end
assignin('base','runFrequency',runFrequency);

% --- Executes on button press in RunExcitations.
function RunExcitations_Callback(hObject, eventdata, handles)
% hObject    handle to RunExcitations (see GCBO)
% eventdata  reserved - to be defined in a future version of MATLAB
% handles    structure with handles and user data (see GUIDATA)

% Hint: get(hObject,'Value') returns toggle state of RunExcitations
if get(hObject,'Value');
    runExcitation = 1;
else
    runExcitation = 0;
end
assignin('base','runExcitation',runExcitation);

% --- Executes on button press in RunTimeTraces.
function RunTimeTraces_Callback(hObject, eventdata, handles)
% hObject    handle to RunTimeTraces (see GCBO)
% eventdata  reserved - to be defined in a future version of MATLAB
% handles    structure with handles and user data (see GUIDATA)

% Hint: get(hObject,'Value') returns toggle state of RunTimeTraces
if get(hObject,'Value');
    runTimeTraces = 1;
else
    runTimeTraces = 0;
end
assignin('base','runTimeTraces',runTimeTraces);

% --- Executes on button press in loadDistr.

```

```

function loadDistr_Callback(hObject, eventdata, handles)
% hObject    handle to loadDistr (see GCBO)
% eventdata  reserved - to be defined in a future version of MATLAB
% handles    structure with handles and user data (see GUIDATA)
[DistrName,DistrPath] = uigetfile('*.DTA;*.txt;*.asc;*.dat','Load
experimental distance distribution');
    assignin('base','DistrName',DistrName);
    assignin('base','DistrPath',DistrPath);
% [xDistr,yDistr] = deerload([DistrPath DistrName(1:end-4)]);

% --- Executes on button press in loadPELDOR.
function loadPELDOR_Callback(hObject, eventdata, handles)
% hObject    handle to loadPELDOR (see GCBO)
% eventdata  reserved - to be defined in a future version of MATLAB
% handles    structure with handles and user data (see GUIDATA)
[PTTname,PTTpath] =
uigetfile('*.DTA;*.txt;*.asc;*.dat','MultiSelect','on','Load PELDOR
time traces');
assignin('base','PTTname',PTTname);
    assignin('base','PTTpath',PTTpath);
% [xPTT,yPTT] = deerload([PTTpath PTTname(1:end-4)]);

% --- Executes on button press in loadSimulationProgram.
function loadSimulationProgram_Callback(hObject, eventdata, handles)
[SimPname,SimPpath] = uigetfile('*.m','MultiSelect','on','Load
Simulation Program');
assignin('base','SimPname',SimPname(1:end-2));
    assignin('base','SimPpath',SimPpath);

function nExperiments_Callback(hObject, eventdata, handles)
% hObject    handle to nExperiments (see GCBO)
% eventdata  reserved - to be defined in a future version of MATLAB
% handles    structure with handles and user data (see GUIDATA)

% Hints: get(hObject,'String') returns contents of nExperiments as
text
%         str2double(get(hObject,'String')) returns contents of
nExperiments as a double
    N = str2double(get(hObject,'String'));% returns contents of
nRotations as a double
    assignin('base','N',N);

% --- Executes during object creation, after setting all properties.
function nExperiments_CreateFcn(hObject, eventdata, handles)
% hObject    handle to nExperiments (see GCBO)
% eventdata  reserved - to be defined in a future version of MATLAB
% handles    empty - handles not created until after all CreateFcns
called

% Hint: edit controls usually have a white background on Windows.
%         See ISPC and COMPUTER.
if ispc && isequal(get(hObject,'BackgroundColor'),
get(0,'defaultUicontrolBackgroundColor'))
    set(hObject,'BackgroundColor','white');
end

```

```

function nRotations_Callback(hObject, eventdata, handles)
% hObject    handle to nRotations (see GCBO)
% eventdata  reserved - to be defined in a future version of MATLAB
% handles    structure with handles and user data (see GUIDATA)

% Hints: get(hObject,'String') returns contents of nRotations as tex
      n = str2double(get(hObject,'String'));% returns contents of
nRotations as a double
assignin('base','n',n);

% --- Executes during object creation, after setting all properties.
function nRotations_CreateFcn(hObject, eventdata, handles)
% hObject    handle to nRotations (see GCBO)
% eventdata  reserved - to be defined in a future version of MATLAB
% handles    empty - handles not created until after all CreateFcns
called

% Hint: edit controls usually have a white background on Windows.
%       See ISPC and COMPUTER.
if ispc && isequal(get(hObject,'BackgroundColor'),
get(0,'defaultUicontrolBackgroundColor'))
    set(hObject,'BackgroundColor','white');
end

function nDispConformers_Callback(hObject2, eventdata, handles)
% hObject    handle to nDispConformers (see GCBO)
% eventdata  reserved - to be defined in a future version of MATLAB
% handles    structure with handles and user data (see GUIDATA)

% Hints: get(hObject,'String') returns contents of nDispConformers as
text
%       str2double(get(hObject,'String')) returns contents of
nDispConformers as a double
      m = str2double(get(hObject2,'String'));% returns contents of
nRotations as a double
assignin('base','m',m);

%Set default values.

function XbandButton_Callback(XbandhObject, eventdata, handles)
if get(XbandhObject,'Value');
set(handles.WbandButton,'Value',0);
B0 = 3496*1e-4;%in Tesla - Xband
assignin('base','B0',B0);
minfreq = 9.5928e9;
maxfreq = 9.9848e9;
assignin('base','minfreq',minfreq);
assignin('base','maxfreq',maxfreq);
set(handles.PumpFreq,'String','9.822 9.822 9.822 9.822 9.822 9.822');
set(handles.ProbeFreq,'String','0.04 0.05 0.06 0.07 0.08 0.09');
set(handles.PumpPulseLength,'String','16 16 16 16 16 16');
set(handles.ProbePiHalfLength,'String','16 16 16 16 16 16');
set(handles.ProbePiLength,'String','32 32 32 32 32 32');
assignin('base','band','xband');
end

```

```

function WbandButton_Callback(WbandhObject, eventdata, handles)
if get(WbandhObject,'Value');
set(handles.XbandButton,'Value',0);
B0 = 3.34727;%in Tesla - Wband
assignin('base','B0',B0);
minfreq = 93.58e9;
maxfreq = 94.41e9;
assignin('base','minfreq',minfreq);
assignin('base','maxfreq',maxfreq);
set(handles.PumpFreq,'String','94.08 94.02 93.975 94.035 94.035
93.94');
set(handles.ProbeFreq,'String','0.0696 0.0696 -0.1008 0.1116 -0.1008
0.21');
set(handles.PumpPulseLength,'String','12 12 12 12 12 12');
set(handles.ProbePiHalfLength,'String','7 7 7 7 7 7');
set(handles.ProbePiLength,'String','14 14 14 14 14 14');
assignin('base','band','wband');
end

```

```

function PumpFreq_Callback(PumpFreqhObject, eventdata, handles)
pumpcentrefreq = get(PumpFreqhObject,'String');
pumpcentrefreq = textscan(pumpcentrefreq,'%s');
pumpcentrefreq = str2double(pumpcentrefreq{1}(1:end,1));
pumpcentrefreq = pumpcentrefreq';
assignin('base','pumpcentrefreq',pumpcentrefreq);

```

```

function PumpFreq_CreateFcn(hObject, eventdata, handles)

```

```

% Hint: edit controls usually have a white background on Windows.
%       See ISPC and COMPUTER.
if ispc && isequal(get(hObject,'BackgroundColor'),
get(0,'defaultUicontrolBackgroundColor'))
    set(hObject,'BackgroundColor','white');
end

```

```

function ProbeFreq_Callback(hObject, eventdata, handles)
probecentrefreq = get(hObject,'String');
probecentrefreq = textscan(probecentrefreq,'%s');
probecentrefreq = str2double(probecentrefreq{1}(1:end,1));
probecentrefreq = probecentrefreq';
assignin('base','probecentrefreq',probecentrefreq);

```

```

function ProbeFreq_CreateFcn(hObject, eventdata, handles)

```

```

% Hint: edit controls usually have a white background on Windows.
%       See ISPC and COMPUTER.
if ispc && isequal(get(hObject,'BackgroundColor'),
get(0,'defaultUicontrolBackgroundColor'))
    set(hObject,'BackgroundColor','white');
end

```

```

function ProbePiLength_Callback(hObject, eventdata, handles)
secondprobepulselength = get(hObject,'String');

```

```

secondprobepulselength = textscan(secondprobepulselength,'%s');
secondprobepulselength =
str2double(secondprobepulselength{1}(1:end,1));
secondprobepulselength = secondprobepulselength';
assignin('base','secondprobepulselength',secondprobepulselength);

```

```

function ProbePiLength_CreateFcn(hObject, eventdata, handles)

```

```

% Hint: edit controls usually have a white background on Windows.
%       See ISPC and COMPUTER.
if ispc && isequal(get(hObject,'BackgroundColor'),
get(0,'defaultUiControlBackgroundColor'))
    set(hObject,'BackgroundColor','white');
end

```

```

function PumpPulseLength_Callback(hObject, eventdata, handles)
pumppulselength = get(hObject,'String');
pumppulselength = textscan(pumppulselength,'%s');
pumppulselength = str2double(pumppulselength{1}(1:end,1));
pumppulselength = pumppulselength';
assignin('base','pumppulselength',pumppulselength);

```

```

function PumpPulseLength_CreateFcn(hObject, eventdata, handles)

```

```

% Hint: edit controls usually have a white background on Windows.
%       See ISPC and COMPUTER.
if ispc && isequal(get(hObject,'BackgroundColor'),
get(0,'defaultUiControlBackgroundColor'))
    set(hObject,'BackgroundColor','white');
end

```

```

function ProbePiHalfLength_Callback(hObject, eventdata, handles)
firstprobepulselength = get(hObject,'String');
firstprobepulselength = textscan(firstprobepulselength,'%s');
firstprobepulselength =
str2double(firstprobepulselength{1}(1:end,1));
firstprobepulselength = firstprobepulselength';
assignin('base','firstprobepulselength',firstprobepulselength);

```

```

function ProbePiHalfLength_CreateFcn(hObject, eventdata, handles)

```

```

% Hint: edit controls usually have a white background on Windows.
%       See ISPC and COMPUTER.
if ispc && isequal(get(hObject,'BackgroundColor'),
get(0,'defaultUiControlBackgroundColor'))
    set(hObject,'BackgroundColor','white');
end

```

```

%Send variables to the base workspace.

```

```

function saveGUIVariables_Callback(hObject, eventdata, handles)
[GUIVarName,GUIVarPath] = uiputfile('*.fig','Save setup variables');
hgsave([GUIVarPath GUIVarName]);%Save the current GUI window

```

```

if evalin('base','exist('FSname','var')));
    FSname = evalin('base','FSname');

```

```

        Fspath = evalin('base','Fspath');
        save([GUIVarPath GUIVarName(1:end-4) 'expFS'],'FSname','Fspath');
    end
    if evalin('base','exist(''DistrName'', 'var''));
        DistrName = evalin('base','DistrName');
        DistrPath = evalin('base','DistrPath');
        save([GUIVarPath GUIVarName(1:end-4)
'expDistr'],'DistrName','DistrPath');
    end
    if evalin('base','exist(''PTTname'', 'var''));
        PTTname = evalin('base','PTTname');
        PTTpath = evalin('base','PTTpath');
        save([GUIVarPath GUIVarName(1:end-4)
'expTimeTrace'],'PTTname','PTTpath');
    end

    if evalin('base','exist(''SimPname'', 'var''));
        SimPname = evalin('base','SimPname');
        SimPpath = evalin('base','SimPpath');
        save([GUIVarPath GUIVarName(1:end-4)
'SimProgram'],'SimPname','SimPpath');
    end
end

```

```
function saveGUIVariables_CreateFcn(hObject, eventdata, handles)
```

```

function LoadGUIVariables_Callback(hObject, eventdata, handles)
[GUIVarName,GUIVarPath] = uigetfile('*.fig','Load setup variables');
    close(gcf)%close the current GUI window
    hgload([GUIVarPath GUIVarName]);%Load the saved GUI window
    expFSCheck = exist([GUIVarPath GUIVarName(1:end-4) 'expFS' '.mat']);
    if expFSCheck == 2
        load([GUIVarPath GUIVarName(1:end-4) 'expFS'])
        assignin('base','FSname',FSname);
        assignin('base','Fspath',Fspath);
    end
    expDistrCheck = exist([GUIVarPath GUIVarName(1:end-4) 'expDistr'
'.mat']);
    if expDistrCheck == 2
        load([GUIVarPath GUIVarName(1:end-4) 'expDistr'])
        assignin('base','DistrName',DistrName);
        assignin('base','DistrPath',DistrPath);
    end
    expTimeTraceCheck = exist([GUIVarPath GUIVarName(1:end-4)
'expTimeTrace' '.mat']);
    if expTimeTraceCheck == 2
        load([GUIVarPath GUIVarName(1:end-4) 'expTimeTrace'])
        assignin('base','PTTname',PTTname);
        assignin('base','PTTpath',PTTpath);
    end

    SimProgramCheck = exist([GUIVarPath GUIVarName(1:end-4) 'SimProgram'
'.mat']);
    if SimProgramCheck == 2
        load([GUIVarPath GUIVarName(1:end-4) 'SimProgram'])
        assignin('base','SimPname',SimPname);
        assignin('base','SimPpath',SimPpath);
    end
end

```

```

function LoadGUIVariables_CreateFcn(hObject, eventdata, handles)

function LoadGUIVariables_DeleteFcn(hObject, eventdata, handles)

function ClearAllVariables_Callback(hObject, eventdata, handles)
evalin('base','clear variables');

function CloseAllWindows_Callback(hObject, eventdata, handles)
evalin('base','close all');

function EditModel_Callback(hObject, eventdata, handles)
EditModel

function Author_CreateFcn(hObject, eventdata, handles)

function text11_CreateFcn(hObject, eventdata, handles)

function OrientationCorrelation_CreateFcn(hObject, eventdata,
handles)

% --- Executes on button press in OrientationCorrelation.
function OrientationCorrelation_Callback(hObject, eventdata, handles)
% hObject      handle to RunExcitations (see GCBO)
% eventdata    reserved - to be defined in a future version of MATLAB
% handles      structure with handles and user data (see GUIDATA)

% Hint: get(hObject,'Value') returns toggle state of
OrientationCorrelation
if get(hObject,'Value');
    OrientationCorrelation = 1;
else
    OrientationCorrelation = 0;
end
assignin('base','OrientationCorrelation',OrientationCorrelation);

```



### A.3.2 Simulation program

%-----This m-file contains the actual simulation program that is loaded via the user interface-----

```
function [] = PsimP1()

wait = waitbar(0,'Calculating conformers');%Open the progress bar
window.

%Read variables from the user interface (UI) and copy them to the
base work
%space.
n = evalin('base','n');%Numner of conformers
m = evalin('base','m');%Number of conformers for graphics
N = evalin('base','N');%Number of experiments
B0 = evalin('base','B0');%Field
runConformers = evalin('base','runConformers');
runOrientations = evalin('base','runOrientations');
runFrequency = evalin('base','runFrequency');
runExcitation = evalin('base','runExcitation');
runTimeTraces = evalin('base','runTimeTraces');
OrientationCorrelation = evalin('base','OrientationCorrelation');
%get model variables from the base workspace that were put there by
the
%Edit model GUI. If the variables were not changed in the GUI use the
%default values.
if evalin('base','exist(''molecularLength'',''var'')');
molecularLength = evalin('base','molecularLength');
else
    molecularLength = 14;
end

if evalin('base','exist(''AspinLabelLength'',''var'')');
    AspinLabelLength = evalin('base','AspinLabelLength');
else
    AspinLabelLength = 4;
end

if evalin('base','exist(''BspinLabelLength'',''var'')');
BspinLabelLength = evalin('base','BspinLabelLength');
else
    BspinLabelLength = 4;
end

if evalin('base','exist(''AxzCorrelationMean'',''var'')');
AxzCorrelationMean = evalin('base','AxzCorrelationMean');
else
    AxzCorrelationMean = 0;
end

if evalin('base','exist(''AxzCorrelationStd'',''var'')');
AxzCorrelationStd = evalin('base','AxzCorrelationStd');
else
    AxzCorrelationStd = 1e-9;
end

if evalin('base','exist(''BxzCorrelationMean'',''var'')');
BxzCorrelationMean = evalin('base','BxzCorrelationMean');
else
    BxzCorrelationMean = 0;
```

```

end

if evalin('base','exist(''BxzCorrelationStd'',''var''));
BxzCorrelationStd = evalin('base','BxzCorrelationStd');
else
    BxzCorrelationStd = 1e-9;
end

if evalin('base','exist(''AxyCorrelationMean'',''var''));
AxyCorrelationMean = evalin('base','AxyCorrelationMean');
else
    AxyCorrelationMean = 0;
end

if evalin('base','exist(''AxyCorrelationStd'',''var''));
AxyCorrelationStd = evalin('base','AxyCorrelationStd');
else
    AxyCorrelationStd = 1e-9;
end

if evalin('base','exist(''BxyCorrelationMean'',''var''));
BxyCorrelationMean = evalin('base','BxyCorrelationMean');
else
    BxyCorrelationMean = 0;
end

if evalin('base','exist(''BxyCorrelationStd'',''var''));
BxyCorrelationStd = evalin('base','BxyCorrelationStd');
else
    BxyCorrelationStd = 1e-9;
end

if evalin('base','exist(''AyzCorrelationMean'',''var''));
AyzCorrelationMean = evalin('base','AyzCorrelationMean');
else
    AyzCorrelationMean = 0;
end

if evalin('base','exist(''AyzCorrelationStd'',''var''));
AyzCorrelationStd = evalin('base','AyzCorrelationStd');
else
    AyzCorrelationStd = 1e-9;
end

if evalin('base','exist(''ByzCorrelationMean'',''var''));
ByzCorrelationMean = evalin('base','ByzCorrelationMean');
else
    ByzCorrelationMean = 0;
end

if evalin('base','exist(''ByzCorrelationStd'',''var''));
ByzCorrelationStd = evalin('base','ByzCorrelationStd');
else
    ByzCorrelationStd = 1e-9;
end

if evalin('base','exist(''molecularLengthMean'',''var''));
molecularLengthMean = evalin('base','molecularLengthMean');
else
    molecularLengthMean = 12;
end

```

```

if evalin('base','exist(''molecularLengthStd'',''var''));
molecularLengthStd = evalin('base','molecularLengthStd');
else
    molecularLengthStd = 1e-9;
end

if evalin('base','exist(''AspinLabelLengthMean'',''var''));
AspinLabelLengthMean = evalin('base','AspinLabelLengthMean');
else
    AspinLabelLengthMean = 4;
end

if evalin('base','exist(''AspinLabelLengthStd'',''var''));
AspinLabelLengthStd = evalin('base','AspinLabelLengthStd');
else
    AspinLabelLengthStd = 1e-9;
end

if evalin('base','exist(''BspinLabelLengthMean'',''var''));
BspinLabelLengthMean = evalin('base','BspinLabelLengthMean');
else
    BspinLabelLengthMean = 4;
end

if evalin('base','exist(''BspinLabelLengthStd'',''var''));
BspinLabelLengthStd = evalin('base','BspinLabelLengthStd');
else
    BspinLabelLengthStd = 1e-9;
end

band = evalin('base','band');
if strcmp(band,'wband')
    experiments = [{'XX'},{'YY'},{'ZZ'},{'YX'},{'YZ'},{'ZX'}];
else
    experiments = [{'40 MHz'},{'50 MHz'},{'60 MHz'},{'70 MHz'},{'80
MHz'},{'90 MHz'}];
end

clc%clears the command window

tic%start the timer

%define constants used later
bohrmagneton = 9.274e-24;
hbar = 1.05457e-34;
mu0 = 4*pi*1e-7;%Permeability of vacuum
g = 2.0023193043718;%the free electron g factor

%Create n conformers with random orientations of spin labels, defined
%through angles. The orientation of spin labels is relative to a
{x,y,z}
%frame that is collinear to the g-matrix frame. The orientation of
the
%biradical (i.e. the interspin vector is defined in a {X,Y,Z} frame.
The
%interspin distance vector starts out to be parallel to the Z-axis.

if OrientationCorrelation==1%Checks if orientation correlation box in

```

```

UI was ticked, then no biradical conformers are created.
if runConformers==1%Checks if the runConformers box in the UI was
ticked

moleculebendAngle = 0*pi/180+(1e-9*pi/180/2).*randn(n,1);

AxzCorrelation =
AxzCorrelationMean*pi/180+(AxzCorrelationStd*pi/180).*randn(n,1);%def
ines the distribution of rotation of spin label A around the y-axis
BxzCorrelation =
BxzCorrelationMean*pi/180+(BxzCorrelationStd*pi/180).*randn(n,1);%sam
e for spin label B
AyzCorrelation =
AyzCorrelationMean*pi/180+(AyzCorrelationStd*pi/180).*randn(n,1);%def
ines the distribution of rotation of spin label A around the x-axis
ByzCorrelation =
ByzCorrelationMean*pi/180+(ByzCorrelationStd*pi/180).*randn(n,1);%the
same for spin label B
AxyCorrelation =
AxyCorrelationMean*pi/180+(AxyCorrelationStd*pi/180).*randn(n,1);%def
ines the angle that the spin label A is rotated about its z-axis,...
%that is the axis that is normal to the plane of the spin label.
BxyCorrelation =
BxyCorrelationMean*pi/180+(BxyCorrelationStd*pi/180).*randn(n,1);%sam
e as above but for spin label B

randomRotation = 1*pi*2*rand(n,1);%This applies equal random rotation
to both spin labels around the Z-axis (interspin vector).
%This equals rotation of the molecule around its Z-axis.

AspinLabelLength = AspinLabelLengthMean +
AspinLabelLengthStd.*randn(n,1);%Length of A spin label in angstrom.
BspinLabelLength = BspinLabelLengthMean +
BspinLabelLengthStd.*randn(n,1);%Length of B spin label in angstrom.

molecularLength = molecularLengthMean +
molecularLengthStd.*randn(n,1);%Length of molecular linker in
angstrom.

%Calculate the coordiantes of the point where the spin labels are
joined to the molecular linker. This is calculated from lengths of
spin labels and molecular linker an bending angles.
spinAstartPosition = zeros(n,3);
spinBstartPosition = zeros(n,3);
for c = 1:n;
spinAstartPosition(c,:) =
[cos(moleculebendAngle(c,1))*(molecularLength(c,1)/2+AspinLabelLength
(c,1)) 0
sin(moleculebendAngle(c,1))*(molecularLength(c,1)/2+AspinLabelLength(
c,1))];
spinBstartPosition(c,:) = [-
cos(moleculebendAngle(c,1))*(molecularLength(c,1)/2+BspinLabelLength(
c,1)) 0
sin(moleculebendAngle(c,1))*(molecularLength(c,1)/2+BspinLabelLength(
c,1))];
end

%Becuse the spin label are represented as vectors
%pointing along the Z-axis.Including rotation of the label around the
Z-axis will not be

```

```

%visible in the graphics. Instead the rotation of the label around
the
%Z-axis (the twist) is introduced in later in the "Orientations" part.

%subtracting (spinAstartPosition-[spinLabelLength 0 0] and then
adding
%this again to spinAstartPosition is done to observe correct
%positioning of the spin centre, and correspondingly the correct
%interspin vector.

spinlabelApositions = zeros(n,3);
for c=1:n;

spinlabelApositions(c,:)=RotateAboutZaxis(AxyCorrelation(c,1))*Rotate
AboutYaxis(AxzCorrelation(c,1))*(spinAstartPosition(c,:)-
[cos(moleculebendAngle(c,1))*(molecularLength(c,1)/2) 0
sin(moleculebendAngle(c,1))*(molecularLength(c,1)/2)]');

spinlabelApositions(c,:)=spinlabelApositions(c,:)+[cos(moleculebendAn
gle(c,1))*(molecularLength(c,1)/2) 0
sin(moleculebendAngle(c,1))*(molecularLength(c,1)/2)];
end

%Calculate the orientation of the spin centre of spin label A for
each
%conformer. The initial structure has the the gz aligned with the
magnetic
%field. This orientation is defined as [0 0 1].The orientation of the
A spin g-matrix is then affected
%by the bending and twisting of the spin label.
spinAorientation = zeros(n,3);
for c=1:n;
    spinAorientation(c,:) =
RotateAboutYaxis(AxzCorrelation(c,1))*RotateAboutYaxis(-
moleculebendAngle(c,1))*[0 0 1]';
end

%-----Define the relative orientation of spin label B for each
conformer-----

%Rotate the B spin label about the molecular Y-axis.
spinlabelBpositions = zeros(n,3);
for c=1:n;

spinlabelBpositions(c,:)=RotateAboutZaxis(BxyCorrelation(c,1))*Rotate
AboutYaxis(BxzCorrelation(c,1))*(spinBstartPosition(c,:)-[
cos(moleculebendAngle(c,1))*(molecularLength(c,1)/2) 0
sin(moleculebendAngle(c,1))*(molecularLength(c,1)/2)]');
    spinlabelBpositions(c,:)=spinlabelBpositions(c,:)+[
cos(moleculebendAngle(c,1))*(molecularLength(c,1)/2) 0
sin(moleculebendAngle(c,1))*(molecularLength(c,1)/2)];
end

%Calculate the orientation of the spin centre of spin label B for
each
%conformer.
spinBorientation = zeros(n,3);

```

```

for c=1:n;
    spinBorientation(c,:) =
RotateAboutYaxis(BxzCorrelation(c,1))*RotateAboutYaxis(moleculebendAn
gle(c,1))*[0 0 1]';
end

%Calculate the interspin distance for each conformer
explicitdistanceAB = zeros(n,1);
explicitdistanceAB(:,1) = sqrt((spinlabelApositions(:,1)-
spinlabelBpositions(:,1)).^2+(spinlabelApositions(:,2)-
spinlabelBpositions(:,2)).^2+(spinlabelApositions(:,3)-
spinlabelBpositions(:,3)).^2);

%Calculate and display statistics
explicitdistanceStd=std(explicitdistanceAB);
explicitdistanceMean=mean(explicitdistanceAB);
disp(['Mean distance = ' num2str(explicitdistanceMean)])
disp(['Distance Std = ' num2str(explicitdistanceStd)])

%Calculate the projection of the interspin vector on the laboratory
frame
%(The frame that has the magnetic field pointing along the Z-axis).

rabprojection = zeros(n,3);
for c=1:n;
    rabprojection(c,:) = (spinlabelApositions(c,:)-
spinlabelBpositions(c,:))/norm(spinlabelApositions(c,:)-
spinlabelBpositions(c,:));
end

waitbar(1/6,wait,'Conformers calculated')
%plot the vectors representing the molecule and spin labels. The
sphere
%represents the laboratory frame.
if evalin('base','ishandle(1)')==1
close 1%If figure 1 was already created, close and and create a new
one.
end
figure(1)
subplot(2,2,1)
[X,Y,Z] = sphere;

dimension = (max(molecularLength)/2+max(AspinLabelLength))+0.5;%This
sets the dimension of the graphics box
axis([-dimension dimension -dimension dimension -dimension
dimension])%define the axis limits of the graphics
for c = 1:m;
line([0 -molecularLength(c,1)/2*cos(moleculebendAngle(c,1))],[0 0],[0
sin(moleculebendAngle(c,1))*molecularLength(c,1)/2]);
line([0 molecularLength(c,1)/2*cos(moleculebendAngle(c,1))],[0 0],[0
sin(moleculebendAngle(c,1))*molecularLength(c,1)/2]);
end
axis square
xlabel('X','FontSize',12)
ylabel('Y','FontSize',12)
zlabel('Z','FontSize',12)
title({'Molecular','Conformers'],'FontWeight','bold','FontSize',12)
set(gca,'Xtick',[])

```

```

set(gca,'Ytick',[])
set(gca,'Ztick',[])
box on

% Draw the spin labels and the interspin vectors
for c=1:m;
line([cos(moleculebendAngle(c,1))*(molecularLength(c,1)/2)
spinlabelApositions(c,1)],[0
spinlabelApositions(c,2)],[sin(moleculebendAngle(c,1))*(molecularLength(c,1)/2)
spinlabelApositions(c,3)],'color','red','LineWidth',2);%spin label A
line([-cos(moleculebendAngle(c,1))*(molecularLength(c,1)/2)
spinlabelBpositions(c,1)],[0
spinlabelBpositions(c,2)],[sin(moleculebendAngle(c,1))*(molecularLength(c,1)/2)
spinlabelBpositions(c,3)],'color','green','LineWidth',2);%spin label B
end

%If experimental distance distribution was loaded then import the
data and
%plot.
if evalin('base','exist('DistrName','var')));
DistrName = evalin('base','DistrName');
DistrPath = evalin('base','DistrPath');
[x3,y3] = deerload([DistrPath DistrName(1:end-4)]);%It is assumed
that the distance distribution is a file from DeerAnalysis.
end
%bin the calculated distances for all conformers
distance = (min(explicitdistanceAB)-
min(implicitdistanceAB)*0.1:0.08:max(implicitdistanceAB) +
max(implicitdistanceAB)*0.1);
[hits,~] = histc(implicitdistanceAB,distance);
hits = hits/max(hits);

figure(1)
subplot(2,2,2)
x3Check = exist('x3','var');
if x3Check == 1
plot_h = plot(distance,hits,'r',x3*10,y3/max(y3),'b');
else
plot_h = plot(distance,hits,'r');
end

set(plot_h,'LineWidth',2);
title({'Distance','Distribution'],'FontWeight','bold','FontSize',12)
xlabel(['Distance [',char(197),']'],'FontSize',12)
ylabel('Probability','FontSize',12)
xlim([min(distance) max(distance)])
ylim([0 1.1])
set(gca,'FontSize',12);

%If these variables have not been defined then save them to the base
%workspace

assignin('base','spinAorientation',spinAorientation);
assignin('base','spinBorientation',spinBorientation);
assignin('base','rabprojection',rabprojection);
assignin('base','AxyCorrelation',AxyCorrelation);
assignin('base','BxyCorrelation',BxyCorrelation);
assignin('base','AyzCorrelation',AyzCorrelation);
assignin('base','ByzCorrelation',ByzCorrelation);

```

```

assignin('base','randomRotation',randomRotation);
assignin('base','explicitdistanceAB',explicitdistanceAB);

%If these variables have been defined then read them from the
workspace
else
    spinAorientation = evalin('base','spinAorientation');
    spinBorientation = evalin('base','spinBorientation');
    rabprojection = evalin('base','rabprojection');
    AxyCorrelation = evalin('base','AxyCorrelation');
    BxyCorrelation = evalin('base','BxyCorrelation');
    AyzCorrelation = evalin('base','AyzCorrelation');
    ByzCorrelation = evalin('base','ByzCorrelation');
    randomRotation = evalin('base','randomRotation');
    explicitdistanceAB = evalin('base','explicitdistanceAB');

end
end

if OrientationCorrelation==0%If the orientation correlation tickbox
is not ticked then do the following;
    if evalin('base','exist(''DistrName',''var'')');%If a distance
distribution was loaded
        DistrName = evalin('base','DistrName');
        DistrPath = evalin('base','DistrPath');
        x3 = mtsslWizardLoad([DistrPath DistrName(1:end-4)]);%Function that
reads the data from a distance distribution file from MTSSL Wizard
program.
        n = length(x3);
        assignin('base','n',n);
        explicitdistanceAB = x3;%Copies the loaded distance vector into the
explicitdistanceAB variable
        distance = (min(explicitdistanceAB)-
min(explicitdistanceAB)*0.1:0.08:max(explicitdistanceAB) +
max(explicitdistanceAB)*0.1);
        [hits,~] = histc(explicitdistanceAB,distance);
        hits = hits/max(hits);

    else
        %Define a Gaussian distance distribution if no distribution
was
        %imported.
        x3 = 25 + 0.5.*randn(n,1);%This can be changed
        explicitdistanceAB = x3;%Copies the gaussian distance
distribution into the explicitdistanceAB variable
        distance = (min(explicitdistanceAB)-
min(explicitdistanceAB)*0.1:0.08:max(explicitdistanceAB) +
max(explicitdistanceAB)*0.1);
        [hits,~] = histc(explicitdistanceAB,distance);
        hits = hits/max(hits);
    end

%plot the imported or Gaussian (created above) distance distribution
figure(1)
subplot(2,2,2)
plot_h = plot(distance,hits,'r');
set(plot_h,'LineWidth',2);
title({'Distance','Distribution'},'FontWeight','bold','FontSize',12)

```



```

xlabel(['Distance [',char(197),']'],'FontSize',12)
ylabel('Probability','FontSize',12)
xlim([min(distance) max(distance)])
ylim([0 1.1])
set(gca,'FontSize',12);

%Calculate and display statistics
explicitdistanceStd=std(explicitdistanceAB);
explicitdistanceMean=mean(explicitdistanceAB);
disp(['Mean distance = ' num2str(explicitdistanceMean)])
disp(['Distance Std = ' num2str(explicitdistanceStd)])
end

%-----
%
%
% Here the orientation of the interspin distance, for each
conformer
% created above, is given a random orientation relative to the z-
axis.
% The relative orientations of the spin centers are also
calculated.
%
%
%-----

waitbar(1/6,wait,'Calculating the orientations')

if runOrientations == 1

%Create random orientations on the half sphere.
%If the sample is to be orientated (in a crystal) theta and phi can
be
%defined by constants.
theta = (pi/2)*(acos(sign(rand(n,1)).*rand(n,1))/(pi/2));%gives a
random theta, sin weighted
phi=pi*2*rand(n,1);%gives a random phi from 0 to 2pi

randomorientations=ones(n,3);
randomorientations(:,1)=(sin(theta).*cos(phi));
randomorientations(:,2)=(sin(theta).*sin(phi));
randomorientations(:,3)=(cos(theta));

%calculate theta, the angle between the interspin vector and the
magnetic
%field, for each orientation.
rABangles=acos(randomorientations(:,3));
thetaForEachPair = ((pi/2) - abs(rABangles -pi/2));

%Plot the random orientations on the sphere
figure(1)
subplot(2,2,3)
[x,y,z]=sphere;

```

```

s=mesh(x,y,z);
set(s,'EdgeColor','b');
axis equal
hold on
plot3(randomorientations(:,1),randomorientations(:,2),randomorientati
ons(:,3),'r. ');
xlabel('X','FontSize',12)
ylabel('Y','FontSize',12)
zlabel('Z','FontSize',12)
title({'Random orientations','of interspin
vectors'},'FontWeight','bold','FontSize',12)
hold off
%the red dots on the sphere represent the orientation of each
generated interspin vector
%in space. A dot that lies on the pole represents an interspin vector
that
%is parallel with the laboratory Z-axis (The magnetic field). A dot
that lies on the X i.e.
%(1,0,0) represents an interspin vector that is perpendicular to the
%laboratory Z-axis.
%-----

%Create the random orientations for the A and B spin centres relative
to
%the interspin vector.

if OrientationCorrelation==1;%Checks if orientation correlation box
was ticked.
    %If the box was ticked then the orientation of spin centers is
    %calculated by using the random orientation given to the
interspin
    %vector and a rotation matrix. Rotations due to flexibility in
the model
    %is included.
    %If the box was not ticked then the spin centers are given a
random
    %orientation.
AspinOrientations=zeros(n,3);
BspinOrientations=zeros(n,3);
for c=1:n;
    AspinOrientations(c,:) =
RotationMatrix(spinAorientation(c,:),rabprojection(c,:))*RotateAboutX
axis(AxyCorrelation(c,1))*RotateAboutZaxis(AyzCorrelation(c,1))*Rotat
eAboutZaxis(randomRotation(c,1))*randomorientations(c,:);
    BspinOrientations(c,:) =
RotationMatrix(spinBorientation(c,:),rabprojection(c,:))*RotateAboutX
axis(BxyCorrelation(c,1))*RotateAboutZaxis(ByzCorrelation(c,1))*Rotat
eAboutZaxis(randomRotation(c,1))*randomorientations(c,:);
end
else
%If Orientation correlation box was not ticked then do this.
%Random orientation of A spin centres
spinAtheta = (pi/2)*(acos(sign(rand(n,1)).*rand(n,1))/(pi/2));%gives
a random theta sin weighted
spinAphi=pi*2*rand(n,1);%gives a random phi from 0 to 2pi
AspinOrientations(:,1)=(sin(spinAtheta).*cos(spinAphi));
AspinOrientations(:,2)=(sin(spinAtheta).*sin(spinAphi));
AspinOrientations(:,3)=(cos(spinAtheta));
%Random orientation of B spin centres
spinBtheta = (pi/2)*(acos(sign(rand(n,1)).*rand(n,1))/(pi/2));%gives
a random theta sin weighted

```

```

spinBphi=pi*2*rand(n,1);%gives a random phi from 0 to 2pi
BspinOrientations(:,1)=(sin(spinBtheta).*cos(spinBphi));
BspinOrientations(:,2)=(sin(spinBtheta).*sin(spinBphi));
BspinOrientations(:,3)=(cos(spinBtheta));
end

%Convert the AspinOrientations into spherical coordinates,
%[THETA,PHI,R] = cart2sph(X,Y,Z), THETA is the angle in the X-Y plane
and
%PHI is the elevation angle.
sphericalAspinOrientations = zeros(n,3);
[sphericalAspinOrientations(:,1),sphericalAspinOrientations(:,2),sphericalAspinOrientations(:,3)] =
cart2sph(AspinOrientations(:,1),AspinOrientations(:,2),AspinOrientations(:,3));
% Convert the BspinOrientations into spherical coordinates
sphericalBspinOrientations = zeros(n,3);
[sphericalBspinOrientations(:,1),sphericalBspinOrientations(:,2),sphericalBspinOrientations(:,3)] =
cart2sph(BspinOrientations(:,1),BspinOrientations(:,2),BspinOrientations(:,3));

waitbar(3/6,wait,'Orientations calculated')

%Plot the random A and B spin orientations on the sphere
subplot(2,2,4)
[x,y,z]=sphere;
h = mesh(x*0.99,y*0.99,z*0.99);
set(h,'EdgeColor','b');
axis equal
hold on
plot3(AspinOrientations(:,1),AspinOrientations(:,2),AspinOrientations(:,3),'r.','MarkerSize',5)
plot3(BspinOrientations(:,1),BspinOrientations(:,2),BspinOrientations(:,3),'k.','MarkerSize',5)
xlabel('X','FontSize',12)
ylabel('Y','FontSize',12)
zlabel('Z','FontSize',12)
title({'Random orientations','of spin centres'},'FontWeight','bold','FontSize',12)
hold off
%The red nd black dots on the sphere represent the g-matrix components of
%the A and B spin centres, respectively, that point in the direction of the magnetic field. These orientations
%are correlated to the interspin orientations that were created above.
For
%this particular model, and assuming no flexibility of the molecule, the gx of spin centres lie parallel to the interspin
%vector. This means that if the interspin vector is parallel to the magnetic field
%(red dot on the z pole (0,0,1) for the molecular orientation) then the gx components of the spin's g-matrix are
%parallel to the magnetic field (red and black dot on the x (1,0,0).
I am
%also assuming that the g- and A-tensors are collinear.
%In summary, these dots on spheres confirm that we have a
%proper distribution of orientations and that the relative orientation of spin centres is correct. The relative

```

```

%orientations of spin centres and their flexibility can be checked by
generating a
%fixed orientation for the interspin vector.

    assignin('base','AspinOrientations',AspinOrientations);
    assignin('base','BspinOrientations',BspinOrientations);

assignin('base','sphericalAspinOrientations',sphericalAspinOrientatio
ns);

assignin('base','sphericalBspinOrientations',sphericalBspinOrientatio
ns);
    assignin('base','thetaForEachPair',thetaForEachPair);

else
    spinAorientation = evalin('base','spinAorientation');
    spinBorientation = evalin('base','spinBorientation');
    sphericalAspinOrientations =
evalin('base','sphericalAspinOrientations');
    sphericalBspinOrientations =
evalin('base','sphericalBspinOrientations');
    thetaForEachPair = evalin('base','thetaForEachPair');
end

%-----
%
%
% Here the resonance frequencies for the spin centers on each
conformer are computed
%
%
%-----

waitbar(3/6,wait,'Calculating the resonance freq.')

if runFrequency == 1;%Only run this if the Run. res. freq. box was
ticked
minfreq = evalin('base','minfreq');
maxfreq = evalin('base','maxfreq');

%Define g-tensor components
gx = 2.0092;
gy = 2.0068;
gz = 2.0030;
%Define 14N hyperfine tensor components
Ax = 10e6;%in MHz
dAx = 5e6;%one standard deviation
Ay = 10e6;
dAy = 5e6;
Az = 101e6;
dAz = 5e6;
%Define line broadening
inhombroadeningx = 10*10^6;%in MHz
inhombroadeningy = 10*10^6;
inhombroadeningz = 10*10^6;
fxx = gx*bohrmagneton*B0/(hbar*2*pi);
fyy = gy*bohrmagneton*B0/(hbar*2*pi);
fzz = gz*bohrmagneton*B0/(hbar*2*pi);

```

```

dgx = inhombroadeningx/fxx;
dgy = inhombroadeningy/fyy;
dgz = inhombroadeningz/fzz;

%Load the experimental field sweep spectrum
if evalin('base','exist('FSname','var')));
FSname = evalin('base','FSname');
FSpath = evalin('base','FSpath');

band = evalin('base','band');
if strcmp(band,'wband')%Check which band was selected in the UI.
[xFS,yFS] = Hiperload([FSpath FSname(1:end-4)]);%Load the imported W-
band field swept spectrum
%-----
%The field positions from Hiper spectrometer are given as field
offsets.
%These lines of code turn the offsets into approximate field
positions.
microwavefrequency = 93.9996e9;
B = (hbar*2*pi*microwavefrequency)/(2.0073*bohrmagneton);
B = (B*1e4)+14.52;
xFS = (xFS+B) *2.804e6;
%-----
else
[xFS,yFS] = eprload([FSpath FSname(1:end-4)]);%Load the imported
X-band field swept spectrum
xFS = xFS*2.808e6;%Convert the field positions into frequency

end
yFS = basecorr(yFS,1,0);
yFS = yFS - yFS(1);
yFS=yFS/max(yFS);
yFSinv = zeros(length(yFS),1);
yFSinv(1:end,1)=yFS(end:-1:1,1);%Reverse the spectrum so it can be
compared to the simulated EPR spectrum, which is in frequency domain.
[~,maxpos] = max(real(yFSinv));%Find the vector position of the
maximum value in the y vector.
B0 = xFS(maxpos,1)/2.808e10;%Read the frequency position in the x
vector that corresponds to the maximum in the y vector and convert it
into field position in Tesla.
minfreq = xFS(1);
maxfreq = xFS(end);
df = 1e6;%1 Mhz step size
freqWidth = minfreq:df:maxfreq;
else
%Use this is if an experimental field sweep was not imported.
df = 1e6;
freqWidth = minfreq:df:maxfreq;%The minfreq and maxfreq are defined
in the UI script.
end

%Calculate resonance frequencies for the A and B spins.
%The second term in the A and B spin spherical coordinates is the
angle from the x-y
%projection to the position vector. The resonance frequency equations
%needs the second term to be the angle from the z-axis to the
projection of
%the position vector in the x-y plane. That is why the second term is
pi/2-(second term).

```

```

%NB! I am calling the random g and A once for each spin and hyperfine
level in
%order to get unique random numbers for each set of spin centres.

```

```

%A spin for ms = 0

```

```

randomgx = gx+dgx.*randn(n,1);
randomgy = gy+dgy.*randn(n,1);
randomgz = gz+dgz.*randn(n,1);

```

```

AresfreqMsZERO = zeros(n,1);

```

```

AresfreqMsZERO(:,1) = (bohrmagneton*B0)/(hbar*2*pi)*...
    sqrt((randomgx.^2.*cos(sphericalAspinOrientations(:,1)).^2.*...
    sin(pi/2-sphericalAspinOrientations(:,2)).^2) +...
    (randomgy.^2.*sin(sphericalAspinOrientations(:,1)).^2.*...
    sin(pi/2-sphericalAspinOrientations(:,2)).^2) + (randomgz.^2.*...
    cos(pi/2-sphericalAspinOrientations(:,2)).^2));

```

```

randomgx = gx+dgx.*randn(n,1);
randomgy = gy+dgy.*randn(n,1);
randomgz = gz+dgz.*randn(n,1);

```

```

%B spin for ms = 0

```

```

BresfreqMsZERO = zeros(n,1);

```

```

BresfreqMsZERO(:,1) = (bohrmagneton*B0)/(hbar*2*pi)*...
    sqrt((randomgx.^2.*cos(sphericalBspinOrientations(:,1)).^2.*...
    sin(pi/2-sphericalBspinOrientations(:,2)).^2) +...
    (randomgy.^2.*sin(sphericalBspinOrientations(:,1)).^2.*...
    sin(pi/2-sphericalBspinOrientations(:,2)).^2) + (randomgz.^2.*...
    cos(pi/2-sphericalBspinOrientations(:,2)).^2));

```

```

randomgx = gx+dgx.*randn(n,1);
randomgy = gy+dgy.*randn(n,1);
randomgz = gz+dgz.*randn(n,1);
randomAx = Ax+dAx.*randn(n,1);
randomAy = Ay+dAy.*randn(n,1);
randomAz = Az+dAz.*randn(n,1);

```

```

%A spin for ms = 1

```

```

AresfreqMsPLUSONE = zeros(n,1);

```

```

AresfreqMsPLUSONE(:,1) = (bohrmagneton*B0)/(hbar*2*pi)*...
    sqrt((randomgx.^2.*cos(sphericalAspinOrientations(:,1)).^2.*...
    sin(pi/2-sphericalAspinOrientations(:,2)).^2) +...
    (randomgy.^2.*sin(sphericalAspinOrientations(:,1)).^2.*...
    sin(pi/2-sphericalAspinOrientations(:,2)).^2) + (randomgz.^2.*...
    cos(pi/2-sphericalAspinOrientations(:,2)).^2) +
sqrt((randomAx.^2.*...
    cos(sphericalAspinOrientations(:,1)).^2.*...
    sin(pi/2-sphericalAspinOrientations(:,2)).^2) +...
    (randomAy.^2.*...
    sin(sphericalAspinOrientations(:,1)).^2.*...
    sin(pi/2-sphericalAspinOrientations(:,2)).^2) + (randomAz.^2.*...
    cos(pi/2-sphericalAspinOrientations(:,2)).^2));

```

```

randomgx = gx+dgx.*randn(n,1);
randomgy = gy+dgy.*randn(n,1);
randomgz = gz+dgz.*randn(n,1);
randomAx = Ax+dAx.*randn(n,1);
randomAy = Ay+dAy.*randn(n,1);
randomAz = Az+dAz.*randn(n,1);

```

```

%B spin for ms = 1
BresfreqMsPLUSONE = zeros(n,1);
BresfreqMsPLUSONE(:,1) = (bohrmagneton*B0)/(hbar*2*pi)*...
    sqrt((randomgx.^2.*cos(sphericalBspinOrientations(:,1)).^2.*...
    sin(pi/2-sphericalBspinOrientations(:,2)).^2) +...
    (randomgy.^2.*sin(sphericalBspinOrientations(:,1)).^2.*...
    sin(pi/2-sphericalBspinOrientations(:,2)).^2) + (randomgz.^2.*...
    cos(pi/2-sphericalBspinOrientations(:,2)).^2)) +
sqrt((randomAx.^2.*...
    cos(sphericalBspinOrientations(:,1)).^2.*...
    sin(pi/2-sphericalBspinOrientations(:,2)).^2) +...
    (randomAy.^2.*...
    sin(sphericalBspinOrientations(:,1)).^2.*...
    sin(pi/2-sphericalBspinOrientations(:,2)).^2) + (randomAz.^2.*...
    cos(pi/2-sphericalBspinOrientations(:,2)).^2));

randomgx = gx+dgx.*randn(n,1);
randomgy = gy+dgy.*randn(n,1);
randomgz = gz+dgz.*randn(n,1);
randomAx = Ax+dAx.*randn(n,1);
randomAy = Ay+dAy.*randn(n,1);
randomAz = Az+dAz.*randn(n,1);

%A spin for ms = -1
AresfreqMsMINUSONE = zeros(n,1);
AresfreqMsMINUSONE(:,1) = (bohrmagneton*B0)/(hbar*2*pi)*...
    sqrt((randomgx.^2.*cos(sphericalAspinOrientations(:,1)).^2.*...
    sin(pi/2-sphericalAspinOrientations(:,2)).^2) +...
    (randomgy.^2.*sin(sphericalAspinOrientations(:,1)).^2.*...
    sin(pi/2-sphericalAspinOrientations(:,2)).^2) + (randomgz.^2.*...
    cos(pi/2-sphericalAspinOrientations(:,2)).^2)) -
sqrt((randomAx.^2.*...
    cos(sphericalAspinOrientations(:,1)).^2.*...
    sin(pi/2-sphericalAspinOrientations(:,2)).^2) +...
    (randomAy.^2.*...
    sin(sphericalAspinOrientations(:,1)).^2.*...
    sin(pi/2-sphericalAspinOrientations(:,2)).^2) + (randomAz.^2.*...
    cos(pi/2-sphericalAspinOrientations(:,2)).^2));

randomgx = gx+dgx.*randn(n,1);
randomgy = gy+dgy.*randn(n,1);
randomgz = gz+dgz.*randn(n,1);
randomAx = Ax+dAx.*randn(n,1);
randomAy = Ay+dAy.*randn(n,1);
randomAz = Az+dAz.*randn(n,1);

%B spin for ms = -1
BresfreqMsMINUSONE = zeros(n,1);
BresfreqMsMINUSONE(:,1) = (bohrmagneton*B0)/(hbar*2*pi)*...
    sqrt((randomgx.^2.*cos(sphericalBspinOrientations(:,1)).^2.*...
    sin(pi/2-sphericalBspinOrientations(:,2)).^2) +...
    (randomgy.^2.*sin(sphericalBspinOrientations(:,1)).^2.*...
    sin(pi/2-sphericalBspinOrientations(:,2)).^2) + (randomgz.^2.*...
    cos(pi/2-sphericalBspinOrientations(:,2)).^2)) -
sqrt((randomAx.^2.*...
    cos(sphericalBspinOrientations(:,1)).^2.*...
    sin(pi/2-sphericalBspinOrientations(:,2)).^2) +...
    (randomAy.^2.*...
    sin(sphericalBspinOrientations(:,1)).^2.*...
    sin(pi/2-sphericalBspinOrientations(:,2)).^2) + (randomAz.^2.*...
    cos(pi/2-sphericalBspinOrientations(:,2)).^2));

```

```

%Combine the resonance frequencies and orientations for A and B spins
when
%ms = 0
ABresfreqMsZERO = [AresfreqMsZERO;BresfreqMsZERO];
spectrumforMsZERO = histc(ABresfreqMsZERO(:,1),freqWidth);%bin the
frequencies

%Combine the resonance frequencies and orientations for A and B spins
when
%ms = 1
ABresfreqMsPLUSONE = [AresfreqMsPLUSONE;BresfreqMsPLUSONE];
spectrumforMsPLUSONE = histc(ABresfreqMsPLUSONE(:,1),freqWidth);

%Combine the resonance frequencies and orientations for A and B spins
when
%ms = -1
ABresfreqMsMINUSONE = [AresfreqMsMINUSONE;BresfreqMsMINUSONE];
spectrumforMsMINUSONE = histc(ABresfreqMsMINUSONE(:,1),freqWidth);

%Add all the hyperfine level spectra
ABresfreq = [ABresfreqMsMINUSONE; ABresfreqMsZERO;
ABresfreqMsPLUSONE];

%Add all spectra
fullspectrum = spectrumforMsZERO + spectrumforMsPLUSONE +
spectrumforMsMINUSONE;

waitbar(4/6,wait,'Resonance freq. calculated')

if evalin('base','ishandle(2)')==1
close 2%close window 2 if it is already open
end

figure(2)
xFSCheck = exist('xFS','var');
fullspectrum = fullspectrum/max(fullspectrum);
fullspectrum = smooth(fullspectrum,2);

if xFSCheck == 1
plot(xFS,yFSinv,'b', freqWidth,fullspectrum,'r')
else
plot(freqWidth,fullspectrum,'r')
end
axis tight
title('Field swept spectra in frequency domain')

%Make the matrix that pairs up the resonace frequencies for spin A
and B
%for every random orientation of the interspin vector and for each
%hyperfine level. The matrix is a nx6 matrix. The 1-3 columns contain
%resonance frequencies for spin A when the hyperfine level is -1, 0
and +1 respectively. Column 4-6 contain the
%same for spin B.
spinpair = zeros(n,6);
spinpair(:,1:6) = [AresfreqMsMINUSONE(:,1) AresfreqMsZERO(:,1)...
AresfreqMsPLUSONE(:,1) BresfreqMsMINUSONE(:,1)...
BresfreqMsZERO(:,1) BresfreqMsPLUSONE(:,1)];

```



```

assignin('base','fullspectrum',fullspectrum);
assignin('base','spinpair',spinpair);
assignin('base','freqWidth',freqWidth);
else
    fullspectrum = evalin('base','fullspectrum');
    spinpair = evalin('base','spinpair');
    freqWidth = evalin('base','freqWidth');
end

%-----
%
%
%       Here the excitation profile for pulses are calculated. The
contribution to the PELDOR
%       signal from each conformer is also computed using the
resonance
%       frequencies and the excitation profiles.
%
%
%-----
waitbar(4/6,wait,'Calculating excitations')
if evalin('base','ishandle(3)')==1
close 3
end
if runExcitation == 1;%If the Run excitations box in the UI was
ticked then perform the following.

n = evalin('base','n');
pumppulselength = evalin('base','pumppulselength')*1e-9;
pumpcentrefreq = evalin('base','pumpcentrefreq')*1e9;%Frequency of
pump pulse in Hz

%Import parameters for detection sequence (probe pulse). The pulse
lengths and frequency are
%defined in the UI.
firstprobepulselength = evalin('base','firstprobepulselength')*1e-
9;%in seconds
secondprobepulselength = evalin('base','secondprobepulselength')*1e-
9;
probecentrefreq = pumpcentrefreq +
evalin('base','probecentrefreq')*1e9;%Frequency of probe pulse in Hz

signalIntensities = zeros(n,N);
signalIntensityWithoutPumpPulse = zeros(1,N);

for expnr = 1:N

omegaA = (pi/2)/firstprobepulselength(1,expnr);
omega2A = pi/secondprobepulselength(1,expnr);
omegaB = pi/pumppulselength(1,expnr);

gaussdistr = 0.011e12;%one standard deviation for the gaussian
function applied to the pulse profiles.
excAtt = 0.88; %Use this to account for less than 100% inversion of

```

```

experimental pulses. This was determined from experiment. Possibly
varies between spectrometers.
pumpProfile =
excAtt*pumpPulseProfile(length(freqWidth),omegaB,pumpcentrefreq(1,expnr),freqWidth,pumpPulseLength(1,expnr));
pumpProfile =
pumpProfile.*(GGaussian(pumpcentrefreq(1,expnr),gaussdistr,freqWidth)
)';

%Calculate the probe profile to plot
probeProfile =
excAtt*observerPulseProfile(length(freqWidth),omegaA,omega2A,probecentrefreq(1,expnr),freqWidth',firstprobepulseLength(1,expnr),secondprobepulseLength(1,expnr));

%Plot the pulse profiles
figure(3)
if N<4
    subplot(1,N,expnr)
else
    subplot(ceil(N/3),3,expnr)
end
plot(freqWidth,fullspectrum/max(fullspectrum),'k',freqWidth,pumpProfile,'b',freqWidth,probeProfile,'r')
title(experiments(1,expnr))
xlabel('Frequency [Hz]')
ylabel('Normalised intensity')
axis tight

%Calculate the amount of excitation for each spin pair.

Ahf = [1 2 3];%this corresponds to the indices of the spinpair matrix
where the A spin resonance frequencies for each 14N hyperfine level
are stored
Bhf = [4 5 6];%this corresponds to the indices of the spinpair matrix
where the B spin resonance frequencies for each 14N hyperfine level
are stored

for ahf = 1:3;
    for bhf = 1:3;

freqA = Ahf(1,ahf); freqB = Bhf(1,bhf);

%Calculate the contribution to the signal from probe excitation on
spin A
fprobeA = zeros(n,1);
fprobeA =
excAtt*observerPulseProfile(n,omegaA,omega2A,probecentrefreq(1,expnr),spinpair(:,freqA),firstprobepulseLength(1,expnr),secondprobepulseLength(1,expnr));

%Calculate the contribution to the signal from the pump pulse on spin
B
fpumpB = zeros(n,1);
fpumpB =

```

```

excAtt*pumpPulseProfile(n,omegaB,pumpcentrefreq(1,expnr),spinpair(:,f
reqB),pumppulselength(1,expnr));
fpumpB =
fpumpB.*(GGaussian(pumpcentrefreq(1,expnr),gaussdistr,spinpair(:,freq
B)));

%Calculate the contribution to the signal from probe excitation on
spin B
fprobeB = zeros(n,1);
fprobeB =
excAtt*observerPulseProfile(n,omegaA,omega2A,probcentrefreq(1,expnr)
,spinpair(:,freqB),firstprobepulselength(1,expnr),secondprobepulselen
gth(1,expnr));

%Calculate the contribution to the signal from the pump pulse on spin
A
fpumpA = zeros(n,1);
fpumpA =
excAtt*pumpPulseProfile(n,omegaB,pumpcentrefreq(1,expnr),spinpair(:,f
reqA),pumppulselength(1,expnr));
fpumpA =
fpumpA.*(GGaussian(pumpcentrefreq(1,expnr),gaussdistr,spinpair(:,freq
A)));

%Calculate the resulting weighting factor to the PELDOR signal for
each spin pair
%by adding together the contributions for each hyperfine level and
then
%dividing the result with (number of hyperfine levels for spin A and
B = 3 x 3 = 9.
xm = zeros(n,1);
xm(:,1) = fpumpA.*fpumpB + fprobeB.*fpumpA;
signalIntensities(:,expnr) = signalIntensities(:,expnr) + xm;

    end
end

signalIntensities(:,expnr) = signalIntensities(:,expnr)/9;

%Calculate the amount of probe pulse excitation for each spin
V0 = zeros(n,1);
for level = 1:3;

freqA = Ahf(1,level); freqB = Bhf(1,level);

vo = zeros(n,1);
vo(:,1) =
observerPulseProfile(n,omegaA,omega2A,probcentrefreq(1,expnr),spinpa
ir(:,freqA),firstprobepulselength(1,expnr),secondprobepulselength(1,e
xpnr)) +...

observerPulseProfile(n,omegaA,omega2A,probcentrefreq(1,expnr),spinpa
ir(:,freqB),firstprobepulselength(1,expnr),secondprobepulselength(1,e
xpnr));

V0(:,1) = V0(:,1) + vo;

```

```

end

V0(:,1) = V0(:,1)/3;%divide by the number of hyperfine levels for
each spin
signalIntensityWithoutPumpPulse(1,expnr) = sum(V0(:,1));%divide the
sum by the number of spin pairs

end

assignin('base','signalIntensities',signalIntensities);
assignin('base','signalIntensityWithoutPumpPulse',signalIntensityWith
outPumpPulse);
else
    %If the Run excitations box in the UI was not ticked then do this.
    signalIntensities = evalin('base','signalIntensities');
    signalIntensityWithoutPumpPulse =
evalin('base','signalIntensityWithoutPumpPulse');
end

waitbar(4/6,wait,'Excitations calculated')

%-----
%
%
%       Here the PELDOR timetraces are computed
%
%-----

waitbar(5/6,wait,'Calculating timetraces - almost done')

if runTimeTraces == 1;%Do this if the Run time traces box was ticked
in the UI.

%setup constants
kN = mu0*bohrmagneton^2*g^2/hbar;
k2 =kN/(4*pi);

tmin = 0*1e-6;%the starting time in seconds for the time traces
tmax = 4*1e-6;%The time delay between the second and third observer
pulses in seconds (time window)
tstep = 5*1e-9;%The increment of the pump pulse in seconds
timewindow = tmin:tstep:tmax;
J = randn(n,1);%use this for the exchange coupling
jcoupling = 0*[3.0+2.2*J 3.0+0.5*J 1.5+1.0*J 2.3+0*J 1.1+1*J
2+0*J]*(2*pi*1e6);%A normal distribution of exchange coupling. The
Exchange coupling is given in MHz

%Prepare some variables
Vintra = cell(1,N);
PELDORtimetrace = cell(1,N);
%Do this if experimental time traces have been loaded via the UI.
if evalin('base','exist(''PTTname'', 'var')');
PTTname = evalin('base','PTTname');
PTTpath = evalin('base','PTTpath');

```

```

band = evalin('base','band');
Xph = cell(1,N);%placeholder for X
Yph = cell(1,N);%placeholder for Y
timescale = cell(1,N);

for expnr = 1:N

%Load the experimental time traces
%The time trace from Hiper are normal text files. They need to be
loaded
%using a different function than time traces from DeerAnalysis.
if strcmp(band,'wband')
    if N>1
[X,Y] = Hiperload ([PTTpath PTTname{expnr}(1:end-4)]);

        else
            [X,Y] = Hiperload([PTTpath PTTname(1:end-4)]);
        end
    else
        if N>1
[X,Y] = deerload([PTTpath PTTname{expnr}(1:end-4)]);

            else
                [X,Y] = deerload([PTTpath PTTname(1:end-4)]);
            end
        end
    end
Xph{1,expnr} = X;
Yph{1,expnr} = Y;
Yph{1,expnr} = Yph{1,expnr}/max(Yph{1,expnr});
[~,indice(1,expnr)]=max(Yph{1,expnr});%find the indice of Y that
contains the maximum number.
Xph{1,expnr} = Xph{1,expnr}-Xph{1,expnr}(indice(1,expnr),1);%shift
the X-axis so the point with the highest intensity (in Y) is at X = 0.

timescale{1,expnr} = Xph{1,expnr}*1e-6;%use X for the timescale so
both experimental and simulated time traces have the same number of
points

for t = 1:1:length(timescale{1,expnr});
    V=0;
    V= signalIntensityWithoutPumpPulse(1,expnr) -
(sum(signalIntensities(:,expnr).*(1-cos(((k2./(explicitdistanceAB*1e-
10).^3).*(1-3.*cos(thetaForEachPair).^2)...
    +jcoupling(:,expnr)).*timescale{1,expnr}(t,1)))));
    Vintra{1,expnr}(t,1) = V;
end
PELDORtimetrace{1,expnr} = Vintra{1,expnr}/max(Vintra{1,expnr});
end

%If experimental time traces were not loaded then do this.
else
    for expnr = 1:N
        for t = 1:1:length(timewindow);
            V=0;
            V= signalIntensityWithoutPumpPulse(1,expnr) -
(sum(signalIntensities(:,expnr).*(1-cos(((k2./(explicitdistanceAB*1e-
10).^3).*(1-3.*cos(thetaForEachPair).^2)...
            +jcoupling(:,expnr)).*timewindow(t)))));

```

```

    Vintra{1,expnr}(t,1) = V;
    end
    PELDORtimetrace{1,expnr} = Vintra{1,expnr}/max(Vintra{1,expnr});
    end
end

%plot the time traces
if evalin('base','ishandle(4)')==1
close 4
end
figure(4)
XCheck = exist('Xph','var');
if XCheck == 1%Check if experimental time trace was loaded or exist
then do the following.
    for expnr = 1:N

        if N<4
            subplot(1,N,expnr)
        else
            subplot(ceil(N/3),3,expnr)
        end
        plot(timescale{1,expnr}*1e6,PELDORtimetrace{1,expnr},'r',Xph{1,expnr}
        ,Yph{1,expnr},'b')
        xlabel('Time [\mu s]')
        xlim([0 max(timescale{1,expnr}*1e6)])
        title(experiments(1,expnr))
        ylim([min(PELDORtimetrace{1,expnr})-0.2 1])
        end
    else
        for expnr = 1:N
            if N<4
                subplot(1,N,expnr)
            else
                subplot(ceil(N/3),3,expnr)
            end
            plot(timewindow*1e6,PELDORtimetrace{1,expnr},'r')
            xlabel('Time [\mu s]')
            xlim([0 max(timewindow*1e6)])
            title(experiments(1,expnr))
            ylim([min(PELDORtimetrace{1,expnr})-0.2 1])

        end
    end
end

end

waitbar(6/6,wait,'Timetraces calculated, phew')

elapsedtime = toc;
disp(['Time it took to simulate = ' num2str(elapsedtime),' s'])
close(wait)
end

```

### A.3.3 Functions used in simulation program

#### **AngleRotation.m**

```
%Creates a 3D rotation matrix for a counterclockwise rotation of
%"rotationangle" radians around the vector [sin(randomphi)
cos(randomphi) 0].
function [Rrot]=AngleRotation(rotationangle,randomphi)
k=[sin(randomphi) cos(randomphi),0];%Constructs a vector to rotate
rotationangle degrees around
kx=[0 -k(1,3) k(1,2);k(1,3) 0 -k(1,1);-k(1,2) k(1,1) 0];%the cross
product in matrix form
Rrot=eye(3,3)+(kx*sin(rotationangle))+((1-
cos(rotationangle))*kx^2);%Calculate the rotation matrix with
Rodrigues' rotation formula
```

#### **AngleTilt.m**

```
%Creates a 3D rotation matrix for a counterclockwise rotation of
%"rotationangle" radians around the vector [cos(randomphi)
sin(randomphi) 0].
function [Rrot]=AngleTilt(rotationangle,randomphi)
k=[cos(randomphi) sin(randomphi),0];%Constructs a vector to rotate
rotationangle degrees around
kx=[0 -k(1,3) k(1,2);k(1,3) 0 -k(1,1);-k(1,2) k(1,1) 0];%the cross
product in matrix form
Rrot=eye(3,3)+(kx*sin(rotationangle))+((1-
cos(rotationangle))*kx^2);%Calculate the rotation matrix with
Rodrigues' rotation formula
```

#### **deerload.m**

```
%Import data from DeerAnalysis
function [X,Y,Sim]=deerload(filepath)
file=[filepath '.dat'];
D=load(file);
X=D(:,1);
Y=D(:,2);
Sim=D(:,3);
```

#### **GGaussian.m**

```
function [gaussian]=GGaussian(mu,sigma,spinfreq)
x = spinfreq;
gaussian = exp(-(x-mu).^2./(2.*sigma.^2))./(sqrt(2.*pi).*sigma);
gaussian = gaussian/max(gaussian);
```

#### **Hiperload.m**

```
%Import data from the HiPER spectrometer. These are simple text file
with only numbers.
function [X,Y,Z]=Hiperload(filepath)
file=[filepath '.txt'];
D=load(file);
X=D(:,1);
Y=D(:,2);
```

#### **mtsslWizardLoad.m**

```
%Import data from the MTSSL wizard program. These are simple text
file with only numbers.
function [X]=mtsslWizardLoad(filepath)
file=[filepath '.txt'];
D=load(file);
X=D(:,1);
```

### **observerPulseProfile.m**

```
%Square pi/2, pi, pi pulse profile
function
[observerPulseProfile]=observerPulseProfile(n,omega,omega2,centrefreq
,spinres,pihalfpulselength,secondpulselength)
observerPulseProfile = zeros(n,1);
observerPulseProfile(:,1) = abs((omega./sqrt(omega.^2 +
(centrefreq.*2.*pi - spinres.*2.*pi).^2).*sin(sqrt(omega.^2 +
(centrefreq.*2.*pi - spinres.*2.*pi).^2).*pihalfpulselength)...
.*(omega2.^4)./(4.*(sqrt(omega2.^2 + (centrefreq.*2.*pi -
spinres.*2.*pi).^2)).^4)).*(1-cos(sqrt(omega2.^2 +...
(centrefreq.*2.*pi -
spinres.*2.*pi).^2).*secondpulselength)).^2));
```

### **pumpPulseProfile.m**

```
%Square pi pulse profile
function
[pumppulseprofile]=pumpPulseProfile(n,omega,centrefreq,spinres,pulsel
ength)
pumppulseprofile = zeros(n,1);
pumppulseprofile(:,1) = ((omega.^2./(2.*(omega.^2 +
(centrefreq.*2.*pi - spinres.*2.*pi).^2))).*(1-cos(sqrt(omega.^2 +
(centrefreq.*2.*pi...
-spinres.*2.*pi).^2).*pulselength)));
```

### **RotateAboutAxis.m**

```
%Creates a 3D rotation matrix for a counterclockwise rotation of
%"randomphi" radians around an axis that is defined by randomphi.
function [Rrot]=RotateAboutAxis(coneAngle,randomphi)
k=[0 cos(randomphi) sin(randomphi)];%This is the molecular y-axis and
it is perpendicular to the vector that is being rotated and after the
rotation.
kx=[0 -k(1,3) k(1,2);k(1,3) 0 -k(1,1);-k(1,2) k(1,1) 0];%the cross
product in matrix form
Rrot=eye(3,3)+(kx.*sin(coneAngle))+((kx^2)*(1-
cos(coneAngle)));%Calculate the rotation matrix with Rodrigues'
rotation formula
```

### **RotateAboutAxis2.m**

```
%Creates a 3D rotation matrix for a counterclockwise rotation of
%"randomphi" radians around an axis that is defined by randomphi.
function [Rrot]=RotateAboutAxis2(coneAngle,randomphi)
k=[zeros(length(randomphi),1) cos(randomphi) sin(randomphi)];%This is
the molecular y-axis and it is perpendicular to the vector that is
being rotated and the rotated vector
k1 = [0 -k(1,3) k(1,2)];
numMatrix = ones(1,length(coneAngle));
kcell = mat2cell(k, numMatrix, 3);
kx(:,1) = {[zeros(length(randomphi),1) -k(:,3) k(:,2)]];
kx2(:,1) = {[k(:,3) zeros(length(randomphi),1) -k(:,1)]];
kx3(:,1) = {[k(:,2) k(:,1) zeros(length(randomphi),1)]];

Rrot=eye(3,3)+(kx.*sin(coneAngle))+((kx.^2)*(1-
cos(coneAngle)));%Calculate the rotation matrix with Rodrigues'
rotation formula
```

### **RotateAboutRab.m**

```
%Creates a 3D rotation matrix for a counterclockwise rotation of
%"rotationangle" radians around the interspin vector. The orientation
of the interspin vector is passed to the function.
function [Rrot]=RotateAboutRab(rab,rotationangle)
k=rab;%This is the molecular x-axis and it is perpendicular to the
```



```

vector that is being rotated and the rotated vector
kx=[0 -k(1,3) k(1,2);k(1,3) 0 -k(1,1);-k(1,2) k(1,1) 0];%the cross
product in matrix form
Rrot=eye(3,3)+(kx.*sin(rotationangle))+((1-
cos(rotationangle))*kx^2);%Calculate the rotation matrix with
Rodrigues' rotation formula

```

#### **RotateAboutXaxis.m**

```

%Creates a 3D rotation matrix for a counterclockwise rotation of
%"rotationangle" radians around the molecular x-axis. The orientation
of the molecular x-axis is defined in the function.
function [Rrot]=RotateAboutXaxis(rotationangle)
k=[1 0 0];%This is the molecular x-axis and it is perpendicular to
the vector that is being rotated and the rotated vector
kx=[0 -k(1,3) k(1,2);k(1,3) 0 -k(1,1);-k(1,2) k(1,1) 0];%the cross
product in matrix form
Rrot=eye(3,3)+(kx.*sin(rotationangle))+((1-
cos(rotationangle))*kx^2);%Calculate the rotation matrix with
Rodrigues' rotation formula

```

#### **RotateAboutYaxis.m**

```

%Creates a 3D rotation matrix for a counterclockwise rotation of
%"rotationangle" radians around the molecular y-axis. The orientation
of the molecular y-axis is defined in the function.
function [Rrot]=RotateAboutYaxis(rotationangle)
k=[0 1 0];%This is the molecular y-axis and it is perpendicular to
the vector that is being rotated and the rotated vector
kx=[0 -k(1,3) k(1,2);k(1,3) 0 -k(1,1);-k(1,2) k(1,1) 0];%the cross
product in matrix form
Rrot=eye(3,3)+(kx.*sin(rotationangle))+((1-
cos(rotationangle))*kx^2);%Calculate the rotation matrix with
Rodrigues' rotation formula

```

#### **RotateAboutZaxis.m**

```

%Creates a 3D rotation matrix for a counterclockwise rotation of
%"rotationangle" radians around the molecular z-axis. The orientation
of the molecular z-axis is defined in the function.
function [Rrot]=RotateAboutZaxis(rotationangle)
k=[0 0 1];%This is the molecular x-axis and it is perpendicular to
the vector that is being rotated and the rotated vector
kx=[0 -k(1,3) k(1,2);k(1,3) 0 -k(1,1);-k(1,2) k(1,1) 0];%the cross
product in matrix form
Rrot=eye(3,3)+(kx.*sin(rotationangle))+((1-
cos(rotationangle)).*kx^2);%Calculate the rotation matrix with
Rodrigues' rotation formula

```

#### **RotationMatrix.m**

```

%Creates a rotation matrix that rotates the vector u to the direction
of the vector v
function [R]=RotationMatrix(u,v)
uvangle=acos(dot(u,v));%calculate the angle between u and v
k=cross(u,v); k = k/norm(k);%calculate the cross product between u
and v and normalise the vector that results.
kx=[0 -k(1,3) k(1,2);k(1,3) 0 -k(1,1);-k(1,2) k(1,1) 0];%the cross
product in matrix form
R=eye(3,3)+(kx.*sin(uvangle))+((1-cos(uvangle))*kx^2);%Calculate the
rotation matrix with Rodrigues' rotation formula

```

**ScalingMatrix.m**

```
%Multiplies each element of a vector by the supplied scalars.  
function [Rscale]=ScalingMatrix(a,b,c)%a is radiusScaling, b is  
heighScaling, c is randompsiA  
Rscale = [1+a*c 1+a*c 1+b*c];
```

### A.3.4 Cooperative twist-stretch dynamics model for short dsDNA

```
%-----Calculate the conformers for non-covalently spin labelled
DNA
clc%clears the command window
n=20000;%number of conformers
m=200;%number of conformers in graphics

molecularorientation=[0 0 1];%Defines the orientation of the molecule
relative to spin labels.

%Define the orientations of spin labels A and B around the molecular
%Z-axis.
psiA = 10;%equilibrium rotation angle in degrees for spin A
psiB = -65;%equilibrium rotation angle in degrees for spin B

dnaRadius = 2.7;%the distance in Angstrom that the spin labels are
shifted away from the center of the DNA helix.

stretchDistribution = 2.25;%Distribution in DNA stretching. One
standard deviation, in angstrom
maxAllowedRotation = 5.5;%the maximum angle the spin labels can
rotate with stretching, in degrees
randomStretch = 0 +(stretchDistribution).*randn(n,1);%stretching with
normal distribution
stretchpsiA = psiA +
(maxAllowedRotation*randomStretch/stretchDistribution);%spin label
rotation coupled to stretching
stretchpsiB = psiB -
(maxAllowedRotation*randomStretch/stretchDistribution);
radiusChange = -3.2/11*randomStretch;%The change in radius is
controlled by the change in DNA length, the stretch. 11 is the number
of basepairs between the spin labels. This equation is from: Marko,
A., Denysenkov, V., Margraf, D., Cekan, P., Schiemann, O., Sigurdsson,
Th. S., Prisner, T. F., Journal of the American Chemical Society,
2011, vol.133 (34), pp. 13375-13379.
flexAngleA = 0*pi/180+(1*pi/180)/2.*randn(n,1);
flexAngleB = 0*pi/180+(1*pi/180)/2.*randn(n,1);

% tiltA = 5*pi/180+(5*pi/180)/2.*randn(n,1);%If the spin labels need
to be tilted around their gx axis.
% tiltB = 5*pi/180+(5*pi/180)/2.*randn(n,1);

spinAheight = 18.8;
spinBheight = -18.8;
spinLabelLength = 9.5;

spinAstartPosition = [spinLabelLength -dnaRadius spinAheight];
spinBstartPosition = [spinLabelLength dnaRadius spinBheight];

%Turn the A spin label around the DNA axis, move it accordingly in
the plane perpendicular to the DNA axis
spinlabelApositions = zeros(n,3);
spinlabelAbackPositions = zeros(n,3);
spinAstartPositions = zeros(n,3);
for c=1:n;
    spinAstartPositions(c,:) = [spinLabelLength -
dnaRadius+radiusChange(c,1) spinAheight];%This line changes the
radius of the DNA upon stretching (moves the spin label either
towards or away from the rotation axis of the DNA duplex). As the DNA
```

```

stretches the radius is decreased, hence the "+radiusChange"
    spinlabelApositions(c,:) = [spinAstartPositions(c,1)
spinAstartPositions(c,2) spinAstartPositions(c,3)+
(randomStretch(c,1)/2)];
    spinlabelApositions(c,:) =
RotateAboutZaxis(stretchpsiA(c,1)*pi/180)*spinlabelApositions(c,:);%
Rotate the spin label
    spinlabelAbackPositions(c,:) =
RotateAboutZaxis(stretchpsiA(c,1)*pi/180)*[0 spinAstartPositions(c,2)
spinlabelApositions(c,3)]';%move the initial point of the spin label
vector accordingly
    %add flexibility to the spin label
    spinlabelApositions(c,:) =
AngleRotation(flexAngleA(c,1),stretchpsiA(c,1)*pi/180)*(spinlabelApos
itions(c,:)-spinlabelAbackPositions(c,:));%add flexibility to the
spin label, up/down motion.
    spinlabelApositions(c,:) =
spinlabelApositions(c,:)+spinlabelAbackPositions(c,:);
end

spinA = zeros(n,3);
spinA = spinlabelApositions;

%Calculate the orientation for the spin centre of spin label A
spinAorientation = zeros(n,3);
for c=1:n;
spinAorientation(c,:) =
AngleRotation(flexAngleA(c,1),stretchpsiA(c,1)*pi/180)*[0 0 1]';
end

%Turn the B spin label around the DNA axis, move it accordingly in
the plane perpendicular to the DNA axis
spinlabelBpositions = zeros(n,3);
spinlabelBbackPositions = zeros(n,3);
spinBstartPositions = zeros(n,3);
for c=1:n;
    spinBstartPositions(c,:) = [spinLabelLength dnaRadius-
radiusChange(c,1) spinBheight];
spinlabelBpositions(c,:) = [spinBstartPositions(c,1)
spinBstartPositions(c,2) spinBstartPositions(c,3) -
(randomStretch(c,1)/2)];
    spinlabelBpositions(c,:) =
RotateAboutZaxis(stretchpsiB(c,1)*pi/180)*spinlabelBpositions(c,:);
    spinlabelBbackPositions(c,:) =
RotateAboutZaxis(stretchpsiB(c,1)*pi/180)*[0 spinBstartPositions(c,2)
spinlabelBpositions(c,3)]';
    %add flexibility to the spin label
    spinlabelBpositions(c,:) = AngleRotation(flexAngleB(c,1),-
stretchpsiB(c,1)*pi/180)*(spinlabelBpositions(c,:)-
spinlabelBbackPositions(c,:));
    spinlabelBpositions(c,:) =
spinlabelBpositions(c,:)+spinlabelBbackPositions(c,:);
end

spinB = zeros(n,3);
spinB = spinlabelBpositions;

%Calculate the orientation for the spin centre of spin label B
spinBorientation = zeros(n,3);

```

```

for c=1:n;
spinBorientation(c,:) =
AngleRotation(flexAngleB(c,1),stretchpsiB(c,1)*pi/180)*[0 0 1]';
end

%Calculate the interspin distance
explicitdistanceAB = zeros(n,1);
explicitdistanceAB(:,1) = sqrt((spinA(:,1)-
spinB(:,1)).^2+(spinA(:,2)-spinB(:,2)).^2+(spinA(:,3)-
spinB(:,3)).^2);

explicitdistanceStd=std(explicitdistanceAB);
explicitdistanceMean=mean(explicitdistanceAB);
disp(['Mean distance = ' num2str(explicitdistanceMean)])
disp(['Distance Std = ' num2str(explicitdistanceStd)])

torsionangleAStd = std(stretchpsiA);
torsionangleBStd = std(stretchpsiB);
disp(['Std for spin A torsion = ' num2str(torsionangleAStd)])
disp(['Std for spin B torsion = ' num2str(torsionangleBStd)])

spinlabelAheightStd = std(spinlabelApositions(:,3));
spinlabelBheightStd = std(spinlabelBpositions(:,3));
disp(['Std for height of spinlabel A = '
num2str(spinlabelAheightStd)])
disp(['Std for height of spinlabel B = '
num2str(spinlabelBheightStd)])

RadiusStd = std(radiusChange);
disp(['Std for DNA duplex radius (Distance from spin label to centre
of helix) = ' num2str(RadiusStd)])

%Calculate the projection of the interspin vector on the magnetic
frame
%(The frame that has the magnetic field pointing along the Z-axis).

rabprojection = zeros(n,3);
for c=1:n;
    rabprojection(c,:) = (spinA(c,:)-spinB(c,:))/norm(spinA(c,:)-
spinB(c,:));
end

if ishandle(1);%Check if figure 1 exists. If it does then it is
closed and a new one generated.
close(1)
else
end
figure(111)
axis([-20 20 -20 20 -20 20])%define the axis limits of the graphics
line([0 0],[0 0],[-20 20])%make the Z-axis
axis square
xlabel('X')
ylabel('Y')
zlabel('Z')
%Draw the spin labels and the interspin vectors
for c=1:m;
line([spinlabelAbackPositions(c,1)
spinA(c,1)],[spinlabelAbackPositions(c,2)
spinA(c,2)],[spinlabelAbackPositions(c,3)
spinA(c,3)],'color','blue');

```

```

line([spinlabelBbackPositions(c,1)
spinB(c,1)], [spinlabelBbackPositions(c,2)
spinB(c,2)], [spinlabelBbackPositions(c,3) spinB(c,3)], 'color', 'red');
end

%Show the distance distribution as a histogram
figure(1)
subplot(2,2,2)
distance = (min(explicitdistanceAB)-2:0.4:max(implicitdistanceAB)+10);
hist(implicitdistanceAB,distance)
title('Distance distribution')

[x3,y3] = deerload('path to file');
figure(11)
[hits,~] = histc(implicitdistanceAB,distance);
hits = hits/max(hits);
plot_h = plot(distance,hits,'r',x3*10,y3/max(y3),'b');
set(plot_h,'LineWidth',2);
% legend('from model','from orientation average')
title('Distance distribution','FontSize',18)
xlabel(['Distance [',char(197),']'],'FontSize',18)
ylabel('Probability','FontSize',18)
xlim([20 70])
set(gca,'FontSize',18);

```

### A.3.5 Harmonic segmented chain (HSC) model for **21**

In this section, the Matlab script describing an harmonic segmented chain model for compound **21** is described. The model used for compound **22** was constructed in a similar manner.

```
clc
eq. 3 in :Jeschke, G., Sajid, M., Schulte, M., Ramezani, N., Volkov,
A., Zimmermann, H., Godt, A., Journal of the American Chemical
Society, 2010, vol. 132 (29), pp. 10107-10117 is treated as
%one standard deviation and not as the variance.

tic;
n=20000;%number of conformers
m=100;%number of conformers in graphics

%I have based my bending variance using bending variances from the
paper above.
% The variance values are converted into one standard deviation by
taking
% the square root of the variance. The variance of the bending angle
is
% 1/(2*F). The variances in the paper are from measurements in o-
terphenyl,

F1 = 20; %Bond between two benzen groups (unknown potential).
F2 = 20; %bond connected to benzen. 25 is the value used by G.
Jeschke.
F3 = 20; %bond connected to an acetylene carbon. 25 is the value used
by G. Jeschke.
F4 = 20; %Nitroxide label flexibility
F5 = 20; %Trityl label flexibility

molsegbend1 = zeros(n,2);
molsegbend2 = zeros(n,2);
molsegbend3 = zeros(n,2);
molsegbend4 = zeros(n,2);
molsegbend5 = zeros(n,2);
molsegbend6 = zeros(n,2);
molsegbend7 = zeros(n,2);

molsegbend1 = 0*pi/180+((1/(2*F3))).*randn(n,2);%There are two
columns of random angles. One column for the A spin side and one
column for the B spin side.

molsegbend2(:,1) = 0*pi/180+((1/(2*F3))).*randn(n,1);%For the A side
segment (right side)
molsegbend2(:,2) = 0*pi/180+((1/(2*F3))).*randn(n,1);%For the B side
segment (left side)

molsegbend3(:,1) = 0*pi/180+((1/(2*F3))).*randn(n,1);
molsegbend3(:,2) = 0*pi/180+((1/(2*F1))).*randn(n,1);

molsegbend4(:,1) = 0*pi/180+((1/(2*F1))).*randn(n,1);
molsegbend4(:,2) = 0*pi/180+((1/(2*F1))).*randn(n,1);
```

```

molsegbend5(:,1) = 0*pi/180+((1/(2*F1))).*randn(n,1);
molsegbend5(:,2) = 0*pi/180+((1/(2*F3))).*randn(n,1);

molsegbend6 = 0*pi/180+((1/(2*F3))).*randn(n,2);
molsegbend7 = 0*pi/180+((1/(2*F3))).*randn(n,1);

AmolsegLength1 = zeros(n,1);
AmolsegLength2 = zeros(n,1);
AmolsegLength3 = zeros(n,1);
AmolsegLength4 = zeros(n,1);
AmolsegLength5 = zeros(n,1);
AmolsegLength6 = zeros(n,1);
AmolsegLength7 = zeros(n,1);

BmolsegLength1 = zeros(n,1);
BmolsegLength2 = zeros(n,1);
BmolsegLength3 = zeros(n,1);
BmolsegLength4 = zeros(n,1);
BmolsegLength5 = zeros(n,1);
BmolsegLength6 = zeros(n,1);

segLengthDistr = 0.13;

AmolsegLength1 = 1.5+segLengthDistr.*randn(n,1);
AmolsegLength2 = 2.8+segLengthDistr.*randn(n,1);
AmolsegLength3 = 1.4+segLengthDistr.*randn(n,1);
AmolsegLength4 = 1.2+segLengthDistr.*randn(n,1);
AmolsegLength5 = 1.4+segLengthDistr.*randn(n,1);
AmolsegLength6 = 2.8+segLengthDistr.*randn(n,1);
AmolsegLength7 = 1.5+segLengthDistr.*randn(n,1);

BmolsegLength1 = 2.8+segLengthDistr.*randn(n,1);
BmolsegLength2 = 1.4+segLengthDistr.*randn(n,1);
BmolsegLength3 = 1.2+segLengthDistr.*randn(n,1);
BmolsegLength4 = 1.4+segLengthDistr.*randn(n,1);
BmolsegLength5 = 2.8+segLengthDistr.*randn(n,1);
BmolsegLength6 = 1.4+segLengthDistr.*randn(n,1);

% molrotphi = 0*pi*rand(n,1);

molsegRotPhi1 = 2*pi*rand(n,2);
molsegRotPhi2 = 2*pi*rand(n,2);
molsegRotPhi3 = 2*pi*rand(n,2);
molsegRotPhi4 = 2*pi*rand(n,2);
molsegRotPhi5 = 2*pi*rand(n,2);
molsegRotPhi6 = 2*pi*rand(n,2);
molsegRotPhi7 = 2*pi*rand(n,2);

randomRotationA = 2*pi*rand(n,1);%random rotation of the spins or
molecule around it's z-axis, i.e. it's initial interspin vector,
%includes the random rotation of the whole molecule and also the
random rotation of the spin centres due to rotation around bonds
randomRotationB = 2*pi*rand(n,1);
Arandomphi = 2*pi*rand(n,1);%use this for the A spin rotations around
the cone, the trityl
Brandomphi = 2*pi*rand(n,1);%use this for the B spin rotations around

```



```

the cone, the nitroxide
Aconeangle = 24*pi/180+(1/(2*F4)).*randn(n,1);%this is for the
nitroxide
Bconeangle = 12.7*pi/180+(1/(2*F5)).*randn(n,1);%this is for the
trityl

AspinLabelLength = zeros(n,1);
BspinLabelLength = zeros(n,1);

AspinLabelLength = 5.8+segLengthDistr.*randn(n,1);%The distance (in
angstrom) from the nitroxide N to the C of the amide group. From MM
model.
BspinLabelLength = 6.0+segLengthDistr.*randn(n,1);%The distance (in
angstrom) from the center of the C center to the O bonded to the
phenyl group. From MM model.

segAPositions1 = zeros(n,3);
segBPositions1 = zeros(n,3);
for c = 1:n;
segAPositions1(c,:) = RotateAboutAxis(-
molsegbend1(c,1),molsegRotPhil(c,1))*[AmolsegLength1(c,1) 0 0]';
segBPositions1(c,:) =
RotateAboutAxis(molsegbend1(c,2),molsegRotPhil(c,2))*[-
BmolsegLength1(c,1) 0 0]';
end

segAPositions2 = zeros(n,3);
segBPositions2 = zeros(n,3);
for c = 1:n;
    segAPositions2(c,:) = RotateAboutAxis(-
molsegbend2(c,1),molsegRotPhi2(c,1)) * ((RotateAboutAxis(-
molsegbend1(c,1),molsegRotPhil(c,1))*[AmolsegLength1(c,1)+AmolsegLeng
th2(c,1) 0 0]')' - segAPositions1(c,:))';
    segAPositions2(c,:) = segAPositions2(c,:) + segAPositions1(c,:);
    segBPositions2(c,:) =
RotateAboutAxis(molsegbend2(c,2),molsegRotPhi2(c,2)) *
((RotateAboutAxis(molsegbend1(c,2),molsegRotPhil(c,2))*[-
BmolsegLength1(c,1)-BmolsegLength2(c,1) 0 0]')' -
segBPositions1(c,:))';
    segBPositions2(c,:) = segBPositions2(c,:) + segBPositions1(c,:);
end

segAPositions3 = zeros(n,3);
segBPositions3 = zeros(n,3);
for c = 1:n;
    segAPositions3(c,:) = RotateAboutAxis(-
molsegbend3(c,1),molsegRotPhi3(c,1)) *...
    ((RotateAboutAxis(-molsegbend1(c,1),molsegRotPhil(c,1))*...
    RotateAboutAxis(-molsegbend2(c,1),molsegRotPhi2(c,1))*...
    [AmolsegLength1(c,1)+AmolsegLength2(c,1)+AmolsegLength3(c,1)
0 0]')' - segAPositions2(c,:))';
    segAPositions3(c,:) = segAPositions3(c,:) + segAPositions2(c,:);

    segBPositions3(c,:) =
RotateAboutAxis(molsegbend3(c,2),molsegRotPhi3(c,2)) *...
    ((RotateAboutAxis(molsegbend1(c,2),molsegRotPhil(c,2))*...
    RotateAboutAxis(molsegbend2(c,2),molsegRotPhi2(c,2))*...
    [-BmolsegLength1(c,1)-BmolsegLength2(c,1)-BmolsegLength3(c,1)
0 0]')' - segBPositions2(c,:))';
    segBPositions3(c,:) = segBPositions3(c,:) + segBPositions2(c,:);
end

```

```

segAPositions4 = zeros(n,3);
segBPositions4 = zeros(n,3);
for c = 1:n;
    segAPositions4(c,:) = RotateAboutAxis(-
molsegbend4(c,1),molsegRotPhi4(c,1)) *...
    ((RotateAboutAxis(-molsegbend1(c,1),molsegRotPhi1(c,1))*...
    RotateAboutAxis(-molsegbend2(c,1),molsegRotPhi2(c,1))*...
    RotateAboutAxis(-molsegbend3(c,1),molsegRotPhi3(c,1))*...

[AmolsegLength1(c,1)+AmolsegLength2(c,1)+AmolsegLength3(c,1)+AmolsegL
ength4(c,1) 0 0]')'- segAPositions3(c,:)');
    segAPositions4(c,:) = segAPositions4(c,:) + segAPositions3(c,:);

    segBPositions4(c,:) =
RotateAboutAxis(molsegbend4(c,2),molsegRotPhi4(c,2)) *...
    ((RotateAboutAxis(molsegbend1(c,2),molsegRotPhi1(c,2))*...
    RotateAboutAxis(molsegbend2(c,2),molsegRotPhi2(c,2))*...
    RotateAboutAxis(molsegbend3(c,2),molsegRotPhi3(c,2))*...
    [-BmolsegLength1(c,1)-BmolsegLength2(c,1)-
BmolsegLength3(c,1)-BmolsegLength4(c,1) 0 0]')' -
segBPositions3(c,:))';
    segBPositions4(c,:) = segBPositions4(c,:) + segBPositions3(c,:);
end

segAPositions5 = zeros(n,3);
segBPositions5 = zeros(n,3);
for c = 1:n;
    segAPositions5(c,:) = RotateAboutAxis(-
molsegbend5(c,1),molsegRotPhi5(c,1)) *...
    ((RotateAboutAxis(-molsegbend1(c,1),molsegRotPhi1(c,1))*...
    RotateAboutAxis(-molsegbend2(c,1),molsegRotPhi2(c,1))*...
    RotateAboutAxis(-molsegbend3(c,1),molsegRotPhi3(c,1))*...
    RotateAboutAxis(-molsegbend4(c,1),molsegRotPhi4(c,1))*...

[AmolsegLength1(c,1)+AmolsegLength2(c,1)+AmolsegLength3(c,1)+AmolsegL
ength4(c,1)+AmolsegLength5(c,1) 0 0]')'- segAPositions4(c,:)');
    segAPositions5(c,:) = segAPositions5(c,:) + segAPositions4(c,:);

    segBPositions5(c,:) =
RotateAboutAxis(molsegbend5(c,1),molsegRotPhi5(c,1)) *...
    ((RotateAboutAxis(molsegbend1(c,2),molsegRotPhi1(c,2))*...
    RotateAboutAxis(molsegbend2(c,2),molsegRotPhi2(c,2))*...
    RotateAboutAxis(molsegbend3(c,2),molsegRotPhi3(c,2))*...
    RotateAboutAxis(molsegbend4(c,2),molsegRotPhi4(c,2))*...
    [-BmolsegLength1(c,1)-BmolsegLength2(c,1)-
BmolsegLength3(c,1)-BmolsegLength4(c,1)-BmolsegLength5(c,1) 0 0]')' -
segBPositions4(c,:))';
    segBPositions5(c,:) = segBPositions5(c,:) + segBPositions4(c,:);
end

segAPositions6 = zeros(n,3);
segBPositions6 = zeros(n,3);
for c = 1:n;
    segAPositions6(c,:) = RotateAboutAxis(-
molsegbend6(c,1),molsegRotPhi6(c,1)) *...
    ((RotateAboutAxis(-molsegbend1(c,1),molsegRotPhi1(c,1))*...
    RotateAboutAxis(-molsegbend2(c,1),molsegRotPhi2(c,1))*...
    RotateAboutAxis(-molsegbend3(c,1),molsegRotPhi3(c,1))*...
    RotateAboutAxis(-molsegbend4(c,1),molsegRotPhi4(c,1))*...
    RotateAboutAxis(-molsegbend5(c,1),molsegRotPhi5(c,1))*...

```

```

[AmolsegLength1(c,1)+AmolsegLength2(c,1)+AmolsegLength3(c,1)+AmolsegLength4(c,1)+AmolsegLength5(c,1)+AmolsegLength6(c,1) 0 0]')'-
segAPositions5(c,:)');
    segAPositions6(c,:) = segAPositions6(c,:) + segAPositions5(c,:);

    segBPositions6(c,:) =
RotateAboutAxis(molsegbend6(c,2),molsegRotPhi6(c,2)) *...
    ((RotateAboutAxis(molsegbend1(c,2),molsegRotPhi1(c,2))*...
    RotateAboutAxis(molsegbend2(c,2),molsegRotPhi2(c,2))*...
    RotateAboutAxis(molsegbend3(c,2),molsegRotPhi3(c,2))*...
    RotateAboutAxis(molsegbend4(c,2),molsegRotPhi4(c,2))*...
    RotateAboutAxis(molsegbend5(c,2),molsegRotPhi5(c,2))*...
    [-BmolsegLength1(c,1)-BmolsegLength2(c,1)-
    BmolsegLength3(c,1)-BmolsegLength4(c,1)-BmolsegLength5(c,1)-
    BmolsegLength6(c,1) 0 0]')' - segBPositions5(c,:))';
    segBPositions6(c,:) = segBPositions6(c,:) + segBPositions5(c,:);
end

segAPositions7 = zeros(n,3);
segBPositions7 = zeros(n,3);
for c = 1:n;
    segAPositions7(c,:) = RotateAboutAxis(-
molsegbend7(c,1),molsegRotPhi7(c,1)) *...
    ((RotateAboutAxis(-molsegbend1(c,1),molsegRotPhi1(c,1))*...
    RotateAboutAxis(-molsegbend2(c,1),molsegRotPhi2(c,1))*...
    RotateAboutAxis(-molsegbend3(c,1),molsegRotPhi3(c,1))*...
    RotateAboutAxis(-molsegbend4(c,1),molsegRotPhi4(c,1))*...
    RotateAboutAxis(-molsegbend5(c,1),molsegRotPhi5(c,1))*...
    RotateAboutAxis(-molsegbend6(c,1),molsegRotPhi6(c,1))*...

[AmolsegLength1(c,1)+AmolsegLength2(c,1)+AmolsegLength3(c,1)+AmolsegLength4(c,1)+AmolsegLength5(c,1)+AmolsegLength6(c,1)+AmolsegLength7(c,1) 0 0]')'- segAPositions6(c,:))';
    segAPositions7(c,:) = segAPositions7(c,:) + segAPositions6(c,:);
end

%Rotate the A spin label about the molecular Y-axis. I don't include
%rotation of the label around the labels X-axis because it will not
be
%visible. Instead the twist of the label around its X-axis is
introduced in the Orientations file.

%subtracting (spinAStartPosition-[spinLabelLength 0 0] and then
adding
%this again to spinAStartPosition is done to observe correct
%positioning of the spin centre, and correspondingly the correct
%interspin vector.
%The RotateAboutXaxis rotates the spin label around the axis of the
%molecule (the blue line). Rotation of the molecule around its axis
is not included in
%the generation of random orientations.
spinlabelApositions = zeros(n,3);
for c=1:n;
    spinlabelApositions(c,:) =
RotateAboutAxis(Aconeangle(c,1),Arandomphi(c,1)) *...
    ((RotateAboutAxis(-molsegbend1(c,1),molsegRotPhi1(c,1))*...
    RotateAboutAxis(-molsegbend2(c,1),molsegRotPhi2(c,1))*...
    RotateAboutAxis(-molsegbend3(c,1),molsegRotPhi3(c,1))*...
    RotateAboutAxis(-molsegbend4(c,1),molsegRotPhi4(c,1))*...
    RotateAboutAxis(-molsegbend5(c,1),molsegRotPhi5(c,1))*...
    RotateAboutAxis(-molsegbend6(c,1),molsegRotPhi6(c,1))*...

```

```

        RotateAboutAxis(-molsegbend7(c,1),molsegRotPhi7(c,1))*...

[AmolsegLength1(c,1)+AmolsegLength2(c,1)+AmolsegLength3(c,1)+AmolsegL
ength4(c,1)+AmolsegLength5(c,1)+AmolsegLength6(c,1)+AmolsegLength7(c,
1)+AspinLabelLength(c,1) 0 0]')' - segAPositions7(c,:))';
    spinlabelApositions(c,:) = spinlabelApositions(c,:) +
segAPositions7(c,:);
end

spinA = zeros(n,3);
spinA(:,1:3) = spinlabelApositions;

%Calculate the orientation for the spin centre of spin label A
spinAorientation = zeros(n,3);
for c=1:n;
    spinAorientation(c,:) = RotateAboutYaxis(Aconeangle(c,1))*...
        RotateAboutYaxis(-molsegbend1(c,1))*...
        RotateAboutYaxis(-molsegbend2(c,1))*...
        RotateAboutYaxis(-molsegbend3(c,1))*...
        RotateAboutYaxis(-molsegbend4(c,1))*...
        RotateAboutYaxis(-molsegbend5(c,1))*...
        RotateAboutYaxis(-molsegbend6(c,1))*...
        [0 0 1]';
end

end

%Rotate the B spin label about the molecular Y-axis.
spinlabelBpositions = zeros(n,3);
for c=1:n;
    spinlabelBpositions(c,:) =
RotateAboutAxis(Bconeangle(c,1),Brandomphi(c,1)) *...
    ((RotateAboutAxis(molsegbend1(c,2),molsegRotPhi1(c,2))*...
    RotateAboutAxis(molsegbend2(c,2),molsegRotPhi2(c,2))*...
    RotateAboutAxis(molsegbend3(c,2),molsegRotPhi3(c,2))*...
    RotateAboutAxis(molsegbend4(c,2),molsegRotPhi4(c,2))*...
    RotateAboutAxis(molsegbend5(c,2),molsegRotPhi5(c,2))*...
    RotateAboutAxis(molsegbend6(c,2),molsegRotPhi6(c,2))*...
    [-BmolsegLength1(c,1)-BmolsegLength2(c,1)-
BmolsegLength3(c,1)-BmolsegLength4(c,1)-BmolsegLength5(c,1)-
BmolsegLength6(c,1)-BspinLabelLength(c,1) 0 0]')' -
segBPositions6(c,:))';
    spinlabelBpositions(c,:) = spinlabelBpositions(c,:) +
segBPositions6(c,:);
end

spinB = zeros(n,3);
spinB(:,1:3) = spinlabelBpositions;

%Calculate the orientation for the spin centre of spin label B
spinBorientation = zeros(n,3);
for c=1:n;
    spinBorientation(c,:) = RotateAboutYaxis(Bconeangle(c,1))*...
    RotateAboutYaxis(-molsegbend1(c,2))*...
    RotateAboutYaxis(molsegbend2(c,2))*...
    RotateAboutYaxis(molsegbend3(c,2))*...
    RotateAboutYaxis(molsegbend4(c,2))*...
    RotateAboutYaxis(molsegbend5(c,2))*...

```

```

        RotateAboutYaxis(molsegbend6(c,2))*...
        [0 0 1]';
end

%Calculate the interspin distance
explicitdistanceAB = zeros(n,1);
explicitdistanceAB(:,1) = sqrt((spinA(:,1)-
spinB(:,1)).^2+(spinA(:,2)-spinB(:,2)).^2+(spinA(:,3)-
spinB(:,3)).^2);

explicitdistanceStd=std(explicitdistanceAB);
explicitdistanceMean=mean(explicitdistanceAB);
disp(['Mean distance = ' num2str(explicitdistanceMean)])
disp(['Distance Std = ' num2str(explicitdistanceStd)])

%Calculate the projection of the interspin vector on the magnetic
frame
%(The frame that has the magnetic field pointing along the Z-axis).

rabprojection = zeros(n,3);
for c=1:n;
    rabprojection(c,:) = (spinA(c,:)-spinB(c,:))/norm(spinA(c,:)-
spinB(c,:));
end

%plot the vectors representing the molecule and spin labels. The
sphere
%represents the laboratory frame.
figure(22)
% subplot(2,2,1)
[X,Y,Z] = sphere;
axis([-20 20 -20 20 -20 20])%define the axis limits of the graphics
for c = 1:m;
line([0 segAPositions1(c,1)],[0 segAPositions1(c,2)],[0
segAPositions1(c,3)]);
line([0 segBPositions1(c,1)],[0 segBPositions1(c,2)],[0
segBPositions1(c,3)]);

line([segAPositions1(c,1) segAPositions2(c,1)],[segAPositions1(c,2)
segAPositions2(c,2)],[segAPositions1(c,3) segAPositions2(c,3)]);
line([segBPositions1(c,1) segBPositions2(c,1)],[segBPositions1(c,2)
segBPositions2(c,2)],[segBPositions1(c,3) segBPositions2(c,3)]);

line([segAPositions2(c,1) segAPositions3(c,1)],[segAPositions2(c,2)
segAPositions3(c,2)],[segAPositions2(c,3) segAPositions3(c,3)]);
line([segBPositions2(c,1) segBPositions3(c,1)],[segBPositions2(c,2)
segBPositions3(c,2)],[segBPositions2(c,3) segBPositions3(c,3)]);

line([segAPositions3(c,1) segAPositions4(c,1)],[segAPositions3(c,2)
segAPositions4(c,2)],[segAPositions3(c,3) segAPositions4(c,3)]);
line([segBPositions3(c,1) segBPositions4(c,1)],[segBPositions3(c,2)
segBPositions4(c,2)],[segBPositions3(c,3) segBPositions4(c,3)]);

line([segAPositions4(c,1) segAPositions5(c,1)],[segAPositions4(c,2)
segAPositions5(c,2)],[segAPositions4(c,3) segAPositions5(c,3)]);
line([segBPositions4(c,1) segBPositions5(c,1)],[segBPositions4(c,2)
segBPositions5(c,2)],[segBPositions4(c,3) segBPositions5(c,3)]);

```

```

line([segAPositions5(c,1) segAPositions6(c,1)],[segAPositions5(c,2)
segAPositions6(c,2)],[segAPositions5(c,3) segAPositions6(c,3)]);
line([segBPositions5(c,1) segBPositions6(c,1)],[segBPositions5(c,2)
segBPositions6(c,2)],[segBPositions5(c,3) segBPositions6(c,3)]);

line([segAPositions6(c,1) segAPositions7(c,1)],[segAPositions6(c,2)
segAPositions7(c,2)],[segAPositions6(c,3) segAPositions7(c,3)]);

end

axis square
xlabel('X','FontSize',10)
ylabel('Y','FontSize',10)
zlabel('Z','FontSize',10)
title('molecule conformers','FontSize',10)
set(gca,'Xtick',[])
set(gca,'Ytick',[])
set(gca,'Ztick',[])
box on

% Draw the spin labels and the interspin vectors
for c=1:m;
line([segAPositions7(c,1) spinA(c,1)],[segAPositions7(c,2)
spinA(c,2)],[segAPositions7(c,3)
spinA(c,3)'],'color','green','LineWidth',2);%spin label A
line([segBPositions6(c,1) spinB(c,1)],[segBPositions6(c,2)
spinB(c,2)],[segBPositions6(c,3)
spinB(c,3)'],'color','red','LineWidth',2);%spin label B
end

%Show the distance distribution as a histogram
figure(1)
subplot(2,2,2)
distance =(25:0.09:38);
hist(explicitdistanceAB,distance)
title('Distance distribution')

[x11,y11] = deerload('path to file');

figure(11)
y11 = -y11;

[hits,~] = histc(explicitdistanceAB,distance);
hits = hits/max(hits);
plot_h = plot(distance,hits,'r',x11*10,y11/max(y11),'b');
set(plot_h,'LineWidth',2);
% legend_h = legend('from model','from orientation average');
% set(legend_h,'FontSize',14)
title('Distance distribution','FontSize',18)
xlabel(['Distance [',char(197),']'],'FontSize',18)
ylabel('Probability','FontSize',18)
xlim([25 38])
% ylim([0 1.1])
set(gca,'FontSize',18);
% set(gca,'Xtick',[26 30 34 38])

```

### A.3.6 Dynamics model for 17

```
tic
n=20000;%number of conformers
m=200;%number of conformers in graphics

moleculebendAngle = 0*pi/180+(10*pi/180/2).*randn(n,1);

randomRotationA = 0*pi*rand(n,1);%random rotation of the spins or
molecule around it's z-axis, i.e. it's initial interspin vector,
%includes the random rotation of the whole molecule and also the
random rotation of the spin centres due to rotation around bonds
randomRotationB = 0*pi*rand(n,1);
Arandomphi = 2*pi*rand(n,1);%use this for the A spin rotations around
the cone.
Brandomphi = 2*pi*rand(n,1);%use this for the B spin rotations around
the cone.
Aconeangle = 25*pi/180+(10*pi/180/2).*randn(n,1);%This defines the
cone angle and variation
Bconeangle = 25*pi/180+(10*pi/180/2).*randn(n,1);

AspinLabelLength = 5.1;%The distance (in angstrom) from the center of
the nitroxide NO bond to the O of the ester group.
BspinLabelLength = 5.1;

molecularLength = 9.95;%The length (in angstrom) between the O of
each ester group.
spinAstartPosition = zeros(n,3);
spinBstartPosition = zeros(n,3);
for c = 1:n;
spinAstartPosition(c,:) =
[cos(moleculebendAngle(c,1))*(molecularLength/2+AspinLabelLength) 0
sin(moleculebendAngle(c,1))*(molecularLength/2+AspinLabelLength)];
spinBstartPosition(c,:) = [-
cos(moleculebendAngle(c,1))*(molecularLength/2+BspinLabelLength) 0
sin(moleculebendAngle(c,1))*(molecularLength/2+BspinLabelLength)];
end

%The RotateAboutXaxis rotates the spin label around the axis of the
%molecule (the blue line). Rotation of the molecule around its axis
is not included in
%the generation of random orientations.
spinlabelApositions = zeros(n,3);
for c=1:n;
spinlabelApositions(c,:) =
RotateAboutAxis(Aconeangle(c,1),Arandomphi(c,1))*(spinAstartPosition(
c,:)-[cos(moleculebendAngle(c,1))*(molecularLength/2) 0
sin(moleculebendAngle(c,1))*(molecularLength/2)]');
spinlabelApositions(c,:) =
spinlabelApositions(c,:)+[cos(moleculebendAngle(c,1))*(molecularLength/2) 0
sin(moleculebendAngle(c,1))*(molecularLength/2)];
end

spinA = zeros(n,3);
spinA(:,1:3) = spinlabelApositions;

%Calculate the orientation for the spin centre of spin label A
spinAorientation = zeros(n,3);
for c=1:n;
```

```

    spinAorientation(c,:) = RotateAboutYaxis(-
Aconeangle(c,1))*RotateAboutYaxis(moleculebendAngle(c,1))*[0 0 1]';
end

%Rotate the B spin label about the molecular Y-axis.
spinlabelBpositions = zeros(n,3);
for c=1:n;
    spinlabelBpositions(c,:) =
RotateAboutAxis(Bconeangle(c,1),Brandomphi(c,1))*(spinBstartPosition(
c,)-[-cos(moleculebendAngle(c,1))*(molecularLength/2) 0
sin(moleculebendAngle(c,1))*(molecularLength/2)]');
    spinlabelBpositions(c,:) = spinlabelBpositions(c,)+[-
cos(moleculebendAngle(c,1))*(molecularLength/2) 0
sin(moleculebendAngle(c,1))*(molecularLength/2)];
end

spinB = zeros(n,3);
spinB(:,1:3) = spinlabelBpositions;

%Calculate the orientation for the spin centre of spin label B
spinBorientation = zeros(n,3);
for c=1:n;
    spinBorientation(c,:) =
RotateAboutYaxis(Bconeangle(c,1))*RotateAboutYaxis(moleculebendAngle(
c,1))*[0 0 1]';
end

%Calculate the interspin distance
explicitdistanceAB = zeros(n,1);
explicitdistanceAB(:,1) = sqrt((spinA(:,1)-
spinB(:,1)).^2+(spinA(:,2)-spinB(:,2)).^2+(spinA(:,3)-
spinB(:,3)).^2);

explicitdistanceStd=std(explicitdistanceAB);
explicitdistanceMean=mean(explicitdistanceAB);
disp(['Mean distance = ' num2str(explicitdistanceMean)])
disp(['Distance Std = ' num2str(explicitdistanceStd)])

%Calculate the projection of the interspin vector on the magnetic
frame
%(The frame that has the magnetic field pointing along the Z-axis).

rabprojection = zeros(n,3);
for c=1:n;
    rabprojection(c,:) = (spinA(c,:)-spinB(c,:))/norm(spinA(c,:)-
spinB(c,:));
end

%plot the vectors representing the molecule and spin labels. The
sphere
%represents the laboratory frame.
figure(1)
subplot(2,2,1)
[X,Y,Z] = sphere;
% S=mesh(X*2,Y*2,Z*2);%Draw the sphere in the centre
% set(S,'EdgeColor','b');
axis([-12 12 -12 12 -12 12])%define the axis limits of the graphics
for c = 1:m;

```



```

line([0 -molecularLength/2*cos(moleculebendAngle(c,1))],[0 0],[0
sin(moleculebendAngle(c,1))*molecularLength/2]);
line([0 molecularLength/2*cos(moleculebendAngle(c,1))],[0 0],[0
sin(moleculebendAngle(c,1))*molecularLength/2]);
end
axis square
xlabel('X','FontSize',18)
ylabel('Y','FontSize',18)
zlabel('Z','FontSize',18)
title('molecule conformers','FontSize',18)
set(gca,'Xtick',[])
set(gca,'Ytick',[])
set(gca,'Ztick',[])
box on

% Draw the spin labels and the interspin vectors
for c=1:m;
line([cos(moleculebendAngle(c,1))*(molecularLength/2) spinA(c,1)],[0
spinA(c,2)],[sin(moleculebendAngle(c,1))*(molecularLength/2)
spinA(c,3)],'color','red','LineWidth',2);%spin label A
line([-cos(moleculebendAngle(c,1))*(molecularLength/2) spinB(c,1)],[0
spinB(c,2)],[sin(moleculebendAngle(c,1))*(molecularLength/2)
spinB(c,3)],'color','red','LineWidth',2);%spin label B
end

% Show the distance distribution as a histogram
figure(10)
subplot(2,2,2)
distance=(min(explicitdistanceAB)-3:0.09:max(explicitdistanceAB+3));
hist(explicitdistanceAB,distance)
title('Distance distribution')
%
[x3,y3]=deerload('path to file');
figure(11)
[hits,~]=histc(explicitdistanceAB,distance);
hits=hits/max(hits);
plot_h=plot(distance,hits,'r',x3*10,y3/max(y3),'b');
set(plot_h,'LineWidth',2);
% legend_h = legend('from model','from orientation average');
% set(legend_h,'FontSize',14)
title('Distance distribution','FontSize',18)
xlabel(['Distance [',char(197),']'],'FontSize',18)
ylabel('Probability','FontSize',18)
xlim([15 21])
ylim([0 1.1])
set(gca,'FontSize',18);

```

### A.3.7 Dynamics model for **19**

This section describes the Matlab script for the construction of a dynamics model for compound **19**. The model for **18** was constructed in a similar manner.

```
% clc%clears the command window

n=20000;%number of conformers
m=50;%number of conformers in graphics.

%-----Define the relative orientation of spin label A for each
conformer-----

%mean+standard deviation*randn(n,m) gives a nxm matrix with random
numbers
%from a normal distribution.

moleculebendAngle = zeros(n,1);
moleculebendAngleUP = 10*pi/180+(5*pi/180/2).*randn(n/2,1);
moleculebendAngleDOWN = -10*pi/180+(-5*pi/180/2).*randn(n/2,1);

randomplace = randperm(n)';
moleculebendAngle = [moleculebendAngleUP;moleculebendAngleDOWN];
moleculebendAngle = moleculebendAngle(randomplace(:,1),1);

AbendAngle = 0*pi/180+(0*pi/180)/2.*randn(n,1);%defines the
distribution of rotation of spin label A around the Y-axis
BbendAngle = 0*pi/180+(0*pi/180)/2.*randn(n,1);%same for spin label B
twistA = 0*pi/180+(0*pi/180)/2.*randn(n,1);%defines the distribution
of rotation of spin label A around the Z-axis
twistB = 0*pi/180+(0*pi/180)/2.*randn(n,1);%the same for spin label B
AkneeAngle = 0*pi/180+(0*pi/180)/2.*randn(n,1);%defines the angle
that the spin label A is rotates about the molecular Z-axis,
%that is the axis that is normal to the plane of the molecule.
BkneeAngle = 0*pi/180+(0*pi/180)/2.*randn(n,1);%same as above but for
spin label B

randomRotation = 1*pi*2*rand(n,1);%This applies equal random rotation
to both spin labels around the Z-axis.
%This equals rotation of the molecule around its Z-axis.

spinLabelLength = 4;%The distance (in angstrom) from the center of
the N-O bond to the center of the C-C bond opposite. From QM model.
molecularLength = 12;

spinAstartPosition = zeros(n,3);
spinBstartPosition = zeros(n,3);
for c = 1:n;
spinAstartPosition(c,:) =
[cos(moleculebendAngle(c,1))*(molecularLength/2+spinLabelLength) 0
sin(moleculebendAngle(c,1))*(molecularLength/2+spinLabelLength)];
spinBstartPosition(c,:) = [-
cos(moleculebendAngle(c,1))*(molecularLength/2+spinLabelLength) 0
sin(moleculebendAngle(c,1))*(molecularLength/2+spinLabelLength)];
```

```

end

%Rotate the A spin label about the molecular Y-axis. Because the spin
labels are represented as lines
%pointing along the Z-axis. Including rotation of the label around the
Z-axis will not be
%visible in the graphics. Instead the rotation of the label around
the Z-axis (the twist) is introduced in the "Orientations" m-file.

%subtracting (spinAstartPosition-[spinLabelLength 0 0] and then
adding
%this again to spinAstartPosition is done to observe correct
%positioning of the spin centre, and correspondingly the correct
%interspin vector.

spinlabelApositions = zeros(n,3);
for c=1:n;

spinlabelApositions(c,:)=RotateAboutZaxis(AkneeAngle(c,1))*RotateAboutYaxis(AbendAngle(c,1))*(spinAstartPosition(c,:)-[cos(moleculebendAngle(c,1))*(molecularLength/2) 0 sin(moleculebendAngle(c,1))*(molecularLength/2)]);

spinlabelApositions(c,:)=spinlabelApositions(c,:)+[cos(moleculebendAngle(c,1))*(molecularLength/2) 0 sin(moleculebendAngle(c,1))*(molecularLength/2)];
end

%Calculate the orientation of the spin centre of spin label A for
each
%conformer. The initial structure has the the gz aligned with the
magnetic
%field, or [0 0 1]. The orientation of the A spin g-tensor is then
affected
%by the bending and twisting of the spin label.
spinAorientation = zeros(n,3);
for c=1:n;
    spinAorientation(c,:) =
    RotateAboutYaxis(AbendAngle(c,1))*RotateAboutYaxis(-
moleculebendAngle(c,1))*[0 0 1]';
end

%-----Define the relative orientation of spin label B for
each %conformer-----

%Rotate the B spin label about the molecular Y-axis.
spinlabelBpositions = zeros(n,3);
for c=1:n;

spinlabelBpositions(c,:)=RotateAboutZaxis(BkneeAngle(c,1))*RotateAboutYaxis(BbendAngle(c,1))*(spinBstartPosition(c,:)-[cos(moleculebendAngle(c,1))*(molecularLength/2) 0 sin(moleculebendAngle(c,1))*(molecularLength/2)]);
    spinlabelBpositions(c,:)=spinlabelBpositions(c,:)+[-
cos(moleculebendAngle(c,1))*(molecularLength/2) 0 sin(moleculebendAngle(c,1))*(molecularLength/2)];
end

%Calculate the orientation of the spin centre of spin label B for

```

```

each
%conformer.
spinBorientation = zeros(n,3);
for c=1:n;
    spinBorientation(c,:) =
RotateAboutYaxis(BbendAngle(c,1))*RotateAboutYaxis(moleculebendAngle(
c,1))*[0 0 1]';
end

%Calculate the interspin distance for each conformer
explicitdistanceAB = zeros(n,1);
explicitdistanceAB(:,1) = sqrt((spinlabelApositions(:,1)-
spinlabelBpositions(:,1)).^2+(spinlabelApositions(:,2)-
spinlabelBpositions(:,2)).^2+(spinlabelApositions(:,3)-
spinlabelBpositions(:,3)).^2);

explicitdistanceStd=std(explicitdistanceAB);
explicitdistanceMean=mean(explicitdistanceAB);
disp(['Mean distance = ' num2str(explicitdistanceMean)])
disp(['Distance Std = ' num2str(explicitdistanceStd)])

%Calculate the projection of the interspin vector on the laboratory
frame
%(The frame that has the magnetic field pointing along the Z-axis).

rabprojection = zeros(n,3);
for c=1:n;
    rabprojection(c,:) = (spinlabelApositions(c,:)-
spinlabelBpositions(c,:))/norm(spinlabelApositions(c,:)-
spinlabelBpositions(c,:));
end

%plot the vectors representing the molecule and spin labels. The
sphere
%represents the laboratory frame.
figure(11)
% subplot(2,2,1)
[X,Y,Z] = sphere;
% S=mesh(X*3,Y*3,Z*3);%Draw the sphere in the centre
% set(S,'EdgeColor','b');
axis([-10 10 -10 10 -10 10])%define the axis limits of the graphics
for c = 1:m;
line([0 -molecularLength/2*cos(moleculebendAngle(c,1))],[0 0],[0
sin(moleculebendAngle(c,1))*molecularLength/2]);
line([0 molecularLength/2*cos(moleculebendAngle(c,1))],[0 0],[0
sin(moleculebendAngle(c,1))*molecularLength/2]);
end
axis square
xlabel('X','FontSize',18)
ylabel('Y','FontSize',18)
zlabel('Z','FontSize',18)
title('molecule conformers','FontSize',18)
set(gca,'Xtick',[])
set(gca,'Ytick',[])
set(gca,'Ztick',[])
box on

% Draw the spin labels and the interspin vectors

```

```

for c=1:m;
line([cos(moleculebendAngle(c,1))*(molecularLength/2)
spinlabelApositions(c,1)], [0
spinlabelApositions(c,2)], [sin(moleculebendAngle(c,1))*(molecularLength/2) spinlabelApositions(c,3)], 'color', 'red', 'LineWidth', 2); %spin
label A
line([-cos(moleculebendAngle(c,1))*(molecularLength/2)
spinlabelBpositions(c,1)], [0
spinlabelBpositions(c,2)], [sin(moleculebendAngle(c,1))*(molecularLength/2) spinlabelBpositions(c,3)], 'color', 'red', 'LineWidth', 2); %spin
label B
end

```

```

%Show the distance distribution as a histogram
figure(1)
subplot(2,2,2)
distance = 15:0.08:25;
hist(explicitdistanceAB,distance)
title('Distance distribution')

```

```

figure(10)
[hits,~] = histc(explicitdistanceAB,distance);
hits = hits/max(hits);
plot(distance,hits)
title('Distance distribution')
xlabel(['Distance [',char(197),']'], 'FontSize', 18)
ylabel('Probability', 'FontSize', 18)
set(gca, 'FontSize', 18);
xlim([19.4 20.2])

```

```

[x3,y3] = deerload('path to file');
figure(11)
[hits,~] = histc(explicitdistanceAB,distance);
hits = hits/max(hits);
plot_h = plot(distance,hits,'r',x3*10,y3/max(y3),'b');
set(plot_h, 'LineWidth', 2);
% legend_h = legend('from model', 'from orientation average');
% set(legend_h, 'FontSize', 14)
title('Distance distribution', 'FontSize', 18)
xlabel(['Distance [',char(197),']'], 'FontSize', 18)
ylabel('Probability', 'FontSize', 18)
xlim([15 21])
ylim([0 1.1])
set(gca, 'FontSize', 18);

```

## A.3.8 Manual for PELDOR simulation program

### 1 Introduction

The program 'peldorsim' is a Matlab script. The program simulates PELDOR time traces and distance distributions from a pre-defined dynamics model. Both X-band and W-band PELDOR experiments are supported. The program uses the 'loadopr' function of the EasySpin toolbox. Therefore, EasySpin has to be installed on the computer. You are on your own if you try to run this program on anything else than Mac OS.

### 2 How to install and start to use peldorsim

After saving the folder 'peldorsim' to your hard drive start Matlab and set the path to the 'peldorsim' folder and all sub-folders. In Matlab's Command Window type peldorsim and the program's user interface will load.

### 3 peldorsim - user interface

The screenshot displays the 'peldorsim' user interface, which is organized into several sections:

- Experimental data:** Contains three 'Load data' buttons for 'Experimental field sweep', 'Distance distribution', and 'Experimental time traces'.
- Simulation program:** Contains 'Load script' and 'Edit model' buttons.
- Clear all:** A button to reset all settings.
- Close all:** A button to close the interface.
- Pulse settings:** A section with five input fields:
  - Pump freq. in GHz: 9.822 9.822 9.822 9.822 9.822 9.822
  - Probe freq. offset in GHz: 0.04 0.05 0.06 0.07 0.08 0.09
  - Pump pi pulse length in ns: 16 16 16 16 16 16
  - Probe pi/2 pulse length in ns: 16 16 16 16 16 16
  - Probe pi pulse length in ns: 32 32 32 32 32 32
- Simulation settings:** A section with several controls:
  - Number of PELDOR experiments to simulate: 1
  - Number of conformers/rotations: 20000
  - Number of displayed conformers: 200
  - Band selection: Radio buttons for X-band (selected) and W-band.
  - Checkboxes for: Run conformers, Run orientations, Run res. freq., Run excitations, Run time traces, and Orientation corr. (all checked).
  - Buttons for 'Run simulation', 'Load', and 'Save'.

(c) Gunnar W. Regnsson

The user interface is split into three sections.

1. Experimental data:

*Experimental field sweep.* - Optional: Here you can load an experimental field swept spectrum. In X-band mode this has to be an Eleksys file. If in W-band mode this has to be a text file where the field positions are in the first column and the intensity data in the second column.

*Distance distribution.* - Optional: Here you can load an experimental distance distribution. This has to be a distance distribution file from DeerAnalysis.

*Experimental time traces.* - Optional: Here you can load experimental time traces. These time traces have to be background corrected with DeerAnalysis. Multiple files can be selected by holding down the command button. The number of selected time traces has to be equal to the number given in *Number of PELDOR experiments to simulate* in the **Simulation settings** section. **Important.** To make sure the imported experimental time traces are in the same order as the pulse variables in the **Pulse setting** section the filename of the experiment that corresponds to the first number of each field in the **Pulse setting** has to start with '1' . The filename of the second experiment has to start with '2' etc.

*Simulation program.* - Required:

*Load script:* Here you select the Matlab program that performs the simulation. The default program is PsimP1.m. The dynamics model is defined within this program. If another dynamics model is to be used it has to be defined in a new simulation program, e.g. PsimP2.m.

*Edit Model:* Press this button to open up the 'Edit Model' window (see section 4). In the new window you can edit a set of variables for the dynamics model defined in the simulation program PsimP(number). In the current version of the peldorsim there is only one simulation program available.

## 2. Pulse settings:

Here are the frequency positions and lengths of the pump and probe pulses defined. The values for each experiment (field position) is given as a list of numbers separated with a single space. By default this section has numbers for six experiments. The number of experiments in this section has to be equal or larger than the number given in *Number of PELDOR experiments to simulate* in the **Simulation settings** section.

## 3. Simulation settings:

*Number of PELDOR experiments to simulate:* The number of PELDOR time traces to simulate is given in this field. By default its one time trace. The number in this field needs to be equal to or larger than the number of items in the **Pulse settings** field. The number in this field also needs to be equal to the number of experimental time traces selected in **Experimental data**.

*Number of conformers/rotations:* This field sets the number of conformers used in the simulation of PELDOR time traces. By default this number is 20,000. It's recommended not to use a number higher than 40,000 for the number of conformers. Since that only results in longer computation time without any visible improvement to the simulated time traces.

*Number of displayed conformers:*

This field sets the number of conformers to display. By default this value is 200. This number has to be equal to or less than the number given in Number of conformers/rotations. The maximum recommended value for this field is 200 since a higher number will make any editing, e.g. rotation and displacement, of the conformers figure very slow. A number less than 100 may not display the true distribution of conformers.

*X-band, W-band:* These button set the frequency band for the simulated PELDOR experiments. The frequency band selected here set the rules for the type of files that can be imported in the **Experimental data** section.

*Run check boxes:* The 5 check boxes in this section control which part of the simulation program should be executed. The order of calculations in the



simulation program is the following: 1. The conformers are calculated. 2. The orientations for all interspin vectors and spin centres is calculated. 3. The resonance frequencies for all spin centres is calculated. 4. The excitations profiles and the amount of excitation for each spin are calculated. 5. Finally the PELDOR time traces are calculated. Unchecking the unwanted parts of the simulation speeds up the calculation of the parts you are interested in. If changes are made to the dynamics model the *Run conformers* and *Run orientations* boxes need to be checked. If only changes are made to the pulse settings then the *Run conformers* and *Run orientations* boxes can be unchecked. If you are only interested in the conformers and distance distribution then uncheck all boxes except *Run conformers*. Unchecking the *Orientation corr.* box will simulate PELDOR time traces assuming there is no orientation correlation. Only the distance distribution from the model and pulse parameters are used for the simulation of time traces. A distance distribution from other sources can be used for the simulations by loading a file via the *Distance distribution* button. The file must contain a number of distances in a single column vector.

*Run simulation:* This button executes the simulation program selected in the **Experimental - Simulation program** section.

*Load:* This button loads a saved instant of the user interface with user-defined parameters and experimental data files.


*Save:* This button save the user interface including all variables and experimental data files. Note the actual experimental data files are not saved, only the path to the files.

*Clear all:* This button clears all variables in the Matlab workspace. If you want to change the imported experimental data or you are having unexplained problems press this button. Only the paths to the imported data files are deleted when this button is pressed.

*Close all:* This button closes all open windows in Matlab, including the user interface to peldorsim.

## 4 Edit Model - user interface

Model



The diagram shows two coordinate systems, one for spin label A (red vector) and one for spin label B (green vector). A blue vector connects the two spin labels. The axes are labeled x, y, and z.

Distance between spin labelled sites [Å]	mean	std
	<input type="text" value="12"/>	<input type="text" value="0"/>
Distance from spin labelled site and A spin centre [Å]	<input type="text" value="4"/>	<input type="text" value="0"/>
Distance from spin labelled site and B spin centre [Å]	<input type="text" value="4"/>	<input type="text" value="0"/>

Label A	mean	std	Label B	mean	std
xz correlation [degrees]	<input type="text" value="0"/>	<input type="text" value="0"/>	xz correlation [degrees]	<input type="text" value="0"/>	<input type="text" value="0"/>
xy correlation [degrees]	<input type="text" value="0"/>	<input type="text" value="0"/>	xy correlation [degrees]	<input type="text" value="0"/>	<input type="text" value="0"/>
yz correlation [degrees]	<input type="text" value="0"/>	<input type="text" value="0"/>	yz correlation [degrees]	<input type="text" value="0"/>	<input type="text" value="0"/>

In the 'Edit Model' window a figure of the model used by the simulation program is displayed. Green and red vectors represent the spin labels. The blue vector connecting the green and red vectors is the distance vector between the spin-labelled sites, not the interspin vector. The vectors labelled x,y and z, positioned at the end of the green and red vectors, define the frame of the **g**- and  $^{14}\text{N}$  hyperfine matrices.

Below the figure you can edit the correlations between XZ, XY and YZ for each label. Correlations are given in degrees and can be distributed with a normal distribution. XZ correlation means that the X and Z tensor components move in the XZ plane. If XZ correlation has a mean value of  $90^\circ$  and standard deviation (std) of 0 (i.e. no distribution) then the spin label is rotated counter clockwise  $90^\circ$  about the Y component. Now the Z component is parallel and the X component perpendicular to the distance vector. The other correlations can be explained in a similar way. The best way to understand this is to edit the values, run simulations (only the conformers check box needs to be

checked) and look at the conformers figure which shows the orientations of spin labels relative to the distance vector.

To the right of the model figure you can edit the length of the distance vector and the length of the spin labels. The distances are given in angstrom ( $\text{\AA}$ ) and are defined as mean value and one standard deviation. The length of the spin label is defined as the distance between the spin-labelled site and the spin label spin centre. The save and load buttons do the same thing as in the peldorsim user interface.

Note. After editing values make sure to press return or click inside a field. Otherwise the values are not updated.

## 5 Output windows

The simulation program returns four figure windows labelled Figure 1 - 4.

Figure 1 contains the molecular conformers. This figure can be rotated using the rotate 3D tool in the figure tool box. Figure 1 also contains the distance distribution. Random orientations of the interspin vectors are displayed as red dots on a sphere. The orientations of spin centres for each conformer are displayed in Figure 1. The tensor components for both spin centres that are parallel with the magnetic field are displayed as red and black dots on a sphere. The figures showing random orientations of interspin vectors and spin centres can be rotated using the rotate 3D tool.

Figure 2 shows the simulated (red) and (if applicable) experimental (blue) field swept EPR spectrum.

Figure 3 shows the simulated field swept EPR spectrum (black) and the pulse profiles for the detection pulses (red) and inversion pulse (blue).

Figure 4 shows the simulated PELDOR time traces (red) and (if applicable) experimental PELDOR time traces (blue).

## 6 Advanced uses

For advanced use of 'peldorsim' a basic knowledge in Matlab's scripting language is required. The simulation program 'PsimP1.m' is thoroughly

commented to make it readable to users. The following scenarios will require advance use of the simulation program:

1. If EPR parameters for the simulation of the field swept spectrum, e.g. g- and  $^{14}\text{N}$  hyperfine coupling values, need to be changed.
2. The need for specific simulation output figures.
3. The need to change the pulse profiles.
4. The need for more elaborate dynamics model.

## **Publications**

### **Research articles**

1. T. E. Edwards, P. Cekan, G. W. Reginsson, S. A. Shelke, A. R. Ferré-D'Amaré, O. Schiemann, S. Th. Sigurdsson. Crystal structure of a DNA containing the planar, phenoxazine-derived bi-functional spectroscopic probe Ç. *Nucleic Acids Research*, (2011), vol. 39 (10), pp. 4419-4426.
2. G. W. Reginsson, R. I. Hunter, P. A.S. Cruickshank, D. R. Bolton, S. Th. Sigurdsson, G. M. Smith, O. Schiemann. W-band PELDOR with 1kW microwave power: Molecular geometry, flexibility and exchange coupling. *Journal of Magnetic Resonance*, (2012), vol. 216, pp. 175-182.
3. G. W. Reginsson, S. A. Shelke, C. Rouillon, M. F. White, S. Th. Sigurdsson, O. Schiemann. Protein-Induced changes in DNA structure and dynamics observed with noncovalent site-directed spin labeling and PELDOR. *Nucleic Acids Research*, vol. 41(1), pp. e11-e11, doi:10.1093/nar/gks817.
4. G. W. Reginsson, N. C. Kunjir, S. Th. Sigurdsson, O. Schiemann. Trityl radicals: Spin Labels for Nanometer Distance Measurements. *Angewandte Chemie, International Edition*, (2012), vol. 18 (43), pp. 13580-13584.

### **Review articles**

1. G. W. Reginsson, O. Schiemann. Pulsed electron-electron double resonance: beyond nanometer distance measurements on biomacromolecules. *The Biochemical Journal*, (2011), vol. 434(3), pp. 353-363.
2. G. W. Reginsson, O. Schiemann. Studying biomolecular complexes with pulsed electron-electron double resonance spectroscopy. *Biochemical Society Transactions* (2011), vol. 39(1), pp. 128-139.

### **Talks at conferences and seminars**

1. PELDOR measurements on nitroxide biradicals and non-covalently spin labelled DNA using HiPER. 44<sup>th</sup> Annual International Meeting of the ESR Spectroscopy Group of the Royal Society of Chemistry, York, UK (2011).
2. Trityl: A new spin label for nanometer distance measurements. 45<sup>th</sup> Annual International Meeting of the ESR Spectroscopy Group of the Royal Society of Chemistry, Manchester, UK (2012).
3. Non-Covalent and Trityl Labelling for Nanometer Distance Measurements with EPR. Interdisziplinäres Seminar. Fortschritte in der Biophysikalischen Chemie, University of Bonn, Bonn, Germany (2012).
4. Trityl: A new spin label for nanometer distance measurements. Second Annual Meeting of the St Andrews Centre of Magnetic Resonance, University of St Andrews, St Andrews, UK (2012).

### **Posters**

1. Trityl: A New Spin Label for Nanometer Distance Measurements. EUROMAR , Frankfurt, Germany (2011).
2. Non-Covalently Spin Labeled DNA and high-field PELDOR measurements. Hirschegg Meeting 2010, Hirschegg, Germany (2010).
3. Biomolecular structure probed by spin labels and EPR. Biology Post Graduate Conference 2011, University of St Andrews, St Andrews, UK (2011).

## **Original research articles**

# Crystal structure of a DNA containing the planar, phenoxazine-derived bi-functional spectroscopic probe Ç

Thomas E. Edwards<sup>1,\*</sup>, Pavol Cekan<sup>2</sup>, Gunnar W. Reginsson<sup>3</sup>, Sandip A. Shelke<sup>2</sup>, Adrian R. Ferré-D'Amaré<sup>4</sup>, Olav Schiemann<sup>3</sup> and Snorri Th. Sigurdsson<sup>2,\*</sup>

<sup>1</sup>Emerald BioStructures, Bainbridge Island, WA 98110, USA, <sup>2</sup>University of Iceland, Science Institute, Dunhaga 3, 107 Reykjavik, Iceland, <sup>3</sup>Biomedical Sciences Research Complex, Centre of Magnetic Resonance, University of St Andrews, North Haugh, St Andrews, KY16 9ST, UK and <sup>4</sup>Howard Hughes Medical Institute and Division of Basic Sciences, Fred Hutchinson Cancer Research Center, Seattle, WA 98102, USA

Received November 22, 2010; Revised January 4, 2011; Accepted January 5, 2011

## ABSTRACT

Previously, we developed the deoxycytosine analog Ç (C-spin) as a bi-functional spectroscopic probe for the study of nucleic acid structure and dynamics using electron paramagnetic resonance (EPR) and fluorescence spectroscopy. To understand the effect of Ç on nucleic acid structure, we undertook a detailed crystallographic analysis. A 1.7 Å resolution crystal structure of Ç within a decamer duplex A-form DNA confirmed that Ç forms a non-perturbing base pair with deoxyguanosine, as designed. In the context of double-stranded DNA Ç adopted a planar conformation. In contrast, a crystal structure of the free spin-labeled base ç displayed a ~20° bend at the oxazine linkage. Density function theory calculations revealed that the bent and planar conformations are close in energy and exhibit the same frequency for bending. These results indicate a small degree of flexibility around the oxazine linkage, which may be a consequence of the antiaromaticity of a 16- $\pi$  electron ring system. Within DNA, the amplitude of the bending motion is restricted, presumably due to base-stacking interactions. This structural analysis shows that the Ç forms a planar, structurally non-perturbing base pair with G indicating it can be used with high confidence in EPR- or fluorescence-based structural and dynamics studies.

## INTRODUCTION

Interconnected with the central importance of the macromolecular structural scaffold, the dynamics or movements

of structural elements play a key role in all biological processes. Electron paramagnetic resonance (EPR) spectroscopy can provide information on both the dynamics as well as the global structure of biological molecules (1–4). For such studies on nucleic acids, several nitroxide spin labels have been developed (5–11). Most of these reporters contain flexible linkers with one or more rotatable bonds between the nitroxide spin label and the nucleic acid. Flexible linkers introduce uncertainty in the measurement of dynamics, or determination of distances between two nitroxide spin labels due to movement of the probe independent of the nucleic acid. Therefore, we designed and synthesized the rigid nitroxide spin-labeled cytidine analog Ç (C-spin) for use in studies of the structure and dynamics of nucleic acids by EPR spectroscopy (12). The nitroxide moiety of this reporter can be reduced with a mild reducing reagent such as sodium sulfide (Na<sub>2</sub>S) to produce a fluorescent nucleoside (Ç<sup>f</sup>), which was used for detection of mismatches in DNA (13,14). Therefore, both EPR and fluorescence spectroscopies can be used with the same spectroscopic label as illustrated in folding studies of the cocaine DNA aptamer (15) and dynamics of DNA hairpin loops (16). Pulsed electron–electron double resonance (PELDOR) has also been used to determine precise distances and angular orientations within Ç-labeled DNAs (17,18). Thus, this bi-functional reporter allows for the study of nucleic acid structure and dynamics via the complementary spectroscopic techniques of fluorescence and EPR.

As with any reporter group used in biophysical experiments, it is important that the probe does not perturb the structure of the biological system of interest. If the reporter group is structurally perturbing, the results obtained from biophysical experiments would falsely report the nature of the macromolecule. Therefore, the effect of the reporter on the structure of the biopolymer

\*To whom correspondence should be addressed. Tel: +1 206 780 8949; Fax: +1 206 780 8547; Email: tedwards@embios.com  
Correspondence may also be addressed to Snorri Th. Sigurdsson. Tel: +354 525 4800; Fax: +354.552.8911; Email: snorrissi@hi.is



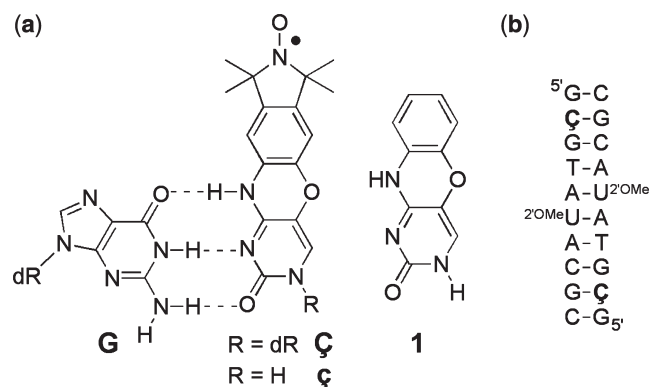


**Figure 1.** (a) Structures of phenoxazine-derived nitroxide spin labels  $\zeta$  and  $\zeta$ , and the unmodified phenoxazine derivative **1**. The spin labels are shown base-paired with guanine (G), with hydrogen bonds indicated by dashed lines. (b) Sequence and secondary structure of the duplex DNA used to obtain a high-resolution crystal structure of a  $\zeta$ -containing DNA helix. dR = 2'-deoxyribose.  $2'OMeU$  = 2'-O-methyluridine.

must be carefully analyzed. Despite the widespread use of spectroscopic probes in biophysical studies, there are very few crystal structures containing covalently bound spectroscopic probes aside from 2-aminopurine for nucleic acids (19–21) and nitroxide spin labels for proteins (22–25). Obtaining a high-resolution crystal structure of a nucleic acid containing a spectroscopic probe remains challenging, and thus most researchers have relied on a variety of biophysical techniques to provide indirect evidence as to whether or not a probe alters the structure of the macromolecule of interest. For example, melting temperature analysis of DNAs containing  $\zeta$  showed only subtle changes in the melting temperatures relative to unlabeled DNAs (16). In addition, EPR studies of dynamics (12,16) and distance measurements (18) aligned well with predicted models. Despite these encouraging biophysical data, no direct structural evidence exists to demonstrate whether or not the reporter  $\zeta$  is structurally perturbing, forms a proper base pair with deoxyguanosine and what may be the preferred conformation. Furthermore, one concern with regards to the structure of the spin-labeled nucleoside was the fact that the phenoxazine-derived nucleobase contains 16  $\pi$ -electrons. This number of electrons in a cyclic  $\pi$ -system indicates antiaromaticity, which could result in non-planarity of the ring system. Because a bend in the nucleobase might affect the use of this probe for biophysical studies, we undertook a detailed analysis of its high-resolution structure.

Here we report a detailed crystallographic characterization of  $\zeta$ . This analysis includes small molecule crystal structures of the  $\zeta$  nucleobase, which has been used for non-covalent spin labeling of nucleic acids containing an abasic site (26), and its phenoxazine analog (**1**) (Figure 1) as well as a 1.7 Å resolution crystal structure of a decamer DNA duplex containing  $\zeta$ . The high-resolution nucleic acid structure demonstrates that within the context of the nucleic acid, the nitroxide spin label  $\zeta$  adopts a planar conformation while forming a standard three hydrogen bond base pair with deoxyguanosine.

These results validate the interpretation of distance and orientation measurements between two  $\zeta$  reporters described previously and provide the basis for further structural and dynamics studies on oligonucleotides with unknown folds.

## MATERIALS AND METHODS

### Small molecule crystallization and structure determination

The nitroxide spin-labeled nucleobase  $\zeta$  was prepared as previously described (26), and the synthesis of phenoxazine **1** is described in the Supplementary Data. Yellow crystals of the  $\zeta$  spin label were obtained by slow evaporation from ethanol. Yellowish-brown crystals of **1** were obtained by slow evaporation from 3:1 dichloromethane:methanol solution. Crystals of  $\zeta$  and **1** were mounted on a Rigaku MM007/Mercury X-ray diffractometer (confocal optics Mo K $\alpha$  radiation, 0.71073 Å). X-ray diffraction experiments were performed at 93 K. Intensity data were collected using accumulated area detector frames spanning at least a hemisphere of reciprocal space for all structures. Data were integrated using Crystal Clear. All data were corrected for Lorentz, polarization and long-term intensity fluctuations. Absorption effects were corrected on the basis of multiple equivalent reflections. The structures were solved by direct methods. Hydrogen atoms bound to carbon were idealized. Structural refinements were obtained with full-matrix least-squares based on F<sup>2</sup> by using the program SHELXTL (27). The theta(max) resolution of the small molecule structure of **1** was 27.52 and the theta(max) resolution of the small molecule structure of  $\zeta$  was 25.3.

### Density function theory calculations

Density function theory (DFT) calculations on the spin-labeled nucleobase  $\zeta$  were performed with the B3LYP functional, the 6-31G\* basis set and unrestricted spin-wave functions using Gaussian03 (28). To obtain a geometry optimized structure and single point energy for the bent spin label, the atoms of the spin label's phenoxazine moiety were frozen to the position obtained from the small molecule crystal structure and hydrogen atoms were added to the vacant positions. The constraints on the phenoxazine moiety were then relaxed to obtain the energy optimized structure and single point energy of the unbent spin label. The vibrational frequencies for both geometry-optimized structures were all positive, indicating the structures represent an energy minimum. The single point energy for the bent and planar spin label was  $-2\,795\,044.283$  kJ/mol and  $-2\,795\,045.594$  kJ/mol respectively. The unbent structure is 1.31 kJ/mol less in energy. The frequency for the bending motion around the oxazine linkage is 18.8 and 28.3  $\text{cm}^{-1}$  for the planar and the bent conformation, respectively.

### DNA crystallization and structure determination

A 10 nt-long DNA containing  $\zeta$  at position 2 and 2'-O-methyl U at position 6 (Figure 1b) was prepared via solid-phase chemical synthesis as described

previously (12,16). The decamer duplex DNA sample containing the nitroxide spin-labeled nucleotide  $\zeta$  was crystallized as described for a similar phenoxazine-containing cytosine analog (29). Crystals were grown at 16°C using the sitting drop vapor diffusion method from 0.4  $\mu$ l of DNA (2.4 mM) mixed with 0.4  $\mu$ l of 10% ( $\pm$ )-2-methane-2,4-pentanediol (MPD), 40 mM sodium cacodylate pH 6.0, 12 mM spermine•HCl, 80 mM NaCl, 12 mM KCl, 12 mM MgCl<sub>2</sub> and equilibrated against a reservoir of 35% MPD. Crystals of the 10 nt-long DNA containing 2'-O-methyl U and  $\zeta$  grew over several months. Most crystals grew as clusters, although one drop contained two single crystals (Supplementary Data). A single crystal was vitrified by plunging into liquid nitrogen and a data set was collected using a Rigaku FR-E<sup>+</sup> SuperBright rotating anode X-ray generator with VariMax HF optics and a Saturn 944<sup>+</sup> CCD detector. The crystal diffracted beyond the resolution limits of the detector at the minimum detector distance (Supplementary Data), and thus a 2 $\theta$  swing of  $-15^\circ$  was used to enhance the resolution limits given the in house X-ray system. Nevertheless, the crystal diffracted beyond the resolution limits of the in house X-ray detection system, as determined by the strong signal in the highest resolution bin ( $I/\sigma = 20$ ; Table 1). The data were reduced with XDS and XSCALE (30). The structure was solved by molecular replacement using PHASER (31) from the CCP4 suite (32) and contained two DNA molecules (i.e. a self-complementary duplex) in the asymmetric unit. The structure was refined with numerous reiterative rounds of refinement in REFMAC (33) and manual building in Coot (34). The final crystallographic model was produced after two additional rounds of refinement in Phenix (35) which utilized a CIF file containing the modified nucleotide linkage definitions generated using the program Jligand (G.N. Murshudov *et al.*, unpublished data).

**Table 1.** Crystallographic statistics for a DNA containing  $\zeta$

Space group	$P2_12_12_1$
Unit cell	$a = 24.71 \text{ \AA}$ , $b = 44.55 \text{ \AA}$ , $c = 45.94 \text{ \AA}$ ; $\alpha = \beta = \gamma = 90^\circ$
Vm	$1.95 \text{ \AA}^3/\text{Da}^a$
Solvent content	57.4%
Resolution	50–1.7 $\text{\AA}$ (1.74–1.70 $\text{\AA}$ ) <sup>b</sup>
$I/\sigma$	54.0 (20.0)
Completeness	94.3% (82.9%)
$R_{\text{merge}}$	0.022 (0.070)
Multiplicity	8.4 (6.4)
Reflections	5613 (354)
Refinement	
$R_{\text{cryst}}$	15.9% (0.138)
$R_{\text{free}}$	19.5% (0.218)
Mean $B$ -factor	$14.5 \text{ \AA}^2$
Number of atoms	
DNA	436
Solvent	83
Total	519

<sup>a</sup>Matthews co-efficient and solvent content calculated based on a predicted duplex DNA MW of 6494 Da.

<sup>b</sup>Values in parenthesis indicated highest of 20 resolution bins for data reduction and highest of four resolution bins for refinement.

## RESULTS AND DISCUSSION

Small molecule crystal structures were determined for the  $\zeta$  nucleobase as well as the phenoxazine analog **1** (Figure 2a and Supplementary Data). The phenoxazine nucleobase **1** adopts a planar conformation with almost no bend at the oxazine linkage between the cytosine and benzene rings (Figure 2a). In contrast,  $\zeta$  adopts a non-planar geometry with a bend of  $\sim 20^\circ$  at the oxazine linkage between the cytosine and benzene rings (Figure 2b and Supplementary Data). In order to rationalize the conformational differences of the phenoxazine moiety, DFT calculations have been performed on  $\zeta$  in the bent conformation as found in the small molecule crystal structure and on  $\zeta$  in the planar conformation as found in the small molecule crystal structure of **1**. These calculations revealed that the bent form is only 1.31 kJ/mol higher in energy than the planar form and that all vibrational frequencies for both conformations are positive. Thus, both conformations are similar energy minima or might actually belong to the same energy minimum. This is supported by the finding that the frequencies for the bending motion differ by only  $10 \text{ cm}^{-1}$  (18 and  $28 \text{ cm}^{-1}$  for the planar and bent conformation, respectively). Taken together, we interpret these results as both conformations belonging to the same energy minimum with a low energy bending motion around the oxazine linkage. Because bending the phenoxazine moiety costs little energy, the surrounding environment such as crystal packing can drive it into either conformation. This raises the question as to whether  $\zeta$  is bent or planar when incorporated into an oligonucleotide structure. Thus, we proceeded to obtain a high-resolution structure of a DNA containing  $\zeta$  to establish the preferred conformation of  $\zeta$  within the context of a nucleic acid.

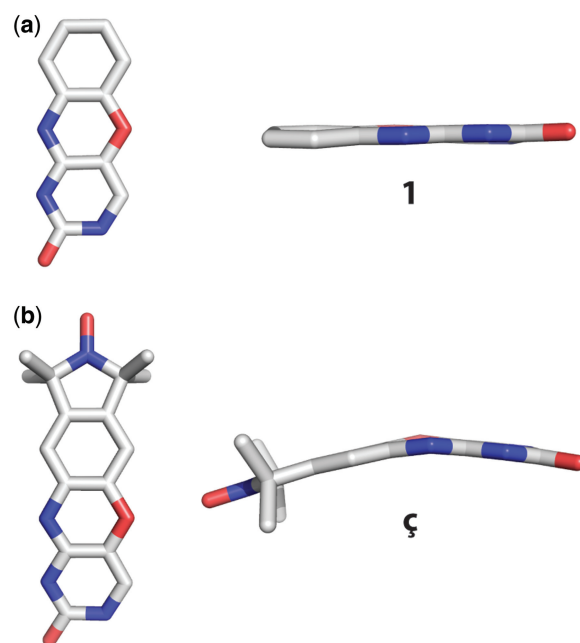


**Figure 2.** Small molecule crystal structures of (a) phenoxazine (**1**) and (b) the nitroxide spin-labeled nucleobase  $\zeta$ .

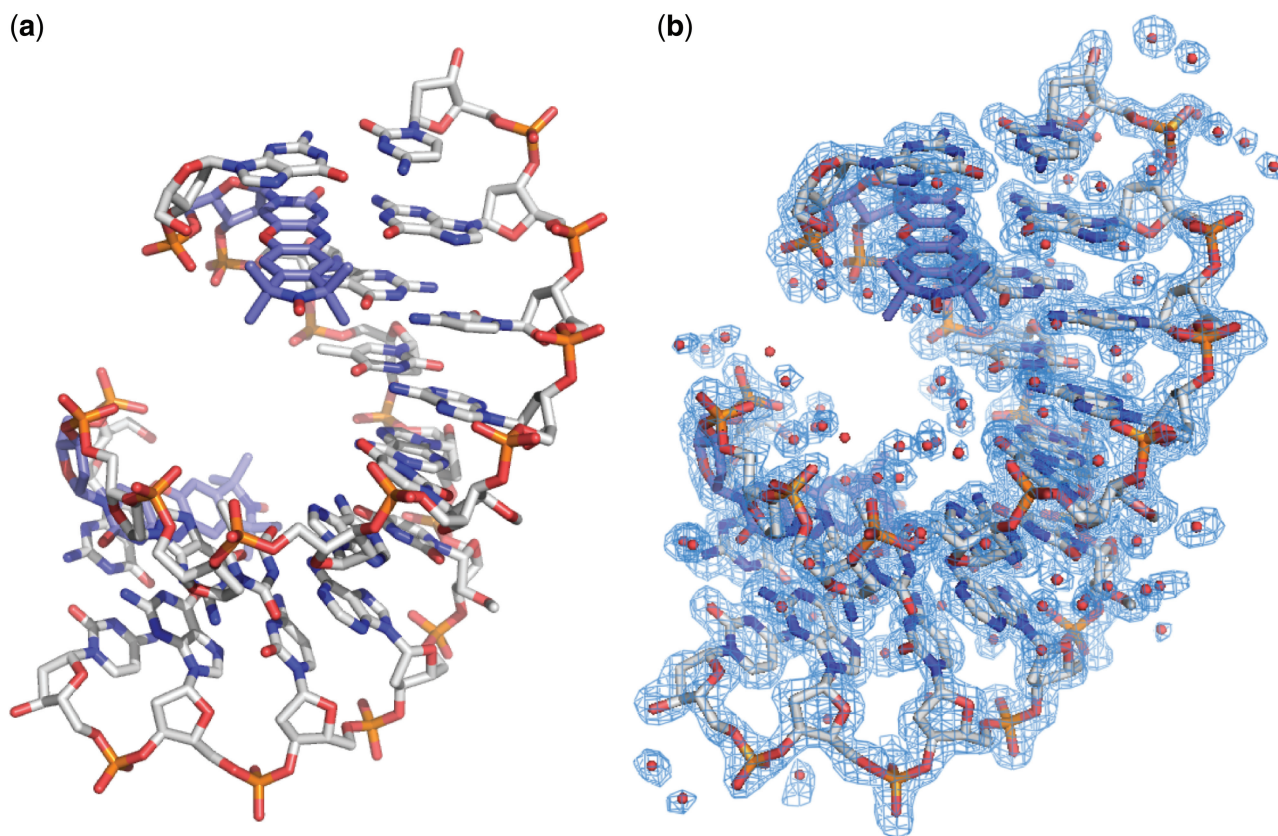


**Figure 3.** Overall crystal structure of a DNA containing Ç. (a) Stick figure representation of an A-form duplex DNA crystal structure containing Ç solved at 1.7 Å resolution. For clarity, Ç is shown in light blue carbon backbone and the remainder of the DNA is shown in gray carbon backbone. (b) Final crystallographic model containing waters overlaid with the  $2|F_o| - |F_c|$  electron density map shown in blue mesh and contoured at 1.0  $\sigma$ .

Initially, we selected two previously reported duplex DNA crystal forms, one A-form (36) and one B-form (37), for incorporation of Ç and subsequent crystallographic structure determination. Each of these crystal forms was chosen because it contained a cytosine residue that in principle had sufficient space within the crystal lattice to accommodate replacement with Ç. We incorporated Ç at positions 4 or 6 of the self-complementary octamer A-form duplex DNA as well as position 9 of the self-complementary dodecamer B-form duplex DNA. Despite producing large, well diffracting crystals using unmodified DNA samples, we observed only thin plate crystals that were unsuitable for structure determination using DNA samples containing Ç (data not shown). Therefore, we sought a different crystal form for incorporation of Ç and structural characterization.

Egli *et al.* (38) reported crystal structures of an A-form decamer DNA duplex with either cytosine or the phenoxazine-derived cytosine analog ‘G-clamp’ (29). These crystal structures contain a 2'-*O*-methoxymethyl T at position 6 that promotes formation of A-form DNA in solution rather than B-form, which is standard for DNA. To our knowledge, the 2'-*O*-methoxymethyl T phosphoramidite is not commercially available, and thus we first produced crystals with a C at position 2 and a 2'-*O*-methyl U at position 6. These crystals diffracted X-rays to better than 2.3 Å resolution in house (data not shown).

Next, a DNA sample was prepared with the nitroxide spin label Ç incorporated into position 2 and a 2'-*O*-methyl U at position 6 (Figure 1b) and resulted in a crystal from which we determined a 1.7 Å resolution crystal structure (Figure 3, Table 1 and Supplementary Data). Crystals suitable for structure determination failed to grow from a sample containing Ç at position 2 with a dT at position 6 (i.e. no 2'-*O*-methyl). EPR spectra of these two Ç-containing samples, one with a 2'-*O*-methyl U at position 6 that should be A-form in solution and one with a dT at position 6 that should be B-form in solution, were found to be nearly identical (Supplementary Data). Thus, there is likely to be little difference in the mobility of the probe in comparison of A- and B-form DNA in solution. Inspection of the electron density maps from our 1.7 Å resolution structure obtained from the DNA sample containing Ç at position 2 and a 2'-*O*-methyl U at position 6 clearly showed the 2'-*O*-methyl group of U6 (Figure 3 and Supplementary Data).

The 1.7 Å resolution crystal structure of the decamer duplex DNA containing Ç at position 2 was initially refined with an abasic site at this position. The resulting omit  $|F_o| - |F_c|$  electron density map showed unambiguous electron density for the Ç nucleobase (Figure 4a). The simulated-annealing omit  $2|F_o| - |F_c|$  electron density map calculated with phases from the refined model was of excellent quality and revealed unambiguously that Ç

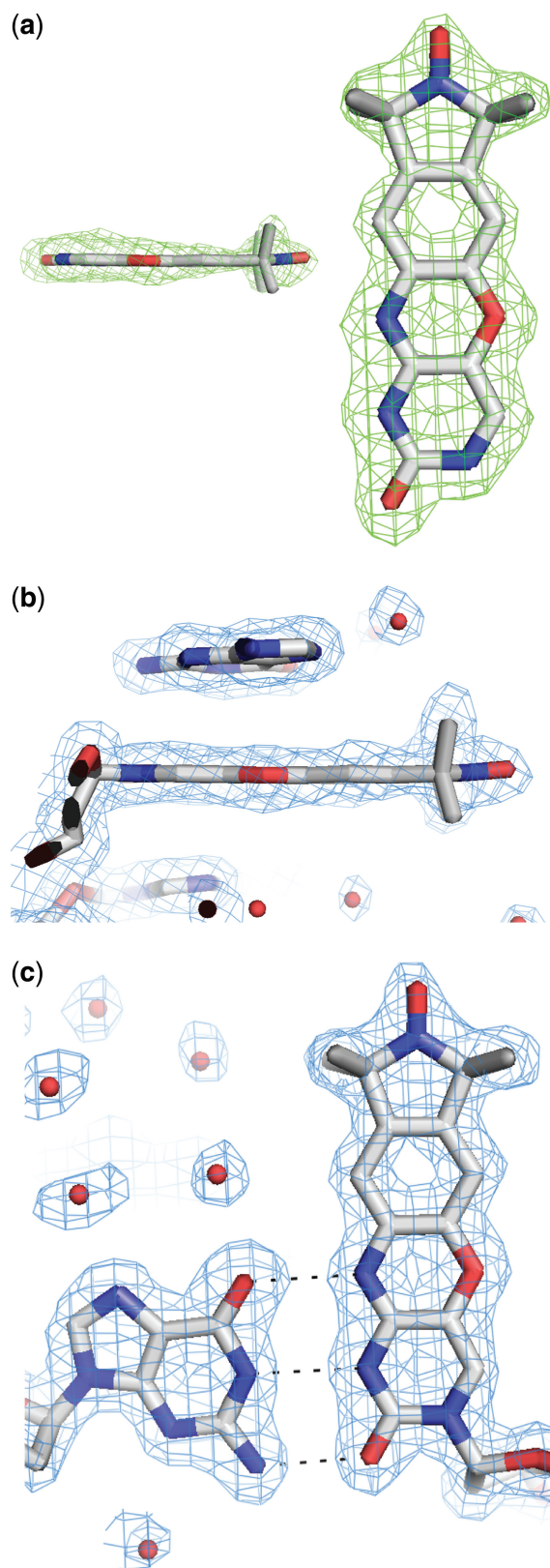


**Figure 4.** Examination of the nitroxide spin-labeled nucleotide Ç within the high-resolution DNA crystal structure. (a) Side- and top-down views of Ç superimposed with the  $|F_o|-|F_c|$  omit electron density map shown in green mesh contoured at  $3.0 \sigma$ . (b) Side view of Ç superimposed with the  $2|F_o|-|F_c|$  electron density map, shown in blue mesh contoured at  $1.0 \sigma$ . (c) Top-down view of the base pair formed by deoxyguanosine and Ç superimposed with the  $2|F_o|-|F_c|$  electron density map shown in blue mesh contoured at  $1.0 \sigma$ . Hydrogen bonds are depicted as dashed lines.

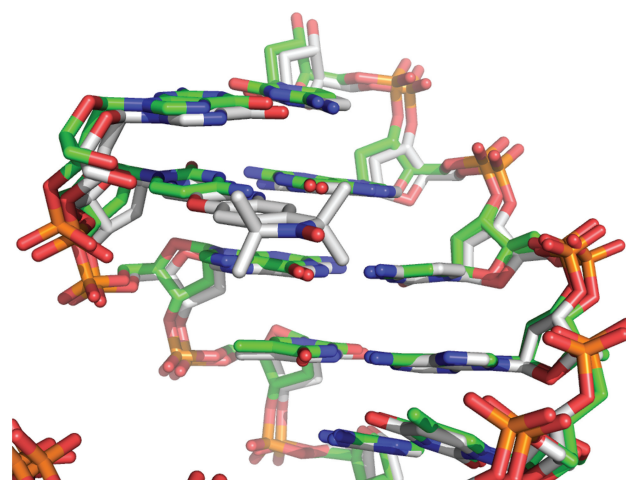


**Figure 5.** Overlay of the  $1.7 \text{ \AA}$  resolution crystal structure of a DNA containing the nitroxide spin-labeled deoxycytosine analog Ç (gray carbon backbone) with a crystal structure containing deoxycytosine at the same position (PDB ID 1DPL, green carbon backbone) (38).

forms a standard base pair with dG9 of the opposite strand with three  $\sim 2.8 \text{ \AA}$  long hydrogen bonds (Figure 4b and c). The structure of the nucleic acid helix containing Ç superimposes closely on a previously reported structure containing a deoxycytidine residue at this position (38) (Figure 5), indicating that Ç does not perturb the DNA structure relative to a standard deoxycytidine residue. EPR spectroscopic analysis showed that Ç had decreased mobility in duplex DNA relative to single-stranded (12,16) or bulged (39) sites and could be used to measure single strand to duplex transitions during folding (15), implying Ç forms a base pair with dG. Furthermore, thermal denaturation experiments showed that the Ç•dG pairing had a similar melting temperature to a dC•dG pair, but showed a decrease in the melting temperature of  $10\text{--}15^\circ\text{C}$  when Ç was paired with dA, dT or dC (12). Combined with the EPR spectroscopy and thermal denaturation results, the high-resolution crystal structure described here shows that Ç is a non-perturbing cytosine analog that forms a Watson–Crick base pair with dG as designed.

The crystal structure shows that within the context of a nucleic acid, Ç adopts a planar geometry (Figure 4b) rather than the bent geometry observed in the crystal structure of ç (Figure 2b). At the oxazine linkage, N4 of Ç is involved in a  $2.9 \text{ \AA}$  hydrogen bond with dG9 of the opposite strand and O5 does not form hydrogen bonds with any water molecules, but rather packs  $3.7 \text{ \AA}$  away from O2P of the Ç phosphate and also C3' of residue G1. This is similar to what was observed for the small molecule crystal structure of phenoxazine 1 alone or the phenoxazine-derived ‘G-clamp’ modified nucleoside (29). At the current resolution limits, no water-mediated interactions were observed off the nitroxide of Ç in the major groove. However, if one extends the model 5' of dG1, it is possible that the nitroxide could make water mediated interactions with the phosphate or base two residues away on the 5' side of Ç. If that residue were a purine, we speculate that additional packing interactions

may be observed with the nitroxide ring. Interestingly, examination of the high-resolution DNA crystal structure shows that the average *B*-factor of the pyrimidine ring (12.9 Å<sup>2</sup>) is lower than either the benzene ring (19.3 Å<sup>2</sup>) or the nitroxide ring (25.2 Å<sup>2</sup>). This demonstrates greater static or dynamic disorder of the nitroxide ring relative to the pyrimidine ring, which could be reflective of the bending motion observed in DFT calculations for the free label **ϕ**. Alternatively, the increased *B*-factors could be reflective of rigid body motion of the entire nucleobase relative to the sugar-phosphate backbone. Nevertheless, the preferred conformation of the nucleobase of **ϕ** in DNA is planar; the amplitude of the bending motion is clearly more restricted within the DNA duplex than observed in the crystal structure of the free label **ϕ**, presumably due to the benefit of van der Waals packing interactions with the 5' deoxyguanosine base (Supplementary Data and below). Although the phenoxazine ring system is formally antiaromatic, it has been shown with 20 and 24  $\pi$  electron N,N-dihydrodiazatetracenes by X-ray crystallography, cyclic voltammetry and nucleus independent chemical shift calculations that they have reduced aromaticity, rather than antiaromaticity (40).

Crystal structures with other phenoxazine-containing compounds include those of the antibiotic actinomycin, which reveal a slight bend at the oxazine linkage (41), and of actinomycin bound to DNA which reveal a planar conformation of the phenoxazine moiety (42–44). We note that there is significant  $\pi$ -stacking interaction of the phenoxazine component of **ϕ** with dG1 (Supplementary Data), as was observed in the G-clamp crystal structure (29) and is consistent with  $\pi$ -stacking in the actinomycin-DNA crystal structures (42–44). Previously, we examined the melting temperature of a series of DNAs to determine the effect of **ϕ**, and in some cases, a +5°C shift in the melting temperature of duplex DNAs containing **ϕ** has been observed (16), which could be consistent with the  $\pi$ -stacking observed in the crystal structure presented here and with other phenothiazine- and phenoxazine-labeled DNA structures (45,46). Increased melting temperatures do not necessarily correlate with  $\pi$ -stacking, but could be due to simple van der Waals packing as observed in crystal structures of a modified deoxycytosine base with a non-aromatic two-ring system (47). Given that the antibiotic actinomycin and **ϕ**/**ϕ** are both observed in planar and bent forms and our DFT calculations show that the bent and planar conformations of **ϕ** are similar in energy and frequency, we predict that other phenoxazine-derived molecules would exhibit a similar general pattern. In summary, the high-resolution crystal structure of a DNA containing **ϕ** showed that the spin label adopts a planar geometry with indicators of modest mobility at the oxazine ring, consistent with small molecule crystal structures, DFT geometry calculations and previously published crystal structures of molecules containing phenoxazine-based compounds, such as actinomycin.

Only a handful of crystal structures of biological macromolecules containing spectroscopic probes have hitherto been reported. We have performed a detailed crystallographic analysis of the nitroxide spin-labeled

deoxycytosine analog **ϕ**. Consistent with previous EPR and fluorescence spectroscopic and thermal stability results, the results presented here demonstrate that **ϕ** is a non-perturbing cytosine analog that forms a Watson–Crick base pair with dG. These results increase the accuracy and interpretation of distance and orientation measurements made with this spectroscopic probe and provide a benchmark for structural characterization of spectroscopic probes.

## DATA BANK ACCESSION CODES

Coordinates and structure factors files have been deposited into the Protein Data Bank with accession code 3OT0.

## SUPPLEMENTARY DATA

Supplementary Data are available at NAR Online.

## ACKNOWLEDGEMENTS

We thank S. Roy and M. Buehl for help with the DFT calculations, A. M. Z. Slawin for X-ray structure determination of nitroxide spin-labeled nucleobase **ϕ** and phenoxazine derivative and A. Gardberg for assistance with JLigand and refinement in Phenix. A.R.F. was a Distinguished Young Scholar in Medical Research of the W.M. Keck Foundation and is an Investigator of the Howard Hughes Medical Institute.

## FUNDING

Icelandic Research Fund (60028021); Research Councils of the UK with a RCUK fellowship (to O.S.); BBSRC (SBSO YBB 016 to O.S. and G.W.) doctoral fellowships (to P.C.); University of Iceland (to S.A.S.); W.M. Keck Foundation, partial (to A.R.F.); Damon Runyon Cancer Research Foundation (DRG-1844-04 to T.E.E.); Emerald BioStructures (to T.E.E.). Funding for open access charge: Icelandic Research Fund (60028021).

*Conflict of interest statement.* None declared.

## REFERENCES

1. Columbus, L. and Hubbell, W.L. (2002) A new spin on protein dynamics. *Trends Biochem. Sci.*, **27**, 288–295.
2. Hubbell, W.L., Cafiso, D.S. and Altenbach, C. (2000) Identifying conformational changes with site-directed spin labeling. *Nat. Struct. Biol.*, **7**, 735–739.
3. Qin, P.Z. and Dieckmann, T. (2004) Application of NMR and EPR methods to the study of RNA. *Curr. Opin. Struct. Biol.*, **14**, 350–359.
4. Schiemann, O. and Prisner, T.F. (2007) Long-range distance determinations in biomacromolecules by EPR spectroscopy. *Q. Rev. Biophys.*, **40**, 1–53.
5. Edwards, T.E. and Sigurdsson, S.T. (2007) Site-specific incorporation of nitroxide spin-labels into 2'-positions of nucleic acids. *Nat. Protoc.*, **2**, 1954–1962.
6. Jakobsen, U., Shelke, S.A., Vogel, S. and Sigurdsson, S.T. (2010) Site-directed spin-labeling of nucleic acids by click chemistry:

- detection of abasic sites in duplex DNA by EPR spectroscopy. *J. Am. Chem. Soc.*, **132**, 10424–10428.
7. Okamoto, A., Inasaki, T. and Saito, I. (2004) Nitroxide-labeled guanine as an ESR spin probe for structural study of DNA. *Bioorg. Med. Chem. Lett.*, **14**, 3415–3418.
  8. Schiemann, O., Piton, N., Plackmeyer, J., Bode, B.E., Prisner, T.F. and Engels, J.W. (2007) Spin labeling of oligonucleotides with the nitroxide TPA and use of PELDOR, a pulse EPR method, to measure intramolecular distances. *Nat. Protoc.*, **2**, 904–923.
  9. Sicoli, G., Wachowius, F., Bennati, M. and Hobartner, C. (2010) Probing secondary structures of spin-labeled RNA by pulsed EPR spectroscopy. *Angew Chem. Int. Ed. Engl.*, **49**, 6443–6447.
  10. Sowa, G.Z. and Qin, P.Z. (2008) Site-directed spin labeling studies on nucleic acid structure and dynamics. *Prog. Nucleic Acid Res. Mol. Biol.*, **82**, 147–197.
  11. Zhang, X.J., Cekan, P., Sigurdsson, S.T. and Qin, P.Z. (2009) *Methods in Enzymology*, Vol. 469. Elsevier pp. 303–328, <http://www.sciencedirect.com/science/bookseries/00766879>.
  12. Barhate, N., Cekan, P., Massey, A.P. and Sigurdsson, S.T. (2007) A nucleoside that contains a rigid nitroxide spin label: a fluorophore in disguise. *Angew Chem. Int. Ed. Engl.*, **46**, 2655–2658.
  13. Cekan, P. and Sigurdsson, S.T. (2008) Single base interrogation by a fluorescent nucleotide: each of the four DNA bases identified by fluorescence spectroscopy. *Chem. Commun.*, 3393–3395.
  14. Gardarsson, H. and Sigurdsson, S.T. (2010) Large flanking sequence effects in single nucleotide mismatch detection using fluorescent nucleoside C(f). *Bioorg. Med. Chem.*, **18**, 6121–6126.
  15. Cekan, P., Jonsson, E.O. and Sigurdsson, S.T. (2009) Folding of the cocaine aptamer studied by EPR and fluorescence spectroscopies using the bifunctional spectroscopic probe C. *Nucleic Acids Res.*, **37**, 3990–3995.
  16. Cekan, P., Smith, A.L., Barhate, N., Robinson, B.H. and Sigurdsson, S.T. (2008) Rigid spin-labeled nucleoside C: a nonperturbing EPR probe of nucleic acid conformation. *Nucleic Acids Res.*, **36**, 5946–5954.
  17. Marko, A., Margraf, D., Cekan, P., Sigurdsson, S.T., Schiemann, O. and Prisner, T.F. (2010) Analytical method to determine the orientation of rigid spin labels in DNA. *Phys. Rev. E Stat. Nonlin. Soft Matter Phys.*, **81**, 021911.
  18. Schiemann, O., Cekan, P., Margraf, D., Prisner, T.F. and Sigurdsson, S.T. (2009) Relative orientation of rigid nitroxides by PELDOR: beyond distance measurements in nucleic acids. *Angew Chem. Int. Ed. Engl.*, **48**, 3292–3295.
  19. Myers, J.C. and Shamoo, Y. (2004) Human UPI as a model for understanding purine recognition in the family of proteins containing the RNA recognition motif (RRM). *J. Mol. Biol.*, **342**, 743–756.
  20. Shandrick, S., Zhao, Q., Han, Q., Ayida, B.K., Takahashi, M., Winters, G.C., Simonsen, K.B., Vourloumis, D. and Hermann, T. (2004) Monitoring molecular recognition of the ribosomal decoding site. *Angew Chem. Int. Ed. Engl.*, **43**, 3177–3182.
  21. Lenz, T., Bonnist, E.Y., Pljevaljcic, G., Neely, R.K., Dryden, D.T., Scheidig, A.J., Jones, A.C. and Weinhold, E. (2007) 2-Aminopurine flipped into the active site of the adenine-specific DNA methyltransferase M.TaqI: crystal structures and time-resolved fluorescence. *J. Am. Chem. Soc.*, **129**, 6240–6248.
  22. Fleissner, M.R., Cascio, D. and Hubbell, W.L. (2009) Structural origin of weakly ordered nitroxide motion in spin-labeled proteins. *Protein Sci.*, **18**, 893–908.
  23. Guo, Z., Cascio, D., Hideg, K. and Hubbell, W.L. (2008) Structural determinants of nitroxide motion in spin-labeled proteins: solvent-exposed sites in helix B of T4 lysozyme. *Protein Sci.*, **17**, 228–239.
  24. Guo, Z., Cascio, D., Hideg, K., Kalai, T. and Hubbell, W.L. (2007) Structural determinants of nitroxide motion in spin-labeled proteins: tertiary contact and solvent-inaccessible sites in helix G of T4 lysozyme. *Protein Sci.*, **16**, 1069–1086.
  25. Hagelueken, G., Ingledew, W.J., Huang, H., Petrovic-Stojanovska, B., Whitfield, C., Elmkami, H., Schiemann, O. and Naismith, J.H. (2009) PELDOR spectroscopy distance fingerprinting of the octameric outer-membrane protein Wza from *Escherichia coli*. *Angew Chem. Int. Ed. Engl.*, **48**, 2904–2906.
  26. Shelke, S.A. and Sigurdsson, S.T. (2010) Noncovalent and site-directed spin labeling of nucleic acids. *Angew Chem. Int. Ed. Engl.*, **49**, 7984–7986.
  27. Sheldrick, G.M. (2008) A short history of SHELX. *Acta Crystallogr. A*, **64**, 112–122.
  28. Frisch, M.J., Trucks, G.W., Schlegel, H.B., Scuseria, G.E., Robb, M.A., Cheeseman, J.R., Montgomery, J.A. Jr, Vreven, T., Kudin, K.N., Burant, J.C. *et al.* (2007). Gaussian, Inc., Wallingford CT, 2004.
  29. Wilds, C.J., Maier, M.A., Tereshko, V., Manoharan, M. and Egli, M. (2002) Direct observation of a cytosine analogue that forms five hydrogen bonds to guanosine: guanidino G-clamp. *Angew Chem. Int. Ed. Engl.*, **41**, 115–117.
  30. Kabsch, W. (2010) Xds. *Acta Crystallogr. D Biol. Crystallogr.*, **66**, 125–132.
  31. McCoy, A.J., Grosse-Kunstleve, R.W., Adams, P.D., Winn, M.D., Storoni, L.C. and Read, R.J. (2007) Phaser crystallographic software. *J. Appl. Crystallogr.*, **40**, 658–674.
  32. The CCP4 suite: programs for protein crystallography. *Acta Crystallogr. D Biol. Crystallogr.*, **50**, 760–763, <http://www.ncbi.nlm.nih.gov/pubmed/15299374>.
  33. Murshudov, G.N., Vagin, A.A. and Dodson, E.J. (1997) Refinement of macromolecular structures by the maximum-likelihood method. *Acta Crystallogr. D Biol. Crystallogr.*, **53**, 240–255.
  34. Emsley, P. and Cowtan, K. (2004) Coot: model-building tools for molecular graphics. *Acta Crystallogr. D Biol. Crystallogr.*, **60**, 2126–2132.
  35. Adams, P.D., Afonine, P.V., Bunkoczi, G., Chen, V.B., Davis, I.W., Echols, N., Headd, J.J., Hung, L.W., Kapral, G.J., Grosse-Kunstleve, R.W. *et al.* (2010) PHENIX: a comprehensive Python-based system for macromolecular structure solution. *Acta Crystallogr. D Biol. Crystallogr.*, **66**, 213–221.
  36. Bingman, C., Li, X., Zon, G. and Sundaralingam, M. (1992) Crystal and molecular structure of d(GTGCAC): investigation of the effects of base sequence on the conformation of octamer duplexes. *Biochemistry*, **31**, 12803–12812.
  37. Sines, C.C., McFail, L., Howerton, S.B., Vanderveer, D. and Williams, L.D. (2000) Cations mediate B-DNA conformational heterogeneity. *J. Am. Chem. Soc.*, **122**, 11048–11056.
  38. Egli, M., Tereshko, V., Teplova, M., Minasov, G., Joachimiak, A., Sanishvili, R., Weeks, C.M., Miller, R., Maier, M.A., An, H. *et al.* (1998) X-ray crystallographic analysis of the hydration of A- and B-form DNA at atomic resolution. *Biopolymers*, **48**, 234–252.
  39. Smith, A.L., Cekan, P., Brewood, G.P., Okonogi, T.M., Alemayehu, S., Hustedt, E.J., Benight, A.S., Sigurdsson, S.T. and Robinson, B.H. (2009) Conformational equilibria of bulged sites in duplex DNA studied by EPR spectroscopy. *J. Phys. Chem. B*, **113**, 2664–2675.
  40. Miao, S., Brombosz, S.M., Schleyer, P.V., Wu, J.L., Barlow, S., Marder, S.R., Hardcastle, K.I. and Bunz, U.H. (2008) Are N,N-dihydrodiazatetracene derivatives antiaromatic? *J. Am. Chem. Soc.*, **130**, 7339–7344.
  41. Schaefer, M., Sheldrick, G.M., Bahner, I. and Lackner, H. (1998) Crystal structures of actinomycin D and actinomycin Z3. *Angew Chem. Int. Ed. Engl.*, **37**, 2381–2384.
  42. Hou, M.H., Robinson, H., Gao, Y.G. and Wang, A.H. (2002) Crystal structure of actinomycin D bound to the CTG triplet repeat sequences linked to neurological diseases. *Nucleic Acids Res.*, **30**, 4910–4917.
  43. Robinson, H., Gao, Y.G., Yang, X., Sanishvili, R., Joachimiak, A. and Wang, A.H. (2001) Crystallographic analysis of a novel complex of actinomycin D bound to the DNA decamer CGATC GATCG. *Biochemistry*, **40**, 5587–5592.
  44. Takusagawa, F., Takusagawa, K.T., Carlson, R.G. and Weaver, R.F. (1997) Selectivity of F8-actinomycin D for RNA:DNA hybrids and its anti-leukemia activity. *Bioorg. Med. Chem.*, **5**, 1197–1207.
  45. Engman, K.C., Sandin, P., Osborne, S., Brown, T., Billeter, M., Lincoln, P., Norden, B., Albinsson, B. and Wilhelmsson, L.M. (2004) DNA adopts normal B-form upon incorporation of highly fluorescent DNA base analogue tC: NMR structure and UV-Vis spectroscopy characterization. *Nucleic Acids Res.*, **32**, 5087–5095.

46. Sandin,P., Borjesson,K., Li,H., Martensson,J., Brown,T., Wilhelmsson,L.M. and Albinsson,B. (2008) Characterization and use of an unprecedentedly bright and structurally non-perturbing fluorescent DNA base analogue. *Nucleic Acids Res.*, **36**, 157–167.
47. Magat Juan,E.C., Shimizu,S., Ma,X., Kurose,T., Haraguchi,T., Zhang,F., Tsunoda,M., Ohkubo,A., Sekine,M., Shibata,T. *et al.* (2010) Insights into the DNA stabilizing contributions of a bicyclic cytosine analogue: crystal structures of DNA duplexes containing 7,8-dihydropyrido [2,3-d]pyrimidin-2-one. *Nucleic Acids Res.*, **38**, 6737–6745.

# Crystal Structure of a DNA Containing the Planar, Phenoxazine-Derived Bi-functional Spectroscopic Probe $\mathbf{\zeta}$

Thomas E. Edwards,<sup>\*,†</sup> Pavol Cekan,<sup>‡</sup> Gunnar W. Reginsson,<sup>||</sup> Sandip A. Shelke,<sup>‡</sup> Adrian R. Ferré-D'Amaré,<sup>§</sup> Olav Schiemann,<sup>||</sup> Snorri Th. Sigurdsson<sup>\*,‡</sup>

<sup>†</sup>Emerald BioStructures, Bainbridge Island, WA 98110 USA; <sup>‡</sup>University of Iceland, Science Institute, Dunhaga 3, 107 Reykjavik, Iceland; <sup>||</sup>Centre for Biomolecular Sciences, Centre for Magnetic Resonance, University of St. Andrews, North Haugh, UK; <sup>§</sup>Howard Hughes Medical Institute and Division of Basic Sciences, Fred Hutchinson Cancer Research Center, Seattle, WA 98102, USA

[tedwards@embios.com](mailto:tedwards@embios.com), [snorrisi@hi.is](mailto:snorrisi@hi.is)

## Supporting Information

General	S2
Synthesis of compound <b>1</b>	S2-S8
<b>Table S1.</b> DFT calculations of $\mathbf{\zeta}$ in a planar conformation	S9
<b>Figure S1.</b> DFT IR spectrum of $\mathbf{\zeta}$ in the planar conformation	S10
Coordinates for $\mathbf{\zeta}$ in the planar conformation from DFT calculations	S11
<b>Table S2.</b> DFT calculations of $\mathbf{\zeta}$ in a bent conformation	S12
<b>Figure S2.</b> DFT IR spectrum of $\mathbf{\zeta}$ in the bent conformation	S13
Coordinates for $\mathbf{\zeta}$ in the bent conformation from DFT calculations	S14
<b>Figure S3.</b> Thermal ellipsoid plot of the small molecule crystal structure of <b>1</b>	S15
<b>Figure S4.</b> Packing of phenoxazine ( <b>1</b> ) within the small molecule crystal lattice	S15
<b>Figure S5.</b> Thermal ellipsoid plot of the small molecule crystal structure of $\mathbf{\zeta}$	S16
<b>Figure S6.</b> Packing of $\mathbf{\zeta}$ within the small molecule crystal lattice	S16
<b>Figure S7.</b> EPR spectra of DNA samples containing $\mathbf{\zeta}$ used in crystallography	S17
<b>Figure S8.</b> Images of DNA crystals containing $\mathbf{\zeta}$	S17
<b>Figure S9.</b> Diffraction pattern of DNA crystal containing $\mathbf{\zeta}$	S15
<b>Figure S10.</b> Model and electron density for 2'-O-methyl U residues	S16
<b>Figure S11.</b> All atom lsq overlay of DNA chains A and B	S16
<b>Figure S12.</b> Stacking of $\mathbf{\zeta}$ with dA1 from DNA chain A	S17
<b>Figure S13.</b> Planarity of $\mathbf{\zeta}$ from DNA chains A and B	S17
Coordinates for crystal structure of <b>1</b>	
Crystallographic Information File (CIF) for crystal structure of <b>1</b>	
Coordinates for crystal structure of $\mathbf{\zeta}$	
Crystallographic Information File (CIF) for crystal structure of $\mathbf{\zeta}$	

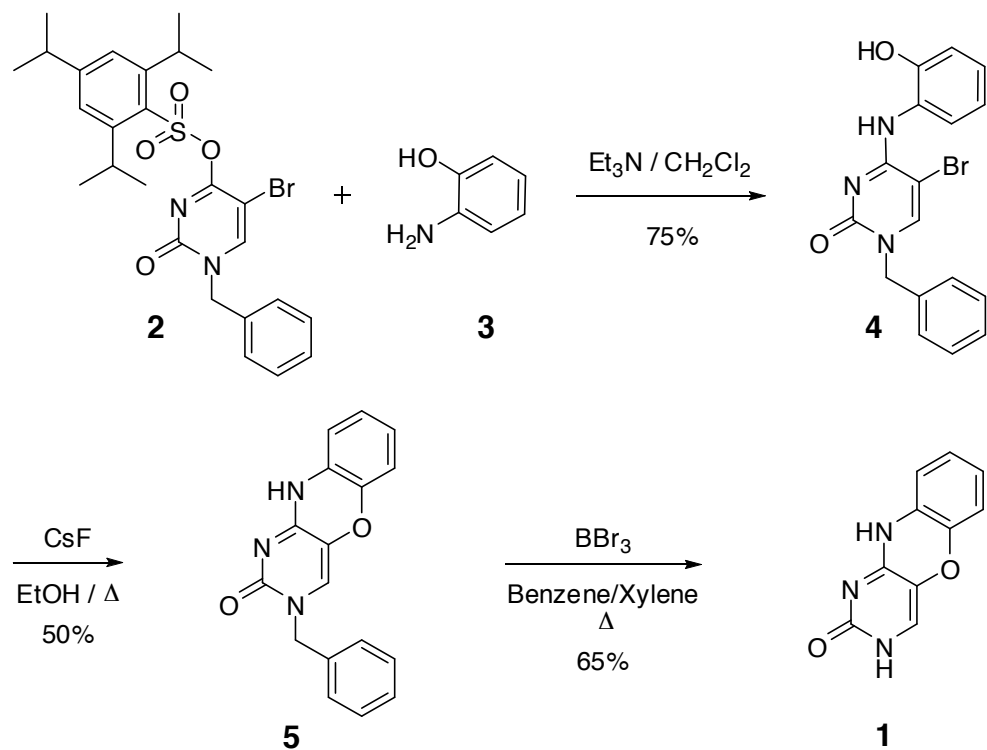


## General

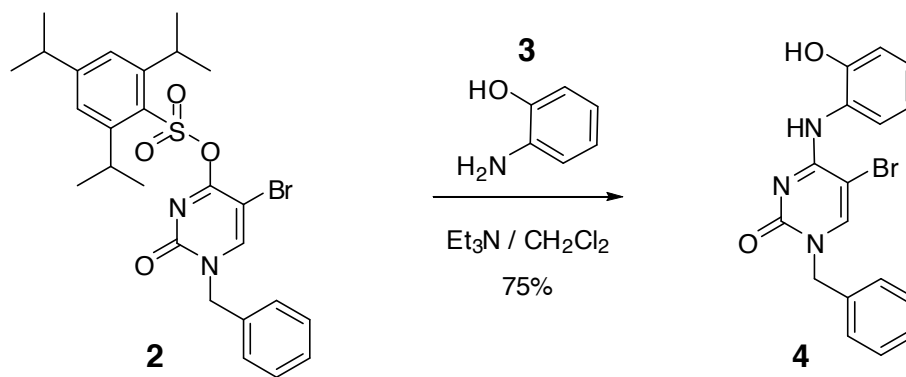
All air and moisture sensitive reactions were performed in oven-dried reaction flasks, under an argon atmosphere. All commercial reagents were purchased from Sigma-Aldrich and used without further purification. Dichloromethane was freshly distilled over calcium hydride before use. Thin layer chromatography (TLC) was performed on glass backed TLC with extra hard layer (Kieselgel 60 F<sub>254</sub>, 250  $\mu$ m, Silicycle) and compounds visualized was by UV light. Silica gel (230-400 mesh, 60 Å) was purchased from Silicycle and used for flash column chromatography. Nuclear magnetic resonance (NMR) spectra were recorded on a Bruker Avance 400 MHz spectrometer and the chemical shifts were reported in parts per million (ppm) relative to the residual proton signal (for <sup>1</sup>H NMR) and the carbon signal (for <sup>13</sup>C NMR) of the deuterated solvents used [*d*<sub>6</sub>-DMSO (2.50 ppm), CDCl<sub>3</sub> (7.26 ppm), *d*<sub>4</sub>-MeOH (4.84 and 3.31 ppm)] for <sup>1</sup>H NMR; [*d*<sub>6</sub>-DMSO (39.52 ppm), CDCl<sub>3</sub> (77.0 ppm), *d*<sub>4</sub>-MeOH (49.05 ppm)] for <sup>13</sup>C NMR. Molecular mass of organic compounds were determined by HR-APCI-MS (Bruker, MicroTof-Q).

## Synthesis of compound 1.

The phenoxazine derivative **1** (Scheme S1) was prepared by following the similar synthetic strategy to that of spin label **ç** (Shelke, S. A.; Sigurdsson, S. T. *Angew Chem Int Ed Engl* **2010**, *in press*; DOI: 10.1002/anie.201002637). The coupling of *O*<sup>4</sup>-sulphonyl-activated 1-benzyl-5-bromo-2-oxo-1,2-dihydropyrimidin-4-yl 2,4,6-triisopropylbenzenesulfonate (**2**) with 2-amino phenol in presence of triethyl amine yielded conjugate **4**, which on treatment with cesium fluoride afforded ring closed phenoxazine derivative **5**. The deprotection of *N**I*-protected benzyl group was facilitated by boron tribromide to give the compound **1**.



**Scheme S1.** Synthesis of compound **1**.

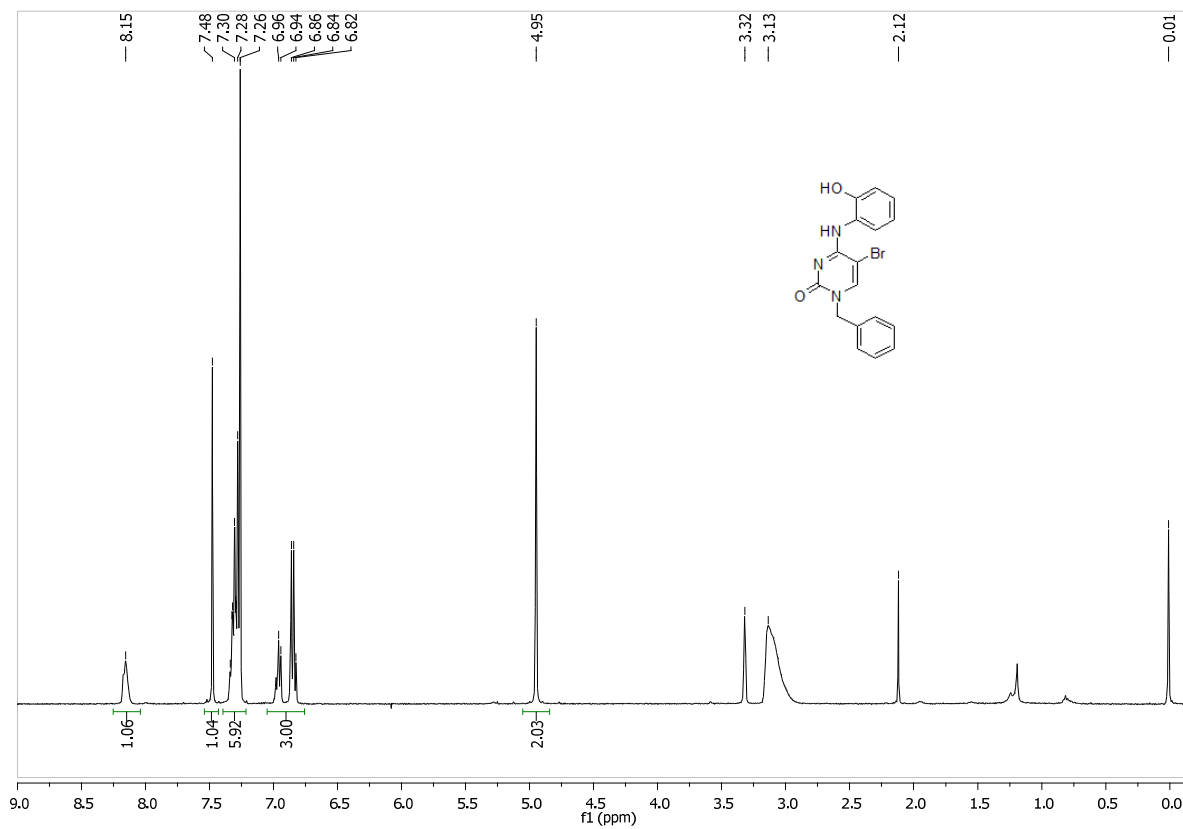


**1-benzyl-5-bromo-4-(2-hydroxyphenylamino) pyrimidin-2(1H)-one (4).** 2-amino phenol (**3**, 0.22 g, 2.01 mmol) was added to a solution of **2** (0.55 g, 1.005 mmol) in CH<sub>2</sub>Cl<sub>2</sub> (10 mL), followed by Et<sub>3</sub>N (0.28 mL, 2 mmol). The resulting reaction mixture was stirred for 36 h in dark, diluted with CH<sub>2</sub>Cl<sub>2</sub> (40 mL) and washed with H<sub>2</sub>O (15 mL), saturated sodium bicarbonate solution (15 mL) and brine (15 mL). The organic layer was dried over anhydrous sodium sulphate and concentrated. The crude product was purified by flash column chromatography using 5% CH<sub>3</sub>OH/CH<sub>2</sub>Cl<sub>2</sub> to yield a pale yellow solid (0.28 g, 75% yield).

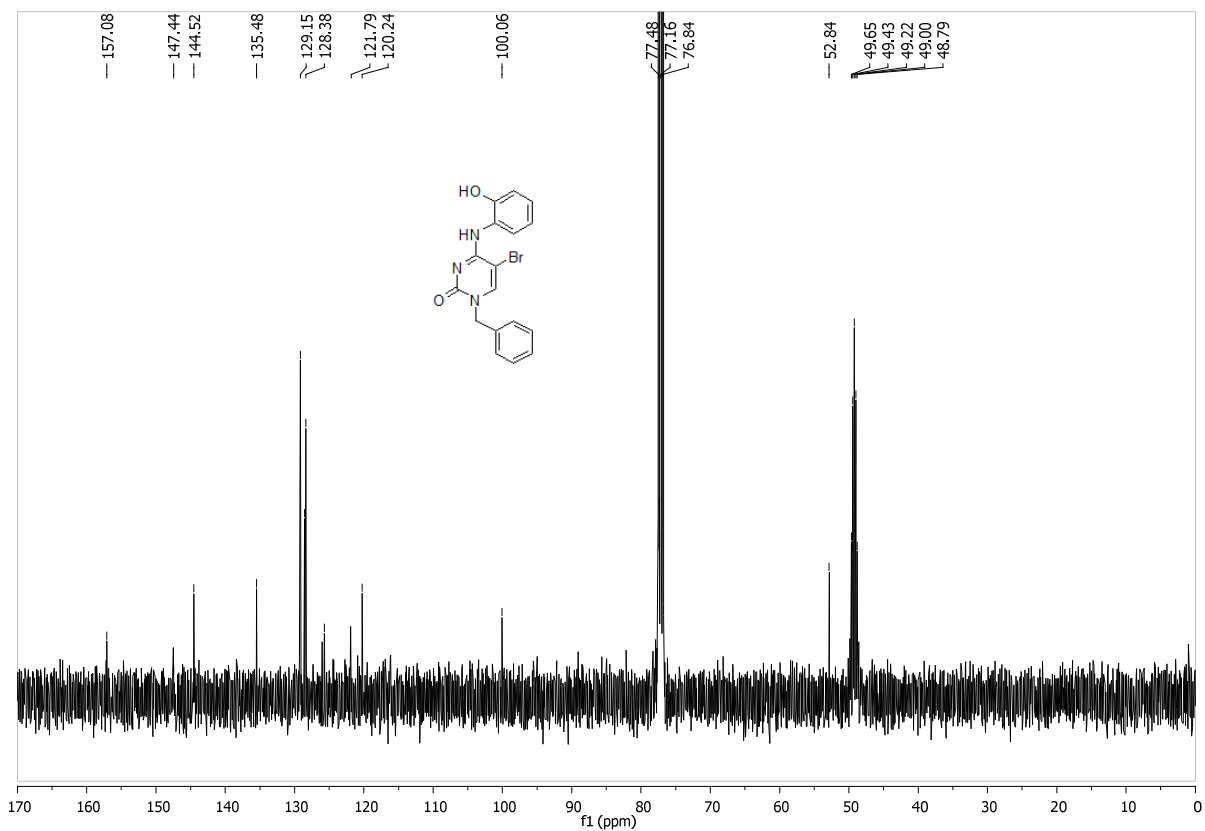
<sup>1</sup>H-NMR (95:5 CDCl<sub>3</sub>:CD<sub>3</sub>OD): δ 8.15 (bs, 1H, ArH), 7.48 (s, 1H, ArH), 7.28-7.32 (m, 5H, ArH), 6.82-6.96 (m, 3H, ArH), 4.95 (s, 2H, CH<sub>2</sub>) ppm.

<sup>13</sup>C NMR (95:5 CDCl<sub>3</sub>:CD<sub>3</sub>OD): δ 157.08, 147.44, 144.52, 135.48, 129.15, 128.38, 121.79, 120.24, 100.06, 52.84 ppm.

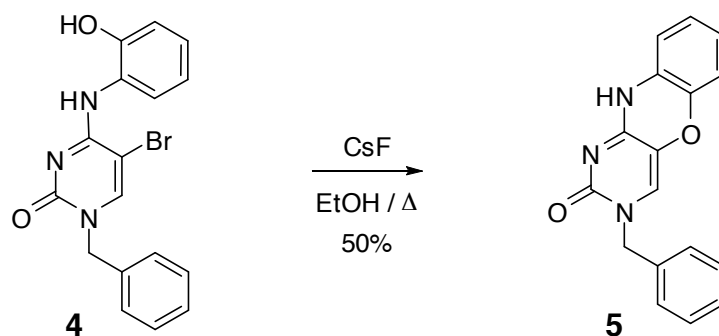
HR-APCI-MS: Calculated for C<sub>17</sub>H<sub>14</sub>BrN<sub>3</sub>O<sub>2</sub> 371.0269, found 372.0357 (M+1).



<sup>1</sup>H NMR Spectrum of 4



<sup>13</sup>C NMR spectrum of 4

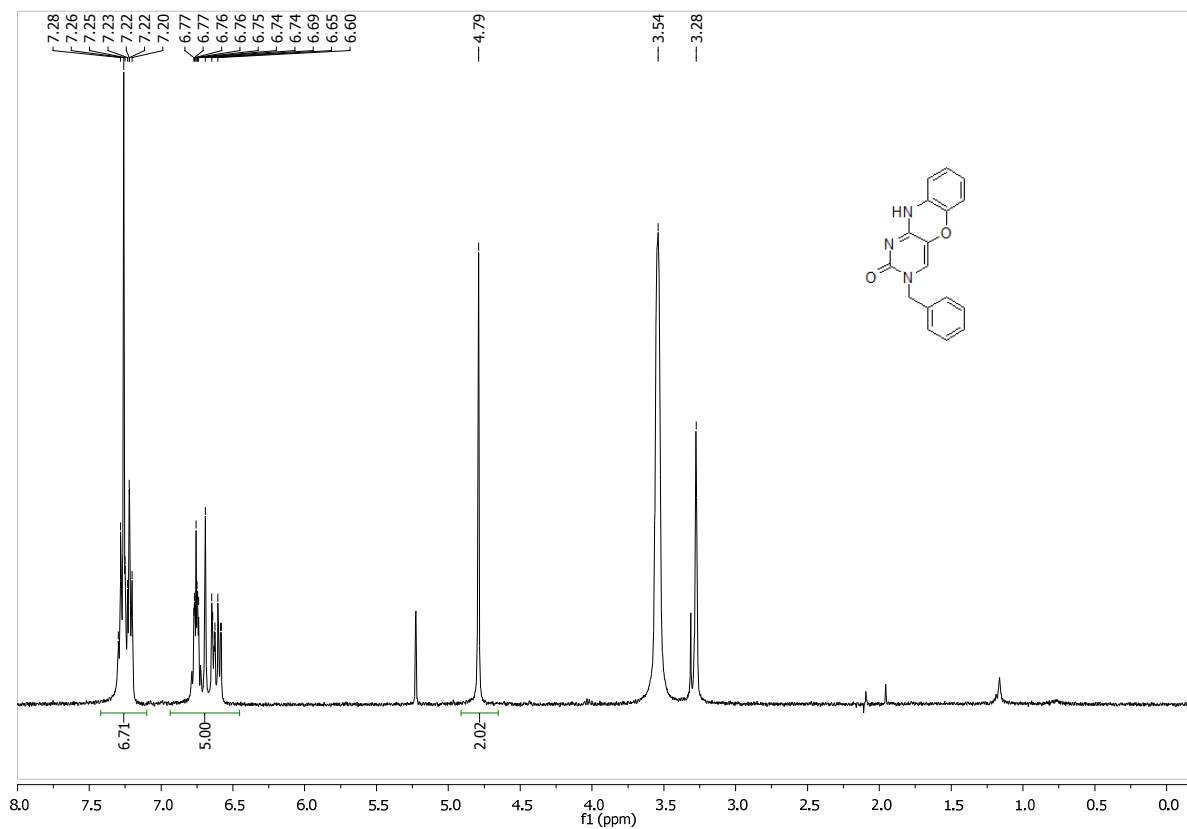


**Compound 5.** A solution of **4** (0.16 g, 0.4298 mmol) in ethanol (5 mL) was treated with CsF (0.65 g, 4.28 mmol) and stirred at 85 °C for 48 h. The solvent was evaporated and the crude product was purified by flash column chromatography using a gradient of 99:1 to 95:5 CH<sub>2</sub>Cl<sub>2</sub>/MeOH, containing 1% aqueous ammonia to give **5** as a pale yellow solid (0.062 g, 50% yield).

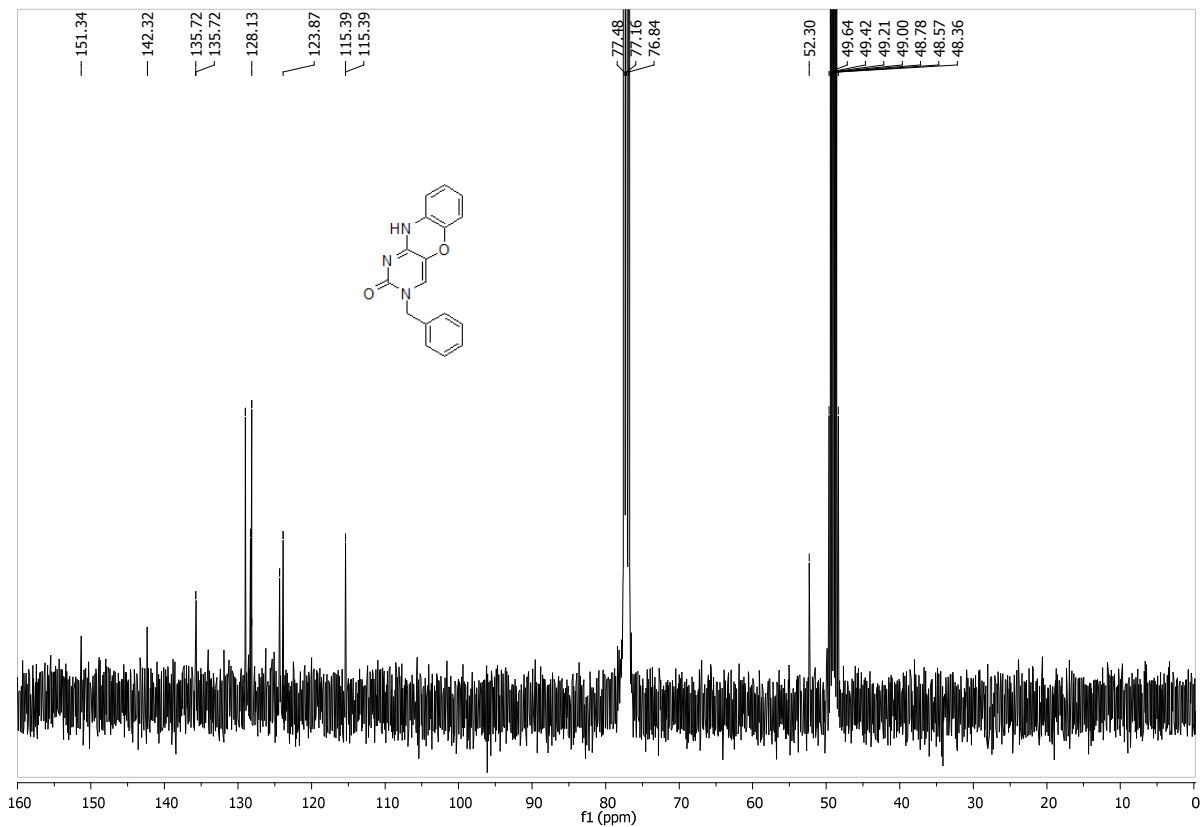
<sup>1</sup>H-NMR (90:10 CDCl<sub>3</sub>:CD<sub>3</sub>OD): δ 7.20-7.28 (m, 5H, ArH), 6.64-6.77 (m, 2H, ArH), 6.69 (s, 1H, ArH), 6.60-6.65 (m, 2H, ArH), 4.79 (s, 2H, CH<sub>2</sub>) ppm.

<sup>13</sup>C NMR (90:10 CDCl<sub>3</sub>:CD<sub>3</sub>OD): δ 151.34, 142.32, 135.72, 128.13, 123.87, 115.39, 52.30 ppm.

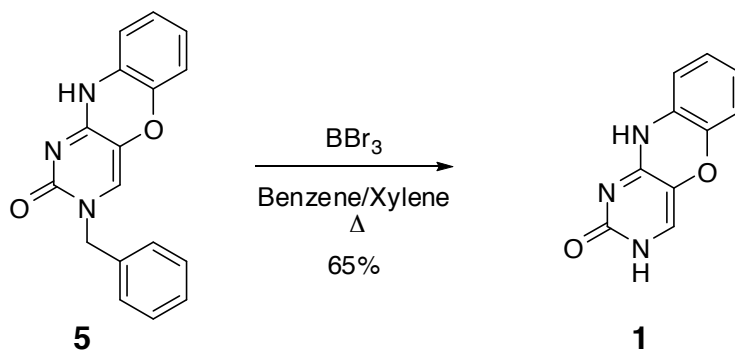
HR-APCI-MS: Calculated for C<sub>17</sub>H<sub>13</sub>N<sub>3</sub>O<sub>2</sub> 291.1008, found 292.1028 (M+1).



<sup>1</sup>H NMR Spectrum of **5**



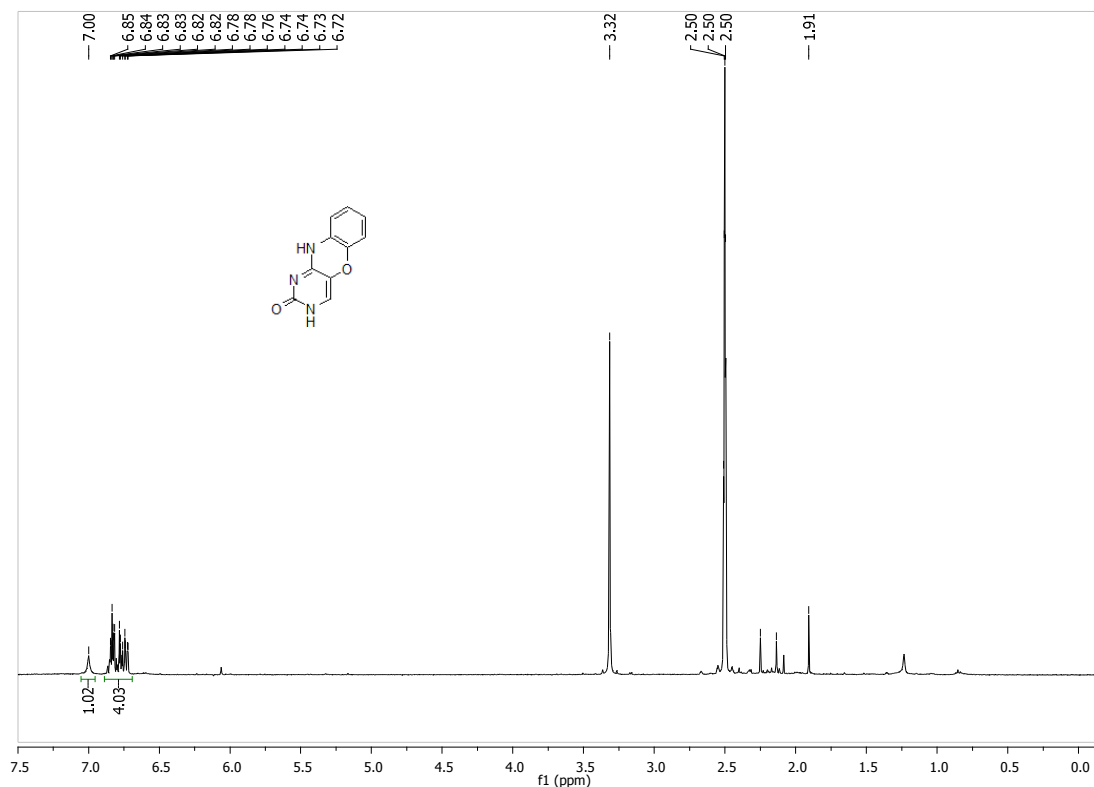
<sup>13</sup>C NMR spectrum of **5**



**Compound 1.** BBr<sub>3</sub> (0.048 mL, 0.5145 mmol) was added to a suspension of **5** (30 mg, 0.1029 mmol) in mixture of benzene and xylene (5 mL, 50:50), and the resulting reaction mixture was stirred at 135 °C for 12 h in a sealed tube before quenching the reaction by addition of methanol (1 mL). The solvent was removed under reduced pressure and the crude product was purified by preparative chromatography using 10% MeOH/CH<sub>2</sub>Cl<sub>2</sub> containing 1% aqueous ammonia to yield a light brown solid (13 mg, 65% yield).

<sup>1</sup>H NMR (*d*<sub>6</sub>-DMSO): δ 6.72-6.85 (m, 4H, ArH), 7.00 (s, 1H, CH) ppm.

HR-APCI-MS: Calculated for C<sub>10</sub>H<sub>7</sub>N<sub>3</sub>O<sub>2</sub> 201.0538, found 202.0466 (M+1).



<sup>1</sup>H NMR spectrum of **1**

**Table S1.** Frequencies and intensities from DFT frequency calculations on the geometry optimized  $\zeta$  spin label in the planar conformation.

Frequencies	Intensities
18.78	0.59
30.56	0.68
51.24	3.86
85.46	2.01
99.13	3.59
117.41	0.88
117.89	1.31
166.19	0.04
207.29	0.92
211.85	0.19
213.68	1.22
215.16	0.11
217.41	0.06
258.45	0.70
259.67	0.28
261.21	0.99
274.94	0.03
299.72	0.18
317.79	9.65
320.38	0.18
345.07	2.75
353.86	0.58
375.79	23.43
391.24	0.14
412.92	9.42
438.78	0.12
461.46	0.42
503.58	9.67
523.23	0.03
527.68	51.87
535.31	0.88
550.43	18.00
571.77	1.68
585.60	1.69
590.09	109.60
602.33	2.59
652.99	6.62
672.45	1.61
688.91	0.41
719.52	1.46
743.12	3.07
749.19	0.83
759.16	27.15
765.11	0.35
781.86	5.20
845.83	13.47
867.89	11.67
867.98	13.26
882.88	8.24
885.24	23.28
888.61	2.84
948.74	0.00

949.57	0.15
952.83	5.96
961.32	2.10
1027.21	0.11
1028.18	0.08
1038.64	1.69
1090.63	0.59
1141.90	35.24
1147.98	25.99
1182.84	0.19
1183.35	15.28
1185.41	18.55
1195.58	132.55
1203.52	5.66
1208.52	10.43
1260.24	9.21
1277.17	37.61
1285.82	11.15
1311.49	13.46
1334.22	6.17
1355.41	20.45
1376.41	467.01
1414.95	0.97
1416.39	26.14
1417.60	13.01
1433.36	0.90
1436.09	23.52
1448.54	210.35
1488.91	53.34
1502.89	0.03
1506.65	342.99
1507.00	2.69
1515.38	0.14
1518.13	2.97
1522.61	219.73
1526.65	65.19
1528.84	139.13
1537.61	6.11
1539.29	1.21
1550.50	175.57
1619.77	547.54
1646.24	6.48
1672.81	31.79
1732.44	131.05
1817.52	805.46
3056.30	0.02
3056.57	32.90
3060.74	30.64
3061.74	0.60
3127.33	0.58
3128.78	17.47
3132.11	50.77
3133.47	7.47

3142.04	0.00
3142.62	14.33
3145.47	5.12
3146.23	42.82
3186.01	8.94
3213.01	2.45
3243.84	3.58
3611.05	60.63
3622.93	101.80



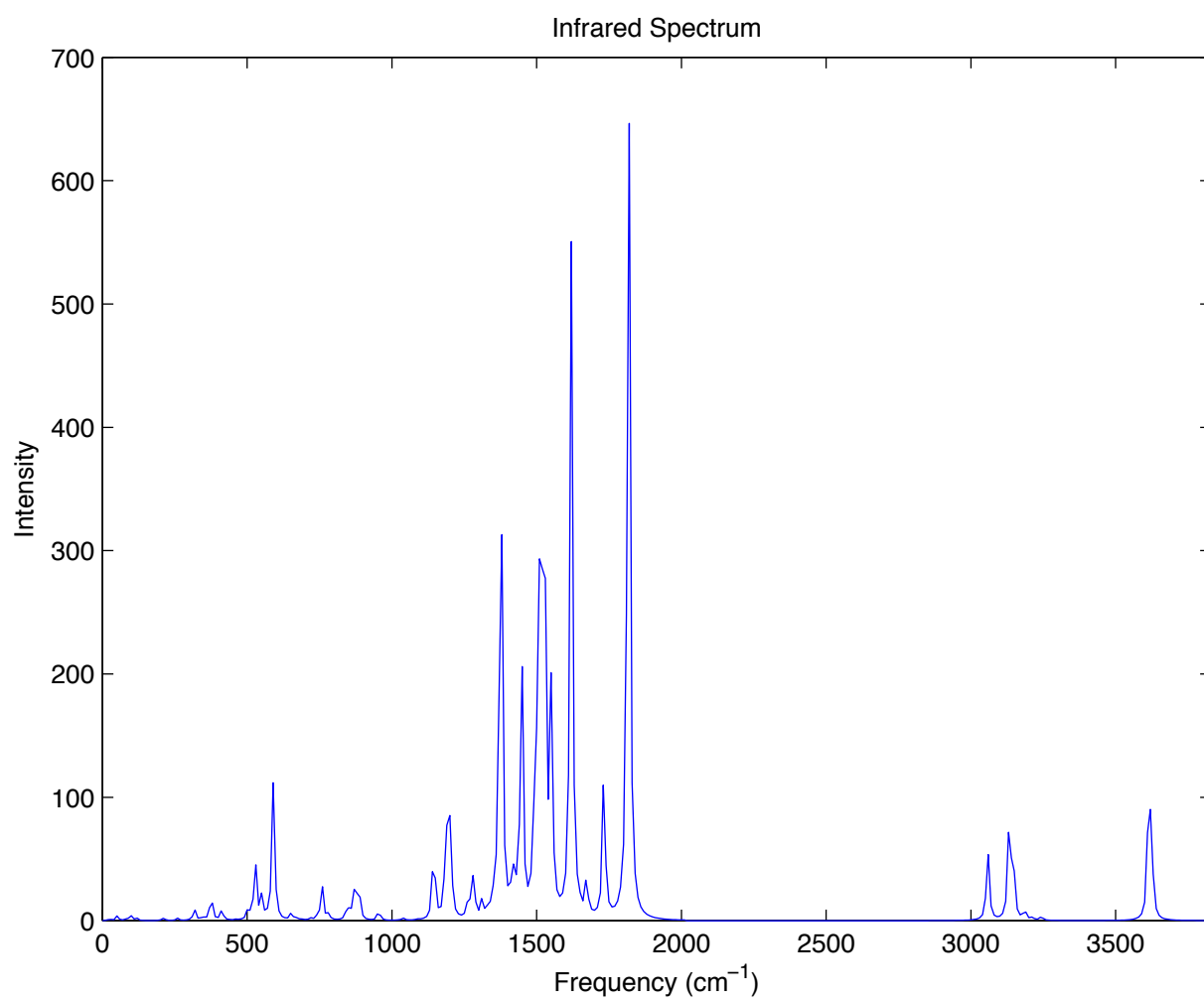


**Figure S1.** DFT IR spectrum of  $\mathbf{\zeta}$  in the planar conformation.

Coordinates for  $\zeta$  in the planar conformation from DFT calculations

O	-4.911925	-3.862008	9.219636
C	-4.103746	-3.743416	8.315366
N	-3.616735	-4.904645	7.662796
C	-2.710704	-4.885853	6.638118
H	-2.402788	-5.831082	6.206707
C	-2.236844	-3.692264	6.206022
O	-1.319957	-3.629393	5.173185
C	-0.873438	-2.384873	4.776238
C	0.047798	-2.335180	3.737106
H	0.373679	-3.267540	3.286294
C	0.521377	-1.094888	3.309327
C	1.517882	-0.816636	2.204907
O	2.313785	1.356977	1.493285
N	1.573640	0.672374	2.271680
C	0.710039	1.310703	3.306418
C	0.074885	0.080600	3.918107
C	-0.848992	0.030752	4.960232
H	-1.203759	0.939007	5.441675
C	-1.329324	-1.205756	5.395929
N	-2.258040	-1.313951	6.438204
C	-2.735926	-2.518884	6.873858
N	-3.603113	-2.538057	7.854164
C	1.025685	-1.244663	0.810406
H	0.015720	-0.868994	0.619027
H	1.011747	-2.336621	0.724899
H	1.699319	-0.839949	0.049083
C	2.919242	-1.390575	2.482284
H	3.262326	-1.119030	3.485449
H	3.626178	-0.988559	1.750284
H	2.911194	-2.483000	2.402180
C	-0.300121	2.246975	2.618277
H	-0.955527	1.688313	1.942915
H	0.241988	2.998529	2.036523
H	-0.921932	2.757870	3.361610
C	1.593729	2.100113	4.289540
H	2.292115	1.436478	4.808788
H	0.978042	2.610478	5.038316
H	2.168910	2.849138	3.737014
H	-3.989101	-5.779783	8.006807
H	-2.609853	-0.489892	6.908492

**Table S2.** Frequencies and intensities from DFT frequency calculations on the geometry optimized  $\zeta$  spin label in the bent conformation.

Frequencies	Intensities
28.31	0.45
41.74	1.06
51.64	3.44
89.80	0.99
95.89	5.10
120.80	1.37
124.32	0.91
166.99	0.05
202.63	1.56
211.87	0.01
214.53	0.06
218.63	0.35
223.38	0.88
257.51	0.54
260.33	0.74
263.94	0.70
279.12	1.17
300.51	0.17
318.17	9.69
325.93	1.08
345.44	2.56
353.68	1.18
378.09	18.75
391.87	0.35
413.48	10.37
438.41	0.70
463.64	0.26
502.31	9.92
523.16	0.48
531.31	4.66
550.85	3.83
559.83	42.13
573.11	4.50
590.78	2.69
598.07	101.96
603.50	34.78
653.52	8.08
674.10	2.20
689.81	0.93
721.42	2.47
744.32	3.29
751.18	1.08
760.19	27.49
765.47	0.18
781.46	5.55
845.82	17.84
868.28	13.75
868.57	11.11
885.32	0.81
887.50	28.03
888.23	5.30
948.17	0.02

948.94	0.36
952.70	5.81
960.93	2.03
1025.55	0.12
1026.31	0.10
1037.87	1.66
1090.38	0.69
1140.86	32.57
1146.90	28.93
1183.70	0.25
1184.30	15.15
1185.55	18.54
1194.95	125.21
1203.46	8.78
1207.35	9.78
1260.64	8.26
1273.81	38.23
1284.43	11.14
1311.57	14.17
1334.35	4.03
1354.44	35.30
1373.85	471.31
1413.59	0.40
1415.20	30.62
1416.26	18.72
1432.03	2.85
1435.28	23.49
1448.62	214.19
1488.70	59.62
1503.81	7.72
1504.55	370.66
1507.85	3.24
1514.70	0.71
1517.24	4.02
1520.69	311.61
1525.94	52.80
1528.24	14.26
1536.80	5.61
1538.41	1.36
1549.01	142.50
1618.47	476.03
1646.10	6.06
1672.84	32.57
1732.41	125.44
1818.41	806.12
3056.39	1.37
3056.72	31.38
3060.95	30.58
3061.98	0.64
3127.48	0.07
3128.81	17.79
3132.33	51.59
3133.65	6.41

3141.87	1.62
3142.70	13.30
3145.45	7.09
3146.34	40.08
3186.29	8.81
3213.21	2.43
3243.65	3.27
3601.93	52.56
3622.01	102.71

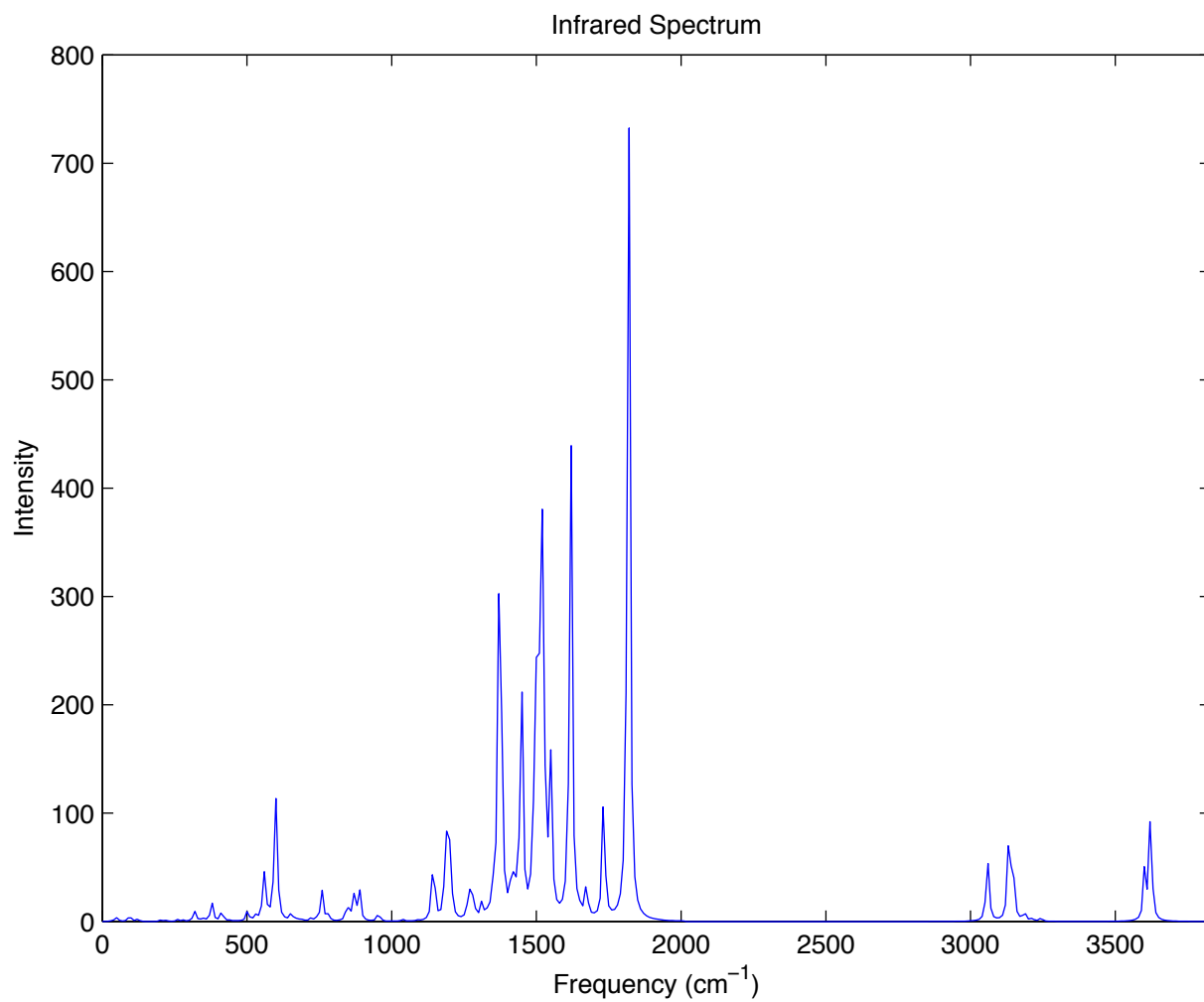


**Figure S2.** DFT IR spectrum of  $\zeta$  in the bent conformation.

Coordinates for  $\zeta$  in the bent conformation from DFT calculations

O	-5.188737	-3.822481	8.916236
C	-4.266471	-3.714672	8.127335
N	-3.764802	-4.875444	7.483490
C	-2.735846	-4.870108	6.582933
H	-2.425860	-5.814143	6.150277
C	-2.137908	-3.691618	6.283641
O	-1.056856	-3.637025	5.423110
C	-0.711337	-2.393927	4.926363
C	0.151494	-2.344974	3.839049
H	0.482470	-3.278134	3.393671
C	0.568038	-1.101970	3.362006
C	1.497357	-0.822270	2.200872
O	2.174243	1.355466	1.386896
N	1.490810	0.669129	2.214072
C	0.687347	1.306931	3.296735
C	0.120654	0.074537	3.968564
C	-0.749147	0.024591	5.056703
H	-1.107633	0.934119	5.532985
C	-1.167161	-1.214588	5.545199
N	-2.040541	-1.331185	6.636733
C	-2.657537	-2.518598	6.934482
N	-3.647848	-2.522819	7.789774
C	0.959404	-1.319457	0.847170
H	-0.074202	-0.994365	0.693279
H	0.990545	-2.413375	0.797584
H	1.577501	-0.912784	0.041070
C	2.933790	-1.327954	2.429286
H	3.311606	-1.008938	3.405652
H	3.587939	-0.922279	1.651647
H	2.968664	-2.421871	2.385013
C	-0.383585	2.213754	2.664328
H	-1.075730	1.632026	2.047686
H	0.104743	2.960849	2.031439
H	-0.959520	2.731583	3.439191
C	1.619534	2.127304	4.207538
H	2.364146	1.484736	4.687555
H	1.045043	2.635921	4.989374
H	2.141298	2.879186	3.607894
H	-4.226475	-5.739463	7.735239
H	-2.451977	-0.502876	7.049081

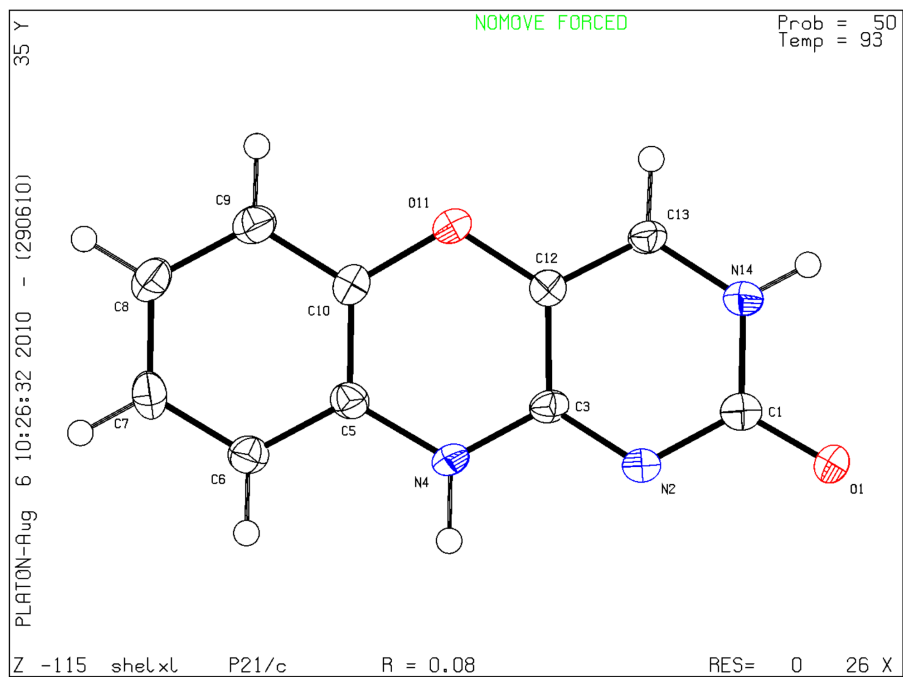


**Figure S3.** Thermal ellipsoid plot of the small molecule crystal structure of **1**.

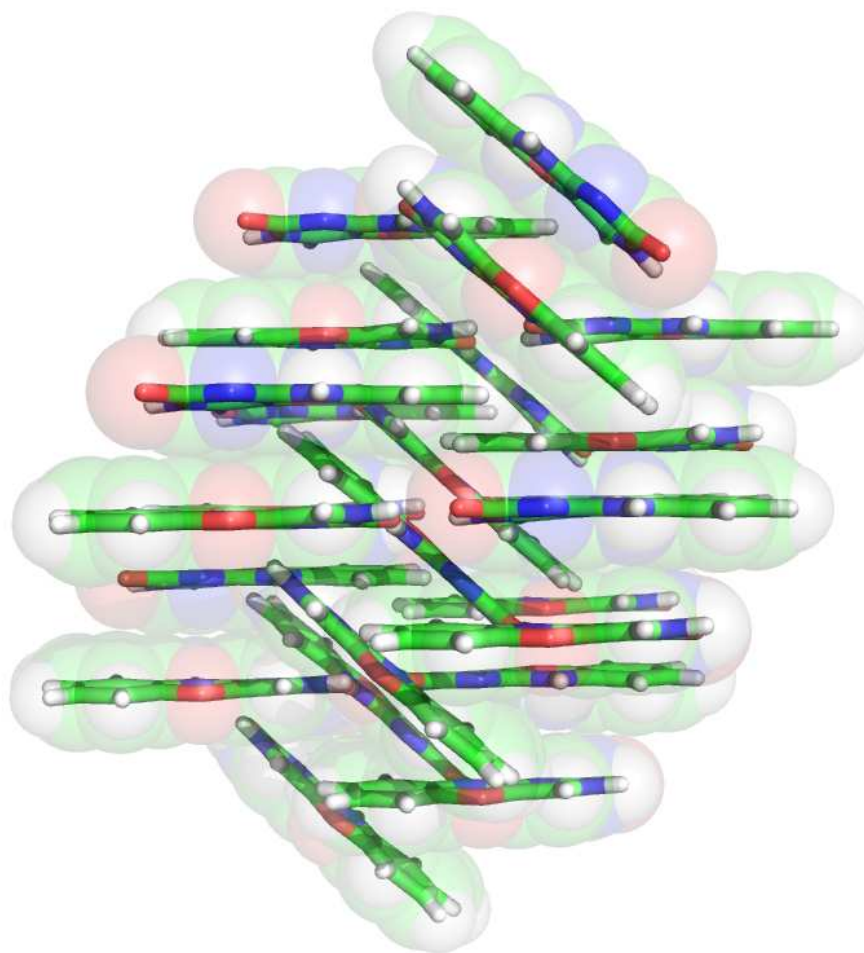


**Figure S4.** Packing of phenoxazine (**1**) within the small molecule crystal lattice.

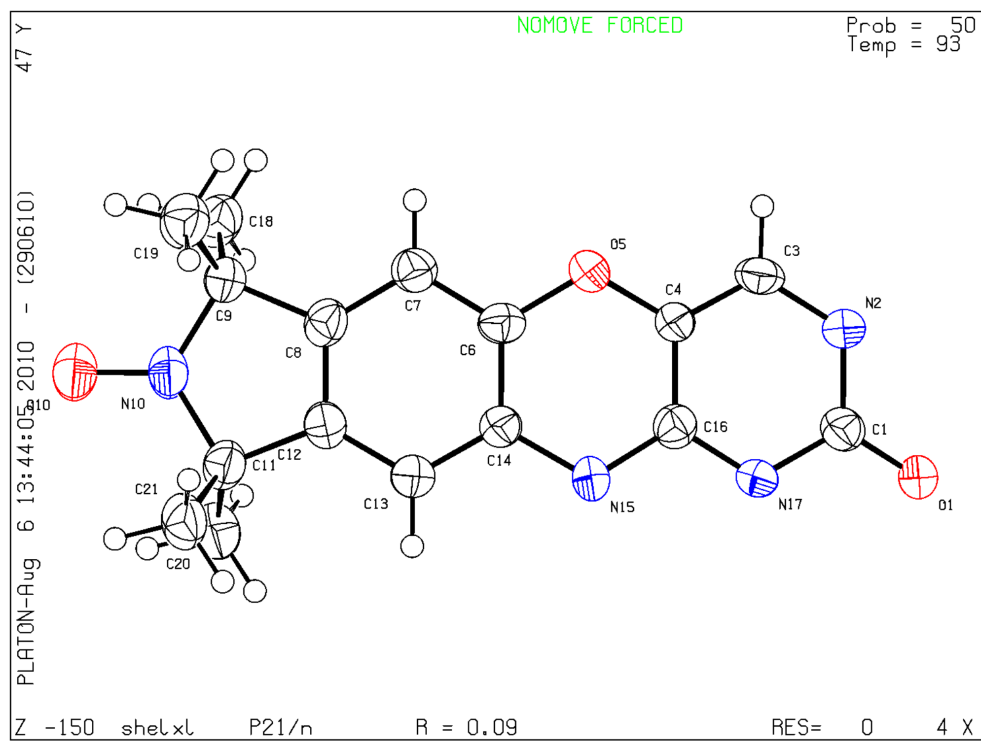


**Figure S5.** Thermal ellipsoid plot of the small molecule crystal structure of  $\bar{q}$ .

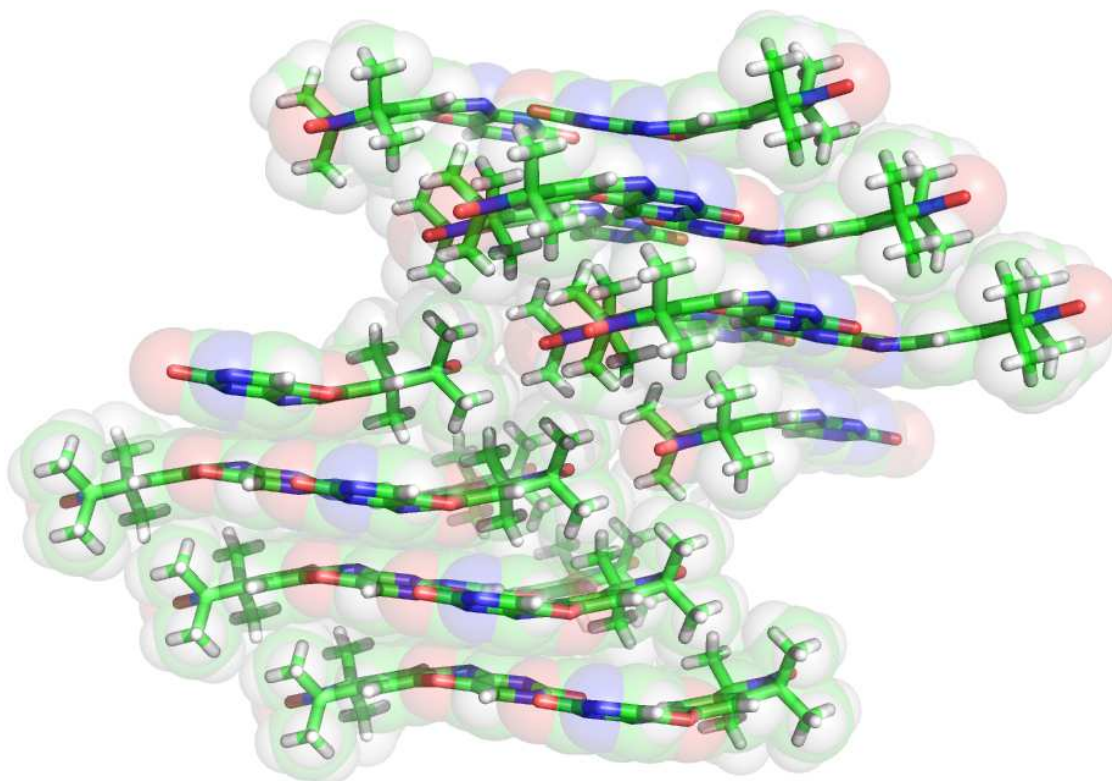


**Figure S6.** Packing of  $\bar{q}$  within the small molecule crystal lattice.

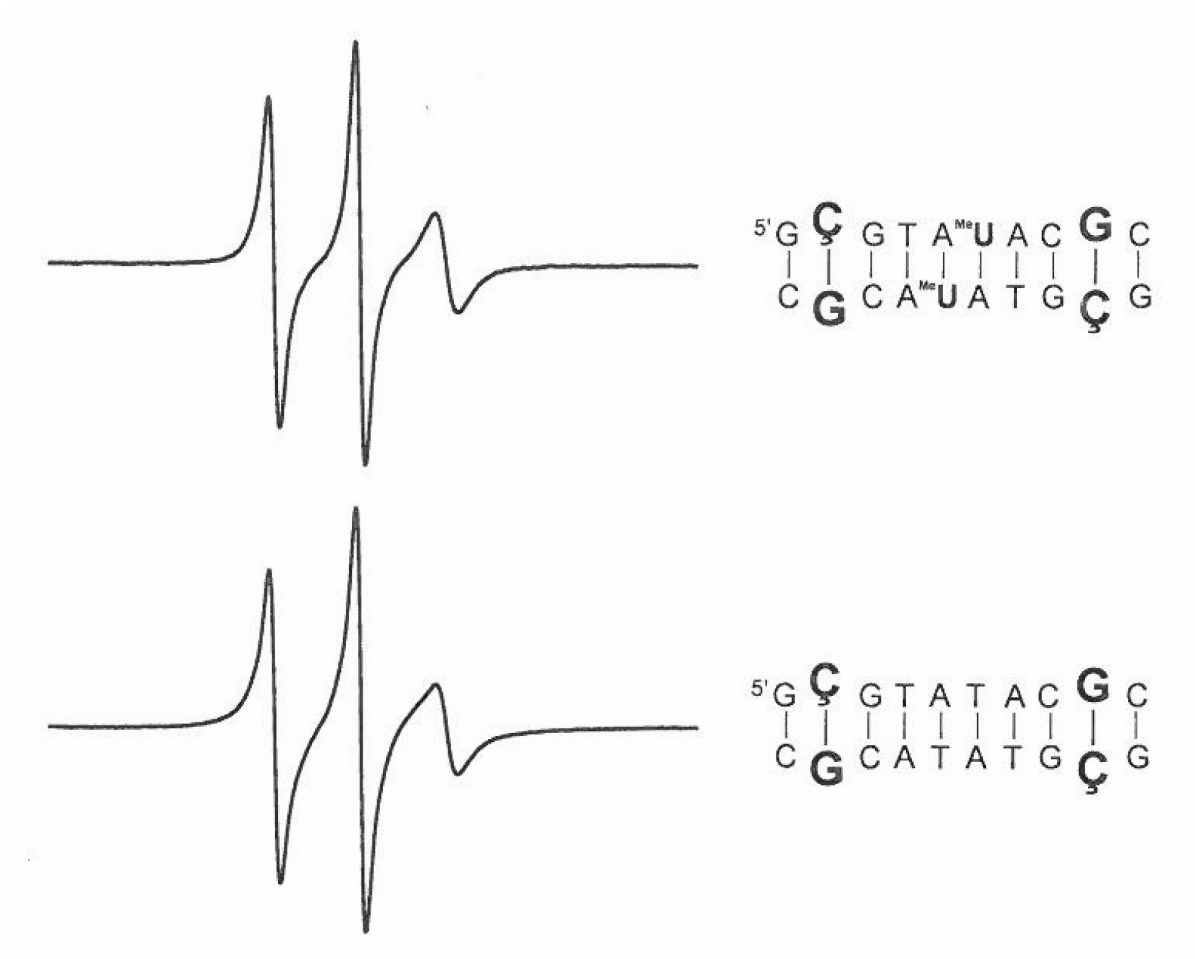


**Figure S7.** EPR spectra of DNA samples containing the nitroxide spin-labeled nucleotide **C** used in crystallography. Spectra were obtained at 22 °C in 10 mM sodium phosphate, 100 mM NaCl, and 0.1 mM EDTA (pH 7.0). The 2'-O-methyl U containing top sample should form A-form DNA whereas the dT containing sample on bottom should form B-form DNA.

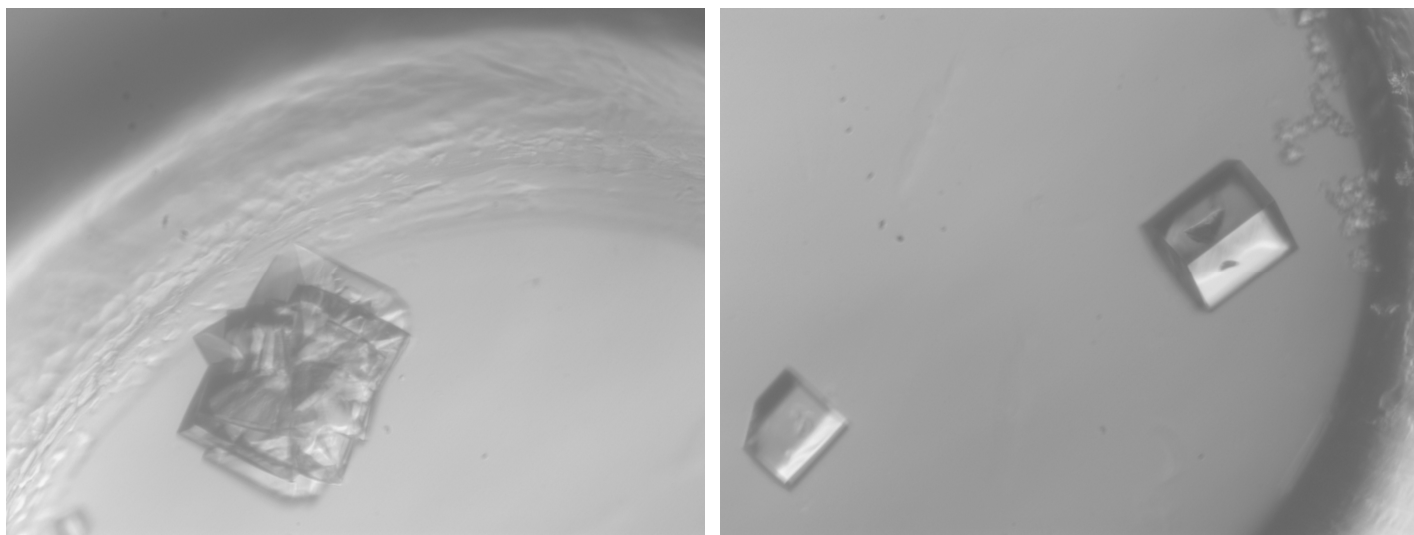


**Figure S8.** Crystals of a 10-nucleotide long DNA containing the rigid nitroxide spin-labeled nucleotide **C**. Crystals typically grew as clusters (left) which are unsuitable for X-ray crystallographic structure determination. However, one drop contained two single crystals (right). The larger crystal was used to determine a 1.7 Å resolution structure. All crystals were yellow in color.



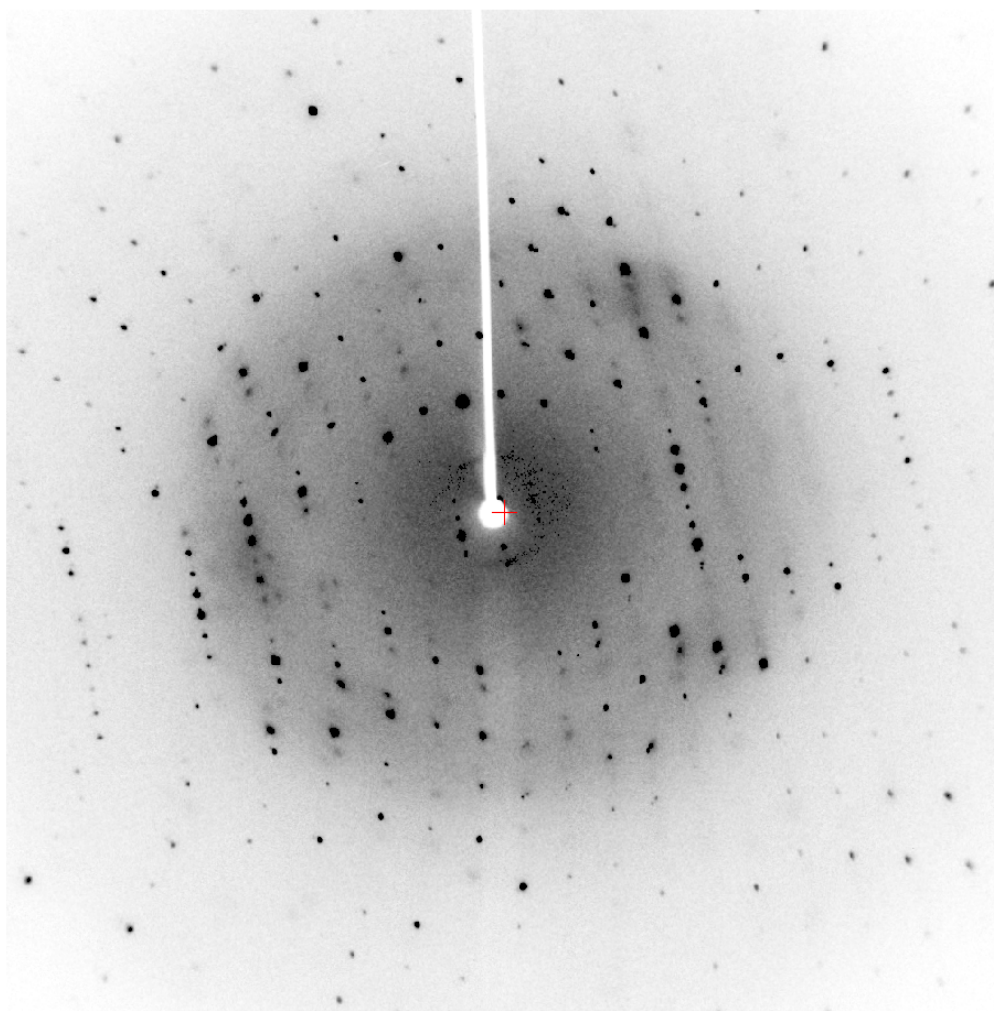


**Figure S9.** Diffraction pattern image of a DNA containing the rigid nitroxide spin-labeled nucleotide **C**.

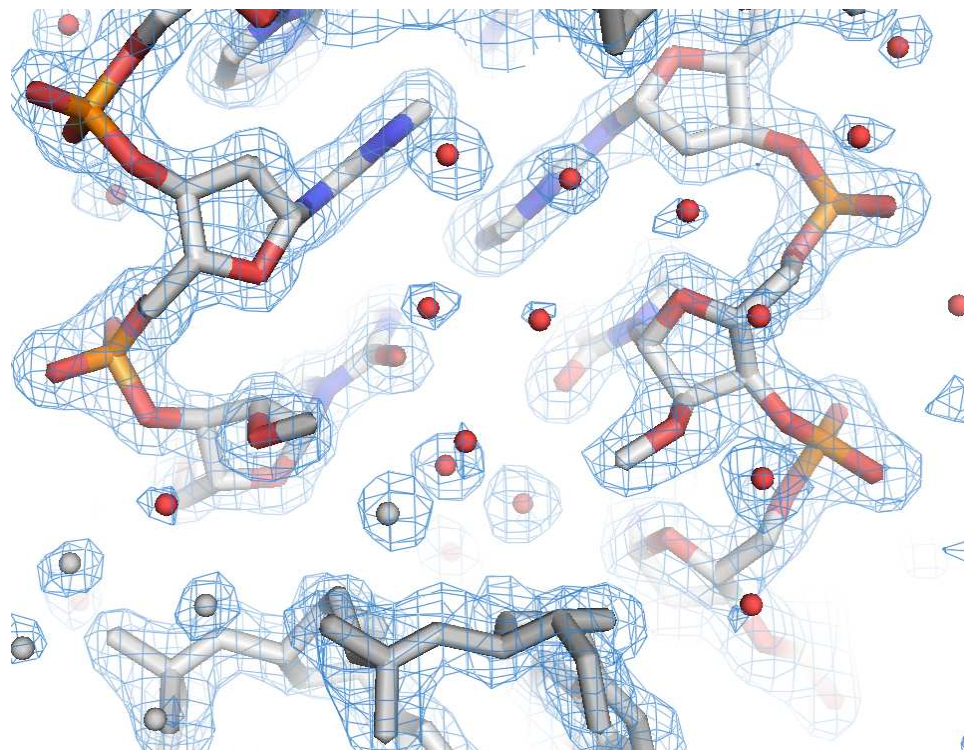


**Figure S10.** Crystal structure of an A-form DNA containing the rigid nitroxide spin-labeled nucleotide **C** showing the 2'-*O*-methyl U residues which promote formation of A-form DNA in solution. Electron density map ( $2F_o - |F_c|$ ) is shown in blue mesh contoured at  $1.0 \sigma$ . Symmetry mate is shown in gray.

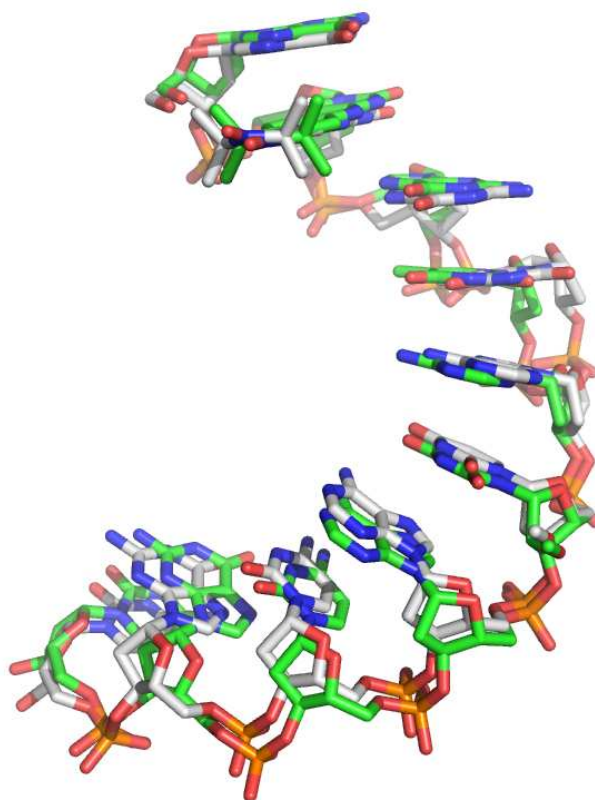


**Figure S11.** All atom LSQ superposition of chains A (gray carbon backbone) and B (green carbon backbone) across all atoms. RMS deviations were  $0.99 \text{ \AA}$  for main chain atoms and  $0.96 \text{ \AA}$  for side chain atoms.

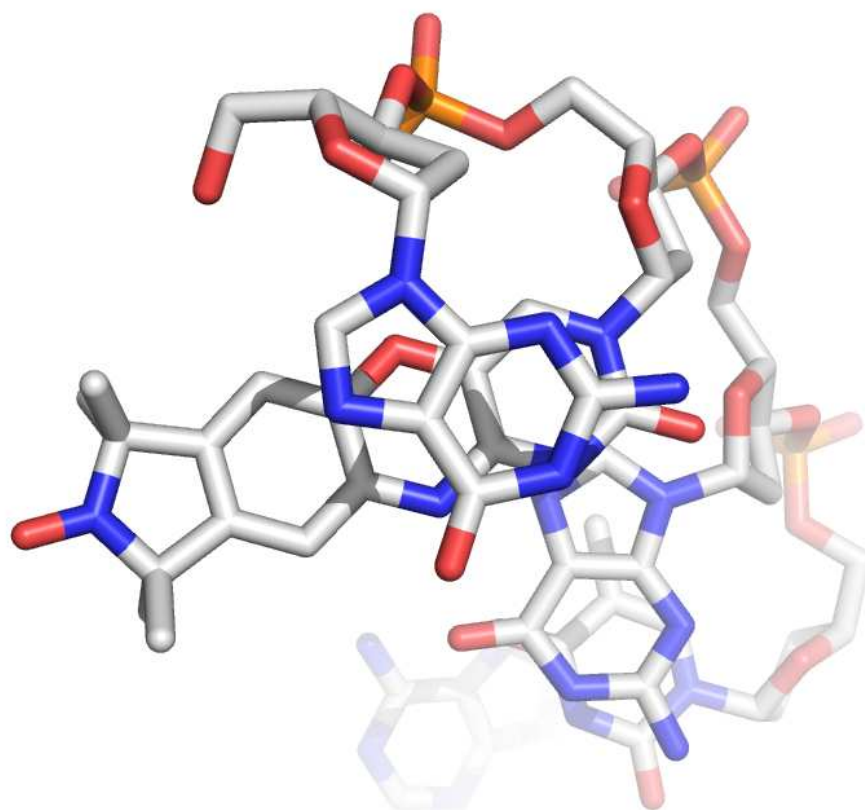


**Figure S12.** Stacking of residue dG1 on top of  $\zeta$ 2 from chain A. For simplicity, only chain A is shown without the complementary chain B.

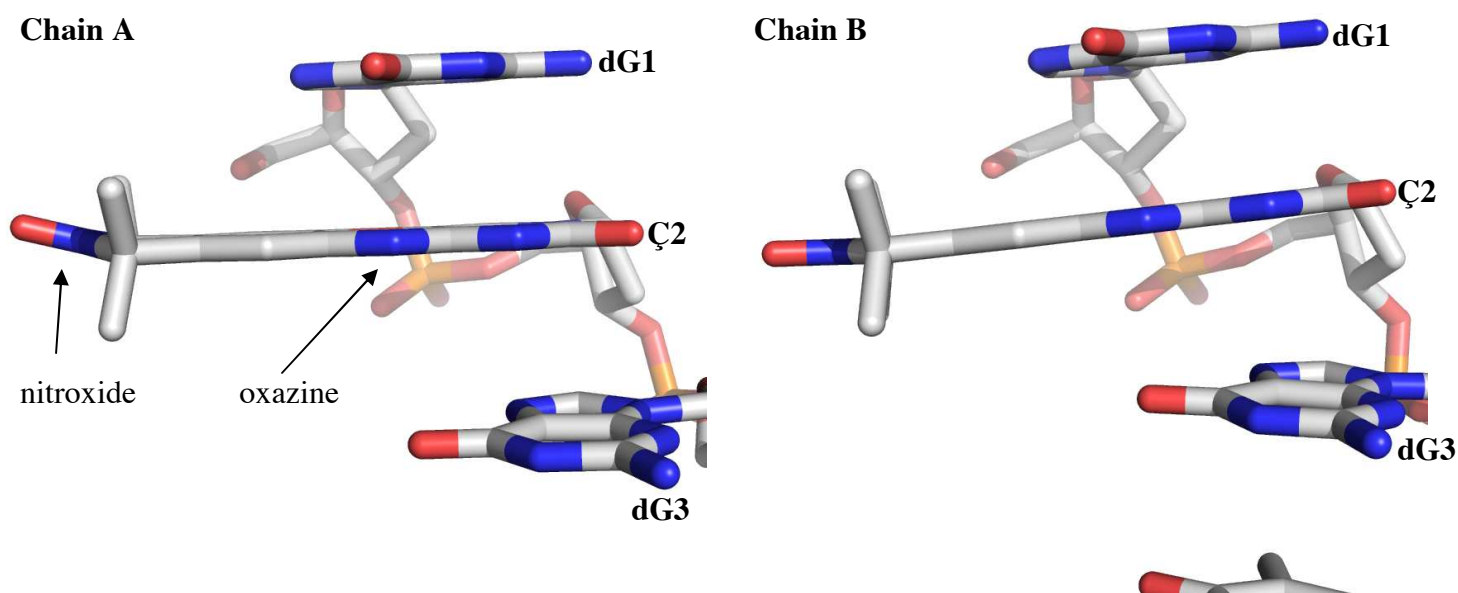


**Figure S13.** View of  $\zeta$  in molecules A (left) and B (right) of the asymmetric unit.  $\zeta$  is planar at the oxazine linkage at both molecules in the asymmetric unit. There appears to be a slight puckering of the nitroxide ring in molecule A, but very little puckering at the nitroxide ring in molecule B. This puckering is expected given that the ring containing the nitroxide is not aromatic (i.e. it is a 3-pyrroline ring).

Coordinates for small molecule crystal structure of **1**

Bond precision: C-C = 0.0075 Å Wavelength=0.71073

Cell: a=9.268(7) b=8.872(6) c=11.160(8)

alpha=90 beta=112.90(3) gamma=90

Temperature: 93 K

Calculated Reported

Volume 845.3(11) 845.3(11)

Space group P 21/c P21/c

Hall group -P 2ybc ?

Moiety formula C10 H7 N3 O2 ?

Sum formula C10 H7 N3 O2 C10 H7 N3 O2

Mr 201.19 201.19

Dx, g cm<sup>-3</sup> 1.581 1.581

Z 4 4

Mu (mm<sup>-1</sup>) 0.115 0.115

F000 416.0 416.0

F000' 416.19

h,k,lmax 12,11,14 11,10,14

Nref 1952 1567

Tmin,Tmax 0.986,0.999 0.986,0.999

Tmin' 0.986

Correction method= MULTI-SCAN

Data completeness= 0.803 Theta(max)= 27.520

R(reflections)= 0.0844( 873) wR2(reflections)= 0.1915( 1567)

S = 1.048 Npar= 136

CRYST1	9.268	8.872	11.160	90.00	112.90	90.00			
SCALE1	0.107897	0.000000	0.045575			0.000000			
SCALE2	0.000000	0.112718	0.000000			0.000000			
SCALE3	0.000000	0.000000	0.097268			0.000000			
ATOM	1	O11	0	0.665	4.644	5.352	1.000	2.11	
ANISOU	1	O11	0	267	250	285	-55	101	-16
ATOM	2	O1	0	-3.028	0.850	6.395	1.000	2.19	
ANISOU	2	O1	0	302	205	324	-64	99	-16
ATOM	3	N2	0	-2.270	2.969	6.814	1.000	1.76	
ANISOU	3	N2	0	206	227	234	-5	42	-16
ATOM	4	N4	0	-1.457	5.089	7.163	1.000	1.85	
ANISOU	4	N4	0	236	213	252	-33	99	9
ATOM	5	N14	0	-1.260	1.594	5.178	1.000	1.82	
ANISOU	5	N14	0	238	236	218	-2	55	-13
ATOM	6	C1	0	-2.208	1.778	6.152	1.000	1.72	
ANISOU	6	C1	0	208	240	205	25	-15	34
ATOM	7	C3	0	-1.369	3.893	6.544	1.000	1.50	
ANISOU	7	C3	0	205	208	159	5	30	54
ATOM	8	C5	0	-0.518	6.108	6.912	1.000	1.74	
ANISOU	8	C5	0	226	250	184	-10	-1	-28
ATOM	9	C6	0	-0.627	7.350	7.512	1.000	1.87	

ANISOU	9	C6	0	260	218	231	19	34	27
ATOM	10	C7	0	0.330	8.332	7.282	1.000	2.23	
ANISOU	10	C7	0	359	199	289	-47	-22	-26
ATOM	11	C8	0	1.408	8.076	6.432	1.000	2.18	
ANISOU	11	C8	0	290	287	252	-85	0	25
ATOM	12	C9	0	1.497	6.829	5.788	1.000	2.08	
ANISOU	12	C9	0	218	310	261	-19	20	-3
ATOM	13	C10	0	0.533	5.875	6.015	1.000	1.82	
ANISOU	13	C10	0	224	217	250	-29	-12	24
ATOM	14	C12	0	-0.310	3.707	5.597	1.000	1.68	
ANISOU	14	C12	0	203	206	228	-7	15	-6
ATOM	15	C13	0	-0.312	2.547	4.909	1.000	1.68	
ANISOU	15	C13	0	209	252	176	-33	45	-9

Crystallographic Information File (CIF) for small molecule crystal structure of **1**

data\_shelxl

\_audit\_creation\_method SHELXL-97  
\_chemical\_name\_systematic  
;  
?  
;  
\_chemical\_name\_common ?  
\_chemical\_melting\_point ?  
\_chemical\_formula\_moiety ?  
\_chemical\_formula\_sum  
'C10 H7 N3 O2'  
\_chemical\_formula\_weight 201.19

loop\_

\_atom\_type\_symbol  
\_atom\_type\_description  
\_atom\_type\_scatter\_dispersion\_real  
\_atom\_type\_scatter\_dispersion\_imag  
\_atom\_type\_scatter\_source  
'C' 'C' 0.0033 0.0016  
'International Tables Vol C Tables 4.2.6.8 and 6.1.1.4'  
'H' 'H' 0.0000 0.0000  
'International Tables Vol C Tables 4.2.6.8 and 6.1.1.4'  
'N' 'N' 0.0061 0.0033  
'International Tables Vol C Tables 4.2.6.8 and 6.1.1.4'  
'O' 'O' 0.0106 0.0060  
'International Tables Vol C Tables 4.2.6.8 and 6.1.1.4'

\_symmetry\_cell\_setting monoclinic  
\_symmetry\_space\_group\_name\_H-M P21/c

loop\_

\_symmetry\_equiv\_pos\_as\_xyz  
'x, y, z'  
'-x, y+1/2, -z+1/2'  
'-x, -y, -z'  
'x, -y-1/2, z-1/2'

\_cell\_length\_a 9.268(7)  
\_cell\_length\_b 8.872(6)  
\_cell\_length\_c 11.160(8)  
\_cell\_angle\_alpha 90.00  
\_cell\_angle\_beta 112.90(3)  
\_cell\_angle\_gamma 90.00  
\_cell\_volume 845.3(11)  
\_cell\_formula\_units\_Z 4  
\_cell\_measurement\_temperature 93(2)  
\_cell\_measurement\_reflns\_used 3143

```

_cell_measurement_theta_min    2.52
_cell_measurement_theta_max    28.24

_exptl_crystal_description     ?
_exptl_crystal_colour          ?
_exptl_crystal_size_max        0.12
_exptl_crystal_size_mid        0.10
_exptl_crystal_size_min        0.01
_exptl_crystal_density_meas    ?
_exptl_crystal_density_diffn   1.581
_exptl_crystal_density_method  'not measured'
_exptl_crystal_F_000           416
_exptl_absorpt_coefficient_mu   0.115
_exptl_absorpt_correction_type  multi-scan
_exptl_absorpt_correction_T_min 0.9863
_exptl_absorpt_correction_T_max 0.9989
_exptl_absorpt_process_details 'Jacobson, R. (1998) Private communication'

_exptl_special_details
;
?
;

_diffn_ambient_temperature     93(2)
_diffn_radiation_wavelength     0.71073
_diffn_radiation_type           MoK\alpha
_diffn_radiation_source         'rotating anode'
_diffn_radiation_monochromator  confocal
_diffn_measurement_device_type  CCD
_diffn_measurement_method       '\w and \f scans'
_diffn_detector_area_resol_mean ?
_diffn_standards_number         ?
_diffn_standards_interval_count ?
_diffn_standards_interval_time  ?
_diffn_standards_decay_%        ?
_diffn_reflns_number            3564
_diffn_reflns_av_R_equivalents  0.0949
_diffn_reflns_av_sigma/netI     0.0943
_diffn_reflns_limit_h_min       -11
_diffn_reflns_limit_h_max        7
_diffn_reflns_limit_k_min       -10
_diffn_reflns_limit_k_max        10
_diffn_reflns_limit_l_min       -12
_diffn_reflns_limit_l_max        14
_diffn_reflns_theta_min         4.78
_diffn_reflns_theta_max         27.52
_reflns_number_total            1567
_reflns_number_gt               873
_reflns_threshold_expression     >2sigma(I)

_computing_data_collection      'CrystalClear (Rigaku Corp., 2004)'

```

```
_computing_cell_refinement      'CrystalClear (Rigaku Corp., 2004)'  
_computing_data_reduction      'CrystalClear (Rigaku Corp., 2004)'  
_computing_structure_solution  'SHELXS-97 (Sheldrick, 1990)'  
_computing_structure_refinement 'SHELXL-97 (Sheldrick, 1997)'  
_computing_molecular_graphics  'Bruker SHELXTL'  
_computing_publication_material 'Bruker SHELXTL'
```

```
_refine_special_details
```

```
;  
Refinement of  $F^2$  against ALL reflections. The weighted R-factor  $wR$  and  
goodness of fit  $S$  are based on  $F^2$ , conventional R-factors  $R$  are based  
on  $F$ , with  $F$  set to zero for negative  $F^2$ . The threshold expression of  
 $F^2 > 2\sigma(F^2)$  is used only for calculating R-factors(gt) etc. and is  
not relevant to the choice of reflections for refinement. R-factors based  
on  $F^2$  are statistically about twice as large as those based on  $F$ , and R-  
factors based on ALL data will be even larger.  
;
```

```
_refine_ls_structure_factor_coef Fsqd  
_refine_ls_matrix_type          full  
_refine_ls_weighting_scheme     calc  
_refine_ls_weighting_details  
'calc w=1/[ $\sigma^2(F_o^2) + (0.0354P)^2 + 3.3437P$ ] where  $P = (F_o^2 + 2F_c^2)/3$ ']  
_atom_sites_solution_primary    direct  
_atom_sites_solution_secondary  difmap  
_atom_sites_solution_hydrogens  geom  
_refine_ls_hydrogen_treatment   constr  
_refine_ls_extinction_method     none  
_refine_ls_extinction_coef       ?  
_refine_ls_number_reflns        1567  
_refine_ls_number_parameters     136  
_refine_ls_number_restraints     0  
_refine_ls_R_factor_all          0.1622  
_refine_ls_R_factor_gt           0.0844  
_refine_ls_wR_factor_ref         0.1915  
_refine_ls_wR_factor_gt          0.1503  
_refine_ls_goodness_of_fit_ref   1.048  
_refine_ls_restrained_S_all      1.048  
_refine_ls_shift/su_max          0.001  
_refine_ls_shift/su_mean         0.000
```

```
loop_
```

```
_atom_site_label  
_atom_site_type_symbol  
_atom_site_fract_x  
_atom_site_fract_y  
_atom_site_fract_z  
_atom_site_U_iso_or_equiv  
_atom_site_adp_type  
_atom_site_occupancy  
_atom_site_symmetry_multiplicity
```



\_atom\_site\_calc\_flag  
\_atom\_site\_refinement\_flags  
\_atom\_site\_disorder\_assembly  
\_atom\_site\_disorder\_group  
O11 O 0.3157(4) 0.5235(4) 0.5206(3) 0.0267(9) Uani 1 1 d ...  
O1 O -0.0352(4) 0.0958(4) 0.6220(3) 0.0277(9) Uani 1 1 d ...  
N2 N 0.0656(5) 0.3346(5) 0.6628(4) 0.0223(9) Uani 1 1 d ...  
N4 N 0.1692(5) 0.5736(5) 0.6967(4) 0.0234(10) Uani 1 1 d ...  
H4 H 0.1195 0.5918 0.7584 0.028 Uiso 1 1 calc R ..  
N14 N 0.1000(4) 0.1797(5) 0.5037(4) 0.0231(10) Uani 1 1 d ...  
H14 H 0.0788 0.0953 0.4586 0.028 Uiso 1 1 calc R ..  
C1 C 0.0421(5) 0.2004(6) 0.5984(5) 0.0217(11) Uani 1 1 d ...  
C3 C 0.1506(5) 0.4388(5) 0.6365(4) 0.0191(11) Uani 1 1 d ...  
C5 C 0.2591(5) 0.6884(6) 0.6723(4) 0.0220(11) Uani 1 1 d ...  
C6 C 0.2747(6) 0.8285(6) 0.7307(5) 0.0236(11) Uani 1 1 d ...  
H6 H 0.2216 0.8491 0.7865 0.028 Uiso 1 1 calc R ..  
C7 C 0.3675(6) 0.9391(6) 0.7083(5) 0.0283(12) Uani 1 1 d ...  
H7 H 0.3781 1.0347 0.7493 0.034 Uiso 1 1 calc R ..  
C8 C 0.4451(6) 0.9103(6) 0.6256(5) 0.0276(12) Uani 1 1 d ...  
H8 H 0.5106 0.9849 0.6118 0.033 Uiso 1 1 calc R ..  
C9 C 0.4254(6) 0.7698(6) 0.5630(5) 0.0263(12) Uani 1 1 d ...  
H9 H 0.4765 0.7492 0.5057 0.032 Uiso 1 1 calc R ..  
C10 C 0.3316(5) 0.6622(6) 0.5851(5) 0.0230(11) Uani 1 1 d ...  
C12 C 0.2217(5) 0.4179(6) 0.5444(4) 0.0212(11) Uani 1 1 d ...  
C13 C 0.1901(5) 0.2871(6) 0.4775(4) 0.0212(11) Uani 1 1 d ...  
H13 H 0.2302 0.2694 0.4123 0.025 Uiso 1 1 calc R ..

loop\_

\_atom\_site\_aniso\_label  
\_atom\_site\_aniso\_U\_11  
\_atom\_site\_aniso\_U\_22  
\_atom\_site\_aniso\_U\_33  
\_atom\_site\_aniso\_U\_23  
\_atom\_site\_aniso\_U\_13  
\_atom\_site\_aniso\_U\_12  
O11 0.034(2) 0.0250(19) 0.0285(18) -0.0016(16) 0.0204(16) -0.0057(16)  
O1 0.038(2) 0.0205(19) 0.032(2) -0.0016(16) 0.0217(17) -0.0065(16)  
N2 0.024(2) 0.023(2) 0.023(2) -0.0016(19) 0.0130(18) -0.0011(18)  
N4 0.031(2) 0.021(2) 0.025(2) 0.0009(19) 0.0190(19) -0.0027(19)  
N14 0.028(2) 0.024(2) 0.022(2) -0.0013(19) 0.0136(18) -0.0006(18)  
C1 0.020(2) 0.024(3) 0.020(2) 0.003(2) 0.007(2) 0.004(2)  
C3 0.022(3) 0.021(3) 0.016(2) 0.005(2) 0.009(2) 0.003(2)  
C5 0.022(3) 0.025(3) 0.018(2) -0.003(2) 0.007(2) -0.002(2)  
C6 0.028(3) 0.022(3) 0.023(3) 0.003(2) 0.012(2) 0.003(2)  
C7 0.033(3) 0.020(3) 0.029(3) -0.003(2) 0.009(2) -0.005(2)  
C8 0.028(3) 0.029(3) 0.025(3) 0.003(2) 0.010(2) -0.007(2)  
C9 0.024(3) 0.031(3) 0.026(3) 0.000(2) 0.012(2) -0.002(2)  
C10 0.022(3) 0.022(3) 0.025(3) 0.002(2) 0.009(2) -0.002(2)  
C12 0.022(3) 0.021(3) 0.023(3) -0.001(2) 0.010(2) -0.001(2)  
C13 0.024(2) 0.025(3) 0.018(2) -0.001(2) 0.011(2) -0.003(2)

\_geom\_special\_details

;  
All esds (except the esd in the dihedral angle between two l.s. planes)  
are estimated using the full covariance matrix. The cell esds are taken  
into account individually in the estimation of esds in distances, angles  
and torsion angles; correlations between esds in cell parameters are only  
used when they are defined by crystal symmetry. An approximate (isotropic)  
treatment of cell esds is used for estimating esds involving l.s. planes.

;

loop\_

\_geom\_bond\_atom\_site\_label\_1  
\_geom\_bond\_atom\_site\_label\_2  
\_geom\_bond\_distance  
\_geom\_bond\_site\_symmetry\_2  
\_geom\_bond\_publ\_flag  
O11 C12 1.375(6) . ?  
O11 C10 1.404(6) . ?  
O1 C1 1.261(6) . ?  
N2 C3 1.319(6) . ?  
N2 C1 1.364(6) . ?  
N4 C3 1.349(6) . ?  
N4 C5 1.408(6) . ?  
N14 C1 1.371(6) . ?  
N14 C13 1.371(6) . ?  
C3 C12 1.432(6) . ?  
C5 C6 1.384(7) . ?  
C5 C10 1.401(7) . ?  
C6 C7 1.391(7) . ?  
C7 C8 1.397(7) . ?  
C8 C9 1.406(7) . ?  
C9 C10 1.376(7) . ?  
C12 C13 1.349(7) . ?

loop\_

\_geom\_angle\_atom\_site\_label\_1  
\_geom\_angle\_atom\_site\_label\_2  
\_geom\_angle\_atom\_site\_label\_3  
\_geom\_angle  
\_geom\_angle\_site\_symmetry\_1  
\_geom\_angle\_site\_symmetry\_3  
\_geom\_angle\_publ\_flag  
C12 O11 C10 116.5(4) . . ?  
C3 N2 C1 118.8(4) . . ?  
C3 N4 C5 121.0(4) . . ?  
C1 N14 C13 121.6(4) . . ?  
O1 C1 N2 121.3(4) . . ?  
O1 C1 N14 119.2(5) . . ?  
N2 C1 N14 119.6(4) . . ?  
N2 C3 N4 118.8(4) . . ?  
N2 C3 C12 123.3(5) . . ?

N4 C3 C12 117.8(4) .. ?  
C6 C5 C10 119.1(5) .. ?  
C6 C5 N4 121.3(4) .. ?  
C10 C5 N4 119.6(5) .. ?  
C5 C6 C7 120.5(4) .. ?  
C6 C7 C8 120.2(5) .. ?  
C7 C8 C9 119.3(5) .. ?  
C10 C9 C8 119.7(5) .. ?  
C9 C10 C5 121.1(5) .. ?  
C9 C10 O11 117.6(4) .. ?  
C5 C10 O11 121.2(4) .. ?  
C13 C12 O11 119.8(4) .. ?  
C13 C12 C3 116.6(4) .. ?  
O11 C12 C3 123.6(4) .. ?  
C12 C13 N14 119.9(4) .. ?

\_diffn\_measured\_fraction\_theta\_max 0.803  
\_diffn\_reflns\_theta\_full 25.00  
\_diffn\_measured\_fraction\_theta\_full 0.945  
\_refine\_diff\_density\_max 0.431  
\_refine\_diff\_density\_min -0.318  
\_refine\_diff\_density\_rms 0.079

Coordinates for small molecule crystal structure of  $\epsilon$

Bond precision: C-C = 0.0064 A Wavelength=0.71073

Cell: a=5.731(2) b=9.162(4) c=31.739(12)

alpha=90 beta=91.230(12) gamma=90

Temperature:93 K

Calculated Reported

Volume 1666.2(11) 1666.0(11)

Space group P 21/n P21/n

Hall group -P 2yn ?

Moiety formula C16 H15 N4 O3 C16 H15 N4 O3

Sum formula C16 H15 N4 O3 C16 H15 N4 O3

Mr 311.32 311.32

Dx,g cm<sup>-3</sup> 1.241 1.243

Z 4 4

Mu (mm<sup>-1</sup>) 0.089 0.089

F000 652.0 696.0

F000' 652.29

h,k,lmax 6,11,38 6,11,38

Nref 3017 2997

Tmin,Tmax 0.997,0.997 0.991,0.997

Tmin' 0.991

Correction method= MULTI-SCAN

Data completeness= 0.993 Theta(max)= 25.300

R(reflections)= 0.0900( 1506) wR2(reflections)= 0.2790( 2997)

S = 1.030 Npar= 227

CRYST1	5.731	9.162	31.739	90.00	91.23	90.00			
SCALE1	0.174505	0.000000	0.003747		0.000000				
SCALE2	0.000000	0.109144	0.000000		0.000000				
SCALE3	0.000000	0.000000	0.031514		0.000000				
ATOM	1	O1	0	-5.434	-3.673	8.544	1.000	3.51	
ANISOU	1	O1	0	491	337	506	-34	179	14
ATOM	2	C1	0	-4.374	-3.680	7.874	1.000	3.13	
ANISOU	2	C1	0	469	337	383	6	14	21
ATOM	3	N2	0	-3.861	-4.838	7.354	1.000	3.06	
ANISOU	3	N2	0	433	317	411	11	87	-34
ATOM	4	C3	0	-2.730	-4.835	6.567	1.000	3.22	
ANISOU	4	C3	0	522	292	410	38	16	-67
ATOM	5	C4	0	-2.100	-3.694	6.300	1.000	2.94	
ANISOU	5	C4	0	458	295	363	26	91	25
ATOM	6	O5	0	-0.948	-3.659	5.525	1.000	3.51	
ANISOU	6	O5	0	553	292	488	14	155	47
ATOM	7	C6	0	-0.561	-2.413	5.046	1.000	3.03	
ANISOU	7	C6	0	427	363	363	27	-5	-47
ATOM	8	C7	0	0.296	-2.366	3.943	1.000	3.21	
ANISOU	8	C7	0	384	395	441	-14	10	-26
ATOM	9	C8	0	0.672	-1.106	3.443	1.000	3.21	
ANISOU	9	C8	0	332	472	416	-46	34	-23
ATOM	10	C9	0	1.504	-0.841	2.210	1.000	3.35	
ANISOU	10	C9	0	379	398	497	-44	96	-12

ATOM	11	O10	0	2.007	1.338	1.269	1.000	4.74	
ANISOU	11	O10	0	663	593	547	-129	173	36
ATOM	12	N10	0	1.422	0.643	2.184	1.000	3.90	
ANISOU	12	N10	0	537	463	484	-128	130	32
ATOM	13	C11	0	0.683	1.276	3.307	1.000	3.49	
ANISOU	13	C11	0	404	489	432	-69	69	-13
ATOM	14	C12	0	0.223	0.063	4.051	1.000	3.07	
ANISOU	14	C12	0	412	385	368	-47	6	19
ATOM	15	C13	0	-0.632	-0.004	5.138	1.000	3.26	
ANISOU	15	C13	0	415	356	470	-9	65	-31
ATOM	16	C14	0	-1.042	-1.225	5.625	1.000	2.82	
ANISOU	16	C14	0	384	343	345	8	25	-1
ATOM	17	N15	0	-2.012	-1.297	6.656	1.000	3.14	
ANISOU	17	N15	0	444	336	415	-64	110	24
ATOM	18	C16	0	-2.608	-2.502	6.881	1.000	3.00	
ANISOU	18	C16	0	405	390	344	-6	-1	0
ATOM	19	N17	0	-3.704	-2.504	7.662	1.000	2.93	
ANISOU	19	N17	0	455	275	383	4	68	-23
ATOM	20	C18	0	0.900	-1.393	0.928	1.000	4.12	
ANISOU	20	C18	0	560	586	418	-43	64	-32
ATOM	21	C19	0	2.939	-1.269	2.332	1.000	4.33	
ANISOU	21	C19	0	462	598	587	-40	58	12
ATOM	22	C20	0	-0.470	2.150	2.766	1.000	4.32	
ANISOU	22	C20	0	558	520	564	-52	17	95
ATOM	23	C21	0	1.636	2.155	4.146	1.000	4.31	
ANISOU	23	C21	0	526	551	560	-188	62	-20
ATOM	24	O31	0	1.349	4.121	0.251	0.500	8.60	
ANISOU	24	O31	0	1488	472	1308	-414	303	23
ATOM	25	C31	0	1.945	4.138	0.871	0.500	12.67	
ANISOU	25	C31	0	2511	537	1766	-688	1615	-253

Crystallographic Information File (CIF) for small molecule crystal structure of **6**

data\_shelxl

\_audit\_creation\_method SHELXL-97  
\_chemical\_name\_systematic ?

\_chemical\_melting\_point ?  
\_chemical\_formula\_moiety 'C16 H15 N4 O3'  
\_chemical\_formula\_sum 'C16 H15 N4 O3'  
\_chemical\_formula\_weight 311.32

loop\_

\_atom\_type\_symbol  
\_atom\_type\_description  
\_atom\_type\_scatter\_dispersion\_real  
\_atom\_type\_scatter\_dispersion\_imag  
\_atom\_type\_scatter\_source  
'C' 'C' 0.0033 0.0016  
'International Tables Vol C Tables 4.2.6.8 and 6.1.1.4'  
'H' 'H' 0.0000 0.0000  
'International Tables Vol C Tables 4.2.6.8 and 6.1.1.4'  
'N' 'N' 0.0061 0.0033  
'International Tables Vol C Tables 4.2.6.8 and 6.1.1.4'  
'O' 'O' 0.0106 0.0060  
'International Tables Vol C Tables 4.2.6.8 and 6.1.1.4'

\_symmetry\_cell\_setting monoclinic  
\_symmetry\_space\_group\_name\_H-M P21/n

loop\_

\_symmetry\_equiv\_pos\_as\_xyz  
'x, y, z'  
'-x+1/2, y+1/2, -z+1/2'  
'-x, -y, -z'  
'x-1/2, -y-1/2, z-1/2'

\_cell\_length\_a 5.731(2)  
\_cell\_length\_b 9.162(4)  
\_cell\_length\_c 31.739(12)  
\_cell\_angle\_alpha 90.00  
\_cell\_angle\_beta 91.230(12)  
\_cell\_angle\_gamma 90.00  
\_cell\_volume 1666.0(11)  
\_cell\_formula\_units\_Z 4  
\_cell\_measurement\_temperature 93(2)  
\_cell\_measurement\_reflns\_used ?  
\_cell\_measurement\_theta\_min ?  
\_cell\_measurement\_theta\_max ?

\_exptl\_crystal\_description ?  
\_exptl\_crystal\_colour yellow  
\_exptl\_crystal\_size\_max 0.10  
\_exptl\_crystal\_size\_mid 0.03  
\_exptl\_crystal\_size\_min 0.03  
\_exptl\_crystal\_density\_meas ?  
\_exptl\_crystal\_density\_diffn 1.243  
\_exptl\_crystal\_density\_method 'not measured'  
\_exptl\_crystal\_F\_000 696  
\_exptl\_absorpt\_coefficient\_mu 0.089  
\_exptl\_absorpt\_correction\_type multi-scan  
\_exptl\_absorpt\_correction\_T\_min 0.9906  
\_exptl\_absorpt\_correction\_T\_max 0.9972  
\_exptl\_absorpt\_process\_details 'Jacobson, R. (1998) Private communication'

\_exptl\_special\_details

;  
?  
;

\_diffn\_ambient\_temperature 93(2)  
\_diffn\_radiation\_wavelength 0.71073  
\_diffn\_radiation\_type MoK $\alpha$   
\_diffn\_radiation\_source 'rotating anode'  
\_diffn\_radiation\_monochromator confocal  
\_diffn\_measurement\_device\_type CCD  
\_diffn\_measurement\_method '\w and \f scans'  
\_diffn\_detector\_area\_resol\_mean ?  
\_diffn\_standards\_number ?  
\_diffn\_standards\_interval\_count ?  
\_diffn\_standards\_interval\_time ?  
\_diffn\_standards\_decay\_% ?  
\_diffn\_reflns\_number 9668  
\_diffn\_reflns\_av\_R\_equivalents 0.1135  
\_diffn\_reflns\_av\_sigma/netI 0.1080  
\_diffn\_reflns\_limit\_h\_min -4  
\_diffn\_reflns\_limit\_h\_max 6  
\_diffn\_reflns\_limit\_k\_min -11  
\_diffn\_reflns\_limit\_k\_max 10  
\_diffn\_reflns\_limit\_l\_min -37  
\_diffn\_reflns\_limit\_l\_max 38  
\_diffn\_reflns\_theta\_min 1.28  
\_diffn\_reflns\_theta\_max 25.30  
\_reflns\_number\_total 2997  
\_reflns\_number\_gt 1506  
\_reflns\_threshold\_expression >2sigma(I)

\_computing\_data\_collection 'CrystalClear (Rigaku Corp., 2004)'  
\_computing\_cell\_refinement 'CrystalClear (Rigaku Corp., 2004)'  
\_computing\_data\_reduction 'CrystalClear (Rigaku Corp., 2004)'  
\_computing\_structure\_solution 'SHELXS-97 (Sheldrick, 1990)'

```
_computing_structure_refinement 'SHELXL-97 (Sheldrick, 1997)'
_computing_molecular_graphics 'Bruker SHELXTL'
_computing_publication_material 'Bruker SHELXTL'
```

```
_refine_special_details
```

```
;
```

Refinement of  $F^2$  against ALL reflections. The weighted R-factor  $wR$  and goodness of fit  $S$  are based on  $F^2$ , conventional R-factors  $R$  are based on  $F$ , with  $F$  set to zero for negative  $F^2$ . The threshold expression of  $F^2 > 2\sigma(F^2)$  is used only for calculating R-factors(gt) etc. and is not relevant to the choice of reflections for refinement. R-factors based on  $F^2$  are statistically about twice as large as those based on  $F$ , and R-factors based on ALL data will be even larger.

```
;
```

```
_refine_ls_structure_factor_coef Fsqd
_refine_ls_matrix_type full
_refine_ls_weighting_scheme calc
_refine_ls_weighting_details
'calc w=1/[\s^2*(Fo^2)+(0.1337P)^2+0.0000P] where P=(Fo^2+2Fc^2)/3'
_atom_sites_solution_primary direct
_atom_sites_solution_secondary difmap
_atom_sites_solution_hydrogens geom
_refine_ls_hydrogen_treatment constr
_refine_ls_extinction_method none
_refine_ls_extinction_coef ?
_refine_ls_number_reflns 2997
_refine_ls_number_parameters 227
_refine_ls_number_restraints 0
_refine_ls_R_factor_all 0.1676
_refine_ls_R_factor_gt 0.0900
_refine_ls_wR_factor_ref 0.2790
_refine_ls_wR_factor_gt 0.2330
_refine_ls_goodness_of_fit_ref 1.030
_refine_ls_restrained_S_all 1.030
_refine_ls_shift/su_max 0.019
_refine_ls_shift/su_mean 0.001
```

```
loop_
```

```
_atom_site_label
_atom_site_type_symbol
_atom_site_fract_x
_atom_site_fract_y
_atom_site_fract_z
_atom_site_U_iso_or_equiv
_atom_site_adp_type
_atom_site_occupancy
_atom_site_symmetry_multiplicity
_atom_site_calc_flag
_atom_site_refinement_flags
_atom_site_disorder_assembly
```



\_atom\_site\_disorder\_group

O1 O -0.9162(6) -0.4009(3) 0.26927(9) 0.0445(9) Uani 1 1 d . . .  
C1 C -0.7338(9) -0.4017(5) 0.24815(14) 0.0396(12) Uani 1 1 d . . .  
N2 N -0.6463(7) -0.5281(4) 0.23177(11) 0.0387(10) Uani 1 1 d . . .  
C3 C -0.4517(9) -0.5278(5) 0.20696(14) 0.0408(12) Uani 1 1 d . . .  
H3A H -0.3951 -0.6169 0.1958 0.049 Uiso 1 1 calc R . .  
C4 C -0.3428(8) -0.4032(5) 0.19854(13) 0.0372(11) Uani 1 1 d . . .  
O5 O -0.1448(6) -0.3993(3) 0.17413(9) 0.0444(9) Uani 1 1 d . . .  
C6 C -0.0791(8) -0.2633(5) 0.15902(13) 0.0384(12) Uani 1 1 d . . .  
C7 C 0.0664(8) -0.2582(5) 0.12426(14) 0.0407(12) Uani 1 1 d . . .  
H7A H 0.1209 -0.3454 0.1116 0.049 Uiso 1 1 calc R . .  
C8 C 0.1301(8) -0.1208(5) 0.10850(14) 0.0406(12) Uani 1 1 d . . .  
C9 C 0.2708(8) -0.0918(5) 0.06964(15) 0.0425(12) Uani 1 1 d . . .  
O10 O 0.3551(6) 0.1460(4) 0.04000(11) 0.0601(11) Uani 1 1 d . . .  
N10 N 0.2562(7) 0.0702(5) 0.06883(12) 0.0495(11) Uani 1 1 d . . .  
C11 C 0.1315(8) 0.1392(5) 0.10423(14) 0.0442(13) Uani 1 1 d . . .  
C12 C 0.0541(8) 0.0069(5) 0.12767(13) 0.0388(12) Uani 1 1 d . . .  
C13 C -0.0910(8) -0.0005(5) 0.16193(14) 0.0413(12) Uani 1 1 d . . .  
H13A H -0.1427 0.0868 0.1749 0.050 Uiso 1 1 calc R . .  
C14 C -0.1608(8) -0.1337(5) 0.17728(13) 0.0358(11) Uani 1 1 d . . .  
N15 N -0.3262(7) -0.1415(4) 0.20976(11) 0.0398(10) Uani 1 1 d . . .  
C16 C -0.4294(8) -0.2731(5) 0.21686(13) 0.0379(11) Uani 1 1 d . . .  
N17 N -0.6177(7) -0.2732(4) 0.24145(11) 0.0371(10) Uani 1 1 d . . .  
C18 C 0.1605(9) -0.1520(6) 0.02924(14) 0.0521(14) Uani 1 1 d . . .  
H18A H -0.0027 -0.1205 0.0270 0.078 Uiso 1 1 calc R . .  
H18B H 0.1673 -0.2589 0.0297 0.078 Uiso 1 1 calc R . .  
H18C H 0.2458 -0.1155 0.0050 0.078 Uiso 1 1 calc R . .  
C19 C 0.5216(9) -0.1386(6) 0.07349(16) 0.0549(14) Uani 1 1 d . . .  
H19A H 0.5914 -0.0983 0.0994 0.082 Uiso 1 1 calc R . .  
H19B H 0.6071 -0.1025 0.0492 0.082 Uiso 1 1 calc R . .  
H19C H 0.5300 -0.2453 0.0743 0.082 Uiso 1 1 calc R . .  
C20 C -0.0717(10) 0.2347(6) 0.08716(16) 0.0547(14) Uani 1 1 d . . .  
H20A H -0.1797 0.1742 0.0704 0.082 Uiso 1 1 calc R . .  
H20B H -0.0096 0.3127 0.0695 0.082 Uiso 1 1 calc R . .  
H20C H -0.1546 0.2777 0.1108 0.082 Uiso 1 1 calc R . .  
C21 C 0.3009(10) 0.2352(6) 0.13065(16) 0.0546(14) Uani 1 1 d . . .  
H21A H 0.4302 0.1751 0.1415 0.082 Uiso 1 1 calc R . .  
H21B H 0.2176 0.2782 0.1543 0.082 Uiso 1 1 calc R . .  
H21C H 0.3625 0.3132 0.1129 0.082 Uiso 1 1 calc R . .

loop\_

\_atom\_site\_aniso\_label  
\_atom\_site\_aniso\_U\_11  
\_atom\_site\_aniso\_U\_22  
\_atom\_site\_aniso\_U\_33  
\_atom\_site\_aniso\_U\_23  
\_atom\_site\_aniso\_U\_13  
\_atom\_site\_aniso\_U\_12  
O1 0.050(2) 0.034(2) 0.0506(18) 0.0014(15) 0.0190(17) -0.0034(15)  
C1 0.047(3) 0.034(3) 0.038(2) 0.002(2) 0.002(2) 0.001(2)  
N2 0.044(2) 0.032(2) 0.041(2) -0.0034(18) 0.0096(19) 0.0010(18)

C3 0.052(3) 0.029(3) 0.041(2) -0.007(2) 0.002(2) 0.004(2)  
 C4 0.046(3) 0.029(3) 0.036(2) 0.003(2) 0.010(2) 0.003(2)  
 O5 0.056(2) 0.0292(18) 0.0488(18) 0.0047(15) 0.0166(17) 0.0015(15)  
 C6 0.043(3) 0.036(3) 0.036(2) -0.005(2) 0.000(2) 0.003(2)  
 C7 0.038(3) 0.039(3) 0.044(3) -0.003(2) 0.002(2) -0.001(2)  
 C8 0.033(3) 0.047(3) 0.042(2) -0.002(2) 0.004(2) -0.005(2)  
 C9 0.038(3) 0.040(3) 0.050(3) -0.001(2) 0.011(2) -0.004(2)  
 O10 0.067(3) 0.059(2) 0.055(2) 0.0036(19) 0.018(2) -0.0128(19)  
 N10 0.054(3) 0.046(3) 0.048(2) 0.003(2) 0.014(2) -0.013(2)  
 C11 0.041(3) 0.049(3) 0.043(3) -0.001(2) 0.008(2) -0.007(2)  
 C12 0.041(3) 0.039(3) 0.037(2) 0.002(2) 0.001(2) -0.005(2)  
 C13 0.042(3) 0.036(3) 0.047(3) -0.003(2) 0.008(2) -0.001(2)  
 C14 0.039(3) 0.034(3) 0.034(2) 0.000(2) 0.003(2) 0.001(2)  
 N15 0.045(2) 0.034(2) 0.042(2) 0.0024(18) 0.0119(18) -0.0064(18)  
 C16 0.040(3) 0.039(3) 0.034(2) 0.000(2) 0.001(2) -0.001(2)  
 N17 0.046(2) 0.027(2) 0.0383(19) -0.0023(17) 0.0077(18) 0.0003(17)  
 C18 0.056(4) 0.059(3) 0.042(3) -0.003(3) 0.007(3) -0.004(3)  
 C19 0.046(3) 0.060(4) 0.059(3) 0.001(3) 0.007(3) -0.004(3)  
 C20 0.056(4) 0.052(3) 0.056(3) 0.009(3) 0.003(3) -0.005(3)  
 C21 0.053(3) 0.055(3) 0.056(3) -0.002(3) 0.007(3) -0.019(3)

\_geom\_special\_details

;  
 All esds (except the esd in the dihedral angle between two l.s. planes)  
 are estimated using the full covariance matrix. The cell esds are taken  
 into account individually in the estimation of esds in distances, angles  
 and torsion angles; correlations between esds in cell parameters are only  
 used when they are defined by crystal symmetry. An approximate (isotropic)  
 treatment of cell esds is used for estimating esds involving l.s. planes.  
 ;

loop\_

\_geom\_bond\_atom\_site\_label\_1  
 \_geom\_bond\_atom\_site\_label\_2  
 \_geom\_bond\_distance  
 \_geom\_bond\_site\_symmetry\_2  
 \_geom\_bond\_publ\_flag  
 O1 C1 1.254(5) . ?  
 C1 N2 1.369(5) . ?  
 C1 N17 1.370(6) . ?  
 N2 C3 1.379(6) . ?  
 C3 C4 1.331(6) . ?  
 C4 O5 1.388(5) . ?  
 C4 C16 1.420(6) . ?  
 O5 C6 1.390(5) . ?  
 C6 C7 1.398(6) . ?  
 C6 C14 1.406(6) . ?  
 C7 C8 1.406(6) . ?  
 C8 C12 1.392(6) . ?  
 C8 C9 1.511(6) . ?  
 C9 N10 1.487(6) . ?

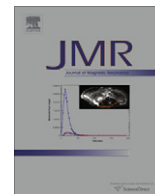
C9 C19 1.502(7) . ?  
C9 C18 1.521(7) . ?  
O10 N10 1.289(5) . ?  
N10 C11 1.486(6) . ?  
C11 C12 1.495(6) . ?  
C11 C21 1.544(7) . ?  
C11 C20 1.545(7) . ?  
C12 C13 1.385(6) . ?  
C13 C14 1.377(6) . ?  
C14 N15 1.417(5) . ?  
N15 C16 1.364(6) . ?  
C16 N17 1.345(6) . ?

loop\_

\_geom\_angle\_atom\_site\_label\_1  
\_geom\_angle\_atom\_site\_label\_2  
\_geom\_angle\_atom\_site\_label\_3  
\_geom\_angle  
\_geom\_angle\_site\_symmetry\_1  
\_geom\_angle\_site\_symmetry\_3  
\_geom\_angle\_publ\_flag  
O1 C1 N2 121.6(4) . . ?  
O1 C1 N17 119.4(4) . . ?  
N2 C1 N17 119.0(4) . . ?  
C1 N2 C3 121.5(4) . . ?  
C4 C3 N2 120.3(4) . . ?  
C3 C4 O5 121.8(4) . . ?  
C3 C4 C16 117.9(4) . . ?  
O5 C4 C16 120.3(4) . . ?  
C4 O5 C6 116.5(3) . . ?  
O5 C6 C7 118.2(4) . . ?  
O5 C6 C14 121.3(4) . . ?  
C7 C6 C14 120.4(4) . . ?  
C6 C7 C8 118.4(4) . . ?  
C12 C8 C7 120.7(4) . . ?  
C12 C8 C9 112.7(4) . . ?  
C7 C8 C9 126.5(4) . . ?  
N10 C9 C19 109.8(4) . . ?  
N10 C9 C8 99.1(4) . . ?  
C19 C9 C8 114.2(4) . . ?  
N10 C9 C18 109.0(4) . . ?  
C19 C9 C18 110.1(4) . . ?  
C8 C9 C18 113.9(4) . . ?  
O10 N10 C11 122.2(4) . . ?  
O10 N10 C9 121.6(4) . . ?  
C11 N10 C9 116.1(4) . . ?  
N10 C11 C12 100.6(4) . . ?  
N10 C11 C21 110.3(4) . . ?  
C12 C11 C21 112.4(4) . . ?  
N10 C11 C20 110.3(4) . . ?  
C12 C11 C20 113.8(4) . . ?

C21 C11 C20 109.2(4) .. ?  
C13 C12 C8 120.1(4) .. ?  
C13 C12 C11 128.3(4) .. ?  
C8 C12 C11 111.4(4) .. ?  
C14 C13 C12 120.3(4) .. ?  
C13 C14 C6 120.1(4) .. ?  
C13 C14 N15 120.4(4) .. ?  
C6 C14 N15 119.4(4) .. ?  
C16 N15 C14 117.6(4) .. ?  
N17 C16 N15 116.9(4) .. ?  
N17 C16 C4 121.9(4) .. ?  
N15 C16 C4 121.2(4) .. ?  
C16 N17 C1 119.3(4) .. ?

\_diffn\_measured\_fraction\_theta\_max 0.995  
\_diffn\_reflns\_theta\_full 25.30  
\_diffn\_measured\_fraction\_theta\_full 0.995  
\_refine\_diff\_density\_max 0.495  
\_refine\_diff\_density\_min -0.361  
\_refine\_diff\_density\_rms 0.086



## W-band PELDOR with 1 kW microwave power: Molecular geometry, flexibility and exchange coupling

Gunnar W. Reginsson<sup>a,b</sup>, Robert I. Hunter<sup>c</sup>, Paul A.S. Cruickshank<sup>c</sup>, David R. Bolton<sup>c</sup>, Snorri Th. Sigurdsson<sup>b</sup>, Graham M. Smith<sup>c,\*</sup>, Olav Schiemann<sup>a,\*</sup>

<sup>a</sup> Biomedical Sciences Research Complex, Centre of Magnetic Resonance, University of St Andrews, St Andrews KY16 9ST, UK

<sup>b</sup> Science Institute, University of Iceland, Dunhaga 3, 107 Reykjavik, Iceland

<sup>c</sup> School of Physics and Astronomy, Centre of Magnetic Resonance, University of St Andrews, St Andrews KY16 9SS, UK

### ARTICLE INFO

#### Article history:

Received 10 November 2011

Revised 9 January 2012

Available online 8 February 2012

#### Keywords:

PELDOR

DEER

Nitroxide spin labels

Orientation selective PELDOR

Exchange coupling

### ABSTRACT

A technique that is increasingly being used to determine the structure and conformational flexibility of biomacromolecules is Pulsed Electron–Electron Double Resonance (PELDOR or DEER), an Electron Paramagnetic Resonance (EPR) based technique. At X-band frequencies (9.5 GHz), PELDOR is capable of precisely measuring distances in the range of 1.5–8 nm between paramagnetic centres but the orientation selectivity is weak. In contrast, working at higher frequencies increases the orientation selection but usually at the expense of decreased microwave power and PELDOR modulation depth. Here it is shown that a home-built high-power pulsed W-band EPR spectrometer (HiPER) with a large instantaneous bandwidth enables one to achieve PELDOR data with a high degree of orientation selectivity and large modulation depths. We demonstrate a measurement methodology that gives a set of PELDOR time traces that yield highly constrained data sets. Simulating the resulting time traces provides a deeper insight into the conformational flexibility and exchange coupling of three bisnitroxide model systems. These measurements provide strong evidence that W-band PELDOR may prove to be an accurate and quantitative tool in assessing the relative orientations of nitroxide spin labels and to correlate those orientations to the underlying biological structure and dynamics.

© 2012 Elsevier Inc. All rights reserved.

### 1. Introduction

Pulsed Electron–Electron Double Resonance (PELDOR or DEER) [1,2] is increasingly being used to determine structures and conformational changes of biologically relevant macromolecules. Using intrinsic paramagnetic centres or site specifically incorporated spin labels into proteins or nucleic acids PELDOR is used to measure the distance between spin centres and to relate distance distributions to conformational states [3–5]. In addition to measuring distances between spin labelled sites, PELDOR can also be used to measure the relative orientation of spin centres [6,7]. Whilst most standard spin labels such as MTSSL are very flexible and known to give a very broad distribution of orientations, new spin labels are now being developed that have less flexibility. Using such rigid spin labels or spin labelling sites with restricted spin label dynamics, orientation-sensitive PELDOR measurements have been demonstrated at X-band frequencies where they have been used to obtain information on relative orientations of spin labels and dynamics. Examples include DNAs spin labelled with the rigid spin label Ç

[8–10], the spin labelled potassium ion channel [11] and copper nitroxide biradical model systems [12,13]. The recent development of the so-called RX nitroxide spin label with two linkers [14,15] also gives hope that in the future protein systems may be spin labelled in a rigid way. Performing PELDOR measurements at 94 GHz (W-band) [7,16–18] or 180 GHz (G-band) [6,10,19] gives a much higher orientation resolution since the *g*-tensors become better resolved, but at the same time the PELDOR modulation depth decreases as a result of less microwave power being available with the spectrometers used. An exception is the W-band PELDOR study by the lab of Goldfarb where a modulation depth of ~20% was achieved with 1 W of power [20]. A deep modulation is important since the dipolar information is contained in the modulation rather than the absolute echo height. All the high-field/high-frequency studies mentioned above also used relatively high *Q* single-mode cavities to improve sensitivity, which limited the available instantaneous bandwidth, restricting the frequency separation between inversion and detection pulses. To invert and detect a full set of orthogonal orientations in a PELDOR experiment requires an effective bandwidth of 250–300 MHz, which previously required lowering the *Q*-value of the cavity substantially with a significant loss of sensitivity. One exception is the promising approach described by Bennati et al. where a bimodal cavity was used to provide separate

\* Corresponding authors.

E-mail addresses: [gms@st-andrews.ac.uk](mailto:gms@st-andrews.ac.uk) (G.M. Smith), [os11@st-andrews.ac.uk](mailto:os11@st-andrews.ac.uk) (O. Schiemann).

tunable cavity resonances for both inversion and detection pulses, although sensitivity was still limited by the available power [16].

In this work we show that these technical limitations can be overcome and high concentration sensitivity measurements can be made over large bandwidths at 94 GHz. Measurements were made on three bisnitroxide model systems (Fig. 1) using a home-built W-band EPR spectrometer with 1 kW pulse microwave power and a flat 1 GHz instantaneous bandwidth (HiPER) [21] obtaining a detailed picture of their molecular geometry, flexibility and exchange coupling.

## 2. Results and discussions

Continuous wave-EPR (CW-EPR) spectra were recorded of all three bisnitroxides on HiPER at 110 K (Fig. 2). All three compounds show a typical cw W-band nitroxide spectrum with no discernible splittings due to dipolar- or exchange couplings. Simulating all three spectra yielded  $g$ -tensor values,  $^{14}\text{N}$  hyperfine coupling values and linewidths that were used for the simulations of the PELDOR time traces (see Table 2).

In the standard terminology for nitroxide orientations in a magnetic field the nitroxide is oriented in the  $x$ -direction when the NO-bond is parallel to the applied magnetic field  $B_0$ , in the  $y$ -direction when  $B_0$  is orthogonal to the  $x$ -direction but in the plane of the five-membered ring system and in the  $z$ -direction when  $B_0$  is orthogonal to the ring plane (Fig. 3, inset).

At W-band frequencies the  $g$ -tensors are sufficiently well resolved that it becomes possible to selectively excite nitroxides with specific orientations. Thus, in an orientation selective PELDOR experiment one excites the “A” spins of nitroxides oriented in a particular direction via the detection pulse sequence and then monitors the effect of inverting the “B” spins of nitroxides oriented in the same or an orthogonal direction. The overall modulation depth is determined by the fraction of  $B$  spins that were excited by the inversion pulse. The modulation frequency and its damping contains information on both the distribution of distances between the spins and the distribution in orientations of the interspin vector with respect to  $B_0$ . In the study described here, we use six separate PELDOR measurements to correlate  $A$  and  $B$  spins with each other that are oriented in either the  $x$ -,  $y$ - or  $z$ -directions with respect to the magnetic field. Thus, we describe six inversion/detection PELDOR correlation measurements in the  $XX$ ,  $YY$ ,  $ZZ$ ,  $YX$ ,  $YZ$  and  $ZX$  directions, where for example  $ZX$  means that we invert the spins oriented in the  $z$ -direction and detect spins oriented in the  $x$ -direction. It is our experience that this measurement methodology gives a highly constrained data set that can be obtained in about 3 h with the described samples and instrumentation.

An echo detected field swept spectrum of each bisnitroxide was used to guide the positioning of the detection and inversion pulses (Fig. 3). Since HiPER works in reflection mode (without a cavity), it is not limited by a cavity band-width and thus allows one to position inversion and detection pulses at any position on the nitroxide

spectrum. This enables one to monitor not only  $XX$ ,  $YY$  and  $ZZ$  correlations but also the cross-correlations  $XY$ ,  $XZ$  and  $YZ$  with large frequency offsets between inversion and detection, e.g. 210 MHz for  $XZ$ .

For each of these six inversion/detection combinations a PELDOR time trace was recorded for each of the three biradicals (Fig. 4a, d, and g). The high sensitivity and high microwave power of the HiPER spectrometer allowed the acquisition of each time trace with an average signal to noise ( $S/N$ ) ratio of 100 and modulation depths as large as 40% in about 30 min. This modulation depth is close to the 50% obtained at X-band [13,22] and considerably larger than the largest modulation depth of 6% for W-band PELDOR on a power-upgraded Bruker Elexsys 680 spectrometer using either a single or dual mode cavity [7,16] and still larger than the modulation of 20% achieved by Goldfarb et al. [20]. Although, it should be kept in mind that the observed PELDOR modulation depth depends also on the relative orientation and degree of correlation between the coupled spin centres. A quantitative analysis of the three sets of time traces are detailed below.

### 2.1. Biradical 1

The set of PELDOR time traces acquired for **1** show a high degree of orientation selection in terms of modulation frequency and modulation depth (Fig. 4a). Fourier transforming the PELDOR time traces gives a clear qualitative picture of the orientations of the nitroxides relative to the vector connecting the spin centres. The  $XX$  experiment shows the largest selection of the parallel dipolar component ( $\theta = 0^\circ$ ) while the  $ZZ$  experiment shows the largest perpendicular dipolar component ( $\theta = 90^\circ$ ). This implies that the orientation of the  $g_x$  tensor component is largely parallel and the  $g_{zz}$  component perpendicular to the molecular backbone/dipolar distance vector. This necessarily means that the orientation of the  $g_x$  tensor component on one nitroxide (spin A) (Fig. 3, inset) is largely perpendicular to the  $g_{zz}$  tensor component of the other nitroxide within the same molecule (spin B). This is supported by the very small modulation in the  $ZX$  time trace.

To obtain a more quantitative picture of the mutual orientation of the nitroxide spin labels and the inherent conformational flexibility of the molecule the PELDOR time traces were simulated with a home-written Matlab® program based on an approach published by the Prisner lab [23]. In a first step, a geometry optimised structure of **1** was obtained from density functional theory (DFT) calculations. The lengths of the molecular linker and nitroxide moieties obtained from that structure were then used as initial geometric values to construct a vector model where each nitroxide including the ester groups and the connecting bridge were represented by three independent vectors (Fig. 5a).

The two nitroxides groups in **1** were allowed to rotate freely around the phenolic bond with the N–O bond ( $g_{xx}$  tensor component) tracing out a cone with a mean opening of  $25^\circ$  and the  $g_{zz}$  and  $g_y$  tensor components having a random position in the

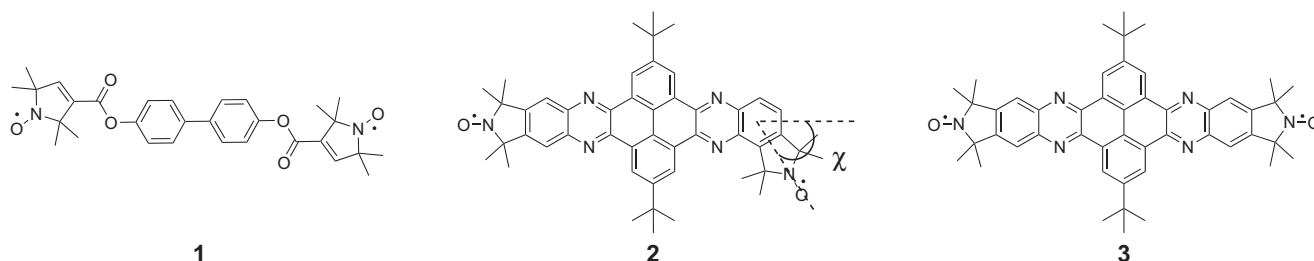
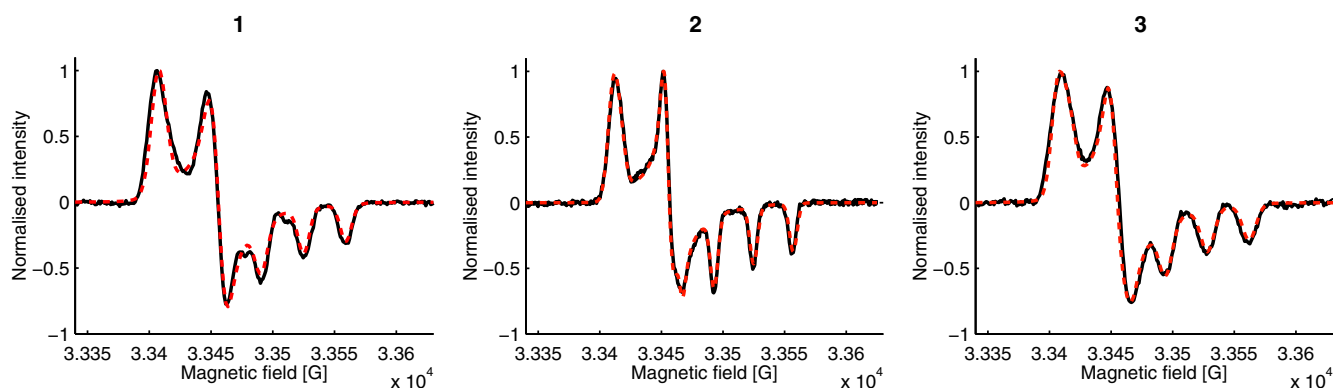
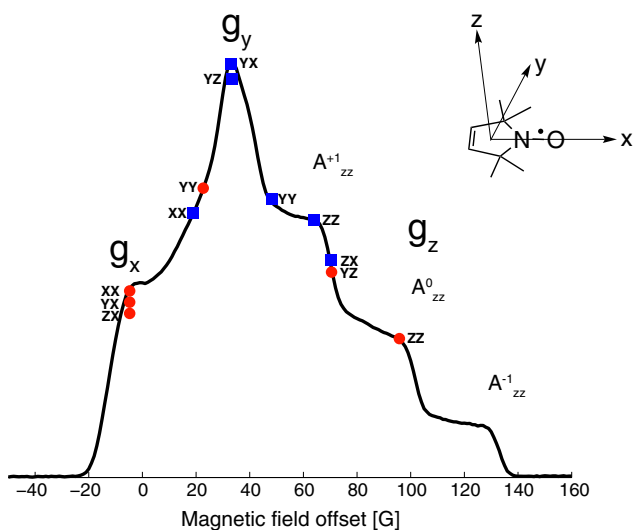


Fig. 1. Structure of nitroxide biradicals **1**–**3**. For **2**,  $\chi$  denotes the angle between the nitroxide  $g_x$  components. Their synthesis is described elsewhere [13,22].



**Fig. 2.** W-band CW-EPR spectra of **1**, **2** and **3** at 110 K (solid black) with simulations overlaid (dashed red). (For interpretation of the references to colour in this figure legend, the reader is referred to the web version of this article.)



**Fig. 3.** An echo detected field sweep of **1**. Red dots and blue squares show the positions of the detection and inversion pulses, respectively. The dots and squares are labelled with their respective PELDOR experiment. The inset shows a nitroxide and the relative orientation of the  $g$ -tensor indicated by arrows. (For interpretation of the references to colour in this figure legend, the reader is referred to the web version of this article.)

$zy$ -plane. The flexibility in the molecular linker was modelled with a single normal distributed bending motion about the biphenyl bond (Fig. 5a). From this ensemble of conformers the intramolecular interspin distance distribution was obtained by measuring the distance between the nitroxide spin centres (defined as the centre of the N–O bond) for each generated molecular conformer. The PELDOR time traces were simulated using the spin-Hamiltonian parameters obtained from the simulation of the CW-EPR spectrum of **1** (Fig. 2a) and the geometrical parameters. The cone angle ( $\alpha$ ) and degree of molecular linker flexibility ( $\beta$ ) were iterated until one set of parameters gave good fits to all six time traces. The structural parameters yielding simulations with the best fit to the experimental time traces (Fig. 4a) are summarised in Table 1. The mean distance of 19.3 Å agrees well with the 19.8 Å obtained from the geometry optimised structure. The cone angle and linker flexibility are in good agreement with previous X-band PELDOR studies on analogous biradical systems [12,13,23]. We were not able to find another set of geometric parameters that were able to fit all six time traces at the same time. We therefore believe that this is a unique solution.

If there is negligible correlation between the orientation of coupled spin centres, the distance distribution is easily obtained by inverting the time-domain data into the distance-domain using Tikhonov regularization, as implemented into DeerAnalysis [24]. However, the time traces here show strong orientation selection indicating strong correlations, which means they cannot be treated individually in DeerAnalysis. In such a case summing up the time traces yields a good approximation to an orientation averaged time trace [25], which may be analysed in DeerAnalysis. This is shown in Fig. 4c for bisnitroxide **1**. The distance distribution agrees very well with the simulated distance distribution from the molecular conformer ensemble apart from a small broad peak in the range 15–17 Å. These smaller distances would correspond to unlikely molecular conformers and are rather artefacts due to incomplete orientation averaging.

## 2.2. Biradical **2** and **3**

Biradicals **2** and **3** [22] were recorded with PELDOR at approximately the same field positions as for **1** (Fig. 4d and g). The set of PELDOR time traces for **2** show a large difference in modulation frequency and depth between field positions. The largest orientation correlations are seen in the XX, ZZ and YX experiments (Fig. 4d). From the Fourier transformed time traces it is seen that the XX and YX experiment show an intense parallel dipolar component and the ZZ experiment an intense perpendicular component (Fig. 4e). This immediately suggests that the  $g_x$  and  $g_y$  tensor components are more parallel than perpendicular to the molecular backbone and the  $g_z$  tensor components are largely perpendicular to the molecular backbone. However, care must be taken in the detailed interpretation as the time traces also show that the relative modulation frequencies of the parallel and perpendicular components are clearly not consistent with a simple dipolar model, where  $\nu_{\parallel} = 2\nu_{\perp}$  suggesting that it is necessary to include an exchange coupling term in the analysis [19].

Thus, to obtain the interspin distance distribution and the relative orientation of the nitroxides from the PELDOR data, the PELDOR time traces were again simulated by using the Hamiltonian parameters obtained from the simulation of the CW-EPR spectrum of **2** (Fig. 2), a geometry model and in addition by taking into account an exchange coupling constant,  $J$  (Fig. 4d). As was done for **1**, distances and angles were obtained from a geometry optimised structure of **2** (Fig. 1) and substituted as initial mean values into a simple vector model (Fig. 5b). In the vector model one nitroxide was aligned such that its  $g_x$  tensor component was parallel to the molecular backbone and the  $g_x$  and  $g_y$  tensor components of the other nitroxide were rotated 60° about its  $g_z$  tensor component.

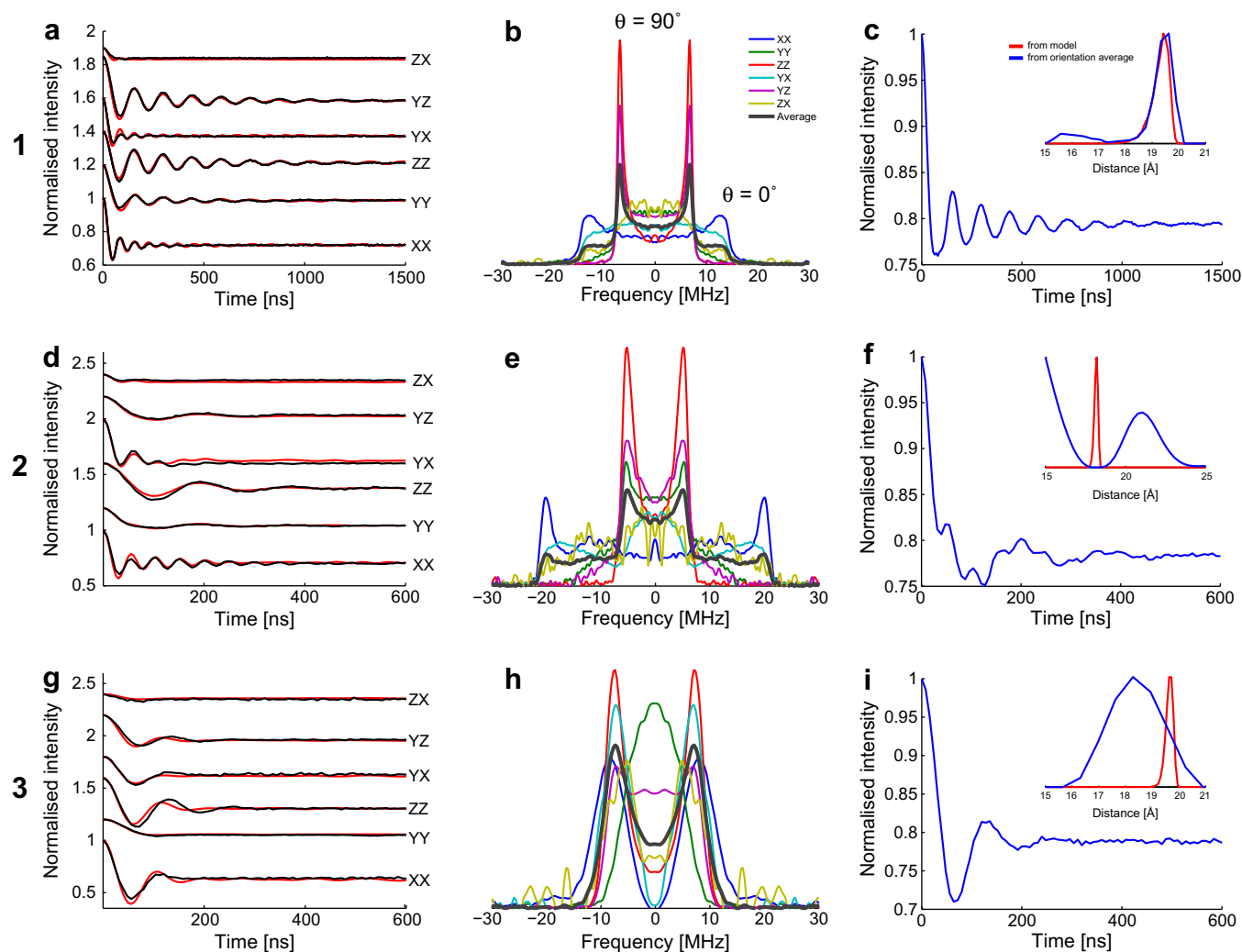


**Fig. 4.** PELDOR data for compounds **1–3**. (a, d, and g) Background corrected time traces (black) with simulated time traces overlaid (red). ZX denotes inversion pulse on  $g_z$  and detection sequence on  $g_x$ , etc. The time traces are displaced on the y-axis for clarity. (b, e, and h) Fourier transformed spectra of the six individual time traces, plus the Fourier transformation of their sum (black line). (c, f, and i) Sum of all time traces and distance distribution from simulation (red) and summed time trace (blue).

The molecular backbone, that now also includes the nitroxide moiety, was allowed to have a discrete bending in the zx plane about the centre of the molecule, described with a normal distribution. Bending of such molecules has also been observed in X-ray crystallographic analysis of analogous compounds [26]. Including an exchange coupling of  $-3.2 \pm 0.8$  MHz and a discrete molecular bending of  $\pm 10^\circ$  with a distribution of  $2.5^\circ$  resulted in the best fit to the experimental PELDOR time traces. The exchange coupling is in excellent agreement with the value determined from the X-band PELDOR data [22]. Including a discrete molecular bending was necessary in order to simulate the observed modulation depth of all six time traces of **2** and indeed also of **3** (see below). In the X-band study [22] a bending of  $\pm 5^\circ$  was added to rectify the distribution in  $J$ , which was required to fit the damping of the time traces. The higher degree of orientation selection at W-band and the possibility to probe different orientation correlations with HiPER verifies and gives a more quantitative picture of this mode. The simulated distance distribution has a mean distance of 18.04 Å with a width of 0.26 Å, in agreement with the distance from the geometry optimised structure (Table 1).

It is interesting to note that at X-band, for molecule **2**, it was difficult to distinguish between two sets of solutions for  $r$  and  $J$

even via simulations [22]. The HiPER PELDOR time traces for **2** were therefore simulated with both of these solution sets. While one solution set agrees with the values used for the simulation in Fig. 4d, the other has an exchange coupling constant of  $-10.5$  MHz and an interspin distance of 20.7 Å [22]. Using the latter set as values for the distance and exchange coupling did not result in simulations with good fits to any of the six time traces (Fig. 6). Therefore, the higher degree of orientation selectivity at W-band makes it easier to determine a unique set of values for the exchange coupling and interspin distance.

Summing up all the experimental time traces for **2** and analysing the orientation averaged time trace with DeerAnalysis yields a broad distance distribution with two major distances. Neither of which agrees with the simulated distance nor represent a realistic molecular conformer (Fig. 4f). The discrepancy between the distance distributions is caused by the inherent exchange coupling which is not accounted for in DeerAnalysis.

The PELDOR time traces of **3** were simulated using the Spin Hamiltonian parameters obtained from cw EPR simulations and using the same vector model and dynamics that were used to simulate the PELDOR time traces of **2** with the exception that the two nitroxide  $g_x$  tensor components are antiparallel (Fig. 1). Including



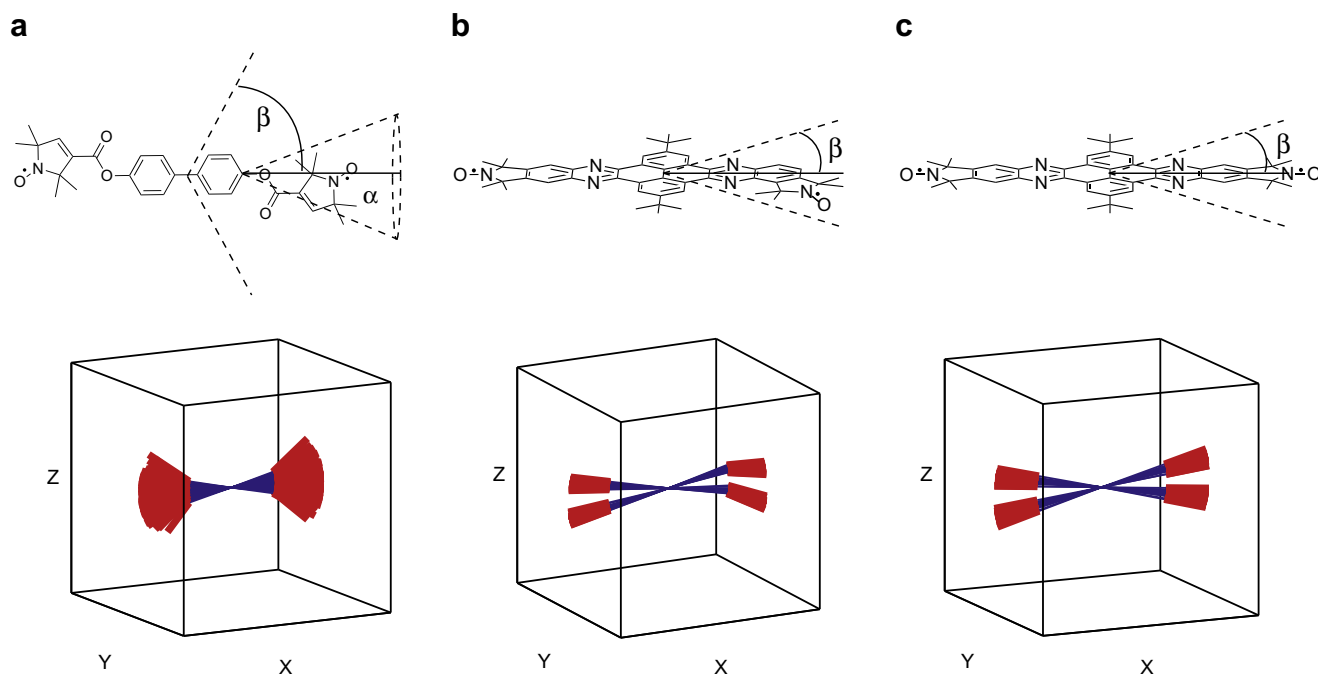


**Fig. 5.** (a–c) Structures and corresponding geometrical vector models used in the simulation program for biradicals **1–3**, respectively. Blue lines represent the connecting bridge. Red lines represent the nitroxide moieties including the ester groups. Each model shows the conformations of 20 conformers. The molecular flexibility is described by the backbone bending angle  $\beta$  and the cone angle  $\alpha$ , describing the flexibility of the nitroxide moiety. (For interpretation of the references to colour in this figure legend, the reader is referred to the web version of this article.)

**Table 1**  
Structural parameters determined from DFT calculations, PELDOR measurements and simulations.

Biradical	$r_{\text{DFT}}$ (Å) <sup>a</sup>	$r_{\text{PELDOR}}$ (Å) <sup>b</sup>	$\alpha$ (°) <sup>c</sup>	$\beta$ (°) <sup>d</sup>	$\chi$ (°) <sup>e</sup>
<b>1</b>	19.8	19.30, 0.34 (0.15, 0.01)	25, 5 (3, 2.5)	0, 5 (5, 2.5)	–
<b>2</b>	18.4	18.04, 0.13 (0.03, 0.01)	–	10, 2.5 (4, 1.4)	60
<b>3</b>	20	19.70, 0.15 (0.03, 0.01)	–	10, 2.5 (3, 1.5)	0

<sup>a</sup> Interspin distances obtained from DFT calculations. The interspin distance was measured between the centres of the NO bonds.

<sup>b</sup> The distance distribution obtained by simulation of the PELDOR time traces is represented as a mean value, standard deviation. The error in the mean value and standard deviation is in brackets. The width of the distance distribution is defined as two times the standard deviation.

<sup>c</sup> The angle of the cone  $\alpha$  is given as a normal distribution with mean value, standard deviation. The error in the mean value and standard deviation is in brackets.

<sup>d</sup> The bending of the backbone  $\beta$  is given as a normal distribution with mean value, standard deviation. The error in the mean value and standard deviation is in brackets.

<sup>e</sup> For **3**, the angle between the  $g_x$  components  $\chi$  is defined as 0°.

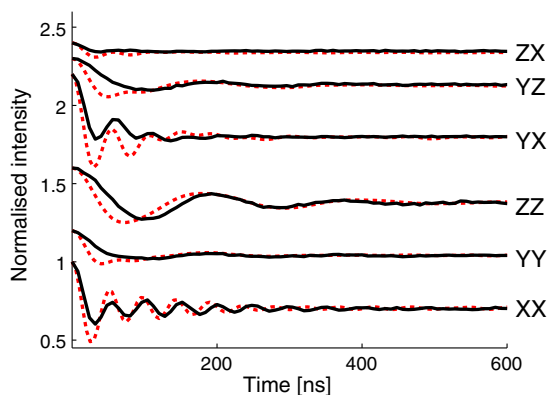


**Fig. 6.** Experimental (solid black) and simulated (dashed red) time traces for bisnitroxide **2**. The simulated time traces were calculated using an interspin distance of 20.7 Å and exchange coupling of  $-10.5$  MHz. (For interpretation of the references to colour in this figure legend, the reader is referred to the web version of this article.)

an exchange coupling constant of  $2.5 \pm 1.7$ , as determined from the X-band data [22], resulted in the best overall fit to the experimental data (Fig. 4g). The simulated distance distribution obtained

from the conformational ensemble has a mean value of 19.7 Å and a width of 0.3 Å, which agrees with the distance from the DFT geometry optimised structure of **3** (Table 1). In contrast, analysing the orientation averaged time trace of **3** gives a single distance with a broad distribution that does not agree with the simulated distance distribution (Fig. 4i) due to the inherent exchange coupling which is not accounted for in DeerAnalysis.

In contrast to biradical **2** the PELDOR time traces for **3** do not show a large difference in modulation frequency (Fig. 4g). This is also revealed in the Fourier transformed time traces that do not show a clear distinction between the parallel and perpendicular dipolar components (Fig. 4h). At X-band, this was also observed and is attributed to the parallel and perpendicular component of the dipolar tensor coinciding due to the presence of an exchange coupling constant [22]. At X-band it was therefore not possible to distinguish between solutions for  $r$  and  $J$  via simulations [22]. One set of solutions had  $r$  approaching infinity and  $J = \pm 8.3$  MHz and the other solution had values used for the simulation in Fig. 4g. Using an interspin distance of 10 m (as an approximation for infinity) and an exchange coupling of  $\pm 8.3$  MHz as initial values for the simulations of the HiPER PELDOR time traces resulted in worse fits, particularly for YY and YZ (Fig. 7).

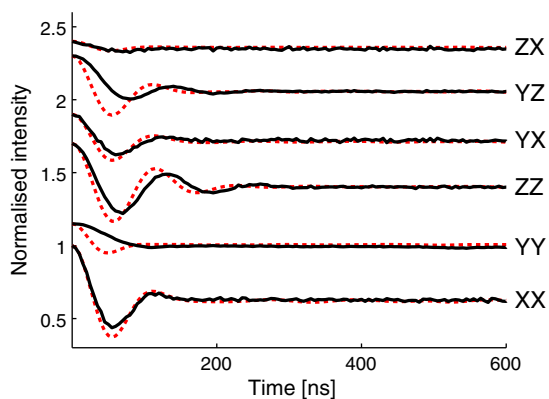


**Fig. 7.** Experimental (solid black) and simulated (dashed red) time traces for bisnitroxide **3**. The simulated time traces were done using an interspin distance of 10 m and an isotropic exchange coupling of 8.5 MHz ( $-8.5$  MHz gives identical solutions). (For interpretation of the references to colour in this figure legend, the reader is referred to the web version of this article.)

As for **2** the higher degree of orientation selection at W-band makes it possible to determine a unique set of values for the exchange coupling and interspin distance.

### 3. Conclusions

We have shown that it is possible to make high sensitivity orientation dependent PELDOR measurements at W-band and quantitatively model the data sets to provide accurate information on the relative orientation and molecular flexibility of semi-rigid and exchange coupled rigid biradicals. The conformational flexibility of the nitroxide spin labels and the molecular linker measured for biradicals **1** were in good agreement with parameters obtained from X-band PELDOR on structurally analogous biradicals [12,23]. From the W-band PELDOR data it became possible to quantitatively determine the relative orientation of the spin labels for **2** and **3**. Specifically, the change in the orientation of the  $g_x$  and  $g_y$  tensor components between **2** and **3** was resolved, which was not possible at X-band [22]. In addition, the conformational distribution of the molecular linker in biradical **2** and **3** was quantitatively determined with less ambiguity than at X-band [22]. By simulating the W-band PELDOR time traces it became possible to unravel the exchange coupling from the PELDOR time traces and to more easily determine a unique set of solutions for the interspin distances and exchange couplings [22]. We have shown that acquiring PELDOR with the HiPER spectrometer, which gives the possibility to probe the correlation between all principal g-tensor components, makes it possible to acquire a detailed picture of spin label orientation and conformational flexibility on a set of semi-rigid and rigid nitroxide biradicals. The results presented in this study set the stage for structural determination on biological systems from measurements of distances, orientations and dynamics using high power, wideband, W-band spectrometers and simulations.

## 4. Experimental

### 4.1. Sample preparation

Biradical **1** (100  $\mu$ M) was dissolved in molten d14 o-terphenyl obtained from Chem Service (98%*C*). The synthesis of **1** has been described elsewhere [13]. Biradicals **2** and **3** (100  $\mu$ M) were dissolved in d-8 toluene obtained from Cambridge Isotope Laboratories Incorporation (99.5%). The samples ( $\sim 50$   $\mu$ L) were shock-frozen in liquid nitrogen before loading into the spectrometer. The synthesis of **2** and **3** have been described elsewhere [22].

### 4.2. Pulse EPR measurements

Pulse EPR measurements were recorded using a home-built W-band EPR spectrometer using a non-resonant sample holder operating in reflection and induction mode, which has been described before [21]. All frequency, phase and pulse control of both inversion and detection frequencies is performed at frequencies near 7.8 GHz, before multiplication to 94 GHz and amplification to beyond 1 kW. The frequency of both low noise inversion and detection pulse sources may be separately phase locked at any frequency within a 1 GHz bandwidth at W-band, which allows complete coverage of the nitroxide spectrum. Phase coherent, heterodyne detection of the detection pulse frequency is performed with an IF frequency of 1800 MHz, with excellent electronic phase stability. The inversion pulse source is not phase related to the local oscillator. High power amplification is performed using an Extended Interaction Klystron Amplifier (EIKA) (CPI, Communications & Power Industries) operating at 94 GHz with a 1 GHz instantaneous bandwidth. Power is transmitted to the sample and to the detector through low loss quasi-optics, where free space isolators provide  $>90$  dB isolation between source and sample and  $>70$  dB isolation between sample and detector. The sample is contained in a 3 mm OD, 2.5 mm ID quartz tube that is placed within a non-resonant sample holder that is designed to be pre-cooled and permit cold sample loading. High isolation ( $>40$  dB) between source and detector is maintained by operating in induction mode. The sample is irradiated by a single linear polarisation and the orthogonal polarisation is detected. This technique also allows conventional, very fast (ns), low power (few Watt) switches to be used for receiver protection. For measurements at cryogenic temperatures a continuous flow helium cryostat (CF935) and a temperature control system (ITC 502) from Oxford instruments were used. All pulsed experiments were performed at 50 K. The PELDOR experiments were done using the four pulse sequence,  $\pi/2(\nu A) - \tau_1 - \pi(\nu A) - (\tau_1 + t) - \pi(\nu B) - (\tau_2 - t) - \pi(\nu A) - \tau_2 - echo$ . The length of the  $\pi/2$  and  $\pi$  detection pulses ( $\nu A$ ) were 8 and 16 ns respectively. The length of the inversion pulse ( $\nu B$ ) varied between 14 and 21 ns, depending on sample and field position. The time delay between the first two detection pulses ( $d_1$ ) was set to 300 ns. The inversion pulse position was incremented by 5 ns. The sequence repetition rate was 2.5 kHz with 3000 shots per point. Interferences from  $^{14}\text{N}$  nuclear modulations, which might be expected and that would show up predominately at the end of the time trace, were not discernible in neither the PELDOR time traces nor the Fourier transformed time traces, and indeed have not yet been seen in any PELDOR experiments using this instrumentation. Each PELDOR time trace for biradicals **1**, **2** and **3** was measured in approximately 30 min.

### 4.3. Data analysis and simulations

A three dimensional homogeneous background model was fitted and subtracted from the experimental PELDOR time traces using DeerAnalysis 2011. The starting time for the background fit was adjusted to minimise any singularity in the dipolar spectrum at zero frequency. The orientation averaged PELDOR time traces were constructed by normalising the original time traces and summing them up. This is also a common strategy for orientation selected NMR residual dipolar coupling patterns [27].

### 4.4. Molecular modelling

Geometry optimised structures of biradicals **1–3** were obtained using density functional theory (DFT) as implemented in the program Orca [28]. DFT calculations were done using the B3LYP functional and 6-31G\* basis set [29].

#### 4.5. CW-EPR simulations

The W-band CW-EPR spectra recorded of **1–3** were simulated using the program EasySpin [30]. All spectra were simulated without including dipolar or exchange couplings. The parameters obtained from the simulations are listed in Table 2.

#### 4.6. PELDOR simulations

PELDOR time traces were simulated with a home-written Matlab® program. A laboratory frame ( $X, Y, Z$ ) is defined, with the applied magnetic field  $B_0$  aligned along the  $Z$ -axis. Within this frame the geometry of the biradicals were represented by a vector model from which the distance vector is calculated (Fig. 8).

Orientation of the  $g$ - and hyperfine-tensors are defined relative to this distance vector. The conformational dynamics of the molecules were represented by creating 20,000 different molecular conformers employing a simple dynamics model including backbone bending about the midpoint and rotation of the nitroxides on a cone [23]. The relative orientations of spin labels and the interspin vector were calculated for each conformer. The interspin distance vector  $\mathbf{r}$  for each conformer was given a  $\sin(\theta)$  weighted random orientation on the half sphere with respect to the laboratory frame and the orientation of the  $g$ - and hyperfine-tensors relative to the laboratory frame calculated. The  $g$ - and hyperfine-tensors were assumed to be collinear.

The resonance frequencies for each spin centre were computed from the respective orientations, the  $g$ -tensor values,  $^{14}\text{N}$  hyperfine coupling values and line width. Calculating the frequencies for each of the  $^{14}\text{N}$  nuclear spin quantum number  $m_i$  yields a total of 120,000 single spin centres.

The excitation profiles for the detection  $I_{v1}$  and inversion  $I_{v2}$  pulses are described by Eqs. (1) and (2) respectively [31],

$$I_{v1} = \frac{\xi}{\zeta} \sin(\zeta t_{\pi/2}) \frac{\xi'^4}{4\xi'^4} [1 - \cos(\zeta' t_{\pi})]^2$$

$$\xi = \frac{\pi/2}{t_{\pi/2}}$$

$$\xi' = \frac{\pi}{t_{\pi}}$$

$$\zeta^2 = \xi^2 + (\omega - \omega_r)^2$$

$$\zeta'^2 = \xi'^2 + (\omega - \omega_r)^2$$
(1)

$$I_{v2} = \frac{\xi'^2}{2\zeta'^2} [1 - \cos(\zeta' t_{\pi})]$$
(2)

where  $(\omega - \omega_r)$  is the frequency offset of the microwave pulses. The lengths of the  $\pi/2$  and  $\pi$  pulses are given by  $t_{\pi/2}$  and  $t_{\pi}$ , respectively.

The contribution from each spin pair to the PELDOR modulation is then computed from the detection of spin  $A$  weighted by the inversion probability of spin  $B$  and the detection of spin  $B$  weighted

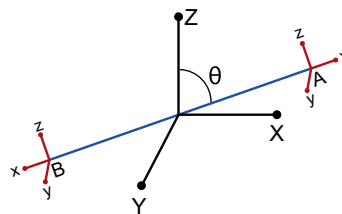


**Fig. 8.** A vector diagram showing the laboratory frame ( $X, Y, Z$ ) and the frames of two connected spin centres  $A$  and  $B$ . The interspin distance is depicted by a blue line with the angle to the applied magnetic field represented by  $\theta$ .

by the inversion probability of spin  $A$  (Eq. (3)). The degree of PELDOR modulation for each spin pair depends on the angle between the interspin vector and the applied magnetic field  $\theta$ , the set of Euler angles that describe the orientation of the  $g$ - and  $A$ -tensors  $\varphi$  and the detection and inversion pulse frequencies,  $\nu_1$  and  $\nu_2$  respectively.

$$\Psi(\theta, \varphi_A, \varphi_B, \nu_1, \nu_2) = I_{v1}(A)(1 - I_{v2}(A))I_{v2}(B)(1 - I_{v1}(B)) + I_{v1}(B)(1 - I_{v2}(B))I_{v2}(A)(1 - I_{v1}(A))$$
(3)

$I_{v1}(A)$  represents excitation of spin  $A$  by the detection sequence. The excitation of spin  $A$  is weighted by the excitation of spin  $B$  by the inversion pulse,  $I_{v2}(B)$ . In case of pulse overlap the detection of spin  $A$  and inversion of spin  $B$  are weighted by the inversion probability of spin  $A$  and detection probability of spin  $B$ ,  $(1 - I_{v2}(A))$  and  $(1 - I_{v1}(B))$  respectively.

Likewise, the intensity of the echo produced by the detection sequence without the inversion pulse is computed by Eq. (4), where  $N$  is the number of molecular conformers.

$$V_0 = \sum_{i=1}^N I_{v1}(A) + I_{v1}(B)$$
(4)

For  $N$  spin pairs, each with a finite number  $R$  of orientations, the intensity of the refocused echo  $V$  with the position of the inversion pulse  $T$  can be described by Eq. (5).

$$V(T) = V_0 + \sum_{i=1}^N \sum_{j=1}^R \Psi^i[\cos(DT) - 1]$$
(5)

$D$  is the dipolar coupling

$$D = \frac{\mu_0 g^2 \beta_e^2}{4\pi\hbar} \frac{1}{r^3} (1 - 3\cos^2(\theta)) + J$$
(6)

where  $\mu_0$  is the permeability of vacuum,  $g$  the isotropic  $g$ -value,  $\beta$  the Bohr magneton,  $\hbar$  the reduced Planck constant,  $r$  the interspin distance and  $J$  the isotropic exchange coupling constant.

By computing  $V_0$  and  $\Psi$ ,  $\theta$  and  $r$  for each molecular conformer and using Eq. (5) the PELDOR time trace is constructed. The calculations of six time traces from 20,000 conformers takes about 14 s

**Table 2**

Parameters used for the simulations of the cw EPR spectra of compounds **1–3**.

Parameters	<b>1</b>	<b>2</b>	<b>3</b>
$g_{xx}, g_{yy}, g_{zz}$	2.0104, 2.0073, 2.0033	2.01, 2.0072, 2.0033	2.0101, 2.0073, 2.0031
$g$ -Strain <sup>a</sup>	0.0004, 0.0003, 0.0001	0.0005, 0.0002, 0.0003	0.0003, 0.0003, 0.0005
$A_{xx}, A_{yy}, A_{zz}$ <sup>b</sup>	8, 6, 96	10, 12, 90	16, 13, 95
$A$ -strain <sup>c</sup>	0, 0, 12	5, 0, 5	1, 1, 5
Linewidth <sup>d</sup>	0.8, 0.13	0.4, 0.02	0.7, 0.11

<sup>a</sup> The  $g$ -strain is given in MHz and listed in the following order ( $x, y, z$ ).

<sup>b</sup> The  $^{14}\text{N}$  hyperfine coupling values are in MHz.

<sup>c</sup> The  $A$ -strain is given in MHz and listed in the following order ( $x, y, z$ ).

<sup>d</sup> The linewidths (Gaussian, Lorentzian) is the peak to peak linewidth in mT.

to compute on a 2.8 GHz Intel processor. The uncertainty in simulation parameters was assessed qualitatively by varying each simulation parameter individually. The difference in a parameter value giving noticeably different simulations was assigned as the error for that variable.

## Acknowledgments

This work was supported by the BBSRC (Grant No. BB/H017917/1), the EPSRC (Grant No. F004583/1) and the Icelandic Research Fund (60028021). G.W.R. acknowledges the School of Biology, University of St Andrews for a SORS (Scottish Overseas Research Students) Scholarship and O.S. thanks the Research Councils of the UK for an RCUK fellowship.

## Appendix A. Supplementary material

Supplementary data associated with this article can be found, in the online version, at doi:10.1016/j.jmr.2012.01.019.

## References

- [1] R.E. Martin, M. Pannier, F. Diederich, V. Gramlich, M. Hubrich, H.W. Spiess, Determination of end-to-end distances in a series of TEMPO diradicals of up to 2.8 nm length with a new four-pulse double electron resonance experiment, *Angew. Chem., Int. Ed.* 37 (1998) 2833–2837.
- [2] A.D. Milov, K.M. Salikhov, M.D. Shirov, Application of the double resonance method to electron spin echo in a study of the spatial distribution of paramagnetic centers in solids, *Sov. Phys. – Solid State* 23 (1981) 565–569.
- [3] G.W. Reginsson, O. Schiemann, Pulsed electron–electron double resonance: beyond nanometre distance measurements on biomacromolecules, *Biochem. J.* 434 (2011) 353–363.
- [4] G.W. Reginsson, O. Schiemann, Studying biomolecular complexes with pulsed electron–electron double resonance spectroscopy, *Biochem. Soc. Trans.* 39 (2011) 128–139.
- [5] G. Jeschke, Y. Polyhach, Distance measurements on spin-labelled biomacromolecules by pulsed electron paramagnetic resonance, *Phys. Chem. Chem. Phys.* 9 (2007) 1895–1910.
- [6] V.P. Denysenkov, T.F. Prisner, J. Stubbe, M. Bennati, High-field pulsed electron–electron double resonance spectroscopy to determine the orientation of the tyrosyl radicals in ribonucleotide reductase, *Proc. Natl. Acad. Sci.* 103 (2006) 13386–13390.
- [7] Y. Polyhach, A. Godt, C. Bauer, G. Jeschke, Spin pair geometry revealed by high-field DEER in the presence of conformational distributions, *J. Magn. Reson.* 185 (2007) 118–129.
- [8] O. Schiemann, P. Cekan, D. Margraf, T.F. Prisner, S.T. Sigurdsson, Relative orientation of rigid nitroxides by PELDOR: beyond distance measurements in nucleic acids, *Angew. Chem., Int. Ed.* 48 (2009) 3292–3295.
- [9] A. Marko, D. Margraf, P. Cekan, S.T. Sigurdsson, O. Schiemann, T. Prisner, Analytical method to determine the orientation of rigid spin labels in DNA, *Phys. Rev. E* 81 (2010) 021911–1–021911–9.
- [10] A. Marko, V.P. Denysenkov, D. Margraf, P. Cekan, O. Schiemann, S.T. Sigurdsson, T. Prisner, Conformational flexibility of DNA, *J. Am. Chem. Soc.* 133 (2011) 13375–13379.
- [11] B. Endeward, J.A. Butterwick, R. MacKinnon, T. Prisner, Pulsed electron–electron double-resonance determination of spin-label distances and orientations on the tetrameric potassium ion channel KcsA, *J. Am. Chem. Soc.* 131 (2009) 15246–15250.
- [12] B.E. Bode, J. Plackmeyer, M. Bolte, T. Prisner, O. Schiemann, PELDOR on an exchange coupled nitroxide copper(II) spin pair, *J. Organomet. Chem.* 694 (2009) 1172–1179.
- [13] B.E. Bode, J. Plackmeyer, T.F. Prisner, O. Schiemann, PELDOR measurements on a nitroxide-labeled Cu(II) porphyrin: orientation selection, spin-density distribution, and conformational flexibility, *J. Phys. Chem. A* 112 (2008) 5064–5073.
- [14] D.M. Bridges, K. Hideg, W.L. Hubbell, Resolving conformational and rotameric exchange in spin labeled proteins using saturation recovery EPR, *Appl. Magn. Reson.* 37 (2010) 363–390.
- [15] M.R. Fleissner, D.M. Bridges, E.K. Brooks, D. Cascio, T. Kálai, K. Hideg, W.L. Hubbell, Structure and dynamics of a conformationally constrained nitroxide side chain and applications in EPR spectroscopy, *Proc. Natl. Acad. Sci. U. S. A.* 108 (2011) 16241–16246.
- [16] I. Tkach, G. Sicoli, C. Höbartner, M. Bennati, A dual-mode microwave resonator for double electron–electron spin resonance spectroscopy at W-band microwave frequencies, *J. Magn. Reson.* 209 (2011) 341–346.
- [17] A. Savitsky, A.A. Dubinskii, M. Flores, W. Lubitz, K. Möbius, Orientation-resolving pulsed electron dipolar high-field EPR spectroscopy on disordered solids: I. Structure of spin-correlated radical pairs in bacterial photosynthetic reaction centers, *J. Phys. Chem. B* 111 (2007) 6245–6262.
- [18] M. Flores, A. Savitsky, M.L. Paddock, E.C. Abresch, A. Dubinskii, M.Y. Okamura, W. Lubitz, K. Möbius, Electron-nuclear and electron–electron double resonance spectroscopies show that the primary quinone acceptor QA in reaction centers from photosynthetic bacteria *Rhodospirillum rubrum* remains in the same orientation upon light-induced reduction, *J. Phys. Chem. B* 114 (2010) 16894–16901.
- [19] V.P. Denysenkov, D. Biglino, W. Lubitz, T. Prisner, M. Bennati, Structure of the tyrosyl biradical in mouse R2 ribonucleotide reductase from high-field PELDOR, *Angew. Chem.* 47 (2008) 1224–1227.
- [20] D. Goldfarb, Y. Lipkin, A. Potapov, Y. Gorodetsky, B. Epel, A.M. Raitisimring, M. Radoul, I. Kaminker, HYSCORE and DEER with an upgraded 95 GHz pulse EPR spectrometer, *J. Magn. Reson.* 194 (2008) 8–15.
- [21] P.A.S. Cruickshank, D.R. Bolton, D.A. Robertson, R.I. Hunter, R.J. Wyld, G.M. Smith, A kilowatt pulsed 94 GHz electron paramagnetic resonance spectrometer with high concentration sensitivity, high instantaneous bandwidth, and low dead time, *Rev. Sci. Instrum.* 80 (2009) 103102–1–103102–15.
- [22] D. Margraf, P. Cekan, T. Prisner, S.T. Sigurdsson, O. Schiemann, Ferro- and antiferromagnetic exchange coupling constants in PELDOR spectra, *Phys. Chem. Chem. Phys.* 11 (2009) 6708–6714.
- [23] D. Margraf, B.E. Bode, A. Marco, O. Schiemann, T.F. Prisner, Conformational flexibility of nitroxide biradicals determined by X-band PELDOR experiments, *Mol. Phys.* 105 (2007) 2153–2160.
- [24] G. Jeschke, I.P. Chechik, A. Godt, H. Zimmermann, J. Banham, C.R. Timmel, J.H. Hilger, DeerAnalysis 2006 – a comprehensive software package for analyzing pulsed ELDOR data, *Appl. Magn. Reson.* 30 (2006) 473–498.
- [25] A. Godt, M. Schulte, H. Zimmermann, G. Jeschke, How flexible are poly(paraphenyleneethynylene)s?, *Angew. Chem., Int. Ed.* 45 (2006) 7560–7564.
- [26] B. Gao, M. Wang, Y. Cheng, L. Wnag, X. Jing, F. Wang, Pyrazine-containing acene-type molecular ribbons with up to 16 rectilinearly arranged fused aromatic rings, *J. Am. Chem. Soc.* 130 (2008) 8297–8306.
- [27] S.E. Ashbrook, Recent advances in solid-state NMR spectroscopy of quadrupolar nuclei, *Phys. Chem. Chem. Phys.* 11 (2009) 6892–6905.
- [28] F. Neese, ORCA – An ab-initio, Density Functional and Semiempirical Program Package, University of Bonn, 2011.
- [29] W.J. Hehre, R. Ditchfield, J.A. Pople, Self-consistent molecular orbital methods. XII. Further extensions of gaussian-type basis sets for use in molecular orbital studies of organic molecules, *J. Chem. Phys.* 56 (1972) 2257.
- [30] S. Stoll, A. Schweiger, EasySpin, a comprehensive software package for spectral simulation and analysis in EPR, *J. Magn. Reson.* 178 (2006) 42–55.
- [31] A. Marko, D. Margraf, H. Yu, Y. Mu, G. Stock, T. Prisner, Molecular orientation studies by pulsed electron–electron double resonance experiments, *J. Chem. Phys.* 130 (2009) 064102–1–064102–9.

# W-Band PELDOR with 1kW Microwave Power: Molecular Geometry, Flexibility and Exchange Coupling

Gunnar W. Reginsson<sup>1,2</sup>, Robert I. Hunter<sup>3</sup>, Paul A. S. Cruickshank<sup>3</sup>, David R. Bolton<sup>3</sup>, Snorri Th. Sigurdsson<sup>2</sup>, Graham M. Smith<sup>3\*</sup>, Olav Schiemann<sup>1\*</sup>

<sup>1</sup>*Biomedical Sciences Research Complex, Centre of Magnetic Resonance, University of St Andrews, St Andrews KY16 9ST, UK.*

<sup>2</sup>*Science Institute, University of Iceland, Dunhaga 3, 107 Reykjavik, Iceland.*

<sup>3</sup>*School of Physics and Astronomy, Centre of Magnetic Resonance, University of St Andrews, St Andrews KY16 9SS, UK.*

\* To whom correspondence should be addressed (e-mail: <mailto:os11@st-andrews.ac.uk>, phone: +44(0)1334-46 3410 or e-mail: [gms@st-andrews.ac.uk](mailto:gms@st-andrews.ac.uk), phone: +44(0)1334-46 2669).

**Supporting information**

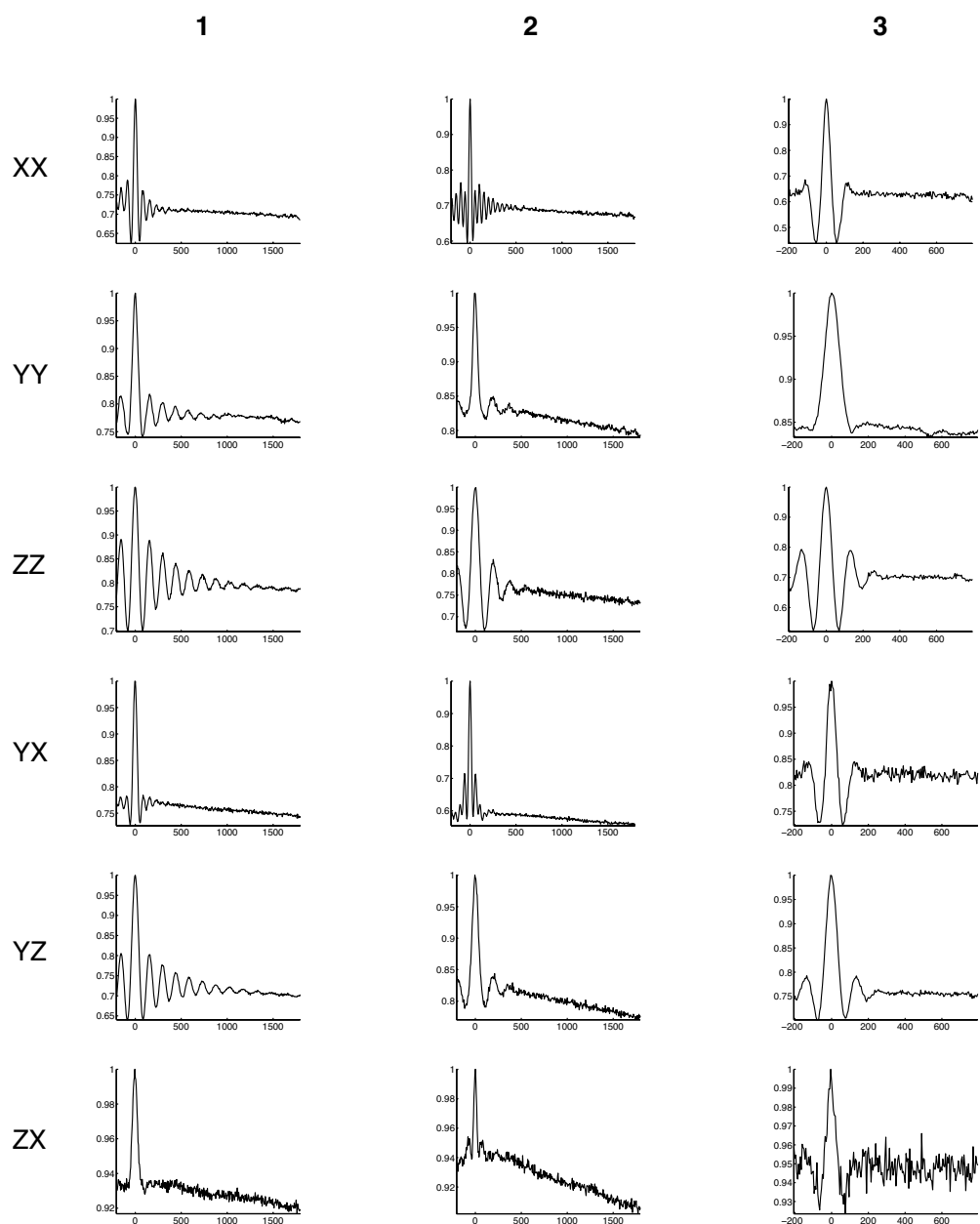


**Figure S1.** Experimental PELDOR time traces for compounds **1** – **3** before background correction. ZX denotes inversion pulse on  $g_z$  and detection sequence on  $g_x$  etc. The time traces are normalized with respect to maximum intensity.

# Protein-induced changes in DNA structure and dynamics observed with noncovalent site-directed spin labeling and PELDOR

Gunnar W. Reginsson<sup>1,2</sup>, Sandip A. Shelke<sup>2</sup>, Christophe Rouillon<sup>3</sup>, Malcolm F. White<sup>3</sup>, Snorri Th. Sigurdsson<sup>2</sup> and Olav Schiemann<sup>1,\*</sup>

<sup>1</sup>Biomedical Sciences Research Complex, Centre of Magnetic Resonance, University of St Andrews, St Andrews KY16 9ST, UK, <sup>2</sup>Science Institute, University of Iceland, Dunhaga 3, 107 Reykjavík, Iceland and <sup>3</sup>Biomedical Sciences Research Complex, University of St Andrews, St Andrews KY16 9ST, UK

Received May 7, 2012; Revised July 23, 2012; Accepted August 5, 2012

## ABSTRACT

Site-directed spin labeling and pulsed electron-electron double resonance (PELDOR or DEER) have previously been applied successfully to study the structure and dynamics of nucleic acids. Spin labeling nucleic acids at specific sites requires the covalent attachment of spin labels, which involves rather complicated and laborious chemical synthesis. Here, we use a noncovalent label strategy that bypasses the covalent labeling chemistry and show that the binding specificity and efficiency are large enough to enable PELDOR or DEER measurements in DNA duplexes and a DNA duplex bound to the Lac repressor protein. In addition, the rigidity of the label not only allows resolution of the structure and dynamics of oligonucleotides but also the determination of label orientation and protein-induced conformational changes. The results prove that this labeling strategy in combination with PELDOR has a great potential for studying both structure and dynamics of oligonucleotides and their complexes with various ligands.

## INTRODUCTION

Nucleic acids play a complex role in biological processes. Therefore, it is of great importance to solve their structure and conformational distribution to understand the structure–function relationship of nucleic acids or nucleic acid/protein complexes. Pulsed electron–electron double resonance (PELDOR or DEER) (1,2), together with site-directed spin labeling (SDSL) (3,4), is increasingly

being used as a method for structure determination of biomolecules (5). PELDOR is a pulsed electron paramagnetic resonance (EPR) technique that is capable of measuring distances in the range of 2–8 nm between spin centers in biological samples (6). Therefore, this method requires that the nucleic acids be labeled with molecules that carry an unpaired electron, the so-called spin labels.

The most widely used family of spin labels is nitroxides (7). These labels can be attached to the sugar, base or phosphate backbone via linkers of different flexibilities, either during chemical synthesis of the nucleic acid or postsynthetically (3,5). Since flexible linkers introduce an unwanted distribution to distance measurements, the determination of precise distances and conformational distribution of nucleic acid becomes more challenging. A way to get around this problem is incorporating rigid spin labels (8,9). The rigid spin label  $\zeta$  (Figure 1a), reported by Sigurdsson *et al.* (9–11), has afforded precise distance measurements, mutual orientation of spin labels and conformational dynamics of nucleic acids through EPR (9, 12–14). However, all of these labeling strategies require covalent attachment of the label and, thus, rather elaborate organic synthesis, which hampers the wide application and dissemination of this technique.

Recently, we have developed a noncovalent SDSL strategy (NC-SDSL) that utilizes spin label  $\zeta$  (15), the nucleobase of the rigid spin label nucleoside  $\zeta$ . Spin label  $\zeta$  binds to the abasic site in duplex DNA by hydrogen bonding with the orphan guanine (G) base present on the complementary strand and by stacking interaction with base pairs flanking the abasic site. Since the DNAs that contains abasic sites are commercially available, the preparation of spin-labeled nucleic acid sample has become as simple as mixing a spin label with a duplex DNA containing abasic sites. Here, we show that

\*To whom correspondence should be addressed. Tel: +44 1334 463410; Fax: +44 1334 462595; Email: os11@st-andrews.ac.uk  
Present address:

Olav Schiemann, Institute of Physical and Theoretical Chemistry, University of Bonn, Bonn 53115, Germany.

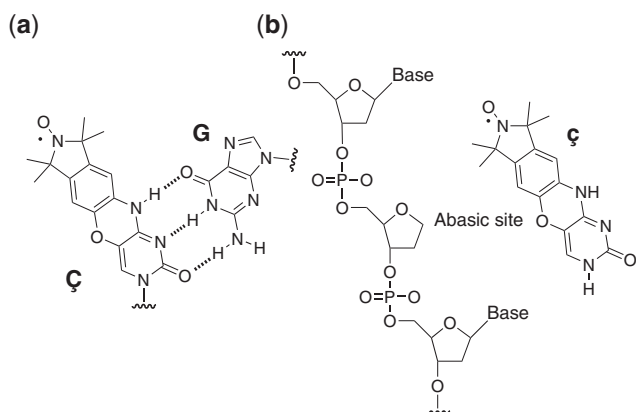


**Figure 1.** Structures of spin labels and abasic site. (a) The rigid spin label  $\zeta$  base paired with G. (b) A DNA oligomer containing an abasic site and the rigid spin label  $\zeta$ .

the specificity and binding efficiency of  $\zeta$  for abasic sites in duplex DNAs (Table 1) are high enough to permit PELDOR measurements with resolved modulations and orientation selectivity. Furthermore, we show on the DNA/Lac repressor system that such measurements can be performed in the presence of DNA-binding proteins and that they enable one to observe DNA bending and dynamics.

## MATERIALS AND METHODS

### General procedures

NaCl and 2-(*N*-morpholino)ethanesulfonic acid (MES) were obtained from Fluka.  $\text{Na}_2\text{HPO}_4 \cdot 6 \text{H}_2\text{O}$ , ethanol and ethylenediaminetetraacetic acid (EDTA) were obtained from Fischer Scientific. Ethylene glycol was obtained from Aldrich. Deuterated ethylene glycol (98%) and deuterium oxide (99%) were obtained from Cambridge Isotope Laboratories.

### Synthesis and purification of DNA oligomers

#### *29-Mer $\zeta$ labeled DNA oligomers were synthesized and purified as previously reported (11)*

DNA oligomers containing abasic sites were synthesized by a trityl-off synthesis on a 1.0  $\mu\text{mol}$  scale (1000 Å CPG columns) using an automated ASM 800 Biosset DNA synthesizer and phosphoramidites with standard protecting groups. 1,2-Dideoxy *D*-ribose CED phosphoramidite was used as a building block for abasic oligomer synthesis. The DNA oligomers were deprotected in concentrated ammonia solution at 55°C for 8 h and purified by 20% denaturing polyacrylamide gel electrophoreses (DPAGE). The oligonucleotides were visualized by ultraviolet (UV) shadowing, and the bands excised from the gel were crushed and soaked in TEN buffer (10 mM Tris pH 7.5, 250 nM NaCl and 1 mM  $\text{Na}_2\text{EDTA}$ ). The DNA elution solutions were filtered through a 0.45- $\mu\text{m}$  polyethersulfone membrane (disposable filter device from Whatman) and desalted using Sep-Pak cartridge (Waters Corporation) according to manufacturer's instructions. After removing the solvent under vacuum, the oligonucleotides were

dissolved in deionized and sterilized water (200  $\mu\text{l}$ ). All commercial phosphoramidites, CPG columns and solutions for DNA synthesis were purchased from ChemGenes Corporation.

29-Mer DNA oligomers containing 19-mer LacI operator sequence and abasic sites were purchased from Eurogentec. Purification was done with DPAGE and quality control by MALDI-TOF mass spectrometry.

The concentration of DNA oligomers was calculated from Beer's law based on measurements of absorbance at 260 nm, using a 50 Bio UV-visible spectrometer from Varian, equipped with a 100  $\mu\text{l}$  cell (optical path length = 1 cm). Extinction coefficients of DNA oligomers were determined using the UV WinLab oligonucleotide calculator (V2.85.04, Perkin Elmer). ssDNA oligomers solutions (1  $\mu\text{l}$ ) were dissolved in sterilized water (99  $\mu\text{l}$ ) and transferred to spectrometer cell for measurements. Sterilized water was used as a reference sample. Evaporation of solvents under vacuum was carried out on an SPD 111-V speed-vac from Savant equipped with vapor trap and vacuum inversion. Preparation of all DNA samples for EPR measurements were done in sterile Biopur Eppendorf tubes (2 ml) with cap.

### Hybridization of oligonucleotides

Hybridization of all DNA oligomers was performed with a PCH-2 heating block from Grant-bio. Complementary DNA strands were annealed according to the following program: 90°C for 2 min, 60°C for 5 min, 50°C for 5 min, 40°C for 5 min, 22°C for 15 min. The DNA samples were stored at -30°C.

### Preparation of dsDNA 1

Synthesized and purified DNA oligomers were reconstituted with sterile water in Biopur Eppendorf tubes (2 ml). Noncovalently spin-labeled DNA duplexes were prepared by mixing appropriate single-stranded DNA oligomers (5 nmol) with two equivalents of spin label  $\zeta$  dissolved in ethanol (10 nmol). The water/ethanol solution was evaporated under vacuum and the dry sample was dissolved in phosphate buffer ( $\text{Na}_2\text{HPO}_4$  10 mM, NaCl 100 mM,  $\text{Na}_2\text{EDTA}$  0.1 mM, pH 7.00) (100  $\mu\text{l}$ ). After annealing the DNA oligomers, the solvent was removed under vacuum. The dry sample was dissolved in sterile water with 20% (v/v) ethylene glycol (100  $\mu\text{l}$ ). All samples were transferred to a quartz EPR tube, rapidly frozen in (1:4 methylcyclohexane:iso-pentane at -165°C) and stored in liquid nitrogen.

### Preparation of dsDNA 2

29-Mer DNA oligomers (4 nmol) were mixed with two equivalents of  $\zeta$  dissolved in ethanol (8 nmol) and annealed in phosphate buffer ( $\text{Na}_2\text{HPO}_4$  10 mM, NaCl 100 mM,  $\text{Na}_2\text{EDTA}$  0.1 mM, pH 7.00) (100  $\mu\text{l}$ ). The solvent was removed under vacuum, and the dry sample was dissolved in MES buffer (MES 20 mM pH 6.0, NaCl 300 mM, in  $^2\text{H}_2\text{O}$ ) (80  $\mu\text{l}$ ) and deuterated ethylene glycol (20  $\mu\text{l}$ ). The sample was transferred to an EPR tube, rapidly frozen in a freezing mixture and stored in liquid nitrogen.



**Table 1.** Sequences for the dsDNAs containing abasic sites that were noncovalently spin labeled

DNA	DNA sequence
dsDNA 1	5'-GATGCGFGCGCGGACTGAC-3' 3'-CTACGCGCGCGCTGAFTG-5'
dsDNA 2	5'-GCGFATTGTGAGCGGATAACAATTTGGCG-3' 3'-CGCGTAACTCGCCTATTGTAAAFCGC-5'

The abasic sites are denoted by F. The bold sequence in dsDNA 2 is the 19-mer Lac repressor consensus sequence.

### Electrophoretic mobility shift assay

Aliquots of LacI from *Escherichia coli* (150  $\mu$ M) in MES buffer (MES 20 mM pH 6.0, NaCl 300 mM, 50% in  $^2\text{H}_2\text{O}$ ) were prepared.  $^{32}\text{P}$ -labeled 29-mer dsDNA (50 nM) was incubated for 20 min at room temperature with two equivalents of  $\zeta$  spin label and Lac repressor, titrated at 0.25, 0.5, 0.75, 1.25, 2.5, 5 and 12.5  $\mu$ M, in MES buffer (MES 20 mM pH 6.0, NaCl 300 mM, 100% in  $^2\text{H}_2\text{O}$ ), before loading onto 12% native acrylamide gel (90 mM Tris-borate, 2 mM EDTA). Gels were run at 130 V for 4 h, exposed to phosphor imaging screen and visualized using a Fuji FLA5000 imager.

### Preparation of dsDNA 2 with lac repressor

29-Mer DNA oligomers (4 nmol) were mixed with two equivalents of  $\zeta$  dissolved in ethanol (8 nmol) and annealed in phosphate buffer ( $\text{Na}_2\text{HPO}_4$  10 mM, NaCl 100 mM,  $\text{Na}_2\text{EDTA}$  0.1 mM, pH 7.00) (100  $\mu$ l). The solvent was removed under vacuum, and the dry sample was dissolved in MES buffer (MES 20 mM pH 6.0, NaCl 300 mM, 50% in  $^2\text{H}_2\text{O}$ ) containing Lac repressor (315  $\mu$ M) (80  $\mu$ l) and deuterated ethylene glycol (20  $\mu$ l). The sample was transferred to an EPR tube and rapidly frozen in a freezing mixture  $\sim$ 10 min after addition of LacI. The sample was stored in liquid nitrogen.

### Preparation of dsDNA 3

29-Mer DNA oligomers (4 nmol) spin labeled with the  $\zeta$  spin label were annealed in phosphate buffer ( $\text{Na}_2\text{HPO}_4$  10 mM, NaCl 100 mM,  $\text{Na}_2\text{EDTA}$  0.1 mM, pH 7.00) (100  $\mu$ l). The solvent was removed under vacuum, and the dry sample was dissolved in MES buffer (MES 20 mM pH 6.0, NaCl 300 mM, in  $^2\text{H}_2\text{O}$ ) (80  $\mu$ l) and deuterated ethylene glycol (20  $\mu$ l). The sample was transferred to an EPR tube, rapidly frozen in a freezing mixture and stored in liquid nitrogen.

### Preparation of dsDNA 3 with lac repressor

29-Mer DNA oligomers (4 nmol) spin labeled with the  $\zeta$  spin label were annealed in phosphate buffer ( $\text{Na}_2\text{HPO}_4$  10 mM, NaCl 100 mM,  $\text{Na}_2\text{EDTA}$  0.1 mM, pH 7.00) (100  $\mu$ l). The solvent was removed under vacuum, and the dry sample was dissolved in MES buffer (MES 20 mM pH 6.0, NaCl 300 mM, 50% in  $^2\text{H}_2\text{O}$ ) containing Lac repressor (315  $\mu$ M) (80  $\mu$ l) and deuterated ethylene glycol (20  $\mu$ l). The sample was transferred to an EPR

tube and rapidly frozen in a freezing mixture  $\sim$ 10 min. after addition of LacI. The sample was stored in liquid nitrogen.

### Pulse EPR measurements

Pulse EPR measurements were done using a Bruker ELEXSYS E580 X-band EPR spectrometer with a standard flex line probe head, housing a dielectric ring resonator (MD4). For measurements at cryogenic temperatures, a continuous-flow helium cryostat (CF935) and a temperature control system (ITC 502) from Oxford instruments were used. All pulsed experiments were performed at 50 K. For PELDOR measurements, a double-microwave frequency setup available from Bruker was used. Microwave pulses were amplified with a TWT amplifier (117X) from Applied Systems Engineering. PELDOR experiments were done using the four-pulse sequence,  $\pi/2(\nu_A) - \tau_1 - \pi(\nu_A) - (\tau_1 + t) - \pi(\nu_B) - (\tau_2 - t) - \pi(\nu_A) - \tau_2 - \text{echo}$ . To eliminate receiver offsets, the  $\pi/2(\nu_A)$  pulse was phase cycled by applying the microwave pulse consecutively through the  $+\langle x \rangle$  and  $-\langle x \rangle$  channels and subtracting the signals. The length of the detection pulses ( $\nu_A$ ) were set to 16 ( $\pi/2$ ) and 32 ns ( $\pi$ ). The frequency of the inversion pulse ( $\nu_B$ ) was set at the maximum of the nitroxide field sweep spectrum, and the length was set to 16 ns. Amplitude and phase of the pulses were set to optimize the refocused echo (RE). The frequency of the detection pulses ( $\nu_A$ ) was 40–90 MHz higher than the frequency of the inversion pulse ( $\nu_B$ ). All PELDOR spectra were recorded with a short repetition time of 4000–5000  $\mu$ s, video amplifier bandwidth of 20 MHz and amplifier gain of 51–57 dB.  $\tau_1$  was set to 200 ns for samples in protonated matrix and to 380 ns for samples in deuterated matrix. Proton and deuterium modulation were suppressed by incrementing  $\tau_1$  by 8 ns eight times and adding the consecutive spectra. The time increment of the inversion pulse was set to either 12 or 30 ns.

### Data analysis, simulation and modeling

Experimental PELDOR time traces were background subtracted and Fourier transformed using DeerAnalysis2011 (16). Distance distributions were generated from orientation average time traces using Tikhonov regularization, as implemented in DeerAnalysis2011. The equilibrium geometry of spin label  $\zeta$  was calculated using density functional theory (DFT) with the B3LYP functional and 6-31 G\* basis set as implemented in Spartan (Wavefunction). B-form DNA structures were modeled with the make-na server from <http://casegroup.rutgers.edu/Biomer/index.html>. Abasic sites were introduced into the DNA duplexes by deleting the corresponding cytosine and replacing the glycosidic bond with hydrogen using PyMol (DeLano Scientific LLC). Simulated PELDOR time traces and distance distributions were done using a Matlab program as previously described (17).

## RESULTS AND DISCUSSIONS

Sequence-specific binding of DNA by proteins regulates transcription and translation processes and thereby

expression of specific genes. Such binding events have been studied by several techniques, such as foot printing (18), photochemical cross-linking (19) and various spectroscopic approaches (20). There are a number of examples of major conformational changes associated with such binding events (21,22). Studying the details of such molecular rearrangements requires high-resolution techniques, such as X-ray crystallography (23) or NMR spectroscopy (24,25). Unfortunately high-resolution structures of nucleic acid/protein complexes are not readily obtained, and static crystal structures give limited information about dynamics that may play a role in the mechanism of gene regulation (26). Solution studies through long-range distance measurements have been performed using fluorescence resonance energy transfer (FRET), but this technique suffers from the flexibility and uncertainty in orientation of the dyes (27). On the other hand, the use of rigid spin labels and PELDOR enables accurate distance measurements and also yields information on orientations (14).

### The PELDOR method

PELDOR can determine distances between two nitroxide spin labels, placed into biopolymers using SDSL (28), through measurement of the dipolar coupling between the two spins. The relationship between dipolar coupling and distance is described by Equation (1) (29):

$$\nu_{\text{dip}} = \frac{52.16}{r^3} (1 - 3 \cos^2 \theta), \quad (1)$$

where 52.16 is the dipolar splitting constant for two nitroxides,  $r$  is the magnitude of the interspin distance vector  $\mathbf{r}$  and  $\theta$  is the angle between the applied magnetic field  $B_0$  and the distance vector. In a four-pulse PELDOR experiment, the intensity of the RE, created from spins in resonance with the detection sequence  $\nu_A$  (spins A), is modulated by the inversion of spins in resonance with the inversion pulse  $\nu_B$  (spins B) (Figure 2). The frequency of this modulation is the dipolar coupling between spins A and B. When the orientation of the spin centers in a molecule is fixed, the modulation frequency and depth of the PELDOR time trace become dependent on the frequency of the detection sequence (9).

### PELDOR measurements on dsDNA 1

dsDNA 1 was mixed with two equivalents of the spin label  $\zeta$  and then hybridized in phosphate buffer containing 20%

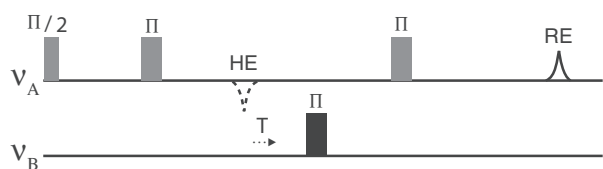


**Figure 2.** The four-pulse PELDOR sequence. The detection sequence  $\nu_A$  is in gray. The inversion pulse  $\nu_B$  is in black. The Hahn echo (HE) and RE are denoted by a broken and solid line, respectively.

ethylene glycol as cryoprotectant. Binding of the spin labels to the abasic sites was confirmed by measuring the noncovalently spin-labeled DNA with continuous wave (CW) EPR at 0 to  $-40^\circ\text{C}$  (Supplementary Information, Supplementary Figure S1). The spin-labeled dsDNA was then measured with four-pulse PELDOR (2), placing the inversion pulse at the center of the nitroxide spectrum and the detection pulse sequence at 40–90 MHz higher frequency (Figure 3). At 90 MHz offset, the detection sequence excites predominantly the  $A_{zz}$  component of the  $^{14}\text{N}$  hyperfine tensor. Decreasing the frequency offset to 40 MHz results in an increased excitation of  $A_{xx}$ ,  $A_{yy}$  and off-diagonal components.

Acquiring the PELDOR experiments at 40–90 MHz offset, in steps of 10 MHz, resulted in the time traces with varying modulation frequency and depth shown in Figure 4a. The PELDOR time trace acquired at 40 MHz offset has a modulation depth  $\Delta$  of about 0.16 (Figure 4c). This modulation depth depends on the relative orientation of the spin labels, the degree of orientation correlation, the ratio between coupled spin pairs in DNA and the total spin concentration (30). Therefore, comparing this modulation depth to one of a DNA with the same base sequence but with the covalently attached spin label  $\zeta$  (which is 100% doubly spin-labeled) gives access to the degree of noncovalent binding, assuming that the relative orientation and the orientation correlation are the same. The covalently labeled DNA duplex, at 40 MHz offset, had a modulation depth of about 0.45 (9). Comparing this to the modulation depth of 0.16 for the noncovalently labeled DNA indicates that  $0.16/0.45 = 36\%$  of the DNA duplexes contain two noncovalently bound spin labels. The same result was obtained at the other frequency offset. The percentage of doubly labeled DNAs could not be increased by increasing the ratio of spin label to duplex nor by varying the flanking bases for both abasic sites (31). Rapidly freezing the noncovalently spin-labeled DNA either before or after cooling the sample to approximately  $-30^\circ\text{C}$  did not affect the modulation depth (data not shown).

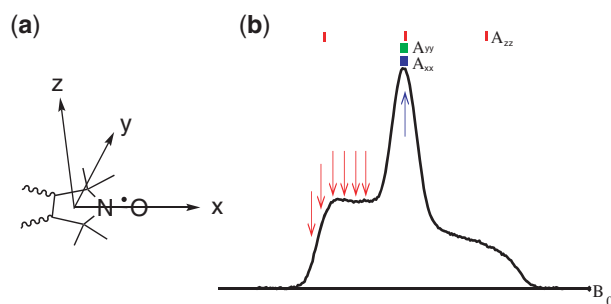


**Figure 3.** The A-tensor frame and EPR spectrum for a nitroxide and the relative orientation of the A-tensor's principal components. (b) A nitroxide EPR spectrum at X-band. The blue arrow indicates the position of the inversion pulse. The red arrows indicate the position of the detection pulses at 40–90 MHz offsets between the frequencies of the detection and inversion pulses. The sticks at the top of the figure show the approximate positions of the  $^{14}\text{N}$  hyperfine coupling components.

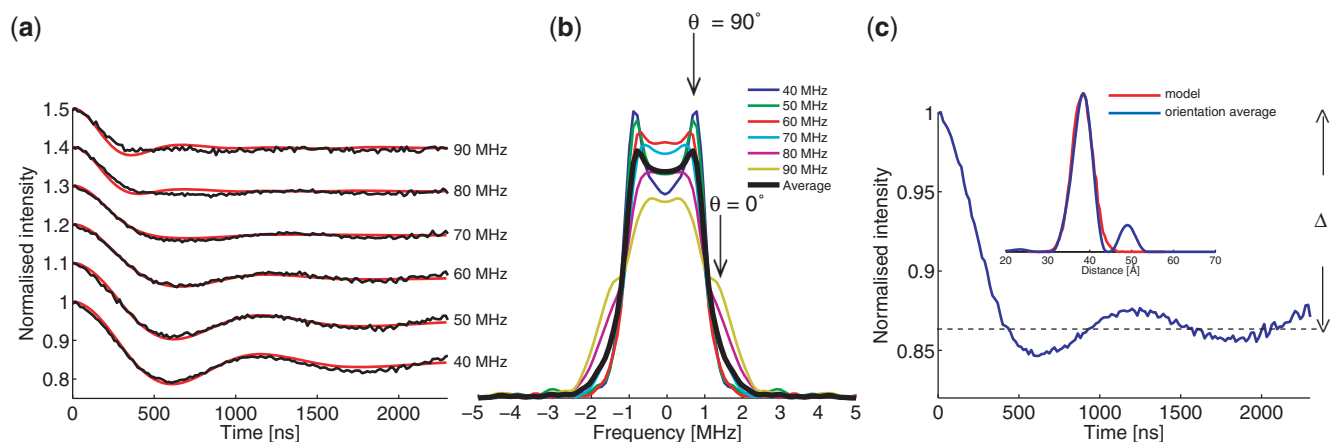


**Figure 4.** PELDOR data for **dsDNA 1**. (a) PELDOR time traces of noncovalently spin-labeled **dsDNA 1** (black) with simulated time traces overlaid (red). The time traces have been background subtracted, normalized and displaced on the y-axis for clarity (original time traces are depicted in the Supplementary Information). (b) Fourier transformation of the experimental time traces and their sum. Arrows point to the perpendicular and parallel components. (c) Orientation-averaged time trace and distance distribution from simulation (red) and summed time trace (blue).  $\Delta$  represents the modulation depth.

The dependence of the dipolar frequency on the frequency offset can be seen in the Fourier transformed time traces in Figure 4b. These show that the parallel component of the dipolar spectrum ( $\theta = 0^\circ$ ) increases in intensity as the detection sequence is moved from 40 to 90 MHz offset. This trend was also observed for the covalently spin labeled dsDNA (9) and indicates that the  $A_{zz}$  components of the rigid spin label  $\zeta$  are approximately parallel to the interspin vector  $\mathbf{r}$  (Figure 5a). Since the PELDOR time traces of the noncovalently spin-labeled dsDNA show that the spin-label orientation is correlated with the orientation of the interspin vector  $\mathbf{r}$ , the distance distribution cannot be obtained from the individual time traces using the program DeerAnalysis2011 (32). Instead, all six time traces recorded at the different spectral positions were added together, as described by Godt *et al.* (33), which yields an orientation-averaged time trace. The resulting orientation-averaged time trace, its Fourier transformation and the corresponding distance distribution are shown in Figure 4b and c. The obtained distance distribution has a mean distance of  $38 \pm 2.2 \text{ \AA}$  (Figure 4c, inset), nearly identical to that previously determined for the covalently spin-labeled **dsDNA 1** ( $37 \pm 1 \text{ \AA}$ ) (9).

To obtain information on the conformational dynamics of the dsDNA and spin label orientation, the PELDOR time traces were simulated with an in-house Matlab<sup>®</sup> program (17) using the cooperative twist-stretch dynamic model for short dsDNA (34,35) (Supplementary Figure S2) that was recently applied by the lab of Prisner (14) for the analysis of PELDOR data obtained from the covalent version of our label. Using identical dynamics parameters as for the covalently spin labeled dsDNA (14), except for the mean distance (see Supplementary Information, Supplementary Table S1), the simulated PELDOR time traces agree well with the experimental time traces (Figure 4a) and yield a distance distribution in agreement with the distribution from the orientation-averaged time trace (Figure 4c). It should also be noted that all six time traces were simulated with the same set

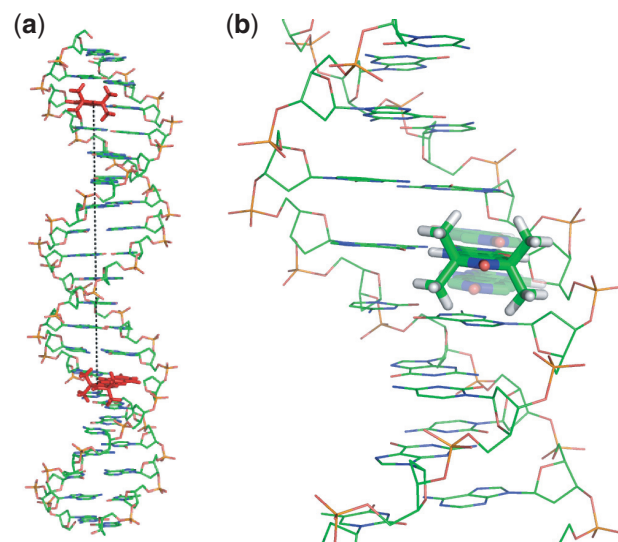


**Figure 5.** Molecular models of the noncovalently spin-labeled **dsDNA 1**. (a) Molecular model of **dsDNA 1** showing the relative positioning of the  $\zeta$  spin labels (red) and the distance vector between them (broken black line). (b) A close-up view of  $\zeta$  (stick representation) within the DNA abasic site. The conformational dynamics of the spin label, as implemented in the PELDOR simulations, are depicted. The transparent spin labels show how the spin labels move away from an equilibrium position upon cooperative twist-stretching of the DNA helix. The conformational dynamics of the DNA helix have been omitted, and the methyl groups of the transparent spin labels have been removed for clarity.

of geometrical parameters. Interspin distances obtained from PELDOR, simulations and modeling DNA duplexes are summarized in Table 2.

### Observing LacI-induced DNA bending by PELDOR

To assess the applicability of noncovalent spin labeling for distance measurements on DNA/protein complexes, the

binding of the Lac repressor protein (LacI) to the consensus Lac operator DNA sequence (Figure 6) was chosen as a proof of principle experiment. The Lac repressor binds specifically to the operator and distorts the DNA from its B-form by bending the center of the operator sequence through an angle of  $\sim 45^\circ$  (37–39). If the LacI protein is able to bind to a DNA containing two abasic sites occupied by the spin label  $\zeta$ , then the accompanied bending of the DNA should manifest in a distance change in the PELDOR experiment.

For this experiment, we used a 29-mer dsDNA that contains a 19-mer Lac consensus sequence and two abasic sites (**dsDNA 2**, Table 1). To verify the binding of the Lac repressor protein (LacI from *Escherichia coli*) to the dsDNA, an electrophoretic mobility shift assay

**Table 2.** Interspin distances for all dsDNA

dsDNA	$r_{\text{DA}}^{\text{a}}$ (Å)	$r_{\text{Simulation}}^{\text{b}}$ (Å)	$r_{\text{MM/X-ray}}^{\text{c}}$ (Å)
<b>dsDNA 1</b>	$38.0 \pm 2.2$	$38.6 \pm 2.5$ ( $0.4 \pm 0.1$ )	38
<b>dsDNA 2</b>	$69.2 \pm 3.8$	$70.0 \pm 4.8$ ( $1 \pm 0.1$ )	73
<b>dsDNA 2 + LacI</b>	$64.6 \pm 4.1$	$65.0 \pm 5.3$ ( $1 \pm 0.1$ )	67

<sup>a</sup>Most probable distance  $\pm$  one standard deviation from orientation-averaged PELDOR time traces using DeerAnalysis 2011.

<sup>b</sup>Most probable distance  $\pm$  one standard deviation. The error in the distance  $\pm$  one standard deviation is in brackets.

<sup>c</sup>Interspin distances obtained from molecular modeling using B-form DNA duplexes. The interspin distance for **dsDNA 2** bound to LacI was estimated by modeling spin labels into the X-ray structure of a 21-mer dsDNA bound to LacI (pdb id. 1LBG).

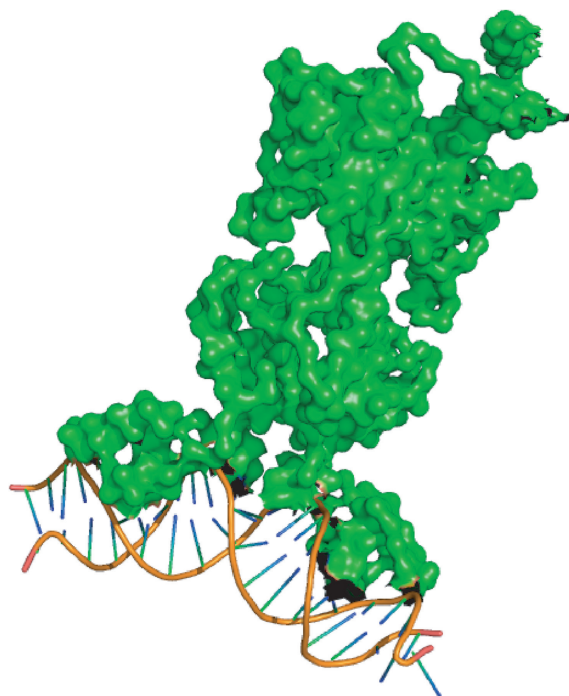


**Figure 6.** Lac repressor dimer bound to a 21-mer symmetric Lac operator (PDB 1LBG) (36). The Lac repressor is represented in surface mode. The Lac operator DNA is represented in cartoon mode.

was used. The 29 base pair DNA duplex with two abasic sites was radiolabeled with  $^{32}\text{P}$  and 50 nM duplex incubated with an increasing concentration of LacI before electrophoresis and imaging. A clear shift of the DNA upon protein binding was observed, yielding an apparent dissociation constant of  $\sim 1 \mu\text{M}$  LacI (Figure 7). This suggests that the protein is fully bound at the concentrations used for EPR experiments. Similar results were obtained whether or not the spin label  $\zeta$  was present. The binding affinity is weaker than that published previously for the Lac repressor using membrane filtering (40), most likely due to the relatively short length of DNA used, the incorporation of two abasic sites and the use of the gel-shift technique, which tends to underestimate binding affinity due to extended incubation times.

The **dsDNA 2** was noncovalently spin labeled with two equivalents of spin label  $\zeta$  and measured with PELDOR at 40–90 MHz frequency offsets, both before and after addition of LacI. The PELDOR time trace of the DNA duplex alone at 40 MHz has a modulation depth of 0.2 (Figure 8a), corresponding to  $\sim 40\%$  doubly spin-labeled duplex DNA. This is comparable to the binding observed for **dsDNA 1**, taking into account the error in determining the modulation depth and different label orientation. The change in the modulation period for **dsDNA 2** is not as visible as for **dsDNA 1** (Figure 8a and b) but increasing the frequency offset from 40 to 90 MHz leads to a decrease in modulation depth. The Fourier transformations of the individual time traces show less pronounced orientation selection for this DNA (Figure 8c and d). This could be due to the increased interspin distance and flexibility or that the angle between the interspin vector and the  $z$  component of the spin labels'  $^{14}\text{N}$  hyperfine coupling tensor ( $A_{zz}$ ) is around  $45^\circ$  (9). To observe at least one full period of the dipolar modulation, the time window had to be extended to  $7 \mu\text{s}$ . This considerably reduces the monitored echo intensity and results in a time trace with worse signal to noise than for **dsDNA 1**.

The distance distribution from the orientation-averaged PELDOR time trace has a mean distance of  $69.2 \text{ \AA}$  (Figure 8e, inset), close to the mean distance of  $68.1 \text{ \AA}$

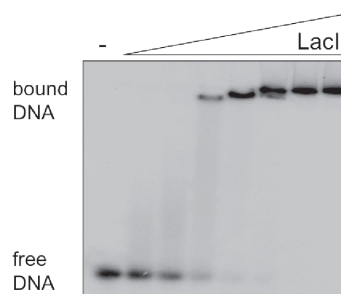


**Figure 7.** Electrophoretic mobility shift assay showing binding of the Lac repressor to the **dsDNA 2** in the presence of the spin label  $\zeta$ . DNA (50 nM) was titrated with 0, 0.25, 0.5, 0.75, 1.25, 2.5, 5 and  $12.5 \mu\text{M}$  LacI dimer before separation by gel electrophoresis and gel visualization. An apparent dissociation constant of  $\sim 1 \mu\text{M}$  was observed. The second, more retarded species observed at high protein concentrations is likely due to the known propensity for LacI to tetramerise.

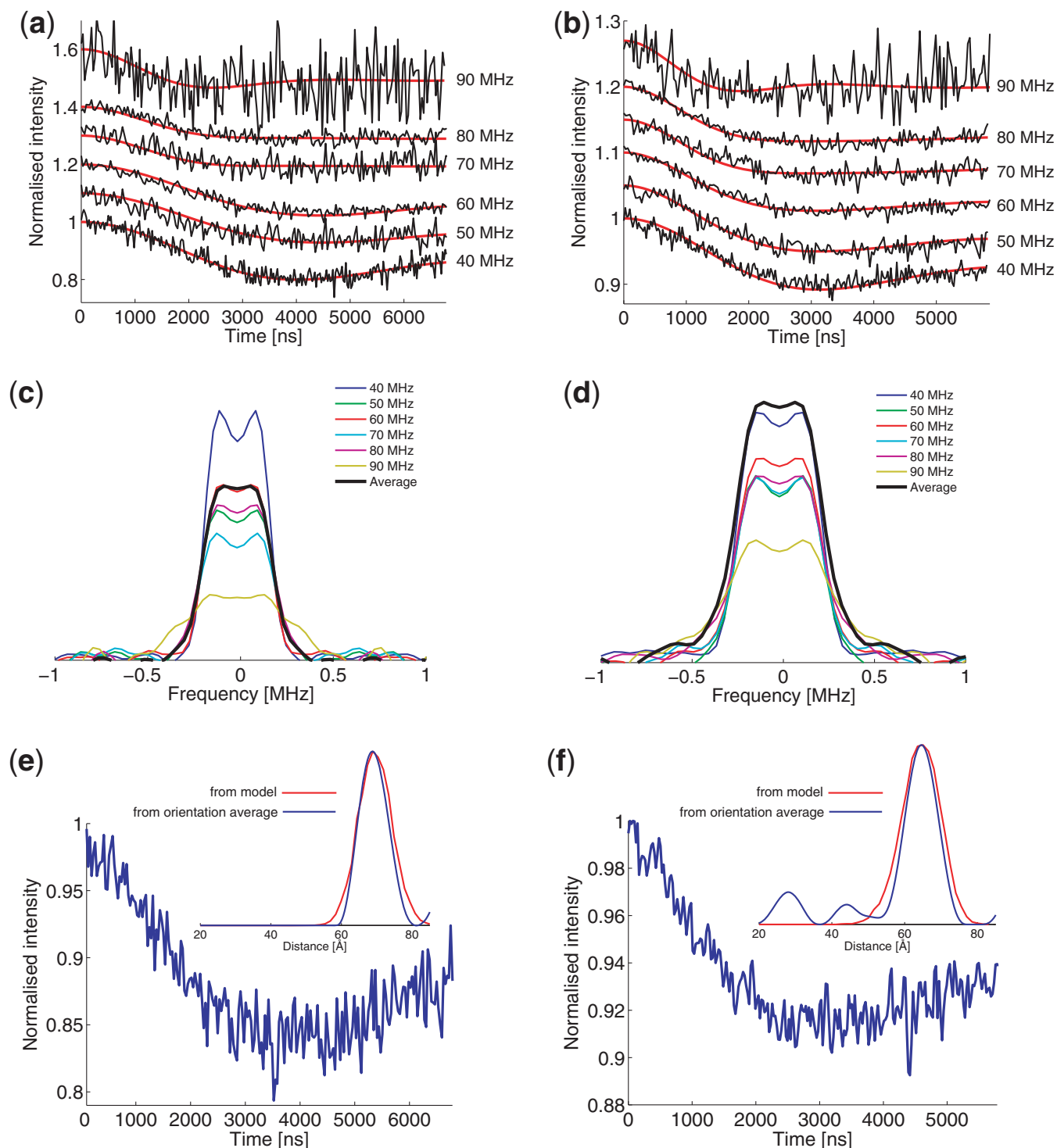


**Figure 8.** PELDOR data for noncovalently spin-labeled **dsDNA 2** with and without LacI at 40–90 MHz offsets. (a) and (b) Background-corrected PELDOR time traces of **dsDNA 2** without and with LacI (black), respectively, overlaid with the corresponding simulated time traces (red). The time traces have been displaced on the y-axis for clarity. Original time traces are shown in the Supplementary Information, Supplementary Figure S5. (c) and (d) are the respective Fourier transformations of the time traces in (a) and (b). The black spectra are the Fourier transformations of the respective summed time traces shown in (e) and (f). (e) and (f) are the summed PELDOR time traces of **dsDNA 2** without and with LacI, respectively. The inset shows the distance distribution obtained from the summed time traces using DeerAnalysis (blue) and the distribution obtained from model-based simulations.

obtained from PELDOR measurements on an identical DNA duplex covalently spin labeled with  $\zeta$  (Supplementary Information, Supplementary Figure S3 and Supplementary Table S2, S3). Simulations of the PELDOR time

traces for **dsDNA 2** using the cooperative twist-stretch dynamics model (14) yields a distance distribution with a mean distance of 70 Å (Figure 8e, inset), which is in good agreement with the result from DeerAnalysis. The

PELDOR time traces for **dsDNA 2** bound to the Lac repressor show a modulation but only a weakly resolved orientation selection (Figure 8b and d). The modulation depth at 40 MHz of 0.1 indicates that 20% of the dsDNA are doubly labeled. The decrease in noncovalent spin labeling efficiency is attributed to deformation of the DNA and abasic sites due to LacI binding, which impedes spin-label binding into the abasic sites. However, the labeling efficiency and specificity are still large enough to yield modulated PELDOR time traces. The distance distribution from the orientation-averaged time trace has a mean distance of 64.6 Å (Figure 8f, inset). Comparing the orientation-averaged PELDOR time traces and distance distributions for **dsDNA 2** and **dsDNA 2+LacI** clearly shows the change in interspin distance upon binding of LacI (Figure 9).

Using the mean distances obtained from the orientation-averaged PELDOR time traces for the bound and unbound duplexes and trigonometry (41) yields a bending angle of 42°, which is in good agreement with a bending angle of ~45° observed from crystal structure (39) and the 48.5° obtained from PELDOR measurements on the covalently spin-labeled DNA (Supplementary Information, Supplementary Figure S4). Although the change in the observed interspin distance corresponds nicely to a 42° bending of the DNA, this approach does not take into account the fact that the spin labels stick out from the DNA helix and change their relative orientation when LacI bends the DNA. Furthermore, addition of time traces acquired at discrete field positions does not represent a complete orientation-averaged time trace (42). This motivated us to simulate the PELDOR time traces of the DNA/LacI complex using a model with the twist-stretch dynamics of the unbound DNA. Assuming that LacI bends the operator DNA symmetrically around the central base pair, which is valid according to the X-ray structure, and using simple trigonometry, it can be estimated that a 42° bending of the DNA should decrease the distance between the two abasic sites by about 4.6 Å and tilt each spin label ~21° toward the interspin vector (Figure 10). Furthermore, to obtain a good fit to the experimental modulation frequency, it

was necessary to increase the equilibrium angle between the N-O axes of the spin labels (torsion angle) by 15°, relative to the angle used for the unbound DNA. This change in the torsion angle can be rationalized by the unwinding of the DNA upon binding to LacI (36). These geometric parameters were then combined with the twist/stretch dynamics model used for the **dsDNA 2**. The geometric and dynamics parameters that resulted in simulations with a good fit to the experimental time traces (Figure 8b) are listed in Supplementary Table S1. These parameters yield a distance distribution with a mean distance of 65 Å, which fits nicely to the distance obtained from DeerAnalysis (Table 2).

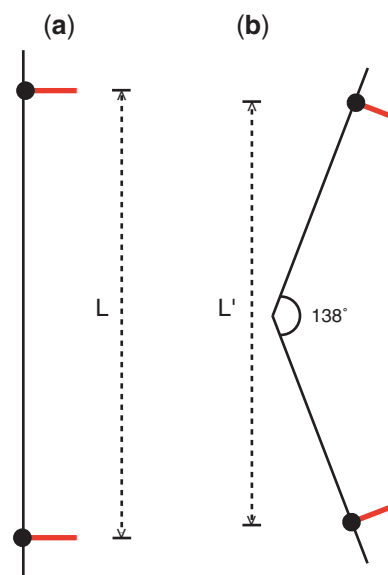


**Figure 10.** Diagram illustrating the change in distance between the DNA abasic sites and spin-label orientation upon DNA bending. The **dsDNA 2** is represented by black solid lines, abasic sites by black circles and spin labels by red lines. (a) Unbound **dsDNA 2**. The distance between the abasic sites (the height between spin labels) is denoted by  $L$ . (b) **dsDNA 2** after being bent 42° about the center by the LacI protein. The distance between the abasic site, which now has become shorter, is denoted by  $L'$ .

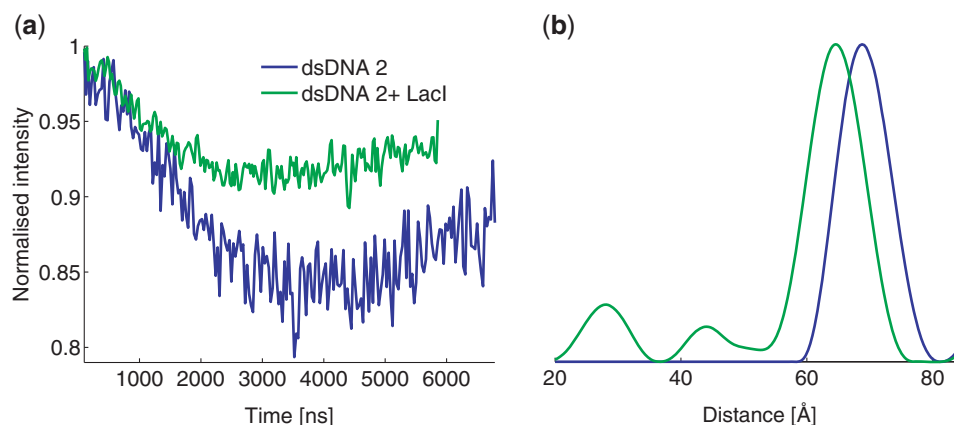


**Figure 9.** Overlay of the PELDOR data for **dsDNA 2** and **dsDNA 2+LacI**. (a) Background-corrected orientation-averaged time traces. (b) Distance distributions from the time traces in (a) obtained by Tikhonov regularization.

## CONCLUSIONS

We have noncovalently spin-labeled dsDNA with the rigid spin label  $\zeta$  and used PELDOR to measure the interspin distance, label orientations and conformational dynamics of DNA duplexes and a DNA/protein complex. We were able to show that the LacI protein binds and bends DNA in the presence of noncovalently bound spin labels. The protein does displace a fraction of the labels but are still bound to enable PELDOR measurements. Measuring this DNA/protein complex enabled us to evaluate the limits for the noncovalent spin labeling method to be close to 70 Å for the maximum distance, 20% for the double spin labeling efficiency and 4.5 Å as a detectable distance change. We have obtained PELDOR time traces that show clear modulation and orientation selectivity. Most importantly, the noncovalent but site-directed labeling strategy, with the rigid spin label  $\zeta$ , simply requires mixing spin label and DNA, followed by PELDOR measurements. Since DNA strands containing abasic sites at specific sites are commercially available, this strategy is widely applicable and should facilitate dissemination of this EPR methodology.

## SUPPLEMENTARY DATA

Supplementary Data are available at NAR Online: Supplementary Tables 1–3, Supplementary Figures 1–5 and Supplementary Information.

## ACKNOWLEDGEMENTS

The authors thank Biljana Petrovic-Stojanovska, BSRC, University of St Andrews, for preparing the LacI protein.

## FUNDING

Biotechnology and Biological Sciences Research Council [BB/H017917/1]; Engineering and Physical Sciences Research Council [F004583/1]; Icelandic Research Fund [110035021]; Scottish Overseas Research Students (SORS) Scholarship from the School of Biology, University of St Andrews (to G.W.R.); Doctoral fellowship from the University of Iceland Research Fund (to S.A.S.); Research Councils of the UK for an RCUK fellowship (to O.S.). Funding for open access charge: Wellcome Trust [091825/Z/10/Z].

*Conflict of interest statement.* None declared.

## REFERENCES

- Milov, A.D., Salikhov, K.M. and Shirov, M.D. (1981) Application of the double resonance method to electron spin echo in a study of the spatial distribution of paramagnetic centers in solids. *Soviet Phys Solid State*, **23**, 565–569.
- Martin, R., Pannier, M., Diederich, F., Gramlich, V., Hubrich, M. and Spiess, H. (1998) Determination of end-to-end distances in a series of TEMPO diradicals of up to 2.8 nm length with a new four-pulse double electron resonance experiment. *Angew. Chem. Int. Ed.*, **37**, 2833–2837.
- Zhang, X., Cekan, P., Sigurdsson, S.T. and Qin, P. (2009) Studying RNA using site-directed spin-labeling and continuous-wave electron paramagnetic resonance spectroscopy. *Methods Enzymol.*, **469**, 303–328.
- Klare, J.P. and Steinhoff, H.-J. (2009) Spin labeling EPR. *Photosynth. Res.* **102**, 377–390.
- Shelke, S.A. and Sigurdsson, S.T. (2012) Site-directed spin labelling of nucleic acids. *Eur. J. Org. Chem.*, **2012**, 2291–2301.
- Schiemann, O. and Prisner, T.F. (2007) Long-range distance determinations in biomacromolecules by EPR spectroscopy. *Q. Rev. Biophys.*, **40**, 1–53.
- Griffith, O.H. and Waggoner, A.S. (1969) Nitroxide free radicals: spin labels for probing biomolecular structure. *Acc. Chem. Res.*, **2**, 17–24.
- Miller, T.R., Alley, S.C., Reese, A.W., Solomon, M.S., McCallister, W.V., Mailer, C., Robinson, B.H. and Hopkins, P.B. (1995) A probe for sequence-dependent nucleic acid dynamics. *J. Am. Chem. Soc.*, **117**, 9377–9378.
- Schiemann, O., Cekan, P., Margraf, D., Prisner, T.F. and Sigurdsson, S.T. (2009) Relative orientation of rigid nitroxides by PELDOR: beyond distance measurements in nucleic acids. *Angew. Chem. Int. Ed.*, **48**, 3292–3295.
- Barhate, N., Cekan, P., Massey, A. and Sigurdsson, S. (2007) A nucleoside that contains a rigid nitroxide spin label: a fluorophore in disguise. *Angew. Chem. Int. Ed.*, **46**, 2655–2658.
- Cekan, P., Smith, A.L., Barhate, N., Robinson, B.H. and Sigurdsson, S.T. (2008) Rigid spin-labeled nucleoside  $\zeta$ : a nonperturbing EPR probe of nucleic acid conformation. *Nucleic Acids Res.*, **36**, 5946–5954.
- Smith, A.L., Cekan, P., Brewood, G.P., Okonogi, T.M., Alemayehu, S., Hustedt, E.J., Benight, A.S., Sigurdsson, S.T. and Robinson, B.H. (2009) Conformational equilibria of bulged sites in duplex DNA studied by EPR spectroscopy. *J. Phys. Chem. B*, **113**, 2664–2675.
- Cekan, P., Jonsson, E.Ö. and Sigurdsson, S.T. (2009) Folding of the cocaine aptamer studied by EPR and fluorescence spectroscopies using the bifunctional spectroscopic probe C. *Nucleic Acids Res.*, **37**, 3990–3995.
- Marko, A., Denysenkov, V., Margraf, D., Cekan, P., Schiemann, O., Sigurdsson, S.T. and Prisner, T.F. (2011) Conformational flexibility of DNA. *J. Am. Chem. Soc.*, **133**, 13375–13379.
- Shelke, S.A. and Sigurdsson, S.T. (2010) Noncovalent and site-directed spin labeling of nucleic acids. *Angew. Chem. Int. Ed.*, **49**, 7984–7986.
- Jeschke, G., Chechik, V., Ionita, P., Godt, A., Zimmermann, H., Banham, J., Timmel, C.R., Hilger, D. and Jung, H. (2006) DeerAnalysis2006—a comprehensive software package for analyzing pulsed ELDOR data. *Appl. Magn. Reson.*, **30**, 473–498.
- Reginsson, G.W., Hunter, R.I., Cruickshank, P.A.S., Bolton, D.R., Sigurdsson, S.T., Smith, G.M. and Schiemann, O. (2012) W-band PELDOR with 1kW microwave power: molecular geometry, flexibility and exchange coupling. *J. Magn. Reson.*, **216**, 175–182.
- Galas, D.J. and Schmitz, A. (1978) DNAase footprinting: a simple method for the detection of protein-DNA binding specificity. *Nucleic Acids Res.*, **5**, 3157–3170.
- Welsh, J. and Cantor, C.R. (1984) Protein–DNA cross-linking. *Trends Biochem. Sci.*, **9**, 505–508.
- Lohman, T.M. and Bujalowski, W. (1991) Thermodynamic methods for model-independent determination of equilibrium binding isotherms for protein-DNA interactions: spectroscopic approaches to monitor binding. *Methods Enzymol.*, **208**, 258–290.
- Rhodes, D., Schwabe, J.W.R., Chapman, L. and Fairall, L. (1996) Towards an understanding of protein-DNA recognition. *Philos. Trans. Roy Soc. B: Biol. Sci.*, **351**, 501–509.
- Luscombe, N.M., Austin, S.E., Berman, H.M. and Thornton, J.M. (2000) An overview of the structures of protein-DNA complexes. *Genome Biol.*, **1**, 001.1–001.10.
- Frederick, C.A., Grable, J., Melia, M., Samudzi, C., Jen-Jacobson, L., Wang, B.-C., Greene, P., Boyer, H.W. and Rosenberg, J.M. (1984) Kinked DNA in crystalline complex with EcoRI endonuclease. *Nature*, **309**, 327–331.
- Prestegard, J.H., Al-Hashimi, H.M. and Tolman, J.R. (2000) NMR structures of biomolecules using field oriented media and residual dipolar couplings. *Q. Rev. Biophys.*, **33**, 371–424.
- Renault, M., Cukkemane, A. and Balducci, M. (2010) Solid-state NMR spectroscopy on complex biomolecules. *Angew. Chem. Int. Ed.*, **49**, 8346–8357.

26. Langowski, J., Benight, A.S., Fujimoto, B.S., Schurr, J.M. and Schomburg, U. (1985) Change of conformation and internal dynamics of supercoiled DNA upon binding of Escherichia coli single-strand binding protein. *Biochemistry*, **24**, 4022–4028.
27. Hillisch, A., Lorenz, M. and Diekmann, S. (2001) Recent advances in FRET: distance determination in protein–DNA complexes. *Curr. Opin. Struct. Biol.*, **11**, 201–207.
28. Steinhoff, H. (2004) Inter- and intra-molecular distances determined by EPR spectroscopy and site-directed spin labeling reveal protein–protein and protein–oligonucleotide interaction. *Biol. Chem.*, **385**, 913–920.
29. Slichter, C.P. (1990) *Principles of Magnetic Resonance*, 3rd edn. Springer, Heidelberg, Germany.
30. Bode, B.E., Margraf, D., Plackmeyer, J., Dürner, G., Prisner, T.F. and Schiemann, O. (2008) Counting the monomers in nanometer-sized oligomers by pulsed electron–electron double resonance. *J. Am. Chem. Soc.*, **129**, 6736–6745.
31. Shelke, S.A. and Sigurdsson, S.T. (2011) Structural changes of an abasic site in duplex DNA affect noncovalent binding of the spin label c. *Nucleic Acids Res.*, **40**, 3732–3740.
32. Jeschke, G. and Polyhach, Y. (2007) Distance measurements on spin-labelled biomacromolecules by pulsed electron paramagnetic resonance. *Phys. Chem. Chem. Phys.*, **9**, 1895–1910.
33. Godt, A., Schulte, M., Zimmermann, H. and Jeschke, G. (2006) How flexible are poly (paraphenyleneethynylene)s? *Angew. Chem. Int. Ed.*, **45**, 7560–7564.
34. Gore, J., Bryant, Z., Nöllmann, M., Le, M.U., Cozzarelli, N.R. and Bustamante, C. (2006) DNA overwinds when stretched. *Nature*, **442**, 836–839.
35. Marko, J. (1997) Stretching must twist DNA. *Europhys. Lett.*, **38**, 183–188.
36. Lewis, M., Chang, G., Horton, N.C., Kercher, M.A., Pace, H.C., Schumacher, M.A., Brennan, R.G. and Lu, P. (1996) Crystal structure of the lactose operon repressor and its complexes with DNA and inducer. *Science*, **271**, 1247–1254.
37. Bahl, C.P., Wu, R., Stawinsky, J. and Narang, S.A. (1977) Minimal length of the lactose operator sequence for the specific recognition by the lactose repressor. *Proc. Natl Acad. Sci. USA*, **74**, 966–970.
38. Bell, C. and Lewis, M. (2000) A closer view of the conformation of the Lac repressor bound to operator. *Nat. Struct. Mol. Biol.*, **7**, 209–214.
39. Lewis, M. (2005) The lac repressor. *C. R. Biol.*, **328**, 521–548.
40. Riggs, A.D., Suzuki, H. and Bourgeois, S. (1970) lac repressor-operator interaction. *J. Mol. Biol.*, **48**, 67–83.
41. Kuznetsov, N.A., Milov, A.D., Koval, V.V., Samoilova, R.I., Grishin, Y.A., Knorre, D.G., Tsvetkov, Y.D., Fedorova, O.S. and Dzuba, S. (2009) PELDOR study of conformations of double-spin-labeled single- and double-stranded DNA with non-nucleotide inserts. *Phys. Chem. Chem. Phys.*, **11**, 6826–6832.
42. Jeschke, G. (2012) Interpretation of dipolar EPR data in terms of protein structure. In: *Structure and Bonding*, Springer-Verlag Berlin Heidelberg, Germany. pp.1–38.



# Protein-Induced Changes in DNA Structure and Dynamics Observed with Noncovalent Site-Directed Spin Labeling and PELDOR

Gunnar W. Reginsson<sup>1,2</sup>, Sandip A. Shelke<sup>2</sup>, Christophe Rouillon<sup>3</sup>, Malcolm F. White<sup>3</sup>, Snorri Th. Sigurdsson<sup>2</sup> and Olav Schiemann<sup>1,\*</sup>

<sup>1</sup> Biomedical Sciences Research Complex, Centre of Magnetic Resonance, University of St Andrews, St Andrews KY16 9ST, UK

<sup>2</sup> Science Institute, University of Iceland, Dunhaga 3, 107 Reykjavík, Iceland.

<sup>3</sup> Biomedical Sciences Research Complex, University of St Andrews, St Andrews KY16 9ST, UK.

\* To whom correspondence should be addressed. Tel: +44(0)1334-463410; Email: os11@st-andrews.ac.uk

## Supporting information

### CW-EPR measurements

CW-EPR spectra were recorded of the  $\zeta$  spin label and the noncovalently spin labeled dsDNA **1** in phosphate buffer with 20% (v/v) ethylene glycol (Figure S1). As the temperature of the  $\zeta$  spin label sample is decreased the linewidth becomes broader due to the decreased rotational correlation time of the spin labels. At -40 °C the sample is completely frozen and the spectrum resembles a rigid nitroxide spectrum as can be seen from the spectrum recorded at -173 °C (Figure S1). As the temperature for the sample of noncovalently spin labeled DNA is decreased from 0 to -10 °C peaks that belong to transitions from spin labels with slow tumbling rate become clear as shown by the \* in Figure S1. Since these peaks are not visible in the  $\zeta$  spin label sample at -10 °C they must belong to spin labels that are bound to DNA, which has a slower tumbling rate in solution. As the temperature is decreased further the intensity of the peaks from slow tumbling spin labels increases, indicating that the fraction of bound spin labels increases with decreased temperature. At -30 °C no contribution from fast tumbling/unbound spin labels is observed, as indicated by the reduced intensity of the corresponding transitions (Figure S1, +). It was observed that both the DNA and the  $\zeta$  spin label samples start to freeze at  $\sim$  -30 °C and become completely frozen at -40 °C. It's possible that the freezing of the sample at -30 °C has an impeding effect on the binding of spin labels to the DNA abasic sites.

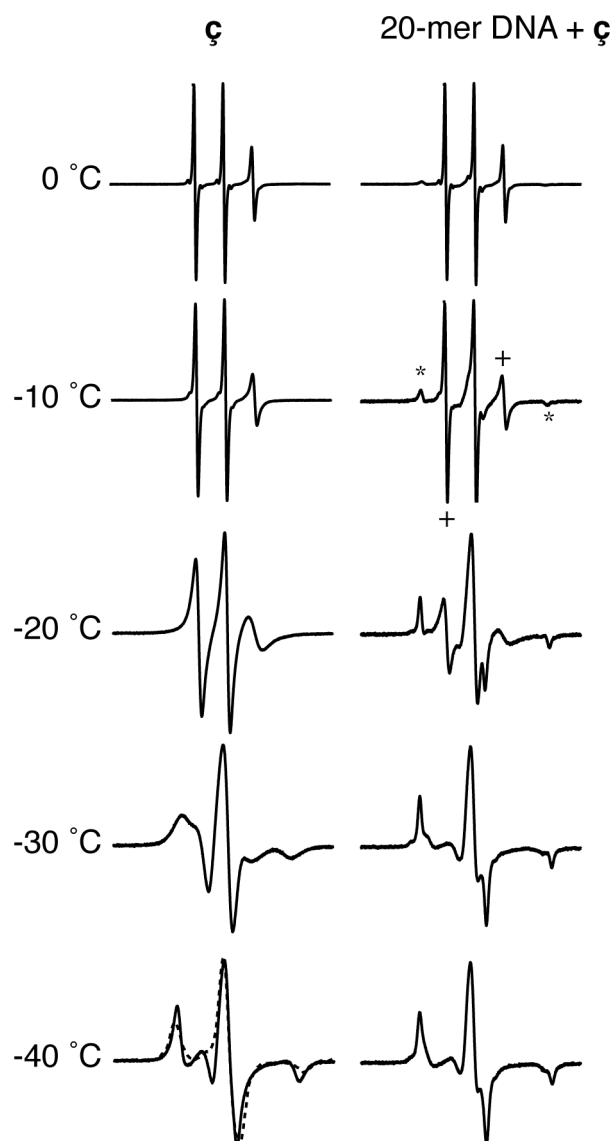


**Figure S1.** CW-EPR spectra of  $\phi$  spin label (left) and noncovalently spin labeled **dsDNA 1** (right) recorded at 0 to -40 °C. The spectrum in dashed line is from the free  $\phi$  spin label at -173 °C. Samples were dissolved in phosphate buffer with 20% ethylene glycol. \* and + symbols show EPR transitions from spin labels bound and unbound to DNA, respectively.

### Simulation of PELDOR time traces

PELDOR time traces and distance distributions were simulated using a geometrical vector model. The conformational distribution and dynamics of the spin labels was modeled using the cooperative twist-stretch dynamic model for short dsDNA (14). Table S1 summarizes the distribution in geometrical parameters used to simulate the PELDOR time traces. The spin labels and their equilibrium positions were represented by vectors, positioned relative to the center of the DNA helix axis. The equilibrium position of the spin labels was obtained from a molecular model of the DNA duplexes with  $\phi$  spin labels docked into the abasic sites (Figure S2). The position of the spin labels was parameterized by defining three variables: DNA radius (R), DNA length (L) and torsion

angle ( $\phi$ ). The equilibrium value for R was defined as the distance the spin labels are shifted away from the center of the DNA helix axis (Figure S2b). R was allowed to have a standard deviation of 0.65 Å as previously determined (1). The equilibrium value for the DNA length was defined as the height between spin labels (Figure S2b) and the distribution in L was given by Eq. S1 (1) where  $\sigma_R$  is the standard deviation in R and n is the number of base pairs between the spin labels.

$$\sigma_L = \frac{\sigma_R * n}{-3.2} \quad \text{Eq. S1}$$

The equilibrium angle between the N-O axes of the spin labels  $\phi$  was determined from the DNA molecular models. The distribution (two standard deviations) in  $\phi$  was previously determined to 22° per helical turn (1). Since the spin labels in **dsDNA 1** and **dsDNA 2** are approximately 1 and 2 helical turns apart, respectively, the distribution in  $\phi$  for **dsDNA 1** and **dsDNA 2** was determined to be 22° and 48°, respectively. The length of the vectors representing the spin labels  $L_\zeta$ , defined as the distance between the center of the N-O bond and the other end of the spin label (Figure S2b), was 11 Å. The equilibrium values for the height and torsion angle between spin labels were adjusted slightly until a good fit to the modulation frequency was obtained. The equilibrium values and distributions in R, L and  $\phi$  for **dsDNA 1**, **dsDNA 2** and **dsDNA 2 +LacI** are summarised in Table S1.

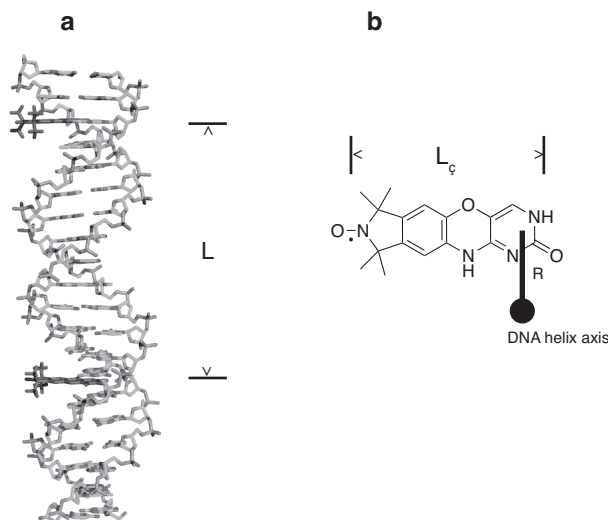


**Figure S2.** Molecular model of DNA and definition of geometric parameters. **a)** Molecular model of **dsDNA 1** with  $\zeta$  spin labels docked inside abasic sites. The spin labels are dark grey. The height between the spin labels, assigned as the DNA length parameter is shown. **b)**  $\zeta$  spin label with illustrations defining the DNA radius R and spin label length  $L_\zeta$ .

Table S1. Geometric parameters used in the molecular model for the simulation of the PELDOR time traces.

dsDNA	DNA Radius (R) [Å]	DNA Length (L) [Å]	Torsion ( $\phi$ ) [°]
<b>dsDNA 1</b>	$2.7 \pm 0.65(0.01)$	$37.2 \pm 2.23(0.03)$	$75 \pm 11(0.2)$
<b>dsDNA 2</b>	$2.7 \pm 0.65(0.01)$	$70 \pm 4.51(0.03)$	$60 \pm 24(0.2)$
<b>dsDNA 2 +LacI</b>	$2.7 \pm 0.65(0.01)$	$65.4 \pm 5.20(0.03)$	$75 \pm 24(0.2)$
<b>dsDNA 3</b>	$2.7 \pm 0.65(0.01)$	$67.6 \pm 4.51(0.03)$	$60 \pm 24(0.2)$
<b>dsDNA 3 +LacI</b>	$2.7 \pm 0.65(0.01)$	$62.1 \pm 5.05(0.03)$	$80 \pm 24(0.2)$

*The DNA radius, DNA length and torsion angle (angle between the spin labels N-O axis) are given as mean value  $\pm$  one standard deviation. The uncertainty in the standard deviation is given within brackets.*

## LacI-induced bending of DNA covalently spin labeled with Ç spin labels

To evaluate the effects from abasic sites and non-covalent spin labeling on the PELDOR measurements of **dsDNA 2** the same 29-mer DNA sequence was covalently spin labeled with the spin label Ç (Table S2) (2) and measured with PELDOR at 40-90 MHz frequency offsets, both before and after addition of LacI.

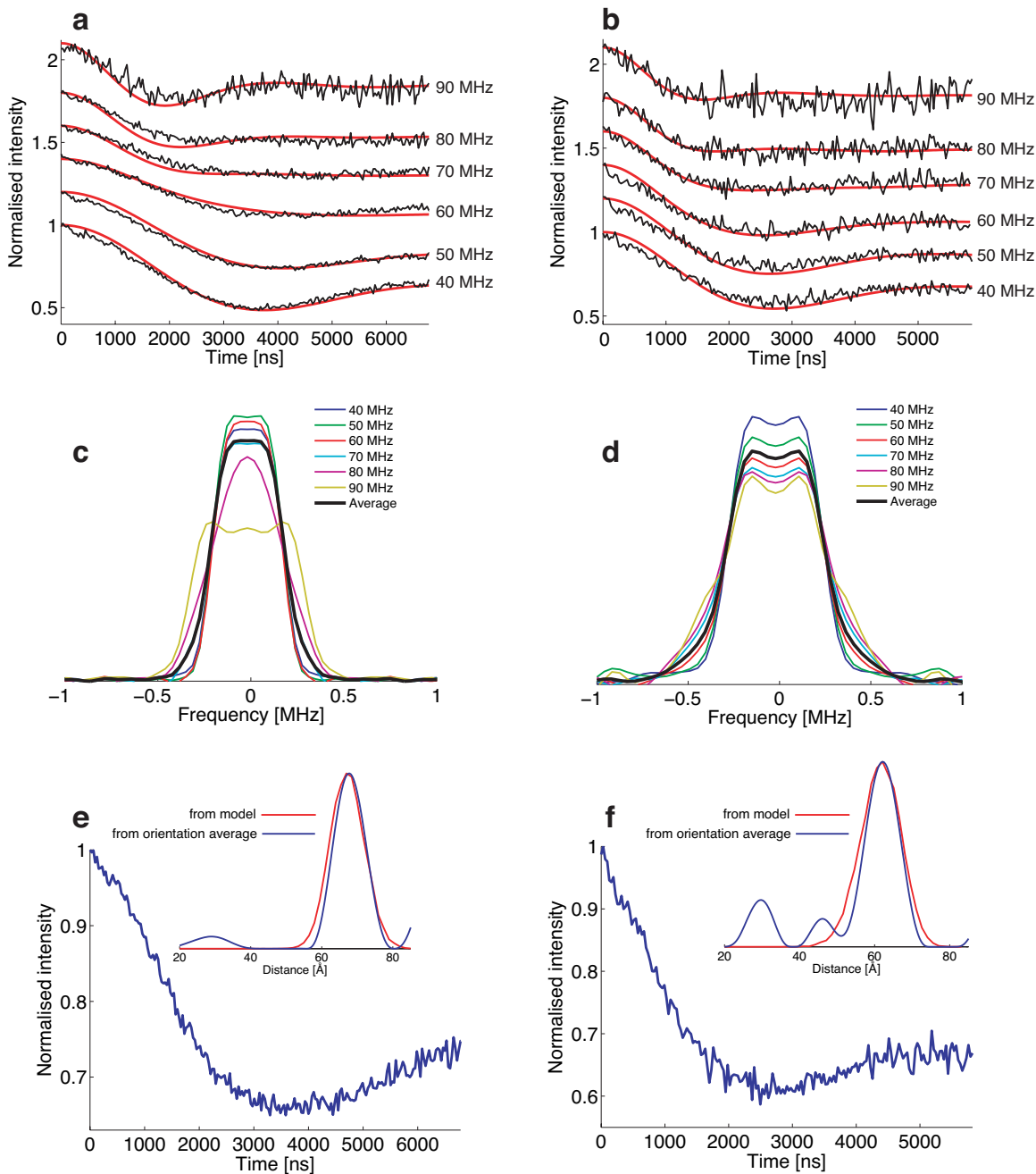
Table S2. Sequence for the dsDNA covalently spin labeled with Ç.

DNA	DNA sequence
<b>dsDNA 3</b>	5'-GCGÇ <b>ATTGTGAGCGGATAACAATTTGGCG</b> -3' 3'-CGCG <b>TAACTCGCCTATTGTTAAACCGC</b> -5'

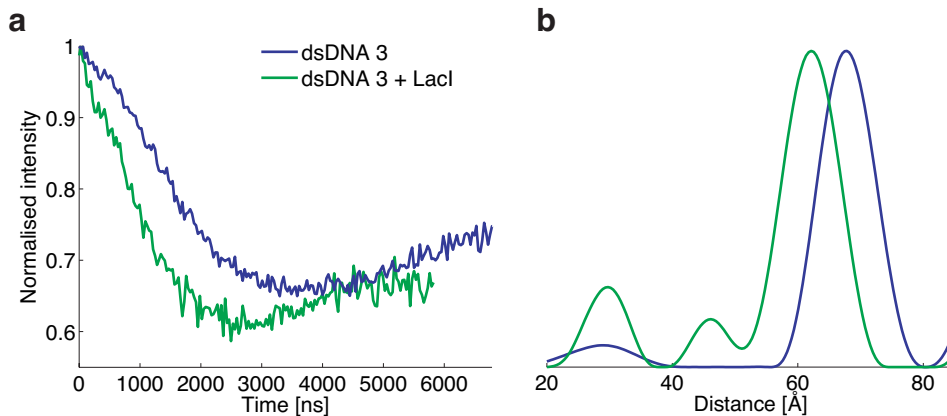
*The spin labels are denoted by Ç. The bold sequence in dsDNA 3 is the 19-mer Lac repressor consensus sequence.*

The PELDOR time traces of **dsDNA 3** with and without LacI show a pronounced modulation at almost all frequency offset and a modulation depth of about 50% at 40 MHz offset (Figure S3a, b). The Fourier transformed time traces show an increased parallel component as the frequency offset is increased from 40 to 90 MHz, which is in agreement with **dsDNA 2** (Figure S3c, d). Analyzing the orientation averaged time traces with Tikhonov regularization yields a mean interspin distance of 68.1 and 62.1 Å for **dsDNA 3** and **dsDNA + LacI**, respectively (Table S3). The change in interspin distance is clearly seen when comparing the orientation averaged time traces and corresponding distance distributions for **dsDNA 3** and **dsDNA 3 + LacI** (Figure S4). Using trigonometry and these mean distances the bending angle of the **dsDNA 3** bound to LacI can be estimated as 48.5°. This is 6.5° larger bending than for the non-covalently spin labeled DNA, **dsDNA 2**.

The PELDOR time traces for **dsDNA 3** were also simulated using the same dynamics model as for simulations of time traces for **dsDNA 2** and the bending angle determined from the orientation averaged time traces of **dsDNA 3** (Table S1). The simulated time traces have an excellent fit to the experimental time traces and the distance distributions from the simulation model fits nicely to the distance distribution from the orientation averaged PELDOR time trace (Figure S3e, f and Table S3). PELDOR measurements on **dsDNA 3** show the mean interspin distance to be 1.1 and 2.5 Å shorter than for the non-covalently spin labeled DNA, **dsDNA 2**. The small difference in the mean interspin distance and LacI induced bending between covalently and non-covalently spin labeled DNAs is most likely due to the structural perturbation from the abasic sites and the exact position of the spin labels within the DNA duplex.



**Figure S3.** PELDOR data for covalently spin-labeled **dsDNA 3** with and without Lacl at 40 to 90 MHz offsets. **a,b)** Background corrected PELDOR time traces of **dsDNA 3** without and with Lacl (black), respectively, overlaid with the corresponding simulated time traces (red). The time traces have been displaced on the y-axis for clarity. Original time traces are shown in figure S5. **c)** and **d)** are the respective Fourier transformations of the time traces in **a)** and **b)**. The black spectra are the Fourier transformations of the respective summed time traces shown in **e)** and **f)**. **e)** and **f)** are the summed PELDOR time trace of **dsDNA 3** without and with Lacl, respectively. The inset shows the distance distribution obtained from the summed time traces using DeerAnalysis (blue) and the distribution obtained from the model based simulations.



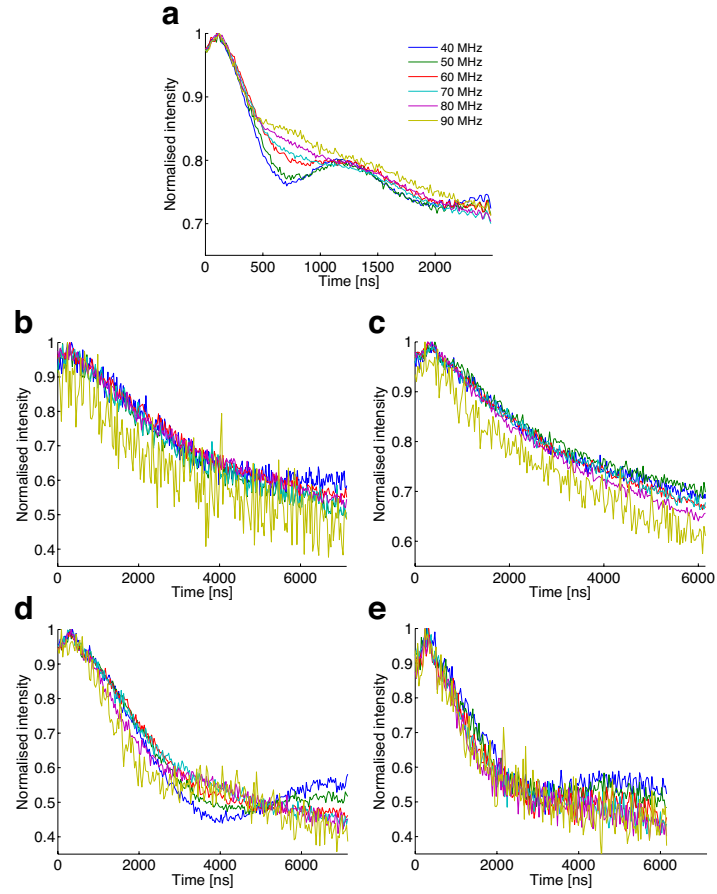
**Figure S4.** Overlay of the PELDOR data for **dsDNA 3** and **dsDNA 3 + Lacl**. **a)** Background corrected orientation averaged time traces. **b)** Distance distributions from the time traces in **a)** obtained by Tikhonov regularization.

Table S3. Interspin distances for **dsDNA 3**

dsDNA	$r_{DA}$ [Å] <sup>a</sup>	$r_{Simulation}$ [Å] <sup>b</sup>	$r_{MM/X-ray}$ [Å] <sup>c</sup>
<b>dsDNA 3</b>	68.1, 4.0	68.0, 4.8 (1, 0.1)	73
<b>dsDNA 3 +Lacl</b>	62.1, 4.1	62.2, 5.3 (1, 0.1)	67

<sup>a</sup> Most probable distance, standard deviation from orientation averaged PELDOR time traces using DeerAnalysis 2011. <sup>b</sup> Most probable distance, standard deviation. The error in the distance, standard deviation is in brackets. <sup>c</sup> Interspin distances obtained from molecular modeling using B-form DNA duplexes. The interspin distance for **dsDNA 3** bound to Lacl was estimated by modeling spin labels into the X-ray structure of a 21-mer dsDNA bound to Lacl (pdb id. 1LBG).

## Original PELDOR time traces



**Figure S5.** Original PELDOR time traces of noncovalently spin labeled a) dsDNA 1, b) dsDNA 2, c) dsDNA 2 + Lacl, d)  $\zeta$  spin labeled dsDNA 3 and e)  $\zeta$  spin labeled dsDNA 3 + Lacl.



## References

1. Marko,A., Denysenkov,V., Margraf,D., Cekan,P., Schiemann,O., Sigurdsson,S.T. and Prisner,T.F. (2011) Conformational Flexibility of DNA. *J. Am. Chem. Soc.*, **133**, 13375–13379.
2. Schiemann,O., Cekan,P., Margraf,D., Prisner,T.F. and Sigurdsson,S.T. (2009) Relative Orientation of Rigid Nitroxides by PELDOR: Beyond Distance Measurements in Nucleic Acids. *Angew. Chem. Int. Ed.*, **48**, 3292–3295.

## Trityl Radicals: Spin Labels for Nanometer-Distance Measurements

Gunnar W. Reginsson,<sup>[a, b]</sup> Nitin C. Kunjir,<sup>[b]</sup> Snorri Th. Sigurdsson,<sup>\*, [b]</sup> and Olav Schiemann<sup>\*, [a, c]</sup>

Structural biology and material sciences are engaging ever-larger complexes, either isolated, in composites or within whole cells. Thus, methods that can provide structural information for these molecular architectures on the relevant length scale are needed. EPR methods, especially pulsed electron–electron double resonance (PELDOR or DEER), have emerged as very powerful tools to quantitatively measure nanometer distances in the range of approximately 1.4 to 8 nm.<sup>[1–4]</sup> Because many of the systems are diamagnetic, site-directed spin labelling is required, usually with nitroxides.<sup>[5,6,7]</sup> Although nitroxides are relatively stable radicals that can be readily incorporated into molecules to be studied by EPR, they have the disadvantage of rather low sensitivity for EPR-based nanometer-distance measurements and require measurements at cryogenic temperatures. Furthermore, they are only stable for minutes under the reducing environment that exists within cells,<sup>[8]</sup> which makes in-cell distance measurements with nitroxides very demanding.<sup>[9]</sup>

Herein, an approach that may overcome some of these limitations by using carbon-centred triarylmethyl (trityl) radicals instead of nitroxides for nanometer-distance measurements is introduced. Specifically, the tetrathiatriaryl-methyl radical **1**<sup>[10]</sup> was used as the spin label (Figure 1), which gave an EPR spectrum with one line only (plus very weak <sup>13</sup>C satellite lines; Figure 1) and has a transverse relaxation time  $T_M$  in the microsecond regime, even at room temperature in the liquid state.<sup>[11,12]</sup> The trityl radical is stabi-

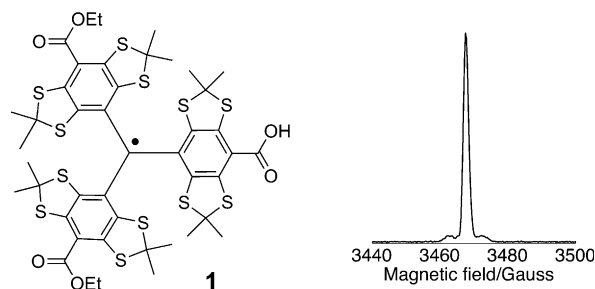


Figure 1. The chemical structure of the trityl spin label **1** and its field-swept X band EPR spectrum.

lized against dimerization by the substituted aryl groups<sup>[13]</sup> and the in-cell survival time is in the range of hours.<sup>[14,15]</sup>

Poly(*para*-phenyleneethynylene)s (PolyPPEs) was chosen to evaluate the potential of trityls as spin labels for nanometer distance measurements. The structure and conformational flexibility of this class of polymers, which have found wide use in material science,<sup>[16,17]</sup> have previously been studied by PELDOR in combination with nitroxide labelling.<sup>[18,19]</sup> Two compounds (**2** and **3**, Scheme 1) were prepared for distance measurements with trityl spin labels. Compound **2** contains one trityl and a typical nitroxide, whereas compound **3** has two trityl groups. The reason for synthesizing a compound with both a trityl and a nitroxide had two purposes: the combination of a trityl label with a nitroxide spin label may be useful for biological heterodimers, and because it enables a direct comparison to PELDOR measurements on bisnitroxides. In both compounds **2** and **3**, the two radicals are connected by a linear tether consisting of aryl and acetylene units that were linked through a series of Sonogashira cross-coupling reactions. Synthesis of the key-linking unit **4** (Scheme 1a), which contains heptyl groups to facilitate adequate solubility of the biradicals, is outlined in Scheme S1 in the Supporting Information. Synthesis of the trityl-nitroxide biradical **2** (Scheme 1a) started with conjugation of nitroxide **12**, prepared by coupling 4-iodobenzoic acid and 4-amino TEMPO (see the Supporting Information), to linker **4** to give compound **13**. The monoacid trityl radical **1**, prepared by limited alkaline hydrolysis of trityl alcohol **14** and subsequent treatment with TFA (see the Supporting Information), was coupled with nitroxide **13** to give the trityl-nitroxide biradical **2**. For synthesis of trityl biradical **3**, complex **1** was coupled with linker **4** to give trityl radical **16** (Scheme 1b), followed by a Pd-catalyzed di-

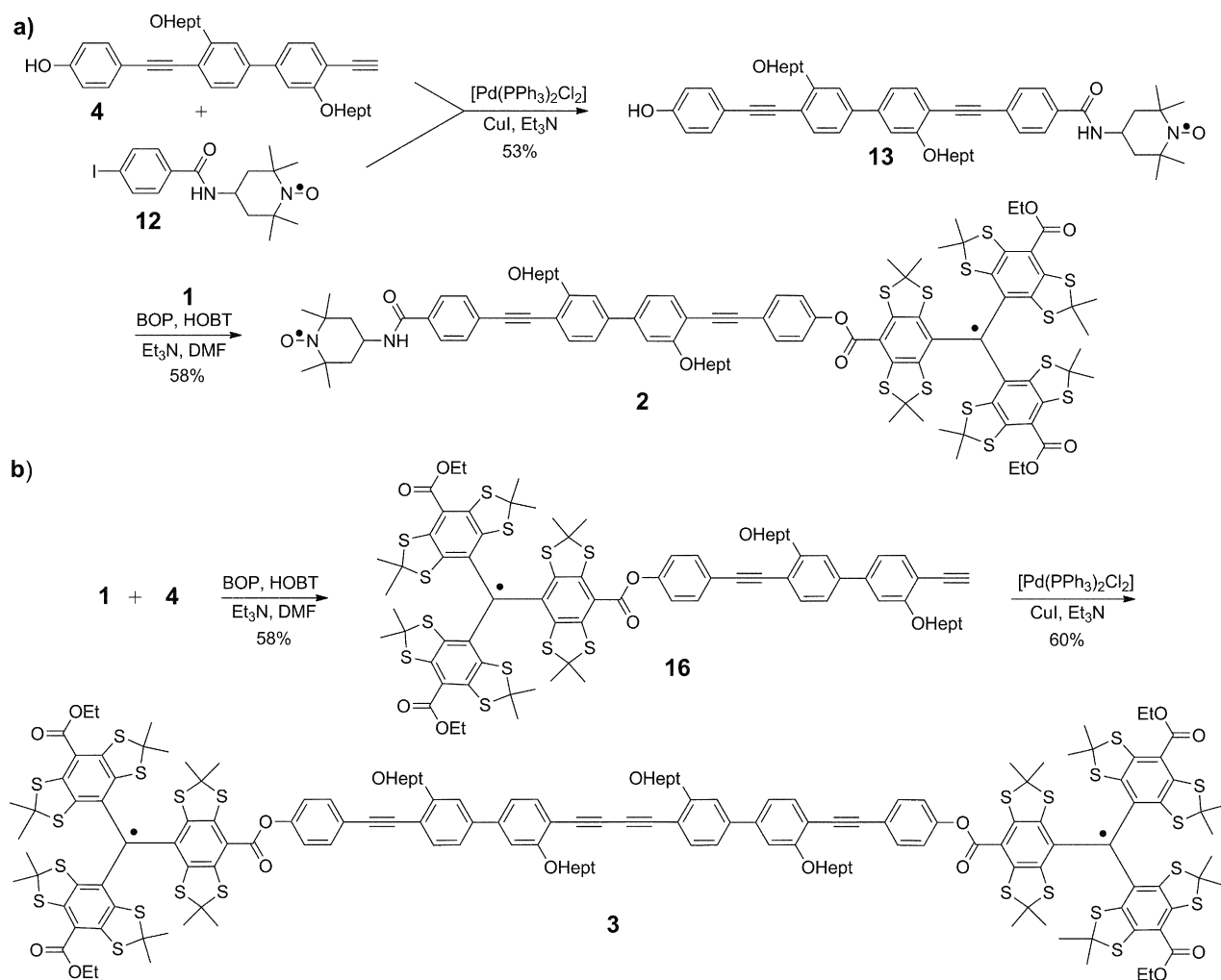
[a] G. W. Reginsson,<sup>+</sup> Prof. O. Schiemann  
Biomedical Sciences Research Complex  
Centre of Magnetic Resonance  
North Haugh, St. Andrews, KY16 9ST (UK)

[b] G. W. Reginsson,<sup>+</sup> N. C. Kunjir,<sup>+</sup> Prof. S. T. Sigurdsson  
Science Institute  
University of Iceland  
Dunhaga 3, 107 Reykjavík (Iceland)  
E-mail: snorrissi@hi.is

[c] Prof. O. Schiemann  
Institute of Physical and Theoretical Chemistry  
University of Bonn  
Wegelerstrasse 12, 53115 Bonn (Germany)  
E-mail: schiemann@pc.uni-bonn.de

[<sup>+</sup>] These authors contributed equally to this work.

Supporting information for this article is available on the WWW under <http://dx.doi.org/10.1002/chem.201203014>.



Scheme 1. Synthesis of a) the trityl-nitroxide biradical **2** and b) the trityl-trityl biradical **3**. HOBT = hydroxybenzotriazole; BOP = benzotriazol-1-yloxy-tris(dimethylamino)-phosphonium hexafluorophosphate.

merization in the presence of CuI under atmospheric oxygen, which gave biradical **3**.

Two-pulse Hahn echo field-swept spectra of compounds **2** and **3** confirmed the presence of the radicals (Figure 2). For compound **2**, the width of the nitroxide spectrum enabled placement of the detection pulses on the nitroxide spectrum, at 30–90 MHz higher frequencies (Figure 2a) than the fre-

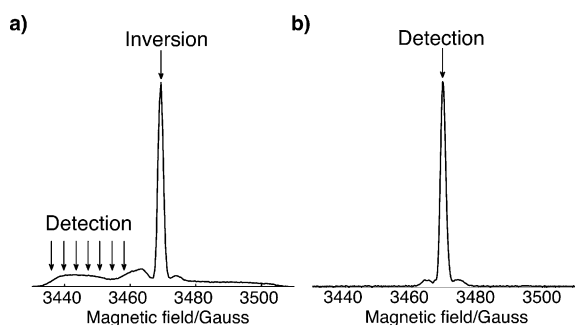


Figure 2. The two-pulse Hahn echo field swept EPR spectra of a) compound **2** and b) compound **3**.

quency of the inversion pulse on the centre of the trityl resonance. Because the trityl peak has a linewidth of only 2 G, the inversion pulse with an excitation bandwidth of 11 G should invert all of the trityl spin centres.

Experimentally, a modulation depth  $\Delta$  of 90% was observed independent of the frequency offset for the detection pulses (Figure 3a). This is twice the modulation depth observed for bisnitroxide systems at X band<sup>[20,21]</sup> and indicates that excitation of the trityl is almost complete. Deviation from the expected 100% is attributed to the inversion pulse not having an excitation profile of an ideal  $\pi$  pulse (see the Supporting Information). Fourier transforms of the time traces showed that the intensity of the perpendicular component ( $\theta = 90^\circ$ ) of the dipolar coupling increases, whereas the intensity of the parallel component ( $\theta = 0^\circ$ ) decreases, if the detection frequency is moved from 30 to 90 MHz offset (Figure 3b). This indicates that orientation-selective PELDOR measurements can still be performed on such mixed trityl/nitroxide-labelled systems, but with much improved modulation depth compared to bisnitroxides.<sup>[22]</sup> To extract the distance distribution, the time traces of the dif-

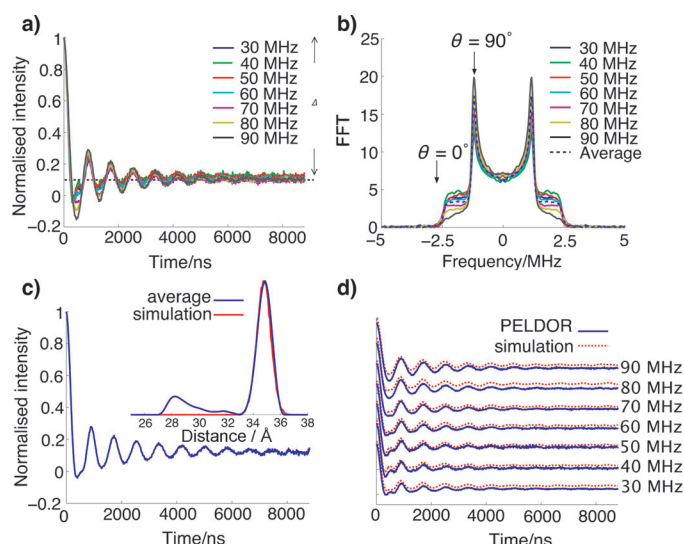


Figure 3. PELDOR data obtained from **2**. a) Background-subtracted time traces. b) Fourier transformed time traces in a). c) Orientation-averaged time trace and distance distributions obtained from Deer analysis (blue line) and by simulations (red line). d) Background-corrected time traces (blue line) and simulated time traces (broken red line). Experimental and simulated time traces have been displaced on the vertical axis for clarity.

ferent frequency offsets (Figure 3a) were added together, and the resulting orientation-averaged time trace (Figure 3c) was analysed with Deer analysis<sup>[23]</sup> (Figure 3c, inset). The obtained mean distance fits to the distance calculated with molecular mechanics (Table 1). The small peak in

Table 1. Interspin distances for **2** and **3** obtained from molecular mechanics, simulations and from PELDOR and DQC, both in combination with Deer analysis. All distances are given as a mean value  $\pm$  two standard deviations.

	$r_{\text{sim}}$ [Å]	$r_{\text{PELDOR}}$ [Å] <sup>[a]</sup>	$r_{\text{DQC}}$ [Å] <sup>[a]</sup>	$r_{\text{MM}}$ [Å]
<b>2</b>	$34.8 \pm 1.1$	$34.8 \pm 1.0$	$34.8 \pm 1.2$	35
<b>3</b>	$48.8 \pm 1.3$	–	$48.9 \pm 1.4$	51

[a] The mean distance  $\pm$  two standard deviations is given for the most probable peak.

the distance distribution from the orientation averaged time trace is attributed to incomplete orientation averaging, because its peak value corresponds to the over weighted parallel component of the dipolar spectrum.

To obtain more information on the conformational dynamics of the system, the PELDOR time traces for **2** were also simulated with a home-written Matlab program, which uses a conformational model and takes orientation selectivity into account.<sup>[24]</sup> The conformational model for **2** was generated by treating the backbone and spin labels as a chain of rigid segments linked by joints (see the Supporting Information).<sup>[18,19]</sup> This dynamics model and one set of EPR parameters were used to reproduce the orientation-selected PELDOR time traces (Figure 3d) and provided an excellent fit to the distance distribution from the orientation-averaged

time trace (inset in Figure 3c and Table 1). Distributions in length and flexibility of segments that resulted in the best fit between simulations and experiment are summarized in Table S2 in the Supporting Information. These results are in excellent agreement with those from Jeschke et al., which studied similar polymers by nitroxide labelling and PELDOR.<sup>[18]</sup> This indicates that the size of the trityl-spin label has no influence on the dynamics of the PolyPPEs, and that the spin density distribution within the trityl label can be neglected.

The narrow spectral width of the trityl centre also prompted us to perform double-quantum coherence (DQC) measurements on compound **2** (Figure 4).<sup>[25,26]</sup> DQC EPR is

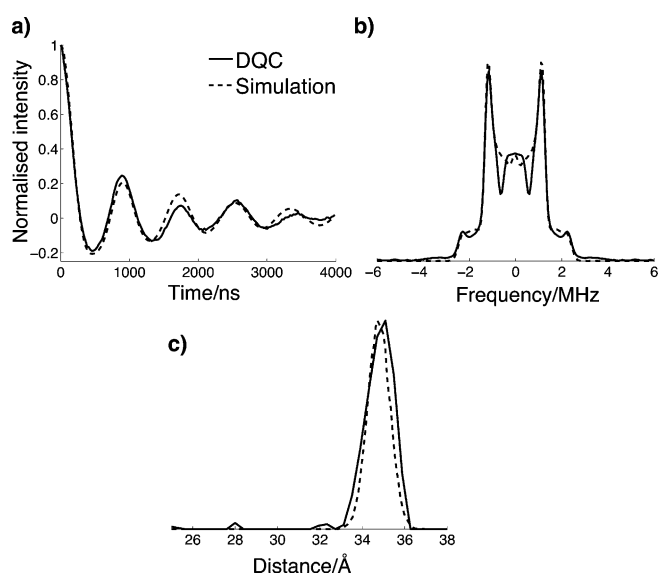


Figure 4. Six-pulse DQC data obtained from **2**. a) Background-corrected time trace (solid line) and simulated time trace (broken line). b) Fourier transformation of the time traces in a). c) Distance distributions from the DQC time trace by using Deer analysis (solid line) and the simulation model (broken line).

an elegant way to solely detect the dipolar electron–electron coupling in a time-domain experiment by introducing a double-quantum coherence filter into the pulse sequence. It was first introduced by the lab of Freed,<sup>[27]</sup> and it only requires one microwave source. In contrast to bisnitroxide biradicals, for which we were not able to obtain DQC time traces on a commercial EPR spectrometer (data not shown), DQC gave very good time traces for compound **2** with almost complete excitation of the whole Pake pattern (Figure 4b). This indicates that it might be sufficient for DQC to completely excite the dipolar coupling on one of the two spin centres. The distance distribution obtained from Deer analysis has a mean value and a standard deviation that is in agreement with the result obtained by PELDOR (Table 1). In addition, the DQC time trace and distance distribution were simulated with the same dynamics model as was used for the PELDOR time traces and gave an excellent fit (Figure 4a and c).

Bistrityl radical **3** gave an EPR spectrum with a width of only 2 G (Figure 2b), which is about a factor 30 narrower compared to a typical bisnitroxide spectrum with a width of about 70 G. This reduced width translates into increased signal intensity for the bistrityl system by roughly the same factor. DQC measurements on **3** gave a time trace with excellent signal-to-noise ratio that is a factor of two better than for a PELDOR time trace obtained for a bisnitroxide under the same conditions (Figure 5a and the Supporting

served for a bisnitroxide radical at 100 K, making PELDOR measurements at this temperature for nitroxide labels with *gem*-dimethyl structure or in matrices others than *ortho*-terphenyl unfeasible.<sup>[28,29]</sup>

In summary, we have demonstrated that trityl radicals can be successfully used as spin labels for nanometer-distance measurements by using pulsed EPR. They provided deep PELDOR modulations in experiments with mixed trityl/nitroxide labels and improved sensitivity in trityl/trityl DQC experiments. The trityl label is certainly more bulky than a nitroxide, but whether this leads to structural distortions, for example, in biological systems will depend on the specific molecular structure and will have to be checked in each individual case as for nitroxides. Please note that a paper from the laboratories of Freed and Hubbell on trityl–trityl distance measurements in the liquid state on proteins appeared, while this paper was being reviewed.<sup>[30]</sup>

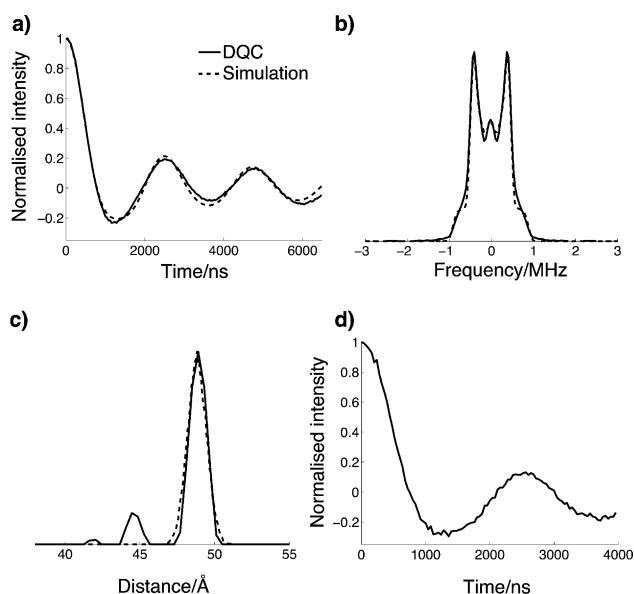


Figure 5. Six-pulse DQC data obtained from **3**. a) Background-corrected time trace (solid line) and simulated time trace (broken line). b) Fourier transform of the time traces in a). c) Distance distributions from the DQC time trace in a) by using Deer analysis (solid line) and the model-based simulation (broken line). d) Background-corrected DQC time trace obtained from **3** at 100 K.

Information). Measurement on **3** with PELDOR gave only electron-spin echo envelope modulation (ESEEM) artefacts due to a strong pulse overlap (see the Supporting Information). The DQC time trace for **3** was simulated by using the same segmented dynamics model as for **2** (Figure 5a and Table S2 in the Supporting Information).

The distance distributions, obtained from Deer analysis and from the model-based simulation are in very good agreement (Figure 5c). The average distance agrees with the distance obtained from molecular-mechanics modelling (Table 1).

The high signal-to-noise ratio and the  $T_M$  relaxation behaviour of **3** prompted us to perform DQC measurements also at higher temperatures. Because the spin system has to be immobile on the time scale of the coupling to be observed, the solvent (toluene) still had to be frozen. Therefore, a temperature of 100 K, at which a time trace with an excellent  $S/N$  of 60:1 could be obtained within 20 h, was chosen (Figure 5d). Compared to 50 K, the  $T_M$  was reduced by a factor of 1.5 and the signal-to-noise ratio was reduced by a factor of 2.7 only. In contrast, no spin echo was ob-

## Acknowledgements

G.W.R. acknowledges the School of Biology, University of St. Andrews for a SORS (Scottish Overseas Research Students) scholarship. S.Th.S. acknowledges financial support from the Icelandic Research Fund (No. 090026021 and 120001021). O.S. acknowledges the DFG for a grant in the Priority Research Program SPP1601 and the research councils of the U.K. for an RCUK fellowship.

**Keywords:** dipolar coupling • double-quantum coherence • EPR spectroscopy • nanostructures • pulsed electron–electron double resonance

- [1] G. W. Reginsson, O. Schiemann, *Biochem. J.* **2011**, *434*, 353–363.
- [2] O. Schiemann, T. F. Prisner, *Q. Rev. Biophys.* **2007**, *40*, 1–53.
- [3] G. Jeschke, Y. Polyhach, *Phys. Chem. Chem. Phys.* **2007**, *9*, 1895–1910.
- [4] J. H. Freed, *Annu. Rev. Phys. Chem.* **2008**, *59*, 655–689.
- [5] *Biological Magnetic Resonance, Vol. 19, Distance Measurements in Biological Systems by EPR*, (Eds.: L. J. Berliner, S. S. Eaton, G. R. Eaton), Kluwer academic/Plenum Publishers, New York, **2000**.
- [6] S. A. Shelke, S. T. Sigurdsson, *Eur. J. Org. Chem.* **2012**, 2291–2301.
- [7] C. Altenbach, T. Marti, H. G. Khorana, W. L. Hubbell, *Science* **1990**, *248*, 1088–1092.
- [8] H. Swartz, N. Khan in *Biological Magnetic Resonance, Vol. 23, Biomedical EPR - Part A: Free Radicals, Metals, Medicine, and Physiology* (Eds.: S. S. Eaton, G. R. Eaton, L. J. Berliner), Kluwer Academic, New York, **2005**, pp. 197–224.
- [9] I. Krstić, R. Hänsel, O. Romainczyk, J. W. Engels, V. Dötsch, T. F. Prisner, *Angew. Chem.* **2011**, *123*, 5176–5180; *Angew. Chem. Int. Ed.* **2011**, *50*, 5070–5074.
- [10] T. Reddy, T. Iwama, H. Halpern, V. Rawal, *J. Org. Chem.* **2002**, *67*, 4635–4639.
- [11] A. Fielding, P. Carl, G. Eaton, S. Eaton, *Appl. Magn. Reson.* **2005**, *28*, 231–238.
- [12] R. Owenius, G. Eaton, S. Eaton, *J. Magn. Reson.* **2005**, *172*, 168–175.
- [13] S. Grimme, P. R. Schreiner, *Angew. Chem.* **2011**, *123*, 12849–12853; *Angew. Chem. Int. Ed.* **2011**, *50*, 12639–12642.
- [14] A. Bobko, I. Dhimitruka, J. Zweier, *J. Am. Chem. Soc.* **2007**, *129*, 7240–7241.
- [15] Y. Liu, F. Villamena, J. Sun, Y. Xu, I. Dhimitruka, *J. Org. Chem.* **2008**, *73*, 1490–1497.

- [16] W. R. Browne, B. L. Feringa, *Nat. Nanotechnol.* **2006**, *1*, 25–35.
- [17] Y. Shirai, A. J. Osgood, Y. Zhao, K. F. Kelly, J. M. Tour, *Nano Lett.* **2005**, *5*, 2330–2334.
- [18] G. Jeschke, M. Sajid, M. Schulte, N. Ramezani, A. Volkov, H. Zimmermann, A. Godt, *J. Am. Chem. Soc.* **2010**, *132*, 10107–10117.
- [19] A. Godt, M. Schulte, H. Zimmermann, G. Jeschke, *Angew. Chem.* **2006**, *118*, 7722–7726; *Angew. Chem. Int. Ed.* **2006**, *45*, 7560–7564.
- [20] B. E. Bode, D. Margraf, J. Plackmeyer, G. Dürner, T. F. Prisner, O. Schiemann, *J. Am. Chem. Soc.* **2007**, *129*, 6736–6745.
- [21] G. Hagelueken, W. J. Inglede, H. Huang, B. Petrovic-Stojanovska, C. Whitfield, H. Elmkami, O. Schiemann, J. H. Naismith, *Angew. Chem.* **2009**, *121*, 2948–2950; *Angew. Chem. Int. Ed.* **2009**, *48*, 2904–2906.
- [22] O. Schiemann, P. Cekan, D. Margraf, T. F. Prisner, S. T. Sigurdsson, *Angew. Chem.* **2009**, *121*, 3342–3345; *Angew. Chem. Int. Ed.* **2009**, *48*, 3292–3295.
- [23] G. Jeschke, V. Chechik, P. Ionita, A. Godt, H. Zimmermann, J. Banham, C. R. Timmel, D. Hilger, H. Jung, *Appl. Magn. Reson.* **2006**, *30*, 473–498.
- [24] G. W. Reginsson, R. I. Hunter, P. A. S. Cruickshank, D. R. Bolton, S. T. Sigurdsson, G. M. Smith, O. Schiemann, *J. Magn. Reson.* **2012**, *216*, 175–182.
- [25] P. Borbat, J. Freed, *Chem. Phys. Lett.* **1999**, *313*, 145–154.
- [26] P. Borbat, H. Mchaourab, J. Freed, *J. Am. Chem. Soc.* **2002**, *124*, 5304–5314.
- [27] S. Saxena, J. Freed, *Chem. Phys. Lett.* **1996**, *251*, 102–110.
- [28] A. Rajca, V. Kathirvelu, K. K. Roy, M. Pink, S. Rajca, S. Sarkar, S. E. Eaton, G. R. Eaton, *Chem. Eur. J.* **2010**, *16*, 5778–5782.
- [29] G. Jeschke, A. Bender, H. Paulsen, H. Zimmermann, A. Godt, *J. Magn. Reson.* **2004**, *169*, 1–12.
- [30] Z. Yang, Y. Liu, P. Borbat, J. L. Zweier, J. H. Freed, W. L. Hubbell, *J. Am. Chem. Soc.* **2012**, *134*, 9950–9952.

Received: August 24, 2012  
Published online: September 20, 2012

# **CHEMISTRY**

---

## **A EUROPEAN JOURNAL**

---

### Supporting Information

© Copyright Wiley-VCH Verlag GmbH & Co. KGaA, 69451 Weinheim, 2012

#### **Trityl Radicals: Spin Labels for Nanometer-Distance Measurements**

**Gunnar W. Reginsson,<sup>[a, b]</sup> Nitin C. Kunjir,<sup>[b]</sup> Snorri Th. Sigurdsson,<sup>\*, [b]</sup> and  
Olav Schiemann<sup>\*, [a, c]</sup>**

chem\_201203014\_sm\_miscellaneous\_information.pdf

## Table of Contents

<b>Experimental</b>	<b>3</b>
<i>General</i>	2
<b>List of abbreviations</b>	<b>3</b>
<b>Organic synthesis procedures</b>	<b>4</b>
<i>Compound 1</i>	5
<i>Compound 2</i>	8
<i>Compound (3)</i>	10
<i>4-((4'-ethynyl-3,3'-bis(heptyloxy)biphenyl-4-yl)ethynyl)phenol (4)</i>	12
<i>3,3'-bis(heptyloxy)-4,4'-diiodobiphenyl (6)</i>	14
<i>2-(4-((3,3'-bis(heptyloxy)-4'-iodobiphenyl-4-yl)ethynyl)phenoxy)tetrahydro-2H-pyran (8)</i>	16
<i>((3,3'-bis(heptyloxy)-4'-((4-(tetrahydro-2H-pyran-2-yloxy)phenyl)ethynyl)biphenyl-4-yl)ethynyl)trimethylsilane (10)</i>	18
<i>2-(4-((4'-ethynyl-3,3'-bis(heptyloxy)biphenyl-4-yl)ethynyl)phenoxy)tetrahydro-2H-pyran (11)</i>	20
<i>Compound 12</i>	22
<i>Compound 13</i>	24
<i>Compound 15</i>	26
<i>Compound (16)</i>	28
<b>CW-EPR</b>	<b>30</b>
<b>Original PELDOR and DQC time traces</b>	<b>32</b>
<b>PELDOR</b>	<b>32</b>
<b>DQC</b>	<b>33</b>
<b>S/N comparison</b>	<b>34</b>
<b>DQC derived distance distribution at 50 and 100 K</b>	<b>34</b>
<b>PELDOR experiments with different inversion/detection positions</b>	<b>35</b>
<b>Excitation profile of inversion pulse and PELDOR modulation depth</b>	<b>37</b>
<b>Data Analysis and Simulations</b>	<b>37</b>
<b>References</b>	<b>39</b>
	1



## Experimental

### General

**EPR:** Pulsed EPR measurements were done on a Bruker ELEXSYS E580 X-band EPR spectrometer equipped with the SpecJet-II and PatternJet-II combination. All pulsed experiments were performed at 50 K unless otherwise stated using a standard flex line probe head with a dielectric ring resonator (MD5) together with a continuous flow helium cryostat (CF935) and a temperature control system (ITC 502) from Oxford Instruments. Continuous wave EPR measurements were performed on a Bruker EMX spectrometer equipped with a liquid nitrogen setup from Oxford Instruments. Samples of **2**, **3** and a nitroxide biradical (inset Figure S6) were dissolved in deuterated toluene to yield a spin concentration of 200  $\mu\text{M}$  and a final volume of 100 microliter. The samples were frozen in liquid nitrogen before the EPR measurements at cryogenic temperatures. Field swept spectra were recorded by detecting the echo created by the Hahn echo pulse sequence  $\pi/2 - \tau - \pi$ . The pulse lengths were 12 and 24 ns for the  $\pi/2$  and  $\pi$  pulse, respectively. The delay  $\tau$  between the pulses was 380 ns. The whole echo was recorded with a 450 ns acquisition window. For the PELDOR measurements a double microwave frequency setup available from Bruker was used. Microwave pulses were amplified with a 1kW TWT amplifier (117X) from Applied Systems Engineering. PELDOR experiments were done using the 4-pulse sequence,  $\pi/2(\nu\text{A}) - \tau_1 - \pi(\nu\text{A}) - (\tau_{1+i}) - \pi(\nu\text{B}) - (\tau_{2-i}) - \pi(\nu\text{A}) - \tau_2 - \text{echo}$ . To eliminate receiver offsets the  $\pi/2(\nu\text{A})$  pulse was phase-cycled. The length of the detection pulses ( $\nu\text{A}$ ) were 16 ns ( $\pi/2$ ) and 32 ns ( $\pi$ ) unless otherwise stated. The frequency of the inversion pulse ( $\nu\text{B}$ ) was set at the maximum of the trityl field sweep spectrum and the length was 16 ns unless otherwise stated. Amplitude and phase of the pulses was set to optimize the refocused echo. All PELDOR spectra were recorded with a shot repetition time of 3000  $\mu\text{s}$ , a video amplifier bandwidth of 20 MHz and an amplifier gain of 51 to 57 dB.  $\tau_1$  was 380 ns, which corresponds to a blind spot for deuterium Larmor frequency. Proton modulation was suppressed by incrementing  $\tau_1$  8 times by 8 ns and adding the consecutive spectra. The time increment of the inversion pulse was 14 ns. The DQC EPR measurements were performed using the six-pulse sequence,  $\pi/2 - \tau_1 - \pi - \tau_1 - \pi/2 - \tau_3 - \pi - \tau_3 - \pi/2 - \tau_2 - \pi - \tau_2 - \text{echo}$ . The dipolar signal was filtered out by a 64-step phase-cycling program.<sup>[1]</sup> To suppress nuclear modulation,  $\tau_1$  and  $\tau_2$  were incremented 4 times by 108 ns and the spectra added together. The initial value for  $\tau_1$  was 280 ns and the initial value for  $\tau_2$  was between 4000 and 6500 ns.  $\tau_3$  was held constant at 30 ns. The DQC time trace was recorded by increasing  $\tau_1$  and decreasing  $\tau_2$  by 20 ns steps. The  $\pi/2$  and  $\pi$  pulse length was 8 and 16 ns, respectively for the DQC EPR measurements on **2** and 12 and 24 ns for the DQC EPR on **3**. The DQC echo was recorded with an acquisition window of 40 ns. The simulations of the DQC time traces were done assuming no orientation selection and complete excitation of the EPR spectrum. The orientation averaged PELDOR time trace was constructed by normalizing the original time traces and adding them. The individual time traces were recorded with the same settings including video amplifier gain and number of scans.

**Synthesis:** All solvents and reagents were purchased from Sigma-Aldrich and stored over molecular sieves (3 Å) prior to use.  $\text{Et}_3\text{N}$  was distilled over calcium hydride prior

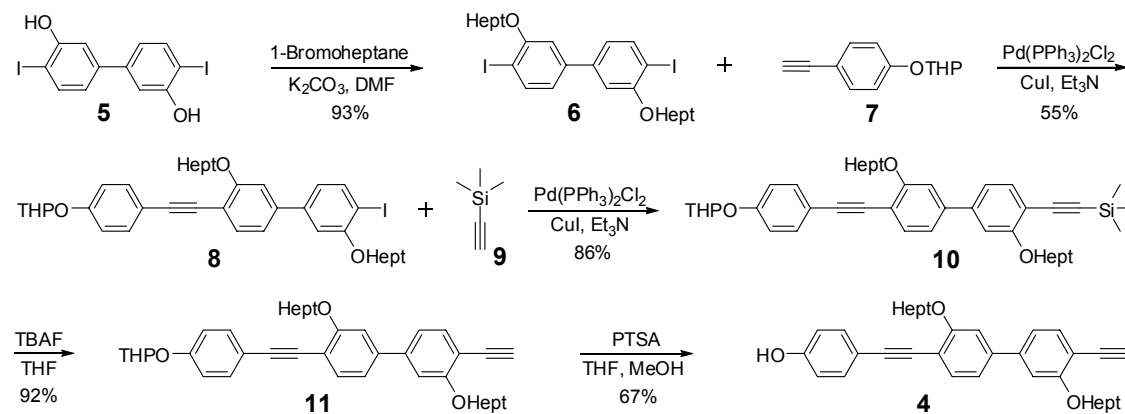
to use. All reactions were carried under an inert atmosphere of argon unless otherwise stated. Neutral silica gel was purchased from Silicycle. Analytical thin layer chromatography (TLC) was performed on silica-coated glass plates (Silicycle 60 F<sub>254</sub>). NMR spectra for all compounds were recorded on an Avance 400 MHz Bruker NMR spectrometer and the chemical shifts were reported parts per million (ppm) relative to the deuterated NMR solvent used [<sup>1</sup>H-NMR CDCl<sub>3</sub> (7.26 ppm), DMSO-*d*<sub>6</sub> (2.50 ppm); <sup>13</sup>C-NMR: CDCl<sub>3</sub> (77.16 ppm), DMSO-*d*<sub>6</sub> (39.52 ppm)]. Due to the paramagnetic nature of nitroxides, the NMR spectra of these compounds show substantial broadening or even absence of the signals, particularly for nuclei close to the radical. Mass spectra were recorded on Bruker, Micro Tof-Q. Compounds **2**, **3** and **16** were purified on RP-HPLC using a GL Sciences Inertsustain C18 14 × 250 mm preparative column with UV detection at 360 nm on Beckman Coulter Gold HPLC. Analytical RP-HPLC samples for the compounds **2**, **3** and **16** were run on same instrument using a GL Sciences Inertsustain C18 4.6 × 150 mm analytical column with UV detection at 360 nm. Solvents gradient for analytical and preparative RP-HPLC were run as described below for compounds **2**, **3** and **16**. Compounds **2**, **3** and **16** were analyzed by MALDI-TOF using an Autoflex III matrix assisted laser desorption/ionization time of flight mass spectrometer (Bruker, Bremen, Germany). The MALDI was operated with a Nb-YAG smartbeam laser of wavelength 354 nm and repetition rate up to 1000 Hz. The spectra were recorded in positive ion mode with operating ion reflectron and pulsed ion extraction (PIE) of 10 ns. The laser power was kept below 50% of total laser power in all measurements. The matrix solution was prepared by dissolving 10 mg of the matrix  $\alpha$ -cyano-4-hydroxy cinnamic acid methyl ester in 1 mL (50:50 V/V) CH<sub>3</sub>CN and 0.1% trifluoroacetic acid in water. Compounds **2** & **16** were dissolved in CH<sub>2</sub>Cl<sub>2</sub> and compound **3** in 50:50 CH<sub>3</sub>CN and EtOAc. The sample spots were prepared by co-spotting 0.5  $\mu$ L of sample solution and 0.5  $\mu$ L of matrix solution on a clean polished steel sample plate. The mixture was allowed to dry at 22 °C. The mass spectra were internally calibrated using peptide calibration standard (nr. 206195, Bruker, Germany) and an in-house prepared calibration standard mixture.

## List of abbreviations

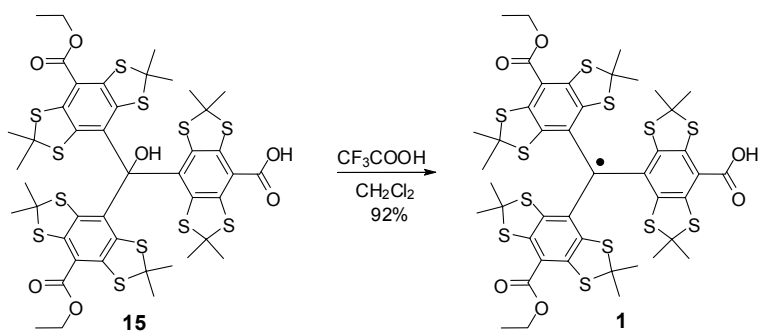
DMF	Dimethylformamide
BOP	Benzotriazol-1-yloxytris(dimethylamino)-phosphonium hexafluorophosphate
HOBt	1-Hydroxybenzotriazole
Et <sub>3</sub> N	Triethylamine
THF	Tetrahydrofuran
PTSA	4-toluensulfonic acid
TBAF	Tetrabutylammonium fluoride
EtOAc	Ethyl acetate
CH <sub>3</sub> CN	Acetonitrile

## Organic synthesis procedures

Scheme S1 shows the synthesis for linker 4, which is referred to in the paper itself. Thus, Scheme 1 and Scheme S1 combined describe the synthetic work in the paper. In the following pages, protocols for individual compounds are detailed.



**Scheme S1.** Synthesis of linker 4.

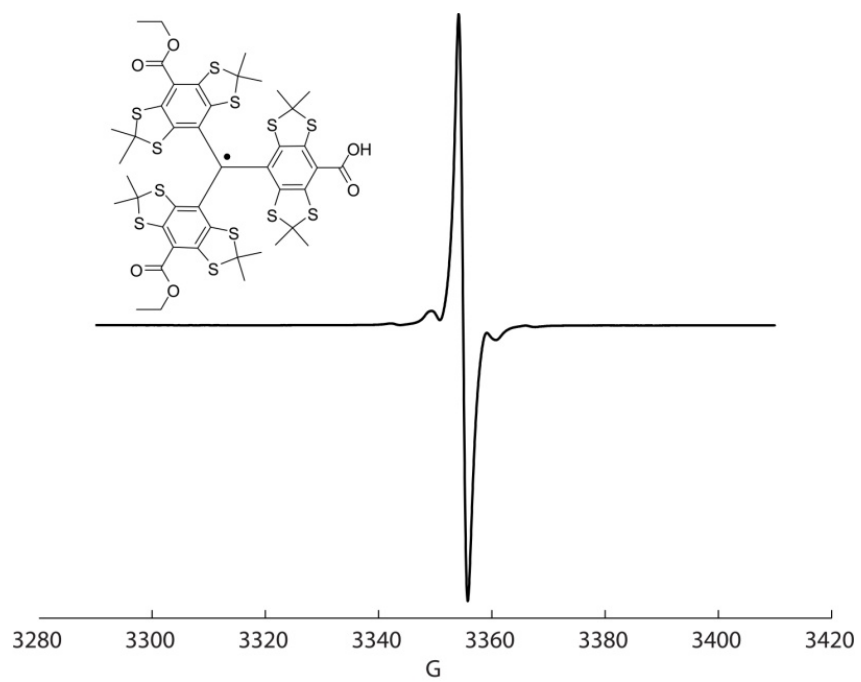


### Compound 1

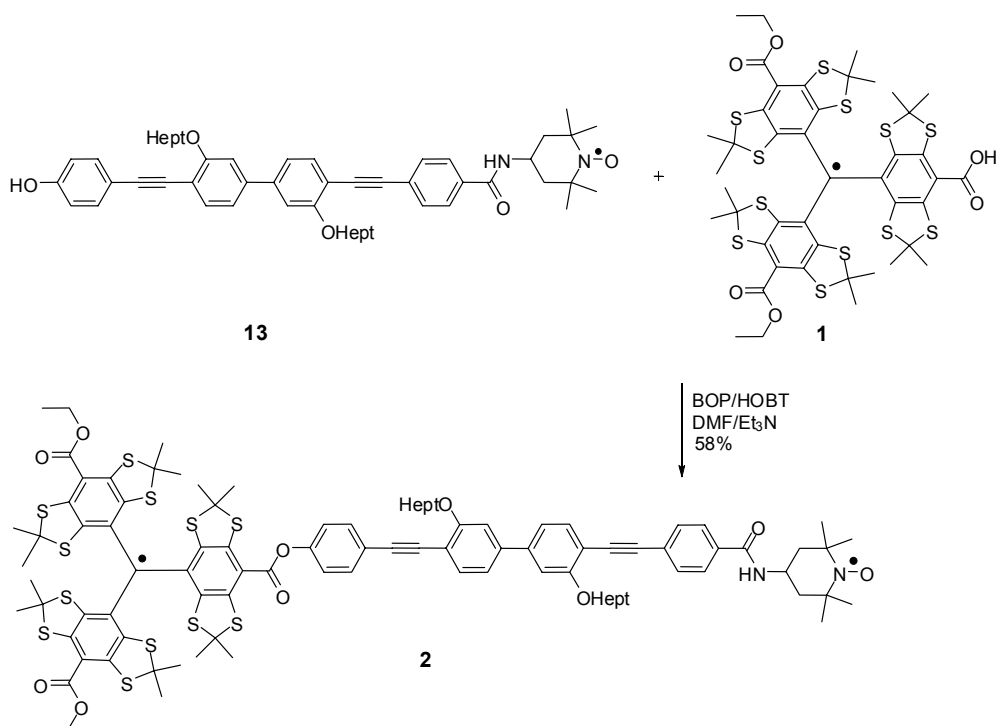
Trifluoroacetic acid (2 mL) was added to a solution of compound **15** (0.200 g, 0.186 mmol) in  $\text{CH}_2\text{Cl}_2$  (5 mL). The reaction mixture was stirred at 25 °C for 2 h and concentrated in *vacuo*. The crude product was purified by column chromatography using neutral silica gel (2:98, MeOH : $\text{CH}_2\text{Cl}_2$ ) to give radical **1** (0.18 g, 92%) as a green solid.

TLC (Silica gel, 10% MeOH/ $\text{CH}_2\text{Cl}_2$ ): Rf (**15**) = 0.60, Rf (**1**) = 0.90.

MS (ESI) calcd. for  $\text{C}_{44}\text{H}_{47}\text{O}_6\text{S}_{12}$  [M+Na] 1077.9919, found 1077.9913.



CW X-band EPR spectrum of **1** (10% MeOH/CH<sub>2</sub>Cl<sub>2</sub> at 22 °C).



## Compound 2

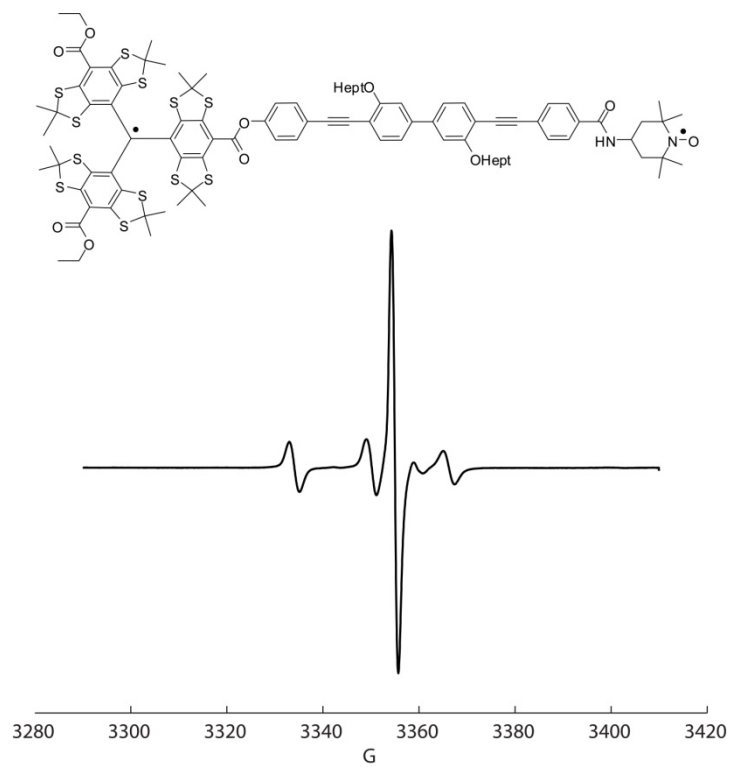
To a solution of compound **13** (0.06 g, 0.075 mmol) and the monoacid trityl radical **1** (0.080 g, 0.075 mmol) in dry DMF (5 mL) were added BOP (0.050 g, 0.113 mmol) and HOBT (0.015 g, 0.113 mmol), followed by addition of Et<sub>3</sub>N (1.5 mL). The reaction mixture was stirred at 25 °C for 12 h and concentrated *in vacuo* to give the crude material, which was purified by column chromatography using neutral silica gel (5:95 to 40:60, EtOAc:hexane) to yield **2** (0.080 g, 58%) as a yellowish green solid.

TLC (Silica gel, 40% EtOAc/hexane): R<sub>f</sub> (**13**) = 0.30, R<sub>f</sub> (**1**) = 0.05, R<sub>f</sub> (**2**) = 0.50.

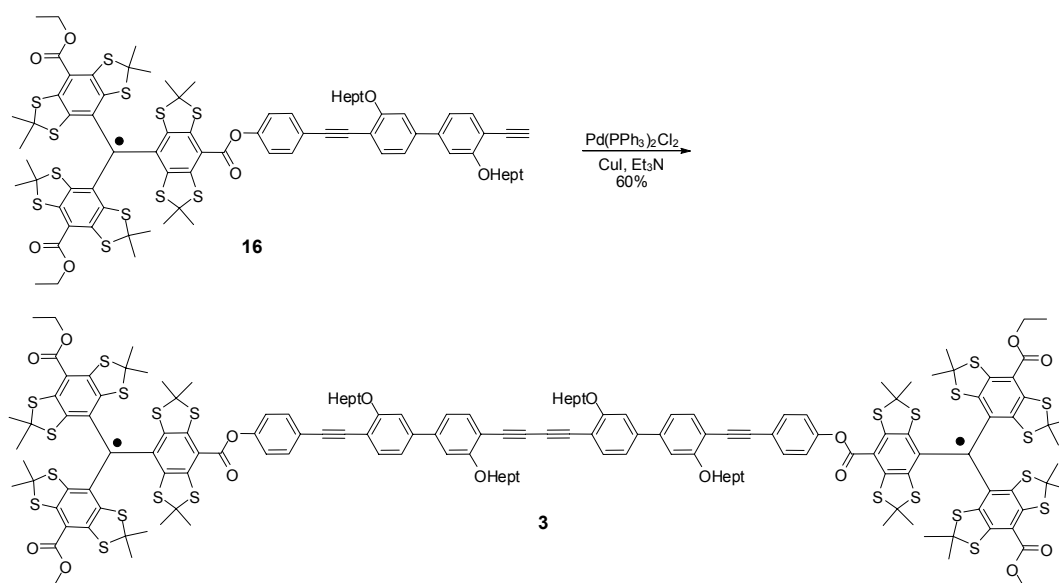
MALDI-TOF: calcd. for C<sub>96</sub>H<sub>108</sub>N<sub>2</sub>O<sub>10</sub>S<sub>12</sub><sup>-</sup> [M<sup>+</sup>] 1832.465, found 1832.469

Preparative HPLC run (Flow rate = 7 mL/min). Solvent A, 100% CH<sub>3</sub>CN; Solvent B, 100% EtOAc; 5 min linear gradient from 0% to 11% B, 11% B isocratic for 35 min. 1 min linear gradient from 11% to 0% B to initial conditions (100% A).

Analytical HPLC run (Flow rate = 1 mL/min). Solvent A, 100% CH<sub>3</sub>CN; Solvent B, 100% EtOAc; 4 min linear gradient from 0% to 25% B, 25% B isocratic for 15 min. 1 min linear gradient from 25% to 0% B to initial conditions (100% A).



CW X-band EPR spectrum of **2** (10% MeOH/CH<sub>2</sub>Cl<sub>2</sub> at 22 °C).



### Compound (3)

Compound **16** (0.030 g, 0.019 mmol) was dissolved in dry THF (3 mL) containing freshly distilled Et<sub>3</sub>N (3 mL). Pd[PPh<sub>3</sub>]<sub>2</sub>Cl<sub>2</sub> (0.001 g, 5 mol %) and CuI (0.0018 g, 8 mol %) were added to the solution in one portion. The mixture was stirred at 25 °C for 12 h in an open air. After completion of the reaction (monitored by TLC), the reaction mixture was diluted with water and extracted with EtOAc (3 × 10 mL). The combined organic layers were washed with water, brine (10 mL) and dried (Na<sub>2</sub>SO<sub>4</sub>). The organic layer was concentrated and the crude mixture was purified by column chromatography using neutral silica gel (5:95 to 40:60, EtOAc:hexane) to give **3** as a green solid (0.018g, 60 %).

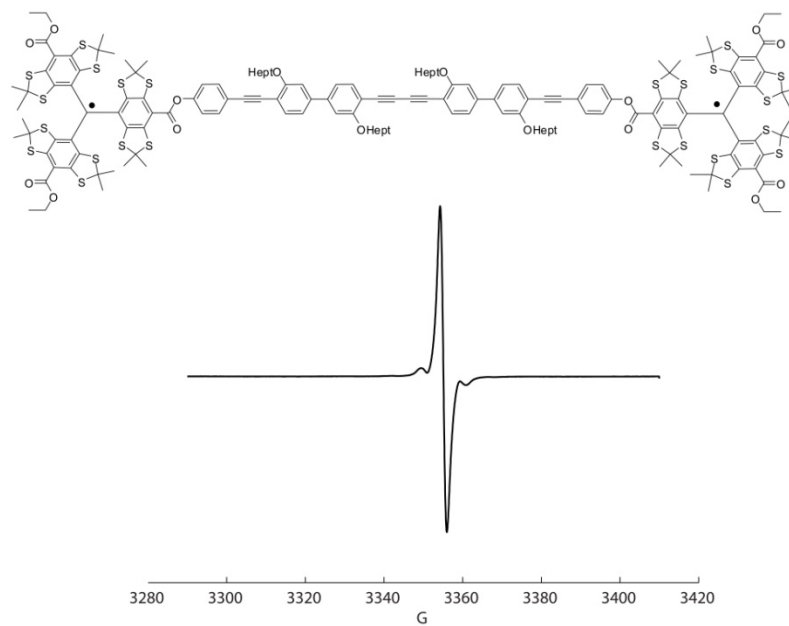
TLC (Silica gel, 40% EtOAc/hexane): R<sub>f</sub> (**16**) = 0.40, R<sub>f</sub> (**3**) = 0.30.

MALDI-TOF: calcd. for C<sub>160</sub>H<sub>172</sub>O<sub>16</sub>S<sub>24</sub><sup>-</sup> [M<sup>+</sup>] 3116.594, found 3116.565.

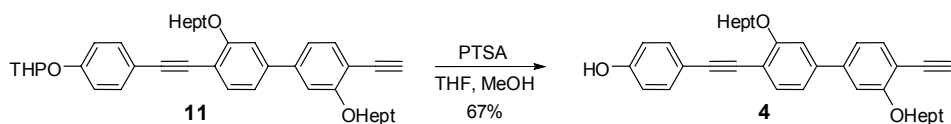
Preparative HPLC (Flow rate = 7 mL/min). Solvent A, 100% CH<sub>3</sub>CN; Solvent B, 100% EtOAc; 3 min linear gradient from 0% to 20% B, 3 min linear gradient from 20% to 80% B, 80% B isocratic for 14 min. 1 min linear gradient from 80% to 0% B to initial conditions (100% A).

Analytical HPLC run (Flow rate = 1 mL/min). Solvent A, 100% CH<sub>3</sub>CN; Solvent B, 100% EtOAc; 3 min linear gradient from 0% to 20% B, 0.5 min linear gradient from 20% to 70% B, 70% B isocratic for 15 min. 1 min linear gradient from 70% to 0% B to initial conditions (100% A).





CW X-band EPR spectrum (10% MeOH/CH<sub>2</sub>Cl<sub>2</sub> at 22 °C) of **3**.



#### 4-((4'-ethynyl-3,3'-bis(heptyloxy)biphenyl-4-yl)ethynyl)phenol (**4**)

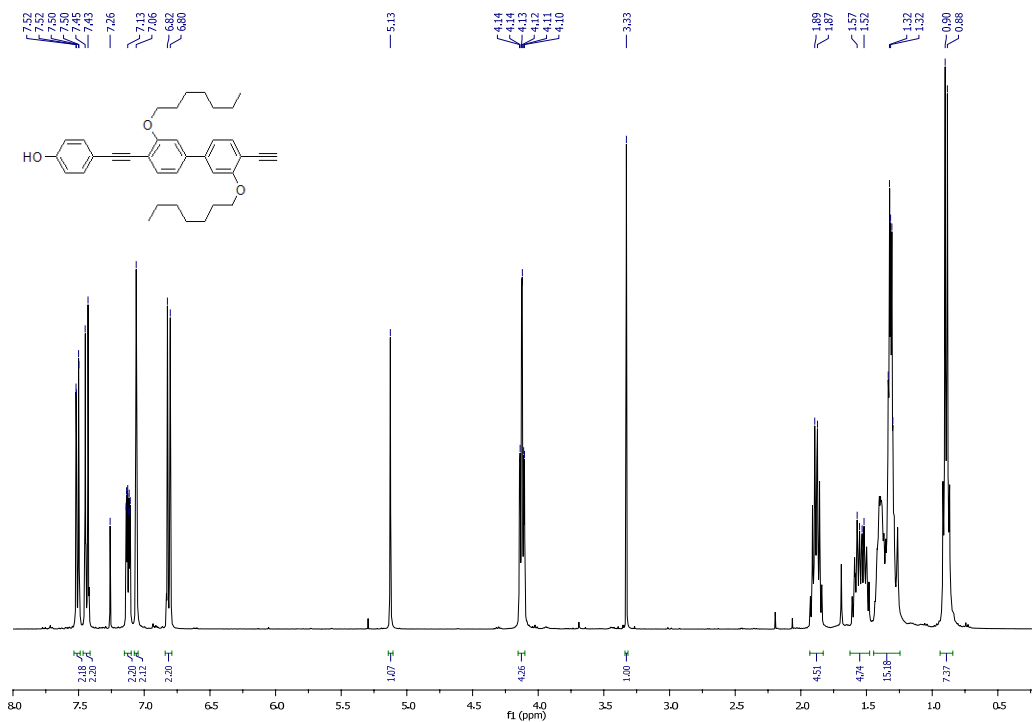
4-toluenesulfonic acid (0.158 g, 0.823 mmol) was added to a solution of compound **11** (0.500 g, 0.823 mmol) in anhydrous THF and methanol (1:1, 10 mL). After stirring the reaction mixture at 25 °C for 12 h, it was diluted with water (10 mL) and extracted with EtOAc (3 × 10 mL). The combined organic layers were washed successively with water (2 × 10 mL) and brine (10 mL). The organic layer was dried over Na<sub>2</sub>SO<sub>4</sub> and concentrated *in vacuo* to give the crude product, which was purified by column chromatography using neutral silica gel (2:98, EtOAc:hexane) to yield **4** (0.290 g, 67%) as a white solid.

TLC (Silica gel, 30% EtOAc/hexane): R<sub>f</sub> (**11**) = 0.70, R<sub>f</sub> (**4**) = 0.50.

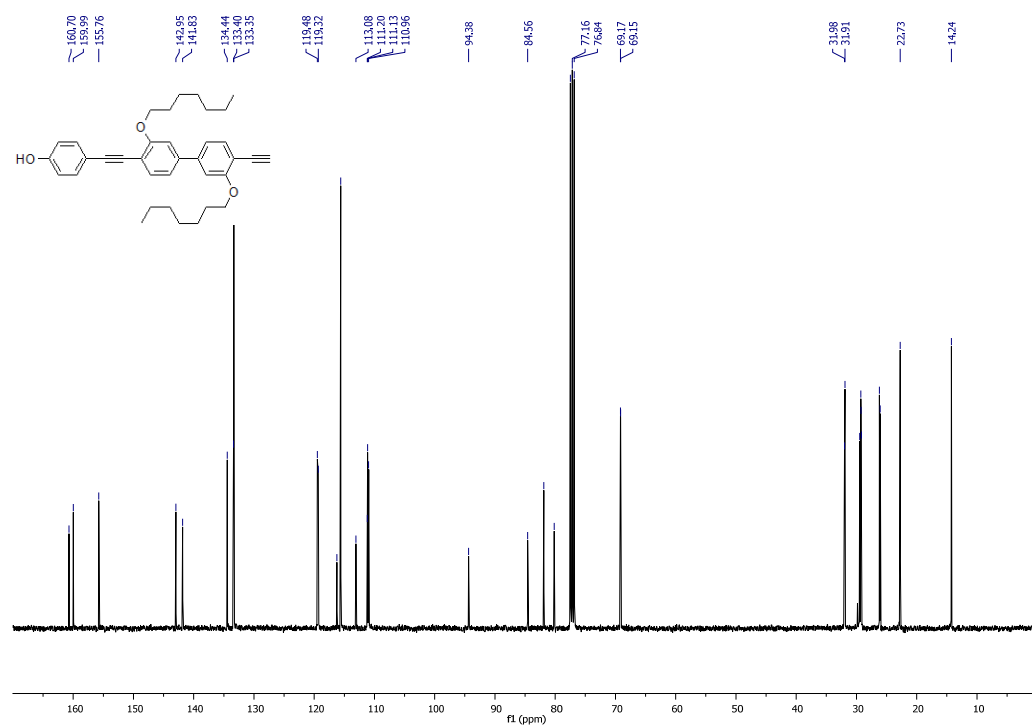
<sup>1</sup>H NMR (CDCl<sub>3</sub>) δ 7.51 (dd, *J* = 7.9, 0.9 Hz, 2H, Ar-*H*), 7.44 (d, *J* = 8.7 Hz, 2H, Ar-*H*), 7.12 (ddd, *J* = 7.9, 3.4, 1.6 Hz, 2H, Ar-*H*), 7.06 (s, 2H, Ar-*H*), 6.81 (d, *J* = 8.7 Hz, 2H, Ar-*H*), 5.13 (s, 1H, OH), 4.12 (td, *J* = 6.5, 2.1 Hz, 4H, OCH<sub>2</sub>), 3.33 (s, 1H, CH), 1.88 (d, *J* = 8.2 Hz, 5H, CH<sub>2</sub>), 1.54 (dd, *J* = 14.4, 6.7 Hz, 5H, CH<sub>2</sub>), 1.32 (dt, *J* = 7.2, 3.5 Hz, 15H, CH<sub>2</sub>), 0.89 (d, *J* = 6.9 Hz, 7H, CH<sub>3</sub>).

<sup>13</sup>C NMR (CDCl<sub>3</sub>) δ 14.24, 22.73, 26.12, 29.28, 31.95, 69.16, 80.17, 81.89, 84.56, 94.38, 110.83-11.33, 113.08, 115.60, 116.23, 119.40, 133.37, 134.44, 141.83, 142.95, 155.76, 159.99, 160.70.

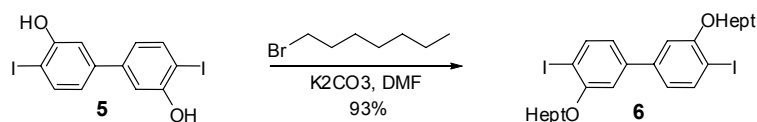
MS (ESI) calcd. for C<sub>36</sub>H<sub>42</sub>O<sub>3</sub> [M+Na] 545.3032, found 545.3026.



**<sup>1</sup>H-NMR (400 MHz, CDCl<sub>3</sub>) spectrum of 4.**



**<sup>13</sup>C-NMR (400 MHz, CDCl<sub>3</sub>) spectrum of 4.**



### 3,3'-bis(heptyloxy)-4,4'-diiodobiphenyl (**6**)

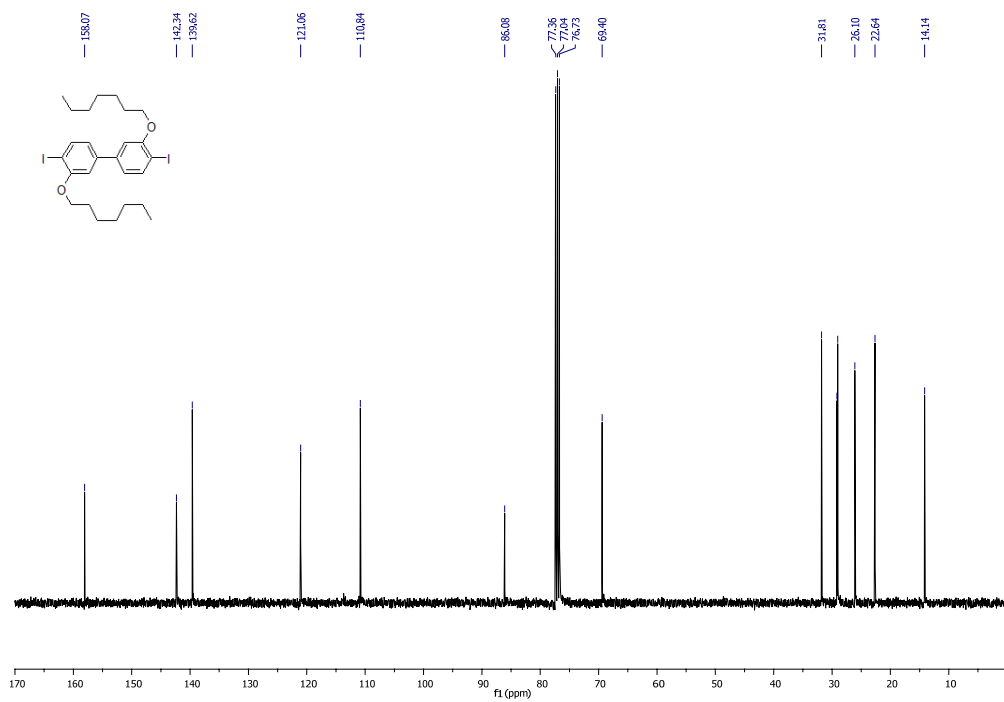
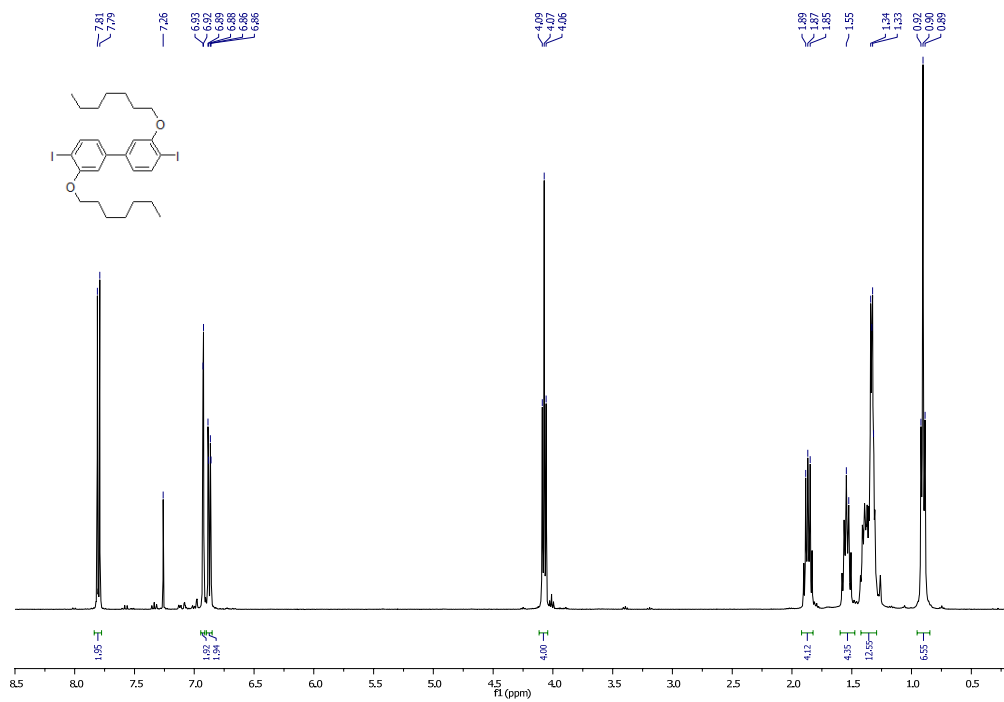
Potassium carbonate (0.947 g, 6.850 mmol) and 1-bromoheptane (1.02 mL, 6.850 mmol) were added to a solution of 4,4'-diiodobiphenyl-3,3'-diol (**5**) (1.000 g, 2.283 mmol) in dry DMF (20 mL) and the reaction mixture was stirred at 80 °C for 5 h. After cooling the reaction mixture to 25 °C, it was diluted with water (15 mL) and extracted with diethyl ether (3 × 30 mL). The combined organic layers were washed successively with water (2 × 20 mL) and brine (20 mL). The organic phase was dried over Na<sub>2</sub>SO<sub>4</sub> and concentrated *in vacuo* to give the crude product, which was purified by column chromatography using neutral silica gel (0.5:99.5, EtOAc:hexane) to yield **6** (1.350 g, 93%) as a white solid.

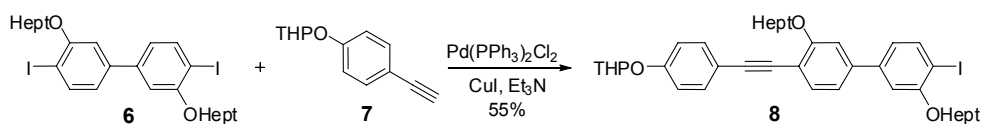
TLC (Silica gel, 30% EtOAc /hexane): R<sub>f</sub> (**5**) = 0.10, R<sub>f</sub> (**6**) = 0.60.

<sup>1</sup>H NMR (CDCl<sub>3</sub>) δ 0.90 (t, *J* = 6.9 Hz, 6H, CH<sub>3</sub>), 1.33 (dd, *J* = 6.4, 3.6 Hz, 13H, CH<sub>2</sub>), 1.54 (d, *J* = 7.9 Hz, 4H, CH<sub>2</sub>), 1.92 – 1.82 (m, 4H, CH<sub>2</sub>), 4.07 (t, *J* = 6.4 Hz, 4H, OCH<sub>2</sub>), 6.87 (dd, *J* = 8.0, 2.0 Hz, 2H, Ar-*H*), 6.92 (d, *J* = 1.9 Hz, 2H, Ar-*H*), 7.80 (d, *J* = 8.0 Hz, 2H, Ar-*H*).

<sup>13</sup>C NMR (CDCl<sub>3</sub>) δ 14.14, 22.64, 26.10, 29.09, 31.81, 69.40, 86.08, 110.84, 121.06, 139.62, 142.34, 158.07.

MS (ESI) calcd. for C<sub>26</sub>H<sub>36</sub>I<sub>2</sub>O<sub>2</sub> [M+Na] 657.0702, found 657.0697.





### 2-(4-((3,3'-bis(heptyloxy)-4'-iodobiphenyl-4-yl)ethynyl)phenoxy)tetrahydro-2H-pyran (8)

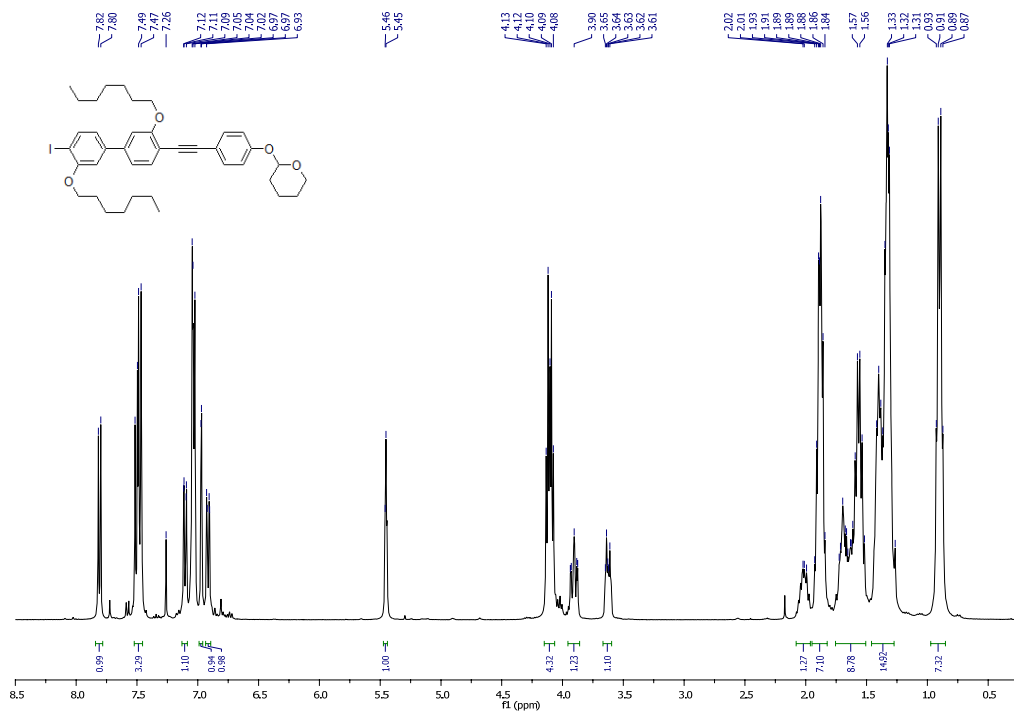
To a solution of compound **6** (0.500 g, 0.788 mmol) and 2-(4-ethynylphenoxy)tetrahydro-2H-pyran (**7**) (0.096 g, 0.472 mmol) and freshly distilled Et<sub>3</sub>N (5 mL) in anhydrous THF (10 mL) were added Pd[PPh<sub>3</sub>]<sub>2</sub>Cl<sub>2</sub> (0.028 g, 5 mol %) and CuI (0.012 g, 8 mol %). The resulting suspension was stirred at 25 °C for 12 h, diluted with water and extracted with EtOAc (3 × 20 mL). The combined organic layers were washed successively with water (2 × 20 mL) and brine (20 mL). The organic phase was dried over Na<sub>2</sub>SO<sub>4</sub> and concentrated *in vacuo* to give the crude product, which was purified by column chromatography using neutral silica gel (1:99, EtOAc:hexane) to yield **8** (0.310 g, 55%) as a white solid.

TLC (Silica gel, 20% EtOAc /hexane): R<sub>f</sub> (**6**) = 0.9, R<sub>f</sub> (**7**) = 0.7, R<sub>f</sub> (**8**) = 0.50.

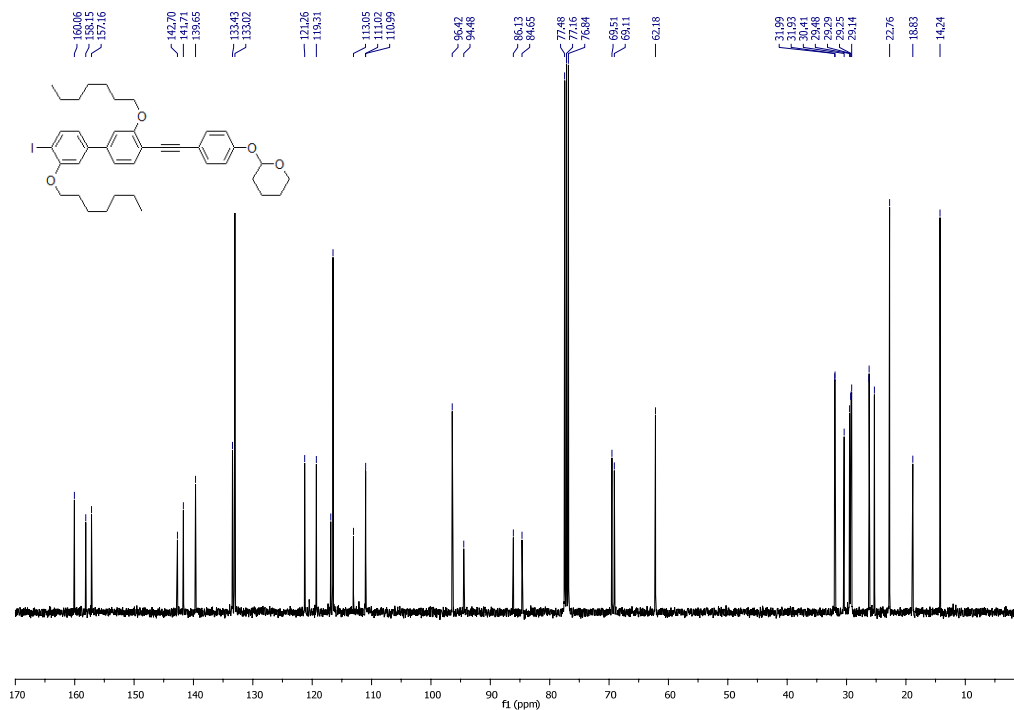
<sup>1</sup>H NMR (CDCl<sub>3</sub>) δ 0.90 (q, *J* = 6.6 Hz, 6H, C-CH<sub>3</sub>), 1.36 (ddd, *J* = 15.0, 10.3, 5.2 Hz, 15H, -CH<sub>2</sub>), 1.76 – 1.51 (m, 9H, -CH<sub>2</sub>), 1.95 – 1.82 (m, 7H, -CH<sub>2</sub>), 2.08 – 1.96 (m, 1H, CH), 3.67 – 3.60 (m, 1H, CH), 3.96 – 3.86 (m, 1H, CH), 4.15 – 4.07 (m, 4H, OCH<sub>2</sub>), 5.46 (d, *J* = 2.9 Hz, 1H, -CH), 6.91 (dd, *J* = 8.1, 1.8 Hz, 1H, Ar-*H*), 6.97 (d, *J* = 1.6 Hz, 1H, Ar-*H*), 7.10 (dd, *J* = 7.9, 1.3 Hz, 1H, Ar-*H*), 7.49 (dd, *J* = 11.8, 8.3 Hz, 3H, Ar-*H*), 7.81 (d, *J* = 8.0 Hz, 1H, Ar-*H*).

<sup>13</sup>C NMR (CDCl<sub>3</sub>) δ 14.24, 18.83, 22.76, 25.30, 26.20, 29.29, 30.41, 31.96, 62.18, 69.11, 69.51, 84.65, 86.13, 94.98, 96.42, 111.01, 113.05, 116.50, 116.88, 119.31, 121.26, 133.02, 133.43, 139.65, 141.71, 142.70, 157.16, 158.15, 160.06.

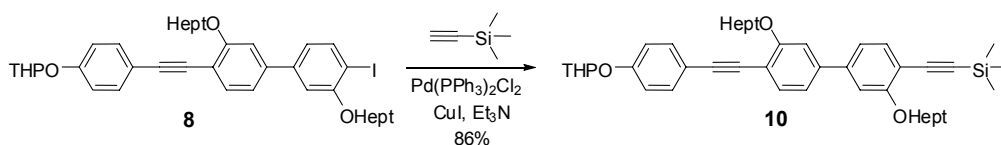
MS (ESI) calcd. for C<sub>39</sub>H<sub>49</sub>IO<sub>4</sub> [M+Na] 731.2573, found 731.2568.



<sup>1</sup>H-NMR (400 MHz, CDCl<sub>3</sub>) spectrum of **8**.



<sup>13</sup>C-NMR (400 MHz, CDCl<sub>3</sub>) spectrum of **8**.



**((3,3'-bis(heptyloxy)-4'-((4-(tetrahydro-2H-pyran-2-yloxy)phenyl)ethynyl)biphenyl-4-yl)ethynyl)trimethylsilane (10)**

To a solution of compound **8** (0.500 g, 0.705 mmol) and trimethylsilylacetylene (0.310 mL, 1.058 mmol) and freshly distilled Et<sub>3</sub>N (5 mL) in anhydrous THF (10 mL) were added Pd[PPh<sub>3</sub>]<sub>2</sub>Cl<sub>2</sub> (0.025 g, 5 mol %) and CuI (0.011 g, 8 mol %). The reaction mixture was stirred at 25 °C for 12 h, diluted with water (10 mL) and extracted with EtOAc (3 × 10 mL). The combined organic layers were washed successively with water (2 × 10 mL) and brine (10 mL). The organic layer was dried over Na<sub>2</sub>SO<sub>4</sub> and concentrated *in vacuo* to give the crude product, which was purified by column chromatography using neutral silica gel (1:99, EtOAc:hexane) to yield **10** (0.410 g, 86%) as a red syrup.

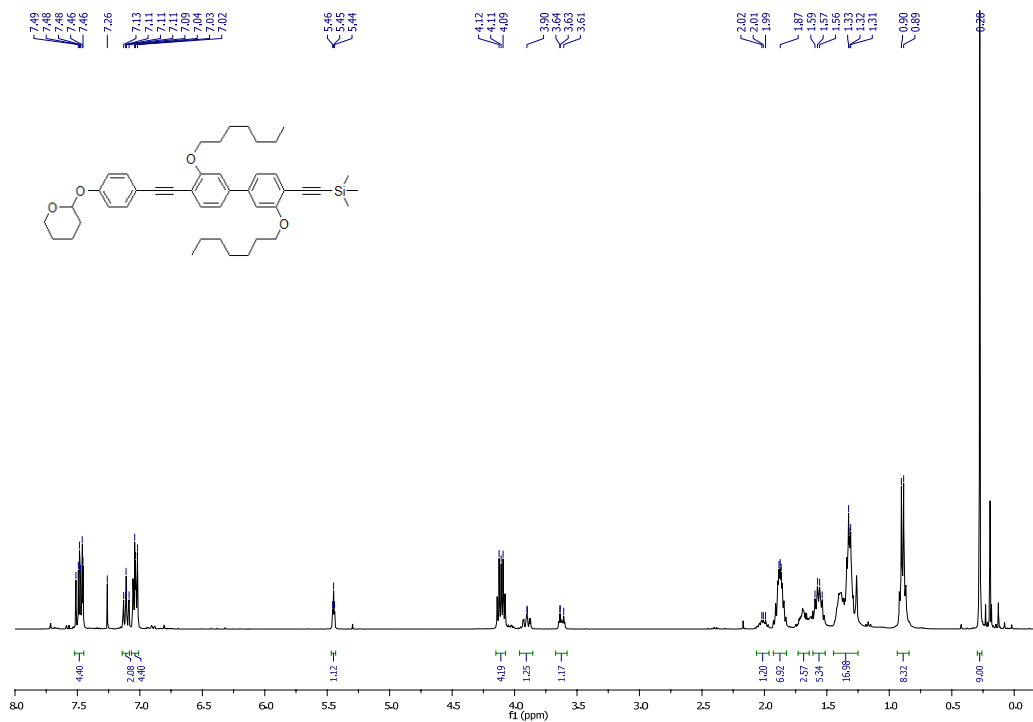
TLC (Silica gel, 20% EtOAc /hexane): R<sub>f</sub> (**8**) = 0.70, R<sub>f</sub> (**10**) = 0.80.

<sup>1</sup>H NMR (CDCl<sub>3</sub>) δ 0.28 (s, 9H, Si-CH<sub>3</sub>), 0.89 (d, *J* = 7.0 Hz, 8H, CH<sub>3</sub>), 1.45 – 1.25 (m, 17H, CH<sub>2</sub>), 1.57 (dd, *J* = 15.0, 8.0 Hz, 5H, CH<sub>2</sub>), 1.68 (ddd, *J* = 11.9, 7.3, 4.0 Hz, 3H, CH<sub>2</sub>), 1.93 – 1.82 (m, 7H, CH<sub>2</sub>), 2.06 – 1.96 (m, 1H, CH), 3.67 – 3.58 (m, 1H, CH), 3.90 (d, *J* = 1.5 Hz, 1H, CH), 4.15 – 4.07 (m, 4H, O-CH<sub>2</sub>), 5.45 (t, *J* = 3.1 Hz, 1H, O-CH), 7.07 – 7.01 (m, 4H, Ar-H), 7.14 – 7.08 (m, 2H, Ar-H), 7.52 – 7.45 (m, 4H, Ar-H).

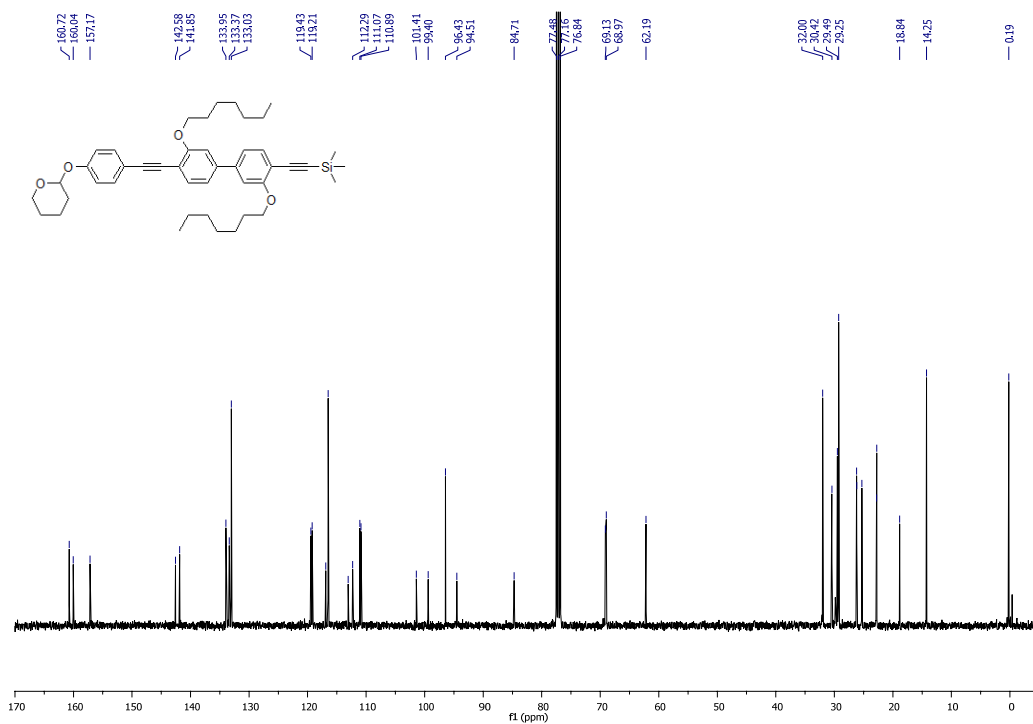
<sup>13</sup>C NMR (CDCl<sub>3</sub>) δ 0.19, 14.25, 18.84, 22.78, 25.30, 26.19, 29.25, 29.49, 30.42, 32.00, 62.19, 69.05, 84.71, 94.51, 96.43, 99.40, 101.41, 110.98, 112.29, 113.06, 116.50, 116.90, 119.21, 119.43, 133.03, 133.37, 133.95, 141.85, 142.58, 157.17, 160.04, 160.72.

MS (ESI) calcd. for C<sub>44</sub>H<sub>58</sub>O<sub>4</sub>Si [M+Na] 701.4002, found 701.3997.

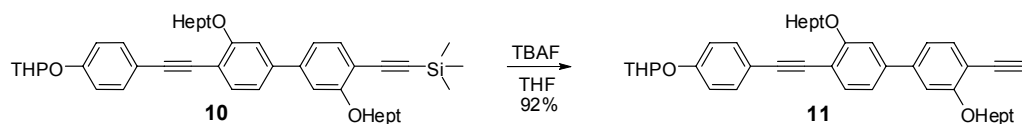




$^1\text{H-NMR}$  (400 MHz,  $\text{CDCl}_3$ ) spectrum of **10**.



$^{13}\text{C-NMR}$  (400 MHz,  $\text{CDCl}_3$ ) spectrum of **10**.



### 2-(4-((4'-ethynyl-3,3'-bis(heptyloxy)biphenyl-4-yl)ethynyl)phenoxy)tetrahydro-2H-pyran (**11**)

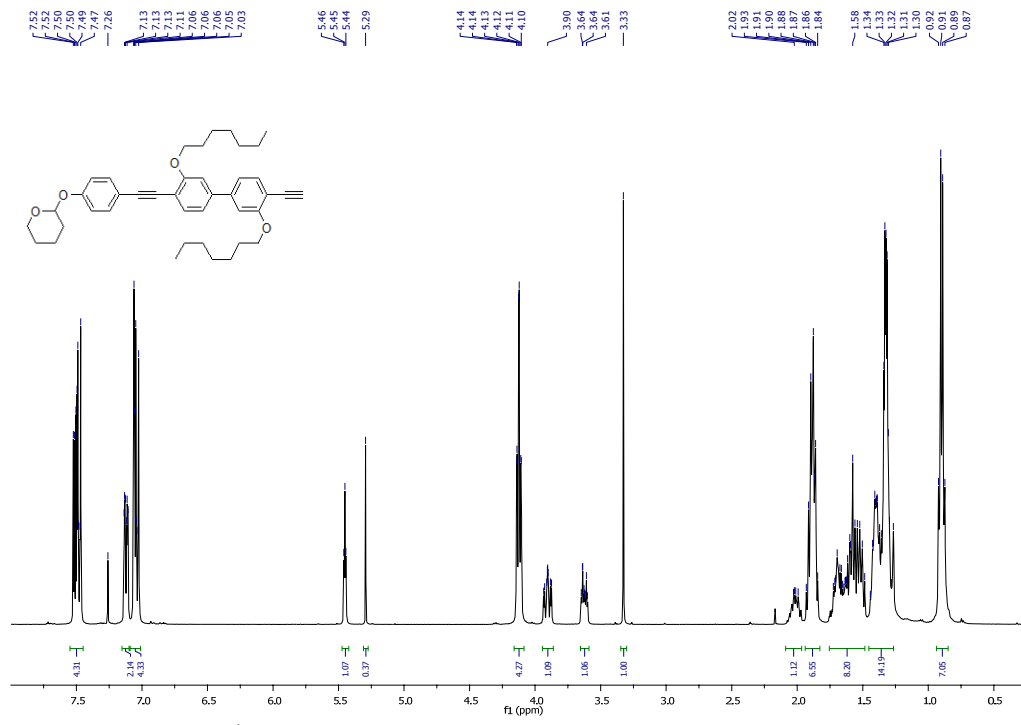
To a solution of compound **10** (0.500 g, 0.736 mmol) in anhydrous THF (10 mL) was added TBAF (0.213 mL, 0.736 mmol) and the reaction mixture was stirred at 25 °C for 2 h, diluted with water (10 mL) and extracted with EtOAc (3 × 10 mL). The combined organic layers were washed successively with water (2 × 10 mL) and brine (10 mL). The organic layer was dried over Na<sub>2</sub>SO<sub>4</sub> and concentrated *in vacuo* to give the crude product, which was purified by column chromatography using neutral silica gel (2:98, EtOAc:hexane) to yield **11** (0.41 g, 92 %) as a yellowish solid.

TLC (Silica gel, 20% EtOAc /hexane): R<sub>f</sub>(**10**) = 0.80, R<sub>f</sub>(**11**) = 0.70.

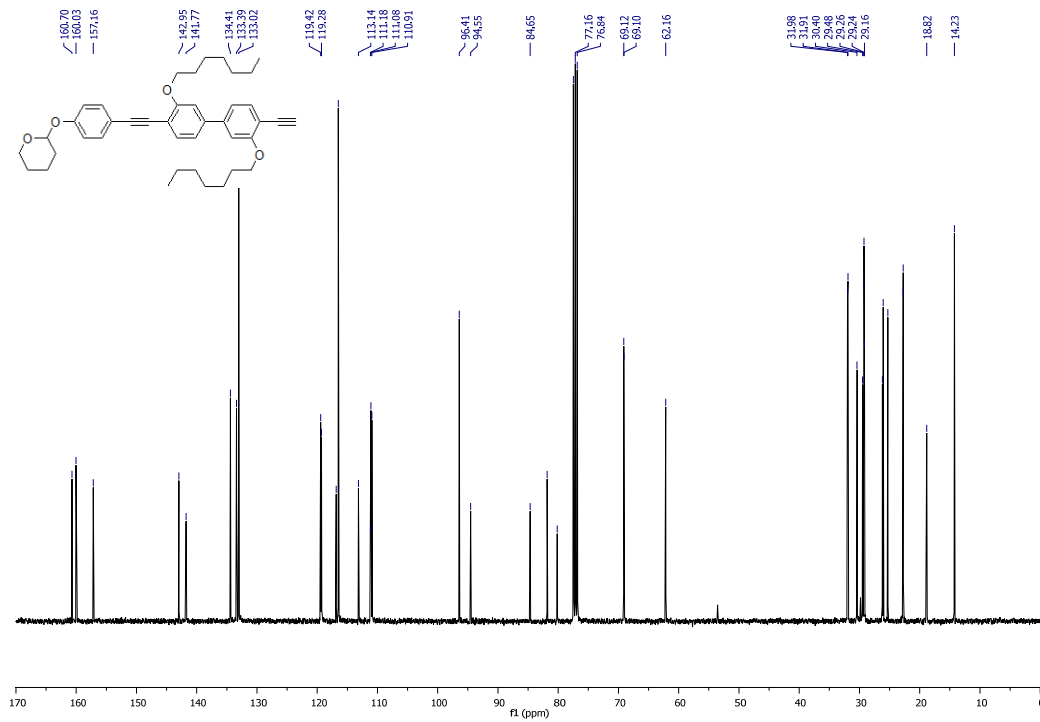
<sup>1</sup>H NMR (CDCl<sub>3</sub>) δ 0.90 (q, *J* = 6.8 Hz, 7H, CH<sub>3</sub>), 1.45 – 1.26 (m, 14H, CH<sub>2</sub>), 1.75 – 1.48 (m, 8H, CH<sub>2</sub>), 1.94 – 1.83 (m, 7H, CH<sub>2</sub>), 2.01 (dd, *J* = 9.0, 4.7 Hz, 1H, CH), 3.33 (s, 1H, CH), 3.62 (ddd, *J* = 8.2, 5.6, 3.2 Hz, 1H, CH), 3.91 (ddd, *J* = 11.4, 9.7, 3.0 Hz, 1H, CH), 4.12 (td, *J* = 6.4, 1.5 Hz, 4H, O-CH<sub>2</sub>), 5.45 (t, *J* = 3.2 Hz, 1H, O-CH), 5.29 (s, 1H, OH), 7.09 – 7.01 (m, 4H, Ar-*H*), 7.12 (ddd, *J* = 7.9, 2.9, 1.6 Hz, 2H, Ar-*H*), 7.49 (ddd, *J* = 8.8, 7.4, 2.7 Hz, 4H, Ar-*H*).

<sup>13</sup>C NMR (CDCl<sub>3</sub>) δ 14.23, 18.82, 22.74, 25.29, 26.12, 29.03-29.39, 29.48, 30.40, 31.94, 62.16, 69.11, 80.16, 81.83, 84.65, 94.55, 96.41, 110.78-111.31, 113.14, 116.49, 116.86, 119.35, 133.02, 133.39, 134.41, 141.77, 142.95, 157.16, 160.03, 160.70.

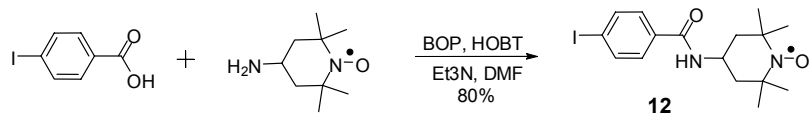
MS (ESI) calcd. for C<sub>41</sub>H<sub>50</sub>O<sub>4</sub> [M+Na] 629.3607, found 629.3601.



<sup>1</sup>H-NMR (400 MHz, CDCl<sub>3</sub>) spectrum of **11**.



<sup>13</sup>C-NMR (400 MHz, CDCl<sub>3</sub>) spectrum of **11**.

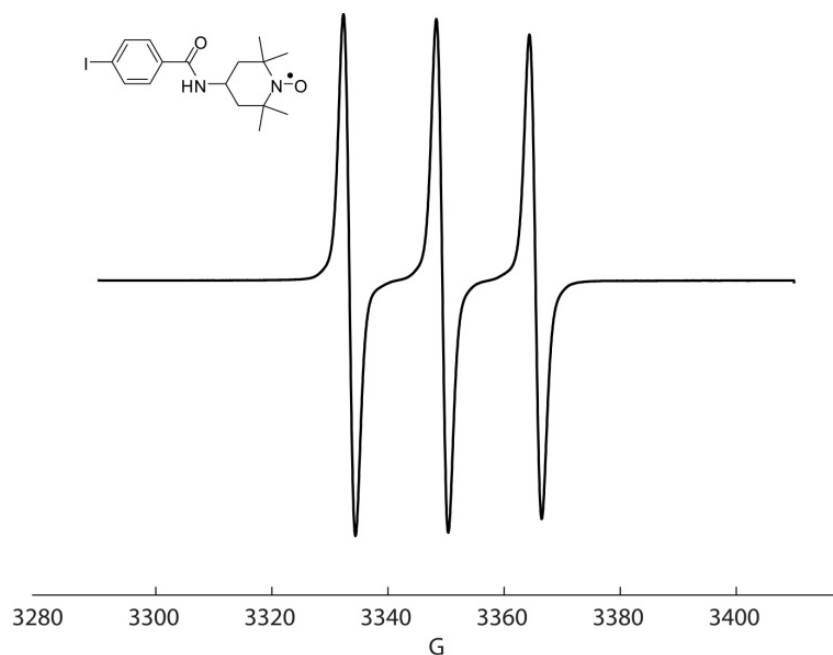


### Compound 12

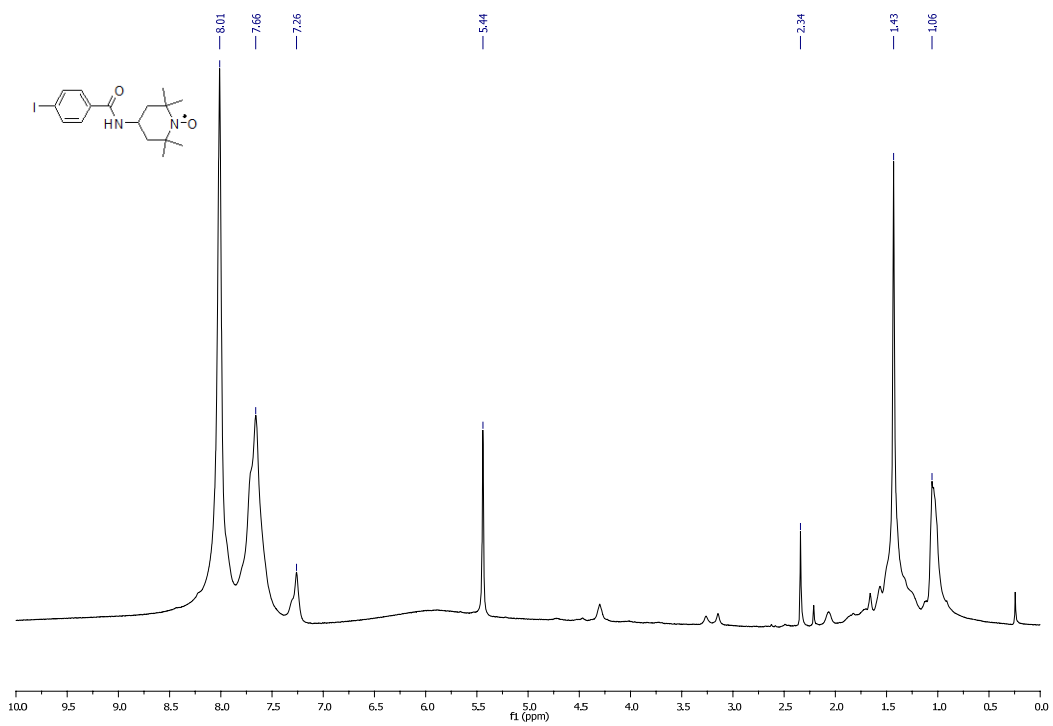
To a solution of 4-iodobenzoic acid (0.500 g, 2.016 mmol) and 4-amino-2,2,6,6-tetramethylpiperidine-1-oxyl (4-amino TEMPO) (0.410 g, 2.42 mmol) and Et<sub>3</sub>N (1.5 mL) in anhydrous DMF (5 mL) were added BOP (1.780 g, 4.032 mmol) and HOBT (0.540 g, 4.032 mmol). The resulting suspension was stirred at 25 °C for 12 h, after which the reaction mixture was concentrated *in vacuo*. The crude product was purified by column chromatography using neutral silica gel (5:95 to 40:60, EtOAc:hexane) to give **12** (0.650 g, 80%) as a red solid.

TLC (Silica gel, 40% EtOAc/hexane): R<sub>f</sub> (**4-amino TEMPO**) = 0.70, R<sub>f</sub> (**12**) = 0.30.

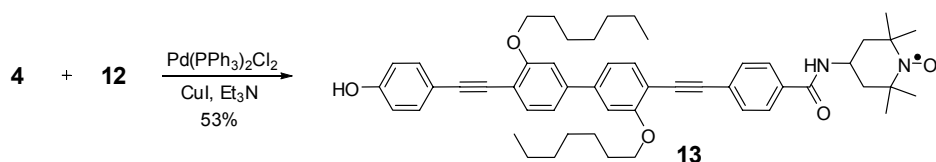
MS (ESI) calcd. for C<sub>16</sub>H<sub>22</sub>IN<sub>2</sub>O<sub>2</sub> [M+Na] 424.0624, found 424.0618.



CW X-band EPR spectrum of **12** (10% MeOH/CH<sub>2</sub>Cl<sub>2</sub> at 22 °C).



$^1\text{H-NMR}$  (400 MHz,  $\text{CDCl}_3$ ) spectrum of **12**.

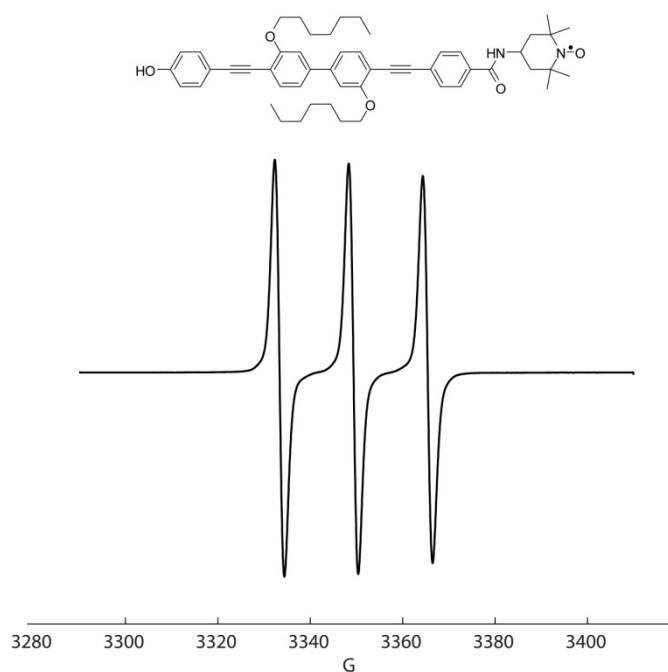


### Compound 13

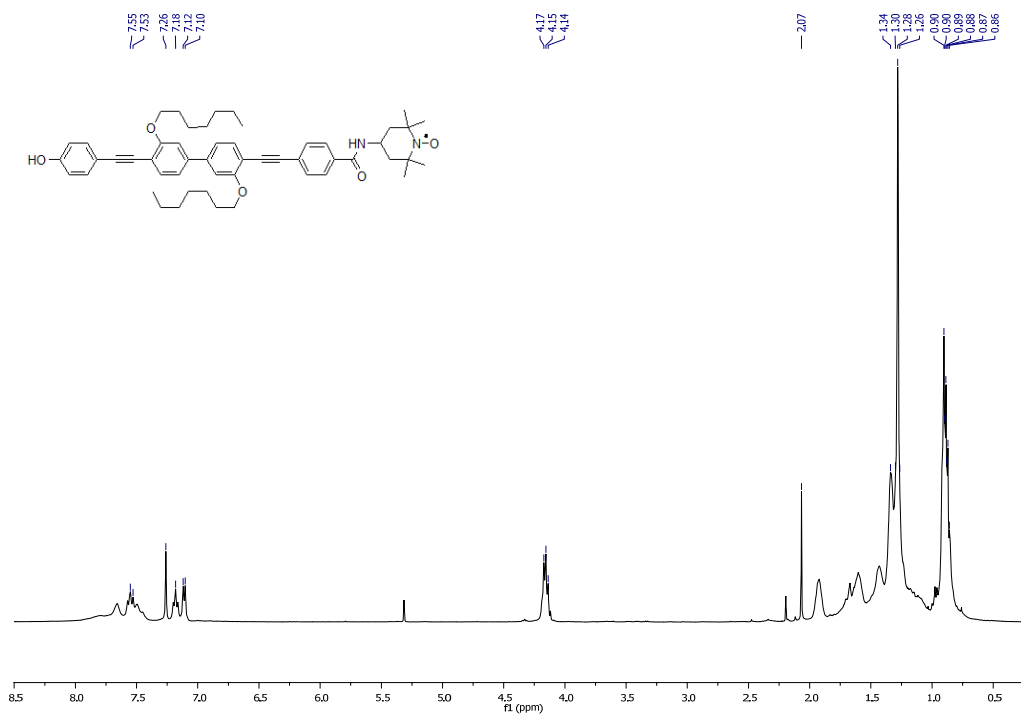
To a solution of compound **4** (0.100 g, 0.191 mmol) and compound **12** (0.110 g, 0.287 mmol) and freshly distilled Et<sub>3</sub>N (5 mL) in anhydrous THF (10 mL) were added Pd[PPh<sub>3</sub>]<sub>2</sub>Cl<sub>2</sub> (0.007 g, 5 mol %) and CuI (0.003 g, 8 mol %) and the reaction mixture was stirred at 25 °C for 12 h. The reaction mixture was diluted with water (20 mL) and extracted with EtOAc (3 × 10 mL). The combined organic layers were washed successively with water (2 × 10 mL) and brine (10 mL). The organic layer was dried over Na<sub>2</sub>SO<sub>4</sub> and concentrated in *vacuo* to give the crude product, which was purified by column chromatography using neutral silica gel (5:95 to 40:60, EtOAc:hexane) to yield **13** (0.080 g, 53%) as a red solid.

TLC (Silica gel, 30% EtOAc/hexane): R<sub>f</sub> (**4**) = 0.50, R<sub>f</sub> (**12**) = 0.40, R<sub>f</sub> (**13**) = 0.30.

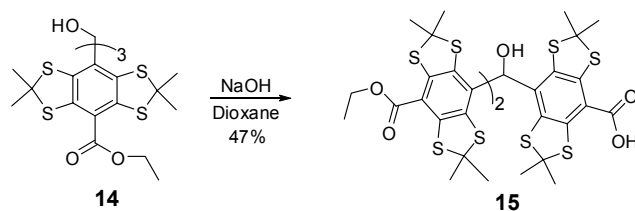
MS (ESI) calcd. for C<sub>52</sub>H<sub>63</sub>N<sub>2</sub>O<sub>5</sub> [M+Na] 818.4635, found 818.4629.



EPR spectrum of **13** (10% MeOH/CH<sub>2</sub>Cl<sub>2</sub> at 22 °C).



<sup>1</sup>H-NMR (400 MHz, CDCl<sub>3</sub>) spectrum of **13**.



## Compound 15

To a solution of compound **14**<sup>[2]</sup> (0.100 g, 0.090 mmol) in dioxane (10 mL), aqueous NaOH (0.003 g in 0.5 mL water, 0.081 mmol) was added and reaction mixture was stirred at 50 °C for 2 h. After cooling the reaction mixture to 25 °C, it was acidified with 2 N HCl and extracted with EtOAc (3 × 10 mL). The combined organic layers were washed successively with water (2 × 10 mL) and brine (10 mL). The organic layer was dried over Na<sub>2</sub>SO<sub>4</sub> and concentrated *in vacuo* to give the crude product, which was purified by column chromatography using neutral silica gel (10:90 to 50:50, EtOAc:hexane) to yield **15** (0.045 g, 47%) as a yellow solid.

TLC (Silica gel, 30% EtOAc/hexane): Rf (**14**) = 0.60, Rf (**15**) = 0.05.

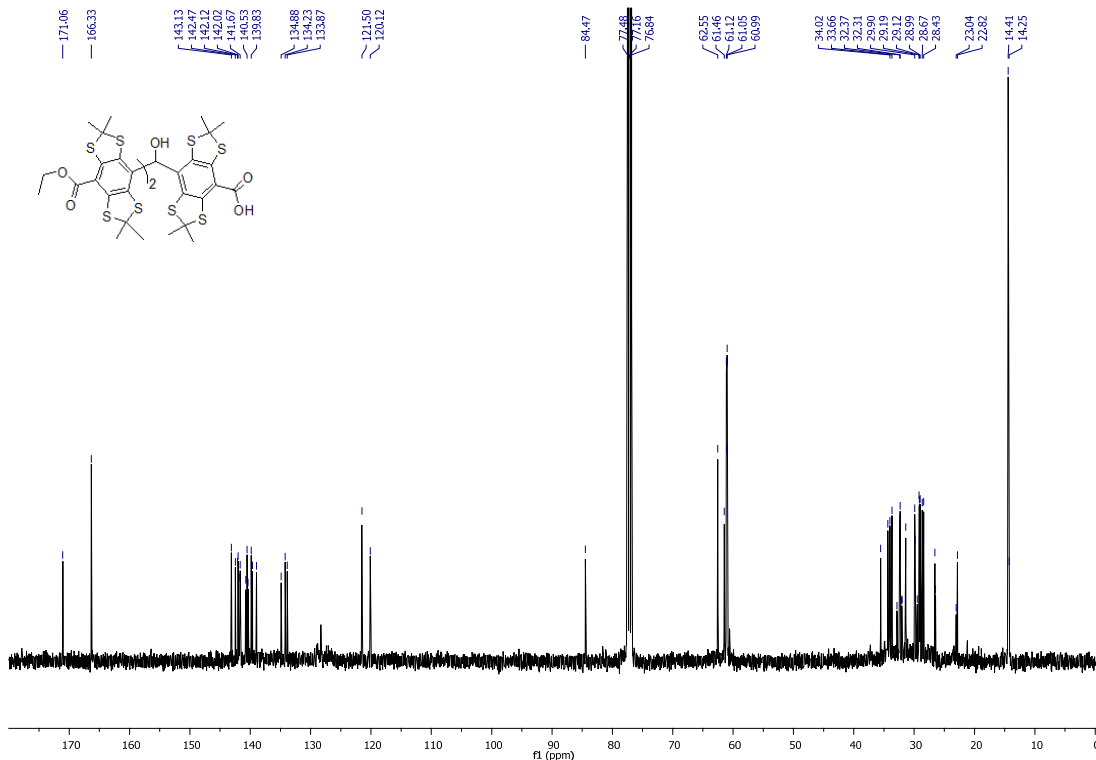
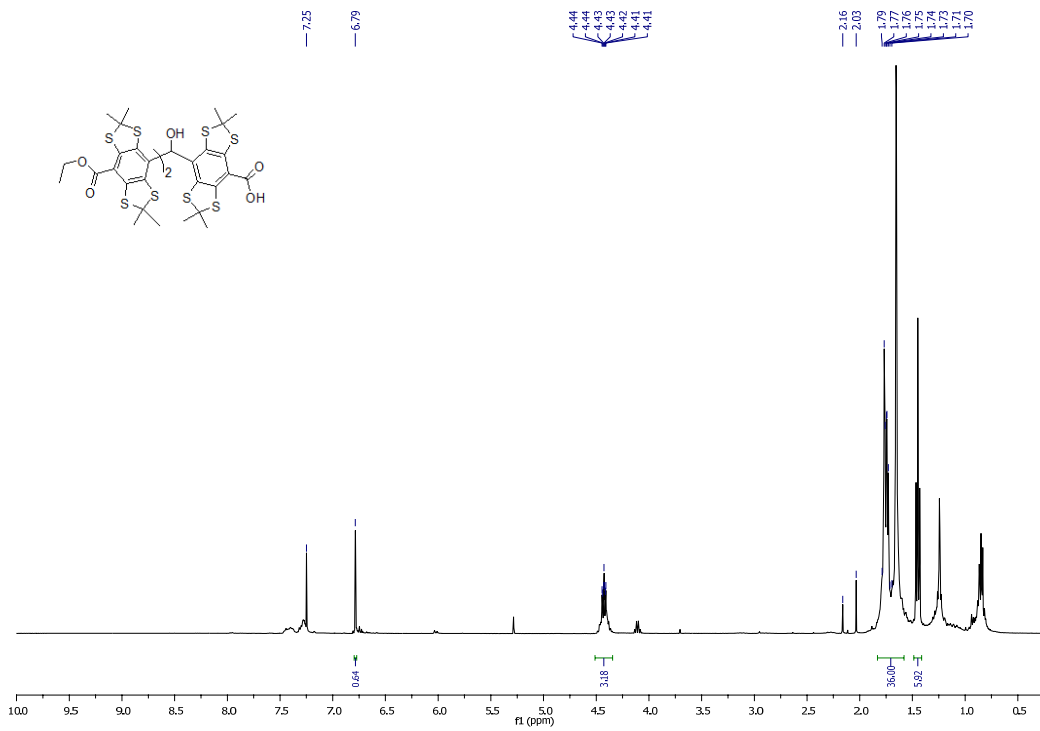
TLC (Silica gel, 10% MeOH/CH<sub>2</sub>Cl<sub>2</sub>): Rf (**14**) = 0.90, Rf (**15**) = 0.6.

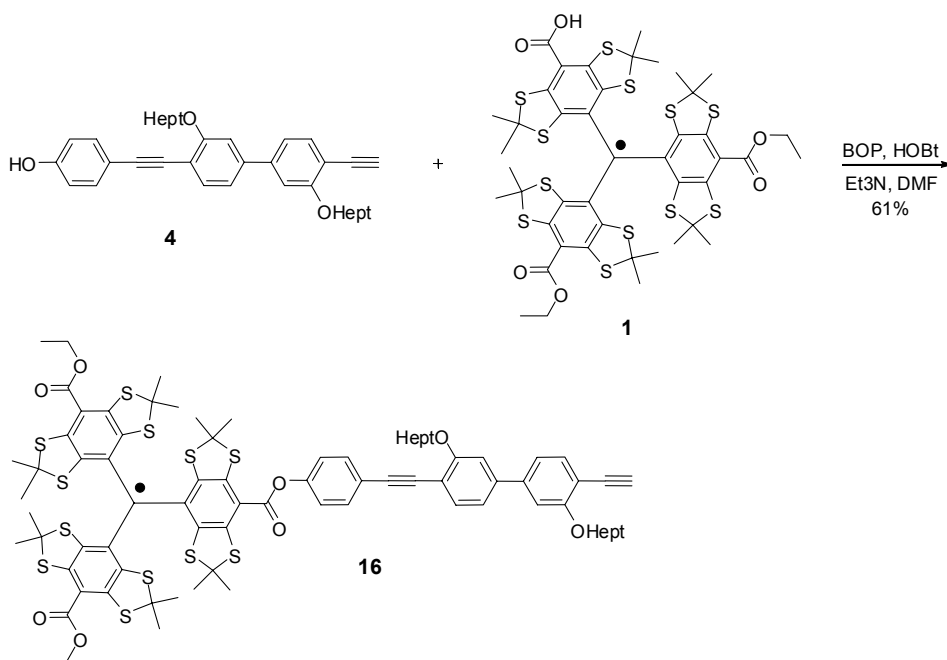
<sup>1</sup>H NMR (CDCl<sub>3</sub>) δ 1.46 (t, *J* = 7.1 Hz, 6H, CH<sub>3</sub>), 1.87 – 1.58 (m, 36H, CH<sub>3</sub>), 4.52 – 4.34 (m, 3H, OCH<sub>2</sub>), 6.80 (s, 1H, OH).

<sup>13</sup>C NMR (CDCl<sub>3</sub>) δ 171.06, 166.33, 143.13, 142.47, 142.07, 141.71, 140.75, 140.45, 139.73, 138.97, 134.88, 134.23, 133.87, 121.50, 120.12, 84.47, 77.48, 77.16, 76.84, 62.55, 61.46, 61.25 – 60.89, 35.56, 34.36, 34.02, 33.66, 32.85, 32.34, 32.04, 31.38, 30.16 – 29.42, 29.45 – 28.92, 28.67, 28.43, 26.51, 23.04, 22.82, 14.33.

MS (ESI) calcd. for C<sub>44</sub>H<sub>48</sub>O<sub>7</sub>S<sub>12</sub> [M+Na] 1094.9946, found 1094.9941.







### Compound (16)

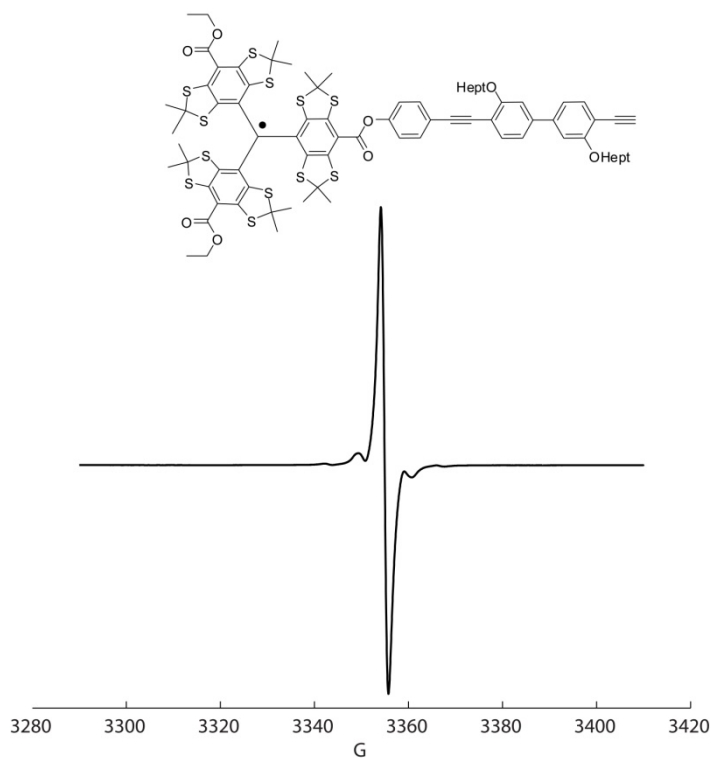
To a solution of trityl radical **1** (0.05 g, 0.04 mmol) and compound **4** (0.025 g, 0.05 mmol) in dry DMF (5 mL) was added BOP (0.04 g, 0.099 mmol) and HOBT (0.011 g, 0.09 mmol) followed by addition of Et<sub>3</sub>N (0.5 mL). The reaction mixture was stirred at 25 °C for 12 h and concentrated to remove DMF and crude obtained was purified by column chromatography using neutral silica gel (5:95 to 40:60, EtOAc:hexane) to give **16** as a green solid (0.045 g, 61 %).

TLC (Silica gel, 40% EtOAc/hexane): Rf (**4**) = 0.50, Rf (**1**) = 0.05, Rf (**16**) = 0.40.

MALDI-TOF: calcd. for C<sub>80</sub>H<sub>87</sub>O<sub>8</sub>S<sub>12</sub> [M<sup>+</sup>] 1559.304, found 1559.336

Preparative HPLC run (Flow rate = 7 mL/min). Solvent A, 100% CH<sub>3</sub>CN; Solvent B, 100% EtOAc; 3 min linear gradient from 0% to 15% B, 15% B isocratic for 37 min. 1 min linear gradient from 15% to 0% B to initial conditions (100% A).

Analytical HPLC run (Flow rate = 1 mL/min). Solvent A, 100% CH<sub>3</sub>CN; Solvent B, 100% EtOAc; 5 min linear gradient from 0% to 20% B, 20% B isocratic for 15 min. 1 min linear gradient from 20% to 0% B to initial conditions (100% A).



CW X-band EPR spectrum of **16** (10% MeOH/CH<sub>2</sub>Cl<sub>2</sub> at 22 °C).

## CW-EPR

Continuous wave electron paramagnetic resonance (CW-EPR) measurements of trityl-nitroxide biradical **2** at 295 and 130 K yielded EPR spectra showing the sharp trityl EPR peak overlapping with the center of the nitroxide EPR spectrum (Figure S1). Simulating the EPR spectra using the EasySpin toolbox<sup>[3]</sup> confirmed a 1:1 ratio of trityl and nitroxide (Table S1).

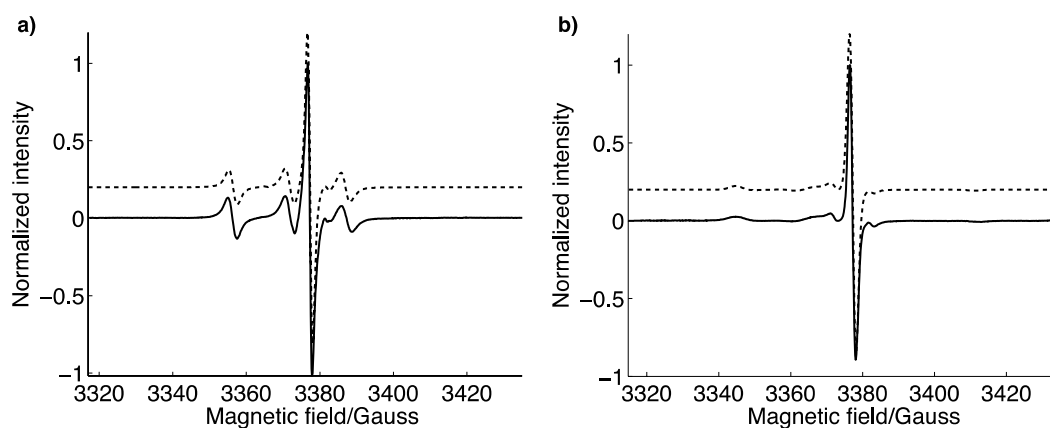


**Figure S1.** CW-EPR spectra of **2**. **a)** CW-EPR spectrum at 295 K (solid line) and simulated spectrum (broken line). **b)** CW-EPR spectrum at 130 K (solid line) and simulated spectrum (broken line). Simulated spectra have been displaced on the vertical axis for clarity.

CW-EPR measurements of trityl biradical **3** at 295 and 130 K yielded EPR spectra containing a single peak and small satellites from <sup>13</sup>C hyperfine coupling (Figure S2). The spectra were simulated using the EasySpin toolbox (Table S1).

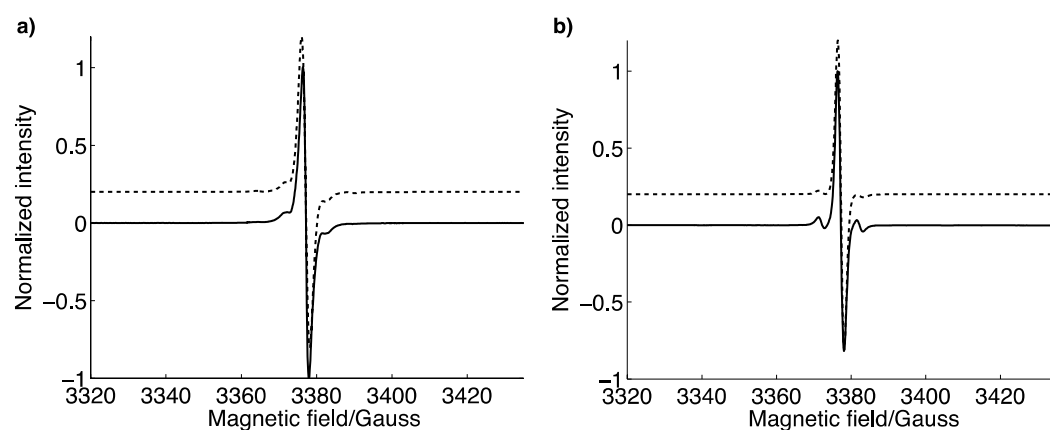


**Figure S2.** CW-EPR spectra of **3**. **a)** CW-EPR spectrum at 295 (solid line) and simulated spectrum (broken line). **b)** CW-EPR spectrum at 130 K (solid line) and simulated spectrum (broken line). Simulated spectra have been displaced on the vertical axis for clarity.

**Table S1.** Simulation parameters for **2** and **3** at 295 and 130 K.

Parameters	<b>2</b>		<b>3</b>
	Nitroxide	Trityl	
$g_{xx}, g_{yy}, g_{zz}$	2.0093, 2.0059, 2.0018	2.0030, 2.0027, 2.0021 <sup>[4]</sup>	2.0030, 2.0027, 2.0021 <sup>[4]</sup>
$A_{xx}, A_{yy}, A_{zz}$ <sup>a</sup>			
<sup>14</sup> N Nitroxide nitrogen	18, 18, 93	-	-
<sup>13</sup> C Central carbon <sup>[5]</sup>	-	20.6, 20.6, 160.1	20.6, 20.6, 160.1
<sup>13</sup> C 1-Phenyl carbon	-	25, 25, 34	25, 25, 34
<sup>13</sup> C 2,6-Phenyl carbon	-	18, 18, 36.7	18, 18, 36.7
Linewidth <sup>b</sup>	295 K	0.12, 0.13	0.10, 0.07
	130 K	0.35, 0.01	0.15, 0.04
Rotational correlation time <sup>c</sup>	$1.4 \cdot 10^{-14}$	$1.4 \cdot 10^{-14}$	$1.4 \cdot 10^{-14}$
Weight	0.5	0.5	-

<sup>a</sup> The hyperfine coupling values are in MHz. Only carbon atoms with the largest hyperfine couplings were included in the simulation for the trityl. <sup>b</sup> The linewidths (Gaussian, Lorentzian) is the peak to peak linewidth in mT. <sup>c</sup>Isotropic rotational correlation times for simulation at 295 K are in seconds.

## Original PELDOR and DQC time traces

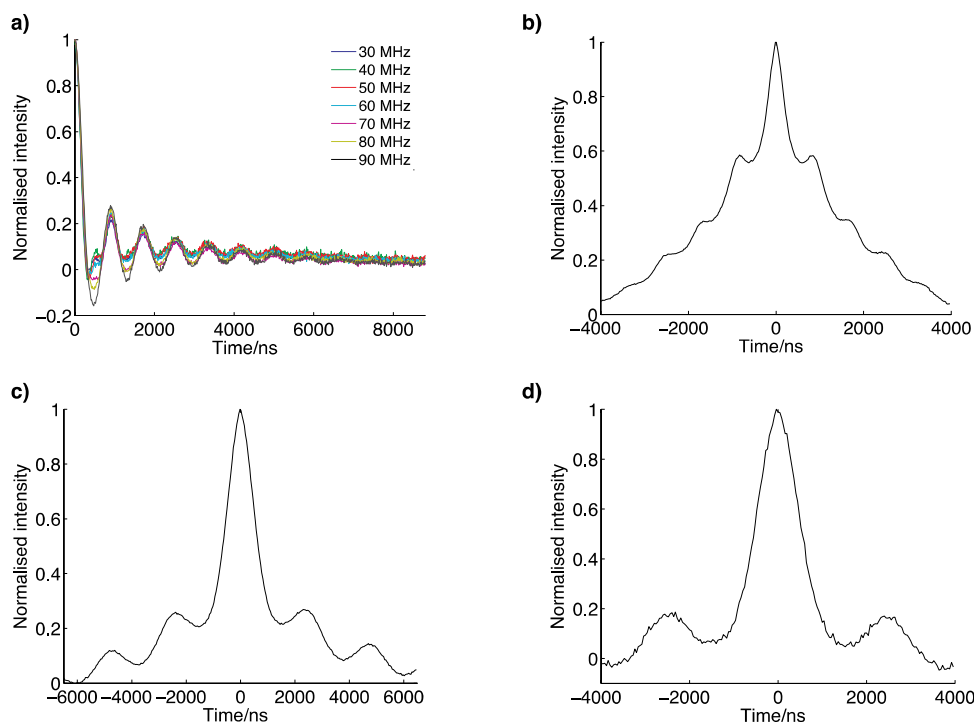


**Figure S3.** Original PELDOR and DQC time traces. **a)** Original PELDOR time traces for **2**. **b)** Original DQC time trace for **2**. **c)** Original DQC time trace for **3**. **d)** Original DQC time trace for **3** at 100 K.

## PELDOR

The trityl biradical **3** was also measured with 4-pulse PELDOR. The detection sequence and inversion pulse were positioned on the center of the trityl peak (Figure S4a). This setup yielded a time trace that only shows modulation from hyperfine interaction between the trityl and deuterium in the solvent (Figure S5), which is attributed to the strong pulse overlap. The length of the inversion pulse was 60 ns. The detection  $\pi/2$  and  $\pi$  pulse lengths were 16 and 32 ns, respectively.

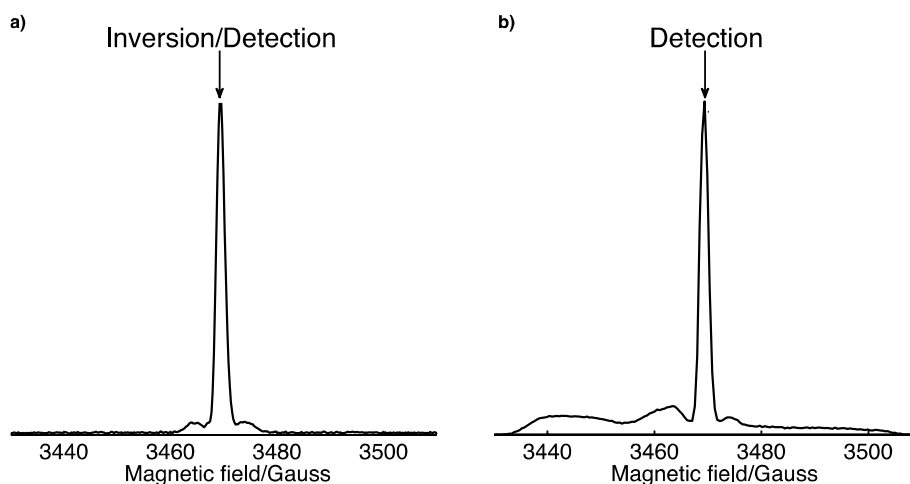


**Figure S4.** 2-pulse echo detected field sweeps at X-band. **a)** Echo detected field sweep of **3**. Position of the inversion pulse and detection sequence used for PELDOR measurement are indicated by the arrow. The small satellites to each side of the sharp peak are from hyperfine interaction to  $^{13}\text{C}$ . **b)** Echo detected field sweep of **2**. The arrow indicates position of the DQC pulse sequence.

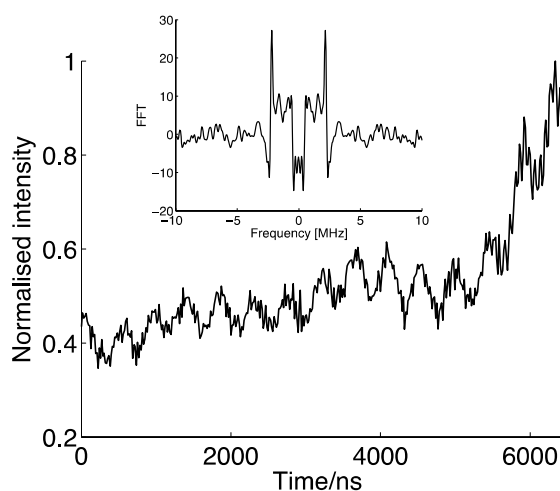


**Figure S5.** 4-pulse PELDOR of **3** and the corresponding dipolar spectrum (inset).

## DQC

Double quantum coherence (DQC) experiments at X-band were performed using a six-pulse sequence with 64-step phase cycling<sup>[1]</sup> (Figure S6). A 2-pulse echo detected field swept spectrum of **2** and **3** was acquired and the microwave frequency positioned at the center of the trityl peak (Figure S4).

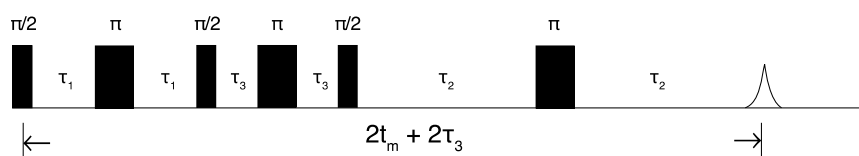


**Figure S6.** Six-pulse DQC sequence. The DQC time trace is recorded by increasing  $\tau_1$  and decreasing  $\tau_2$ .  $t_m = \tau_1 + \tau_2$  and  $\tau_3$  are kept constant.

## S/N comparison

To compare the signal to noise ratio (S/N) for PELDOR and DQC, a semi-rigid nitroxide biradical<sup>[6]</sup> (Figure S7 inset), with the same concentration and volume as the bistrityl **3**, was measured with PELDOR at 50 K (Figure S7). The inversion pulse was set to the center of the nitroxide spectrum and the observer pulse sequence at 80 MHz higher frequency. Measuring the absolute noise of the PELDOR and DQC time traces reveals that the S/N is a factor of 1.7 better for the DQC measurement.

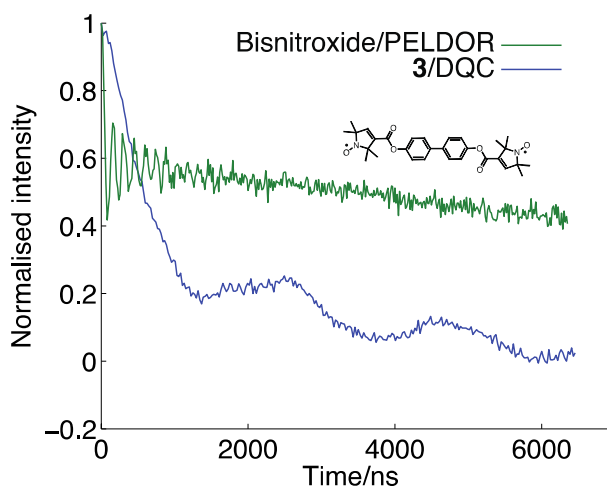


**Figure S7.** PELDOR on bisnitroxide and DQC on **3** at 50 K. Both time traces were recorded for 25 minutes.

## DQC derived distance distributions at 50 and 100 K

The distance distributions obtained from DQC on **3** at 50 and 100 K are in excellent agreement with respect to the mean and most probable distance. The width of the distance distribution at 100 K is a little bit broader (Figure S8).

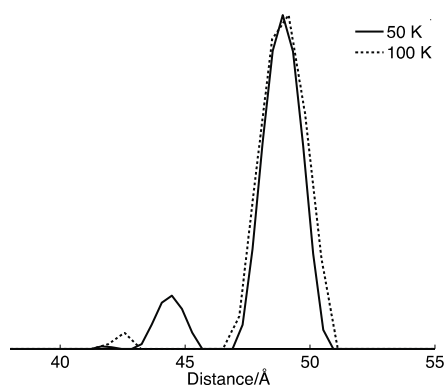


**Figure S8.** Distance distributions obtained from DQC on **3** at 50 K (solid line) and 100 K (broken line).



## PELDOR experiments with different inversion/detection positions

We performed two more PELDOR experiments on the trityl-nitroxide biradical **2**. First, the PELDOR inversion pulse was positioned on the nitroxide spectrum and the detection pulse sequence on the trityl spectrum (70 MHz offset) (Figure S9a). The idea of this setup was to increase the S/N on the expense of the modulation depth. Acquiring a PELDOR time trace with this setup resulted in a time trace with a modulation depth of still 25% but considerably reduced S/N (Figure S9b,c). Two pulse ESEEM measurements at 50 K revealed a  $T_2$  of 2.8  $\mu\text{s}$  and 8.4  $\mu\text{s}$  for the trityl and nitroxide radicals, respectively. Furthermore, placing the detection sequence on the trityl results in a PELDOR echo with a comparable intensity, but which is broader by a factor of 3.4, relative to the echo obtained with the detection on the nitroxide. The reduced S/N for the PELDOR time trace is therefore attributed to the shorter  $T_2$  for trityl at 50 K and the broader PELDOR echo. In the second experiment the inversion and observer pulses were positioned on the nitroxide spectrum with a separation of 168 MHz, (Figure S9a). Since the sample does not contain any bisnitroxide compound, this setup should actually not give an intramolecular dipolar modulation. However, the PELDOR time trace reveals a shallow modulation with a depth of 6% (Figure S9b,c). The dipolar modulation is attributed to the side bands of the inversion pulse exciting a small portion of the trityl spectrum in the frequency domain (Figure S9a). Analysis of the time trace yields a distance distribution (data not shown) in agreement with the distribution obtained from PELDOR experiments where the detection sequence was placed on the nitroxide and the inversion pulse on the trityl.

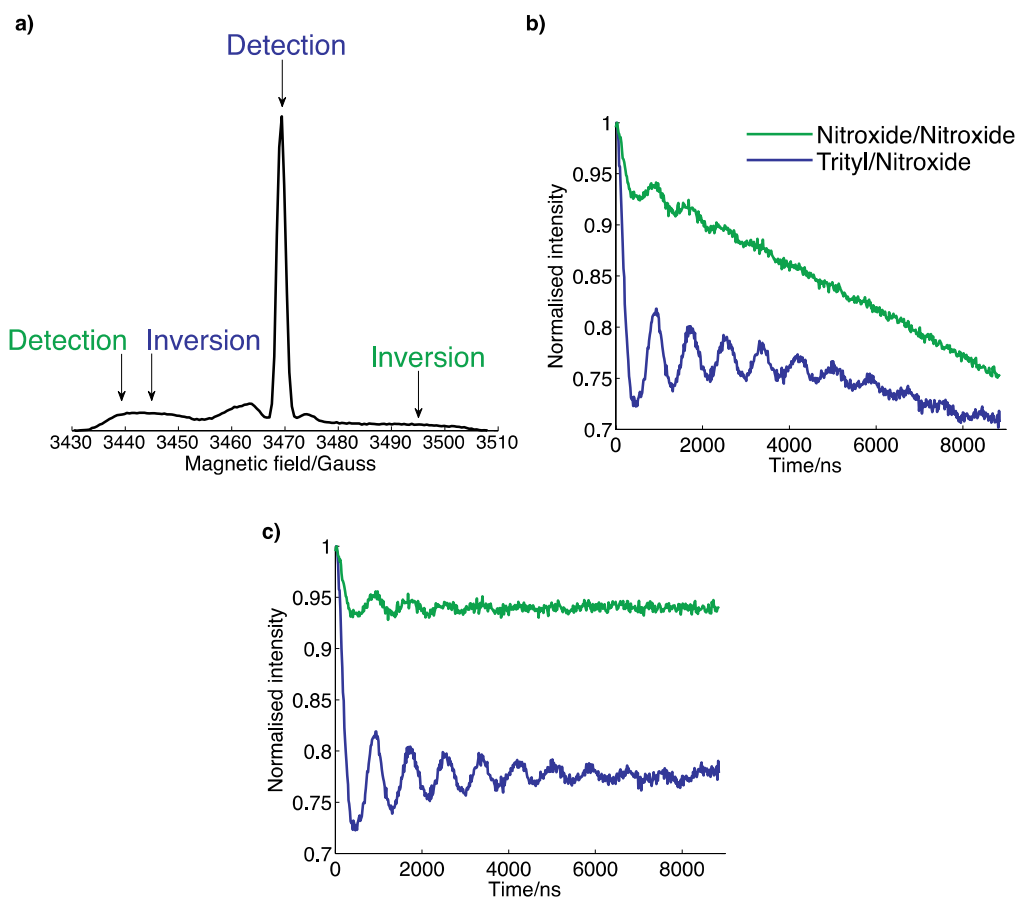


**Figure S9.** PELDOR experiments with different inversion/detection position on **2**: **a)** Echo detected field swept spectrum of **2** and positions of the inversion and detection pulses. **b)** Original PELDOR time traces of **2** obtained by positioning the detection pulse sequence on the trityl spectrum and inversion pulse on the nitroxide spectrum (blue) and detection and inversion pulses on the nitroxide spectrum (green). **c)** Background corrected time traces in **b)**.

## Excitation profile of inversion pulse and PELDOR modulation depth

The excitation profile for a 16 ns  $\pi$  pulse was evaluated from a frequency swept spectrum (Figure S10b). Simulating the PELDOR time traces for **2** using a theoretical excitation profile<sup>[7]</sup> for an ideal square inversion pulse results in time traces with 100% modulation depth. Using an excitation profile that approximates the experimentally determined profile results in simulated time traces with 90% modulation depth, in agreement with the experimental PELDOR time traces. Simulated PELDOR time traces at 70 MHz offset using the theoretical and experimental  $\pi$  pulse profiles are shown as an example in Figure S10a.

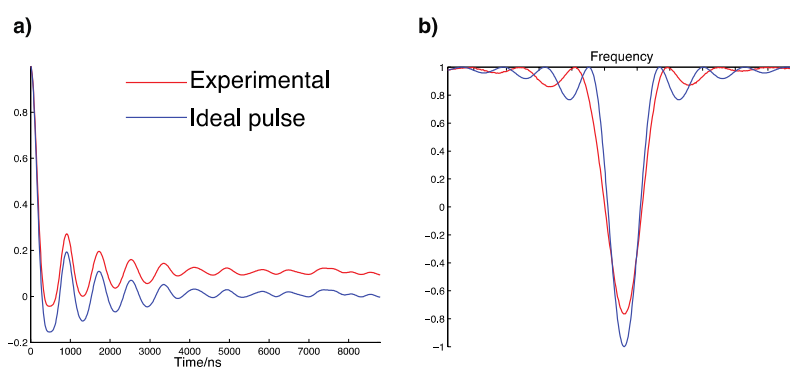


**Figure S10.** Simulated PELDOR time traces and excitation profiles. a) Simulated PELDOR time traces for **2** at 70 MHz offset using a theoretical (blue) and experimental (red) excitation profile for the inversion pulse. b) Theoretical (blue) and experimental (red) excitation profiles for a 16 ns  $\pi$  pulse.

## Data Analysis and Simulations

The PELDOR time traces were background corrected by fitting an exponential function (Eq.1) to the experimental time traces using the function `exponfit` from the EasySpin toolbox<sup>[3]</sup> and then subtracting the fitted function from the experimental time trace.

$$a + b * e^{-kx} \quad \text{Eq. 1}$$

Since DQC time traces were recorded to each side of the zero-time, the data points on each side were added together to make a single time trace from zero time to the maximum of the time window. The DQC time traces were background corrected in the same way as the PELDOR data with the exception for the DQC time trace of **2**, which had a background that fitted better to a polynomial of degree 5. The reason for this might be that the nitroxide spectrum is not fully excited. The starting point for the fitting of the exponential and polynomial functions to the experimental DQC time trace was chosen such that the fit between the background corrected and simulated time trace was optimized. Dipolar spectra and distance distributions from PELDOR and DQC data were then obtained from the background corrected time traces using DeerAnalysis2011.<sup>[8]</sup> To obtain more information on the conformational dynamics of the system, the PELDOR and DQC time traces for **2** and **3** were simulated with a home-written Matlab program which uses a conformational model and takes orientation selectivity into account.<sup>[9]</sup> The simulations of the DQC time traces were

done assuming no orientation selection and complete excitation of the EPR spectrum. The simulated PELDOR and DQC time traces and distance distributions were obtained from 20,000 conformers. These conformers were generated by using a harmonic segmented chain (HSC) model (Figure S11).<sup>[10,11]</sup> We define as one segment: each benzene ring, the bonds between the center of the nitroxide NO bond and the carbon atom of the amide group, the bonds between the trityl radical center and the oxygen atom of the ester group and each remaining bond between atoms in the molecules. These rigid segments are allowed to bend with a normal distribution  $\theta_i$  and rotate uniformly between 0 and  $2\pi$  ( $\phi$ ) about the atoms, which act as joints. Mean length of the segments and bending angles  $\theta_i$  were obtained from molecular mechanics calculations. The mean lengths of the segments are: 2.8 Å (benzen), 1.5 Å (benzen-benzen bond), 1.4 Å (benzene-acetylene bond), 1.2 Å (acetylene), 1.5 Å (benzene-oxygen bond), 1.4 Å (benzene-carbon bond), 5.8 Å (nitroxide spin label), 6 Å (trityl spin label). The mean bending angles for all segments within the molecular linkers is 0°. For the nitroxide and trityl spin label segments the mean bending angles are 24° and 12.7°, respectively. Distributions in length and flexibility of segments that resulted in the best fit between simulations and experiment are summarized in Table S2.

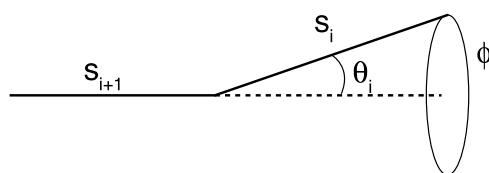


**Figure S11.** Segmented chain model. Each rigid segment  $s_i$  is allowed to bend and rotate about its joint with  $\theta_i$  and  $\phi$ , respectively. The bending angles  $\theta_i$  are the bending angles for the molecular linker-, nitroxide spin label- and trityl spin label- segments  $\theta_S$ ,  $\theta_N$ ,  $\theta_T$ , respectively. They are described by a normal distribution and the torsion angle  $\phi$  is uniformly distributed between 0 and  $2\pi$ .

**Table S2.** Dynamics parameters used for conformational model of **2** and **3**.

	$\sigma_r^{[a]}$	$\theta_S^{[b]}$	$\theta_N^{[b]}$	$\theta_T^{[b]}$
<b>2</b>	0.13(0.03)	$0 \pm 2.9(1)$	$24(3) \pm 2.9(1)$	$12.7(3) \pm 2.9(1)$
<b>3</b>	0.13(0.03)	$0 \pm 2.9(1)$	-	$12.7(3) \pm 2.9(1)$

[a]  $\sigma_r$  describes the average standard deviation in the length of each segment.<sup>[8]</sup> [b]  $\theta_S$ ,  $\theta_N$ ,  $\theta_T$ , describe the bending angle  $\theta_i$  of the molecular linker-, nitroxide spin label- and trityl spin label- segments, respectively. All segments within the molecular linker have the same bending distribution  $\theta_S$ . The degree of bending for each segment is described as the mean value  $\pm$  two standard deviations. Number in bracket is the error of the corresponding parameter.

## References

- [1] P. P. Borbat, in *Biological Magnetic Resonance, Vol. 19* (Eds.:L.J. Berliner, S.S. Eaton and G.R. Eaton), Kluwer Academic/Plenum Publishers, New York, **2000**, pp. 383–459.
- [2] T. Reddy, T. Iwama, H. Halpern, V. Rawal, *J. Org. Chem.* **2002**, *67*, 4635–4639.
- [3] S. Stoll, A. Schweiger, *J. Magn. Reson.* **2006**, *178*, 42–55.
- [4] A. J. Fielding, P. J. Carl, G. R. Eaton, S. S. Eaton, *Appl. Magn. Reson.* **2005**, *28*, 231–238.
- [5] M. K. Bowman, C. Mailer, H. J. Halpern, *J. Magn. Reson.* **2005**, *172*, 254–367.
- [6] B. Bode, J. Plackmeyer, T. Prisner, O. Schiemann, *J. Phys. Chem. A.* **2008**, *112*, 5064–5073.
- [7] G. Jeschke and Y. Polyhach, *Phys. Chem. Chem. Phys.* **2007**, *9*, 1895–1910.
- [8] G. Jeschke, V. Chechik, P. Ionita, A. Godt, H. Zimmermann, J. Banham, C. R. Timmel, D. Hilger, H. Jung, *Appl. Magn. Reson.* **2006**, *30*, 473–498.
- [9] G. W. Reginsson, R. I. Hunter, P. A. S. Cruickshank, D. R. Bolton, S. T. Sigurdsson, G. M. Smith, O. Schiemann, *J. Magn. Reson.* **2012**, *216*, 175–182.
- [10] G. Jeschke, M. Sajid, M. Schulte, N. Ramezani, A. Volkov, H. Zimmermann, A. Godt, *J. Am. Chem. Soc.* **2010**, *132*, 10107–10117.
- [11] A. Godt, M. Schulte, H. Zimmermann, G. Jeschke, *Angew. Chem. Int. Ed. Engl.* **2006**, *45*, 7560–7564.